CARBON NANOTUBES – POLYMER NANOCOMPOSITES

Edited by **Siva Yellampalli**

INTECHWEB.ORG

Carbon Nanotubes – Polymer Nanocomposites
Edited by Siva Yellampalli

Published by InTech
Janeza Trdine 9, 51000 Rijeka, Croatia

Publishing Process Manager Viktorija Zgela
Technical Editor Teodora Smiljanic
Cover Designer Jan Hyrat
Image Copyright Lerche&Johnson, 2010. Used under license from Shutterstock.com

First published July, 2011
Printed in Croatia

A free online edition of this book is available at www.intechopen.com
Additional hard copies can be obtained from orders@intechweb.org

Carbon Nanotubes – Polymer Nanocomposites, Edited by Siva Yellampalli
p. cm.
ISBN 978-953-307-498-6

Contents

Preface

Carbon nanotubes, discovered by Iijima in 1991, have been one of the most interesting materials with exotic properties for the last twenty years. Carbon nanotubes are typically considered as molecular-scale tubes of graphitic carbon. Depending on numbers of carbon layers, they are categorized as single-walled and multi-walled nanotubes. The unique structure provides nanotubes with extraordinary mechanical and electrical properties. The outstanding properties that these materials possess have opened new interesting research areas in nanoscience and nanotechnology.

Although nanotubes are very promising in a wide variety of fields, application of individual nanotubes for large scale production has been limited. The main limitations, which hinder its use, are difficulty in structure control, existence of impurities, and poor processability. In order to improve their practical applications, bulk nanotube materials have recently attracted increasing attentions, particularly by formation of composites with polymers. Here nanotubes may provide good mechanical, electrical, and thermal properties, while polymers enable them with high flexibility, low cost, and easy fabrication.

This book focuses on the preparation and property analysis of polymers with carbon nanotubes. The book has been divided into three parts. The first part deals with fabrication and property analysis of new carbon nanotube structures. The second part deals with preparation and characterization of polymer composites with CNTs followed by the various applications of polymers with CNTs in third part.

A list of chapters is given below. The following description provides a glimpse on the content in each book's chapter.

Part 1. Fabrication and Property Analysis of Carbon Nanotubes

Chapter 1. Growth of Vertically Aligned Carbon Nanotubes by DC Plasma Chemical Vapor Deposition
In this chapter a method to fabricate vertically aligned carbon nanotubes is presented. This method produces CNTs that are highly aligned perpendicular to the substrate surface more than those electrically oriented after dispersion on a substrate. Large area of vertically aligned CNTs has a variety of applications such as field electron emitters for cathode ray lighting tubes, field emission displays etc.

Chapter 2. Carbon Nanotubes Engineering Assisted by Natural Biopolymers
The latest ten-year progress on key topics for CNT engineering assisted by biopolymers has been reviewed. The methods to obtain dispersion, purification and specific chiral separation for CNTs assisted by biopolymers have been developed.

Chapter 3. Elastic Properties of Carbon Nanotubes
An equivalent model is established in this chapter based on the basic principles of the anisotropic elasticity and composite mechanics for the anlaysis of the elastic properties of graphite sheet at the nanometer scale. With this equivalent model, the relationship between the nanotube structure and the graphite sheet is built up and the radial scale effect of the elastic properties of CNTs is investigated.

Part 2. Preparation and Characterization of Polymer Composites with CNTs

Chapter 4. Polymer Carbon Nanotube Nanocomposites
This section starts with nanoparticle polymer fabrication. This chapter provides in-depth information on the preparation, alignment, properties and applications of CNT polymers.

Chapter 5. Functionalization of Carbon Nanotubes
This chapter focuses on the frequently used methods to functionalize CNTs namely covalent and non-covalent strategies. It also discusses the frequent methods and alternative methods that have been developed in the recent past for facile manipulation and processing in physiological environments to overcome difficulties in processing CNTs.

Chapter 6. Preparation and Applicability of Vinyl Alcohol Group Containing Polymer/MWNT Nanocomposite Using a Simple Saponification Method
In this chapter the properties and applicability of highly porous VOH group polymer/MWNT nanocomposites produced by simple saponification method have been investigated.

Chapter 7. Reinforcement Effects of CNTs for Polymer Based Nanocomposites
In this chapter different reinforcement effects of two kinds of CNTS (MWCNT-7 and VGCF) in two types of nanocomposites (three phase hybrid CFRP laminates and two phase CNT/polymer nanocomposites) have been presented with results.

Chapter 8. Characterization of Nanotube-Reinforced Polymer Composites
The chapter focuses on the structure and morphology of the polymer nanotube composites and the consequences of these structures on their performance.

Chapter 9. Carbon Nanotubes as Conductive Filler in Segregrated Polymer Composites - Electrical Properties
In this chapter the conductivity of PVC/MWCNT and UHMWPE/MWCNT composites under different conditions is presented with analysis of the variation of conductivity under different conditions.

Chapter 10. Conductivity Percolation of Carbon Nanotubes in Polyacrylamide Gels
This chapter focuses on testing the critical phenomena of the gelation and conductivity as a function of MWNTs concentration. Through experimental results it is observed that if polymer systems, which are initially of isolator character, are doped with carbon nanotubes of nano dimensions and if the amount of such addition exceeds a critical value then the composite gel systems with carbon nanotubes addition become capable of electrically converting into conductor structure.

Chapter 11. Electrical Properties of CNT Based Polymeric Matrix Nanocomposites
In this chapter a detailed study on the experimental conductivity and scaling laws thereof, for the four polymer matrix-polyvinyl butyral, Polydimethylsiloxane, Epilox™ and Henkel Resin Hysol EA-9360 as a function of CNTs volume fraction, is presented.

Chapter 12. Polymer Composites with Carbon Nanotubes in Alignment
This chapter discusses the preparation of aligned nanotube/polymer arrays, films and fibers with emphasis on the improved mechanical, electrical and sensing properites.

Chapter 13. Silanization of Carbon Nanotubes: Surface Modification and Polymer Nanocomposites
This chapter focuses on the importance of silanization to link nanotubes to other nanoforms or other materials. It also demonstrates that silanization process is an effective way to significantly improve the interface and therefore the properties in polymer nanocomposites.

Chapter 14. Prediction of the Elastic Properties of Single Walled Carbon Nanotune Reinforced Polymers: A Comparative Study of Several Micromechanical Models
This chapter investigates four homogenization schemes and validates them against FE analysis of unit cells or representative volume elements (RVEs) for the prediction of the elastic properties of SWNT/Polymer composites.

Chapter 15. About Grafting of Single-Walled Carbon Nanotubes on the Oligo-N-Vinyl Carbazole and Copolymer Involving N-Vinylcarbazole and Hexylthiophene
This chapter starts with a study of the evolution of the structural and optical properties of composites based on oligo-N-Vinyl carbazole mixed with SWNTs as a function of the solvent nature and temperature annealing, then it proceeds to describing the grafting process between carbon nanotubes and the OVK molecules through theoretical studies based on Density Functional Theory (DFT).

Chapter 16. Giant Moment Enhancement of Magnetic Nanoparticles Embedded in Multi-Walled Carbon Nanotubes : Consistent with Ultrahigh Temperature Superconductivity
In this chapter detailed magnetic properties of multi-walled carbon nanotubes embedded with Ni, Fe and Fe magnetic nanoparticles are presented along with possible microscopic mechanisms for high temperature superconductivity in carbon nanotubes.

Chapter 17. Carbon Nanotubes Influence on Balk and Surface Properties of the Optical Materials
Influence of the carbon nanotubes on alignment ability, polarization features, dynamic, photoconductive and photorefractive characteristics as well as on mechanical hardness and spectral parameters have been presented.

Part 3. Applications

Chapter 18. The Application of Carbon Nanotube to Bone Cement
In this chapter various systems of bone cement reinforced with carbon nanotube were fabricated and the mechanical properties of the bone cement were characterized using tensile as well as compressive analysis and dynamic mechanical analysis.

Chapter 19. Single Walled Carbon Nanotubes as a Molecular Heater for Thermoresponsive Polymer Gel Composite
Utilization of single walled carbon nanotubes (SWNTs) as photon antenna that serves as an effective molecular heater around the NIR regions is presented.

Acknowledgements

I would like to thank the authors of the chapters in this book for their excellent contributions and for the effort involved in getting their work published. I am certain that the material published in this book will be of a great help and genuinely appreciated by students, professors and researchers around the world.

Dr. Siva Yellampalli
VTU Extension Centre
UTL Technologies Ltd
Bangalore, Karnataka-560022
India

Part 1

Fabrication and Property Analysis of Carbon Nanotubes

1

Growth of Vertically Aligned Carbon Nanotubes by RF-DC Plasma Chemical Vapor Deposition

Yasuaki Hayashi, Hideto Sawada and Hideyuki Takagi
Kyoto Institute of Technology
Japan

1. Introduction

Large-area, vertically aligned CNTs have a variety of applications like field electron emitters for cathode ray lighting tubes (Saito et al., 1998), field emission displays (FED) (Sohn et al., 2001; Wang et al., 2001), backlight flat lamps in liquid-crystal displays (Bonard et al., 2001; Yoo et al., 2007), X-ray sources (Yue et al., 2002; Haga et al., 2004), as well as large surface-area electrodes for super-capacitors (Frackowiak et al., 2000; Futaba et al., 2006; McDonough et al., 2009), because of their higher aspect ratio and longer lifetime. A high electric field in the sheath generated in plasma enables self-standing and vertically aligned growth of carbon nanotubes (CNT) on substrates during plasma enhanced-chemical vapor deposition (PE-CVD). Power sources of direct-current (DC) with and without hot-filaments (Ren et al., 1998; Huang et al., 1998; Hayashi et al., 2001; Chhowalla et al., 2001), microwave (Sung et al., 1999; Murakami et al., 2000; Hayashi et al., 2002; Kojima et al., 2005), and radio-frequency (RF) (Hirao et al., 2001; Delzeit et al., 2002; Honda et al., 2003; Sato et al., 2006) have been utilized for generating plasma in vertically aligned growth of CNT by PE-CVD. DC plasma can generate the sheath of high electric field on the cathode. High electric filed sheath can also be generated on RF electrode by self-bias, but only under lower gas pressure (Hirao et al., 2001; Kaneko et al., 2005). Both DC and RF plasmas have the potential for large-area growth of CNT. Higher density plasma can be generated by DC or microwave power sources.

Vertically aligned CNTs are grown owing to a pull-up force exerted by the high electric field in the sheath formed on a substrate.Increasing the gas pressure makes the sheath thinner to form a higher electric field on the substrate without increasing ion bombardment energy (Hayashi et al., 2010). Therefore, DC plasma has the potential to grow vertically aligend CNTs on a large-area substrate under high gas pressure. The problem of applying DC plasma for the growth of CNTs is the instability of DC glow discharge by occasionally generated arcing. Hence, a new plasma CVD method called RF-DC plasma CVD was developed (Hayashi et al., 2006; Hayashi et al., 2010). This method applies DC plasma under assistance of RF plasma for discharge stabilization. It was demonstrated that, with an increase in the RF power, the firing potential of DC discharge decreases and the DC discharge current for the same discharge voltage increases. These features of RF-DC plasma mean that the impedance of DC discharge decreases under RF plasma generation. Arcing occurs occasionally at the cusped points on the electrodes, where high electric fields exist.

Stable glow discharge can continue with less frequent arcing under the condition of low impedance. Thus, with the generation of RF plasma, the DC glow discharge is more stable.
The perpendicular alignment of CNTs grown by PE-CVD on a substrate surface is more than that of CNTs oriented electrically after dispersion on the substrate. However, the density of aligned CNTs grown by PE-CVD as well as thermal CVD is too high to decrease the electric field at their tips. The density by PE-CVD is of the order of $10^9/cm^2$, which corresponds to an average spacing between CNTs of a few hundred nm. In comparison, the density of CNTs formed by thermal CVD is of the order of $10^{10}/cm^2$. The enhancement factor of electric field at the tip of CNT decreases with the increase in spacing between them because of the field-screening effect. It was calculated that the maximum density of field electron emission is obtained when the spacing between CNTs is comparable to their height (Nilsson, 2000; Suh, 2002; Jo, 2003). The spacing for CNTs grown by PE-CVD is generally much larger than the height. Therefore, to increase the density of field electron emission from aligned CNTs, the density of CNTs should be reduced by controlling the growth or by the method of post-treatment. For example, the growth of pattered arrays was controlled using electron beam lithography of catalyst (Teo, 2002), or by post-treatment carried out by a process with energetic plasma ions (Weng, 2004).
This chapter first shows the features of RF-DC PE-CVD plasma obtained through the diagnostics by the method of Langmuir probe, and the result of CNT growth analysis. Second, it shows the increase in density of field electron emission by the dip-dry method of post treatment, which is simple and suitable for vertically aligned CNTs grown over large-area.

2. Vertically aligned CNT growth by RF-DC PE-CVD

2.1 Experimental system of RF-DC PE-CVD

Figure 1 shows the schematic of the RF-DC plasma CVD system. Three electrodes (i. e., a 13.56 MHz RF electrode, a grounded electrode, and a DC cathode) are vertically fixed parallel to each other in a vacuum chamber. The distance between the RF and the grounded electrode is 10 mm, and that between the DC cathode and grounded electrode is 15 mm. The DC cathode, which is round in shape with 110 mm in diameter, having a hole at the center, also plays the role of a substrate holder. A substrate up to 75×75 mm^2 can be mounted on the cathode. An RF plasma is generated between the RF electrode and the grounded electrode, while a DC plasma is generated between the DC cathode and the grounded electrode. The grounded electrode is ring-shaped to facilitate passage of a part of the RF generated plasma into the space of DC discharge. The inside of the ring is covered with a mesh or wires, or is left without them. RF power induces not more than 500 W to the RF electrode. a negative bias not more than 650 V is applied to the cathode electrode. Substrate temperature is measured with a pyrometer at the backside of the substrate or on the surface of the substrate through the center hole of the RF electrode.

2.2 Features of RF-DC plasma

Figure 2 shows the relationship between the voltage and the current of DC discharge with and without RF plasmas in pure hydrogen, measured in the RF-DC plasma CVD system. The current shows average values measured with increasing and decreasing voltage. The firing potential without RF plasma was approximately 300 V, which decreased to a voltage of around 100 V with RF plasma. The discharge voltage decreased from 350 V to 270 V

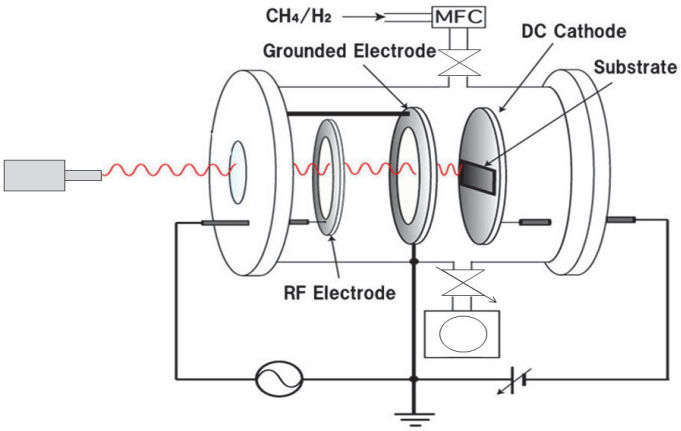

Fig. 1. Schematic of the RF-DC plasma CVD system. RF plasma and DC plasma are generated between RF electrode and grounded electrode and between DC cathode and grounded electrode, respectively.

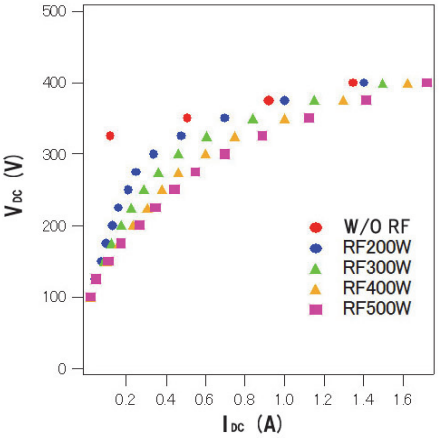

Fig. 2. Relationship between voltage and current of DC discharge with and without RF plasma in pure hydrogen.

at 0.5 A current, and from 380 V to 340 V at 1.0 A current by the generation of RF plasma with a power of 500 W. The impedance of DC discharge decreased with the increase of RF power.

In DC plasma, arcing occasionally occurs at cusped points on the surface of an electrode because high electric fields are formed there. During the fluctuation of plasma state, the electric field at a cusped point accidentally exceeds the value of arcing induction. In order to prevent arcing, DC voltage should be lowered to within the limit of discharge continuation. Thus, stable DC discharge with less arcing is expected under the condition of low impedance.

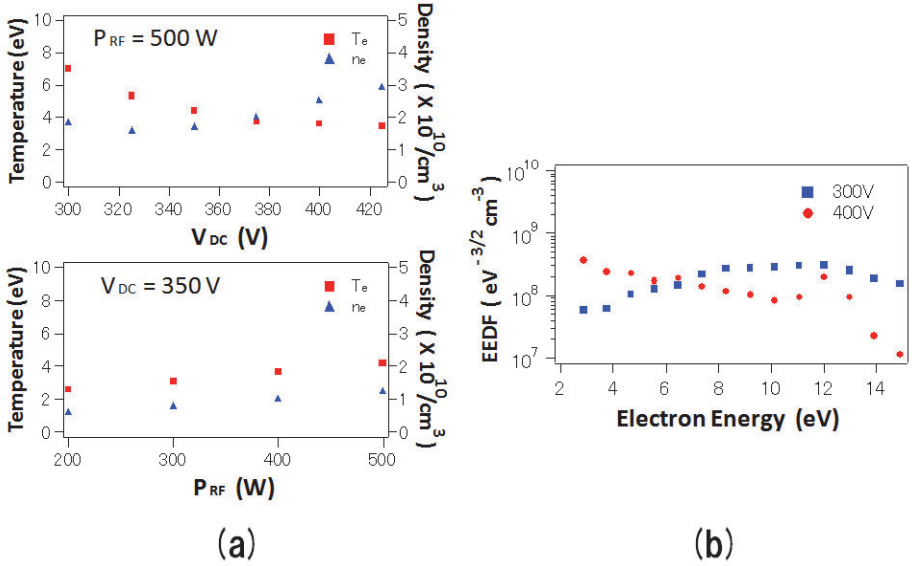

Fig. 3. Features of RF-DC plasma. (a) DC voltage and RF power dependence of electron temperature (T_e) and electron density (n_e). (b) Electron energy distribution function (EEDF) for DC voltage of 300 V and 400 V with RF power of 500 W.

The plasma diagnostics of RF-DC plasma was carried out by the method of Langmuir probe. The tip of Langmuir probe was a tungsten wire of 0.3 mm in diameter and 10 mm in length. The probe was set parallel to the cathode surface at a distance of 10 mm and its longitudinal center at 10 mm from the center axis of electrodes. The diagnostic result is shown in Fig.3. Figure 3(a) shows the dependence of electron temperature and density on DC voltage under a constant RF power of 500 W (upper), as well as their dependence on RF power under a constant DC voltage of 350 V (lower). The electron temperature decreases with increase of DC voltage or with decrease of RF power. In other words, higher electron temperature is obtained under a larger influence of RF plasma. Electron density gradually increases with increase in DC voltage and RF power. Typical electron energy distribution function (EEDF) for DC voltage of 300 and 400 V with RF power of 500 W is shown in Fig.3(b). Comparatively higher energy electrons exist under the condition of higher RF power, i. e., they increase with the increase in ratio of RF power to DC discharge voltage. Because the binding energy of H-H and C-H is 4.5 eV and 4.3 eV, respectively, electrons of energy higher than these values promote the dissociation of hydrogen and hydrocarbon molecules in a plasma. Active species for the growth of CNTs are produced by such energetic electrons.

2.3 Growth of vertically aligned CNTs

Iron foil substrates of 0.2 mm thickness, which had been ultrasonically cleaned in ethanol, were fixed onto the cathode electrode. They were pretreated before CNT growth in a pure hydrogen plasma under a DC voltage of 350 V with RF power of 500 W and pressure of 2200 Pa for 15 min. Methane gas was added to hydrogen by 20% under the same operating

pressure during the growth of CNTs for 15 min. The DC voltage was increased from 470 V to 620 V to maintain the substrate temperature at 700 °C throughout the pretreatment and growth process. For comparing the effect of RF plasma, CNT growth was also carried out with a lower RF power of 300 W at the same substrate temperature.

2.3.1 Vertically aligned CNTs

Figure 4 shows scanning electron microscopy (SEM) images of vertically aligned CNTs, grown with an RF power of 500 W. Multi-walled CNTs of several tens of nm in diameter and several microns in length are observed. The density of the CNTs is of the order of $10^9/cm^2$. All of the CNTs have catalyst iron particles at their tips. Individual CNT grew self-standing without sticking to each other by the van der Waals attraction. Such vertically aligned CNTs were observed to grow all over the surface of the iron foil substrate of 75 mm × 75 mm dimension (Hayashi et al., 2010). CNTs grown with RF power of 300 W showed similar alignment in growth as shown in Fig.4. The length of CNTs was found to be about 6 μm. Raman analysis of the CNTs showed the peak height ratio of Graphite to Defect (G/D) vary between 1.1 and 1.3.

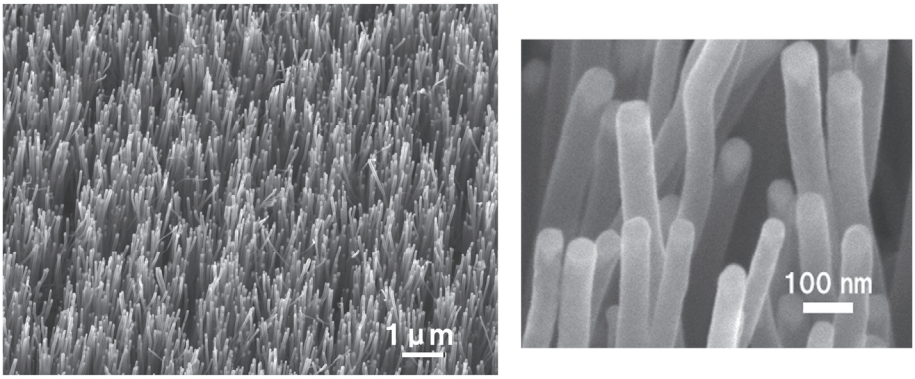

Fig. 4. SEM images of vertically aligned CNTs.

2.3.2 Early stages of growth of vertically aligned CNTs

To analyze the early stages of vertically aligned growth of CNTs, the substrate surface was observed by SEM. The SEM images of substrate surface after 1 min growth of CNTs under the condition of RF power of 300 W (a) and 500 W (b) are shown in Fig.5. They show isolated or strung particles of more or less 100 nm and smaller particles of a few to several tens of nm in sizes. The smaller particles are observed more remarkably for the 500 W RF power (Fig.5(b)). Some short fibers of few tens of nm in diameter, which should be the sprouts of CNTs, are observed in magnified oblique views. The fibers grown with 500 W RF power are longer than those with 300 W RF power. The result means that the initial growth of CNT with 500 W RF power is faster than that with 300 W RF power. As was discussed in section 2.2, because electron temperature increases with the increase of RF power, more active species for the growth of CNTs are produced under the condition of 500 W RF power. However, the diameter of the short fibers is smaller than that of the vertically grown CNTs in Fig.4. The growth of CNT can be explained by the vapor-liquid-solid (VLS) growth model (Tibbetts,

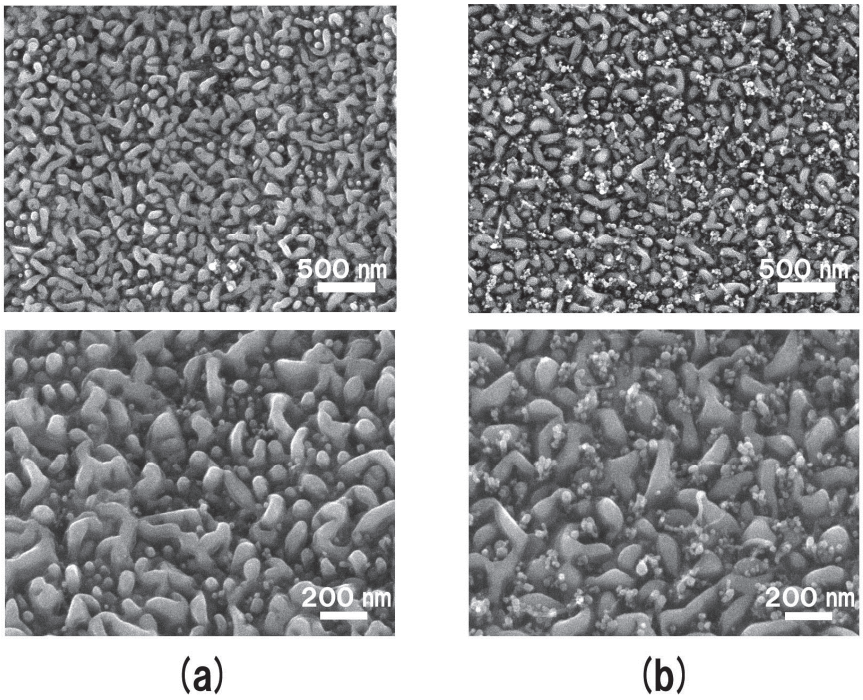

Fig. 5. SEM images of substrate surface after 1 min growth with RF power of (a) 300 W and (b) 500 W. Upper and lower images are top and magnified oblique views, respectively.

1984; Kanzow & Ding, 1999; Hayashi et al., 2005), which advocates that thinner CNTs grow faster because smaller catalyst ion particles absorb and extract carbon faster. Therefore, the thicker CNTs that are observed in Fig.4 should grow later and survive ion bombardment.

3. Field emission properties and post treatment of vertically aligned CNTs

3.1 Field emission properties of vertically aligned CNTs

Field emission properties of vertically aligned CNTs grown by RF-DC PE-CVD were investigated under the application of high voltage in the base pressure of 4×10^{-5} Pa. Negative bias voltage was applied to the CNTs on an iron substrate with a grounded counter electrode. The two electrodes were spaced at 240 μm apart. Figure 6 shows the dependence of the field emission current per unit area (which is defined as if electrons emit uniformly over 0.3 cm in diameter) on the applied voltage (a) and its Fowler-Nordheim plot (b) for CNTs grown by RF-DC PE-CVD at RF power of 500 W. The slope 'b' of linear relation of Fowler-Nordheim plot in higher applied voltage (lower 1/V) is expressed as

$$b = -6.83\times10^{7}\, d\, \phi^{3/2}/\beta \ (V) \tag{1}$$

,where d, ϕ and β are electrode spacing (in cm), the work function (in eV) and field-enhancement factor, respectively (Ishikawa et al., 1993; Forbes, 1999). When d = 240 μm and ϕ = 4.7 eV (Gao et al., 2001) $\beta = 1.7\times10^{3}$ is obtained for the slope in Fig.6(b), by eq. (1).

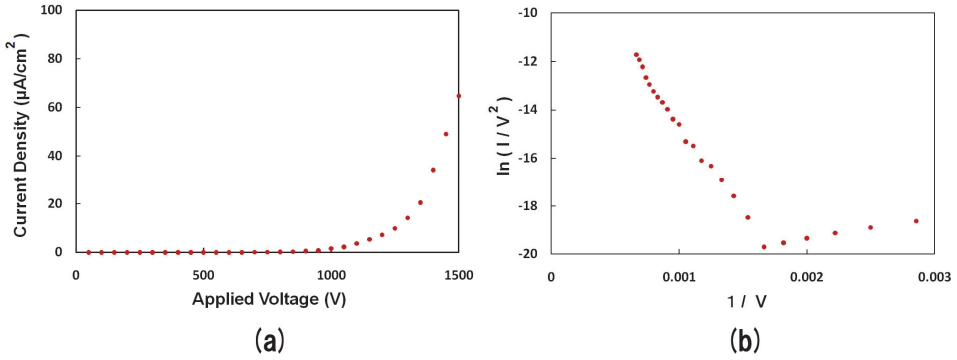

Fig. 6. Relationship between field emission current and applied voltage for CNTs grown by RF-DC PE-CVD with RF power of 500 W. (a) Dependence of current density on applied voltage. (b) Fowler-Nordheim plot of The data shown in (a).

3.2 Effect of post treatment of vertically aligned CNTs

The density of vertically aligned CNTs grown by CVD is so high that the field-screening effect (Nilsson et al., 2000; Suh et al., 2002; Jo et al., 2003) decreases electron emission current as a result of decrease of field-enhancement factor. In order to increase emission current by restricting the field-screening effect, the dip-dry post-treatment method was carried out to assemble vertically aligned CNTs into conics. Such a post-treatment had been done by embedding CNTs into a silicon dioxide, followed by HF etching, water rinsing, and nitrogen drying (Busta et al., 2004). However, in this case, approximately only ten CNTs were bundled together, which is not enough for the purpose. Therefore, we developed a simpler and effective post-treatment process, in which CNTs were first dipped in ethanol or distilled water, and air dried. The SEM images of CNTs post-treated by above method are shown in Fig.7 and Fig.8.

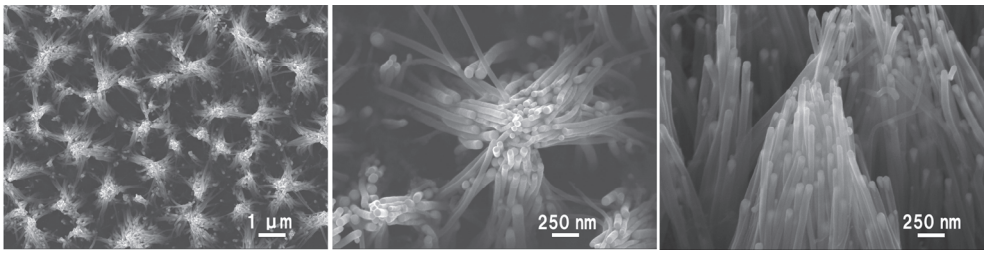

Fig. 7. SEM images of post treated vertically aligned CNTs. The left two are top views and the right is an oblique view.

Figure 7 shows that CNTs are bundled at the tips while their bottoms are left at stuck positions on the substrate. They form conics and decrease the number of electron emission sites. The mechanism of CNT bundling can be explained by the fact that capillary and surface tension forces of solutions act on CNTs at their flexible tips during drying (Busta et al., 2004; Futaba et al., 2006; Hayamizu et al., 2008) and that the tips of CNTs gather to each other by the van der Waals interactions after they are completely dried.

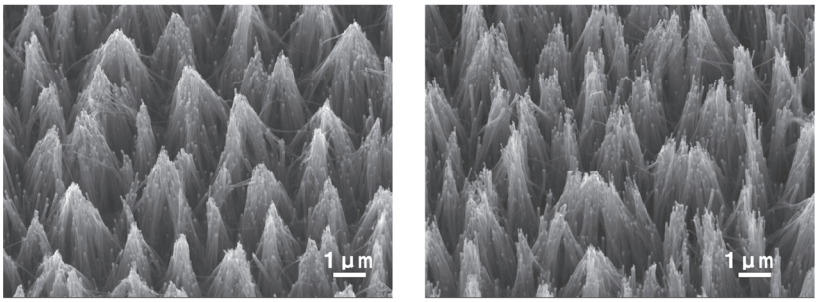

Fig. 8. SEM images of post treated vertically aligned CNTs; (a) dipped and dried in ethanol, (b) dipped and dried in distilled water.

The density of as-grown CNTs shown in Fig.4 was 4.4×10^{9} cm^{-2}. The number of CNT bundles after post-treatment in ethanol and distilled water was 3.9×10^{7} cm^{-2} and 2.2×10^{7} cm^{-2}, respectively. The result means that around 100 CNTs were bundled by the post-treatment in ethanol and more than 100 CNTs in distilled water. The tips of bundled CNTs post-treated in ethanol are more tightly stuck together compared to those post-treated in distilled water (Fig.8). The surface tension of ethanol at 20 °C is 22.40 mN/m, while that of distilled water at 20 °C is 72.75 mN/m. Since higher surface tension gathers larger number of CNTs against restoring force from the bottom during drying, more CNTs are bundled in distilled water than in ethanol. After complete drying, the restoring force spreads out bundled CNTs competing with the van der Waals attractive force, especially for bundles formed by larger number of CNTs.

The field emission properties of post-treated CNTs and as-grown ones were compared. Small chips, which were cut from a sheet of 50 mm × 50 mm vertically aligned CNTs on an iron foil grown by RF-DC PE-CVD, were used for the measurement. The relationship measured between field emission current and applied voltage are shown in Fig.9. Highest current density is obtained for CNTs post-treated in ethanol. It is followed by CNTs post-treated in distilled water, and then by the as-grown CNTs. The field-enhancement factors for post-treated CNTs in ethanol, distilled water, and as-grown ones, evaluated from the slope in the Fowler-Nordheim plot were 2.9×10^{3}, 2.0×10^{3}, and 1.8×10^{3}, respectively. The result indicates that the evaluated field-enhancement factors reflect the field-screening effect.

4. Summary

Large-area, vertically aligned CNTs were grown by DC plasma-enhanced CVD under RF plasma assistance. The firing potential and discharge current in a DC plasma was found to decrease with an increased power of RF plasma. In the plasma, stable glow discharge continued with less arcing. Higher energy electrons increased with the increasing ratio of RF power to DC discharge voltage. They promoted radical production in plasma, leading to increase in CNT growth rate.

Field emission properties of as-grown and post-treated vertically aligned CNTs, grown by RF-DC PE-CVD, were investigated. Dip-dry post-treatment in ethanol was effective for

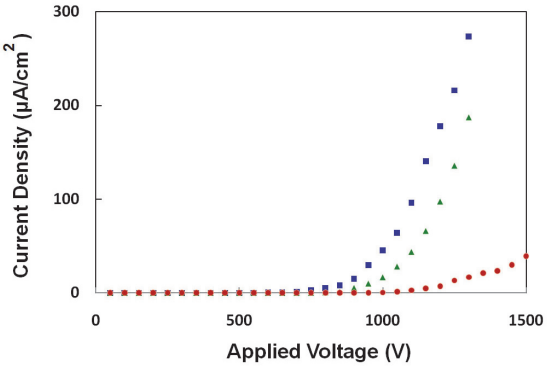

Fig. 9. Relationship between field emission current and applied voltage for as-grown CNTs (red circles) and post-treated CNTs in distilled water (green triangles) and in ethanol (blue rectangles).

reducing the density of field-emission sites, leading to a restriction of the field-screening effect, increasing the field-enhancement factor and consequently improving the field emission property of vertically aligned CNTs.

5. Acknowledgment

The authors thank Mr. Takashi Nakamura and Mr. Kazunori Odani for experimental assistance, and thank Ms. Risa Utsunomiya in Nissin Electric Co. Ltd. for partly supporting the present work.

6. References

Bonard, J. ; Stoeckli, T. ; Noury, O. & Chatelain A. (2001). Field emission from cylindrical carbo nanotube cathodes : Possibilities for lumininescent tubes, *Applied Physics Letters*, 78, 2775-2777.

Busta, H ; Tolt, Z. ; Montgomery, J. & Feinerman, A. (2004). Field Emission from Teepee-shaped Carbon Nanotube Bundles, *Technical Digest of the 17th International Vacuum Nanoelectronics Conference : IVNC 2004*, 30-31.

Chhowalla, M. ; Teo, K. B. K. ; Ducati, C. ; Rupesinghe, N. L. ; Amaratunga, G. A. J. ; Ferrari, A. C. ; Roy, D. ; Robertson, J. & Milne, W. I. (2001). Growth process conditions of vertically aligned carbon nanotubes using plasma enhanced chemical vapor deposition, *Journal of Applied Physics*, 90, 5308-5317.

Delzeit, L. D. ; McAninch, I. ; Crude, B. A. ; Hash, D. ; Chen, B. ; Han, J. & Meyyappan, M. (2002). *Journal of Applied Physics*, 91, 6027-6033.

Forbes, R. G. (1999), Field emission : New theory for the derivation of emission area from a Fowler-Nordheim plot, *Journal of Vacuum Science and Technology B*, 17, 526-533.

Frackowiak, E. ; Metenier, K. ; Bertagna, V. & Beguin, F. (2000). Supercapacitor electrodes from multiwalled carbon nanotubes, *Applied Physics Letters*, 77, 2421-2423.

Futaba, D. N. ; Hata, K. ; Yamada, T. ; Hiraoka, T. ; Hayamizu, Y.; Kakudate, Y. ; Tanaike, O. ; Hatori, H. ; Yumura, M. & Iijima, S. (2006). Shape-engineerable and highly densely

packes single-walled carbon nanotubes and their application as super-capacito electrodes, *Nature Materials*, 5, 987-994.

Gao, R. ; Pan, Z. & Wang, Z. L. (2001). Work function at the tips of multiwalled carbon nanotubes, *Applied Physics Letters*, 78, 1757-1759.

Haga, A. ; Senda, S. ; Sakai, Y. ; Mizuta, Y. ; Kita, S. & Okuyama, F. (2004). Aminiature x-ray tube, *Applied Physics Letters*, 84, 2208-2210.

Hayamizu, Y. ; Yamada, T. ; Mizuno, K. ; Davis, R. C. ; Futaba, D. N. ; Yumura, M. & Hata, K. (2008). Integrated three-dimensional microelectromechanical devices from processable carbon nanotube wafers, *Nature Nanotechnology*, 3, 289-294.

Hayashi, H. ; Koga, M. ; Kashirajima, J. ; Takahashi, K. ; Hayashi, Y. & Nishino, S. (2002). Large-Scale Synthesis of Aligned Carbon Nanotubes by Surface-Wave-Excited Microwave-Plasma-Enhanced Chemical Vapor Deposition, *Japanese Journal of Applied Physics*, 41, L1488-L1491.

Hayashi, Y. ; Negishi, T. & Nishino, S. (2001). Growth of well-aligend carbon nantubes on nickel by ho-filament-assisted dc plasma chemical vapor deposition in a CH_4/H_2 plasma, *Journal of Vacuum Scinece and Technology A*, 19, 1796-1799.

Hayashi, Y. ; Watanabe, Y. ; Ueda, K. & Nishino, S. (2005). Analyses of Early Stages of Vertically Aligned Carbon Nantube Grwoth by Plasma-Enhanced Chemical Vapor Deposition, *Japanese Journal of Applied Physics*, 44, 1549-1553.

Hayashi, Y. ; Fukumura, T. ; Isshiki, T. & Utsunomiya, R. (2006). Highly Alogned Growth of Carbon Nanotubes by RF-Plasma-Assisted DC Plasam Chemical Vapor Deposition at High Pressure, *Japanese Journal of Applied Physics*, 45, 8308-8310.

Hayashi, Y. ; Fukumura, T. ; Odani, K. ; Matsuba, T. & Utsunomiya, R. (2010). Growth of well-aligned carbon nanotubes by RF-DC plasma chemical vapor deposition, *Thin Solid Films*, 518, 3506-3508.

Hirao, T. ; Ito, K. ; Furuta, H. ; Yap, Y. K. ; Ikuno, T. ; Honda, S. ; Mori, Y. ; Sasaki, T. & Oura, K. (2001). Formation of Vertically Aligned Carbon Nantoubes by Dual-RF-Plasma Chemical Vapor Deposition, *Japanese Journal of Applied Physics*, 40, L631-L634.

Honda, S. ; Katayama, M. ; Lee, K. ; Ikuno, T. ; Ohkura, S. ; Oura, K. ; Furuta, H. & Hirao, T. (2003). Low Temperature Synthesis of Aligned Carbon Nanotubes by Inductively Couolpled Plasma Chemical Vapor Deposition Using Pure Methane, *Japanese Journal of Applied Physics*, 4, L441-L443.

Huang, Z. P. ; Xu, J. W. ; Ren, Z. F. ; Wang, J. H. ; Siegal, M. P. & Provencio, P. N. (1998). Growth of highly oriented carbon nanotubes by plasma-enhanced hot filmanet chemical vapor deposition, *Applied Physics Letters*, 73, 3845-3847.

Ishikawa, J. ; Tsuji, H. ; Inoue, K. ; Nagao, M. ; Sasaki, T, ; Kaneko, T. & Gotoh, Y. (1993). Estimation of Metal-Deposited Field Emitters for the Micro Vacuum Tube, *Japanese Journal of Applied Physics*, 32, L342-L345.

Jo, S. H. ; Tu, Y. ; Huang, Z. P. ; Carnahan, D. L. ; Wang, D. Z. & Ren. Z. F. (2003). Effect of lenght and spacing of vertically aligend carbon nanotubes on field emission properties, *Applied Physics Letters*, 82, 3520-3522.

Kaneko, T.; Matsuoka, H.; Hatakeyama, R. & Tohji, K. (2005). Effects of Ion Bombardment on Carbon Nanotube Formation in Strongly Magnetized Glow-Discharge Plasmas, *Japanese Journal of Applied Physics*, 44, 1543-1548.

Knazow, H & Ding. A. (1999). Formation mechanism of single-wall carbon nanotubes on liquid-metal partciles, *Physical Review B*, 60, 11180-11186.

Kojima, Y. ; Kishimoto, S. ; Ohno, Y. ; Sakai, A & Mizutani, T. (2005). Growth of High-Quality Carbon Nanotubes by Grid-Inserted Plasma-Enhanced Chemical Vapor Deposition for Field Emitters, *Japanese Journal of Applied Physics*, 44, 2600-2602.

McDonough, J. R. ; Choi, J. W. ; Yang, Y. ; Mantia, F. L. ; Zhang, Y. & Cui, Y. (2009). Carbon nanofiber supercapacitors with large areal capacitances, *Applied Physics Letters*, 95, 243109- 1-3.

Murakami, H. ; Hirakawa, M. ; Tanaka, C. & Yamakawa, H. (2000). Field emission from well-aligned, patterned, carbon nanotube emittes, *Applied Physics Letters*, 76, 1776-1778.

Nilsson, L. ; Groening, O. ; Emmenegger, C. ; Kuettel, O. ; Schaller, E. ; Schlapbach, L. ; Kind, H. ; Bonard, J-M. & Kem, K. (2000). Scanning field emission from patterned carbon nanotube films, *Applied Physics Letters*, 76, 2071-2073.

Ren, Z. F. ; Huang, Z. P. ; Xu, J. W. ; Wang, J. H. ; Bush, P. ; Siegal, M. P. & Provencio, P. N. (1998). Synthesis of Large Arrays of Well-Aligend Carbon Nanotubes on Glass, *Science*, 282, 1105-1107.

Saito, Y. ; Umemura, S. & Hamaguchi, K. (1998). Cathode Ray Tube Lighting Elements with Carbon Nanotube Field Emitters, *Japanese Journal of Applied Physics*, 37, L346-L348.

Sato, G. ; Kato, T. ; Oohara, W. & Hatakeyama, R. (2006). Production and application of reactive plasmas using helicon-wave discharge in very low magnetic fileds, *Thin Solid Films*, 506-507, 550-554.

Sohn, J. I. ; Lee, S. ; Song, Y. ; Choi, S. ; Cho, K. & Nam, K. (2001). Patterened selective growth of carbon nanotubes and large field emission from vertically well-aligned carbon nanotube field emission arraays, *Applied Physics Letters*, 78, 901-903.

Suh, J. S. ; Jeong, K. S. ; Lee, J. S. & Han, I. (2002). Study of the field-screening effect of highly ordered carbon nanotube arrays, *Applied Physics Letters*, 80, 2392-2394.

Tsai, S. H. ; Chao, C. W. ; Lee, C. L. & Shih, H. C. (1999).Bias-enganced nucleation and growth of the aligned carbon nanotubes with open ends under microwave plasma synthesis, *Applied Physics Letters*, 74, 3462-3464.

Teo, K. B. K. ; Chhowalla, M. ; Amaratunga, G. A. J. ; Milne, W. I. ; Pirio, G. ; Legagneux, P. ; Wyczisk, F. ; Pribat, D. & Hask, D. G. (2002). Field emission from dense, sparse, and pattaered arrays of carbon nanofibers, *Applied Physics Letters*, 80, 2011-2013.

Tibbetts, G. G. (1984). WHY ARE CARBON FILAMNETS TUBLRAR ?, *Journal of Crystal Growth*, 66, 632-638.

Wang, Q. H.; Yan, M. & Chnag, R. P. H. (2001). Flat panel display prototype using gated carbon nanotube field emitters, *Applied Physics Letters*, 76, 2071-2073.

Weng, C. H. ; Leou, K. C. ; Wei, H. W. ; Juang, Z. Y. ; Wei, M. T. ; Tung, C. H. & Tsai C. H. (2004). Structural transformation and field emission enhancement of carbon nanofibers by energetic argon plasma post-treatment, *Applied Physics Letters*, 85, 4732-4734.

Yoo, H. ; Sung, W. ; Yoon, S. ; Kim, Y. & Joo, S. (2007). Novel Triode-Type Field Emission and Appropriate Driving Method for Flat Lamp Using Carbon Nanofibers Grwn by Plasma Enhanced Chemical Vapor Deposition, *Japanese Journal of Applied Physics*, 46, 4381-4385.

Yue, G. Z. ; Qui, Q. ; Gao, B. ; Cheng, Y. ; Zhang, J. ; Shimoda, H. ; Chang, S. ; Lu, J. P. & Zhou, O. (2002). Generation of continuous and pulsed diagnostic imaging x-ray radiation using a carbon-nanotube-based filed-emission cathode, *Applied Physics Letters*, 81, 355-357.

2

Carbon Nanotubes Engineering Assisted by Natural Biopolymers

Luhua Lu, Ying Hu, Chunrui Chang and Wei Chen
i-Lab, Suzhou Institute of Nano-Tech and Nano-Bionics, Chinese Academy of Sciences
China

1. Introduction

For the application of carbon nanotubes (CNTs), there are many practical problems to be solved. Large scale as-produced CNT especially single-walled CNTs (SWCNTs) inevitably contain impurities that produced in their growth process（Huo, et al. 2008) As-produced SWCNTs normally are of different chirality (Kataura, et al. 1999) Untreated CNTs are of high surface area and align into big bundles for their strong Van Der Waals attraction. The high aspect ratio and strong attraction between CNTs further leads to the physically entanglement of CNT ropes. The strong aggregation of CNTs gives rise to a highly complex network makes their uniformly dispersion into other substances hard to be achieved (Mitchell, et al. 2002). Engineering CNTs thus need variety of technologies to achieve CNT purification, separation, dispersion, stabilization, alignment, functionalization and organization (Baughman, et al. 2002). Many physical and chemical approaches have been developed to achieve these goals since the discovery of CNTs (Tasis, et al. 2006). On the route to the engineering of CNTs, biopolymer covalently and noncovalently functionalization of CNTs has been found to be promising way in highly effective realization these technologies. Initial great progress on dispersion of CNTs (Barisci, et al. 2004), CNT liquid crystal phase formation (Badaire, et al. 2005) and selective chiral SWCNTs enrichment (Zheng, et al. 2003) assisted by biopolymer DNA reveal that biopolymers are promising agents for high quality CNT materials preparation, which has soon attracted wide attentions on biopolymers assisted CNT engineering. Now widely obtainable, large scale production and low price agent polysaccharides have been found to be easier and commercially acceptable for achieving such goals. High concentration CNTs single dispersion and stabilization could be simply achieved by varieties of polysaccharides such as chitosan (Zhang, et al. 2007), gellan gum (Panhuis, et al. 2007), hydraulic acid (Moulton,et al. 2007) and etc. Physical purification of CNTs by chitosan funcitonalization has been approved to be easy processing and effective (Yang, et al. 2006). Aligning CNTs through liquid crystal phase of CNTs dispersed by polysaccharides has also been developed. The stable dispersed CNTs by biopolymers were further introduced into biomedical applications such as tissue engineering and drug delivery system, which broaden the application range of CNTs. For the bioactivity of biopolymers, their composites with CNTs provide excellent sensing performance. The biomimetic actuation based on CNT/biopolymer devices have also initially been shown to be of large and fast actuation displacement under low voltage electrical stimulation.

2. Supramolecular self-assembly of biopolymers onto CNT surface

To engineering CNTs, such as dispersion CNTs into solution for further manipulation or preparing CNT composite materials, functionalization of CNTs is usually adopted. There are two approaches for CNT functionalization, covalent and noncovalent as illustrated in figure 1 (Hirsch, 2002). Prestine CNT surface could be chemically modified through oxidation and grafting processing or reversibly absorbing amphiphilic molecules.

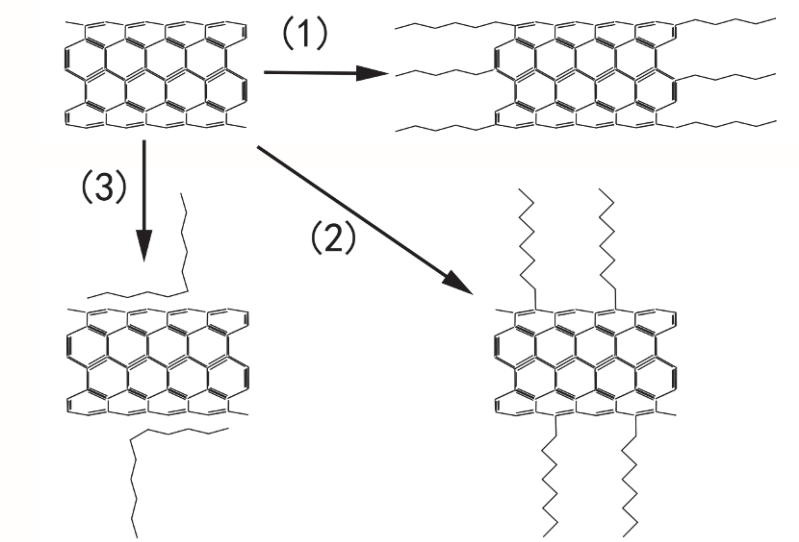

Fig. 1. Schematic illustration for the covalent end (1) and side wall (2) functionalization of CNTs by oxidation and grafting reaction and noncovalent (3) functionalization of CNTs by surface absorbing amphiphilic molecules.

The covalent bond attaches functional groups on the side wall or end of CNTs to obtain desired functions. Covalent approach inevitably changes the intrinsic electrical, mechanical and thermal properties of CNTs, which are important for their variety of applications. However, the strong covalent bond between molecules and CNTs also has advantages in many aspects (Balasubramanian, et al. 2005; Dyke, et al. 2004; Banerjee, et al. 2005). For example, it could reinforce interfacial adhension between CNTs and composite matrix. Covalently functionalized CNTs could be used as stable nano-template for further supramolecular assemble of target molecules. Covalently functionalization of CNT could be controlled to adjust electrical performance of functionalized CNTs that may have higher sensitivity of target molecules.

The noncovalent functionalization of CNTs based on the supramolecular chemistry theory (Lehn, 1985) studies the organization of molecules with CNTs through weak interactions that provide variety of functions without changing CNT properties. The weakly absorbed biopolymers could be removed by varying the solution environment, which favours the realization of CNT excellent electrical, mechanical, thermal and interfacial performances. The surpramolecular chemistry of CNTs for the noncovalent functionalization of CNT (Zhao, & Stoddart 2009) has thus been intensively studied for the CNT engineering. In this

field, of biopolymer noncovalent functionalization of CNT has attracted great attentions for their important roles in variety of CNT applications.

Earlier than theoretical understanding the interaction mechanism between biopolymers and CNTs, helical crystallization of proteins on CNTs has been experimentally observed earlier in 1999 and attributed to order structure of hydrophobic CNT surface (Balavoine, et al. 1999). Later researches have shown that CNTs are effective on reinforcing the crystallization of biopolymers such as bombyx mori silk, poly(L-lactide), poly(ε-caprolactone), polyhydroxyalkanoates and streptavidin. (Levi, et al. 2004; Ayutsede, et al. 2006; Yun, et al. 2008; Wu, et al. 2006). To understand the mechanism of CNT induced biopolymer crystallization, FTIR online test method was adopted to analyze the influence of CNTs on the crystallization of biopolymer poly(L-Lactide) and reveal that CNT reinforced biopolymer crystallization is originated from surface induced biopolymer conformational order. (Hu, et al. 2009) A recent study also show that CNT could reinforce the piezoelectric actuation performance of regenerated cellulose while the reinforced crystalline is in agreement with it. (Yun, et al. 2007).

The widely used polysaccharides amylose (Kim, et al. 2003), chitosan (Zhang, et al. 2007), hydraulic acid (Moulton, et al. 2007), gellan gum [Panhuis, et al. 2007] and cytlodextrin (Komatsu, et al. 2008) have been found to be helically wrapped on CNT surface. As has been shown in figure 2, the biopolymer chitosan helically wrapped on CNT surface, which favour CNT solubilisation in water. Some theoretical calculations prove the helical wrapping on CNTs is the optimal configuration for polymers of rigid molecular chains (Xie, et al. 2005; Gurevitch, et al. 2007). Recent experiment revealed that the absorption of biopolymer chitosan on CNT surface influence by the deacetylation degree of chitosan molecular chain (Iamsamai, et al. 2010). Low deacetylation degree provide more hydrophobic sections that favour the absorption of chitosan on CNT surface and results in better stability of CNT suspension in the experiment though high deacetylation degree provide higher electrostatic repulsive force that should favour the stabilization of CNTs as colloidal. This interesting solution behaviour of chitosan wrapped CNTs reveals that the interaction between biopolymer and CNT surface is more important for their stabilization than the traditional key issues that determine colloidal behaviours.

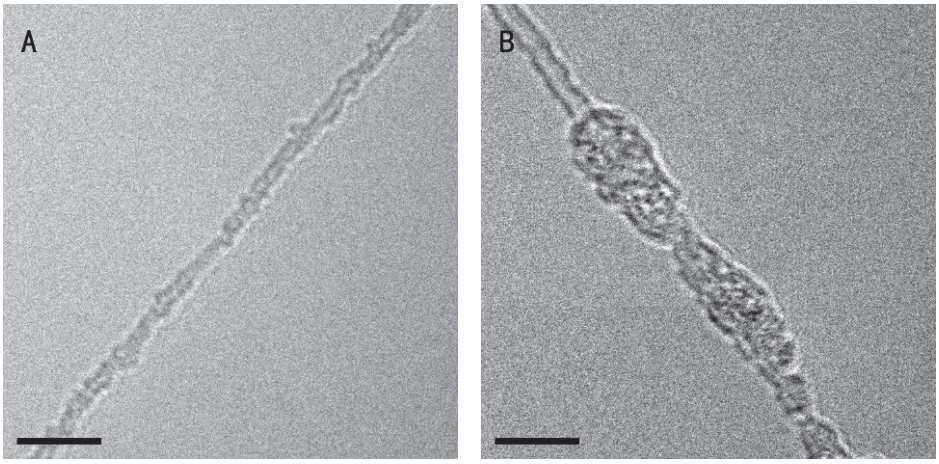

Fig. 2. (A) Single helical and (B) double helical wrapped CNTs, scale bar 5 nm.

The interaction between DNA and CNT surface has been intensively studied (Johnson, et al. 2010; Gao, et al. 2008; Shtogun, et al. 2007). DNA molecular chain composes of four bases adenine (A), cytosine (C), guanine (G), and thymine (T). They have been experimentally and theoretically approved to be of high affinity contact with CNT sidewalls. Very recent research compared the energy variation for the binding of four bases with CNT in water. The interactions of water-CNT, water-bases and base-CNT have been found to important for the binding free energy of the four bases with CNT in water separately. As a result the base's affinity for CNT binding follows the trend G>A>T>C. Base–CNT interactions are dominated by π–π stacking interactions with solvent and entropic effects playing a minor. The sequence of DNA motifs further influences their absorption on CNT surface and their stability in water.

3. Dispersion and stabilization of CNTs assisted by biopolymers

The initially works on studying the cooperation of biopolymers with CNTs were to assist CNT dispersion (Kim, et al. 2003). To understand the dispersion and stabilization of CNTs in water by biopolymers, we should first study the interaction between CNTs and water for the assembly of biopolymer onto CNT surface is mostly achieved in water environment and the assembly indeed forms on the CNT-water interface of unpolar-polar interfacial inducement force. As we have mentioned above, pristine CNTs have the strong attendance to aggregate in water making their dispersion in water without surface treatment hard. In recent years there have been a lot of researches on understanding the mechanism of CNT aggregation in water. A typical molecular dynamic stimulation has theoretically attributed the aggregation of CNTs to the solvation interaction of polar water molecules around unpolar CNTs surface (Walther, et al. 2001). This solvation interaction causes the hydrogen atoms of water molecules point to the surface of CNTs, leading to higher orientation of water molecules around CNT surface than that in the bulk water. The orientated water molecules give a rise in the energy of those molecules around CNTs and force CNT aggregate into bundles to minimize the system energy rise.

Some very initially works has been done to solve this problem by the chemical modification of CNT surface, transferring hydrophobic unpolar CNT surface into hydrophilic polar one. However, the chemical modification of CNT create large amount of defects on CNT surface, leading to the variation of intrinsic CNT electronic structure, which changes the electric performance of CNTs and limits the application of CNTs in variety of fields (Robinson, et al. 2006).

For comparison, physical approach that is called noncovalent functionalization has been found to be a promising method for the preservation of intrinsic CNT surface structure and their variety of properties. This approach was initially proposed in 2001 for the PVP assisted dispersion of CNT in water (O'Connell, et al. 2001). The supramolecular self assembly of small molecules such as lipid derivatives on CNT surface has been detailed studied in 2003 (Richard, et al. 2003). The CNT-water interface direction the ordered structure of lipid derivatives onto CNT surface could lower the system energy. After that, non-covalent functionalization of CNTs by supramolecular self-assembly of biopolymers on CNT surface has been found to be of excellent effect for CNT dispersion. Gum Arabia, the ancient biopolymer dispersant was introduced to stabilize SWCNTs. The dispersion could be

concentrated into suspension of SWCNT concentration as high as 150 mg/mL, the highest concentration for SWCNTs (Bandyopadhyaya,et al. 2002). The Hyaluronic acid functionalized CNTs at high concentration of 10mg/mL shows anisotropic birefringence phenomenon, indicating the liquid crystal phase of biopolymer functionalized CNTs.

Within all those biopolymers functionalized CNTs, Chitosan wrapped CNT is one of most important one for their potential application in variety of fields, such as drug delivery, tissue engineering, electrochemical sensing and actuation. Chitosan wrapped CNTs could be directly dispersed at concentration of 3mg/mL (Lynam, et al. 2007). However, chitosan wrapped CNT could only stabilized in acidic solution. In year 2007 Zhang et al. investigate solution behaviours of chitosan wrapped CNTs (Zhang, et al. 2007). To reveal the influence of electrostatic interaction on the stabilization of chitosan wrapped CNT, derivates of chitosan has been used as shown in figure 3. The groups that containing $-NH_2$ and –COOH would only be charged in acidic and basic environment separately while the group $CH_2CHOHCH_2CN(CH_3)_3^+Cl^-$ charges in the whole pH range.

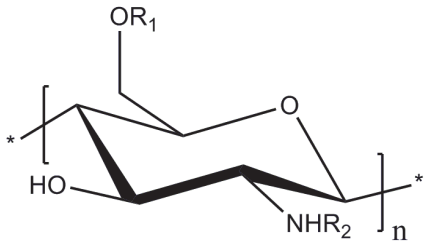

R_1=H or CH_2COOH

R_2=H
or CH_2COOH
or $C{=}OCH_2CH_2COOH$
or $CH_2CHOHCH_2CN(CH_3)_3^+Cl^-$

Fig. 3. Molecular structure of chitosan and its derivates

The comparative characterization indicates that electrostatic repulsive force of the charged chitosan and its derivate molecular chains could stabilize their wrapped CNTs. The aggregation of chitosan and its derivate wrapped CNTs happens when they were discharged by changing the pH value of their suspension. When the pH value of suspension for chitosan wrapped CNTs is higher than 6.59, the $-NH_3^+$ group deprotonated into $-NH_2$ and precipitate could be observed. The CNTs functionalized by chitosan derivates that contains COOH group deprotonate in acidic environment of pH lower than 4.66 aggregate. The chitosan derivate containing group $CH_2CHOHCH_2CN(CH_3)_3^+Cl^-$ show no aggregation in whole pH range. But the aggregation mechanism has not been fully understood. Amylase, which has very similar structure of chitosan and no charge group on its molecular chain, can also stabilize CNT in water. As has been mentioned above, the impact of deacelytation degree on CNT stabilization reveals the electrostatic force is not the dominant fact for chitosan wrapped CNT stabilization. Some research found that the ammonia group in chitosan molecular chain has strong affinity to CNT surface (Long, et al. 2008). Previous research has also shown that the interaction between chitosan and CNT are chiral dependant. Considering chitosan itself aggregates in water in the neutral and basic pH range while chitosan oligosaccharide, which has the same molecular structure of chitosan but shorter chain length, could be solubilized in neutral and basic solution, the molecular chain length should also has impact on chitosan wrapped CNT stabilization. Thus the full image of chitosan wrapped CNTs stabilization mechanism is still complicated and unclear. Further investigation is needed.

4. Purification and selective enrichment SWCNTs by biopolymers

Commercially available CNTs large scale produced by either arc discharge or chemical vapor deposition methods inevitably contain carbonaceous impurities as shown in figure 4. Those impurities not only largely lower the performance of CNTs and their composite materials but also invalid the manipulation of CNTs as micro system devices. To remove those impurities, purification of CNTs has been studied for more than ten years. Though lots of chemical approach has been widely studied for multi-walled CNTs and few-walled CNTs, purification of SWCNTs is still a problem for the chemical durability of SWCNT is too weak to be remained when the carbonaceous impurity removed.

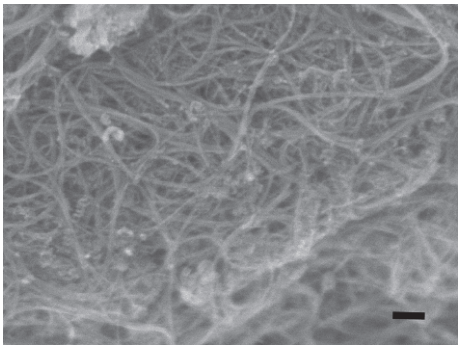

Fig. 4. Scanning electron microscopic image for raw SWCNTs, scale bar 100 nm.

Impurities and CNTs are of different elements, structure, size, density, which lead to their different chemical and colloidal behaviours. The surface properties of impurities should also be different from that of CNTs especially the interaction with biopolymers. In this aspect, biopolymers show incomparable efficiency. In year 2002, amylose functionalized SWCNTs could be purified for the better affinity of amylose to SWCNTs than carbonaceous impurities. (Star, et al. 2002). In our experiment, as shown in figure 5, we also found that gellan gum functionalized SWCNTs could also be separated from carbonaceous impurities by centrifuging their co-suspension (Lu, & Chen, 2010).

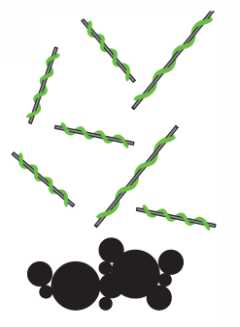

Fig. 5. Purification of CNTs by the stonger affinity of biopolymer onto CNTs (the upper suspended units) than that of impurities (the bottom aggregated units)

Beside the removal of carbonaceous impurity, further purification of SWCNTs requires sorting SWCNTs of different chiralities. Biopolymers are not only capable of separating SWCNT from carbonaceous impurities but also show high efficiency on selective enriching specific chiral SWCNTs. As we know that metallic and semiconducting SWNTs are different in several aspects, in addition to their obvious differences in electrical conductivity, including static polarizability and surface characteristics, chemical reactivity, and so forth. They are also associated with SWNTs of different diameters.

In year 2003 Zheng et al found that anionic exchange column could separate ssDNA wrapped metallic SWCNTs from that of semiconductive ones (Zheng, et al. 2003). It was attributed to the different polarizability of metallic and semiconductor SWCNTs, which results in their different interaction of negative charged ssDNA that wrapped on them. Further detailed design of ssDNA sequence, selective harvesting of 12 major single-chirality SWCNT could be achieved through ion-exchange chromatography (Tu, et al. 2009). Separation of chiral SWCNTs could also be achieved by polysaccharides. Chitosan was found to have ability for the enrichment of small-diameter semiconducting SWNTs by preserve the as-dispersed suspension overnight without centrifugation or any other physical treatment (Yang, 2006). After that, another polysaccharide agarose were introduced to separate metallic and semiconducting SWCNTs (Tanaka, et al. 2009; Tanaka, December 2009; Tanaka, et al. 2010; Liu, et al. 2010). The suspension of single dispersed SWCNTs by surfactant SDS was mixed with agarose gel for gelation. The gel containing SDS-dispersed SWCNTs was frozen, thawed, and squeezed to yield a solution of enriched (70%) metallic SWCNTs. The semiconducting SWCNTs (95%) were left in the gel (Tanaka, & Suga, 2009). The same separation was later demonstrated on column based gel chromatography (Tanaka, & Nishide, 2009). The mechanism for agarose assisted separation of chiral SWCNTs is unclear. Some very recent involvement found that the separation effect originated from two main factors, the unique interaction of semiconductor SWCNTs with agarose gel and exfoliation of SDS molecules from SDS functionalized SWNT entities which may cause the precipitation of semiconductor SWCNTs in the gel (Li, et al. 2010). Thus understanding the role of SDS in the separation, it is possible to further optimize the purification of each fraction and develop a more effective and low-cost separation strategy. This method is more amenable to scaling up than the density gradient ultracentrifugation or ion-exchange chromatography.

5. Formation of CNT liquid crystal phase assisted by biopolymers

Single CNT is anisotropic unit for the high aspect ratio of cylindrical graphene nanostructure. The excellent performance such as electrical, mechanical and thermal performance of CNTs refers to the performance in axis direction. However, the bulk materials of CNTs show no anisotropic performance for their disordered structure. Thus the alignment of CNTs is of great value to obtain high performance CNT bulk materials. Though aligned CNT arrays could be obtained by CVD method, they are normally perpendicular to that of membrane surface. And a more important fact is that the large-scale macroscopic membrane is hard to obtain, which seriously limits the realization of their full potential. In recent years, aligning CNTs by processing disordered CNTs (Jin, et al. 1998; Safadi, et al. 2002; De Heer, et al. 1995, Casavant, 2003; Vigolo, et al. 2000) with external forces, such as electrical force, mechanical force, and liquid flow, has been widely studied. In this field, we have (Chen, et al. 2005) explored the method of aligning CNTs in polyurethane

by solvent-polymer interaction. Using this method, the Young's modulus of composite material has been obviously increased. But the weight fraction of CNTs in the polymer matrix is so low that the anisotropic performances of CNTs are still not well embodied.

Fig. 6. Schematic illustration of CNT phase transition from isotropic (left) to anisotropic (right) phase

Since the discovery of CNT alignment in liquid crystal phase in 2003 (Song, et al. 2003), the formation of CNTs liquid crystal phase has been extensively studied. CNT liquid crystal is lytropic, which caused by the volume effect of high aspect ratio CNTs as illustrated in figure 6 (Zhang, et al. 2006). To obtain CNT liquid crystal phase, high CNT concentration is needed and has been obtained by dispersion CNTs in super strong acid solution (Davis, et al. 2009; Davis, et al. 2004; Rai, et al. 2006). However, those solutions are not suitable for composite material preparation, which the mild solution processing is required.

For biopolymer could disperse CNT at high concentration, the anisotropic birefringence phenomenon of liquid crystal phase was earlier found in 2005 for DNA stablized CNTs (Badaire, et al. 2005). Later the spontaneous nematic phase separation of CNTs stabilized in aqueous biological hyaluronic acid solutions was also observed (Moulton, et al. 2007).The initially obtained SWNT dispersion is isotropic single-phase. Over time, the uniform isotropic phase separated into dispersions containing birefringent nematic domains in equilibrium with an isotropic phase. The time required for phase separation to occur depends on the concentration of SWNT and hyaluronic acid. The attractive interactions between the SWNT and HA shifts the onset of the phase separation toward lower concentration. This phase separation is accompanied by an increase in the dispersion viscosity with this increase qualitatively matching the degree of phase separation. The further development in 2008 has shown that mechanical shearing could uniformly align lyotropic nematic aqueous suspensions in thin cells (Zamora-Ledezma, et al. 2008) by drying the nematic CNT suspension, homogeneous anisotropic CNT thin films can be prepared. To quantitatively estimate the dichroic ratio of CNTs, optical transmission between parallel or crossed polarizers was characterized and analyzed. The order parameter for the anisotropic thin film was measured using polarized Raman spectroscopy and found to be quite weak. It was attributed to the possible entanglement of the CNTs and the intrinsic viscoelastic behavior of the CNT suspensions. In our very recent work, we found that the purity of CNTs is crucially important for CNT alignment (Lu, & Chen, 2010). Highly purified CNTs showed dominant nematic phase of domains as large as hundred micrometers as shown in figure 7a. The mechanical shearing treatment for the CNT liquid crystal phase could further obtain wavy aligned CNTs of typical band structure of polarizing microscope image as shown in figure 7b. The ordered parameter for this aligned was found to be as high as 0.88. The anisotropic electrical performance was characterized. The calculated resistivity in the parallel direction is as low as 1.477×10^{-4} Ωm, about one fourteenth of resistance in perpendicular direction.

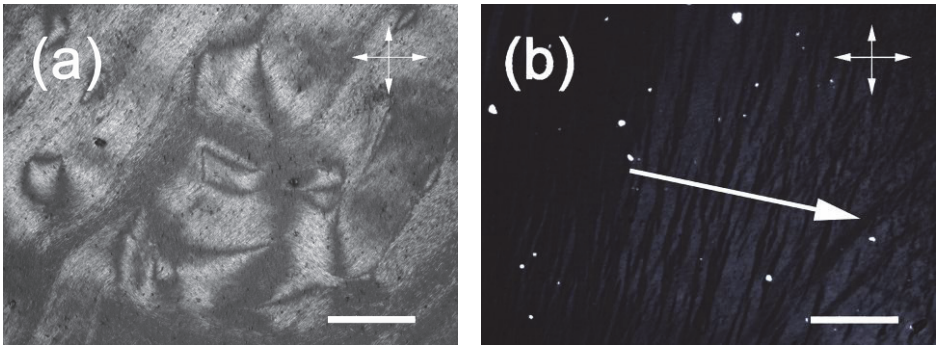

Fig. 7. Polarizing bireflection microscopic images for solid state composite membrane obtained from (a) unsheared and (b) sheared condensed gellan gum/CNT suspension between cross polarizers (scale bar 200 μm)

6. Biopolymer/CNT hybrids for drug delivery

CNTs especially SWCNTs are of surface area as high as 2600 m2/g, which is very suitable to be drug carrier for biomedical applications. Alberto Bianco initially introduced CNT as a template for presenting bioactive peptides to the immune system (Pantarotto, et al. 2003). B-cell epitope of the foot-and mouth disease virus (FMDV) was covalently attached to the amine groups functionalized CNTs. As a result, the peptides around the CNT adopt the appropriate secondary structure due to the recognition by specific monoclonal and polyclonal antibodies. The immunogenic features of peptide–CNT conjugates were subsequently assessed in vivo (Pantarotto, et al. 2003). Immunisation of mice with FMDV peptide–nanotube conjugates elicited high antibody responses as compared with the free peptide. These antibodies were peptide-specific since antibodies against CNT were not detected. In addition, the antibodies displayed virus-neutralising ability. The use of CNT as potential novel vaccine delivery tools was validated by interaction with the complement (Salvador-Morales, et al. 2006). The complement is that part of the human immune system composed of a series of proteins responsible for recognising, opsonising, clearing and killing pathogens, apoptotic or necrotic cells and foreign materials. Pristine CNT activate the complement following both the classical and the alternative way by selective adsorption of some of its proteins. Because complement activation is also involved in immune response to antigens, this might support the enhancement of antibody response following immunisation with peptide–CNT conjugates.

Kam et al. initially tried to deliver ssRNA into cells through functionalized CNTs in year 2005 (Kam, et al. 2005). Later, researchers have found that functionalized CNTs can cross the cell membrane (Martin, et al. 2003; Pantarotto, et al. 2004). Carbon nanotubes can be used to facilitate delivery of DNA or any bioactive agent to cells. While they can be functionalized to attach either electrostatically or covalently to DNA and RNA, the remaining unfunctionalized and hydrophobic portions of the nanotubes can be attracted to the hydrophobic regions of the cells. Biotin functionalized carbon nanotubes were bound to fluorescent dyes were capable of intercellular transport of fluorescent streptavidin (Kam, et al. 2004). Besides heterogeneous functionalization, carbon nanotubes could provide localized delivery of therapeutic agents triggered by external sources. Previously, it was

shown that carbon nanotubes absorb NIR light at wavelengths that are optically transparent to native tissue. For example, irradiation with a 880nm laser pulses can induce local heating of SWNTs in vitro thereby releasing its molecular cargo without harming cells or can be internalized within a cancer cell and with sufficient heating kill the cell (Kam, et al. 2005). This could allow selective delivery of drugs to certain cell types, helping to control the distribution of such cells throughout the engineered tissue. Modulated release of dexamethasone from chitosan/CNT composite has been show to be faster than traditional method (Naficy, et al. 2009).

7. Biopolymer/CNT composite as tissue scaffolds

CNTs are famous filler for reinforcing the mechanical performance of polymer matrix. Thus the very important aspect in biomedical application of CNTs is for structural support. By dispersing a small fraction of CNTs into a polymer, significant improvements in the mechanical strength of the composite have been observed. For example, MWCNTs blended with chitosan showed significant improvement in mechanical properties compared with those of chitosan (Wang, et al. 2005). The composite composed of 2wt% MWNT shown more than doubled Young's modulus and tensile strength compared to neat chitosan. Tuning of the mechanical properties of the polymer can be adjusted depending on CNT loading and with the need of very small amounts may counterbalance their high structure stability. In vitro work has shown that several different cells types have been successfully grown on CNT/biopolymer composites. MacDonald found that blends of SWNT with collagen support smooth muscle cell growth (MacDonald, et al. 2005). L929 mouse fibroblasts have been successfully grown on CNT scaffolds (Correa-Duarte, et al. 2004) Abarrategi et al. demonstrates the use of scaffolds composed of a major fraction of MWCNT (up to 89wt%) and a minor one of chitosan, and with a well-defined microchannel porous structure as biocompatible and biodegradable supports for culture growth. Cell adhesion, viability and proliferation onto the external surface of MWCNT/CHI scaffolds with C2C12 cell line (myoblastic mouse cell), which is a multipotent cell line able to differentiate towards different phenotypes under the action of some chemical or biological factors, has been evaluated in vitro and quantified by MTT assays. The evolution of the C2C12 cell line towards an osteoblastic lineage in presence of the recombinant human bone morphogenetic protein-2 (rhBMP-2) has also been studied both in vitro (e.g., following the appearance of alkaline phosphatase activity) and in vivo (e.g., by implantation of MWCNT/chitosan scaffolds adsorbed with rhBMP-2 in muscle tissue and evaluation of the ectopic formation of bone tissue) (Abarrategi, et al. 2008).

8. Biopolymer/CNT composite sensor

Tracking biological behaviours of cells, organs, blood and etc are of great value for the development of biomedical engineering. CNTs are of high. To monitor engineered tissues, we could use implantable sensors capable of relaying information extracorporeally. Such a sensor would provide real time data related to the physiological relevant parameters such as pH, pO2, and glucose levels. CNT/biopolymer composites are of excellent mechanical performance as has been mentioned above. The good biocompatibility with high electrical and electrochemical sensitivity is advantages for implantable biosensor application. The very initial research found that noncovalently functionalzed CNTs could detect serum

proteins, including disease markers, autoantibodies, and antibodies. (Chen, et al. 2003) High-density nanotube device microarrays have been synthesized and fabricated for proteomics applications, aimed at detecting large numbers of different proteins inva multiplex fashion by using purely electrical transducers. These arrays are attractive because no labelling is required and all aspects of the assay can be carried out in solution phase. The bionanomultilayer biosensor of CNTs and horseradish peroxidase was prepared by layer-by-layer assembly and can be successfully applied to detect hydrogen peroxide, which presented a linear response for hydrogen peroxide from 0.4 to 12.0 μM with a detection limit of 0.08 μM. The MWNTs in the biosensor provided a suitable microenvironment to retain HRP activity and acted as a transducer for improving the electron transfer and amplifying the electrochemical signal of the product of the enzymatic reaction exhibited a fast, sensitive and stable response. (Liu, et al. 2008) DNA aptamer is highly selective and has been used as molecular recognition elements to functionalize CNT preparing filed effect transistor, which has shown high effect detecting two important enzymes elastase and thrombin. The lowest detection limit of the sensor used in their work is around 10 nM. For the selective absorption of DNA on to CNT surface, the supramolecular structure of DNA and CNT could be made used for sensing DNA by it modified CNT electronic properties. The developed fully electronic DNA sensors based on CNT field effect devices has achieved and found to be a effective approach for further understanding of DNA/CNT interaction mechanism. (Tang, et al. 2006)

An important composite biosensor is based on Chitosan/CNT. Chitosan is the only cationic biopolymer. For the solution sensitivity of positive charged amino groups in the chitosan molecular chain, it has variety important biological functions in tissue engineering, immune and drug delivery. (Rinaudo, et al. 2006) Chitosan/CNT composite material has been found to be of good biocompatibility for neutral cells growth. (Thompson, et al. 2009) Their suspension coated on glass carbon substrate could detect NaDH in a fast response time ($t_{90\%}$<5 s). The susceptibility of chitosan to chemical modifications has been made used for covalently immobilizing glucose dehydrogenase (GDH) in the chitosan/CNT films using glutaric dialdehyde (GDI). The stability and sensitivity of the GC/CNT/Chitosan/GDI/GDH biosensor allowed for the interference-free determination of glucose in the physiological matrix (urine). In pH 7.40 phosphate buffer solutions, linear least-squares calibration plots over the range 5-300 μM glucose (10 points) had slopes 80 mA $M^{-1}cm^{-2}$ and correlation coefficient 0.996. Its detection limit was 3 μM glucose. (Zhang, et al. 2004) A composite of MWCNTs-chitosan was used as a matrix for entrapment of lactate dehydrogenase onto a glassy carbon electrode in order to fabricate amperometric biosensor. (Tsai, et al. 2007) CNT-chitosan-lactate dehydrogenase nanobiocomposite film exhibits the abilities to raise the current responses, to decrease the electrooxidation potential of β-nicotinamide adenine dinucleotide and to prevent the electrode surface fouling. The optimized biosensor for the determination of lactate shows a sensitivity of 0.0083 A M^{-1} cm^{-2} and a response time of about 3 s. The proposed biosensor retained 65% of its original response after 7 days. The immobilization of acetylcholinesterase (AChE) on CNTs/chitosan composite was also proposed. (Du, et al. 2007) Based on the inhibition of organophosphorous insecticide to the enzymatic activity of AChE, using triazophos as a model compound, the conditions for detection of the insecticide were explored. The inhibition of triazophos was proportional to its concentration in two ranges, from 0.03 to 7.8 μM and 7.8 to 32 μM with a detection limit of 0.01 μM. A 95% reactivation of the inhibited AChE could be regenerated for using pralidoxime iodide within 8 min. The

constructed biosensor processing prominent characteristics and performance such as good precision and reproducibility, acceptable stability and accuracy, fast response and low detection limit has potential application in the characterization of enzyme inhibitors and detection of toxic compounds against to enzyme.

9. Biopolymer/CNT composite actuator

Biopolymer/CNT composite actuators were initially found to play important role for smart drug delivery. A novel gelatin-CNTs hybrid hydrogel was synthesized. [Li, December 2003] Cooperation with CNT could maintain the stability of the hybrid hydrogel without cross-linking at 37.8 ^{o}C. It have also been noticed that the novel hybrid hydrogel with or without crosslinking can be used in protein separating. Silk fibroin in the sol state can interact with nanotubes through hydrophobic interactions. (Kim, et al. 2009) The pH-sensitive properties of the CNTs dispersed with silk fibroin has been investigated and believed to have potential value for the preparation of novel biomaterials for cancer detection and treatment. Composite gel of chitosan/CNT has also been found to be of improved actuation performance under pH and electrical field stimulation. (Ozarkar, et al. 2008) Modulated release of dexamethasone from their composite has been show to be faster than traditional method (Naficy, et al. 2009). Electrochemical investigation has shown that the chitosan/CNT composite electrodes can foster prolific L929 cell growth and stimulate the cells growth. (Whitten, et al. 2007; Lynam, et al. 2009) In the history of piezoelectric material development, the first discovered piezoelectric polymer is biopolymer cellulose by testing the piezoelectricity of wood. (Fukada, et al. 1955) Lately, the piezoelectricity has also been found in the invertebrate exoskeletons, including crap shell, and bone. (Zilberstein, et al. 1972; Yamashiro, et al. 1989; Fukuda, et al. 1957) Molecular level research approved that the those piezoelectricity comes from biopolymers such chitin, collagen, DNA, which reveals that piezoelectricity is a fundamental properties of biological tissues and may comes from the directed dipole of chemical bond in their ordered structure. (Fukada, 1964 &1975; Ando, 1976; Shamos, 1967). A recent study also show that CNT could reinforce the piezoelectric actuation performance of regenerated cellulose while the reinforced crystalline is in agreement with it. (Yun, et al. 2007) For the structure of biopolymer near CNT surface is directed, single units of biopolymer/CNT at nanoscale could be obtained, which could be further developed as important electromechanical actuator and sensor as nano-electro-mechanical-system for implant biomedical devices. As has been mentioned above, chitosan is a mutifuctional biopolymer involved in variety of biological tissues' formation and functions. It has been widely studied not only as sensor but also actuator for variety of usages.

Because chitosan is a very effective agent for stabilization of CNTs, we have initially constructed a high speed, highly stable, full solid chitosan/CNT bimorph electrochemical composite actuator. (Lu, & Chen, 2010) For the high weight fraction of CNTs in uniform chitosan/CNT composite electrode, the conductivity of composite electrode could reach as high as 34.25 $S.cm^{-1}$, which was made use for reinforcing the electrochemical charging and discharging ability of bimorph structure, as illustrated in figure 8. The bending actuation performance of 15mm long composite strip show 2 mm/s high speed actuation performance under a 3 V low voltage stimulation. This performance is higher than most of traditional IPMC actuator strip while no heavy metal element is needed, which is important for biomedical and harptic interface applications.

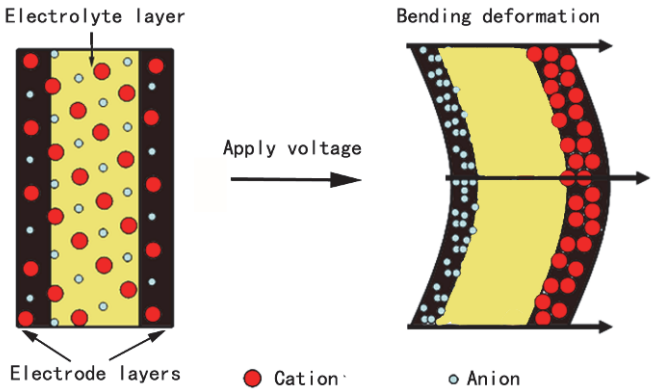

Fig. 8. Schematic illustration for the bending actuation mechanism of bimorph CNT composite, the applied voltage redistribute the cations and anions from the raw state (left) to a new balanced state (right).

CNTs are of excellent electrical conductivity, thermal stability and conductivity. Their temperature could be periodically changed in wide frequency range by electrothermal energy transition under periodical electrical current control. CNTs temperature waving leads to the countering temperature waving of a very thin gas layer surrounded them, which can be achieved by the high frequency range thermal variation of CNTs for the low thermal conductivity of gas induced thermal energy accumulation in very short time. In the thermal actuation system, the periodical thermal accumulation induced equivalent adiabatic expansion and shrinkage of surrounded thin layer gas medium. This character gives birth to the nanoscale loudspeaker. (Xiao, et al. 2008) On realized that by replacing gas medium with chitosan that helically wrapped on CNTs, we could obtain an electrothermal stimulated macroscopic composite actuator. The electrothermal actuation performance of chitosan/CNT composite has thus been detailed studied (Hu, et al. 2010). Biopolymer chitosan functionalized CNTs uniformly distributed as a network in bulk material reversible actuating polymer matrix in the frequency lower than 10 Hz, which is close to organisms' behaviors. The cyclic test shows that the reversible electrothermal actuation could be achieved for more than 3 thousand times. It is believed to be of great value for not only high sensitivity engineering actuation materials but also electrical current controllable drug release system that attached to skin.

10. Conclusion

In summary, the latest ten year progress on key topics for CNT engineering assisted by biopolymers has been reviewed. The dispersion, purification and specific chiral separation for CNTs assisted by biopolymers have been successful achieved. Moreover, their cooperation broaden the application range of CNTs into biomedical fields especially drug delivery and tissue engineering. The cooperation of biopolymers with CNTs provides impresive sensing and actuation performances that traditional materials can't reach. Varieties of technologies for biopolymer assisted CNTs engineering have been developed and thus belived to be of great potential for further applications.

11. Acknowledgment

The corresponding author, Professor Wei Chen, would like to thank National Natural Science Foundation of China (10704051), National Basic Research Program of China (2010CB934700), Science and Technology Program of Suzhou (ZXG0713), Science and Technology Support Key Project from Jiangsu Province (BE2009643), and Special Foundation of President of The Chinese Academy of Sciences.

12. References

Abarrategi, A.; Gutierrez, M.; Moreno-Vicente, C.; Hortiguela, M. J.; Ramos, V.; Lopez-Lacomba, J.; Ferrer, M. & del Monte, F. (2008). Multiwall carbon nanotube scaffolds for tissue engineering purposes, Biomaterials, Vol.29, No.1, (January 2008), pp. 94–102, ISSN 0142-9612

Ando,Y. & Fukada, E. (1976). Piezoelectric Properties of Oriented Deoxyribonucleate Films, Journal of Polymer Science: Polymer Physica Edition, Vol.14, No.1,(January 1976), pp. 63-79, ISSN 0098-1273

Ayutsede, J.; Gandhi, M.; Sukigara, S.; Ye, H.; Hsu, C. M.; Gogotsi, Y. & Ko, F. (2006). Carbon Nanotube Reinforced Bombyx mori Silk Nanofibers by the Electrospinning Process, Biomacromolecules, Vol.7, No.1, (January 2006), pp. 208-214, ISSN 1525-7797

Badaire, S.; Zakri, C.; Maugey, M.; Derre, A.; Barisci, J. N.; Wallace, G. G. & Poulin P. (2005) Liquid Crystal of DNA Stabilized Carbon Nanotubes. Adv. Mater., Vol.17, No.13, (March 2005), pp. 1673-1676, ISSN 0935-9648

Balasubramanian, K.; Burghard, M. (2005). Chemically Functionalized Carbon Nanotubes, Small, Vol.1, No.2, (February 2005), pp. 180-192, ISSN 1613-6829

Balavoine, F.; Schultz, P.; Richard, C.; Mallouh, V.; Ebbesen, T. W. & Mioskowski, C. (1999). Helical Crystallization of Proteins on Carbon Nanotubes: A First Step towards the Development of New Biosensors, Angew. Chem. Int. Ed., Vol.38, No.13/14, (July 1999), pp. 1912-1915, ISSN 1433-7851

Bandyopadhyaya, R.; Nativ-Roth, E.; Regev, O.& Yerushalmi-Rozen, R.; (2002). Stabilization of Individual Carbon Nanotubes in Aqueous Solutions, Nano Letters, Vol.2 No.1,(January 2002), pp 25–28, ISSN 1530-6984

Barisci, J. N.; Tahham, M.; Wallace, G. G.; Badaire, S.; Vangien, T.; Maugey, M. & Poulin, P. (2004). Properties of Carbon Nanotube Fibers Spun from DNA-Stabilized Dispersions, Adv. Funct. Mater., Vol.14, No.2, (February 2004), pp. 133-138, ISSN 1616-301X

Banerjee, S.; Hemraj-Benney, T. & Wong, S. S. (2005). Covalent surface chemistry of single-walled carbon nanotubes, Adv. Mater., Vol.17, No.1, (January 2005), pp. 17-29, ISSN 0935-9648

Baughman, R. H.; Zakhidov, A. A.; & de Heer, W. A. (2002). Carbon Nanotubes—the Route Toward Applications, Science, Vol.297, No.5582, (August 2002), pp.787-792 ISSN 0036-8075

Casavant, M. J.; Walters, D. A.; Schmidt, J. J.; Smalley, R. E. Neat Macroscopic Membranes of Aligned Carbon Nanotubes, J. Appl. Phys., Vol.93, No.4, (February 2003), pp. 2153–2156, ISSN 0021-8979

Chen, W.; Tao, X. (2005) M. Self-Organizing Alignment of Carbon Nanotubes in Thermoplastic Polyurethane. Macromol. Rapid Commun., Vol.26, No.22, (November 2005), pp. 1763–1767, ISSN 1022-1336

Chen, R. J.; Bangsaruntip, S.; Drouvalakis, K. A.; Kam, N. W. S.; Shim, M.; Li, Y.; Kim, W.; Utz, P. J. & Dai, H. (2003). Noncovalent functionalization of carbon nanotubes for highly specific electronic biosensors, PNAS, Vol.29, No.9, (April 2003), pp. 4984-4989, ISSN 0027-8424

Correa-Duarte, M. A.; Wagner, N.; Rojas-Chapana, J.; Morsczeck, C.; Thie, M. & Giersig M. (2004). Fabrication and biocompatability of carbon nanotube-based 3D networks as scaffolds for cell seeding and growth, Nano Lett., Vol.4, No.11, (November 2004), pp. 2233–6, ISSN 1530-6984

Davis, V. A.; Parra-Vasquez, A. G.; Green, M. j.; Rai, P. K.; Behabtu, N.; Prieto, V.; Booker, R. D.; Schmidt, J.; Kesselman, E.; Zhou, W.; Fan, H.; Adams, W. W.; Hauge, R. H.; Fischer, J. E.; Cohen, Y.; Talmon, Y.; Smalley, R. E. & Pasquali, M. (2009) True solutions of single-walled carbon nanotubes for assembly into macroscopic materials, Nature Nanotechnology, Vol.4, No.12, (December 2009), pp. 830-834, ISSN 1748-3387

Davis, V. A. Ericson, L. M.; Parra-Vasquez, A. G.; Fan, H.; Wang, Y.; Prieto, V.; Longoria, J. A.; Ramesh, S.; Saini, R. K.; Kittrell, C.; Billups, W. E.; Adams, W. W.; Hauge, R. H.; Smalley, R. E. & Pasquali, M. (2004), Phase Behavior and Rheology of SWNTs in Superacids, Macromolecules, Vol.37, No.1, (January 2004), p. 154-160, ISSN 0024-9297

Du, D.; Huang, X.; Cai, J. & Zhang, A. (2007). Amperometric detection of triazophos pesticide using acetylcholinesterase biosensor based on multiwall carbon nanotube–chitosan matrix, Sensors and Actuators B, 127, No.2, (November 2007), pp. 531-535, ISSN 0925-4005

De Heer, W. A.; Bacsa, W. S.; Chatelain, A.; Gerfin, T.; Humphrey-Baker, R.; Forro, L. & Ugarte, D. (1995). Aligned Carbon Nanotube Films: Production and Optical and Electronic Properties. Science, Vol.268, No.5212, (May 1995), pp. 845–847, ISSN 0036-8075

Dyke, C. A.; Tours, J. M. (2004). Covalent functionalization of single-walled carbon nanotubes for materials applications, J. Phys. Chem. A, Vol.108, No.51, (December 2004) pp. 11151-11159, ISSN 1089-5639

Fukada, E. (1955). Piezoelectricity of Wood, J. Phys. Soc. Jpn., Vol.10, No.2, (February 1955), pp. 149-154, ISSN 0031-9015

Fukuda, E.; Yasuda, I. (1957). On the Piezoelectric Effect of Bone, J. Phys. Soc. Jap., Vol.12, No.10, October 1957, pp. 1158-62, ISSN 0031-9015

Fukada, E. & Sasaki, S. (1975). Piezoelectricity of α-chitin, Journal of Polymer Science: Polymer Physics Edition, Vol.13, No.9, (September 1975), pp. 1845–1847, ISSN 0098-1273

Fukada, E. & Yasuda, I. (1964). Piezoelectric Effects in Collagen, Japanese Journal of Applied Physics, Vol.3, No.2, (February 1964), pp. 117-121, ISSN 0021-4922

Gao, X.; Xing, G.; Yang, Y.; Shi, X.; Liu, R.; Chu, W.; Jing, L.; Zhao, F.; Ye, C.; Yuan, H.; Fang, X.; Wang, C. & Zhao, Y. (2008). Detection of Trace Hg2+ via Induced Circular Dichroism of DNA Wrapped Around Single-Walled Carbon Nanotubes, J. Am. Chem. Soc., Vol.130, No.29, (July 2008), pp. 9190–9191, ISSN 0002-7863

Gurevitch, I., Srebnik, S. (2007) Monte Carlo simulation of polymer wrapping of nanotubes, Chem. Phys. Lett. Vol.444, No.1-3, (January 2007) pp.96-100, ISSN 0009-2614

Hirsch, A. (2002). Functionalization of Single-Walled Carbon Nanotubes, Angew. Chem. Int. Ed., Vol.41, No.11, (June 2002), pp. 1853-1859, ISSN 1433-7851

Hu, X.; An, H.; Li, Z.; Geng, Y.; Li, L. & Yang, C. (2009). Origin of Carbon Nanotubes Induced Poly(L-Lactide) Crystallization: Surface Induced Conformational Order, Macromolecules, Vol.42, No.8, (April 2009), pp. 3215–3218, ISSN 0024-9297

Hu, Y.; Chen, W.; Lu, L. H.; Liu, J. H. & Chang, C. R. (2010). Electromechanical Actuation with Controllable Motion Based on a Single-Walled Carbon Nanotube and Natural Biopolymer Composite, ACS Nano, Vol.4, (June 2010), pp. 3498–3502, ISSN 1936-0851

Huo, X. P.; Chang, L. & Cheng, H. M. (2008). Purification of carbon nanotubes, Carbon, Vol.46, No.15, (December 2008), pp.2003-2025, ISSN 0008-6223

Iamsamai, C.; Hannongbua, S.; Ruktanonchai, U.; Soottitantawat, A. & Dubas, S. T. (2010). The effect of the degree of deacetylation of chitosan on its dispersion of carbon nanotubes, Carbon Vol.48, No.1, (January 2010), pp. 25-30, ISSN 0008-6223

Jin, L.; Bower, C.; Zhou, O. (1998) Alignment of Carbon Nanotubes in a Polymer Matrix by Mechanical Stretching. Appl. Phys. Lett., Vol.73, No.9, (August 1998), pp. 1197–1199, ISSN 0003-6951

Johnson, R. R.; Johnson, A. T. C. & Klein, M. L. (2010). The Nature of DNA-Base–Carbon-Nanotube Interactions, Small, Vol.6, No.1, (January 2010), pp. 31–34, ISSN 1613-6829

Kataura, H.; Kumazawa, Y.; Maniwa, Y.; Umezu, I.; Suzuki, S.; Ohtsuka, Y. & Achiba, Y. (1999). Optical properties of single-wall carbon nanotubes, Synthetic Metals, Vol.103, No.1-3, (June 1999), pp. 2555-2558, ISSN 0379-6779

Kam, N. W. S.; Jessop, T. C.; Wender, P. A. & Dai, H. (2004). Nanotube molecular transporters: internalization of carbon nanotube–protein conjugates into mammalian cells, J Am Chem Soc., Vol.126, No.22, (June 2004), pp. 6850–1, ISSN 0002-7863

Kam, N. W. S.; O'Connell, M.; Wisdom, J. A. & Dai, H. (2005). Carbon nanotubes as multifunctional biological transporters and near-infrared agents for selective cancer cell destruction, Proc Natl Acad Sci, Vol.102, No.33, (August 2005), pp. 11600–5, ISSN 0027-8424

Kam, N. W. S.; Liu, Z. & Dai, H. (2005). Functionalization of carbon nanotubes via cleavable disulfide bonds for efficient intracellular delivery of siRNA and potent gene silencing, J. Am. Chem. Soc., Vol.127, No.36, (September 2005), pp. 12492–12493, ISSN 0002-7863

Kim, H.; Yoon, S.; Kwon, S. & Jin, H. (2009). pH-Sensitive Multiwalled Carbon Nanotube Dispersion with Silk Fibroins, Biomacromolecules, Vol.10, No.1, (January 2009), pp. 82–86, ISSN 1525-7797

Kim, O. K.; Je, J.; Baldwin, J. W.; Kooi, S.; Pehrsson, P. E. & Buckley, L. J. (2003) Solubilization of Single-Wall Carbon Nanotubes by Supramolecular Encapsulation of Helical Amylose, J. Am. Chem. Soc., Vol.125, No.15, (April 2003), pp. 4426-4427, ISSN 0002-7863

Komatsu, N. (2008). Heterocyclic Supramolecular Chemistry of Fullerenes and Carbon Nanotubes, In: Heterocyclic Supramolecules I, Volume 1, Kiyoshi Matsumoto, pp. 161–198, Springer, ISBN 978-3-540-68189-2, Berlin Heidelberg, German

Lehn, J. M. (1985) Supramolecular chemistry: receptors, catalysts, and carriers, Science, Vol.227 No.4689, (February 1985), pp. 849-856, ISSN 0036-8075

Levi, N.; Czerw, R.; Xing, S.; Iyer, P. & Carroll, D. L. (2004). Properties of Polyvinylidene Difluoride-Carbon Nanotube Blends, Nano Lett., Vol.4, No.7, (July 2004), pp. 1267-1271, ISSN 1530-6984

Li, H. B.; Jin, H. H.; Zhang, J.; Wen, X. N.; Song, Q. j. & Li, Q. W. (2010) Understanding the Electrophoretic Separation of Single-Walled Carbon Nanotubes Assisted by Thionine as a Probe, J. Phys. Chem. C, Vol.114, No.45, (November 2010), pp. 19234–19238, ISSN 1932-7447

Liu, H.; Feng, Y.; Tanaka, T.; Urabe, Y. & Kataura, H. (2010). Diameter-Selective Metal/Semiconductor Separation of Single-wall Carbon Nanotubes by Agarose Gel, J. Phys. Chem. C, Vol.114, No.20, (May 2010), pp. 9270–9276, ISSN 1932-7447

Lu, L. H.; Chen, W. (2010). Large-Scale Aligned Carbon Nanotubes from Their Purified, Highly Concentrated Suspension, ACS Nano, Vol.4, No.2, (February 2010), pp. 1042-1048, ISSN 1936-0851

Li, H.; Wang, D. Q.; Chen, H. L.; Liu, B. L. & Gao, L. Z. (2003). A Novel Gelatin–Carbon Nanotubes Hybrid Hydrogel, Macromol. Biosci., Vol.3, No.12, (December 2003), pp. 720–724, ISSN 1616-5187

Liu, L.; Zhang, F.; Xi, F.; Chen, Z. & Lin, X. (2008). Uniform bionanomultilayer constructed with soluble multiwall carbon nanotubes and its application as biosensor, Journal of Electroanalytical Chemistry, Vol.623, No.2, (November 2008), pp. 135–141, ISSN 1572-6657

Long, D.; Wu, G. & Zhu, G. (2008). Noncovalently Modified Carbon Nanotubes with Carboxymethylated Chitosan: A Controllable Donor-Acceptor Nanohybrid, Int. J. Mol. Sci., Vol.9, No.2, (February 2008), pp. 120-130, ISSN 1422-0067

Lu, L. H.; Chen, W. (2010) Biocompatible Composite Actuator: A Supramolecular Structure Consisting of the Biopolymer Chitosan, Carbon Nanotubes, and an Ionic Liquid, Adv. Mater., Vol.22, No.33, (September 2010), pp. 3745-3748, ISSN 0935-9648

Lynam, C.; Moulton, S. E. & Wallace, G. G. (2007). Carbon-nanotube biofibers, Vol.19, No9, (May 2007), pp. 1244-1248, ISSN 0935-9648

Lynam, C.; Grosse, W. & Wallace, G. G. (2009) Carbon-Nanotube Biofiber Microelectrodes, J. Electrochem. Soc., Vol.156, No.7, (July 2009), pp. 117-121, ISSN 0013-4651

Martin, C. R.; Kohli, P. (2003). The emerging field of nanotube biotechnology, Nature Rev.: Drug Discovery, vol.2, No.1, (January 2003), pp. 29–37, ISSN 1474-1776

MacDonald, R. A.; Laurenzi, B. F.; Viswanathan, G.; Ajayan, P. M.; Stegemann, J. P.; Collagen–carbon nanotube composite materials as scaffolds in tissue engineering, J Biomed Mater Res, Vol.74A, No.3, (September 2005), pp. 489–96, ISSN 0021-9304

Mitchell, C. A.; Bahr, J. L.; Arepalli, S.; Tour, J. M. & Krishnamoorti, R. (2002). Dispersion of functionalized carbon nanotubes in polystyrene, Macromolecules, (November 2002), Vol. 35, No.23, pp. 8825-8830, ISSN 0024-9297

Moulton, S. E.; Maugey, M.; Poulin, P. & Wallace, G. G. (2007). Liquid Crystal Behavior of Single-Walled Carbon Nanotubes Dispersed in Biological Hyaluronic Acid Solutions. J. Am. Chem. Soc. Vol.129, No.8, (August 2007), 9452–9457, ISSN 0002-7863

Naficy, S.; Razal, J. M.; Spinks, G. M.; Wallace, G. G. (2009). Modulated release of dexamethasone from chitosan–carbon nanotube films, Sensors and Actuators A, Vol.155, No.1, (October 2009), pp. 120–124, ISSN 0924-4247

O'Connell, M. J.; Boul, P.; Ericson, L. M.; Huffman, C.; Wang, Y.; Haroz, E.; Kuper, C.; Tour, J.; Ausman, K. D. & Smalley, R. E. (2001). Reversible water-solubilization of single-walled carbon nanotubes by polymer wrapping, Chem. Phys. Lett., Vol.342, No.3-4, (July 2001), pp. 265-271, ISSN 0009-2614

Ozarkar, S. Jassa, M. Agrawal, A. K. (2008). pH and electrical actuation of single walled carbon nanotube/chitosan composite fibers, Smart Mater. Struct., Vol.17, No.5, (October 2008), pp. 055016.1-055016.8, ISSN 0964-1726

Panhuis, M.; Heurtematte, A.; Small, W. R. & Paunov, V. N. (2007). Inkjet Printed Water Sensitive Transparent Films from Natural Gum-Carbon Nanotube Composites. Soft Matter, (April 2007), Vol.3, No.7, pp. 840–843, ISSN 1744-683X

Pantarotto, D.; Partidos, C. D.; Graff, R.; Hoebeke, J.; Briand, J. P.; Prato, M. & Bianco, A. (2003). Synthesis, Structural characterization and immunological properties of carbon nanotubes functionalized with peptides. J Am Chem Soc, Vol.125, No.20, (May 2003), 6160-6164, ISSN 0002-7863

Pantarotto, D.; Partidos, C. D.; Hoebeke, J.; Brown, F.; Kramer, E.; Briand, J. P.; Muller, S.; Prato, M. & Bianco, A. (2003) Immunization with peptide-functionalized carbon nanotubes enhances virusspecific neutralizing antibody responses, Chem Biol, Vol.10, No.10, (October 2003), pp. 961-966, ISSN 1074-5521

Pantarotto, D.; Briand, J. P.; Prato, M. & Bianco, A. (2004). Translocation of bioactive peptides across cell membranes by carbon nanotubes, Chem. Commun., No.1, (January 2004), pp. 16–17, ISSN 1359-7345

Rai, P. K.; Pinnick, R. A.; Parra-Vasquez, A G.; Davis, V. A.; Schmidt, H. K.; Hauge, R. H.; Smalley, R. E. & Pasquali, M. (2006). Isotropic-Nematic Phase Transition of Single-Walled Carbon Nanotubes in Strong Acids, J. Am. Chem. Soc., Vol.128, No.2, (January 2006), pp. 591-595, ISSN 0002-7863

Richard, C.; Balavoine, F.; Schultz, P.; Ebbesen, T. W. & Mioskowski, C. (2003) Supramolecular self-assembly of lipid derivatives on carbon nanotubes, Science, Vol.300, No.5620, (May 2003) pp. 775-778, ISSN 0036-8075

Rinaudo, M. (2006) Chitin and chitosan : Properties and applications, Progress in polymer science, (July 2006), Vol.31, No.7, pp. 603-632, ISSN 0079-6700

Robinson, J. A.; Snow, E. S.; Badescu, S. C.; Reinecke, T. L. & Perkins, F. K. (2006). Role of Defects in Single-Walled Carbon Nanotube Chemical Sensors, Nano Letters, Vol.6, No.8, (August 2006), pp. 1747-1751, ISSN 1530-6984

Safadi, B.; Andrews, R. & Grulke, E. A. (2002). Multiwalled Carbon Nanotube Polymer Composites: Synthesis and Characterization of Thin Films, J. Appl. Polym. Sci. Vol.84, No.14, (June 2002), pp. 2660–2669, ISSN 0021-8995

Salvador-Morales, C.; Flahaut, E.; Sim, E.; Sloan, J.; Green, M. L. H. & Sim, R. B. (2006). Complement activation and protein adsorption by carbon nanotubes, Mol Immunol, Vol.43, No.3, (February 2006), pp. 193-201, ISSN 0161-5890

Shamos, M. H. & Lavine, L. S. (1967). Piezoelectricity as a Fundamental Property of Biological Tissues, Nature, Vol.213, No. 1967, pp. 267-269, ISSN 0028-0836

Shtogun, Y. V.; Woods, L. M. & Dovbeshko, G. I. (2007) Adsorption of Adenine and Thymine and Their Radicals on Single-Wall Carbon Nanotubes, J. Phys. Chem. C, Vol.111, No.49, (December 2007), 18174–18181, ISSN 0002-7863

Song, W. H.; Kinloch, I. A. & Windle, A. H. (2003) Nematic Liquid Crystallinity of Multiwall Carbon Nanotubes. Science, Vol.302, No.5649, (November 2003), pp. 1363 ISSN 0036-8075

Star, A.; Steuerman, D. W.; Heath, J. R. & Stoddart, J. F. (2002). Starched Carbon Nanotubes, Angew. Chem., Int. Ed., (July 2002), Vol.41, No.14, pp. 2508-2512, ISSN 1433-7851

Tang, X.; Bansaruntip, S.; Nakayama, N.; Yenilmez, E.; Chang, Y. & Wang, Q. (2006). Carbon Nanotube DNA Sensor and Sensing Mechanism, Nano Letters, Vol.6, No.8, (August 2006), 1632-1636, ISSN 1530-6984

Tanaka, T.; Jin, H. H.; Miyata, Y.; Fuji, S.; Suga, H.; Naitoh, Y.; Minari, T.; Miyadera, T.; Tsukagoshi, K. & Kataura, H. (2009). Simple and Scalable Gel-Based Separation of Metallic and Semiconducting Carbon Nanotubes, Nano Lett., Vol.9, No.4, (April 2009), 1497-1500, ISSN 1530-6984

Tanaka, T.; Jin, H. H.; Miyata, Y.; Fuji, S.; Nishide, D. & Kataura, H. (2009) Mass separation of metallic and semiconducting single-wall carbon nanotubes using agarose gel, Phys. Status Solidi B, Vol.246, No.11–12, (December 2009) pp. 2490–2493 ISSN 0370-1972

Tanaka, T.; Urabe, Y.; Nishide, D.; Liu, H.; Asano, S.; Nishiyama, S. (2010) Kataura, H. (2010). Metal/semiconductor separation of single-wall carbon nanotubes by selective adsorption and desorption for agarose gel, Phys. Status Solidi B Vol.247, No.11–12, (December 2010), pp. 2867–2870, ISSN 0370-1972

Tasis, D.; Tagmatarchis, N.; Bianco, A. & Prato, M. (2006) Chemistry of carbon nanotubes, Chem. Rev., Vol.106, No.3, (March 2006) pp. 1105-1136 ISSN 0009-2665

Thompson, B. C.; Moulton, S. E.; Gilmore, K. J.; Higgins, M. J.; Whitten, P. G. & Wallace, G. G. (2009). Carbon nanotube biogels, Carbon, (April 2009), Vol.47, No.5, pp. 1282 – 1291, ISSN 0008-6223

Tsai, Y.; Chena, S. & Liaw, H. (2007). Immobilization of lactate dehydrogenase within multiwalled carbon nanotube-chitosan nanocomposite for application to lactate biosensors, Sensors and Actuators B, Vol.125, No.2, (August 2007), pp. 474-481, ISSN 0925-4005

Tu, X.; Manohar, S.; Jagota, A. & M. Zheng, (2009). DNA sequence motifs for structure-specific recognition and separation of carbon nanotubes, Nature, Vol.460, No.7252, (July 2009), pp. 250-253, ISSN 0028-0836

Vigolo, B.; Penicaud, A.; Coulon, C.; Sauder, C.; Pailler, R.; Journet, C.; Bernier, P. & Poulin, P. (2000). Macroscopic Fibers and Ribbons of Oriented Carbon Nanotubes, Science, Vol.290, No.5495, (November 2000), pp. 1331–1334, ISSN 0036-8075

Wang, S. F.; Shen, L.; Zhang, W. D. & Tong, Y. J. (2005). Preparation and mechanical properties of chitosan/carbon nanotubes composites, Biomacromolecules, Vol.6, No.6, (November 2005), pp. 3067–72, ISSN 1525-7797

Whitten, P. G.; Gestos, A. A.; Spinks, G. M.; Gilmore, K. J. & Wallace, G. G. (2007) Free standing carbon nanotube composite bio-electrodes, Journal of Biomedical Materials Research Part B, Vol.82, No.1, (July 2007), pp. 37–43, ISSN 1552-4973

Walther, J. H.; Jaffe,R.; Halicioglu,T.& Koumoutsakos, P. (2001) Carbon nanotubes in water: structural characteristics and energetics, J. Phys. Chem. B, Vol.105, No.41, (October 2001), pp. 9980- 9987, ISSN 1520-6106

Wu, T.; Chen, E. (2006). Crystallization Behavior of Poly(e-caprolactone)/Multiwalled Carbon Nanotube Composites, Journal of Polymer Science: Part B: Polymer Physics, Vol.44, No.3, (February 2006), pp. 598–606, ISSN 0887-6266

Xiao, L. Chen, Z. Feng, C. Liu, L. Bai, Z. Q. Wang, Y. Qian, L. Zhang, Y. Li, Q. Jiang, K. Fan, S. S. (2008). Flexible, Stretchable, Transparent Carbon Nanotube Thin Film

Loudspeakers, Nano Lett., Vol.8, No.12, (December 2008), pp. 4539-4545, ISSN 1530-6984

Xie, Y. H.; Soh, A. K. (2005) Investigation of non-covalent association of single-walled carbon nanotube with amylose by molecular dynamics simulation, Materials Letters, Vol.59, No.8/9, (April 2005) pp. 971-975, ISSN 0167-577X

Yamashiro, T. (1989). Measurement of Piezoelectric Constants of a Crab Shell, Japanese Journal of Applied Physics, Vol.28, No.11, November 1989, 2327 -2328, ISSN 0021-4922

Yang, H.; Wang, S. C.; Mercier, P. & Akins, D. L. (2006). Diameter-selective dispersion of single-walled carbon nanotubes using a water-soluble, biocompatible polymer, Chem. Commun., Vol.45, No.13, (April 2006), 1425–1427, ISSN 1359-7345

Yun, S. I.; Gadd, G. E.; Latella, B. A.; Lo, V.; Russell, R. A.; Holden, P. J.; Yun, S. I.; Gadd, G. E.; Latella, B. A.; Lo, V.; Russell, R. A. & Holden, P. J. (2008). Mechanical Properties of Biodegradable Polyhydroxyalkanoates/Single Wall Carbon Nanotube Nanocomposite Films, Polymer Bulletin, Vol.61, No.2, (August 2008), pp. 267–275, ISSN 0170-0839

Yun, S.; Kim, J. (2007) A bending electro-active paper actuator made by mixing multi-walled carbon nanotubes and cellulose, Smart Mater. Struct., Vol.16, No.4, (August 2007), pp. 1471-1476, ISSN 0964-1726

Zamora-Ledezma, C.; Blanc, C.; Maugey, M.; Zakri, C.; Poulin, P. & Anglaret, E. (2008). Anisotropic Thin Films of Single-Wall Carbon Nanotubes from Aligned Lyotropic Nematic Suspensions, Nano Lett., Vol.8, No.12, (December 2008), 4103–4107, ISSN 1530-6984

Zhang, J. P.; Wang, Q.; Wang, L. & Wang, A. (2007). Manipulated dispersion of carbon nanotubes with derivatives of chitosan, Carbon, Vol.45 No.9 (May 2007), pp. 1911–1920, ISSN 0008-6223

Zhang, S. J.; Kinloch, I. A. & Windle, A. H. (2006). Mesogenicity Drives Fractionation in Lyotropic Aqueous Suspensions of Multiwall Carbon Nanotubes, Nano Lett., Vol.6, No.3, (March 2006), pp. 568-572, ISSN 1530-6984

Zhang, M.; Smith, A. & Gorski, W. (2004). Carbon Nanotube-Chitosan System for Electrochemical Sensing Based on Dehydrogenase Enzymes, Anal. Chem., Vol.76, No.17, (September 2004), pp. 5045-5050, ISSN 0003-2700

Zhao, Y. L.; Stoddart, J. F. (2009) Noncovalent Functionalization of Single-Walled Carbon Nanotubes, Accounts of chemical research, Vol.42, No.8, (August 2009), pp. 1161-1171, ISSN 0001-4842

Zheng, M.; Jagota, A.; Semke, E. D.; Diner, B. A.; Mclean, R. S.; Lusting, S. R.; Richardson, R. E. & Tassi, N. G. (2003). DNA-assisted dispersion and separation of carbon nanotubes, Nat. Mater., Vol.2., No.5, (May 2003), pp. 338-342, ISSN 1476-1122

Zilberstein, R. M. (1972). Piezoelectric Activity in Invertebrate Exoskeletons, Nature, Vol.235, No.5334, (January 1972), pp. 174–175, ISSN 0028-0836

3

Elastic Properties of Carbon Nanotubes

Qiang Han and Hao Xin
School of Civil Engineering and Transportation
South China University of Technology
Guangzhou
People's Republic of China

1. Introduction

The geometric structure of carbon nanotubes (CNTs) can be considered to be the curling of graphene (graphite sheet) (Gao & Li, 2003; Shen, 2004). The physical parameters of carbon in graphite are widely adopted in the molecule dynamics (MD) simulations or other theoretical studies of CNTs, such as the bond energy and length of C-C, the bond angle of C-C-C, etc (Belytschko et al., 2002; Mayo et al., 1990; Xin et al., 2007, 2008). Previous researches have shown that the elastic modulus of small CNTs changes a lot when the radius varies. However, the elastic modulus of CNTs fairly approaches that of graphene, while the radius of CNTs is large enough. Therefore, it is necessary to have a clear understanding of the mechanical properties of graphene for the further realization of the properties of CNTs.

Numerous researchers carried out experiments to measure the effective elastic modulus of CNTs (Krishnan et al.,1998; Poncharal et al., 1999). They reported the effective Young's modulus of CNTs ranging from 0.1 to 1.7 TPa, decreasing as the diameter increased, and the average was about 1.0~1.2 TPa. MD simulations have provided abundant results for the understanding of the buckling behavior of CNTs. The Young's modulus of the CNTs was predicted about 1.0~1.2 TPa through various MD methods (Jin & Yuan, 2003; Li & Chou, 2003; Lu, 1997). Hu et al. (Hu et al., 2007) proposed an improved molecular structural mechanics method for the buckling analysis of CNTs, based on Li and Chou's model (Hwang et al., 2010) and Tersoff-Brenner potential (Brenner, 1990). Due to the different methods employed on various CNTs in these researches, the reported data scattered around an average of 1.0 TPa.

The elastic properties were also discussed in the theoretical analysis by Govinjee and Sackman (Govinjee and Sackman, 1999) based on Euler beam theory, which showed the size dependency of the elastic properties at the nanoscale, which does not occur at continuum scale. Harik (Harik, 2001) further proposed three non-dimensional parameters to validate the beam assumption, and the results showed that the beam model is only proper for CNTs with small radius. Liu et al (Liu et al., 2001) reported the decrease of the elastic modulus of CNTs with increase in the tube diameter. Shell model was also used in some researches (Wang et al., 2003), to study axially compressed buckling of multi-walled CNTs. And studies by Sudak (Sudak, 2003) reported that the scale effect of CNTs should not be ignored. Wang et al (Wang et al., 2006) investigated the buckling of CNTs and the results showed that the critical buckling load drawn with the classical continuum theory is higher than that

with considering the scale effect. There are some other researches also reporting clear scale effect on the vibration of CNTs (Wang & Varadan, 2007; Zhang et al., 2005). Li and Chou (Li & Chou, 2003) put forward a truss model for CNTs and their studies showed the radius-dependence of elastic modulus of SWCNTs. Finite element analysis (FEA) is also employed in researches on the mechanical properties of CNTs (Yao & Han, 2007, 2008; Yao et al., 2008). An equivalent model is established in this chapter, based on the basic principles of the anisotropic elasticity and composite mechanics, for the analysis of the elastic properties of graphite sheet at the nanometer scale. With this equivalent model, the relationship between the nanotube structure and the graphite sheet is built up, and the radial scale effect of the elastic properties of CNTs is investigated.

2. Constitutive equations of orthotropic system

The essential difference between the basic equations of anisotropic materials and those of isotropic ones is in their constitutive equations, which means the usage of the anisotropy Hooke law for the anisotropic constitutive equation and the isotropy one for the other. The phenomenon reflected from the anisotropy equations is more accurate than from the isotropy ones, though this distinction also makes the calculation with the anisotropy equations much more complicated.

One of the anisotropic systems, with three mutually perpendicular principal axes of elasticity, is called an orthotropic system (Fig. 1). If the three principal axes of elasticity are defined as x_1, x_2 and x_3, the constitutive equation of orthotropic system can be obtained as follow,

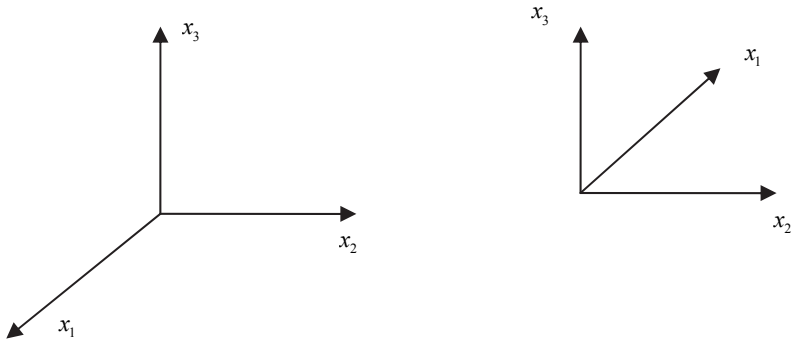

Fig. 1. The principal elastic axes of orthotropic system: a) right-hand coordinate system; b) left-hand coordinate system

$$\begin{Bmatrix} \varepsilon_1 \\ \varepsilon_2 \\ \varepsilon_3 \\ \varepsilon_4 \\ \varepsilon_5 \\ \varepsilon_6 \end{Bmatrix} = \begin{bmatrix} S_{11} & S_{12} & S_{13} & & & \\ S_{12} & S_{22} & S_{23} & & & \\ S_{13} & S_{23} & S_{33} & & & \\ & & & S_{44} & & \\ & & & & S_{55} & \\ & & & & & S_{66} \end{bmatrix} \begin{Bmatrix} \sigma_1 \\ \sigma_2 \\ \sigma_3 \\ \sigma_4 \\ \sigma_5 \\ \sigma_6 \end{Bmatrix} \tag{1}$$

And the inverse function of the equation (1) is,

$$\begin{Bmatrix} \sigma_1 \\ \sigma_2 \\ \sigma_3 \\ \tau_{23} \\ \tau_{31} \\ \tau_{12} \end{Bmatrix} = \begin{bmatrix} C_{11} & C_{12} & C_{13} & & & \\ C_{12} & C_{22} & C_{23} & & & \\ C_{13} & C_{23} & C_{33} & & & \\ & & & C_{44} & & \\ & & & & C_{55} & \\ & & & & & C_{66} \end{bmatrix} \begin{Bmatrix} \varepsilon_1 \\ \varepsilon_2 \\ \varepsilon_3 \\ \gamma_{23} \\ \gamma_{31} \\ \gamma_{12} \end{Bmatrix} \tag{2}$$

where,

$$\begin{cases} S_{\substack{11 \\ 22 \\ 33}} = (C_{\substack{22 \\ 33 \\ 11}} C_{\substack{33 \\ 11 \\ 22}} - C^2_{\substack{23 \\ 31 \\ 12}}) / C \\ S_{\substack{23 \\ 31 \\ 12}} = (C_{\substack{21 \\ 32 \\ 13}} C_{\substack{31 \\ 12 \\ 23}} - C_{\substack{23 \\ 31 \\ 12}} C_{\substack{11 \\ 22 \\ 33}}) / C \\ S_{\substack{44 \\ 55 \\ 66}} = 1 / C_{\substack{44 \\ 55 \\ 66}} \\ C = C_{11}C_{22}C_{33} - C_{11}C^2_{23} - C_{22}C^2_{31} - C_{33}C^2_{12} + 2C_{12}C_{23}C_{31} \end{cases} \tag{3}$$

Equation (3) is also correct if we make exchanges of C for S and S for C.

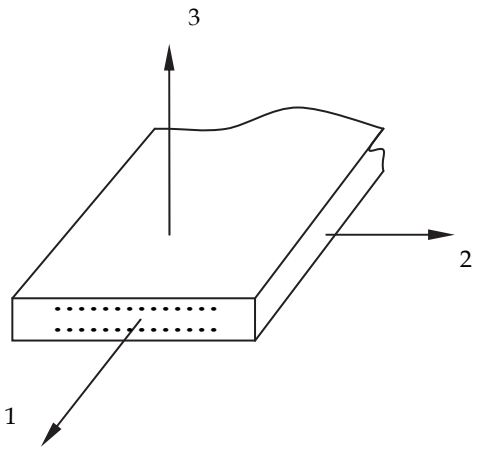

Fig. 2. Sketch of macroscopic homogeneous orthotropic material

The unidirectional fiber composed composite materials can be treated as orthotropic systems, for which the three axes in the right-handed coordinate system in Fig. 2 are the principal material axes and the axis 1 is along the fiber length. Thus, the components of equation (1) can be given minutely in detail,

$$
\begin{aligned}
\varepsilon_1 &= S_{11}\sigma_1 + S_{12}\sigma_2 + S_{13}\sigma_3 = \frac{1}{E_1}\sigma_1 - \frac{\nu_{12}}{E_2}\sigma_2 - \frac{\nu_{13}}{E_3}\sigma_3 \\
\varepsilon_2 &= S_{21}\sigma_1 + S_{22}\sigma_2 + S_{23}\sigma_3 = -\frac{\nu_{21}}{E_1}\sigma_1 + \frac{1}{E_2}\sigma_2 - \frac{\nu_{23}}{E_3}\sigma_3 \\
\varepsilon_3 &= S_{31}\sigma_1 + S_{32}\sigma_2 + S_{33}\sigma_3 = -\frac{\nu_{31}}{E_1}\sigma_1 - \frac{\nu_{32}}{E_2}\sigma_2 + \frac{1}{E_3}\sigma_3 \\
\gamma_{23} &= S_{44}\tau_{23} = \frac{1}{G_{23}}\tau_{23} \\
\gamma_{31} &= S_{55}\tau_{31} = \frac{1}{G_{31}}\tau_{31} \\
\gamma_{12} &= S_{66}\tau_{12} = \frac{1}{G_{12}}\tau_{12}
\end{aligned}
\tag{4}
$$

where,

$$
\begin{cases}
S_{ij} = S_{ji} \\
\dfrac{\nu_{ij}}{E_j} = \dfrac{\nu_{ji}}{E_i}
\end{cases}
\tag{5}
$$

3. Macro-mechanics fundamental principle of composite material

3.1 Constitutive equations of monolayer under plane stress

The monolayer composite with unidirectional fiber can be considered as a homogeneous orthotropic material in the macro analysis. Fig. 3 displays the three principal material axes and the axis 3 is perpendicular to the mid-plane of the monolayer. Suppose the monolayer is in a plane stress state, there are the in-plane stresses,

$$
\sigma_1, \quad \sigma_2, \quad \tau_{12}(\sigma_6) \tag{6}
$$

and the out-plane stresses,

$$
\sigma_3 = \tau_{23}(\sigma_4) = \tau_{13}(\sigma_5) = 0 \tag{7}
$$

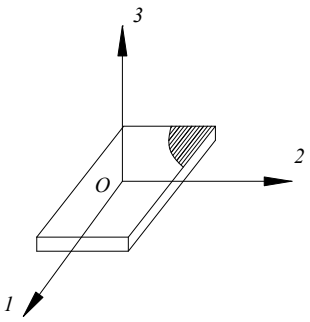

Fig. 3. Sketch of monolayer composite with unidirectional fiber

Thus, the constitutive equation (1) can be given in two parts as follows,

$$\begin{aligned} &\varepsilon_3 = S_{31}\sigma_1 + S_{32}\sigma_2 = -\frac{\nu_{31}}{E_1}\sigma_1 - \frac{\nu_{32}}{E_2}\sigma_2 \\ &\gamma_{23} = 0, \quad \gamma_{31} = 0 \end{aligned} \tag{8}$$

$$\begin{aligned} &\varepsilon_1 = S_{11}\sigma_1 + S_{12}\sigma_2 = \frac{1}{E_1}\sigma_1 - \frac{\nu_{12}}{E_2}\sigma_2 \\ &\varepsilon_2 = S_{21}\sigma_1 + S_{22}\sigma_2 = -\frac{\nu_{21}}{E_1}\sigma_1 + \frac{1}{E_2}\sigma_2 \\ &\gamma_{12} = S_{66}\tau_{12} = \frac{1}{G_{12}}\tau_{12} \end{aligned} \tag{9}$$

The equation (8) is for the out-plane strain and the equation (9) for the in-plane strain. And the equation (9) can also be written in a matrix form,

$$\begin{Bmatrix} \varepsilon_1 \\ \varepsilon_2 \\ \gamma_{12} \end{Bmatrix} = \begin{bmatrix} S_{11} & S_{12} & 0 \\ S_{21} & S_{22} & 0 \\ 0 & 0 & S_{66} \end{bmatrix} \begin{Bmatrix} \sigma_1 \\ \sigma_2 \\ \tau_{12} \end{Bmatrix} \text{ or } \left\{\varepsilon^1\right\} = [S]\left\{\sigma^1\right\} \tag{10}$$

where $[S]$ is the axis flexibility matrix. The equation (10) can also be given as,

$$\begin{Bmatrix} \varepsilon_1 \\ \varepsilon_2 \\ \gamma_{12} \end{Bmatrix} = \begin{bmatrix} \frac{1}{E_1} & -\frac{\nu_{12}}{E_2} & 0 \\ -\frac{\nu_{21}}{E_1} & \frac{1}{E_2} & 0 \\ 0 & 0 & \frac{1}{G_{12}} \end{bmatrix} \begin{Bmatrix} \sigma_1 \\ \sigma_2 \\ \tau_{12} \end{Bmatrix} \tag{11}$$

The inverse of the equation (10) is available,

$$\begin{Bmatrix} \sigma_1 \\ \sigma_2 \\ \tau_{12} \end{Bmatrix} = \begin{bmatrix} Q_{11} & Q_{12} & 0 \\ Q_{21} & Q_{22} & 0 \\ 0 & 0 & Q_{66} \end{bmatrix} \begin{Bmatrix} \varepsilon_1 \\ \varepsilon_2 \\ \gamma_{12} \end{Bmatrix} \text{ or } \left\{\sigma^1\right\} = [Q]\left\{\varepsilon^1\right\} \tag{12}$$

where $[Q]$ is the converted axis stiffness matrix at the plane stress state. Q_{ij} in equation (12) and C_{ij} in equation (2) have the following relations,

$$\begin{aligned} &Q_{11} = C_{11} - C_{13}C_{13} / C_{33} \\ &\underset{22}{\overset{12}{}} \quad \underset{22}{\overset{12}{}} \quad \underset{23}{\overset{13}{}} \quad \underset{23}{\overset{23}{}} \\ &Q_{66} = C_{66} \end{aligned} \tag{13}$$

The values of the flexibility and stiffness in equation (11) and equation (13) can be obtained through micromechanics calculations or experiments.

3.2 Off-axis flexibility and stiffness of monolayer under plane stress

The off-axis flexibility and stiffness are often used in the mechanical analysis on the unidirectional fiber monolayer. As displayed in Fig. 4, axes 1 and 2 are along the principal axes of material, x and y are off-axis, and the anticlockwise angle from x-axis to the 1-axis is positive. Thus, we obtain,

$$\begin{Bmatrix}\sigma_1\\ \sigma_2\\ \tau_{12}\end{Bmatrix}^x = \begin{bmatrix}\cos^2\theta & \sin^2\theta & -2\sin\theta\cos\theta\\ \sin^2\theta & \cos^2\theta & 2\sin\theta\cos\theta\\ \sin\theta\cos\theta & -\sin\theta\cos\theta & \cos^2\theta-\sin^2\theta\end{bmatrix}\begin{Bmatrix}\sigma_1\\ \sigma_2\\ \tau_{12}\end{Bmatrix}^1 \quad \text{or} \quad \{\sigma^x\}=[T]\{\sigma^1\} \tag{14}$$

and

$$\begin{Bmatrix}\sigma_1\\ \sigma_2\\ \tau_{12}\end{Bmatrix}^1 = \begin{bmatrix}\cos^2\theta & \sin^2\theta & 2\sin\theta\cos\theta\\ \sin^2\theta & \cos^2\theta & -2\sin\theta\cos\theta\\ -\sin\theta\cos\theta & \sin\theta\cos\theta & \cos^2\theta-\sin^2\theta\end{bmatrix}\begin{Bmatrix}\sigma_1\\ \sigma_2\\ \tau_{12}\end{Bmatrix}^x \quad \text{or} \quad \{\sigma^1\}=[T]^{-1}\{\sigma^x\} \tag{15}$$

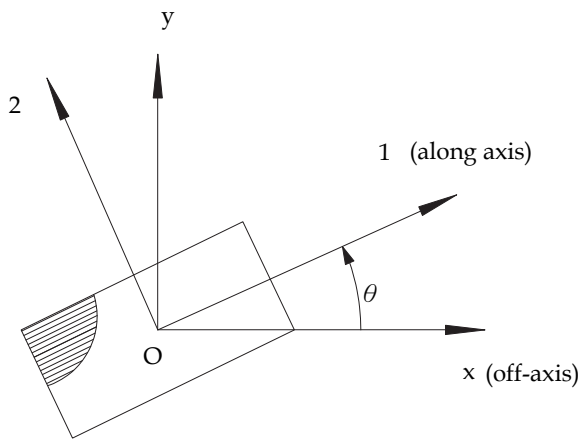

Fig. 4. Sketch of coordinate transformation between the axis and off-axis of monolayer with unidirectional fibers

If, we set,

$$[R]=\begin{bmatrix}1 & & \\ & 1 & \\ & & 2\end{bmatrix} \tag{16}$$

$$[F]=[R][T][R]^{-1}\begin{bmatrix}\cos^2\theta & \sin^2\theta & -\sin\theta\cos\theta\\ \sin^2\theta & \cos^2\theta & \sin\theta\cos\theta\\ 2\sin\theta\cos\theta & -2\sin\theta\cos\theta & \cos^2\theta-\sin^2\theta\end{bmatrix} \tag{17}$$

the follow can be obtained,

$$\{\varepsilon^x\}=[F]\{\varepsilon^1\} \tag{18}$$

It should be known from the equation (15) and (17) that,

$$[F]^T=[T]^{-1} \tag{19}$$

So that,

$$[F]^{-1}=[T]^T \tag{20}$$

Thus, the inverse function of the equation (18) is,

$$\{\varepsilon^1\}=[F]^{-1}\{\varepsilon^x\}=[T]^T\{\varepsilon^x\} \tag{21}$$

With these relations, the follows can be given,

$$\begin{gathered}\{\sigma^x\}=[T]\{\sigma^1\}=[T][Q]\{\varepsilon^1\}=[T][Q][T]^T\{\varepsilon^x\}\\ \text{or } \{\sigma^x\}=[\bar{Q}]\{\varepsilon^x\}\end{gathered} \tag{22}$$

and

$$\begin{gathered}\{\varepsilon^x\}=[F]\{\varepsilon^1\}=[F][S]\{\sigma^1\}=[F][S][T]^{-1}\{\sigma^x\}=[F][S][F]^T\{\sigma^x\}\\ \text{or } \{\varepsilon^x\}=[\bar{S}]\{\sigma^x\}\end{gathered} \tag{23}$$

The equation (22) and (23) are the constitutive equations in the Oxy coordinate system, where the off-axis stiffness $[\bar{S}]$ and the off-axis flexibility $[\bar{Q}]$ are given as follows,

$$[\bar{Q}]=\begin{bmatrix}\bar{Q}_{11} & \bar{Q}_{12} & \bar{Q}_{16}\\ \bar{Q}_{21} & \bar{Q}_{22} & \bar{Q}_{26}\\ \bar{Q}_{61} & \bar{Q}_{62} & \bar{Q}_{66}\end{bmatrix}=[T][Q][T]^T \tag{24}$$

$$[\bar{S}]=\begin{bmatrix}\bar{S}_{11} & \bar{S}_{12} & \bar{S}_{16}\\ \bar{S}_{21} & \bar{S}_{22} & \bar{S}_{26}\\ \bar{S}_{61} & \bar{S}_{62} & \bar{S}_{66}\end{bmatrix}==[F][S][F]^T \tag{25}$$

In the above two equations,

$$\bar{Q}_{ij} = \bar{Q}_{ji}, \quad \bar{S}_{ij} = \bar{S}_{ji} \tag{26}$$

The off-axis stiffness is,

$$\begin{aligned}
\bar{Q}_{11} &= Q_{11}\cos^4\theta + 2(Q_{12} + 2Q_{66})\sin^2\theta\cos^2\theta + Q_{22}\sin^4\theta \\
\underset{22}{\bar{Q}}_{12} &= \underset{66}{Q}_{12} + (Q_{11} + Q_{22} - 2Q_{12} - 4Q_{66})\sin^2\theta\cos^2\theta \\
\underset{26}{\bar{Q}}_{16} &= \pm(\underset{22}{Q}_{11} - Q_{12} - 2Q_{66})\sin\theta\cos^3\theta \mp (\underset{11}{Q}_{22} - Q_{12} - 2Q_{66})\sin^3\theta\cos\theta
\end{aligned} \tag{27}$$

And the off-axis flexibility,

$$\begin{aligned}
\bar{S}_{11} &= S_{11}\cos^4\theta + (2S_{12} + S_{66})\sin^2\theta\cos^2\theta + S_{22}\sin^4\theta \\
\bar{S}_{12} &= S_{12} + (S_{11} + S_{22} - 2S_{12} - S_{66})\sin^2\theta\cos^2\theta \\
\bar{S}_{66} &= S_{66} + 4(S_{11} + S_{22} - 2S_{12} - S_{66})\sin^2\theta\cos^2\theta \\
\underset{26}{\bar{S}}_{16} &= \pm(2\underset{22}{S}_{11} - 2S_{12} - S_{66})\sin\theta\cos^3\theta \mp (2\underset{11}{S}_{22} - 2S_{12} - S_{66})\sin^3\theta\cos\theta
\end{aligned} \tag{28}$$

3.3 Constitutive equations in classical laminated plate theory

The so-called classical laminated plate theory or the classical laminate theory, refers to the use of the straight normal hypothesis in elastic shell theory, neglects a number of secondary factors, and has been an acknowledged laminated plate theory. In the classical laminated plate theory, the transverse shear strain γ_{23} and γ_{31}, and the normal direction strain ε_3 are supposed to be zero.

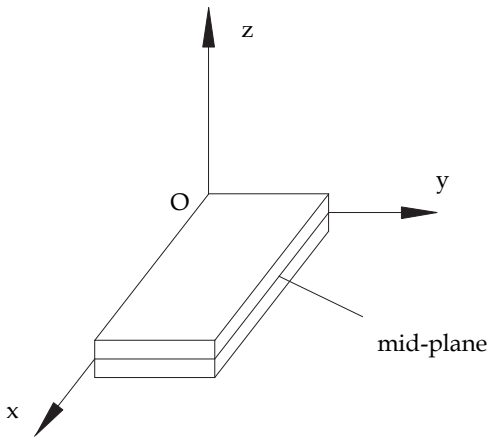

Fig. 5. Sketch of laminated thin plate and the Cartesian coordinates

As a result of straight normal assumption, the deformation of laminated plate can be described with the mid-plane deformation. If the mid-plane strain is ε^0 and thickness of

each layer in the laminated plate is the same, the mid-plane stress of an n-layers laminated plate is

$$\left\{\sigma^0\right\} = \frac{1}{n}\sum_{k=1}^{n}\left\{\sigma^{(k)}\right\} = \frac{1}{n}\sum_{k=1}^{n}\left(\left[\bar{Q}\right]^{(k)}\left\{\varepsilon^0\right\}\right) = \left[\frac{1}{n}\sum_{k=1}^{n}\left(\left[\bar{Q}\right]^{(k)}\right)\right]\cdot\left\{\varepsilon^0\right\} \tag{29}$$

where σ^0 is the mid-plane stress of the laminated plate, $\sigma^{(k)}$ is the stress of the *k*th layer, $\left[\bar{Q}\right]^{(k)}$ is the converted stiffness of the *k*th layer.

4. Equivalent model of graphite sheet

4.1 The basic idea of the equivalent model

All the C atoms in the graphite sheet are connected with the σ bonds and the bonds form a hexagonal structure (Fig.6). Fig. 7 is a schematic diagram of the graphite sheet, thick solid lines in which represent the C-C bond in graphite. If each C-C bond is longer (shown in thin lines), that will form a network structure, as shown in Fig. 8.

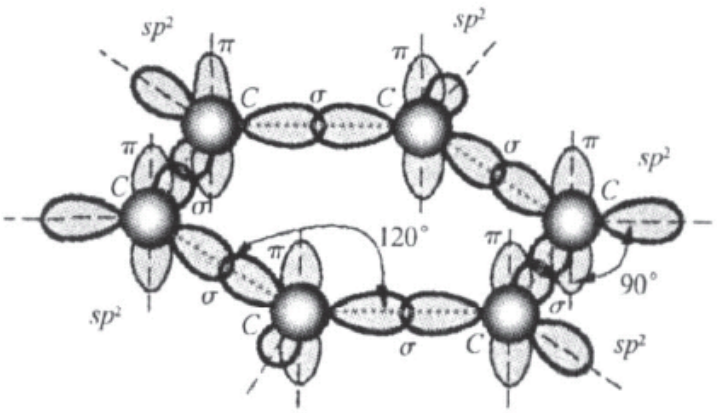

Fig. 6. The bonding relationship in C-C covalent bonds

As can be seen from Fig. 8, the network structure is formed by the three groups of parallel fibers and they are into 60 degree angles with each other. If we consider each group of fiber as a composite monolayer, the mechanical properties of the entire network structure can be obtained with the laminated plate theory. Comparing Fig. 7 and Fig. 8, we find that the network structure in Fig. 8 can also be formed if the three graphite sheets in Fig. 7 are staggered and stacked one on top of the other.

In summary, here we put forward a new original equivalent model used to study the mechanical properties of graphite sheet. The analysis steps are, treat the network structure shown in Fig. 8 as a laminated composite plate with three layers orthotropic monolayer of unidirectional fiber (each fiber in the monolayer is just the covalent C-C bond in series), the mechanical properties of fiber can be deduced from the physical parameters of graphite, and the 1/3 of the converted stiffness of the network structure can be considered as the converted stiffness of the graphite sheet at the plane stress state.

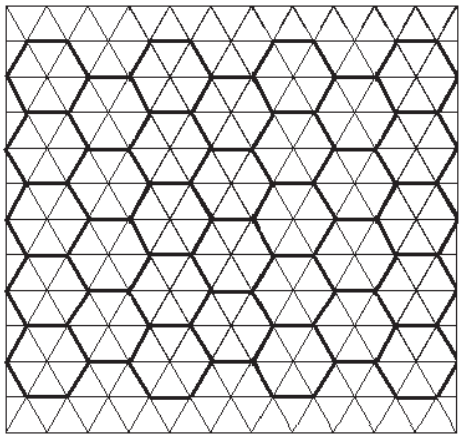

Fig. 7. The atomic structure of a graphite sheet

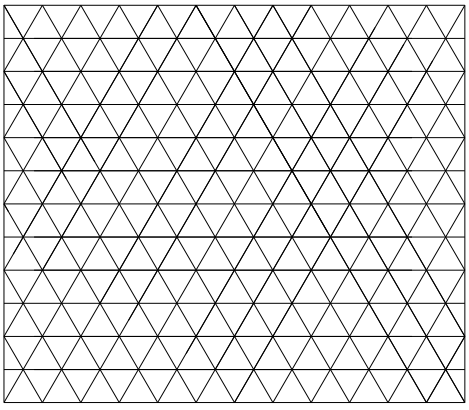

Fig. 8. Effective network structure of laminated graphite sheets

4.2 Mechanical properties of graphite sheet at plane stress state

The hexagonal plane composed of the σ bonds is defined as the σ-plane, and the energy of interactions between any C atoms in the σ-plane are considered to be functions of the position of the C atoms. With all the weak interactions (e.g. the electronic potential, the van der Waals interactions) neglected, the total potential energy of the graphite sheet can be expressed as.

$$U_{graphite} = U_r + U_\theta \tag{30}$$

where U_r is the axial stretching energy of C-C bond, U_θ is the C-C-C bond angle potential. Establish a local coordinate system in the σ-plane with the C-C bond direction as the x′ axis (Fig. 9), we can obtain the whole potential,

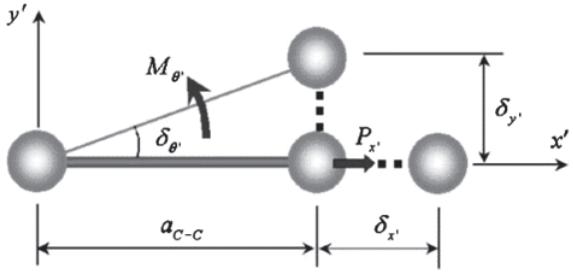

Fig. 9. Local element coordinates of C-C bond in graphite

$$U_{C-C} = U_{x'} + U_{\theta'} \tag{31}$$

where $U_{x'}$ is the axial stretching energy of C-C bond in the local coordinate system and $U_{\theta'}$ the angle bending energy. According to the basic principles of molecular mechanics, the two bond energy can be written as:.

$$\begin{aligned} U_{x'} &= \frac{1}{2} k_{x'} \cdot \delta_{x'}^2 \\ U_{\theta'} &= \frac{1}{2} k_{\theta'} \cdot \delta_{\theta'}^2 \end{aligned} \tag{32}$$

where $\delta_{x'}$ and $\delta_{\theta'}$ are the displacement, $k_{x'}$ and $k_{\theta'}$ are the MD force field constants.

4.3 Elastic constants of monolayer in the equivalent model

If we consider the C-C bond as a single elastic fiber in the equivalent model, and the 1 axis for the fiber is defined as the axial direction of the C-C bond, we have,

$$K_1 = k_{x'} \tag{33}$$

$$E_1 = \frac{K_1 \cdot a_{C-C}}{A_{C-C}} = \frac{k_{x'} \cdot a_{C-C}}{A_{C-C}} \tag{34}$$

where K_1 is the elastic stiffness factor of the fiber at the 1 direction, a_{C-C} and A_{C-C} are the C-C bond length and the cross-sectional area of the equivalent fiber, E_1 is the elastic modulus of the fiber at the 1 direction.

The 2 axis for the fiber is defined as the vertical direction of the C-C bond in the σ-plane. The fiber interactions at the 2 direction are mainly reflected through the C-C-C angle bending potential (Fig. 10).

Set K_2 to be the elastic stiffness factor of the fiber at the 2 direction, we obtain,

$$2 \cdot \left[2 \cdot \frac{1}{2} k_{\theta'} \cdot \delta_{\theta}^2 + \frac{1}{2} k_{\theta'} \cdot (2\delta_{\theta})^2 \right] = \frac{1}{2} K_2 \cdot \delta_2^2 = \frac{1}{2} K_2 \cdot (2 \cdot a_{C-C} \cdot \delta_{\theta} \cdot \sin\frac{\pi}{6})^2 \tag{35}$$

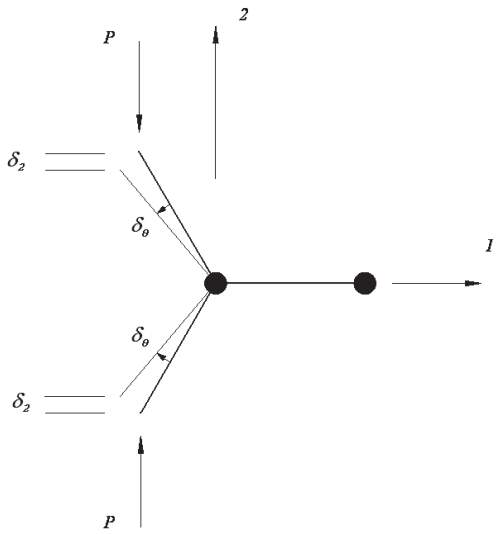

Fig. 10. Loading on the direction 2 of fiber in the equivalent model of graphite

$$K_2 = \frac{12 \cdot k_{\theta'}}{a_{C-C}^2} \tag{36}$$

$$E_2 = \frac{1}{2} \frac{K_2 \cdot \sqrt{3} \cdot a_{C-C}}{t \cdot (a_{C-C} + a_{C-C} \cdot \sin\frac{\pi}{6})} = \frac{\sqrt{3} K_2}{3t} = \frac{4\sqrt{3} k_{\theta'}}{3t \cdot a_{C-C}^2} \tag{37}$$

where δ_θ and δ_2 are the C-C-C angle change and the displacement at the 2 direction when the model is loaded at the 2 direction, t is the effective thickness of the equivalent fiber layer, E_2 is the elastic modulus of the fiber at the 2 direction.

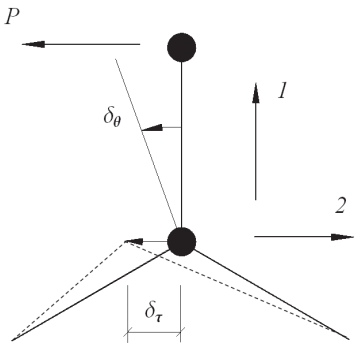

Fig. 11. Shearing deformation of the fiber in the equivalent model of graphite

When the fiber layer in the equivalent model is subjected to a shearing force P (Fig. 11), there will be a horizontal displacement δ_τ for the equivalent fiber element and an angle deflection δ_θ. As to the displacement of the bottom atom in of the figure, it can be obtained,

$$P = 2 \cdot [K_1 \cdot (\delta_\tau \cdot \cos\frac{\pi}{6})] = \sqrt{3} K_1 \delta_\tau \tag{38}$$

The strain energy induced by the angle deflection δ_θ of a fiber is,

$$2 \cdot (2 \cdot \frac{1}{2} k_{\theta'} \cdot \delta_\theta^2) = \frac{1}{2} P \cdot a_{C-C} \cdot \delta_\theta \tag{39}$$

Substitute equation (38) into (39), we obtain,

$$a_{C-C} \cdot \delta_\theta = \frac{\sqrt{3} K_1 \delta_\tau \cdot a_{C-C}^2}{4 k_{\theta'}} = \frac{\sqrt{3} K_1}{K_2 / 3} \delta_\tau \tag{40}$$

Therefore, the shearing deformation of the fiber element in the equivalent model is,

$$\bar{\delta}_\tau = \delta_\tau + a_{C-C} \cdot \delta_\theta = (1 + \frac{3\sqrt{3} K_1}{K_2}) \delta_\tau \tag{41}$$

According to the definition of the elastic shear modulus:

$$G_{12} = \frac{\tau_{12}}{\gamma_{12}} \tag{42}$$

for the fiber element in the equivalent model, there is:.

$$G_{12} = \frac{P / (t \cdot 2 \cdot a_{C-C} \cdot \cos\frac{\pi}{6})}{\frac{1}{2} \bar{\delta}_\tau / a_{C-C}} = \frac{2P}{\sqrt{3} \bar{\delta}_\tau \cdot t} \tag{43}$$

We substitute equation (38) and (41) into (43), and get

$$G_{12} = \frac{2 K_1 \delta_\tau}{t \bar{\delta}_\tau} = \frac{2 K_1}{t (1 + \frac{3\sqrt{3} K_1}{K_2})} \tag{44}$$

4.4 Test for the mechanical constants of the monolayer in the equivalent model

From equation (34), (37) and (44), we obtain the mechanical constants of the monolayer in the equivalent model E_1, E_2 and G_{12}, of which E_1 and E_2 are independent quantities, G_{12} is a function of E_1 and E_2. Both E_1 and E_2 are related to MD parameters of the C-C bond energy There are several empirical potentials and relevant parameters for C-C bond energy. In this section, the following potential energy function and parameters are used to verify the equivalent model provided in this chapter. The Morse potential is employed for the bond

stretching action and harmonic potential for the angle bending. The short-range potential caused by the deformation of C-C bond is described as bellow,

$$U_r = K_r(1 - e^{-\beta(r_{ij} - r_0)})^2 \tag{45}$$

$$U_\theta = \frac{1}{2}K_\theta(\theta_{ijk} - \theta_0)^2 \tag{46}$$

where U_r and U_θ are the potentials of bond stretching and angle bending, K_r and K_r are the corresponding force constants. r_{ij} represents the distance between any couple of bonded atoms, θ_{ijk} represents all the possible angles of bending, r_0 and θ_0 are the corresponding reference geometry parameters of grapheme. β defines the steepness of the Morse well. The values of all these parameters are listed in Table 1.

Bond	$K_r = 478.9\text{KJ/mol}$ ， $\beta = 21.867\text{nm}^{-1}$ ， $r_0 = 0.142\text{nm}$
Angle	$K_\theta = 418.4\text{KJ/mol}$ ， $\theta_0 = 120.00^o$

Table 1. Parameters for C-C bond in MD

Comparing equation (32) and (45), using the data in Table 1, we can obtain:

$$K_1 = k_{x'} = \beta^2 \cdot 2K_r = 760.4 \text{ nN/nm} \tag{47}$$

We substitute data in Table 1 into equation (36), and get

$$K_2 = \frac{12 \cdot k_{\theta'}}{a_{C-C}^2} = 413.48 \text{ nN/nm} \tag{48}$$

There are other scholars working on the C-C stretching force constants through experiments or theoretical calculations, who reported the values along the C-C bond like 729 nN/nm, 880 nN/nm, 708 nN/nm and so on. They also obtained the constants at the direction perpendicular to the C-C bond, 432 nN/nm and 398 nN/nm (Yang & Zeng, 2006). Noting equation (47) and (48), we can see that the data obtained here based on the current equivalent model are in good agreement with the results from other researchers.

5. Elastic properties of graphite sheet

5.1 Flexibility of monolayer in the equivalent model

Graphite sheet can be considered as the network structure formed by the three groups of parallel fibers which are into 60 degree angles with each other. Based on the result of the last section, we can get the axial flexibility of the fiber monolayer,

$$[S]^{(1)} = \begin{bmatrix} \frac{1}{E_1} & -\frac{\nu_{12}}{E_2} & 0 \\ -\frac{\nu_{21}}{E_1} & \frac{1}{E_2} & 0 \\ 0 & 0 & \frac{1}{G_{12}} \end{bmatrix} \tag{49}$$

where it has $\frac{\nu_{12}}{E_2} = \frac{\nu_{21}}{E_1}$. E_1, E_2 and G_{12} can be calculated according to the equation (34), (37) and (44). If we consider ν_{21} to be 0.3 with reference to the parameters of general materials, assume the fiber thickness of 0.34nm, and apply the data in Table 1, the follows can be calculated,

$$\begin{aligned} &E_1 = 1.190 \text{ TPa}, \quad E_2 = 0.702 \text{ TPa}, \quad G_{12} = 0.424 \text{ TPa} \\ &\frac{\nu_{12}}{E_2} = \frac{\nu_{21}}{E_1} = 0.252 \end{aligned} \tag{50}$$

Substituting the values in equation (50) into equation (49), we get the axis flexibility of the monolayer,

$$[S]^{(1)} = \begin{bmatrix} 0.8403 & -0.252 & 0 \\ -0.252 & 1.4245 & 0 \\ 0 & 0 & 2.360 \end{bmatrix} \tag{51}$$

where the unit of the values is 10^{-3} nm^2/nN .
Substituting $\theta = \pi / 3$ and the values in equation (51) into equation (28), we get the off-axis flexibility of the 60^o and -60^o monolayers,

$$\left[\bar{S}\right]^{(60^o)} = \begin{bmatrix} 1.2038 & -0.1743 & -0.3444 \\ -0.1743 & 0.9097 & -0.1650 \\ -0.3444 & -0.1650 & 2.6693 \end{bmatrix} \tag{52}$$

$$\left[\bar{S}\right]^{(-60^o)} = \begin{bmatrix} 1.2038 & -0.1743 & 0.3444 \\ -0.1743 & 0.9097 & 0.1650 \\ 0.3444 & 0.1650 & 2.6693 \end{bmatrix} \tag{53}$$

The unit of the values is also 10^{-3} nm^2/nN in the last two equations.

5.2 Elastic properties of the equivalent model of graphite

The graphite sheet is a whole layer structure with no delamination and the strain did not change in the thickness. Thus we can use formula (29) to calculate the stiffness,

$$\left[\bar{Q}\right] = \frac{1}{3}\sum_{k=1}^{3}\left[\bar{Q}\right]^{(k)} \tag{54}$$

where $\left[\bar{Q}\right]$ is the converted stiffness of the graphite sheet, $\left[\bar{Q}\right]^{(k)}$ is the stiffness of the kth layer in the equivalent model. The flexibility of the graphite sheet is,

$$\left[\bar{S}\right]=\left[\bar{Q}\right]^{-1}=3/\sum_{k=1}^{3}\left[\bar{Q}\right]^{(k)} \tag{55}$$

Substituting the values in equation (51) ~ (53) into (55), we can obtain,

$$\left[\bar{S}\right]=\frac{3}{\{[S]^{(1)}\}^{-1}+\{\left[\bar{S}\right]^{(60^{\circ})}\}^{-1}+\{\left[\bar{S}\right]^{(-60^{\circ})}\}^{-1}}=\begin{Bmatrix}1.0251 & -0.2063 & 0\\ -0.2063 & 1.0251 & 0\\ 0 & 0 & 2.4628\end{Bmatrix} \tag{56}$$

where the unit of the values is $10^{-3}\ \mathrm{nm}^2/\mathrm{nN}$.

A series of well acknowledged experiment values (Yang & Zeng, 2006) of elastic constants of perfect graphite are listed in Table 2. Data obtained in current work are in good agreement with those results, which justifies the present equivalent model. It should be noticed that there is an obvious error of the S_{12}. However, S_{12} has little effect on the mechanical properties of the graphite sheet, the error on it will not influence the reasonable application of the current equivalent model in the mechanics analysis of graphite.

Items	S_{11} / 10^{-3} nm^2/nN	S_{12} / 10^{-3} nm^2/nN	S_{66} / 10^{-3} nm^2/nN
Experiment	0.98	-0.16	2.28
Current	1.0251	-0.2063	2.4628
Error	4.60%	28.94%	8.02%

Table 2. Data obtained in current work and elastic constants of perfect graphite crystals from other experiment

Both the result in equation (56) and the data listed in Table 2 indicate that the graphite is in-plane isotropic at plane stress state. And according to the classical theory of composite mechanics, it is known that the π/m laminated plates with $m\geq 3$ are in-plane isotropic. We can see that the graphite sheets being in-plane isotropic is mainly due to their special structure of C-C-C angles.

According to the points made above, we try to explain why the elastic properties of CNTs are anisotropic to some extent. One of the possible reasons is that the curling at different curvature from graphene to CNTs makes the C-C-C angles change (e.g. the angles in an armchair CNT with 1nm diameter are not fixed 120^{o}, but about 118 ^{o}), for which the quasi-isotropy of graphite sheet is disrupted and the orthotropy introduced. Having an general realization of the CNTs, one should find that the change of the C-C-C angle is obviously related to the change of CNT radius, especially when it is a small tube in diameter. Thus, the

orthotropy of CNTs is diameter related, which is in good agreement with the other research results referring to the mechanical properties of CNTs changing due to their various radial size. The changes of C-C-C angles are also somehow related to the chirality of CNTs. However, the extent of the changes of chiral angles is about 0^o ~30^o, and the change of C-C-C induced by the difference of chiral angles is little when to curl the graphite sheet at the same curvature. It agrees with that many studies reporting that the difference of elastic properties among various chiral CNTs decreases with the increase in the diameter of CNTs.

5.3 Elastic properties of the equivalent model with various C-C-C bond angles

The C-C-C bond angles will change from the constant 120^o to smaller values when the graphite sheet curling to CNTs. In the same way, the angles between the fibers in the equivalent model will change to less than $\pi/3$ and the effect of the change on the elastic properties of the model will be investigated in this section.

Substituting equation (51) and the angle θ' between the fibers (responding to the changed C-C-C angles) into equation (28), we can obtain the off-axis flexibility of θ' and $-\theta'$ monolayers, $\left[\bar{S}\right]^{(\theta')}$ and $\left[\bar{S}\right]^{(-\theta')}$. Substitute those two into equation (55) to get the approximate converted flexibility of the equivalent model (responding to the changed C-C-C angles):

$$\left[\bar{S}_{\theta'}\right] = \frac{3}{\{[S]^{(1)}\}^{-1} + \{\left[\bar{S}\right]^{(\theta')}\}^{-1} + \{\left[\bar{S}\right]^{(-\theta')}\}^{-1}} \tag{57}$$

The elastic modulus of the equivalent model responding to the graphite with changed C-C-C angles, at the direction of 0^o fiber or at the vertical direction, can be obtained from equation (57). The variation of the modulus with the changes of the C-C-C angles are displayed in Fig. 12 and Fig. 13, and also displayed the variation of G_{12}, ν_{12} and ν_{21} in Fig.14~Fig.16.

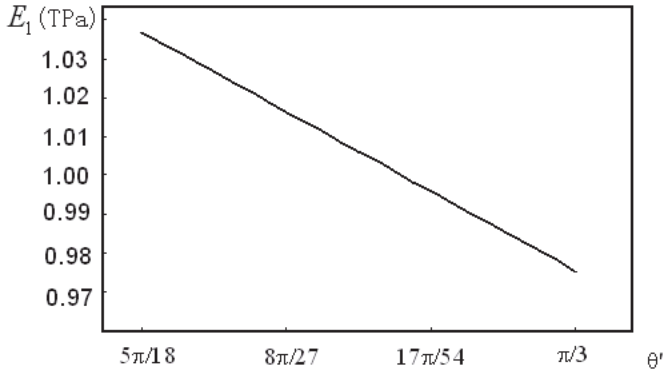

Fig. 12. Elastic modulus of the equivalent model of graphene along the 0^o fiber

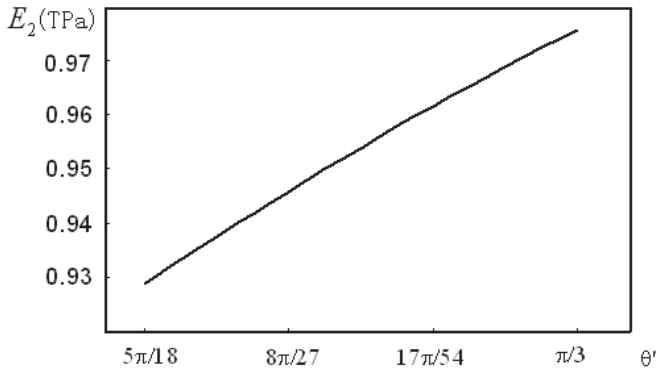

Fig. 13. Elastic modulus of the equivalent model of graphene at perpendicular direction to the 0^o fiber

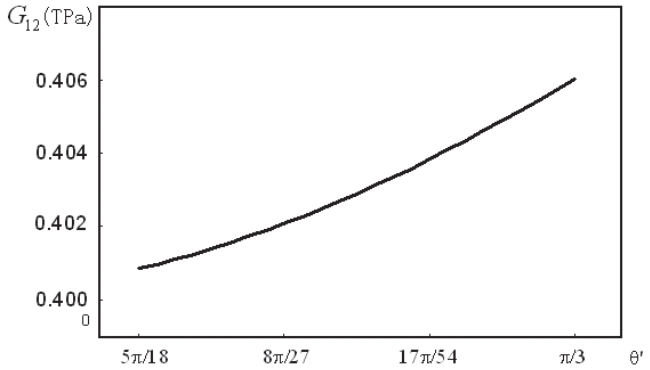

Fig. 14. G_{12} of the equivalent model of graphene

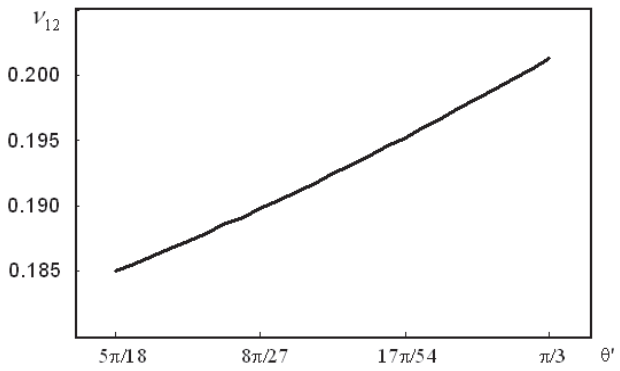

Fig. 15. ν_{12} of the equivalent model of graphene

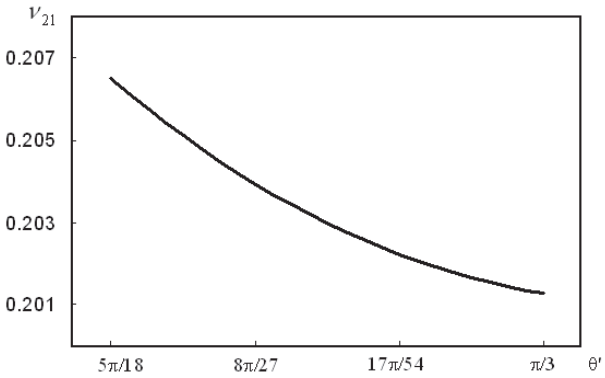

Fig. 16. ν_{21} of the equivalent model of graphene

We can see from Fig. 12 and Fig. 13 that the elastic modulus along the 0° fiber of the equivalent model of graphene almost increases linearly, and the elastic modulus at the vertical direction decreases, with the decrease in the C-C-C angle. And Fig. 14 ~ Fig. 16 show that the G_{12}, ν_{12} and ν_{21} of the equivalent model also changes a lot with the changes of the C-C-C angle.

6. Scale effect of elastic properties of CNTs

6.1 Equivalent model of single-walled carbon nanotubes (SWCNTs)

CNTs can be considered as curling graphite sheet. The C-C-C bond angles will change from the constant 120° to smaller values when the graphite sheet curling to CNTs and the change of the C-C-C angle is related to the radius of the formed CNTs. According to that, we consider CNTs same as graphene with changed C-C-C angles and the elastic properties of CNTs are consistent with those of graphene with changed C-C-C angles.

6.1.1 Zigzag SWCNTs

Taking the zigzag SWCNTs as an example, we study the effect of the changing in diameter of SWCNTs on the value of C-C-C angle. The SWCNT structure and the geometric diagram are shown in Fig. 17, with which we can obtain,

$$\begin{aligned} \sin\angle DBF &= \frac{DF}{DB} \\ \sin\angle CEF &= \frac{CF}{CE} \end{aligned} \tag{58}$$

With $DF = CF$, the last equation becomes,

$$\sin\angle DBF = \frac{CE}{DB}\cdot\sin\angle CEF \approx \frac{\sqrt{3}}{2}\sin\angle CEF \tag{59}$$

where the $\angle BDE$ does not change a lot when the graphene curls to the SWCNT so that we make $\frac{CE}{DB}=\frac{DE}{DB}\approx\frac{\sqrt{3}}{2}$.

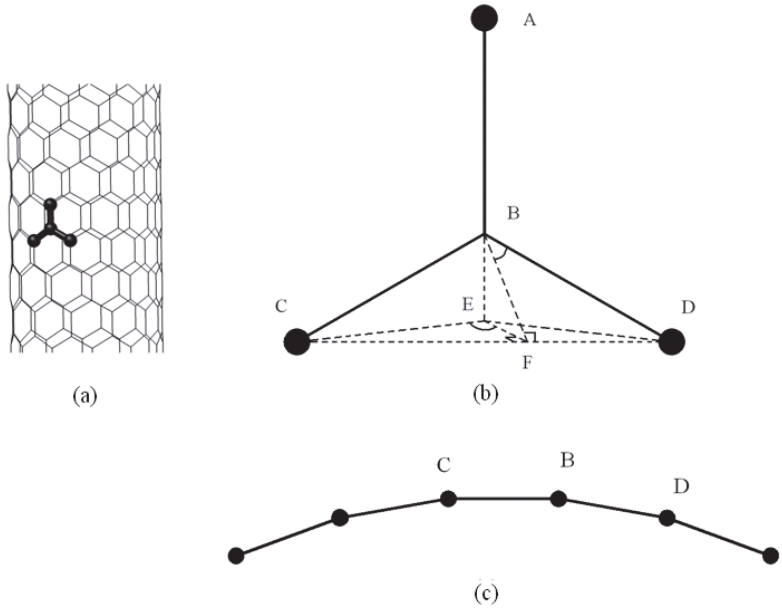

Fig. 17. C-C-C angles in the zigzag SWCNTs

For an (m, 0) zigzag SWCNT, it has,

$$\angle CEF=\frac{(m-1)\pi}{2m} \tag{60}$$

The diameter of the tube is,

$$d_{cnt}=0.0783\cdot m \quad \text{nm} \tag{61}$$

Substituting equation (61) and (60) into (59), we get,

$$\sin\angle DBF=\frac{\sqrt{3}}{2}\sin\left[\frac{\pi}{2}\left(1-\frac{0.0783}{d_{cnt}}\right)\right] \tag{62}$$

Thus, with the diameter of the zigzag SWCNT provided, setting the AB direction in Fig. 17 as the direction of the 0^o fiber, we can calculate the C-C-C angles in zigzag SWCNTs as,

$$\theta^{'}=\text{Arc}\sin\left\{\frac{\sqrt{3}}{2}\cdot\sin\left[\frac{\pi}{2}\left(1-\frac{0.0783}{d_{cnt}}\right)\right]\right\} \tag{63}$$

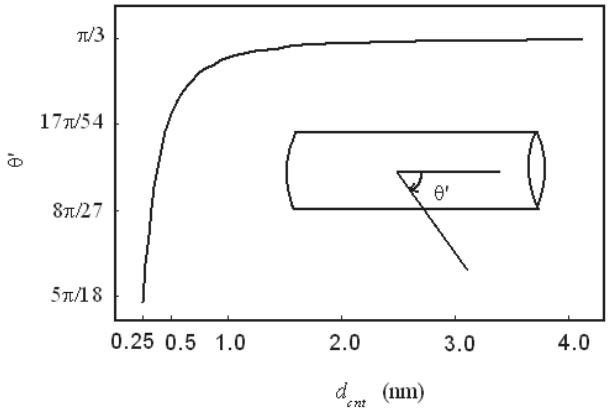

Fig. 18. Different C-C-C angles in zigzag SWCNTs with different diameters

The curve drawn from equation (63) is displayed in Fig. 18, which shows that the smaller the tube radius is the more sensitive the changing in C-C-C angle is. For the SWCNTs with diameter 0.4nm, 1.0nm, 2.0nm and 4.0nm, the C-C-C angles in the tubes decrease 7.3%, 1.2%, 0.3% and 0.08% from 120^o in the graphene.

6.1.2 Armchair SWCNTs

Taking the armchair SWCNTs as another example, we study the effect of the changing in diameter of SWCNTs on the value of C-C-C angle. The SWCNT structure and the geometric diagram are shown in Fig. 19, with which we can obtain,

$$\begin{aligned} \tan\angle DBG &= \frac{GD}{GB} \\ \tan\angle EBH &= \frac{HE}{HB} \end{aligned} \tag{64}$$

With $HE = GD$, the last equation becomes,

$$\tan\angle EBH = \frac{HE}{HB} = \frac{GB}{HB}\cdot\tan\angle DBG \approx \frac{\sqrt{3}}{\cos\angle HBG} \tag{65}$$

where the $\angle CBD$ does not change a lot when the graphene curls to the armchair SWCNT so that we make $\tan\angle DBG = \tan\dfrac{\angle CBD}{2} \approx \sqrt{3}$.

For an (m, m) armchair SWCNT, it has,

$$\angle HBG = \frac{\pi}{2m} \tag{66}$$

The diameter of the tube is,

$$d_{cnt} = 0.0783\cdot\sqrt{3}m \quad \text{nm} \tag{67}$$

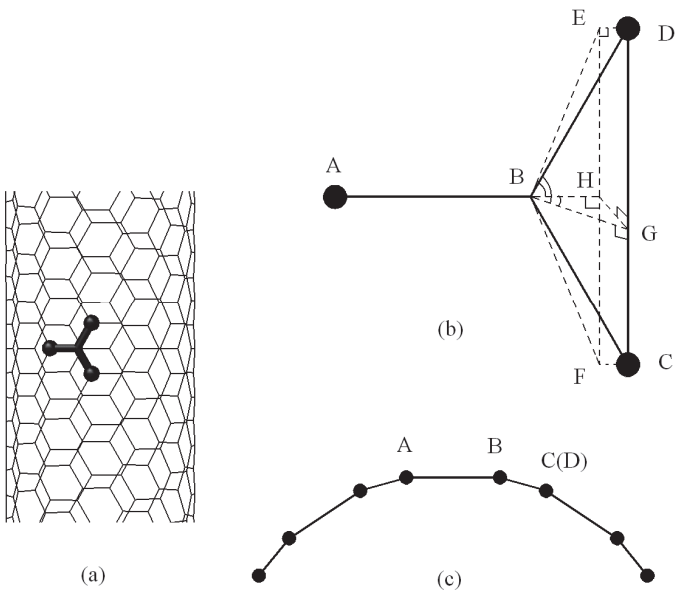

Fig. 19. C-C-C angles in the armchair SWCNTs

Substituting equation (67) and (66) into (65), we get,

$$\tan \angle EBH = \frac{\sqrt{3}}{\cos\left(\dfrac{0.0783\sqrt{3}\cdot\pi}{2d_{cnt}}\right)} \tag{68}$$

Thus, with the diameter of the armchair SWCNT provided, setting the AB direction in Fig. 19 as the direction of the 0^o fiber, we can calculate the C-C-C angles in armchair SWCNTs as,

$$\theta^{'} = \mathrm{Arc}\tan\frac{\sqrt{3}}{\cos\left(\dfrac{0.0783\sqrt{3}\cdot\pi}{2d_{cnt}}\right)} \tag{69}$$

The curve drawn from equation (69) is displayed in Fig. 20, which shows, as for the zigzag SWCNTs, that the smaller the tube radius is the more sensitive the changing in C-C-C angle is. For the armchair SWCNTs with diameter 0.4nm, 1.0nm, 2.0nm and 4.0nm, the C-C-C angles in the tubes decrease 5.9%, 0.94%, 0.23% and 0.06% from 120^o in the graphene. Comparing the armchair SWCNTs with the zigzag ones with same diameter, the changing in C-C-C angle in the armchair SWCNTs is smaller.

6.2 Scale effect of elastic properties of SWCNTs

With the usual continuum model of nanotubes, many researchers use the same isotropic material constants for CNTs with different radius so that the changes of the material properties due to changes in the radial size of CNTs can not be taken into account. In this

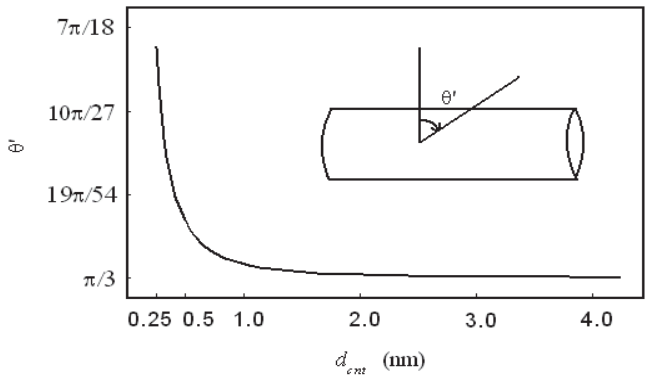

Fig. 20. Different C-C-C angles in armchair SWCNTs with different diameters

section, axial deformation of the SWCNTs with different diameter is analyzed with the finite element method to study the effect of the changes of the material properties for CNTs with different radius on the mechanical properties.

According to the theoretical model described above in this chapter, changes in the elastic properties of CNTs are mainly attributed to the changes of the C-C-C angles when to make CNTs by curling the graphene. The C-C-C angles in CNTs are related to the tube radius, while the corresponding C-C-C angles in the graphene induce varying degrees of anisotropy. Thus, we should choose different anisotropic material parameters for different radial size CNTs based on the parameters of the graphene with different C-C-C angles. Some elastic constants of graphite sheet and SWCNTs are listed in Table 3, the values for SWCNTs calculated with equation (57), (63) and (69). The subscript 1 and 2 in the table identify the along-axis direction of SWCNTs and the circumferential direction.

In the finite element simulation, the same axial strain is applied to each SWCNT, with one end of the tube fixed and at the other end imposed the axial deformation. The length of the tube is 6nm and the axial compression strain is 5%. Two series of the elasticity parameters, the isotropic ones (from equation (56)) and the anisotropic ones (from equation (57)), are both tried to obtain the axial forces in SWCNTs for comparison. With the results of the FEA, we use the following equation to define the scale effect of SWCNTs,

$$\xi = \frac{R_{\mathrm{ANISO}} - R_{\mathrm{ISO}}}{R_{\mathrm{ISO}}} \tag{70}$$

where R_{ANISO} and R_{ISO} are the axial forces obtained with the anisotropic parameters and the isotropic ones. The scale effect of SWCNTs with different radial size is shown in Fig. 21.

FEA results show that the anisotropy of the SWCNTs gradually increased with the decreases in the diameter, leading to more and more obvious scale effect. It can be seen from Fig. 21 that compared with the armchair SWCNTs the zigzag ones show more apparent scale effect and the scale effect of SWCNTs with diameter greater than 2nm is negligible (<0.05%), for tubes with any chirality. However, for zigzag SWCNTs with very small diameter, the scale effect could be very obvious up to 4.4%. That is in good agreement with the other researcher's results. Thus, the scale effect should be considered in the accurate calculation about the mechanical behaviour of small SWCNTs.

C-C-C angles			Mechanical parameters					conclusion
Graphene			$E = 0.9755$ TPa , $G = 0.406$ GPa , $\upsilon = 0.201$					Isotropic
SWCNTs			E_1 (TPa)	E_2 (TPa)	G_{12} (TPa)	υ_{12}	υ_{21}	–
	Diameter (nm)	C-C-C angle (o)						
Zig-zag	0.4	55.6298	1.00221	0.956849	0.403246	0.193494	0.202667	Anisotropic
	0.6	57.9833	0.987757	0.967253	0.404666	0.197574	0.201762	Anisotropic
	1.0	59.2586	0.980001	0.972556	0.405521	0.199891	0.201421	Anisotropic
	2.0	59.8129	0.976654	0.974786	0.405908	0.200919	0.201304	Isotropic
	3.0	59.9167	0.976029	0.975199	0.405982	0.201112	0.201284	Isotropic
	4.0	59.9531	0.97581	0.975343	0.406008	0.20118	0.201277	Isotropic
Arm-chair	0.4	63.5548	0.988636	0.954613	0.40873	0.200935	0.208097	Anisotropic
	0.6	61.5715	0.981558	0.966161	0.407195	0.201043	0.204247	Anisotropic
	1.0	60.5640	0.977735	0.972147	0.406448	0.201172	0.202328	Anisotropic
	2.0	60.1408	0.976084	0.974682	0.406142	0.201242	0.201532	Isotropic
	3.0	60.0626	0.975776	0.975152	0.406086	0.201256	0.201385	Isotropic
	4.0	60.0352	0.975667	0.975317	0.406066	0.201261	0.201334	Isotropic

Table 3. Elastic constants of graphite sheet and SWCNTs

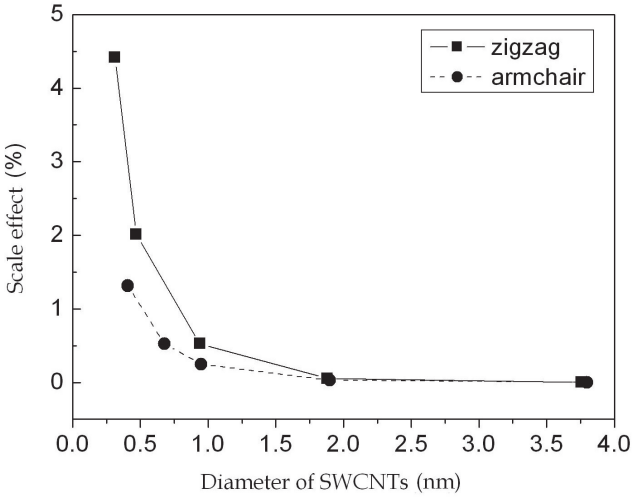

Fig. 21. Scale effect of SWCNTs with different diameters

With the data in Table 3 and the results from Fig. 21 we can see that, for SWCNTs with diameter greater than 2nm, the change of C-C-C angle due to the change in tube diameter is negligible so that the tubes could be treated as isotropic materials with the elastic parameters of graphene. For SWCNTs with diameter smaller than 1nm, the change of C-C-C angle due to the change in tube diameter should not be neglected and it is better for the tubes to be treated as anisotropic materials with the elastic parameters calculated from equation (57), (63) and (69).

7. Conclusion

A new equivalent continuum model is presented to theoretically investigate the elastic properties of the graphite sheet. By comparison, the equivalent model can properly reflect the actual elasticity status of graphite sheet. Further more this equivalent model is employed to study the radial scale effect of SWCNTs.

The C-C-C bond angles will change from the constant 120^o to smaller values when the graphite sheet curling to CNTs. The change of the C-C-C angle is obviously related to the change in CNT radius. Then the relationship between the anisotropy and the changes of the C-C-C angles of CNTs is deduced. The present theory not only clarify some puzzlement in the basic mechanical research of CNTs, but also lay the foundations for the application of continuum mechanics in the theoretical analysis of CNTs.

Based on above theory the scale effect of CNTs is studied. It is showed that the scale effect of the zigzag CNTs is more significant than the armchair ones. For SWCNTs with diameter greater than 2nm, the change of C-C-C angle due to the change in tube diameter is negligible so that the tubes could be treated as isotropic materials with the elastic parameters of graphene, and the scale effect could also be neglected no mater what chirality they are. However, for SWCNTs with diameter smaller than 1nm, the change of C-C-C angle due to the change in diameter should not be neglected (the scale effect neither) and it is better for

the tubes to be treated as anisotropic materials with the elastic parameters calculated from corresponding equations.

It is theoretically demonstrated that the graphite sheet is in-plane isotropic under plane stress, which is mainly due to their special structure of C-C-C angles. Any deformation of the graphite molecule making changes in the C-C-C angles, e.g. curling, will introduce anisotropic elastic properties. That provides a direction for applying the composite mechanics to the research in the mechanical properties of CNTs, and also has laid an important foundation.

8. Acknowledgment

The authors wish to acknowledge the supports from the Natural Science Foundation of Guangdong Province (8151064101000002, 10151064101000062).

9. References

Brenner, D.W. (1990). Empirical potential for hydrocarbons for use in simulating the chemical vapor deposition of diamond films. *Phys.Rev. B*, Vol.42, No.15, (November 1990), pp. 9458-9471, ISSN 1098-0121

Gao; X.L. & Li; K. (2003). Finite deformation continuum model for single-walled carbon nanotubes. *International Journal of Solids and Structures*, Vol.40, No.26, (December 2003), pp. 7329-7337, ISSN 0020-7683

Govindjee; S. & Sackman; J. L. (1999). On the use of continuum mechanics to estimate the properties of nanotubes. *Solid State Commun.* Vol.110, No.4, (March 1999), pp. 227–230, ISSN 0038-1098

Harik; V.M. (2001a). Ranges of applicability for the continuum-beam model in the mechanics of carbon-nanotubes and nanorods. *Solid State Commun.*, Vol.120, No.7-8, (October 2001), pp. 331-335, ISSN 0038-1098

Hu; N, Nunoya; K, Pan; D, Okabe; T. & Fukunaga; H. (2007). Prediction of buckling characteristics of carbon nanotubes. *International Journal of Solids and Structures*, Vol.44, No.20, (October 2007), pp.6535-6550, ISSN 0020-7683

Jin; Y. & Yuan; F.G. (2003). Simulation of elastic properties of single-walled carbon nanotubes. *Compos. Sci. Technol.*, Vol.63, No. 11, (August 2003), pp. 1507-1515, ISSN 0266-3538

Krishnan; A., Dujardin; E., Ebbessen; T.W., Yianilos; P. N. & Treacy; M. M. J. (1998). Young's modulus of single-walled nanotubes. *Phys. Rev. B,* Vol.58, No.20, (November 1998), pp. 14013~14019, ISSN 1098-0121

Li; C.Y. & Chou; T.W. (2003). Elastic moduli of multi-walled carbon nanotubes and the effect of van der Waals forces. *Compos. Sci. Technol.,* Vol.63, No.11, (August 2003), pp. 1517-1524, ISSN 0266-3538

Liu; J.Z., Zheng; Q.S. & Jiang; Q. (2001). Effect of a Rippling Mode on Resonances of Carbon Nanotubes. *Phys. Rev. Lett.*, Vol.86, No.21, (May 2001), pp. 4843-4846, ISSN 0031-9007

Lu; J.P. (1997). Elastic properties of carbon nanotubes and nanoropes. *Phys. Rev. Lett.,* Vol.79, No.7, (August 1997), pp. 1297-1300, ISSN 0031-9007

Mayo; S.L., Olafson; B.D. & Goddard III; W.A. (1990). Dreiding: a generic force field for molecular simulations. *J Phys Chem,* Vol.94, No.26, (December 1990), pp. 8897-8909, ISSN 1932-7447

Poncharal; P., Wang; Z.L., Ugarte; D. & W.A. de Heer. (1999). Electrostatic deflections and electromechanical resonances of carbon nanotubes. *Science,* Vol.283, No.5407, (May 1999), pp. 1513-1516, ISSN 0036-8075

Shen; H.S. (2004). Postbuckling prediction of double-walled carbon nanotubes under hydrostatic pressure. *International Journal of Solids and Structures,* Vol.41, No.9-10, (May 2004), pp. 2643-2657, ISSN 0020-7683

Sudak; L.J. (2003). Column buckling of multiwalled carbon nanotubes using nonlocal continuum mechanics. *J. Appl. Phys.,* Vol.94, No.11, (November 2003), pp. 7281-7287, ISSN 0021-8979

Wang; C.Y., Ru; C.Q. & Mioduchowski; A. (2003a). Axially compressed buckling of pressured multiwall carbon nanotubes. *International Journal of Solids and Structures,* Vol.40, No.5, (July 2003), pp. 3893-3911, ISSN 0020-7683

Wang; Q., Varadan; V.K. & Quek; S.T. (2006). Small scale effect on elastic buckling of carbon nanotubes with nonlocal continuum models. *Physics Letters A,* Vol.357, No.2, (September 2006), pp. 130-135, ISSN 0375-9601

Wang; Q. & Varadan; V.K. (2007). Application of nanlocal ealstic shell theory in wave propagation analysis of carbon nanotubes. *Smart Mater. Struct.,* Vol.6, No.1 (February 2007), pp. 178-190, ISSN

Xin; H., Han; Q. & Yao; X.H. (2007). Buckling and axially compressive properties of perfect and defective single-walled carbon nanotubes. *Carbon*, Vol.45, No.13, (November 2007), pp. 2486-2495, ISSN 0008-6223

Xin; H., Han; Q. & Yao; X.H. (2008). Buckling of defective single-walled and double-walled carbon nanotubes under axial compression by molecular dynamics simulation. *Compos. Sci. Technol.,* Vol.68, No.7-8, (June 2008), pp. 1809-1814, ISSN 0266-3538

Yang; X.G., & Zeng; P. (2006). Numerical simulation of anisotropic mechanical Properties of nano-graphite crystals. *Journal of basic science and engineering,* Vol.14, No.3 (Sep tember 2006), pp. 375-383, ISSN 1005-0930

Yao; X.H. & Han; Q. (2007). Postbuckling prediction of double-walled carbon nanotube under axial compression. *Eur. J. Mech .A-Solid,* Vol.26, No.1, (January-February 2007), pp. 20-32, ISSN 0997-7538

Yao; X.H. & Han; Q. (2008). Torsional buckling and postbuckling equilibrium path of double-walled carbon nanotubes. *Compos. Sci. Technol.,* Vol.68, No.1, (January 2008), pp. 113-120, ISSN 0266-3538

Yao; X.H., Han; Q. & Xin; H. (2008). Bending buckling behaviors of single- and multi-walled carbon nanotubes. *Computational Materials Science,* Vol.43, No.4, (October 2008), pp. 579-590, ISSN 0927-0256

Zhang; Y.Q., Liu; G.R. & Xie; X.Y. (2005). Free transverse vibrations of double-walled carbon nanotubes using a theory of nonlocal elasticity. *Phys. Rev. B,* Vol.71, (May 2005), pp. 195404:1-7, ISSN 1098-0121

Yang; X.G., & Zeng; P. (2006). Numerical simulation of anisotropic mechanical Properties of nano-graphite crystals. *Journal of basic science and engineering,* Vol.14, No.3 (September 2006), pp. 375-383, ISSN 1005-0930

Part 2

Preparation and Characterization of Polymer Composites with CNTs

4

Polymer/Carbon Nanotube Nanocomposites

Veena Choudhary and Anju Gupta
Centre for Polymer Science and Engineering
Indian Institute of Technology Delhi
India

1. Introduction

Polymer is a versatile material having many unique properties like low density, reasonable strength, flexibility, easy processibilty, etc. However, the mechanical properties of these materials are inadequate for many engineering applications. Hence, there is a continuous search towards new polymeric materials with improved properties. Initially, blending of different class of polymer was used to fabricate new materials with unique properties. However, blending lead to only marginal improvement in physical properties which were still inadequate for engineering applications. So to improve the strength and stiffness of polymer materials different kinds of organic and inorganic fillers were used. It was observed that strength and stiffness of long fibers reinforced thermosetting polymer is comparable to metals at a fraction of their weight. As a result of which these material were used in aircraft and in sport equipment. However, processing of these materials is very difficult; therefore small fiber or particle reinforced composites were developed. The common particle fillers used were silica, carbon black , metal particles etc. But significantly high filler loading was required to achieve desired mechanical property, which thus increased cost and made processibility difficult. So to achieve high mechanical properties at lower filler loading, nanofillers were used. The nanofiller reinforced polymer matrix is known as polymer nanocomposite.

Polymer nanocomposites are a new class of composite materials, which is receiving significant attention both in academia and industry. As nano fillers are only a few nanometers (~10,000 times finer than a human hair) in dimension, it offers ultra-large interfacial area per volume between the nano-element and polymer matrix. As a result, the nanofiller reinforced composites exhibit enhanced toughness without sacrificing stiffness or optical clarity. It also possesses greater thermal and oxidative stability, better barrier, mechanical properties as well as unique properties like self-extinguishing behavior. Compared to different range of nanofillers, carbon nanotubes (CNTs) have emerged as the most promising nanofiller for polymer composites due to their remarkable mechanical and electrical properties (Ishikawa, 2001; Kracke & Damaschke, 2000). Currently, one of the most intriguing applications of CNTs is the CNT/polymer nanocomposites (Cai, 2000; Fiege, 1999; Gomes, 1999; Hersam, 1998; Ruiz, 1998). For the last two decades, a lot of research work has been done on evaluating the potential of CNTs as filler for polymer nanocomposites. In the present chapter, we will briefly discuss on CNTs and their properties, different fabrication methods of polymer nanocomposites and their mechanical, electrical and thermal properties.

2. Carbon nanotubes (CNTs)

CNTs are long cylinders of covalently bonded carbon atoms which possess extraordinary electronic and mechanical properties. There are two basic types of CNTs: single-wall carbon nanotubes (SWCNTs) which are the fundamental cylindrical structure and multi-wall carbon nanotubes (MWCNTs) which are made of coaxial cylinders (Fig. 1), having interlayer spacing close to that of the interlayer distance in graphite (0.34 nm). These cylindrical structures are only few nanometre in diameter, but the cylinder can be tens of microns long, with most end capped with half of a fullerene molecule. It was first discovered by M. Endo in 1978, as part of his Ph.D. work at the University of Orleans in France, but real interest in CNTs started when Iijima (1991) first reported it in 1991. The field thrives after that and the first polymer composites using CNT as filler was reported by Ajayan et al (1994).

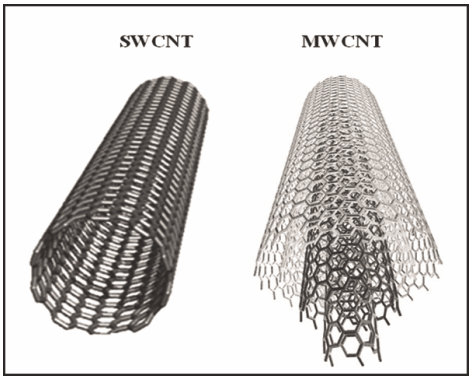

Fig. 1. Schematic diagrams of single-wall carbon nanotube (SWCNT) and multi-wall carbon nanotube (MWCNT)

2.1 Synthesis of carbon nanotubes

CNTs can be prepared using three methods which includes arc discharge, laser ablation and chemical vapor deposition (CVD). Most of these processes take place in vacuum or with process gases. CVD growth of CNTs can occur in vacuum or at atmospheric pressure. High quality and large quantities of nanotubes can be synthesized by these methods.

i. Arc discharge

The carbon arc discharge method, initially used for producing C_{60} fullerenes, is the most common and perhaps easiest way to produce CNTs. But this technique produces graphitic impurities such as carbon soot containing amorphous carbon, anions and fullerens. In this method an inert gas atmosphere is created in the reaction vessel by passing an inert gas at controlled pressure. Two graphitic rods constitute the electrodes, between which a potential difference is applied. As the rods are brought closer, a discharge occurs, resulting in formation of plasma (Fig. 2). The deposit, which contains CNTs, forms on the large negative electrode (cathode) while the smaller positive electrode (anode) is consumed. When a metal catalyst is used along with graphite, a hole is drilled in the carbon anode and it is filled with a mixture of metal and graphite powder. In this case, most nanotubes are found in soot deposited on the arc chamber wall.

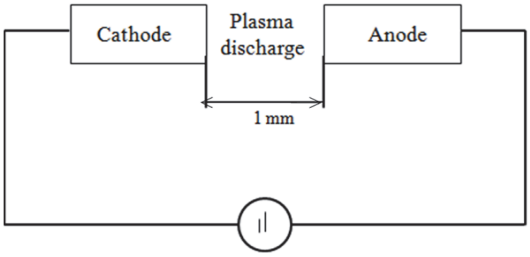

Fig. 2. Plasma arc discharge setup

ii. Laser ablation

Laser ablation uses an intense laser pulse to vaporize a carbon target, which also contains small amount of metals such as nickel and cobalt and is placed in a tube furnace at 1200°C. As the target is ablated, inert gas is passed through the chamber carrying the grown nanotubes on a cold finger for collection (Fig. 3). This method mainly produces SWCNT in the form of ropes.

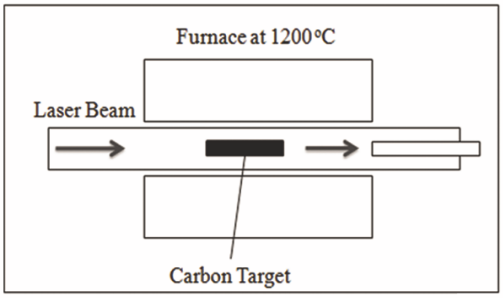

Fig. 3. Laser ablation setup

iii. Chemical vapor deposition

In this process a mixture of hydrocarbon, metal catalyst along with inert gas is introduced into the reaction chamber (Fig. 4a). During the reaction, nanotubes form on the substrate by the decomposition of hydrocarbon at temperatures 700–900°C and atmospheric pressure. The diameter of nanotubes that are to be grown are related to the size of the metal particles. This mechanism of CNT growth is still being studied. In Figure 4b two growth modes can be seen. The first 'tip growth mode' where, the catalyst particles can stay at the tips of the growing nanotube during the growth process and second 'base growth mode' where, catalyst particles remain at the nanotube base, depending on the adhesion between the catalyst particle and the substrate (Fig. 4b). This technique offers more control over the length and structure of the produced nanotubes compared to arc and laser methods. This process can also be scaled up to produce industrial quantities of CNTs. A number of reviews (Awasthi, 2005; Monthioux, 2002; Thostenson, 2001) are available which briefly discusses on these production techniques.

2.2 Properties of carbon nanotubes

The determination of physical properties of CNTs is relatively more difficult compared to other fillers due to very small size of CNTs. However a number of experimental studies

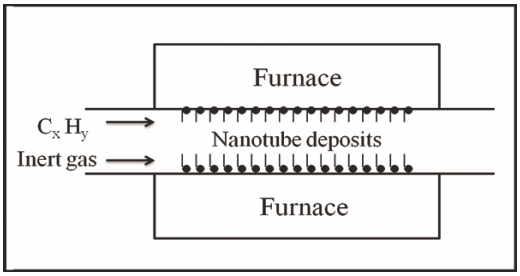

Fig. 4a. Chemical vapor deposition setup

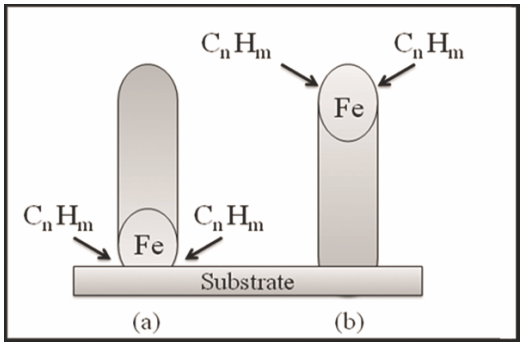

Fig. 4b. Growth modes for CVD (a) base growth mode and (b) tip growth mode

have been carried out on the direct determination of mechanical properties of individual CNTs (Yu et al., 2000a). The stiffness of CNTs was first determined by observing the amplitude of thermal vibrations in transmission electron microscopy (TEM) and the average stiffness values of 1.8 TPa and 1.25 TPa (Yu et al., 2000b) were reported for MWCNTs and SWCNTs, respectively. The in-situ tensile tests on individual MWCNTs and ropes of SWCNTs was performed by carrying out a stress-strain measurement using a "nanostressing stage" operating inside a scanning electron microscope (SEM). Experimental results showed that strength of outer shell of MWCNT ranged from 11 to 63 GPa at fracture strains of up to 12% and modulus values ranged from 270 to 950 GPa (Yu et al., 2000b). It was observed that strength of nanotubes depends on the number of defects, as well as interlayer interactions in MWCNTs and bundles of SWCNTs. Structural defects as well as bends or twists significantly affect mechanical strength of CNTs (Kane & Mele, 1997). Theoretical studies of the electronic properties of SWCNTs, suggest that nanotube shells can be either metallic or semiconducting, depend critically on helicity (Fig. 5) (Saito, 1992; Hamada, 1992; Mintmire, 1992). Tans et al. (1997) first, experimentally showed that there are indeed metallic and semiconducting SWCNTs, which verified the theoretical predictions. It was observed that due to poor control on synthesis, on average, approximately 1/3 of SWCNTs formed are metallic and 2/3 semiconductors (Odom et al., 1998). The room temperature conductivity of metallic SWCNT was found to be 10^5 to 10^6 S/m and for semiconducting tubes about 10 S/m. The conductivity of SWCNT is close to the in-plane conductivity of graphite [10^6 S/m (Charlier & Issi 1996)]. Conductivities of individual MWCNTs have been reported in the range of 10^7 to 10^8 S/m (Ebbesen et al., 1996),

depending on the helicities of the outermost shells or the presence of defects (Dai et al., 1996). The axial thermal conductivity of individual, perfect CNTs is reported to be as high as 3300 W/m/K (Kim et al., 2001).

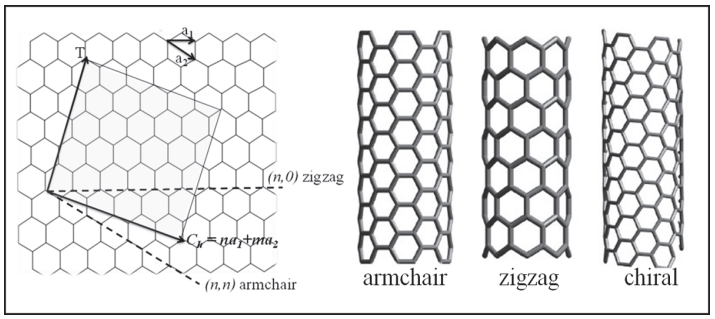

Fig. 5. A sheet of graphene rolled to show formation of different types of single walled carbon nanotube

3. Functionalization of carbon nanotubes

For a nanocomposite, a good dispersion of the filler within the host matrix is very important. At the same time it is also important to stabilize the dispersion to prevent re-aggregation of the filler. These tasks are particularly very challenging in case of nanofillers since the extremely large surface area lead to strong tendency to form agglomerates. CNTs are very well known to form aggregates during compounding and hence various techniques have been used to overcome this problem like use of sonication or mechanical mixing during the fabrication of nanocomposite which generally help in dispersing CNTs. But the most effective way to resolve this problem is surface functionalization of CNTs. Surface functionalization helps in stabilizing the dispersion, since it can prevent re-aggregation of nanotubes and also leads to coupling of CNT with polymeric matrix. Coupling between CNT and polymer matrix is also very important for efficient transfer of external stress to nanotube. In recent years, various methods have been developed for surface functionalization of CNT which includes functionalization of defect groups, covalent functionalization of sidewalls, non-covalent functionalization, e.g., formation of supramolecular adducts with surfactants or polymers (Fig. 6). Although surface functionalization leads to significant improvement in CNT dispersion and stress transfer but this method also causes deterioration of intrinsic properties of CNTs. Covalent functionalization often lead to tube fragmentation and the non-covalent functionalization results in poor exfoliation. Alteration of CNT properties lead to poor reinforcement and conductivity. Hence, it becomes obvious that dispersion and stabilization are not simple issues and compromises have to be made depending on the applications (Hirsch, 2002).

3.1 Covalent functionalization of sidewall

Local strain in CNTs, which arises from either pyramidalization or misalignment of π-orbitals of the sp^2-hybridized carbon atoms, makes nanotubes more reactive than a flat graphene sheet, thereby paving the path to covalently attach chemical species to nanotubes (Banerjee et al., 2005). Covalent functionalization of CNTs can be achieved by introducing

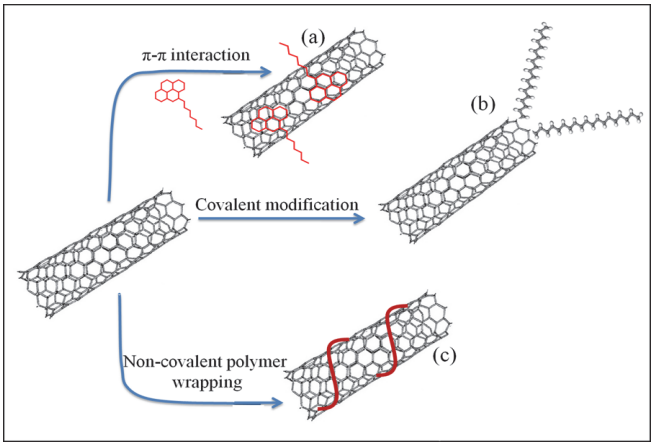

Fig. 6. Possibilities for the functionalization of SWCNTs a) л-л interaction; b) defect group functionalization ; c) non-covalent functionalization with polymers

some functional groups on defect sites of CNTs (Fig. 7) by using oxidizing agents such as strong acids, which results in the formation of carboxylic or hydroxyl groups (-COOH, -OH) on the surface of nanotubes (Coleman, 2000, 2006, Singh, 2009). This type of functionalization is known as defect group functionalization. Such functionalization improves nanotube dispersion in solvents and polymers and imparts high stability in polar solvents. For example, Feng et al. (2008) reported that oxidation of MWCNTs with HNO_3/H_2O_2 and HNO_3/H_2SO_4 introduces some carboxylic groups on CNTs, which enhanced their stability in water at room temperature for more than 100 days. As a result, the water-stable nanotubes can easily be embedded in water soluble polymers such as poly(vinyl alcohol) (PVA), giving CNT/polymer nanocomposites with homogeneous dispersion of CNTs (Zhao et al., 2008). Oxidized nanotubes also show excellent stability in other solvents such as caprolactam, which is used in the production of polyamide (PA6) (Gao et al., 2005). Studies on acid functionalization of CNTs have shown significant improvement in interfacial bonding between CNTs and polymer matrices, which have been shown to give a stronger nanotube–polymer interaction, leading to improved Young's modulus and mechanical strength (Gao, 2006; Sui, 2008; Yuen, 2008a, 2008b, 2008c; Luo, 2008; Rasheed, 2006a, 2006b; Sahoo, 2006; Wong, 2007).

Polymer molecules can also be grafted on the surface of CNTs in presence of these active functional groups (–COOH, -NH_2, -OH). Grafting of polymer chain on CNTs can be carried out either by 'grafting from' or 'grafting to' technique (Coleman, 2000, 2006; Liu, 2005). The grafting-from approach is based on the initial immobilization of initiators onto the nanotube surface, followed by in-situ polymerization with the formation of polymer molecules attached to CNTs. The advantage of this approach is that polymer-functionalized nanotubes with high grafting density can be prepared. However, this process needs a strict control of the amounts of initiator and substrate. The grafting from technique is widely used for the preparation of poly(methyl methacrylate) (PMMA) and related polymer grafted nanotubes. For example, Qin et al. (2004) reported the preparation of poly(n-butyl methacrylate) grafted SWCNTs by attaching n-butyl methacrylate (nBMA) to the ends and sidewalls of SWCNT via atom transfer radical polymerization (ATRP) using methyl 2-bromopropionate as the

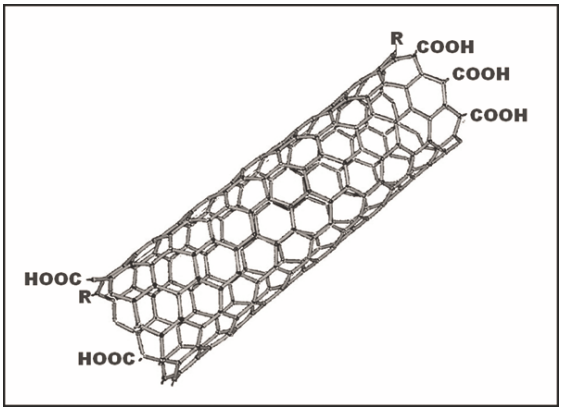

Fig. 7. Covalent functionalization of carbon nanotubes on defects sites

free radical initiator. A similar approach was reported by Hwang et al. (2004) for the synthesis of PMMA grafted MWCNTs by potassium persulfate initiated emulsion polymerization reactions and use of the grafted nanotubes as a reinforcement for commercial PMMA by solution casting.

On the other hand, in case of grafting-to approach, attachment of already functionalized polymer molecules to functionalized nanotube surface takes place via appropriate chemical reactions. One of the first examples of 'grafting to' approach was published by Fu et al (2001). In this work carboxylic acid groups on the nanotube surface were converted to acyl chlorides by refluxing the samples with thionyl chloride. Then the acyl chloride functionalized CNTs were reacted with hydroxyl groups of dendritic poly(ethylene glycol) (PEG) polymers via the esterification reactions. The grafting-to method was applied for the preparation of epoxy-polyamidoamine–SWCNT composites (Sun et al., 2008). An advantage of this method is that, commercially available polymers containing reactive functional groups can be utilized.

3.2 Non-covalent functionalization with surfactant or polymer

The non-covalent functionalization has unique ability of preserving the intrinsic properties of nanotube which is very important for its electrical and thermal conductivity. Various studies have shown that surfactant or wrapping with polymer can lead to individualization of nanotube in aqueous or organic solvent. (Moore, 2003; Matarredona, 2003; Vigolo , 2000; Regev, 2004; Grossiord, 2005; Curran, 1998; Coleman, 2000; O'Connell, 2001). Moore *et al.* studied various anionic, cationic and non-ionic surfactants and polymers to determine their ability to disperse nanotube in aqueous media. They reported that size of the hydrophilic group of surfactant or polymer play a key role in nanotube dispersion. It was also observed that surfactant alone is not capable of suspending nanotubes effectively and vigorous sonication is required (Matarredona et al., 2003). Polymers such as poly(*m*-phenylene-*co*- 2,5-dioctoxy-*p*-phenylenevinylene) (PmPV) can be used to wrap around nanotube in organic solvents such as $CHCl_3$ (Coleman et al., 2000). Polar side chain containing polymer, such as poly(vinyl pyrrolidone) [PVP] or poly(styrene sulfonate) [PSS] gave stable solutions of SWCNT/polymer complexes in water (O'Connell et al., 2001). The thermodynamic driving force for wrapping of polar polymer on nanotube is the need to avoid unfavorable

interactions between the non-polar tube walls and the polar solvent (water). To disperse the nanotube in non-polar polymer matrices, such as polyolefins, polymerization-filling technique (PFT) was used. In this process nanotube is first dispersed with catalyst and co-catalyst and followed by polymerization (Dubois & Alexandre, 2006). This technique leads to individualization of nanotube and allows the homogeneous dispersion of nanotubes upon melt blending.

4. CNT/polymer nanocomposites

In order to utilize CNTs and their extra ordinary properties in real-world applications, CNT/polymer nanocomposites were developed. Currently, polymer composite is the biggest application area for CNTs. These nanocomposites are being utilized in different fields including transportation, automotive, aerospace, defense, sporting goods, energy and infrastructure sectors. Such wide range applications of such materials are due to their high durability, high strength, light weight, design and process flexibility. CNT/polymer nanocomposites are also used as electrostatic discharge (ESD) and electromagnetic interference (EMI) shielding material because of high electrical conductivity of this material. However, the effective utilization of CNTs for fabricating nanocomposites strongly depends on the homogeneous dispersion of CNTs throughout the matrix without destroying their integrity. Furthermore, good interfacial bonding is also required to achieve significant load transfer across the CNT–matrix interface, a necessary condition for improving the mechanical properties of composites. So it is very important to achieve high degree of CNT dispersion during processing without affecting its property. In the following section we will discuss about the different processing techniques and properties of CNT/polymer nanocomposite.

4.1 Processing of CNT/polymer nanocomposites

From the above discussion, it is very clear that CNTs have strong tendency to form aggregates due to their large surface area. These aggregates persist unless high shear forces are applied e.g., vigorous mixing of the polymer. But such mixing often damages nanotube structures, compromising their properties. Therefore, the biggest challenge is to fully disperse individual nanotubes in the matrices to realize full potential of CNTs. Surface modification of CNTs have somewhat helped in dispersing CNT but long term stability is still a real challenge. Nevertheless, several approaches have been successfully adopted to obtain intimate mixing of nanotubes with polymer matrices, including dry powder mixing, solution blending, melt mixing, in-situ polymerization and surfactant-assisted mixing.

i. Solution processing

The most common method for preparing CNT/polymer nanocomposites involves mixing of CNT and polymer in a suitable solvent. The benefit of solution blending is rigorous mixing of CNTs with polymer in a solvent which facilitates nanotube de-aggregation and dispersion. This method consists of three steps: dispersion of nanotubes in a suitable solvent, mixing with the polymer (at room temperature or elevated temperature) and recovery of the nanocomposite by precipitating or casting a film. Both organic and aqueous medium have been used to produce CNT/polymer nanocomposites [Bandyopadhyaya, 2002; Pei, 2008; Wu, 2007; Cheng, 2008]. In this method dispersion of nanotube can be achieved by magnetic stirring, shear mixing, reflux or most commonly, ultrasonication. Sonication can be provided in two forms, mild sonication in a bath or

high-power sonication. The use of high-power ultrasonication for a long period of time can shorten the nanotube length, i.e. reduces the aspect ratio, which is detrimental to the composite properties (Badaire et al., 2004).

To minimize this problem, surfactants have been used to disperse higher loadings of nanotubes (Islam, 2003; Barrau, 2003; Bryning, 2005a). Islam et al. (2003) reported that SWCNT (20 mg/mL) can be dispersed in water by using 1% sodium dodecylbenzene sulfonate as surfactant and low power, high-frequency (12 W, 55 kHz) sonication for 16-24 h. However, it has a major drawback of retaining surfactant in the nanocomposites which deteriorate the transport properties of nanocomposites. Bryning et al. (2005a) prepared SWCNT/epoxy nanocomposites and showed that the thermal conductivity of composite is much lower if surfactant is used for SWCNT dispersion.

In solvent blending, slow evaporation step often lead to CNT aggregation. To overcome this problem, CNT/polymer suspension can be kept on a rotating substrate [spin-casting (Lamy de la Chapelle et al., 1999)] or can be dropped on a hot substrate [drop-casting (Benoit, et al., 2001)] to expedite the evaporation step. Coagulation [developed by Du et al. (Du et al., 2003)] is another method, which involves pouring of a CNT/polymer suspension into an excess of non-solvent. This lead to entrapment of SWCNT by precipitating polymer chains which inturn prevents the SWCNT from bundling. The method is very successful in case of PMMA and polyethylene [PE] nanocomposites (Haggenmueller et al., 2006).

ii. Melt blending

While solution processing is a valuable technique for both nanotube dispersion and nanocomposite formation, it is less suitable for industrial scale processes. For industrial applications, melt processing is a preferred choice because of its low cost and simplicity to facilitate large scale production for commercial applications. In general, melt processing involves the melting of polymer pellets to form a viscous liquid and application of high shear force to disperse the nanofillers such as CNTs. Successful examples of melt blending include MWCNT/polycarbonate (Poetschke et al., 2003) MWCNT/ nylon-6, (Liu, 2004; Zhang, 2004) SWCNT/polypropylene, (Bhattacharya et al., 2003) and SWCNT/polyimide (Siochi et al., 2004) nanocomposites. Although melt blending is very simple, but high shear force and high temperature can deteriorate nanocomposite property, as high shear force which is required to achieve CNT dispersion can also lead to CNT fragmentation. So an optimum shear stress is required to achieve desired dispersion at lowest possible damage of CNTs.

The use of high temperature is also very critical, as high temperature enhances CNT dispersion by lowering the viscosity but too high temperature can degrade the polymer intrinsic properties. So optimization of temperature is also very important. To overcome these challenges many modification in melt compounding has been made like : Haggenmueller et al. (2000) combined the solution and melt blending by subjecting a solvent cast SWCNT/polymer film to several cycles of melt pressing. An approach developed by Jin et al (2002) introduces polymer-coated MWCNT (rather than pristine MWCNT) into the polymer melt to promote compatibilization. However optimization of processing conditions is an important issue, not just for different nanotube types, but for the whole range of polymer–nanotube combinations (Dubois & Alexandre, 2006).

iii. In-situ polymerization

In recent years, in-situ polymerization has been extensively explored for the preparation of polymer grafted nanotubes and processing of corresponding polymer composite materials. The main advantage of this method is that it enables grafting of polymer macromolecules

onto the walls of CNTs. In addition, it is a very convenient processing technique, which allows the preparation of nanocomposites with high nanotube loading and very good miscibility with almost each polymer matrix. This technique is particularly important for the preparation of insoluble and thermally unstable polymers, which cannot be processed by solution or melt processing. Depending on required molecular weight and molecular weight distribution of polymers, chain transfer, radical, anionic, and ring-opening metathesis polymerizations can be used for in-situ polymerization processing. Initially, in-situ radical polymerization was applied for the synthesis of PMMA/MWCNT nanocomposites (Jia, 1999; Velasco-Santos, 2003; Putz, 2004). More recently (Wu, 2009) studied the mechanical and thermal properties of hydroxyl functionalized MWCNTs/acrylic acid grafted PTT nanocomposites and showed a significant enhancement in thermal and mechanical properties of PTT matrix due to the formation of ester bonds between –COOH groups of acrylic acid grafted PTT and –OH groups of MWCNTs.

In-situ polymerization was also very useful for the preparation of polyamide/CNT polymer nanocomposites. Park et al. (2002) also reported the synthesis of SWCNT reinforced polyimide nanocomposites by in-situ polymerization of diamine and dianhydride under sonication. Epoxy nanocomposites comprise the majority of reports using in-situ polymerization methods, (Schadler, 1998; Zhu, 2003, 2004; Gong, 2000; Ajayan, 2000; Moniruzzaman, 2006a) where the nanotubes are first dispersed in the resin followed by curing the resin with the hardener. Zhu et al. (2003) prepared epoxy nanocomposites by this technique using carboxylated end-cap SWCNT and an esterification reaction to produce a composite with improved tensile modulus. It is important to note that as polymerization progresses and the viscosity of the reaction medium increases, the extent of in-situ polymerization reactions might be limited.

In general, in -situ polymerization can be applied for the preparation of almost any polymer nanocomposites containing CNTs which can be non-covalently or covalently bound to polymer matrix. Non-covalent binding between polymer and nanotube involves physical adsorption and wrapping of polymer molecules through van der Waals and л–л interactions. The role of covalently functionalized and polymer grafted nanotubes will be considered in more detail below.

5. Alignment of carbon nanotubes in nanocomposites

The superior properties of CNTs offer exciting opportunities for new nanocomposites, but the important limitation for some potential applications of CNTs come from the fact that randomly oriented nanotubes embedded in polymer matrices have exhibited substantially lower electrical and thermal conductivities than expected (Fischer, 1997; Hone, 1999). Nanotube alignment can be obtained prior to composite fabrication or during composite fabrication or after composite fabrication by in-situ polymerization (Raravikar, 2005; Feng, 2003), mechanical stretching (Jin et al., 1998), melt fiber spinning (Haggenmueller, 2000, 2003), electrospinning (Gao, 2004; Hou, 2005; Ko, 2003) and application of magnetic or electric field (Ma, 2008; Componeschi, 2007). Haggenmueller et al. (2000) have tried a combination of solvent casting and melt mixing methods to disperse single-walled CNTs in PMMA films and subsequently melt spun into fibers. However, only the melt mixing method was found to be successful in forming continuous fibers. Ma et al. (2008) studied alignment and dispersion of functionalized nanotube composites of PMMA induced by electric field and obtained significant enhancement in dispersion quality and alignment

stability for oxidized MWCNTs as compared to pristine MWCNTs. Camponeschi et al. (2007) found that orientation and alignment of CNTs embedded in the epoxy under a magnetic field increased and showed improvement in mechanical properties of the resulting nanocomposites. Gao et al. (2004) prepared SWCNT/poly(vinyl pyrrolidone) fibres by electrospinning using electrostatic forces and found SWCNT exhibit good alignment and dispersion. Xie et al. (2005) showed that enhanced dispersion and alignment of CNTs in polymer matrices greatly improve mechanical, electrical, thermal, electrochemical, optical and super-hydrophobic properties of CNT/polymer nanocomposites. Safadi et al. (2002) prepared PS/MWCNT nanocomposite films by spin casting at high speed (2200 rpm) and found that MWCNTs were aligned in specific angles relative to the radial direction: 45° and 135° on average. The presence of ~2.5 vol.% MWCNTs doubles the tensile modulus and transforms the film from insulating to conducting. Thostenson & Chou (2002) found that tensile strength and modulus of melt drawn PS/MWCNT composite films increased by 137 and 49% respectively, compared to the undrawn PS film.

6. Properties of CNT/polymer nanocomposites

Incorporation of CNT in polymer matrix resulted in a significant change in mechanical, electrical and thermal properties of polymer matrices. Various factors that influence property modification are processing techniques, type of CNT, aspect ratio and CNT content. It is generally observed that a particular processing method which is good for one property may not be good for another. One such example is surface modification of CNT which generally enhances the mechanical properties but deteriorates the electronic properties. So it is very important to optimize the various conditions to obtain the nanocomposite with desired properties. A number of studies have been aimed at evaluating the mechanical, electrical and thermal properties of CNT/polymer nanocomposite under different conditions and filler loading.

6.1 Mechanical properties of CNT/polymer nanocomposites

The excellent mechanical properties of CNTs, as discussed above, suggest that incorporation of very small amount of CNTs into a polymer matrix can lead to structural materials with significantly high modulus and strength. Significant advancement has been made in improving the mechanical properties of polymer matrix by mixing small fraction of CNTs. Qian et al. (2000) reported that adding 1 wt.% MWCNTs in the PS by solution-evaporation method, results in 36–42 and ~25% improvements in tensile modulus and tensile strength, respectively. Biercuk et al. (2002) have also reported increase of indentation resistance (Vickers hardness) by 3.5 times on adding 2 wt. % SWCNTs in epoxy resin. Cadek et al. (2002) also found significant improvement in the modulus and hardness (1.8 times and 1.6 times) on addition of 1 wt% MWCNTs in PVA matrix. Homogeneous dispersion and alignment of CNTs in polymer matrix had a significant effect on the properties of resulting composites. Velasco-Santos et al. (2003) reported that by enhancing the dispersion of CNT by using an in-situ polymerization, the storage modulus of PMMA/MWCNT nanocomposites at 1 wt.% of MWCNTs at 90^{o}C increased by 1135%.

Although, addition of CNTs lead to enhancement of mechanical properties of the polymer matrix but the improvement is still well below the expected value. At current stage, the extraordinary properties of CNTs are still not fully utilized in polymer composites. Many

research works have indicated that poor adhesion between the matrix and nanotube is the limiting factor in imparting the excellent mechanical properties of nanotubes in composites. As load transfer from matrix to CNTs play a key role in mechanical properties of the nanocomposite, good interfacial bonding is very important. Load transfer between the matrix and filler depends on the interfacial shear stress between the two (Schadler et al., 1998). A high interfacial shear stress will transfer the applied load to the filler over a short distance and a low interfacial shear stress will require a long distance. There are three main load transfer mechanisms operating between a matrix and filler.

a. Micro-mechanical interlocking

This is the amount of load transfer due to mechanical interlocking which is very poor in nanotube composites because of the atomically smooth surface of nanotubes. As CNTs has some surface defects like varying diameter and bends/twist due to non-hexagonal defects, along a CNT, mechanical interlocking do play a role in CNT–polymer adhesion.

b. Chemical bonding between filler and matrix

A chemical bond either ionic or covalent significantly improves the interfacial interaction between matrix and filler that enables a stress transfer.

c. Weak van der Waals bonding between filler and matrix

The van der Waals interaction arises from the molecular proximity and is the only mode of interaction between CNTs and the matrix in absence of chemical bonding.

Hence, formation of chemical bonding between CNT and polymer can significantly improve the mechanical properties of nanocomposites. Recently, Blake et al. (2004) developed butyl-lithium-functionalized MWCNTs which can be covalently bonded to chlorinated polypropylene (CPP). The CPP/MWCNT was then compounded with CPP/tetrahydrofuran (THF) solution to obtain CPP/MWCNT nanocomposites. They showed that on addition of 0.6 vol% MWCNT, the modulus increased by three times and both tensile strength and toughness (measured by the area under the stress–strain curve) increased by 3.8 times (from 13 to 49 MPa) and 4 times (from 27 to 108 J/g), respectively. Bal & Samal (2007) showed that the amine functionalized CNTs get completely dispersed in polymer matrix in comparison to unmodified CNTs. Telescopic pull-out was also observed in case of functionalized MWCNTs (Gojny et al., 2005). It was observed that although CNTs get pulled out from the matrix the outer wall still remained in the matrix. This is possible because only weak van der Waals forces are present between the various concentric tubes of the MWCNT where as the outer tube is covalently bonded to the matrix. Such a pull-out process suggests that efficient load transfer occurs from matrix to the outer tube, due to strong covalent bonding between epoxy matrix and CNT.

These observations suggest that the efficiency of property improvement depends on the type of CNT, processing techniques and the compatibility between CNT and host matrix. Although chemical functionalization of CNT can improve the compatibility between CNT and polymer which inturn improves the mechanical properties but it has a deteriorating effect on the other properties of nanocomposites such as electrical and thermal conductivity. However, the rapid growth of this field suggests the solution to these problems are not very far and in coming few years' desire of obtaining super strong polymer material will be realized.

6.2 Electrical properties of CNT/polymer nanocomposites

With exceptional mechanical properties, CNTs also possess very high intrinsic electrical conductivity. The electrical conductivity of individual CNTs ranged between 10^7 to 10^8 S/m that is comparable to metals (Ebbesen et al., 1996). Very high electrical conductivity of CNTs

have helped to impart conductivity in highly insulating material like polymer by fabricating polymer nanocomposites. The enhancement in electrical conductivity of insulating polymer by several orders of magnitude has been achieved with a very small loading (0.021 wt %) of nanotubes in the polymer matrices, which helped in preserving other performance aspects of the polymers such as optical clarity, mechanical properties, low melt flow viscosities, etc. As a result, these conducting materials are in growing demand in different application area such as transparent conductive coatings, electrostatic dissipation, electrostatic painting and electromagnetic interference shielding applications.

The electrical conductivity of CNT reinforced polymer nanocomposites depends on many factors including type of CNTs, aspect ratio, surface functionalization and CNT content. The electrical conductivity of nanocomposite increases with increasing CNT loading till a critical filler concentration where a dramatic increase in conductivity is observed. This critical filler concentration is called electrical percolation threshold concentration. At percolation threshold concentration, filler forms a three-dimensional conductive network within the matrix, hence electron can tunnel from one filler to another, and in doing so it overcomes the high resistance offered by insulating polymer matrix. The percolation threshold is typically determined by plotting the electrical conductivity as a function of the reduced mass fraction of filler and fitting with a power law function (Fig. 8). As formation of percolating networks depends on both intrinsic conductivity and aspect ratio of the filler, the nanotube/polymer nanocomposites exhibit very low percolation threshold because of high conductivity and high aspect ratio of CNTs. Bryning et al. (2005b) studied the effect of aspect ratio on percolation threshold concentration by preparing SWCNT/epoxy nanocomposites with nanotubes from two different sources, HiPco and laser oven, having aspect ratios of ~150 and ~380 respectively. They reported a smaller percolation threshold with the higher aspect ratio nanotubes. Similar observation was also made by Bai & Allaoui (2003); they found more than 8-fold decrease in threshold concentration in MWCNT/epoxy composites when the MWCNT length was increased from 1 to 50 μm. In general, the minimum percolation threshold concentration for SWCNT/polymer nanocomposite is 0.0021wt % in epoxy matrix (Martin et al., 2004). For different polymer systems it ranged from 0.0021 to 15 wt% CNT loading (Bauhofer & Kovacs, 2009). These studies show that the percolation threshold concentration and nanocomposite conductivity also depends on polymer type, synthesis method, aspect ratio of CNTs, disentanglement of CNT agglomerates, uniform spatial distribution of individual CNTs and degree of alignment [Bryning, 2005b; Moniruzzaman , 2006b; Du, 2005].

Another factor which significantly affects the electrical conductivity of nanocomposite is the chemical functionalization of CNTs because it disrupts the extended π-conjugation of nanotubes and thereby reduces the electrical conductivity of isolated nanotubes. Sulong et al. (2009) showed that incorporation of acid and octadecylated functionalized MWCNT in epoxy matrix decreased the electrical conductivity of nanocomposites. Similar results have also been reported by Park et al (2009). Hence, it is important to optimize the modification condition or reagent to achieve minimum deterioration of electronic properties of CNTs.

Nevertheless, significant improvement in electrical conductivity of polymer on CNT addition lead to the development of CNT/polymer conductive nanocomposites for electronics, automotive and aerospace applications with uses such as electrostatic dissipation, electromagnetic interference (EMI) shielding, multilayer printed circuits, and

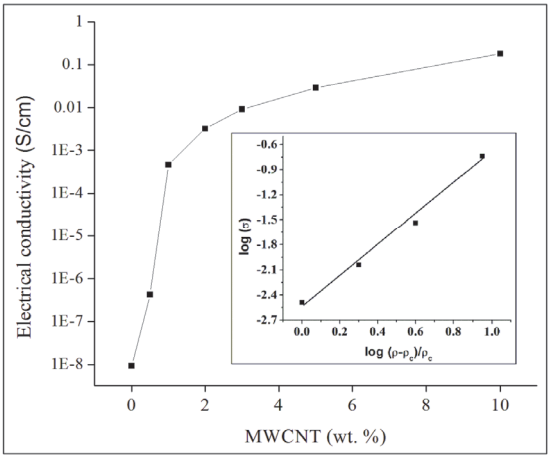

Fig. 8. Plot of dc electrical conductivity (σ) vs weight fraction of MWCNT in PTT/MWCNT composites [inset shows the log-log plot of σ vs $[(\rho- \rho_c)/\rho_c]$

conductive coatings (Baughman, 2002; Dresselhaus, 2004; Holt, 2006; Martel, 1998; Minoux, 2005; Zhang, 2005). The rapid development of electrical industry, demands fabrication of light weight and effective EMI shielding material for the protection of workspace and environment from radiation coming from computers and telecommunication equipment as well as for protection of sensitive circuits. Thus electrically conducting polymer nanocomposites have received much attention recently compared to conventional metal-based EMI shielding materials (Chung, 2001; Joo & Epstein, 1994; Kim, 2003; Yang, 2005a), because of their light weight, resistance to corrosion, flexibility and processing advantages. The use of CNT have significantly reduced the filler loading required to achieve desired EMI SE, thus reduced the cost and weight of the material (Chung, 2001; Micheli, 2009; Sundararaj & Al-Saleh, 2009; Yang, 2005b).

The effect of aspect ratio on EMI SE was shown by Sundararaj & Al-Saleh. They reported that SE of 1 mm thick shielding plate made of 7.5 vol% MWCNT/polypropylene (PP) nanocomposite was much higher (35 dB) than 7.5 vol% (HS-CB)/PP composite (18 dB) in the X-band frequency range. Yang et al. (2005b) studied the EMI shielding behavior of MWCNT/PS nanocomposites and achieved SE of ~20 dB at 7 wt % MWCNT loading. Although, lower value of SE of CNT composites have also been reported, e.g., Liu et al. (2007) achieved only ~17 dB at 20 wt% MWCNTs loading in polyurethane (PU) whereas Kim et al. (2004) reported ~27 dB SE at 40 wt% CNT loading for MWCNT/PMMA films. These observations suggest that SE of CNT filled polymer nanocomposite depends on many factors including fabrication techniques, purity of CNT, dispersion etc. Recently significant efforts have been made in understanding the EMI shielding mechanisms of polymer nanocomposite as it is very important for the best utilization of shielding capabilities of material and for designing nanocomposite at lowest possible filler loading and cost. Three types of EMI shielding mechanisms have been proposed, namely: reflection, absorption and multiple reflections [Sundararaj & Al-Saleh, 2009; Chung, 2001; Liu, 2007]. Some previous studies have shown that in MWCNT/polymer nanocomposites, SE is mainly absorption dominated where as SWCNT/polymer nanocomposites are mainly reflection dominated

material. The application area of EMI shielding materials depends on the dominant shielding mechanism like absorption based EMI shielding materials are used in radar, microwave communication technology, stealth (self concealing) technology, microwave darkroom and anti-EMI coating application.

6.3 Thermal properties

Thermal properties of a composite are equally important as its mechanical and electrical properties because it gives more freedom in selecting processing conditions and also application area. It is observed that incorporation of CNTs in polymer matrices results in increase of glass transition, melting and thermal decomposition temperatures due to hindered chain and segmental mobility of the polymers. To improve the thermal endurance of CNT/polymer nanocomposites, surfactant as the wetting agent were also incorporated. Gong (2000) and Velasco-Santos et al. (2003) reported that addition of 1 wt.% CNTs with a surfactant in epoxy and PMMA matrix increased the glass transition temperature by ~25 and ~40 °C respectively. Incorporation of CNTs in polymer matrices also enhances the rate of crystallization by acting as nucleating sites [Deshpande & Jape, 2009; Zhang, 2008] which in-turn reduces the processing time and enhances mechanical strength. There are reports according to which addition of CNTs in polymer matrix can hinder the crystallization of polymer matrices (Jin, 2007; Diez-Pascual, 2009). Our recent study on MWCNT/PTT nanocomposite suggested that presence of MWCNTs in PTT matrix delays the crystallization and lead to formation of bigger crystallites (Gupta & Choudhary, 2010).

Thermal stability and melting temperature of polymer matrices were improved in presence of CNTs. Kashiwagi et al. (2000) found that the thermal decomposition temperature of polypropylene in nitrogen increases by ~12 °C on 2 vol. % MWCNTs loading. Because of the excellent thermal conductivity of CNTs, incorporation of CNTs significantly improves the thermal transport properties of polymer nanocomposites which lead to its usage as printed circuit boards, connectors, thermal interface materials, heat sinks, and other high-performance thermal management systems. Choi et al. (2003) reported 300% increase in thermal conductivity of epoxy matrix at room temperature on 3 wt % SWCNT loading and an additional increase (10%) when aligned magnetically. Biercuk et al. (2002) prepared an epoxy nanocomposite with 1 wt % raw (not purified) laser-oven SWCNT and showed a 125% increase in thermal conductivity at room temperature. Alignment of CNTs also plays an important role in improving the transport properties of a material. Choi et al. (2003) found 10% increase in thermal conductivity of epoxy composite with aligned MWCNTs in comparison to non-aligned MWCNTs.

7. Application of CNT/polymer nanocomposites

With their excellent range of properties, CNTs have opened up a new age of advanced multifunctional materials. Incorporation of CNTs in polymer matrices provides materials that could be used for many high performance engineering applications. Currently, the most widespread use of CNT nanocomposites is in electronics. These nanocomposites could be used to shield electromagnetic interference and as electrostatic-discharge components. The microwave-absorbing capability of nanotubes could be exploited to heat temporary housing structures and may have applications in space exploration. Thin layers of nanotubes on plastics might also be used in transparent conducting composites. High mechanical strength

of these nanocomposites could be utilized to make some high-end sporting goods such as tennis rackets, baseball bat etc, and thus delivering superior performance. In short, the biggest market for CNT nanocomposites will undoubtedly be for high-value applications that can absorb the added costs, which includes commercial sectors such as electronics especially aerospace (which requires lightweight, high-strength, high-temperature-resistant composites) and energy (for example, in nanotube-reinforced rubber seals for large oil recovery platforms). Once the cost of nanotubes becomes comparable to that of carbon fibre (or even to that of the much cheaper reinforcing agent, carbon black), commodities such as nanotube-filled rubber tyres could become a reality.

8. Conclusion and future scope

Studies on CNT/polymer nanocomposite suggests that CNT has great potential in altering the properties of polymer matrices. The quality of CNT/polymer nanocomposites depends on many factors including type of CNTs, chirality, purity, defect density, aspect ratio, % loading, dispersion, alignment and interfacial adhesion between the nanotube and polymer matrix. A lot of research work has been carried out to improve the quality of CNTs and processing techniques. The biggest challenge in realizing the full potential of CNTs is to achieve homogeneous dispersion of CNTs so that maximum filler surface area will be available for load-transfer between filler and matrix. The functionalization of nanotubes provides a convenient route to improve dispersion and stress transfer between CNT and polymer matrix, but more improvement in this field is required to preserve the intrinsic properties of CNTs. It is important to focus on different methods of noncovalent functionalization of nanotubes and discover a route which can improve the dispersion and compatibility without negatively affecting the composite properties. The actual task of dispersing the CNTs in polymer matrix is performed during its manufacturing. The three major processing techniques namely, solution, melt and in-situ polymerization have their unique advantages in fabricating CNT/polymer nanocomposite. Although solution blending produces high quality composite but melt compounding is much simpler and provide option for large scale production. Recently, in-situ polymerization is also showing great potential in fabricating CNT/polymer nanocomposite. The success of processing technique is directly related to performance of composite. The maximum improvement in mechanical properties of polymer matrix is observed in case of in-situ polymerization which produces covalent bond between CNT and polymer matrix. However it negatively influences the electronic properties of the composite. The increase in electrical conductivity of polymer material on CNT addition is the biggest advantage of fabricating CNT/polymer nanocomposite. As significant improvement in electrical conductivity is observed at very low CNT loading, CNT/polymer nanocomposite is finding application as light weight, low cost and highly effective ESD and EMI shielding material. The thermal properties of the polymer matrix also modified by CNT addition like CNT increases the glass transition, melting and thermal decomposition temperatures. CNT also influences the crystallization rate and percentage crystallinity by acting as nucleating agent. Improvement in both crystallization rate and percentage crystallinity enhances its mechanical and processing properties. So finally we can conclude that CNT is ideal filler for fabricating polymer composite but some serious challenges need to be addressed before fully realizing the extraordinary properties of CNT in polymer nanocomposite.

9. References

Ajayan, P. M., Stephan, O., Colliex, C., & Trauth, D. (1994). Aligned carbon nanotube arrays formed by cutting a polymer resin-nanotube composite. *Science,* Vol. 265, pp. 1212-1214, ISSN 0036-8075

Ajayan, P. M., Schadler, L. S., Giannaris, C., & Rubio, A. (2000). Single-walled carbon nanotube-polymer composites: strength and weakness. *Adv. Mater.,* Vol. 12, pp. 750-753, ISSN 0935-9648

Awasthi, K., Srivastava, A., & Srivastava, O. N. (2005). Synthesis of carbon nanotubes. *J Nanosci Nanotechnol,* Vol. 5, pp. 1616-1636, ISSN 1550-7033

Badaire, S., Poulin, P., Maugey, M., & Zakri, C. (2004). In Situ Measurements of Nanotube Dimensions in Suspensions by Depolarized Dynamic Light Scattering. *Langmuir,* Vol. 20, pp. 10367-10370, ISSN 0743-7463

Bai, J. B., & Allaoui, A. (2003). Effect of the length and the aggregate size of MWNTs on the improvement efficiency of the mechanical and electrical properties of composites - experimental investigation. *Composites, Part A,* Vol. 34A, pp. 689-694, ISSN 1359-835X

Bal, S., & Samal, S. S. (2007). Carbon nanotube reinforced polymer composites - a state of the art. *Bull. Mater. Sci.,* Vol. 30, pp. 379-386, ISSN 0250-4707

Bandyopadhyaya, R., Nativ-Roth, E., Regev, O., & Yerushalmi-Rozen, R. (2002). Stabilization of individual carbon nanotubes in aqueous solutions. *Nano Lett.,* Vol. 2, pp. 25-28, ISSN 1530-6984

Banerjee, S., Hemraj-Benny, T., & Wong, S. S. (2005). Covalent surface chemistry of single-walled carbon nanotubes. *Adv. Mater.,* Vol. 17, pp. 17-29, ISSN 0935-9648

Barrau, S., Demont, P., Perez, E., Peigney, A., Laurent, C., & Lacabanne, C. (2003). Effect of palmitic acid on the electrical conductivity of carbon nanotubes-epoxy resin composites. *Macromolecules,* Vol. 36, pp. 9678-9680, ISSN 0024-9297

Baughman, R. H., Zakhidov, A. A., & de Heer, W. A. (2002). Carbon nanotubes-the route toward applications. *Science,* Vol. 297, pp. 787-792, ISSN 0036-8075

Bauhofer, W., & Kovacs, J. Z. (2009). A review and analysis of electrical percolation in carbon nanotube polymer composites. *Compos. Sci. Technol.,* Vol. 69, pp. 1486-1498, ISSN 0266- 3538

Benoit, J. M., Corraze, B., Lefrant, S., Blau, W. J., Bernier, P., & Chauvet, O. (2001). Transport properties of PMMA-Carbon Nanotubes composites. *Synth. Met.,* Vol. 121, pp. 1215-1216, ISSN 0379-6779

Bhattacharyya, A. R., Sreekumar, T. V., Liu, T., Kumar, S., Ericson, L. M., & Hauge, R. H. (2003). Crystallization and orientation studies in polypropylene/single wall carbon nanotube composite. *Polymer,*Vol. 44, pp. 2373-2377, ISSN 0032-3861

Biercuk, M. J., Llaguno, M. C., Radosavljevic, M., Hyun, J. K., Johnson, A. T., & Fischer, J. E. (2002). Carbon nanotube composites for thermal management. *Appl. Phys. Lett.,* Vol. 80, pp. 2767-2769, ISSN 0003-6951

Blake, R., Gun'ko, Y. K., Coleman, J., Cadek, M., Fonseca, A., & Nagy, J. B. (2004). A Generic Organometallic Approach toward Ultra-Strong Carbon Nanotube Polymer Composites. *J. Am. Chem. Soc.,* Vol. 126, pp. 10226-10227, ISSN 0002-7863

(a) Bryning, M. B., Milkie, D. E., Islam, M. F., Kikkawa, J. M., & Yodh, A. G. (2005). Thermal conductivity and interfacial resistance in single-wall carbon nanotube epoxy composites. *Appl. Phys. Lett.,* Vol. 87, pp. 161909/161901-161909/161903, ISSN 0003-6951

(b) Bryning, M. B., Islam, M. F., Kikkawa, J. M., & Yodh, A. G. (2005). Very low conductivity threshold in bulk isotropic single-walled carbon nanotube-epoxy composites. *Adv. Mater.,* Vol. 17, pp. 1186-1191, ISSN 0935-9648

Cadek, M., Coleman, J. N., Barron, V., Hedicke, K., & Blau, W. J. (2002). Morphological and mechanical properties of carbon-nanotube-reinforced semicrystalline and amorphous polymer composites. *Appl. Phys. Lett.,* Vol. 81, pp. 5123-5125, ISSN 0003-6951

Cai, L., Tabata, H., & Kawai, T. (2000). Self-assembled DNA networks and their electrical conductivity. *Appl. Phys. Lett.,* Vol. 77, pp. 3105-3106, ISSN 0003-6951

Charlier, J. C., & Issi, J. P. (1996). Electrical conductivity of novel forms of carbon. *J. Phys. Chem. Solids,* Vol. 57, pp. 957-965, ISSN 0022-3697

Cheng, F., Imin, P., Maunders, C., Botton, G., & Adronov, A. (2008). Soluble, discrete supramolecular complexes of single-walled carbon nanotubes with fluorene-based conjugated polymers. *Macromolecules,* Vol. 41, pp. 2304-2308, ISSN 0024-9297

Choi, E. S., Brooks, J. S., Eaton, D. L., Al-Haik, M. S., Hussaini, M. Y., & Garmestani, H. (2003). Enhancement of thermal and electrical properties of carbon nanotube polymer composites by magnetic field processing. *J. Appl. Phys.,* Vol. 94, pp. 6034-6039, ISSN 0021-8979

Chung, D. D. L. (2001). Electromagnetic interference shielding effectiveness of carbon materials. *Carbon,* Vol. 39, pp. 279-285, ISSN 0008-6223

Coleman, J. N., Dalton, A. B., Curran, S., Rubio, A., Davey, A. P., & Drury, A. (2000). Phase separation of carbon nanotubes and turbostratic graphite using a functional organic polymer. *Adv. Mater.,* Vol. 12, pp. 213-216, ISSN 0935-9648

Coleman, J. N., Khan, U., Blau, W. J., & Gunko, Y. K. (2006). Small but strong: A review of the mechanical properties of carbon nanotube-polymer composites. *Carbon,* Vol. 44, pp. 1624-1652, ISSN 0008-6223

Camponeschi, E., Vance, R., Al-Haik, M., Garmestani, H., & Tannenbaum, R. (2007). Properties of carbon nanotube-polymer composites aligned in a magnetic field. *Carbon,* Vol. 45, pp. 2037-2046, ISSN 0008-6223

Curran, S. A., Ajayan, P. M., Blau, W. J., Carroll, D. L., Coleman, J. N., & Dalton, A. B. (1998). A composite from poly(m-phenylenevinylene-co-2,5-dioctoxy-p-phenylenevinylene) and carbon nanotubes. A novel material for molecular optoelectronics. *Adv. Mater.,* Vol. 10, pp. 1091-1093, ISSN 0935-9648

Dai, H., Wong, E. W., & Lieber, C. M. (1996). Probing electrical transport in nanomaterials: conductivity of individual carbon nanotubes. *Science,* Vol. 272, pp. 523-526, ISSN 0036-8075

Deshpande, V. D., & Jape, S. (2009). Nonisothermal crystallization kinetics of nucleated poly(ethylene terephthalate). *J. Appl. Polym. Sci.,* Vol. 111, pp. 1318-1327, ISSN 0021-8995

Dıez-Pascual, A. M.; Naffakh, M.; Gomez, M. A.; Marco, C.; Ellis, G.; & Simard B. (2009). Development and characterization of PEEK/carbon nanotube composites. *Carbon,* Vol. 4 7, pp. 3079–3090, ISSN 0008-6223

Dresselhaus, M. S. (2004). Applied physics: Nanotube antennas. *Nature,* Vol. 432, pp. 959-960, ISSN 0028-0836

Du, F., Fischer, J. E., & Winey, K. I. (2005). Effect of nanotube alignment on percolation conductivity in carbon nanotube/polymer composites. *Phys. Rev. B: Condens. Matter Mater. Phys.,* Vol. 72, pp. 121404/121401-121404/121404, ISSN 1098-0121

Du, F., Fischer, J. E., & Winey, K. I. (2003). Coagulation method for preparing single-walled carbon nanotube/poly(methyl methacrylate) composites and their modulus, electrical conductivity, and thermal stability. *J. Polym. Sci., Part B: Polym. Phys.,* Vol. 41, pp. 3333-3338, ISSN 0887-6266

Dubois, P., & Alexandre, M. (2006). Performant clay/carbon nanotube polymer composites. *Adv. Eng. Mater.,* Vol. 8, pp. 147-154, ISSN 1438-1656

Ebbesen, T. W., Lezec, H. J., Hiura, H., Bennett, J. W., Ghaemi, H. F., & Thio, T. (1996). Electrical conductivity of individual carbon nanotubes. *Nature,* Vol. 382, 54-56, ISSN 0028-0836

Feng, J., Sui, J., Cai, W., & Gao, Z. (2008). Microstructure and mechanical properties of carboxylated carbon nanotubes/poly(L-lactic acid) composite. *J. Compos. Mater.,* Vol. 42, pp.1587-1595, ISSN 0021-9983

Feng, W., Bai, X. D., Lian, Y. Q., Liang, J., Wang, X. G., & Yoshino, K. (2003). Well-aligned polyaniline/carbon-nanotube composite films grown by in-situ aniline polymerization. *Carbon,* Vol. 41, pp. 1551-1557, ISSN 0008-6223

Fiege, G. B. M., Altes, A., Heiderhoff, R., & Balk, L. J. (1999). Quantitative thermal conductivity measurements with nanometer resolution. *J. Phys. D: Appl. Phys.,* Vol. 32, pp. L13-L17, ISSN 0022-3727

Fischer, J. E., Dai, H., Thess, A., Lee, R., Hanjani, N. M., & Dehaas, D. L. (1997). Metallic resistivity in crystalline ropes of single-wall carbon nanotubes. *Phys. Rev. B: Condens. Matter,* Vol. 55, pp. R4921-R4924, ISSN 1098-0121

Fu, K., Huang, W., Lin, Y., Riddle, L. A., Carroll, D. L., & Sun, Y.-P. (2001). Defunctionalization of Functionalized Carbon Nanotubes. *Nano Lett.,* Vol. 1, pp. 439-441, ISSN 1530-6984

Gao, J., Zhao, B., Itkis, M. E., Bekyarova, E., Hu, H., & Kranak, V. (2006). Chemical engineering of the single-walled carbon nanotube-nylon 6 interface. *J. Am. Chem. Soc.,* Vol. 128, pp. 7492-7496, ISSN 0002-7863

Gao, J., Itkis, M. E., Yu, A., Bekyarova, E., Zhao, B., & Haddon, R. C. (2005). Continuous Spinning of a Single-Walled Carbon Nanotube-Nylon Composite Fiber. *J. Am. Chem. Soc.,* Vol. 127, pp.3847-3854, ISSN 0002-7863

Gao, J., Yu, A., Itkis, M. E., Bekyarova, E., Zhao, B., & Niyogi, S. (2004). Large-scale fabrication of aligned single-walled carbon nanotube array and hierarchical single-walled carbon nanotube assembly. *J. Am. Chem. Soc.,* Vol. 126, pp. 16698-16699, ISSN 0002-7863

Gojny, F. H., Wichmann, M. H. G., Fiedler, B., Bauhofer, W., & Schulte, K. (2005). Influence of nano-modification on the mechanical and electrical properties of conventional

fibre-reinforced composites. *Composites, Part A,* Vol. 36A, pp. 1525-1535, ISSN 1359-835X

Gomes, S., Trannoy, N., & Grossel, P. (1999). DC thermal microscopy: study of the thermal exchange between a probe and a sample. *Meas. Sci. Technol.,* Vol. 10, pp. 805-811, ISSN 0957-0233

Gong, X., Liu, J., Baskaran, S., Voise, R. D., & Young, J. S. (2000). Surfactant-assisted processing of carbon nanotube/polymer composites. *Chem. Mater.,* Vol. 12, pp. 1049-1052, ISSN 0897-4756

Grossiord, N., Loos, J., & Koning, C. E. (2005). Strategies for dispersing carbon nanotubes in highly viscous polymers. *J. Mater. Chem.,* Vol. 15, pp. 2349-2352, ISSN 0959-9428

Gupta, A.; & Choudhary, V. (2010). Isothermal and non-Isothermal crystallization kinetics and morphology of poly(trimethylene terephthalate)/multiwalled carbon nanotube composites. *Macromole. Symp.*, Vol. 290, pp. 56-69, ISSN 1022-1360

Haggenmueller, R., Fischer, J. E., & Winey, K. I. (2006). Single wall carbon nanotube/polyethylene composites: nucleating and templating polyethylene crystallites. *Macromolecules,* Vol. 39, pp. 2964-2971, ISSN 0024-9297

Haggenmueller, R., Gommans, H. H., Rinzler, A. G., Fischer, J. E., & Winey, K. I. (2000). Aligned single-wall carbon nanotubes in composites by melt processing methods. *Chem. Phys. Lett.,* Vol. 330, pp. 219-225, ISSN 0009-2614

Haggenmueller, R., Zhou, W., Fischer, J. E., & Winey, K. I. (2003). Production and characterization of highly aligned single-walled carbon nanotubes in polymer composites. *J. Nanosci.Nanotechnol.*, Vol. 3, pp. 105-110, ISSN 1550-7033

Hamada, N., Sawada, S., & Oshiyama, A. (1992). New one-dimensional conductors: graphitic microtubules. *Phys. Rev. Lett.,* Vol. 68, pp. 1579-1581, ISSN 0031-9007

Hersam, M. C., Hoole, A. C. F., O'Shea, S. J., & Welland, M. E. (1998). Potentiometry and repair of electrically stressed nanowires using atomic force microscopy. *Appl. Phys. Lett.,* Vol. 72, pp. 915-917, ISSN 0003-6951

Hirsch, A. (2002). Functionalization of single-walled carbon nanotubes. *Angewandte Chemie International Edition,* Vol. 41, pp. 1853-1859, ISSN 0570-0833

Holt, J. K., Park, H. G., Wang, Y., Stadermann, M., Artyukhin, A. B., & Grigoropoulos, C. P. (2006). Fast mass transport through sub-2-nanometer carbon nanotubes. *Science,* Vol. 312, pp. 1034-1037, ISSN 0036-8075

Hone, J., Whitney, M., & Zettl, A. (1999). Thermal conductivity of single-walled carbon nanotubes. *Synth. Met.,* Vol. 103, pp.2498-2499, ISSN 0379-6779

Hou, H., Ge, J. J., Zeng, J., Li, Q., Reneker, D. H., & Greiner, A. (2005). Electrospun polyacrylonitrile nanofibers containing a high concentration of well-aligned multiwall carbon nanotubes. *Chem. Mater.,* Vol. 17, pp. 967-973, ISSN 0897-4756

Hwang, G. L., Shieh, Y.-T., & Hwang, K. C. (2004). Efficient load transfer to polymer-grafted multiwalled carbon nanotubes in polymer composites. *Adv. Funct. Mater.,* Vol. 14, pp. 487-491, ISSN 1616-301X

Islam, M. F., Rojas, E., Bergey, D. M., Johnson, A. T., & Yodh, A. G. (2003). High weight fraction surfactant solubilization of single-wall carbon nanotubes in water. *Nano Lett.,* Vol. 3, pp. 269-273, ISSN 1530-6984

Iijima, S. (1991). Helical microtubules of graphitic carbon. *Nature,* Vol. 354, pp. 56-58, ISSN 0028-0836

Ishikawa, H., Fudetani, S., & Hirohashi, M. (2001). Mechanical properties of thin films measured by nanoindenters. *Appl. Surf. Sci.,* Vol. 178, pp. 56-62, ISSN 0169-4332

Jia, Z., Wang, Z., Xu, C., Liang, J., Wei, B., & Wu, D. (1999). Study on poly(methyl methacrylate)/carbon nanotube composites. *Mater. Sci. Eng., A,* Vol. A271, pp. 395-400, ISSN 0921-5093

Jin, J.; Song, M.; & Pan F. (2007) A DSC study of effect of carbon nanotubes on crystallization behaviour of poly(ethylene oxide). *Thermo. Acta*, Vol. 45, pp. 25–31, ISSN 0040-6031

Jin, Z., Pramoda, K. P., Goh, S. H., & Xu, G. (2002). Poly(vinylidene fluoride)-assisted melt-blending of multi-walled carbon nanotube/poly(methyl methacrylate) composites. *Mater. Res. Bull.,* Vol. 37, pp. 271-278, ISSN 0025-5408

Jin, L., Bower, C., & Zhoua, O. (1998). Alignment of carbon nanotubes in a polymer matrix by mechanical stretching. *Appl. Phys. Lett.,* Vol. 73, pp. 1197-1202, ISSN 0003-6951

Joo, J., & Epstein, A. J. (1994). Electromagnetic radiation shielding by intrinsically conducting polymers. *Appl. Phys. Lett.,* Vol. 65, pp. 2278-2280, ISSN 0003-6951

Kashiwagi, T., Gilman, J. W., Butler, K., Harris, R. H., Shields, J. R., & Asano, A. (2000). Flame retardant mechanism of silica gel/silica. *Fire Mater.,* Vol. 24, pp. 277-289, ISSN 0308-0501

Kane, C. L., & Mele, E. J. (1997). Size, shape, and low energy electronic structure of carbon nanotubes. *Phys. Rev. Lett.,* Vol. 78, pp. 1932-1935, ISSN 0031-9007

Kim, P., Shi, L., Majumdar, A., & McEuen, P. L. (2001). Thermal transport measurements of individual multiwalled nanotubes. *Phys. Rev. Lett.,* Vol. 87, pp. 215502/215501-215502/215504, ISSN 0031-9007

Kim, H. M., Kim, K., Lee, C. Y., Joo, J., Cho, S. J., & Yoon, H. S. (2004). Electrical conductivity and electromagnetic interference shielding of multiwalled carbon nanotube composites containing Fe catalyst. *Appl. Phys. Lett.,* Vol. 84, pp. 589-591, ISSN 0003-6951

Kim, S. H., Jang, S. H., Byun, S. W., Lee, J. Y., Joo, J. S., & Jeong, S. H. (2003). Electrical properties and EMI shielding characteristics of polypyrrole-nylon 6 composite fabrics. *J. Appl. Polym. Sci.,* Vol. 87, pp.1969-1974, ISSN 0021-8995

Ko, F., Gogotsi, Y., Ali, A., Naguib, N., Ye, H., & Yang, G. (2003). Electrospinning of continuous carbon nanotube-filled nanofiber yarns. *Adv. Mater.,* Vol. 15, pp. 1161-1165, ISSN 0935-9648

Kracke, B., & Damaschke, B. (2000). Measurement of nanohardness and nanoelasticity of thin gold films with scanning force microscope. *Appl. Phys. Lett.,* Vol. 77, pp. 361-363, ISSN 0003-6951

Lamy de la Chapelle, M., Stephan, C., Nguyen, T. P., Lefrant, S., Journet, C., & Bernier, P. (1999). Raman characterization of singlewalled carbon nanotubes-PMMA composites. *Synth. Met.,* Vol. 103, pp. 2510-2512, ISSN 0379-6779

Luo, J.-T., Wen, H.-C., Wu, W.-F., & Chou, C.-P. (2008). Mechanical research of carbon nanotubes/PMMA composite films. *Polym. Compos.,* Vol. 29, pp. 1285-1290, ISSN 0272-8397

Liu, P. (2005). Modifications of carbon nanotubes with polymers. *Eur. Polym. J.,* Vol. 41, pp. 2693-2703, ISSN 0014-3057

Liu, Z., Bai, G., Huang, Y., Ma, Y., Du, F., & Li, F. (2007). Reflection and absorption contributions to the electromagnetic interference shielding of single-walled carbon nanotube/polyurethane composites. *Carbon,* Vol. 45, pp.821-827, ISSN 0008-6223

Liu, T., Phang, I.Y., Shen, L., Chow, S.Y., & Zhang, W-D. (2004). Morphology and Mechanical Properties of Multiwalled Carbon Nanotubes Reinforced Nylon-6 Composites. *Macromolecules*, Vol. 37, pp. 7214-7222, ISSN 0024-9297

Ma,C., Zhang, W., Zhu, Y., Ji, L., Zhang, R., Koratkar, N.,& Liang J. (2006). Alignment and dispersion of functionalized carbon nanotubes in polymer composites induced by an electric field. *Carbon,* Vol. 46, pp. 706-720, ISSN 0008-6223

Martel, R., Schmidt, T., Shea, H. R., Hertel, T., & Avouris, P. (1998). Single- and multi-wall carbon nanotube field-effect transistors. *Appl. Phys. Lett.,* Vol. 73, pp. 2447-2449, ISSN 0003-6951

Martin, C. A., Sandler, J. K. W., Shaffer, M. S. P., Schwarz, M. K., Bauhofer, W., & Schulte, K. (2004). Formation of percolating networks in multi-wall carbon-nanotube-epoxy composites. *Compos. Sci. Technol.,* Vol. 64, pp. 2309-2316, ISSN 0266- 3538

Matarredona, O., Rhoads, H., Li, Z., Harwell, J. H., Balzano, L., & Resasco, D. E. (2003). Dispersion of single-walled carbon nanotubes in aqueous solutions of the anionic surfactant NaDDBS. *J. Phys. Chem. B,* Vol. 107, pp. 13357-13367, ISSN 1089-5647

Micheli, D., Pastore, R., Apollo, C., Marchetti, M., Gradoni, G., & Moglie, F. (2009). Carbon based nanomaterial composites in RAM and microwave shielding applications, *9th IEEE Conf. Nanotechnol., pp.* 226-235, ISBN 978-1-4244-4832-6, Genoa, 26-30 July, 2009

Minoux, E., Groening, O., Teo, K. B. K., Dalal, S. H., Gangloff, L., & Schnell, J.-P. (2005). Achieving high-current carbon nanotube emitters. *Nano Lett.,* Vol. 5, pp. 2135-2138, ISSN 1530-6984

Mintmire, J. W., Dunlap, B. I., & White, C. T. (1992). Are fullerene tubules metallic? *Phys. Rev. Lett.,* Vol. 68, pp. 631-634, ISSN 0031-9007

(a) Moniruzzaman, M., Du, F., Romero, N., & Winey, K. I. (2006). Increased flexural modulus and strength in SWNT/epoxy composites by a new fabrication method. *Polymer,* Vol. 47, pp. 293-298, ISSN 0032-3861

(b) Moniruzzaman, M., & Winey, K. I. (2006). Polymer composites containing carbon nanotubes. *Macromolecules,* Vol. 39, pp. 5194-5205, ISSN 0024-9297

Monthioux, M. (2002). Filling single-wall carbon nanotubes. *Carbon,* Vol. 40, pp. 1809-1823, ISSN 0008-6223

Moore, V. C., Strano, M. S., Haroz, E. H., Hauge, R. H., Smalley, R. E., & Schmidt, J. (2003). Individually suspended single-walled carbon nanotubes in various surfactants. *Nano Lett.,* Vol. 3, pp. 1379-1382, ISSN 1530-6984

O'Connell, M. J., Boul, P., Ericson, L. M., Huffman, C., Wang, Y., & Haroz, E. (2001). Reversible water-solubilization of single-walled carbon nanotubes by polymer wrapping. *Chem. Phys. Lett.,* Vol. 342, pp. 265-271, ISSN 0009-2614

Odom, T. W., Huang, J., Kim, P., & Lieber, C. M. (1998). Atomic structure and electronic properties of single-walled carbon nanotubes. *Nature,* Vol. 391, pp. 62-64, ISSN 0028-0836

Park, C., Ounaies, Z., Watson, K. A., Crooks, R. E., Smith, J., & Lowther, S. E. (2002). Dispersion of single wall carbon nanotubes by in-situ polymerization under sonication. *Chem. Phys. Lett.,* Vol. 364, pp. 303-308, ISSN 0009-2614

Park, O-K., Jeevananda, T., Kim, N. H., Kim, S.-i., & Lee, J. H. (2009). Effects of surface modification on the dispersion and electrical conductivity of carbon nanotube/polyaniline composites. *Scr. Mater.,* Vol. 60, pp. 551-554, ISSN 1359-6462

Pei, X., Hu, L., Liu, W., & Hao, J. (2008). Synthesis of water-soluble carbon nanotubes via surface initiated redox polymerization and their tribological properties as water-based lubricant additive. *Eur. Polym. J.,* Vol. 44, pp. 2458-2464, ISSN 0014-3057

Poetschke, P., Bhattacharyya, A. R., Janke, A., & Goering, H. (2003). Melt mixing of polycarbonate/multi-wall carbon nanotube composites. *Compos. Interfaces,* pp. 389-404, ISSN 1568-5543

Putz, K. W., Mitchell, C. A., Krishnamoorti, R., & Green, P. F. (2004). Elastic modulus of single-walled carbon nanotube/poly(methyl methacrylate) composites. *J. Polym. Sci., Part B: Polym. Phys.,* Vol. 42, pp. 2286-2293, ISSN 0887-6266

Qian, D., Dickey, E. C., Andrews, R., & Rantell, T. (2000). Load transfer and deformation mechanisms in carbon nanotube-polystyrene composites. *Appl. Phys. Lett.,* Vol. 76, pp. 2868-2870, ISSN 0003-6951

Qin, S., Qin, D., Ford, W. T., Resasco, D. E., & Herrera, J. E. (2004). Functionalization of single-walled carbon nanotubes with polystyrene via grafting to and grafting from methods. *Macromolecules,* Vol. 37, pp. 752-757, ISSN 0024-9297

Raravikar, N. R., Schadler, L. S., Vijayaraghavan, A., Zhao, Y., Wei, B., & Ajayan, P. M. (2005). Synthesis and characterization of thickness-aligned carbon nanotube-polymer composite films. *Chem. Mater.,* Vol. 17, pp. 974-983, ISSN 0897-4756

(a) Rasheed, A., Dadmun, M. D., & Britt, P. F. (2006). Polymer-nanofiber composites: enhancing composite properties by nanofiber oxidation. *J. Polym. Sci., Part B: Polym. Phys.,* Vol. 44, pp. 3053-3061, ISSN 0887-6266

(b) Rasheed, A., Chae, H. G., Kumar, S., & Dadmun, M. D. (2006). Polymer nanotube composites: Correlating intermolecular interaction to ultimate properties. *Polymer,* Vol. 47, pp. 4734-4741, ISSN 0032-3861

Regev, O., ElKati, P. N. B., Loos, J., & Koning, C. E. (2004). Preparation of conductive nanotube-polymer composites using latex technology. *Adv. Mater.,* 16, 248-251, ISSN 0935-9648

Ruiz, F., Sun, W. D., Pollak, F. H., & Venkatraman, C. (1998). Determination of the thermal conductivity of diamond-like composite films using a scanning thermal microscope. *Appl. Phys. Lett.,* Vol. 73, pp. 1802-1804, ISSN 0003-6951

Safadi, B., Andrews, R., & Grulke, E. A. (2002). Multiwalled carbon nanotube polymer composites: synthesis and characterization of thin films. *J. Appl. Polym. Sci.,* Vol. 84, pp. 2660-2669, ISSN 0021-8995

Sahoo, N. G., Jung, Y. C., Yoo, H. J., & Cho, J. W. (2006). Effect of functionalized carbon nanotubes on molecular interaction and properties of polyurethane composites. *Macromol. Chem. Phys.,* Vol. 207, pp. 1773-1780, ISSN 1521-3935

Saito, R., Fujita, M., Dresselhaus, G., & Dresselhaus, M. S. (1992). Electronic structure of chiral graphene tubules. *Appl. Phys. Lett.,* Vol. 60, pp. 2204-2206, ISSN 0003-6951

Schadler, L. S., Giannaris, S. C., & Ajayan, P. M. (1998). Load transfer in carbon nanotube epoxy composites. *Appl. Phys. Lett.,* Vol. 73, pp. 3842-3844, ISSN 0003-6951

Singh, P., Campidelli, S., Giordani, S., Bonifazi, D., Bianco, A., & Prato, M. (2009). Organic functionalisation and characterisation of single-walled carbon nanotubes. *Chem Soc Rev,* Vol. 38, pp. 2214-2230, ISSN 0306-0012

Siochi, E. J., Working, D. C., Park, C., Lillehei, P. T., Rouse, J. H., & Topping, C. C. (2004). Melt processing of SWCNT-polyimide composite fibers. *Composites, Part B,* Vol. 35B, pp. 439-446, ISSN 1359- 8368

Sui, G., Zhong, W. H., Yang, X. P., Yu, Y. H., & Zhao, S. H. (2008). Preparation and properties of natural rubber composites reinforced with pretreated carbon nanotubes. *Polym. Adv. Technol.,* Vol. 19, pp. 1543-1549, ISSN 1042- 7147

Sulong, A. B., Muhamad, N., Sahari, J., Ramli, R., Md Deros, B., & Park, J. (2009). Electrical conductivity behavior of chemical functionalized MWCNTs epoxy composites. *European Journal of Scientific Research.* Vol. 29, pp. 13-21, ISSN 1450-216X

Sun, L., Warren, G. L., O'Reilly, J. Y., Everett, W. N., Lee, S. M., & Davis, D. (2008). Mechanical properties of surface-functionalized SWCNT/epoxy composites. *Carbon,* Vol. 46, pp. 320-328, ISSN 0008-6223

Sundararaj, U. & Al-Saleh, M. H., (2009). Electromagnetic interference shielding mechanisms of CNT/polymer composites. *Carbon,* Vol. 47, pp. 1738-1746, ISSN 0008-6223

Tans, S. J., Devoret, M. H., Dal, H., Thess, A., Smalley, R. E., & Geerligs, L. J. (1997). Individual single-wall carbon nanotubes as quantum wires. *Nature,* Vol. 386, pp. 474-477, ISSN 0028-0836

Thostenson, E. T., Ren, Z., & Chou, T. W. (2001). Advances in the science and technology of carbon nanotubes and their composites: a review. *Compos. Sci. Technol.,* Vol. 61, pp. 1899-1912, ISSN 0266- 3538

Thostenson, E. T., & Chou, T.-W. (2002). Aligned multi-walled carbon nanotube-reinforced composites: processing and mechanical characterization. *J. Phys. D: Appl. Phys.,* Vol. 35, pp. L77-L80, ISSN 0022-3727

Velasco-Santos, C., Martinez-Hernandez, A. L., Fisher, F. T., Ruoff, R., & Castano, V. M. (2003). Improvement of thermal and mechanical properties of carbon nanotube composites through chemical functionalization. *Chem. Mater.,* Vol. 15, pp. 4470-4475, ISSN 0897-4756

Vigolo, B., Penicaud, A., Coulon, C., Sauder, C., Pailler, R., & Journet, C. (2000). Macroscopic fibers and ribbons of oriented carbon nanotubes. *Science,* Vol. 290, pp. 1331-1334, ISSN 0036-8075

Wong, K.-K., Shi, S.-Q., & Lau, K.-T. (2007). Mechanical and thermal behavior of a polymer composite reinforced with functionalized carbon nanotubes. *Key Eng. Mater.,* Vol. *334-335*, pp. 705-708, ISSN 1013-9826

Wu, C.-S. (2009). Synthesis and characterization of poly(trimethylene terephthalate) composites incorporating multi-walled carbon nanotubes. *J. Appl. Polym. Sci.,* Vol. 114, pp. 1633-1642, ISSN 0021-8995

Wu, H.-X., Qiu, X.-Q., Cao, W.-M., Lin, Y.-H., Cai, R.-F., & Qian, S.-X. (2007). Polymer-wrapped multiwalled carbon nanotubes synthesized via microwave-assisted in situ emulsion polymerization and their optical limiting properties. *Carbon,* Vol. 45, pp. 2866-2872, ISSN 0008-6223

Xie, X.-L., Mai, Y.-W., & Zhou, X.-P. (2005). Dispersion and alignment of carbon nanotubes in polymer matrix: A review. *Mater. Sci. Eng., R,* Vol. R49, pp. 89-112, ISSN 0927-796X

(a) Yang, Y., Gupta, M. C., Dudley, K. L., & Lawrence, R. W. (2005). Conductive carbon nanofiber-polymer foam structures. *Adv. Mater.,* Vol. 17, pp. 1999-2003, ISSN 0935-9648

(b) Yang, Y., Gupta, M. C., Dudley, K. L., & Lawrence, R. W. (2005). Novel carbon nanotube-polystyrene foam composites for electromagnetic interference shielding. *Nano Lett.,* Vol. 5, pp. 2131-2134, ISSN 1530-6984

(a) Yu, M.-F., Files, B. S., Arepalli, S., & Ruoff, R. S. (2000). Tensile loading of ropes of single wall carbon nanotubes and their mechanical properties. *Phys. Rev. Lett.,* Vol. 84, pp. 5552-5555, ISSN 0031-9007

(b) Yu, M.-F., Lourie, O., Dyer, M. J., Moloni, K., Kelly, T. F., & Ruoff, R. S. (2000). Strength and breaking mechanism of multiwalled carbon nanotubes under tensile load. *Science,* Vol. 287, pp. 637-640, ISSN 0036-8075

(a) Yuen, S.-M., & Ma, C.-C. M. (2008). Morphological, electrical, and mechanical properties of multiwall carbon nanotube/polysilsesquioxane composite. *J. Appl. Polym. Sci.,* Vol. 109, pp. 2000-2007, ISSN 0021-8995

(b) Yuen, S.-M., Ma, C.-C. M., Chuang, C.-Y., Yu, K.-C., Wu, S.-Y., & Yang, C.-C. (2008). Effect of processing method on the shielding effectiveness of electromagnetic interference of MWCNT/PMMA composites. *Compos. Sci. Technol.,* Vol. 68, pp. 963-968, ISSN 0266- 3538

(c) Yuen, S.-M., Ma, C.-C. M., Teng, C.-C., Wu, H.-H., Kuan, H.-C., & Chiang, C.-L. (2008). Molecular motion, morphology, and thermal properties of multiwall carbon nanotube/polysilsesquioxane composite. *J. Polym. Sci., Part B: Polym. Phys.,* Vol. 46, pp. 472-482, ISSN 0887-6266

Zhang, W. D., Shen, L., Phang, I. Y., & Liu, T. (2004). Carbon nanotubes reinforced nylon-6 composite prepared by simple melt-compounding. *Macromolecules,* 37, 256-259, ISSN 0024-9297

Zhang, M., Fang, S., Zakhidov, A. A., Lee, S. B., Aliev, A. E., & Williams, C. D. (2005). Strong, transparent, multifunctional, carbon nanotube sheets. *Science,* Vol. 309, pp. 1215-1219, ISSN 0036-8075

Zhang, S., Minus, M. L., Zhu, L., Wong, C.-P., & Kumar, S. (2008). Polymer transcrystallinity induced by carbon nanotubes. *Polymer,* Vol. 49, pp. 1356-1364, ISSN 0032-3861

Zhao, B., Wang, J., Li, Z., Liu, P., Chen, D., & Zhang, Y. (2008). Mechanical strength improvement of polypropylene threads modified by PVA/CNT composite coatings. *Mater. Lett.,* Vol. 62, pp. 4380-4382, ISSN 0167-577X

Zhu, J., Kim, J., Peng, H., Margrave, J. L., Khabashesku, V. N., & Barrera, E. V. (2003). Improving the dispersion and integration of single-walled carbon nanotubes in epoxy composites through functionalization. *Nano Lett.,* Vol. 3, pp. 1107-1113, ISSN 1530-6984

Zhu, J., Peng, H., Rodriguez-Macias, F., Margrave, J. L., Khabashesku, V. N., & Imam, A. M. (2004). Reinforcing epoxy polymer composites through covalent integration of functionalized nanotubes. *Adv. Funct. Mater.,* Vol. 14, pp. 643-648, ISSN 1616-301X

5

Functionalization of Carbon Nanotubes

In-Yup Jeon[1], Dong Wook Chang[2],
Nanjundan Ashok Kumar[1] and Jong-Beom Baek[1]
[1]*Interdisciplinary School of Green Energy/Institute of Advanced Materials & Devices, Ulsan National Institute of Science and Technology (UNIST), Ulsan,*
[2]*Department of Chemical Engineering, Case Western Reserve University, Cleveland, Ohio,*
[1]*South Korea*
[2]*USA*

1. Introduction

Albeit initially reported by a Russian group and reported again by Oberlin and co-workers (Oberlin et al., 1976), carbon nanotubes (CNTs) were first brought to the attention of greater scientific community by Ijima in 1991. It was not until 1991 that CNTs came to limelight unfolding its exotic properties. Following this report, academic interest in this one-dimensional nanomaterial has grown remarkably and phenomenal number of research are being carried out worldwide. Its outstanding properties such as high mechanical strength, flexibility and impressive electrical and thermal conductivity make itself attractive and potential candidate for various applications. Despite CNTs's exceptional properties, there are two main limitations that hinder its use. The surface energy of CNTs is significantly different from that of matrices such as common organic solvents or polymers and CNTs may not have chemical affinity to the organic matrices and thus, the dispersion of CNTs into matrices is the biggest obstacle in practice (Song et al., 2005). In addition, the seamless surface of CNTs cannot provide physical interaction between CNTs and matrix (Ajayan et al., 2000). The modification of CNTs with other materials, makes it the most attractive and ultimate candidate for a plethora of applications which includes nanodevices, to organic electronics. In terms of the practical challenges that must be addressed to expand CNTs application scope in various potential fields of nanotechnology; many protocols have been proposed and considerable amount of research work is being focused on the interfacial molecular engineering of CNTs, aiming at improving their state of interaction with macromolecules, mainly to optimize the final properties of the hybrid nanomaterials. These protocols to prepare such hybrid composites have triggered burgeoning interest and to realize most of these applications practically, CNTs are most frequently functionalized with various kinds of technologically important polymers to improve the properties of the end material. Such assemblies have already suggested that the functionalization of polymers to CNTs draws equal importance in materials development for future applications in constructing optoelectronic devices. This chapter will focus and discuss the frequently used methods to functionalize CNTs namely; covalent and non-covalent strategies. Of particular importance, this chapter will also shed light on the 'pros and cons' of the frequent methods and alternative methods that have been developed in the recent past which can open the

path for their facile manipulation and processing in physiological environments and also to overcome difficulties in processing CNTs.

2. Carbon nanotubes

CNT is one of carbon allotropes such as diamond, graphite, graphene, fullerene and amorphous carbon. But, it is the one-dimensional carbon form which can have an aspect ratio greater than 1000 makes it interesting (Figure 1). The bonding in carbon nanotubes is sp^2, with each atom joined to three neighbours, as in graphite. CNTs are rolled-up graphene sheets (graphene is an individual graphite layer). This type of structural bonding, which is stronger than the sp^3 bonds found in diamond, provides the molecules with their unique strength. Under high pressure, nanotubes can merge together, trading some sp^2 bonds for sp^3 bonds, giving the possibility of producing strong, unlimited length wires through high-pressure nanotube linking.

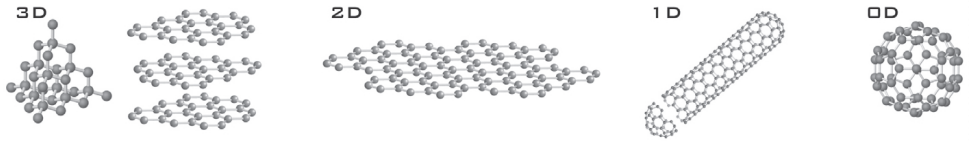

Fig. 1. Crystal structures of different allotropes of carbon. (Left to right) Three-dimensional diamond and graphite (3D); two-dimensional graphene (2D); one-dimensional nanotubes (1D); and zero-dimensional buckyballs (0D) (Mikhail & Katsnelson, 2007).

The properties of nanotubes depend on atomic arrangement (on how the sheets of graphite are 'rolled'), the diameter and length of the tubes, and morphology, or nano structure. Single walled nanotubes (SWNTs) consist of a single sheet of graphene rolled seamlessly to form a cylinder with diameter of order of 1 nm and length of up to centimeters (Bethune et al., 1993; Ijima et al., 1993). Multi-walled nanotubes (MWNTs) consist of an array of such cylinders formed concentrically and separated by 0.35 nm, similar to the basal plane separation in graphite (Ijima 1991). MWNTs can have diameters from 2 to 100 nm and lengths of tens of microns. Apart from these two main types, there was also the few-walled carbon nanotube (FWNTs) that was reported and found to have peculiar properties, often with much better structural integrity (Hutchinson et al. 2001).

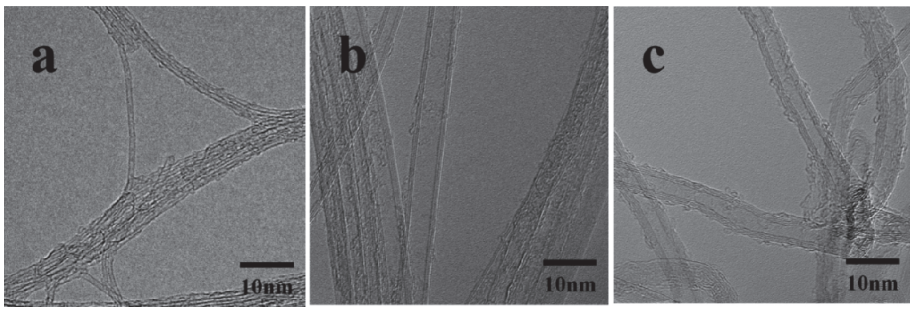

Fig. 2. TEM images of different types of CNTs: (a) single-walled carbon nanotubes; (b) few-walled carbon nanotubes; (c) multi-walled carbon nanotubes (Huo et al. 2009).

SWNTs are formed by rolling a sheet of graphene into a cylinder along an (m, n) lattice vector in the graphene (Figure 3). The (m, n) indices determine the diameter and chirality. Three types of SWNTs are revealed with these values: when $n = m$, the nanotube is called "armchair" type (= 0°); when $m = 0$, then it is of the "zigzag" type (= 30°). Otherwise, when n ≠ m, it is a "chiral" tube and takes a value between 0° and 30°. The value of (m, n) determines the chirality of the nanotube and affects the optical, mechanical and electronic properties. For typical diameters, all armchair SWNTs and one-third of all zigzag nanotubes are metallic, the rest are semiconducting (Hamada et al.; 1992).

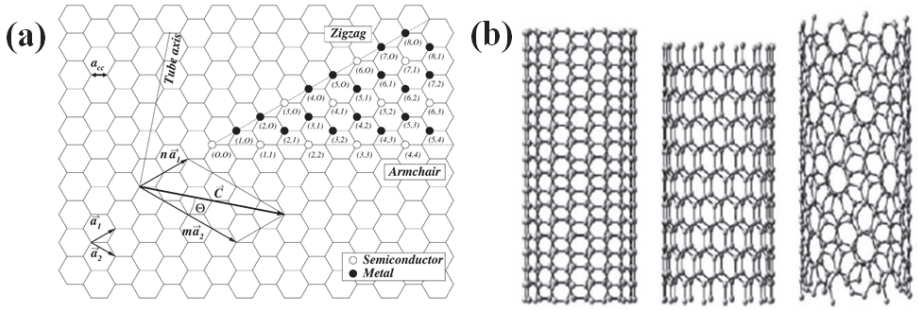

Fig. 3. (a) definition of the chiral vector describing the unit cell of a SWNT (Belin & Epron 2005); (b) CG images of armchair (n, n), zigzag (n, 0), and chiral nanotubes (Popov 2004).

It is clear that CNTs have many advantages over other materials in terms of mechanical, electrical and thermal properties although there is no consensus on the exact properties of CNTs (Table 1). Theoretical and experimental results have shown unusual mechanical properties with Young' modulus as high as 1.2 TPa and tensile strength of 50–200 GPa (Qian et al.; 2002). The relatively high values of modulus and strength values have been measured on high quality SWNT and arc discharge MWNT. However, CVD-MWNT was measured to have a modulus of 0.45 TPa and tensile strength of ~4 GPa (Xie et al.; 2000). The much larger variation in modulus for CVD-MWNT compared to arc-MWNT strongly suggests that the modulus is very sensitive to defect concentration and type.

Depending on the relationship between this axial direction and the unit vectors describing the hexagonal lattice, CNTs can either be metallic or semi-metallic. Semi-metallic nanotubes have band gaps that scale inversely with diameter, ranging from approximately 1.8 eV for very small diameter nanotubes to 0.18 eV for the widest possible stable SWNT (Elliot et al.; 2004). In addition, carrier mobility as high as 105 cm²/Vs have been observed in semi-conducting nanotubes (Kim et al.; 2004). Superconductivity has also been observed in SWNTs at the transition temperatures of 5 K (Tang et al.; 2001). CNTs are also very conductive for phonons. Theory predicts a room temperature thermal conductivity of up to 6000 W/m· K (Che et al.; 2000 & Osman et al.; 2001) but, the values around 200 W/m· K have been measured (Hone et al.; 2002). These properties offer CNTs great potential for wide applications in field emission, conducting plastics, thermal conductors, energy storage, conductive adhesives, thermal interface materials, structural materials, fibers, catalyst supports, biological applications, air and water filtration, ceramics to name a few (Thostenson et al. 2001; Ajayan et al.; 2003; Coleman et al.; 2006).

Property	Carbon nanotubes	Graphite
Lattice structure	(Cylindrical) hexagonal lattice helicity Nanotubes: ropes, tubes arranged in triangular lattice with lattice parameters of a =1.7 nm, tube-tube distance = 0.314	Planar hexagonal, plane-to-plane distance c=0.335
Specific gravity	0.8-1.8 gcc^{-1} (theoretical)	2.26 gcc^{-1}
Elastic modulus	~1 TPa for SWNT ~0.3-1 TPa for MWNT	1 TPa (in-plane)
Strength	50-500 GPa for SWNT 10-50 GPa for MWNT	
Resistivity	~5-50 micro-ohm cm	50 (in-plane)
Thermal conductivity	3000 W $m^{-1}K^{-1}$ (theoretical)	3000 $Wm^{-1}K^{-1}$ (in-plane) 6 $Wm^{-1}K^{-1}$ (c axis)
Thermal expansion	Negligible (theoretical)	-1 × 10^{-6} K^{-1} (in-plane) 29 × $10^{-6}K^{-1}$ (c axis)
Oxidation in air	>700 °C	450-650 °C

Table 1. Theoretical and experimentally measured properties of carbon nanotubes (Schadler 2004).

The synthesis methods for CNTs include arc-discharge (Journet et al. 1997), laser ablation (Rinzler et al. 1998), gas-phase catalytic growth from carbon monoxide (Nikolaev et al. 1999) and chemical vapor deposition (CVD) from hydrocarbons (Ren et al 1999 & 2007). The arc-discharge and laser ablation are well established in producing high-quality and nearly perfect nanotube structures. But, due to their scale-up limitations the production cost is too hight hence limiting its access. During the synthesis process, impurities in the form of catalyst particles, amorphous carbon and non-tubular fullerenes are also produced. Thus, subsequent purification steps are required to separate the tubes. The gas-phase catalytic growth with carbon monoxide as the carbon source yielded in quantity high-purity single walled nanotubes at the highest accessible temperature and pressure (1200 °C, 10 atm). However, this method is not economically practical due to high temperature and pressure of the synthesis conditions. The CVD process tended to tend nanotubes with fewer impurities and was more amenable to large-scale processing. Therefore, the CVD method has the highest potential to produce a large quantity and high purity of CNTs.

method	arc discharge	laser ablation	chemical vapor deposition
description	arc evaporation of graphite in the presence of inert gas; CNT formed on electrodes during quenching	vaporization of graphite target by laser; CNT formed on receiver during quenching	decomposition of hydrocarbons over transition metal catalyst to form CNT
operating temperature	> 3000 °C	> 3000 °C	< 1200 °C
operating pressure	50 – 7600 Torr generally under vacuum	200 – 750 Torr generally under vacuum	760 – 7600 Torr
advantages	good quality CNTs	good quality CNTs; single conformation SWNT formed (10, 10)	easy scale up; synthesis on templates possible
disadvantages	difficult to scale up	difficult to scale up; expensive	quality of CNT not as good

Table 2. Comparison of the established techniques for CNT synthesis (See et al. 2007).

3. Functionalization of carbon nanotubes

The main problem with the majority of popular synthetic methods is that they produce samples yielding a mixture of various diameters and chiralities of nanotubes that are normally contaminated with metallic and amorphous impurities. Thus, post-synthesis chemical processing protocols (Strano et al.; 2004 & Li et al.; 2002) that purify tubes that can also separate individual tubes according to diameter and chirality by taking advantage of their differential reactivities are often the only viable routes to rational and predictable manipulation of the favorable electronic and mechanical properties of these materials (Niyogi et al.; 2002 & Tasis et al.; 2003).

The full potential of CNTs as reinforcements has been severely limited due to poor interfacial interaction, van der Waals interaction, between CNTs and polymer matrix. The nature of dispersion problem for CNTs is rather different from other conventional fillers, such as spherical particles and carbon fibers, because CNTs are characteristic of small diameter in nanometer scale with high aspect ratio (>1000) and thus possessing large surface area. In addition, the commercialized CNTs are supplied in the form of heavily entangled bundles, resulting in inherent difficulties in dispersion.

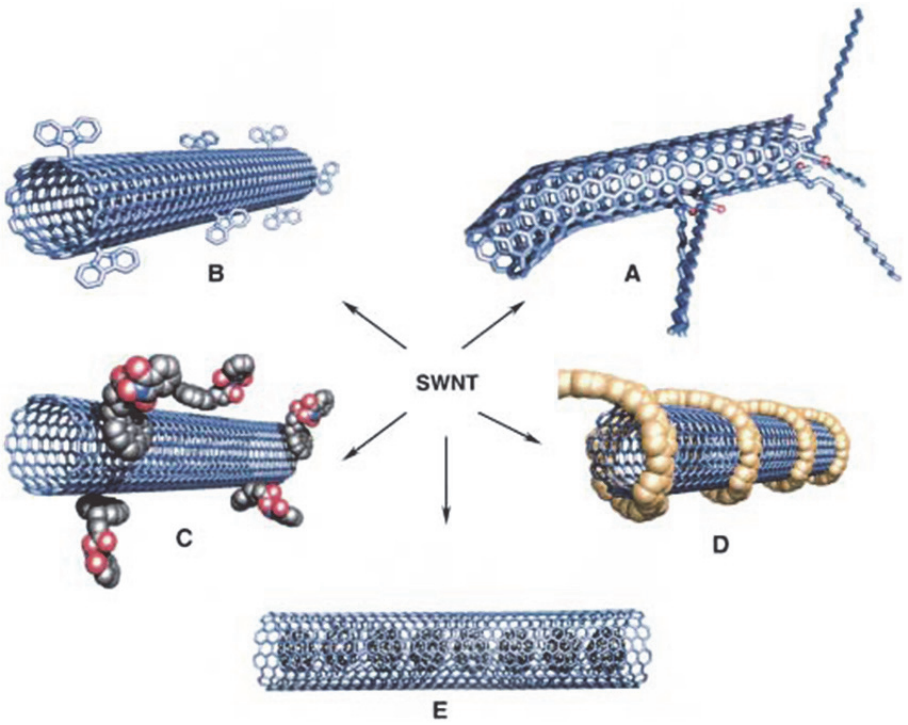

Fig. 4. Functionalization possibilities for SWNTs: a) defect-group functionalization, b) covalent sidewall functionalization, c) non-covalent exohedral functionalization with surfactants, d) non-covalent exohedral functionalization with polymers, and e) endohedral functionalization with, for example, C_{60}. For methods B-E, the tubes are drawn in idealized fashion, but defects are found in real situations (Hirsch 2002).

To resolve those problems, it has been directed towards developing methods to modify surface properties of CNTs. These approaches can be simply divided into chemical (covalent) and physical (noncovalent) functionalization as interactions between active materials and CNTs. The characterization corresponding to these methods are summarized in Figure 4.

3.1 Covalent functionalization

The end caps of nanotubes tend to be composed of highly curved fullerene-like hemispheres, which are therefore highly reactive, as compared with the side walls (Hirsch 2002 & Sinnott 2002). The sidewalls themselves contain defect sites such as pentagon-heptagon pairs called Stone-Walls defects, sp^3-hybrideized defects, and vacancies in the nanotube lattice (Figure 5) (Hirsch 2002).

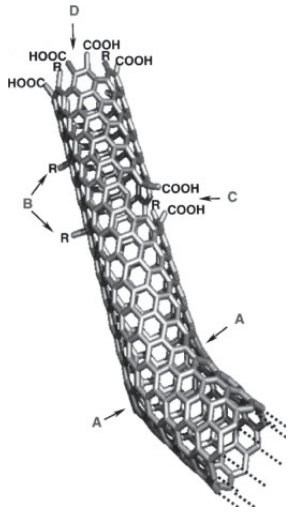

Fig. 5. Typical defects in a SWNT. a) five-or seven-membered rings in the carbon framework, instead of the normal six-membered ring, leads to a bend in the tube. b) sp^3-hybrideized defects (R=H and OH). c) carbon framework damaged by oxidative conditions, which leaves a hole lined with –COOH groups. d) open end of the SWNT, terminated with COOH groups. Besides carboxyl termini, the existence of which has been unambiguously demonstrated, other terminal groups such as -NO_2, -OH, -H, and =O are possible (Hirsch 2002).

Chemical functionalization is based on the covalent bond of functional groups onto carbon form of CNTs. It can be performed at the end caps of nanotubes or at their sidewalls which have many defects. Direct covalent sidewall functionalization is associated with a change of hybridization from sp^2 to sp^3 and a simultaneous loss of p-conjugation system on graphene layer (Figure 6). This process can be made by reaction with some molecules of a high chemical reactivity. In the first approach, fluorination of CNTs has become popular for initial investigation of the covalent functionalization because the CNTs sidewalls are expected to be inert (Bianco et al.; 2008 & Mickelson et al.; 1998). The fluorinated CNTs have C-F bonds that are weaker than those in alkyl fluorides (Kelly et al. 1993) and thus

providing substitution sites for additional functionalization (Touhara et al.; 2002). Successful replacements of the fluorine atoms by amino, alkyl and hydroxyl groups have been achieved (Stevens et al.; 2003). Other methods, including cycloaddition, such as Diels-Alder reaction, carbene and nitrene addition (Hu et al. 2003), chlorination, bromination (Unger et al. 2002), hydrogenation (Kim et al.; 2002), azomethineylides (Tagmatarchis 2004) have also been successfully employed.

Another method is defect functionalization of CNTs. These intrinsic defects are supplemented by oxidative damage to the nanotube framework by strong acids which leave holes functionalized with oxygenated functional groups (Chen et al.; 1998). In particular, treatment of CNTs with strong acid such as HNO_3, H_2SO_4 or a mixture of them (Esumi et al.; 1996 & Liu et al.; 1998), or with strong oxidants such as $KMnO_4$ (Yu et al.; 1998), ozone (Sham et al.; 2006), reactive plasma (Wang et al.; 2009) tend to open these tubes and to subsequently generate oxygenated functional groups such as carboxylic acid, ketone, alcohol and ester groups, that serve to tether many different types of chemical moieties onto the ends and defect sites of these tubes. These functional groups have rich chemistry and the CNTs can be used as precursors for further chemical reactions, such as silanation (Ma et al.; 2006), polymer grafting Sano et al. 2001 & Kong et al. 2003), esterification (Hamno et al. 2002), thiolation (Liu et al.; Science 1998), and even some biomolecules (Coleman et al.; 2006). The CNTs functionalized by the covalent methods has good advantage which that was soluble in various organic solvents because the CNTs possess many functional groups such as polar or non-polar groups.

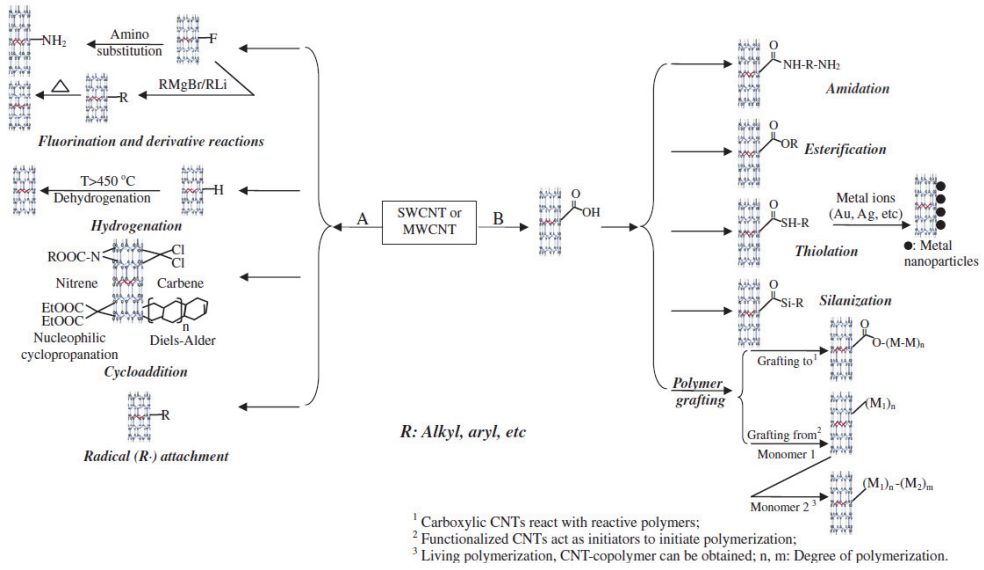

Fig. 6. Strategies for covalent functionalization of CNTs (A: direct sidewall functionalization; B: defect functionalization) (Ma et al.; 2010).

However these methods have two major drawbacks. First, during the functionalization reaction, especially along with damaging ultrasonication process (Figure 7), a large number

of defects are inevitably created on the CNT sidewalls, and in some extreme cases, CNTs are fragmented into smaller pieces (Figure 8). Namely, the carbon hybridization of CNTs was changed from sp^2 to sp^3. These damaging effects result in severe degradation in mechanical properties of CNTs as well as disruption of π electron system in nanotubes. The disruption of π electrons is detrimental to transport properties of CNTs because defect sites scatter electrons and phonons that are responsible for the electrical and thermal conductions of CNTs, respectively. Secondly, concentrated acids or strong oxidants are often used for CNT functionalization, which are environmentally unfriendly. Therefore, many efforts have been put forward to developing methods that are convenient to use, of low cost and less damage to CNT structure.

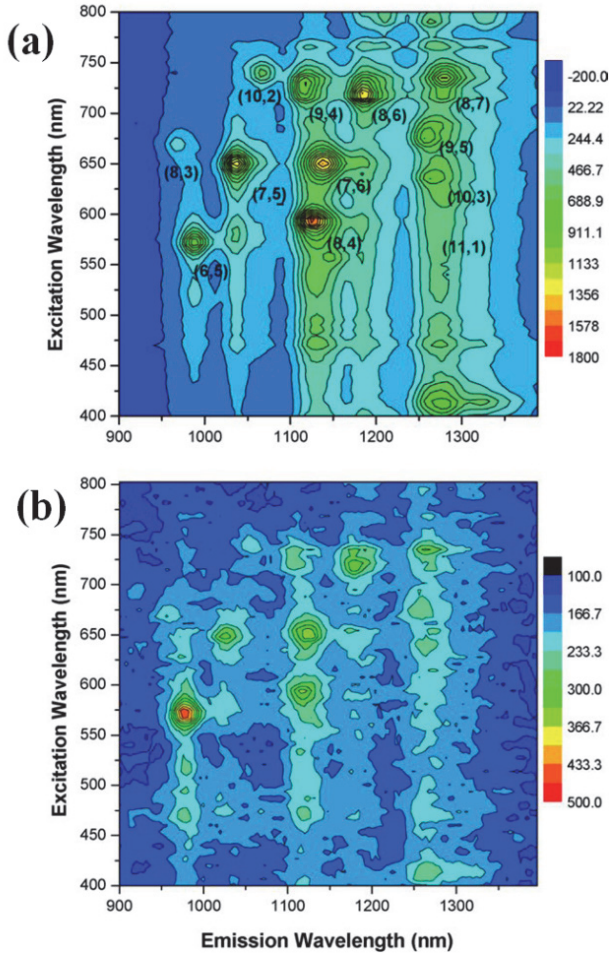

Fig. 7. (a) fluorescence excitation profile of sodium cholate-suspended SWNT in water, (b) profile of the same SWNT after 10min of probe-tip sonication conducted without controlling temperature (Heller et al.; 2005).

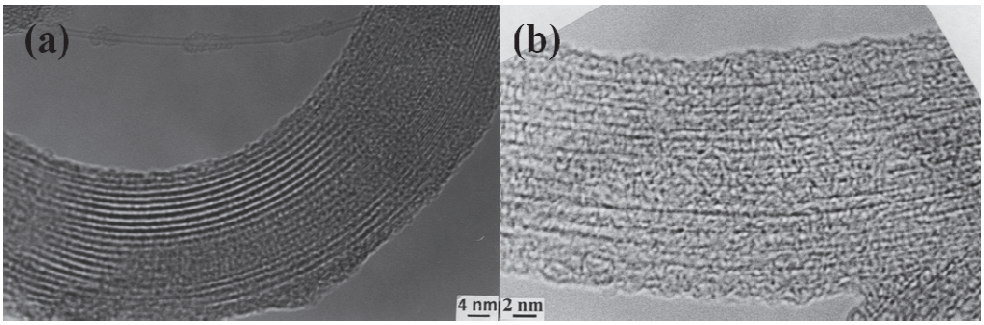

Fig. 8. TEM images: (a) as prepared SWNTs rope; (b) acid treated SWNTs rope (Monthioux et al.; 2001).

3.2 Non-covalent functionalization

The advantage of non-covalent functionalization is that it does not destroy the conjugated system of the CNTs sidewalls, and therefore it does not affect the final structural properties of the material. The non-covalent functionalization is an alternative method for tuning the interfacial properties of nanotubes. The CNTs are functionalized non-covalently by aromatic compounds, surfactants, and polymers, employing π-π stacking or hydrophobic interactions for the most part. In these approaches, the non-covalent modifications of CNTs can do much to preserve their desired properties, while improving their solubilities quite remarkably. It will summarize as followed: aromatic small molecule absorption, polymer wrapping, surfactants, biopolymers and endohedral method.

Aromatic molecules, such as pyrene, porphyrin, and their derivatives, can and do interact with the sidewalls of CNTs by means of π-π stacking interactions, thus opening up the way for the non-covalent functionalization of CNTs (Figure 9). Dai and co-workers have reported a general and attractive approach to the non-covalent functionalization of CNTs sidewalls and the subsequent immobilization of biological molecules onto CNTs with a high degree of control and specificity (Dai et al.; 2001). Hecht et al. fabricated CNTs/FET devices functionalized non-covalently with a zinc porphyrin derivative, was used to detect directly a photo induced electron transferring within the zinc porphyrin derivative-CNTs system (Hecht et al.; 2006). (Hu et al.; 2008) prepared CdSe-CNTs hybrids by self-assembling the pyrene-functionalized CdSe (pyrene/CdSe) nanoparticles onto the surfaces of the CNTs.

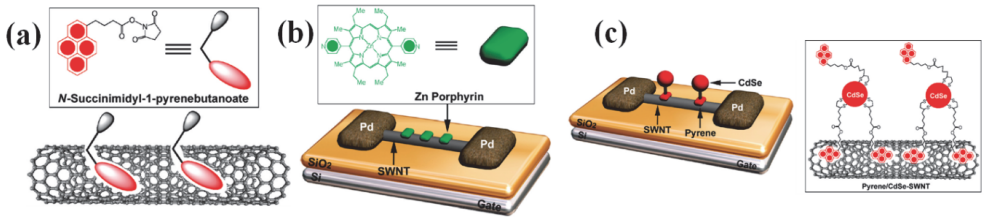

Fig. 9. Aromatic small-molecule based non-covalent functionalization: (a) *N*-succinimidyl-1-pyrenebutanoate coated CNTs; (b) zinc porphyrin-coated CNTs; (c) pyrene/CdSe coated CNTs (Zhao et al. 2009).

Polymers, especially conjugated polymers, have been shown to serve as excellent wrapping materials for the non-covalent functionalization of CNTs as a result of π-π stacking and van der Waals interactions between the conjugated polymer chains containing aromatic rings and the surfaces of CNTs (Figure 10) (Star et al.; 2001, 2002, 2003 Cheng et al.; 2006 & Yi et al.; 2008). Those has reported some organic-soluble conjugated poly(*m*-phenylenevinylene)-co-(2,5-dioctoxy-*p*phenylene) vinylene (PmPV) (Star et al.; 2001) poly(2,6-pyridinlenevinylene)- co-(2,5-dioctoxy-*p*-phenylene)vinylene (PPyPV) (Steuerman et al.; 2002), poly-(5-alkoxy-*m*-phenylenevinylene)-co-(2,5-dioctoxy-*p*-phenylene)- vinylene (PAmPV) (Star et al.; 2003), and stilbene-like dendrimers(Star et al.; 2002), to investigate their non-covalent functionalization for CNTs.

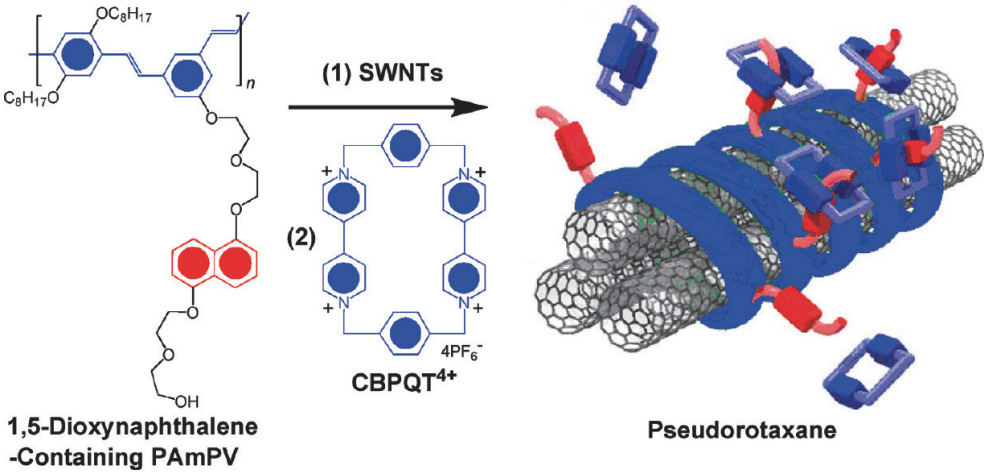

Fig. 10. The side arms of the 1,5-dioxynaphthalene containing PAmPV-decorated CNTs hybrids associate with cyclobis(paraquat-p-phenylene) ($CBPQT^{4+}$) rings (Zhao et al.; 2006).

In addition, surfactants polymers have also been employed to functionalize CNTs (Figure 11). The physical adsorption of surfactant on the CNTs surface lowered the surface tension of CNTs that effectively prevented the aggregation of CNTs. Furthermore, the surfactant-treated CNTs overcame the van der Waals attraction by electrostatic/steric repulsive forces. The efficiency of this method depended strongly on the properties of surfactants, medium chemistry and polymer matrix. The relation between surfactants and CNTs studied previously as followed: (i) non-ionic surfactants, such as polyoxyethylene 8 lauryl or $C_{12}EO_8$ (Gong et al.; 2000), polyoxyethylene octylphenylether (Triton X-100) (Vaisman et al.; 2006), (ii) anionic surfactants, such as sodium dodecylsulfate (SDS), sodium dodecylbenzenesulfonate (NaDDBS), poly(styrene sulfate) (PSS) (Islam et al.; 2003 & Yu et al.; 2007) (iii) cationic surfactants, such as dodecyl tri-methyl ammoniumbromide (DTAB) (Whitsitt et al.; 2003), cetyltrimethylammounium 4-vinylbenzoate (Kim et al.; 2007). Although surfactants may be efficient in the solubilization of CNTs, they are known to be permeable plasma membranes. They are toxic for biological applications. Therefore, the use of surfactant-stabilized CNTs complexes is potentially limited for biomedical applications (Klumpp et al.; 2006).

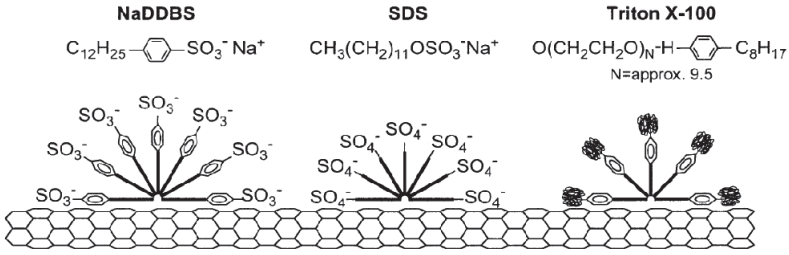

Fig. 11. The schematic representation of how surfactants may adsorb onto the CNTs surface (Islam et al 2003).

The solubilization of CNTs with biological components is certainly more appropriate towards integration of this new type of material with living systems (Figure 12). The biomacromolecules for non-covalent functionalization of CNTs has included simple saccharides and polysaccharides (Barone et al.; 2006; Star et al.; 2002; Chambers et al.; 2003 &

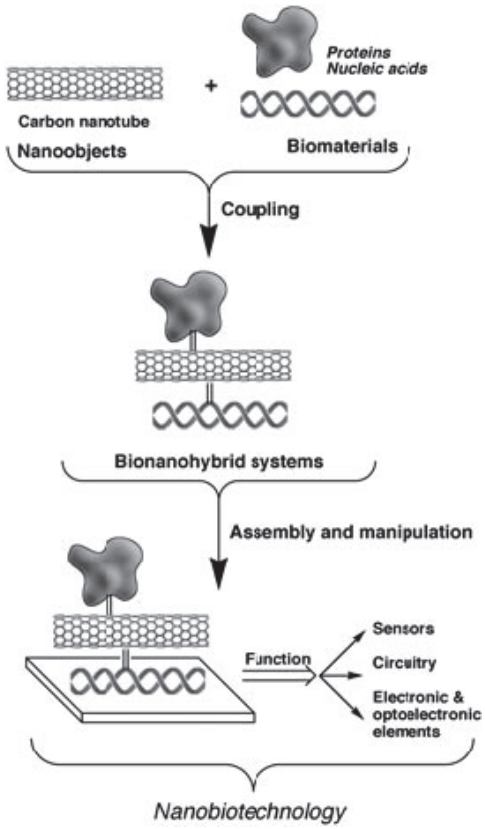

Fig. 12. The conceptual generation of biomolecules-CNTs conjugates and their assembly to yield functional devices.

Ikeda et al.; 2007), proteins (Chen et al.; 2001), enzymes, DNA, etc. Various biomaterials such as *n*-decyl-*β*-Dmaltoside (Ishibashi et al.; 2006), γ-cyclodextrin (Chambers et al.; 2003), *η*-cyclodextrin (Dodzuik et al.; 2003), chitosan (Yan et al.; 2008), pullulan (Kim et al.; 2003) and phospholipid-dextran (Goodwin et al.; 2009) have been used for the non-covalent functionalization of CNTs. They have been aided due to the fact that such saccharides and polysaccharides have almost no light absorption in UV-vis wavelength region, so that the CNTs hybrids can be characterized by photochemical experiments and also the saccharide- and polysaccharide-coated CNTs hybrids are usually biocompatible and may be applicable for many medicinal purposes.

3.3 Alternative routes for the functionalization of carbon nanotubes

Though various methods for enhancing the interaction between CNTs and polymers were adopted in the recent past, the two main routes; namely covalent and non-covalent functionalization generally provided. As discussed earlier, both methods had their own merits depending on the platform. Additionally, the traditional covalent functionalization strategy of CNT is most frequently initiated by chemical acid oxidation acid treatment. However, dramatic amounts of induced defects during functionalization hinder the intrinsic mobility of carriers along CNTs, which is not preferred in any case. This method not only functionalizes the nanotube surfaces with carboxylic acid groups but leaves behind detrimental structures, hence hampering their potential for practical applications and can also compromise the mechanical properties of the nanotubes. Therefore, as a common rule, and a now widespread approach to alleviate these problems is to find alternative routes such as an effective functionalization method that can not only introduce high density and homogenous surface functional groups, which enhance the compatibility between CNTs and the foreign matrix, but allow direct grafting and has little or no structural damage to the CNTs, thus, optimizing their properties for various applications.

Method		Principle	Possible damage to CNTs	Easy to use	Interaction with polymer matrix[a]	Re-agglomeration of CNTs in matrix
Chemical method	Side wall	Hybridization of C atoms from sp^2 to sp^3	√	×	S	√
	Defect	Defect transformation	√	√	S	√
Physical method	Polymer wrapping	Van der Waals force, π–π stacking	×	√	V	×
	Surfactant adsorption	Physical adsorption	×	√	W	×
	Endohedral method	Capillary effect	×	×	W	√

[a] S: Strong; W: Weak; V: Variable according to the miscibility between matrix and polymer on CNT.

Table 3. Advantage and disadvantage of various CNT functionalization methods (Ma et al.; 2010).

To overcome this challenge, Baek et al. (2005; 2004; 2006; 2007; 2010) have reported an efficient route to covalently functionalize CNTs via direct Friedel-Crafts acylation technique (Figure 13). This kind of covalent grafting of the nanotubes is a promising strategy to not only improve nanotube dispersion but also provide a means for creating microscopic interlinks. On the whole, this kind of surface functionalization not only enhances the reactivity, but also improves the specificity and provides an avenue for further chemical modification of CNTs. Considerable achievements have been made in enhancing the various functionalities of CNT-polymer nanocomposites, generally not achievable for each of the components individually. The approach is conceptualized on the basis of our foray into the

CNT chemistry using 'direct' Friedel-Crafts acylation technique which has superior operational simplicity. Not only a mild and an alternative route to functionalize CNTs, this strategy was previously shown to be a less-destructive and/or nondestructive reaction condition for the efficient dispersion and functionalization of carbon nanomaterials. As a result, CNT damage from severe chemical treatments including oxidation and sonication can be avoided to a larger extent. Thus, maximum enhanced properties can be expected from improved dispersion stability as well as chemical affinity with matrices.

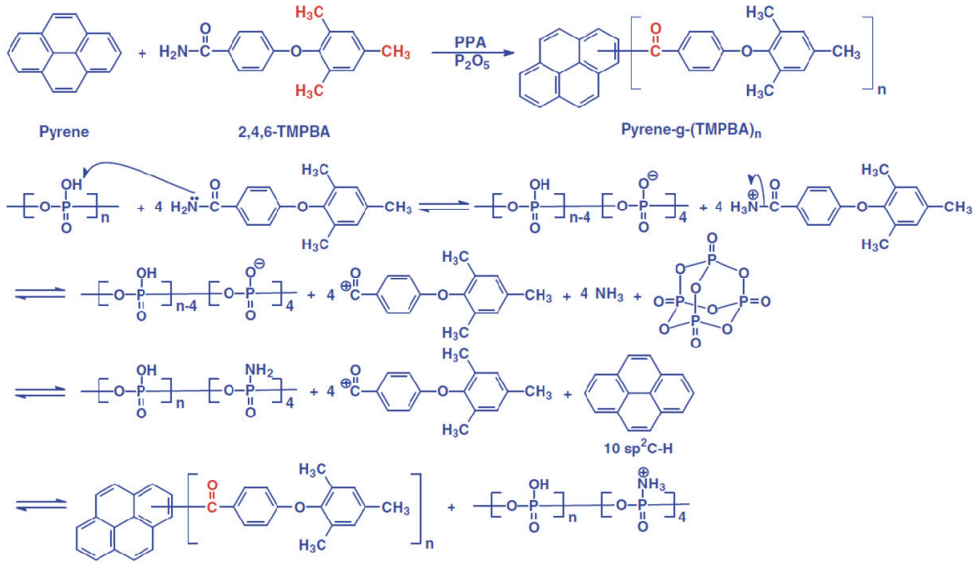

Fig. 13. Friedel-Crafts acylation reaction of pyrene as a miniature graphene and organic material in poly(phosphoric acid)/phosphorous pentoxide medium (Jeon et al.; 2010).

4. Conclusion and outlook

In light of the continuous progress of nanotechnology and material science over the last two decades, CNT based materials have opened new pathways for developing novel functional materials. In summary, CNTs were always been regarded as new and interesting type of materials, especially for energy and electronic applications. All types of CNTs are being investigated with equal importance. While few strategies have been developed so that the handling and manipulation of CNTs be relatively easier, on the whole there is much room for investigations in areas such as supercapacitors. Very recent reports show CNT based supercapacitor devices with better capacitor performance. Precisely, the combination of CNTs with particular macromolecules that offer to enhance the conductivity of the material is one interesting research. Particularly, the large electrochemical window and the environmental stability draw critical importance on such materials. Furthermore, the extension of these functional methods to the 2D forms of carbon namely graphene based materials are also now a fast growing area. While the quest for new materials are always on,

the research on CNT based materials in special fields such as doping are still open for investigations and discussion.

5. Acknowledgment

This research work was supported by World Class University (WCU), US-Korea NBIT, and Mid-Career Researcher (MCR) programs through the National Research Foundation (NRF) of Korea funded by the Ministry of Education, Science and Technology (MEST) and the U.S. Air Force Office of Scientific Research (AFOSR).

6. References

Radushkevich O.L.V. & Lukyanovich V.M. (1952). *Zurn. Fisic. Chim*. 28, 88- 95.

Oberlin A.; Endo M.; & Koyama T. (1976). Filamentous growth of carbon through benzene decomposition. *J. Cryst. Growth 32*, 335-349.

Iijima, S. (1991). Helical microtubules of graphitic carbon. *Nature* 354, 56-58.

Song, Y. S. & Youn, J. R. (2005). Influence of dispersion states of carbon nanotubes on physical properties of epoxy nanocomposites. *Carbon 43*, 1378-1385.

Ajayan, P.M.; Schadler, L.S.; Giannaris, C. & Rubio, A. (2000). Single-Walled Carbon Nanotube–Polymer Composites: Strength and Weakness. *Adv. Mater. 12*, 750-753.

Mikhail, I. Katsnelson. (2007). Graphene: carbon in two dimensions. Materials Today 10, 20-27.

Bethune, D.S.; Kiang, C.H.; Devries, M.S.; Gorman, G.; Savoy, R.; Vazquez J, et al. (1993). Cobalt-catalyzed growth of carbon nanotubes with singleatomic-layerwalls. *Nature* 363 (6430), 605–607.

Iijima, S. & Ichihashi T. (1993). Single-shell carbon nanotubes of 1-nm diameter. *Nature* 363, (6430), 603–605.

Hutchison, J.L.; Kiselev, N.A,; Krinichnaya, E.P.; Krestinin, A.V.; Loutfy, R.O.; Morawsky, A.P.; Muradyan, V.E.; Obraztsova, E.D.; Sloan, J.; Terekhov, S.V. & Zakharov, D.N. (2001). Double-walled carbon nanotubes fabricated by a hydrogen arc discharge method. *Carbon* 39, 761-770.

Hou, Y.; Tang, J.; Zhang, H.; Qian, C.; Feng, Y. & Liu, J. (2009). Functionalized Few-Walled Carbon Nanotubes for Mechanical Reinforcement of Polymeric Composites. *ACS Nano* 3, 1057-1062.

Hamada, N., Sawada, S. & Oshiyama, A. (1992). New one-dimensional conductors: Graphitic microtubules *Phys. Rev. Lett.* 68, 1579-1581.

Belin, T. & Epron, F. (2005). Characterization methods of carbon nanotubes: A review. *Mater. Sci. Eng., B 119*, (2), 105-118.

Popov, V.N. (2004). Carbon nanotubes: Properties and application. *Mater. Sci. Eng., R 43* (3), 61-102.

Qian, D.; Wagner, G.J.; Liu, W.K.; Yu, M.F. & Ruoff R.S. (2002). Mechanics of carbon nanotubes. *Appl. Mech. Rev.* 55, 495–533.

Xie, S.; Li, W.; Pan, Z.; Chang, B. & Sun, L. (2000). Mechanical and physical properties on carbon nanotube. *J. Phys. Chem. Solids* 61, (7), 1153–1158.

Schadler, L.S. (2004). Polymer-Based and Polymer-Filled Nanocomposites, in Nanocomposite Science and Technology (eds P. M. Ajayan, L. S. Schadler and P. V. Braun), Wiley-VCH Verlag GmbH & Co. KGaA, Weinheim.

Elliott, J.A.; Sandler, J.K.W; Windle, A.H.; Young, R.J. & Shaffer, M.S.P. (2004) Collapse of single-wall carbon nanotubes is diameter dependent. *Phys. Rev. Lett.* 92(9), 1–4.

Kim, B.M. & Fuhrer, A.M.S. (2004). Properties and applications of high-mobility semiconducting nanotubes. *J. Phys: Condens. Matter* 16(18) R553–R580.

Tang, Z.K.; Zhang, L.Y,; Wang, N.; Zhang, X.X.; Wen, G.H.; Li, G.D.; et al. (2001). Superconductivity in 4 Angstrom single-walled carbon nanotubes. Science 292, (5526), 2462–2465.

Che, J.W.; Cagin, T. & Goddard, W.A. (2000). Thermal conductivity of carbon nanotubes. *Nanotechnology* 11, (2), 65–69.

Osman, M.A. & Srivastava, D. (2001) Temperature dependence of the thermal conductivity of single-wall carbon nanotubes. *Nanotechnology* 12, (1), 21–24.

Hone. J.; Llaguno, M.C.; Biercuk, M.J.; Johnson, A.T.; Batlogg, B.; Benes, Z.; et al. (2002) Thermal properties of carbon nanotubes and nanotube-based materials. *Appl. Phys. A – Mater. Sci. Process* 74, (3), 339–343.

Thostenson, E.T. Ren, Z.F. & Chou, T.W. (2001). Advances in the science and technology of CNTs and their composites: a review. *Compos. Sci. Technol.* 61, 1899–1912.

Ajayan, P.M.; Schadler, L.S. & Braun, P.V. Nanocomposite science and technology. Weinheim: Wiley-VCH; 2003. p. 77–80.

Coleman, J.N.; Khan, U. & Gunko, Y.K. (2006). Mechanical reinforcement of polymers using carbon nanotubes. *Adv. Mater.* 18, 689–706.

Journet, C.; Maser, W.K.; Bernier, P.; Loiseau, A.; de la Chapelle M.L.; Lefrant, S.; et al. (1997). Large-scale production of single-walled carbon nanotubes by the electric-arc technique *Nature* 388, 756-758.

Rinzler, A.G.; Liu, J.; Dai, H.; Nikolaev, P.; Huffman, C.B.; Rodriguez Macias, F.J. et al. (1998). Large-scale purification of single-wall carbon nanotubes: process, product, and characterization. *Appl.Phys. A* 1998, 67, 29-37.

Nikolaev, P.; Bronikowski, M.J.; Bradley, R.K.; Fohmund, F.; Colbert, D.T.; Smith K.A.; et al. (1999). Gas-phase catalytic growth of single-walled carbon nanotubes from carbon monoxide. *Chem. Phys. Lett.* 313, 91-97.

Ren, Z.F.; Huang, Z.P.; Xu, J.W.; Wang, D.Z.; Wen, J.G.; Wang, J.H.; et al. (1999). Growth of a single freestanding multiwall carbon nanotube on each nanonickel dot. *Appl. Phys. Lett.* 75, 1086-1088.

Ren, Z.F.; Huang, Z.P.; Xu, J.W.; Wang, J.H.; Bush, P.; Siegal, M.P.; et al. (1998). Synthesis of Large Arrays of Well-Aligned Carbon Nanotubes on Glass. *Science.* 282, 1105-1107.

See, C.H. & Harris, A.T. (2007). A Review of Carbon Nanotube Synthesis via Fluidized-Bed Chemical Vapor Deposition. *Ing. Eng. Chem. Res.* 46, 997-1012.

Strano, M.S.; Kyke, C.A.; Usrey, M.L.; Barone, P.W.; Allen, M.J.; Shan, H.; Kittrell, C.; Hauge, R.H.; Tour, J.M. & Smalley, R.E. (2003). Electronic Structure Control of Single-Walled Carbon Nanotube Functionalization *Science* 301, 1519-1522.

Li, H.; Zhou, B.; Lin, Y.; Gu, L.; Wang, W.; Fernando K.A.S.; Kumar, S.; Allard, L.F. & Sun, Y.–P. (2004). Selective Interactions of Porphyrins with Semiconducting Single-Walled Carbon Nanotube. *J. Am. Chem. Soc.* 126, 1014-1015.

Niyogi, S.; Hamon, M.A.; Hu, H.; Zhao, B.; Bhowmik, P.; Sen, R.; Itkis, M.E. & Haddon, R.C. (2002) Chemistry of Single-Walled Carbon Nanotubes. *Acc. Chem. Res.* 35, (12), 1105-1113.

Tasis, D.; Tagmatarchis, N.; Georgakilas, V. & Prato, M. (2003). Soluble Carbon Nanotubes. *Chem. Eur. J.* 9, (17), 4000-4008.

Hirsch, A. (2002). Functionalization of Single-Walled Carbon Nanotubes. *Angew, Chem, Int. Ed.* 41, (11), 1853-1859.

Sinnott, S.B. (2002). Chemical Functionalization of Carbon Nanotubes. Journal of Nanoscience and Nanotechnology *J. Nanosc. Nanotechnol.* 2, 113-123.

Bianco, A.; Prato, M.; Kostarelos, K. & Bianco, A. (2008). Functionalized Carbon Nanotubes in Drug Design and Discovery. *Acc. Chem. Res.* 41, (1), 60-68.

Mickelson, E.T.; Huffman, C.B.; Rinzler, A.G.; Smalley, R.E.; Hauge, R.H. & Margrave, J.L. (1998) Fluorination of single-wall carbon nanotubes. *Chem. Phys. Lett.* 296, (1-2), 188-194.

Kelly, K.F.; Chiang, I.W.; Mickelson, E.T., et al. (1993). Insight into the mechanism of sidewall functionalization of single-walled nanotubes: an STM study. *Chem. Phys. Lett.* 313, 445–450

Touhara. H.; Inahara, J.; Mizuno T.; et al. (2002). Fluorination of cup-stacked carbon nanotubes, structure and properties. *Fluorine Chem.*114, 181–188.

Stevens, J.L.; Huang, A.Y.; Peng, H.; et al. (2003). Sidewall amino-functionalization of SWNTs through fluorination and subsequent reactions with terminal diamines. *Nano Lett*. 3, 331–336.

Hu, H.; Zhao, B.; Hamon, M.A.; et al. (2003). Sidewall functionalization of single-walled carbon nanotubes by addition of dichlorocarbene. J. Am. Chem. Soc.125, 14893–14900.

Unger, E.; Graham, A.; Kreupl, F.; Liebau, M.; Hoenlein, W., (2002). Electrochemical functionalization of multi-walled carbon nanotubes for solvation and purification. *Curr. Appl. Phys.* 2, 107–111.

Kim, K.S.; Bae, D.J.; Kim, J.R.; Park, K.A.; Lim, S.C.; Kim, J.J.; Choi, W.B.; Park, C.Y. & Lee, Y.H. (2002). Modification of Electronic Structures of a Carbon Nanotube by Hydrogen Functionalization. *Adv. Mater*. 14, (24), 1818-1821

Tagmatarchis, N. & Prato, M.J. (2004). Functionalization of carbon nanotubes via 1,3-dipolar cycloadditions. *J. Mater. Chem.* 14, 437–439.

Chen, J.; Hamon, M.A.; Hu, H.; Chen, Y.; Rao, A.M.; Eklund, P.C.; Haddon, R.C. (1998). Solution Properties of Single-Walled Carbon Nanotubes. *Science* 282, (5386), 95-98.

Esumi, K.; Ishigami, M.; Nakajima, A.; Sawada, K. & Honda, H. (1996). Chemical treatment of carbon nanotubes. *Carbon* 34, 279–281.

Liu, J.; Rinzler, A.G.; Dai, H.; Hafner, J.H.; Bradley, R.K.; Boul, P.J.; et al. (1998). Fullerene Pipes. *Science* 280, 1253-1256.

Yu, R.; Chen, L.; Liu, Q.; Lin, J.; Tan, K.-L.; Ng, S.C.; Chan, H S.O.; Xu, G.-Q. & Hor, T.S.A. (1998). Platinum Deposition on Carbon Nanotubes via Chemical Modification. *Chem. Mater.* 10, 718–722.

Sham, M.-L. & Kim, J.-K., (2006). Surface functionalities of multi-wall carbon nanotubes after UV/Ozone and TETA treatments. *Carbon* 44, (4), 768-777.

Wang, S.C.; Chang, K.S. & Yuan, C.J. (2009). Enhancement of electrochemical properties of screen-printed carbon electrodes by oxygen plasma treatment. *Electrochimica Acta* 54, (21), 4937-4943.

Ma, P.C.; Kim, J.K. & Tang, B.Z. (2006). Functionalization of carbon nanotubes using a silane coupling agent. *Carbon* 44, 3232–3238.

Sano, M.; Kamino, A.; Okamura, J. & Shinkai, S. (2001). Self-Organization of PEO-graft-Single-Walled Carbon Nanotubes in Solutions and Langmuir−Blodgett Films. *Langmuir* 17, (17), 5125-5128.

Kong, H.; Gao, C. & Yan, D. (2003). Controlled Functionalization of Multiwalled Carbon Nanotubes by in Situ Atom Transfer Radical Polymerization. *J. Am. Chem. Soc.* 126, 412-413.

Hamon, M.A.; Hui, H. & Bhowmik P. (2002). Ester-functionalized soluble single-walled carbon nanotubes. *Appl. Phys. A.* 74, 333–338.

Coleman, J.N.; Khan, U. & Gun'ko, Y.K. (2006). Mechanical Reinforcement of Polymers Using Carbon Nanotubes. *Adv. Mater.* 18, 689–706.

Ma, P.-C.; Siddiqui, N.A.; Marom, G. & Kim, J.-K. (2010). Dispersion and functionalization of carbon nanotubes for polymer-based nanocomposites: A review. *Composites: Part A* 41, 1345-1364.

Heller D.A., Barone, P.W., Strano, M.S. (2004). Sonication-induced changes in chiral distribution: A complication in the use of single-walled carbon nanotube fluorescence for determining species distribution. *Carbon* 43, 651-673.

Monthioux M., Smith B.W., Burteaux B., Claye A., Fischer, J.E. & Luzzi, D.E. (2001). Sensitivity of single-wall carbon nanotubes to chemical processing: an electron microscopy investigation. *Carbon* 39, (8), 1251-1272.

Chen, R. J.; Zhang, Y.; Wang, D. & Dai, H. (2001). Noncovalent Sidewall Functionalization of Single-walled carbon nanotubes for protein immobilization. *J. Am. Chem. Soc. 123*, 3838–3839.

Hecht, D.S.; Ramirez, R.J.A.; Briman, M.; Artukovic, E.; Chichak, K.S.; Stoddart, J.F. & Gruner, G. (2006). Bioinspired detection of light using a porphyrin-sensitized singlewall nanotube field effect transistor. *Nano Lett. 6*, 2031–2036.

Hu, L.; Zhao, Y.-L.; Ryu, K.; Zhou, C.; Stoddart, J.F.; Gruner, G. Light-induced charge transfer in pyrene/CdSe-SWNT hybrids. *Adv. Mater.* 2008, *20*, 939–946.

Zhao, Y.-L. & Stoddart, J.F. (2009). Noncovalent Functionalization of Single-Walled Carbon Nanotubes. *Acc. Chem. Res*. 42, (8), 1161-1171

Star, A.; Stoddart, J.F.; Steuerman, D.; Diehl, M.; Boukai, A.; Wong, E.W.; Yang, X.; Chung, S.-W.; Choi, H. & Heath, J.R. (2001). Preparation and Properties of Polymer-Wrapped Single-Walled Carbon Nanotubes. *Angew. Chem., Int. Ed.* 2001, *40*, 1721–1725.

Steuerman, D.W.; Star, A.; Narizaano, R.; Choi, H.; Ries, R.S.; Nicolini, C.; Stoddart, J.F. & Heath, J.R. (2002). Interactions between conjugated polymers and singlewalled carbon nanotubes. *J. Phys. Chem. B 106*, 3124–3130.

Star, A.; Liu, Y.; Grant, K.; Ridvan, L.; Stoddart, J.F.; Steuerman, D.W.; Diehl, M.R.; Boukai, A. & Heath, J.R. (2003). Noncovalent side-wall functionalization of singlewalled carbon nanotubes. *Macromolecules 36*, 553–560.

Star, A. & Stoddart, J.F. (2002). Dispersion and solubilization of single-walled carbon nanotubes with a hyperbranched polymer. *Macromolecules 35*, 7516–7520.

Cheng, F.; & Adronov, A. (2006). Noncovalent functionalization and solubilization of carbon nanotubes by using a conjugated Zn-porphyrin polymer. *Chem. Eur. J. 12*, 5053–5059.

Yi, W.; Malkovskiy, A.; Chu, Q.; Sokolov, A. P.; Colon, M.L.; Meador, M. & Pang, Y. (2008). Wrapping of single-walled carbon nanotubes by a π-conjugated polymer: The role of polymer conformation-controlled size selectivity. *J. Phys. Chem. B 112*, 12263–12269.

Gong, X.; Liu, J.; Baskaran, S.; Voise, R.D. & Young, J.S. (2000). Surfactant-Assisted Processing of Carbon Nanotube/Polymer Composites. *Chem. Mater.* 12 (4), 1049-1052.

Vaisman, L.; Marom, G. & Wagner, H.D. (2006). Dispersions of Surface-Modified Carbon Nanotubes in Water-Soluble and Water-Insoluble Polymers. *Adv. Funct. Mater.* 16 (3), 357-363

Islam, M.F.; Rojas, E.; Bergey, D.M.; Johnson, A.T.; Yodh, A.G. (2003). High Weight Fraction Surfactant Solubilization of Single-Wall Carbon Nanotubes in Water. *Nano Lett.* 3 (2), 269-273

Yu, J.; Grossiord, N.; Koning, C.E. & Loos, J. (2007). Controlling the dispersion of multi-wall carbon nanotubes in aqueous surfactant solution. *Carbon* 45 (3), 618-623.

Whitsitt, E.A. & Barron, A.R., (2003). Silica Coated Single Walled Carbon Nanotubes. *Nano Lett.* 3, (6), 775-778.

Kim, T.H.; Doe, C.; Kline, S.R. & Choi, S.M. (2007). Water-Redispersible Isolated Single-Walled Carbon Nanotubes Fabricated by In Situ Polymerization of Micelles. *Adv. Mater.* 19, (7), 929-933.

Klumpp, C.; Kostarelos, K.; Prato, M.; & Bianco, A. (2006). Functionalized carbon nanotubes as emerging nanovectors for the delivery of therapeutics. *Biochim. Biophys. Acta, (BBA) - Biomembranes* 1758, (3), 404-412.

Barone, P.W.; & Strano, M.S. (2006). Reversible Control of Carbon Nanotube Aggregation for a Glucose Affinity Sensor. *Angew. Chem., Int. Ed. 45*, 8138–8141.

Star, A.; Steuerman, D.W.; Heath, J.R. & Stoddart, J.F. (2002)Starched carbon nanotubes. *Angew. Chem., Int. Ed. 41*, 2508–2512.

Chambers, G.; Carroll, C.; Farrell, G.F.; Dalton, A.B.; McNamara, M.; in het Panhuis, M.; & Byrne, H.J. (2003). Characterization of the interaction of gamma cyclodextrin with single-walled carbon nanotubes. *Nano Lett. 3*, 843–846.

Ikeda, M.; Hasegawa, T.; Numata, M.; Sugikawa, K.; Sakurai, K.; Fujiki, M. & Shinkai, S. (2007). Instantaneous inclusion of a polynucleotide and hydrophobic guest

molecules into a helical core of cationic 1,3-glucan polysaccharide. *J. Am. Chem. Soc. 129*, 3979–3988.

Chen, R.J.; Zhang, Y.; Wang, D. & Dai, H. (2001). Single-walled carbon nanotubes for protein immobilization. *J. Am. Chem. Soc. 123*, 3838–3839.

Ishibashi, A. & Nakashima, N. (2006). Individual dissolution of single-walled carbon nanotubes in aqueous solution of steroid or sugar compounds and their Raman and Near-IR spectral properties. *Chem. Eur. J. 12*, 7595–7602.

Dodziuk, H.; Ejchart, A.; Anczewski, W.; Ueda, H.; Krinichnaya, E.; Dolgonos, G. & Kutner, W. (2003). Water solubilization, determination of the number of different types of single-wall carbon nanotubes and their partial separation with respect to diameters by complexation with *η*-cyclodextrin. *Chem. Commun.* 986–987.

Yan, L.Y.; Poon, Y.F.; Chan-Park, M.B.; Chen, Y.; Zhang, Q. (2008). Individually dispersing single-walled carbon nanotubes with novel neutral pH water-soluble chitosan derivatives. *J. Phys. Chem. C 112*, 7579–7587.

Kim, O.-K.; Je, J.; Baldwin, J.W.; Kooi, S.; Pehrsson, P.E.; & Buckley, L.J. (2003). Solubilization of single-walled carbon nanotubes by supramolecular encapsulation of helical amylase. *J. Am. Chem. Soc. 125*, 4426–4427.

Goodwin, A.P.; Tabakman, S.M.; Welsher, K.; Sherlock, S.P.; Prencipe, G. & Dai, H. (2009). Phospholipid-dextran with a single coupling point: A useful amphiphile for functionalization of nanomaterials. *J. Am. Chem. Soc. 131*, 289–296.

Baek, J.-B.; Lyons, C.B.; & Tan, L.-S. (2004). Covalent modification of vapour-grown carbon nanofibers via direct Friedel-Crafts acylation in polyphosphoric acid. *J. Mater, Chem.* 14 (13), 2052-2056.

Baek, J.-B.; Lyons, C.B. & Tan, L.-S. (2004). Grafting of Vapor-Grown Carbon Nanofibers via in-Situ Polycondensation of 3-Phenoxybenzoic Acid in Poly(phosphoric acid). *Macromolecules 37* (22), 8278-8285.

Lee, H.-J.; Oh, S.-J.; Choi, J.-Y.; Kim, J.W.; Han, J.; Tan, L.-S. & Baek, J.-B. (2005). In Situ Synthesis of Poly(ethylene terephthalate) (PET) in Ethylene Glycol Containing Terephthalic Acid and Functionalized Multiwalled Carbon Nanotubes (MWNTs) as an Approach to MWNT/PET Nanocomposites. *Chem. Mater.* 17, (20), 5057-5064.

Oh, S.-J.; Lee, H.-J.; Keum, D.-K.; Lee, S.-W.; Wang, D. H.; Park, S.-Y.; Tan, L.-S. & Baek, J.-B. (2006). Multiwalled carbon nanotubes and nanofibers grafted with polyetherketones in mild and viscous polymeric acid. *Polymer* 47, (4), 1132-1140.

Choi, J.-Y.; Oh, S.-J.; Lee, H.-J.; Wang, D. H.; Tan, L.-S. & Baek, J.-B. (2007). In-Situ Grafting of Hyperbranched Poly(ether ketone)s onto Multiwalled Carbon Nanotubes via the A3 + B2 Approach. *Macromolecules* 40, (13), 4474-4480.

Choi, J.-Y.; Han, S.-W.; Huh, W.-S.; Tan, L.-S. & Baek, J.-B. (2007). In situ grafting of carboxylic acid-terminated hyperbranched poly(ether-ketone) to the surface of carbon nanotubes. *Polymer* 48, (14), 4034-4040.

Wang, D.H.; Arlen, M.J.; Baek, J.-B. & Tan, L.-S. (2007). Nanocomposites Derived from a Low-Color Aromatic Polyimide (CP2) and Amine-Functionalized Vapor-Grown Carbon Nanofibers: In Situ Polymerization and Characterization. *Macromolecules* 40, (17), 6100-6111.

Jeon, I.-Y.; Choi, E.-K.; Bae, S.-Y. & Baek, J.-B., (2010). Edge-Functionalization of Pyrene as a Miniature Graphene via Friedel–Crafts Acylation Reaction in Poly(Phosphoric Acid). *Nanoscale Res. Lett*. 5, (10), 1686-1691.

6

Preparation and Applicability of Vinyl Alcohol Group Containing Polymer/MWNT Nanocomposite Using a Simple Saponification Method

Eun-Ju Lee[1], Jin-San Yoon[1], Mal-Nam Kim[2] and Eun-Soo Park[3*]
[1]*Department of Polymer Science and Engineering, Inha University, Incheon 402-751,*
[2]*Department of Life Science, Sangmyung University, Seoul 110-743,*
[3*]*Youngchang Silicone Co., Ltd., 481-7, Gasan-Dong, Kumchun-Gu, Seoul 153-803 Korea*

1. Introduction

Polymer nanocomposites are increasingly desirable as coating, packaging, filtering and structural materials in a wide range of aerospace, automobiles, membrane, and electrical engineering applications [Mai and Yu, 2006; Ray and Bousmina, 2008]. This is due to our increased ability to analyze, synthesize, and manipulate a broad range of nanofillers and significant investment by laboratories and research centers in industry, government, and academia. In addition, polymers possess general advantages of low cost, lightweight, design flexibility, easy processing, and corrosion resistance. The polymer nanocomposites are one kind of composite materials comprising of nanometer-sized particles, typically at least one dimension less than 100 nm, which are uniformly dispersed in and fixed to a polymer matrix. In this way, the nanoparticles are acting like additives to enhance performance and thus are also termed nanofillers or nano-inclusions [Ramanathan et. al., 2007; Vaisman et. al. 2007]. The nanofillers can be plate-like, high aspect ratio nanotubes, and lower aspect ratio or equiaxed nanoparticles. Frequently employed inorganic nanofillers include metals and metal oxides, semiconductors, clay minerals, and carbon-based materials such like carbon blacks, carbon fibers, graphite and carbon nanotubes (CNTs).

CNTs have received much attention for their unique structural, mechanical, and electronic properties as well as their broad range of potential applications [Kim and Park, 2008; Kang et al. 2008; Xu et. al., 2008; Kumar, 2002; Wong et al., 1998]. CNTs are cylinder-shaped macromolecules with a radius as small as a few nanometers, which can be grown up to 20 cm in length [Zhu et. al., 2002]. Their properties depend on the atomic arrangement, chirality, diameter, and length of the tube and the overall morphology. They exist in one of two structural forms, single-walled carbon nanotube (SWNT) or multi-walled carbon nanotube (MWNT). SWNTs are best described as a 2-D graphene sheet rolled into a tube with pentagonal rings as end caps [Harris, 2004]. SWNTs have aspect ratios of 1000 or more and an approximate diameter of 1 nm. Similarly, MWNTs can be described as multiple

layers of concentric graphene cylinders also with pentagonal ring end caps. Conventional MWNT diameters range from 2-50 microns [Harris, 2004]. Measurements using in situ transmission electron microscopy and atomic force microscopy have produced estimates that Young's modulus of CNTs is approximately 1 TPa [Treacy et. al., 1996; Wong et. al. 1997]. For comparison, the stiffest conventional glass fibers have Young's modulus of approximately 70 GPa, while carbon fibers typically have modulus of about 800 GPa. CNTs can accommodate extreme deformations without fracturing and also have the extraordinary capability of returning to their original, straight, structure following deformation [Harris, 2004]. In addition, they are excellent electrical conductors and have very high thermal conductivities. Many of these exceptional properties can be best exploited by incorporating the nanotubes into polymer matrix, and the preparation of nanotube containing composite materials is now a rapidly growing subject.

Recently, our group has developed a process of simple saponification to make highly porous nanocomposites. In this process, at least one vinyl acetate (VAc) containing polymer or blend is dissolved in an appropriate solvent and a suitable viscosity of the solution is achieved. A functonalized nanotube was dispersed in polymer solution and then the polymer suspension was precipitated/saponified in alkaline non-solvent. This causes separation of the heterogeneous polymer suspension into a solid nanocomposite and liquid solvent phase. After rinsing off the coagulant and drying, sponge-like structure of connected matrix polymer and nanotube were obtained. Production parameters that affect the pore structure and properties include polymer and nanotube concentration, VAc content in polymer, saonification time and temperature, and precipitation media. These factors can be varied to produce porous structure with a large range of pore sizes, and altering chemical, thermal and mechanical properties. Porous materials are heterogeneous systems with complex micro-structure [Roberts and Knackstedt, 1996]. These systems are diphase composites with a solid matrix and gaseous filler [Mills et. al., 2003]. Physical and mechanical properties of such heterogeneous systems depend not only on the nature of the materials but on their morphology as well [Garboczi, 2000]. Materials with highly pore structure and controlled pore volume have potentials in a wide range of applications such as cell culture media, enzyme immobilization, organic electronics, membranes, absorbents, supports for liquid chromatography, ion-exchange applications, bio-separators, metal recovery and tissue engineering [Kanny et. al., 2002; Benson, 2003; Sears, et. al., 2010; Zeleniakiene, 2006]. It was the objective of the study reported here to use new approaches to produce vinyl alcohol (VOH) group containing polymer/MWNT nanocomposites with high porosity and to study their properties and applicability.

2. Preparation and properties of highly porous nanocomposites

Using CNTs as a property enhancing nanofiller for a high performance, lightweight composite is one of the lynchpins of nanocomposite research. The exceptional and unique properties of CNTs offer a great advantage for the production of improved composites. However, use of CNT reinforcements in polymer composites has been a challenge because of the difficulties in optimizing the processing conditions to achieve good dispersion and load transfer. Thus initial published results showed only modest improvement in mechanical properties with MWNT nanofillers [Thostenson and Chou, 2002]. One of the

major problems in the production of nanocomposites involving the use of nanofiller particles is the aggregation of the nanoparticles that severely limits the filler loading level. To improve dispersion, several techniques have been attempted, including the use of surfactants, sonication, and other mixing methods. Recent work has demonstrated superior dispersion of MWNTs in polymers by functionalization of the nanotubes to compatibilize them with solvents and the matrix polymers [Chiu and Chang, 2007; Wu et. al., 2006; Balasubramanian and Burghard, 2005; Yoon et. al., 2004]. The improved dispersion of nanotubes with functional groups has been accompanied by increased mechanical properties of the nanocomposite. Among of them, electron-beam irradiations are potent to induce the uniform and consistent modification of the MWNTs because of the high amount of energy, they impart to the atoms via the primary knock-on atom mechanism. This study investigated the preparation, properties and applicability of various VOH group conataing nanocomposites with high porosity through simple saponification method using electron-beam irradiated MWNT.

2.1 Functionalization of MWNT by electron-beam irradiation

CNTs are often formed in entangled ropes with 10–100 CNTs per bundle depending on the method of synthesis. They can be produced by a number of methods: direct-current arc discharge, laser ablation, thermal and plasma enhanced chemical vapour deposition (CVD) process [Lau and Hui, 2002]. The method of production affects the level of purity of the sample and whether SWNTs or MWNTs are formed. Impurities exist as catalysis particles, amorphous carbons and non-tubular fullerenes [Thostenson et. al., 2001]. Fig. 1 shows the SEM image and EDX analysis result of MWNT produced by a CVD process without any purification. As-received MWNT contain some impurities and entangle into a bulk piece. EDX results of the pristine MWNT show small peaks which are corresponding to Fe, Si and S. The Si peak has its origin in silicon substrate whereas the other peaks are due to the precursor gases present in the gas mixture and catalyst. The Pt peaks was due to the platinum sputtering process during SEM sample preparation. Average diameter and average length of MWNT were 15 nm and 20 μm, respectively.

The MWNT were electron-beam irradiated in air at room temperature using an electron-beam accelerator. Irradiation dose of 800, 1000, and 1200 kGy were used, respectively. Fig. 2. demonstrates a higher magnification SEM micrographs of MWNT before and after

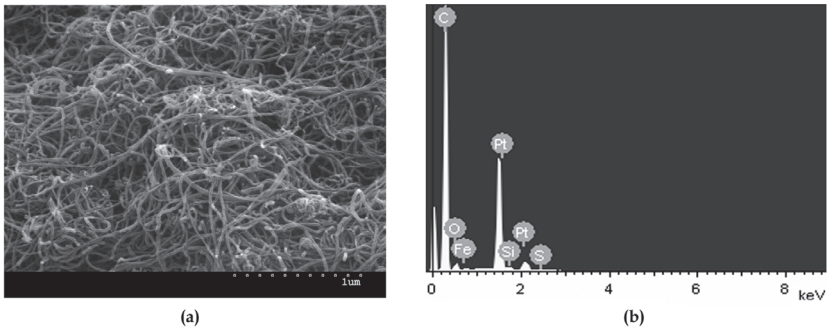

Fig. 1. SEM image and EDX analysis result of the pristine MWNT

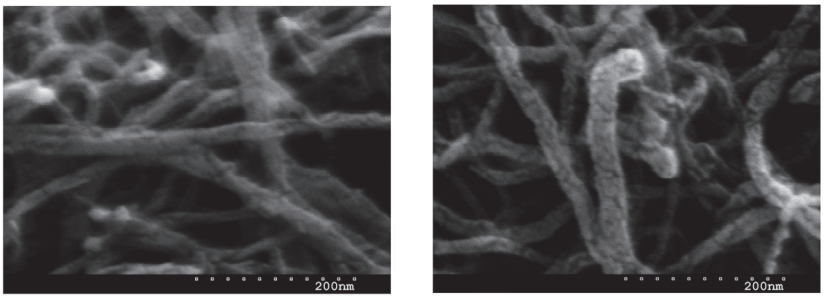

Fig. 2. SEM micrographs of the surface morphology of pristin MWNT and MWNT1200

treatment with the electron-beam irradiation. The pristine MWNT has relatively smooth surface without extra phase or stain attached on its sidewall. Although the electron-beam irradiation increased up to 1000 kGy, the surface appearance did not changed compare to the pristine MWNT. After the 1200 kGy EB irradiation, the smooth surface was disappeared, many wrinkled structure were formed, and the surface roughness increased. In general, the surface of the synthesized CNT is smooth and relatively defects free. However, stresses can induce Stone Wales transformations, resulting in the formation of heptagons and concave areas of deformation on the nanotubes [Thostenson et. al., 2001].

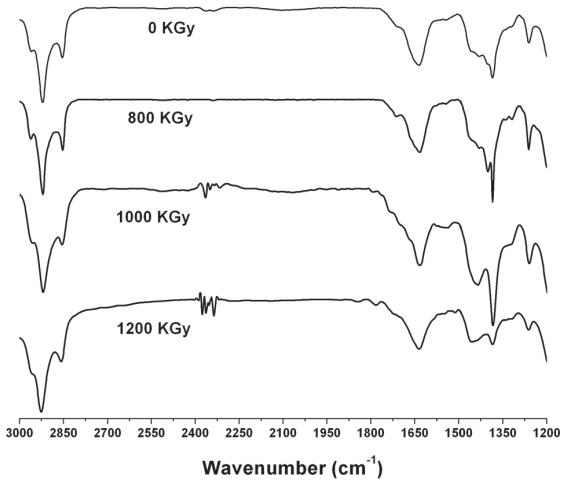

Fig. 3. FTIR spectra of the electron-beam irradiated MWNT

The pristine MWNT and electron-beam irradiated MWNT were further characterized by FTIR spectroscopy. The pristine MWNT exhibit the peaks of C-C bond stretching appeared in the range of 3000–2800 cm^{-1}. FTIR spectra of MWNT after electron-beam irradiation more than 1000 kGy showed new peaks at 1782 cm^{-1} due to the C=O bond resulting from C=O stretch of the carboxyl and carbonyl groups (Fig. 3). Element analysis presented a decrease in the hydrogen/carbon ratio up to 1000 kGy. After the 1200 kGy irradiation, the hydrogen

/carbon ratio was significantly increased. This indicated that low irradiation dose clean the impurities of MWNT, but the increase of irradiation doses could affect surface roughness and chemical composition.

2.2 Preparation of porous VOH group containing polymer/MWNT nanocomposites

Highly porous VOH group containing polymer nanocomposite particles were created by simple saponification method. A VAc group containing polymer/MWNT/toluene suspension was saponification by dropwise addition to KOH in alcohol solution which saponifying the VAc groups in polymer selectively. The VAc group containing polymer used in this study was poly(ethylene-*co*-vinyl acetate) (EVA, VAc content 28 and 40 wt%) and poly(vinyl acetate) (PVAc). The heterogeneous suspension was stirred at room temperature for ambient time, and then the solution was filtrated, and washed with methanol. The approximate size of the prepared particles is 30-50 μm. The abbreviation of the sample name, EVA40/MWNT1200, for example, means that the content of VAc in the EVA was 40 wt % and MWNT was electron-beam irradiated 1200 kGy does.

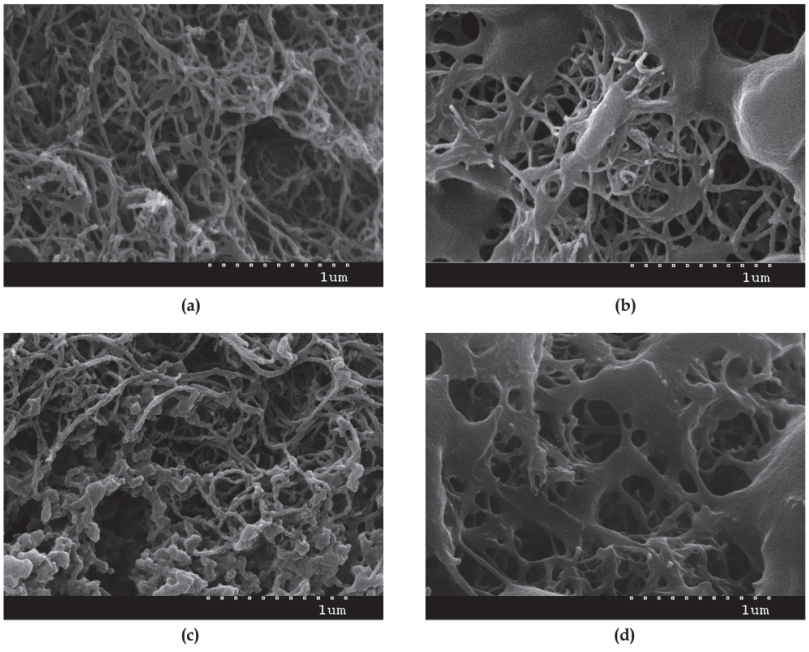

Fig. 4. SEM micrographs of the 3h-saponified PVAc/MWNT1200 (a: ethanol/KOH, c: methanol/KOH), EVA40/MWNT1200 (b: ethanol/KOH) and EVA28/MWNT1200 (d: ethanol/ KOH) coagulants

After rinsing off the coagulant and drying, sponge-like structure of connected matrix polymer and MWNT were obtained. This causes separation of the heterogeneous polymer suspension into a solid nanocomposite and liquid solvent phase. The precipitated coagulants form a porous structure containing a network of uniform open pores. Production

parameters that affect the pore structure and properties significantly include the MWNT concentration, the VAc content in polymer, the precipitation media and the saonification time. At low polymer/MWNT suspension concentrations, the particles were less porous and the precipitated polymer phase had a granular structure consisting of aggregates of precipitated polymer micelles. While at high concentrations, void porosity was increased and the precipitated polymer phase became a spongy-like structure. It was also found that as the VAc content in polymer was decreased, the average pore size increased and number was decreased. In sharp contrast, the irradiation does of MWNT was not affected in pore size and structure. The pore size was obtained directly by image analysis from higher magnification SEM micrographs. Pore size control can be achieved with sub-nanometer 10 to 200 nm range by selecting the matrix materials and the saponification conditions

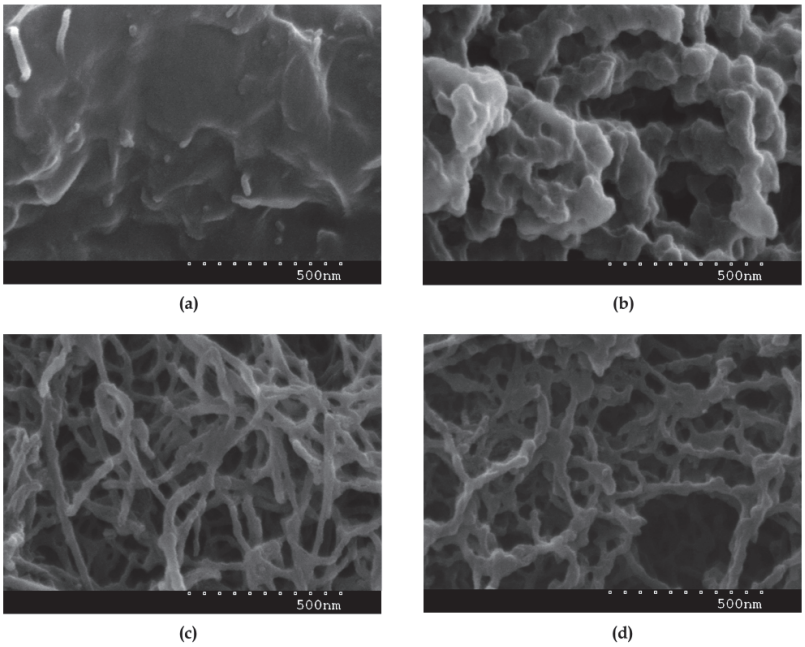

Fig. 5. SEM micrographs of the saponified PVAc/MWNT1200 in methanol/KOH along with that of its corresponding saponification time [(a) precipitated in hexane, (b) 1 h, (c) 3 h, and (d) 6 h]

Fig. 5 represents the SEM image of PVAc/MWNT1200 coagulant surface prepared using methanol/KOH solution as the saponification time. The surface of the PVAc/MWNT1200 coagulant shows a dense skin layer, which appears to be nonporous. The formation of the skin layer and lack of an interconnected pore structure is likely due to the rapid precipitation where the rate of inter-diffusion depends on the value of the solubility parameters of the solvent and non-solvent. As the saponification time increase, the PVAc/ MWNT1200 nanocomposite coagulant form a porous structure containing a network of open-cell pores at the nanometer length scale.

2.3 Mechanical properties of EVOH/MWNT nanocomposites

Table 1 demonstrates the tensile properties of the electron-beam irradiated MWNT (MWNT1200) filled EVA nanocomposites before and after saponification in KOH/metanol solutuion. PVAc/MWNT1200/toluene and EVA/MWNT1200/toluene suspensions were prepared with MWNT1200 loadings of 10 wt%. The suspensions were solvent-casting onto a PTFE film-supporting surface and the prepared film was subsequently hot pressed to sheet of uniform thickness. Dumbbell specimens for tensile tests were prepared in accordance with IEC 60811-1-1 specification. Tensile properties of samples were determined with a universal test machine. The hot-pressed sheets of PVAc/MWNT-10% nanocomposite are very brittle and can not be perform the tensile test.

Sample code	Tensile properties	
	Tensile strength (MPa)	Elongation at break (%)
EVA28	10.6 ± 0.9	1472 ± 106
EVA28/MWNT1200-10%	8.9 ± 0.8	162 ± 20
EVA28/MWNT1200-10%-6h	17.6 ± 2.0	412 ± 50
EVA40	9.0 ± 1.0	1625 ± 156
EVA40/MWNT1200-10%	7.2 ± 0.9	522 ± 59
EVA40/MWNT1200-10%-6h	18.7 ± 2.3	756 ± 81

Table 1. Tensile properties of the hot-pressed specimens

As shown Table 1, addition of 10 wt% of MWNT1200 reduced the tensile strength of EVA28 and EVA40 by 16 and 20 %, respectively. This means that MWNT1200 contents were at values of 10 wt%, the MWNT did not disperse uniformly and they formed agglomerations in the polymer matrix. In addition the elongation at break of both nanocomposites decreased with the presence of filler that indicates interference by the filler in the mobility or deformability of the matrix. It is noteworthy that tensile strength and elongation at break of nanocomposite samples prepared by simple saponification method were significantly increased than those of corresponding unsponified ones. After 6h saponification time, the tensile strength of EVA28/MWNT1200-10% and EVA40/MWNT1200-10% was increased by about 98 and 160 %, respectively. This is indicated that saponification process enhances the overall dispersion state of the MWNT nanofibers due to enhanced interactions between the filler and the polymer matrix.

2.4 Resistivity of saponified VAc containing polymer/MWNT nanocomposites

The surface electrical resistance of the hot-pressed films (80 mm length × 10 mm width) was detected by a megohmmeter according to ASTM D 257. The charge time was 10 s, and the current stress of the measurements was 5000 V at 20 ± 1 °C. Volume resistivity (ρ_v) of prepared films was calculated by use of equation (1).

$$\rho_v = \frac{AR_v}{L} \tag{1}$$

Where A, R_v and L represent the area of the effective electrode (cm^2), measured resistance (Ω), and distance between electrodes (cm), respectively.

Fig. 6 show a rapid decrease in ρ_v of PVAc/MWNT1200, EVA40/MWNT1200, EVA28/MWNT1200 nanocomposites with increasing MWNT content. This rapid decrease is characteristic of the loading level at which the MWNT particles begin to come into contact with one another to form a electroconductive network. As MWNT particles are loaded in a polymer matrix over a percolation threshold concentration, the nanocomposite becomes an electrical conductor at room temperature. The percolation threshold of the PVAc/ MWNT1200, EVA28/MWNT1200, and EVA40/MWNT1200 nanocomposites formed by solution mixing was approximately 2.5, 2.5 and 5 wt%, respectively due to the advantageous effect of composites with higher aspect ratios compared with spherical or elliptical fillers in forming conducting networks in the polymer matrix.

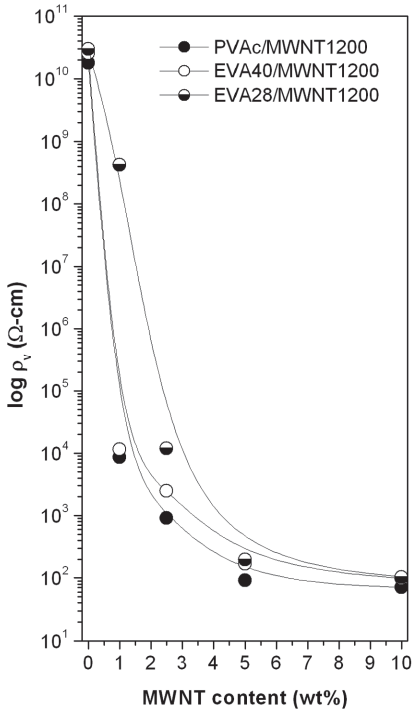

Fig. 6. ρ_v change of the PVAc/MWNT1200, EVA40/MWNT1200 and EVA28/MWNT1200 nanocomposites with increasing MWNT content

The electron transport in CNT assemblies is different from that in individual nanotubes. It has been reported that SWNT fibers exhibit room temperature resistivity in the range of 1 $\times 10^{-4}$ to 7×10^{-4} Ω-cm, which is nearly 100 times higher than that of single CNT. The resistivity of MWNT fibers are one or two orders of magnitude higher than that of SWNT fibers [Zhang et. al., 2004; Zhu et. al, 2006]. Such large differences between single nanotubes and fiber assemblies may arise from high impurity content such as amorphous carbon and catalytic particles in the fibers, which may profoundly affect electron transport by causing significant scattering, and contact resistances between nanotubes [Li, 2007]. Therefore, two

approaches can be used to improve the electrical conductivity of polymer/CNT nanocomposites: 1) reduce the impurity content of CNTs by post treatments [Li, 2007]; 2) minimize the contact distances between nanotubes by enhancing the dispersity of individual nanotubes.

Fig. 7 shows the dependence of ρ_v change for PVAc/MWNT1200, EVA40/MWNT1200 and EVA28/MWNT1200 nanocomposite films with the saponification time. Among them, PVAc/MWNT1200 nanocomposite showed lowest ρ_v and it has also the lowest ρ_v after saponification process. It can be also founded that the ρ_v almost maintained with saponification time. This may be because of the easy dispersion of MWNT particles in the rubbery phase and hence the high VAc polymers disperse the fillers well. The EVA28 and EVA40 consists of more crystalline phase and hence the MWNT particles find it more difficult to disperse and hence form relatively more agglomerations, whereas in high VAc grades, the amount of free volume is more and hence the fillers can disperse relatively easily [George and Bhowmick, 2009]. In sharp contrast, the ρ_v of saponified EVA40/MWNT1200 and EVA28/MWNT1200 nanocomposites decreased significantly with the saponification time. An increase of VOH units would raise the intermolecular interaction between EVOH molecules, and it enhanced crystallization of EVOH molecules. When the matrix polymer crystallinity increased, filler particles segregate to the non-crystalline interlamellar and interspherulitic regions and forms more inter-connective pathways, which results in lowering the resistivity [Lee et. al., 2011].

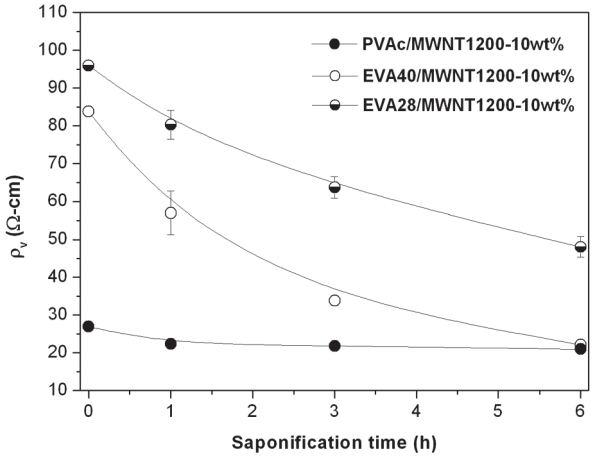

Fig. 7. ρ_v change of PVAc/MWNT1200, EVA40/MWNT1200 and EVA28/MWNT1200 nanocomposite powders with saponification time

In fact, this can be confirmed from XRD spectra of EVA28 in Fig. 8. On curve, there is a strong diffraction peak at $2\theta=20.8°$ and a weak diffraction peak at $2\theta=5.8°$. These diffraction peaks attribute to the crystallization of the main chain. Both the relative intensity increment and the peak shift at higher 2θ with the saponification time is a strong indication of the increased crystallinity of the saponified samples relative to the pure EVA28. All the observations are in accordance with the tensile properties discussed above.

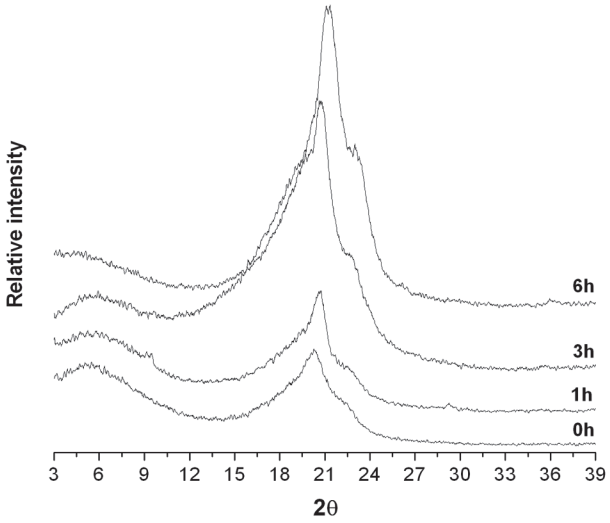

Fig. 8. XRD spectra of the saponified EVA28 along with that of its corresponding saponification time

3 Applicability of VOH group containing polymer/MWNT nanocomposites

3.1 Positive temperature coefficient (PTC) heating elements

Electroconductive polymer nanocomposites are becoming increasingly useful because of their unique combination of metallic electroconductivity and polymer properties. Currently, there are several methods that can be used to impart electroconductivity to polymers: doping of intrinsically electroconductive polymers, incorporation of electroconductive additives into an insulating polymer matrix and coating of fibers with metals or electroconductive chemicals. Applicability of VOH group containing polymer/MWNT nanocomposites can be used in a variety of industrial applications such as heating elements, temperature sensors and current limiters [Kim and Park, 2008; Park et. al., 2004; Park et. al., 2005; Park, 2005; Park, 2006]. This is mainly due to their positive temperature coefficient (PTC) of resistivity. It has been well accepted that the strong PTC effect of them is caused by an increase in the average inter particle distance of filler, which is created by the large thermal expansion that occurs as a result of the melting of the polymer crystals [Park et. al., 2003].

Fig. 9 indicates resistivity-temperature behavior of the saponified EVA28/MWNT-10wt% nanocomposites. All nanocomposites exhibited both negative temperature coefficient (NTC) and PTC effect. A NTC indicates that resistivity decreases with temperature; a PTC indicates that resistance increases with temperature. However, this NTC effect could be eliminated easily by chemical or electron-bam radiation crosslinking. As the saponification time increased, the PTC maximum peak temperature of nanocomposites is shifted at higher temperatures. A reproducible PTC composite should have high PTC effect to prevent the composite from overheating and relatively low room temperature resistivity to ensure sufficient thermal output. From Fig. 9, 3h- and 6h-saponified nanocomposites showed good PTC behavior with high melting temperature. They have great potential for use in industrial applications such like PTC heating elements and coating materials for surface film heater.

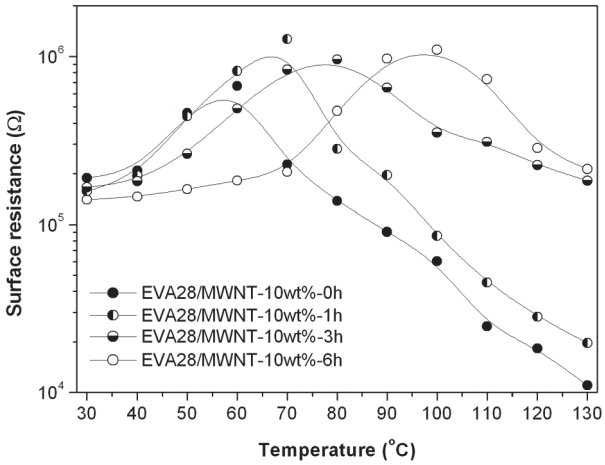

Fig. 9. PTC peak temperature change of the EVA28/MWNT-10wt% nanocomposites with saponification time

3.2 Electromagnetic interference (EMI) shielding materials

As electromagnetic radiation, particularly that at high frequencies tend to interfere with electronics, EMI shielding of both electronics and radiation source is needed and is increasingly required by governments around the world [Chung, 2001]. The radiation may be either electromagnetic in nature, such as X-rays and gamma rays, or charged particles, such as beta particles and electrons. The lifetime and efficiency of them can be increased by the effective shielding. Generally, highly electroconductive materials such like metals are used for shielding application. However, metals have their own shortcomings like heavy weight, susceptibility to corrosion, wear, and physical rigidity [Wu et al., 2006]. The polymer nanocomposites filled with carbon materials are attractive for EMI shielding materials which helps to reduce or eliminate the seams in the housing that is the shield. Many researches have been conducted to improve the EMI shielding of polymer materials by coating an electroconductive layer on the surface, incorporating electroconductive fillers, or utilizing electroconductive polymers. Among various electroconductive fillers that have been utilized, CNT is one of the most promising candidates, not only because of its good electrical conductivity but also because of its ability to improve mechanical properties. Recently, the mass production of MWNT causes price reduction. The MWNT is more affordable for EMI shielding material application in nanocomposites [Wu et. al., 2006].

3.3 Antibacterial agents

In our previously study [Lee et. al., 2011], it is curious to observe that saponified EVA had some antimicrobial activity against *Staphylococcus aureus* (*S. aureus*) and *Escherichia coli* (*E. coli*). Antibacterial activity of EVA28 powders was gradually increased with saponification time. 6h-saponified EVA extirpated 45 and 57% of the viable cells of *S. aureus and E. coil*, respectively. As shown in Fig. 10, it possesses a porous structure that can adsorb various ions and organic molecules easily in its pores and on its surfaces. Bacterial growth or

movement may be restricted by porous media physical conditions. Bacteria are small living organism; their length change between 0.5-10 μm and their diameters are between 0.2-10 μm. Porosity networks with pore throat sizes narrower than the bacterial cell diameter prevent bacterial penetration into these regions [Fredrickson et al., 1997]. Porous regions are diffusion-limited or that are experiencing biomass sloughing due to rapid flow-induced shear forces [Applegate and Bryers, 1991] may be less likely to harbour significant bacterial populations. Furthermore, CNTs have been recently demonstrated to possess antimicrobial properties, and their relevant activities were ascribed to the behaviour of 'nanodart' with the proposed physical damage mechanism [Kang et. al., 2008].

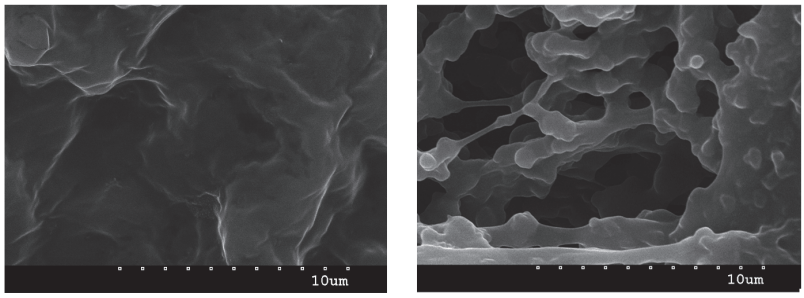

Fig. 10. SEM micrographs of the EVA28 (a) and 6h-saponified EVA28 (b) in ethanol/KOH solution

3.4 Membrane for purification and separation

The development of advanced membrane technologies with controlled and novel pore architectures is important for the achievement of more efficient and cost effective purification. Present polymeric membranes are well known to suffer from a trade off between selectivity and permeability, and in some cases are also susceptible to fouling or exhibit low chemical resistance [Sears, et. al., 2010]. Due to the simplicity of their preparation, Bucky-papers were one of the first macroscopic structures fabricated from CNTs [Baughman et. al., 1999; Kim et. al., 2006]. The Bucky-paper is used to describe a mat of randomly entangled CNTs prepared by filtration [Kim et. al., 2006; Endo et. al., 2003] or alternative papermaking processes. CNTs are known to have a strong tendency to aggregate due to van der Waals interactions, and it is these van der Waals interactions which also hold the CNTs together into a cohesive Bucky-paper. Longer, narrower and more pure CNTs typically lead to stronger Bucky-papers with higher tensile strengths. With increasing MWNT diameter, the attractive van der Waals forces between CNTs become less effective, leading to Bucky-papers with lower tensile strength and poor cohesiveness. This can be improved to some extent through functionalization of MWNTs or the addition of polymers [Xu et. al., 2008]. Recently, EVOH membranes have attracted plenty of research interest in fields of biomedical science and water treatment because of its good blood compatibility and hydrophilicity [Guerra et. al. 1995; Young et. al., 1997]. As noted in the previous section, highly porous EVOH/MWNT nanocomposites with higher tensile strength were easily prepared by simple saponification method. As such they are of interest for applications such

like direct contact membrane distillation, capacitive deionization, and filtration of particles including bacteria and viruses.

3.5 Carriers of catalyst and functional materials

The highly porous nature of materials enables their use as carriers [Benson, 2003]. High surface area and controlled pore size distribution available as the raw material to the shape or monolith forming process. Capillary forces are quite strong, and will tightly contain many substances for slow release. In some cases, an encapsulation step may be required to ensure long term retention of contained substances. In one experiment, an accelerator component was placed into highly porous spheres, retained, and premixed with an adhesive. The two parts were mixed without fear of reaction since capillary forces prevented viscous liquids from escaping. Later, the reaction was initiated when the beads were crushed or heated to the activation temperature [Benson, 2003]. In addition any catalytic material attached to highly porous nanocomposite surfaces would have more efficient interaction with reactants due to large cavities and interconnected pores. As a main constituent for carrier materials provide a controlled surface area and porosity for the final catalytic system. This unique structure permits reactants to flow into spheres, interact with catalysts, form products, and still allows room for products to flow out and away from newly arriving reactants. Such accessibility of the catalyst to reactants is important for rapid and efficient reactions. Carboxyl groups and other functional groups could be modified on the MWNT surface [Chiu and Chang, 2007].

3.6 Chromatography and bio-processing

Large interconnected cavities contained within chemically stable EVOH containing polymer/MWNT nanocomposites are ideally suited for liquid chromatography applications, including bio-processing. Because cavities of them are relatively uniform and are individually connected through a network of smaller pores, sample molecules find clear ingress and egress through the matrix, and diffusion limitations characteristic of conventional porous polymers are absent [Benson, 2003]. Therefore, mass transfer characteristics are extremely attractive. The focus of bio-processing is using living cells to make desired products, which is commonly carried out in a bioreactor. Downstream processing from this reactor gives concentrated and purified products. Separation of proteins and other biopolymers on conventional porous polymers occurs only in the outside few angstroms of the spheres [Krijgsman, 1992]. In contrast, because of the interconnections, separation on porous MWNT nanocomposites occurs throughout the entire volume of particles. Furthermore, since there are no needs to be modified by coating the surface with a hydrophillic polymer to avoid low recovery, pressure drop through columns of these particles is extremely low. In addition, the synthetic polymer-based media is their resistance to extreme chemical conditions, such as pH. These properties, and the suitability of such structures for containment and separation of biopolymers, make them ideal candidates for bio-processing applications.

3.7 Polymeric fillers

Surface modification of filler is an important topic. Fillers are commonly incorporated into polymeric resin compositions in order to modify the properties of the resin. However, most inorganic fillers have a naturally hydrophilic surface which is therefore not easily wetted by

polymeric resin compositions which are generally hydrophobic. This problem is especially acute when the resin is in the form of a low-viscosity liquid because under these conditions it is difficult to dissipate sufficient energy in the composition by mechanical agitation to effect dispersion of the inorganic filler in the polymeric resin. A further disadvantage of conventional inorganic fillers is that they generally have associated with them a small, but significant, quantity of water. EVOH copolymers have been widely used as food packages, biomedical and pharmaceutical industries due to their excellent gas barrier properties, high resistance to oils, good mechanical strength and harmlessness to health [Okaya and Ikari, 1992]. They also have significant potential for polymeric filler and inorganic filler surface modifier due to their combined effect of hydrophilicity, as a consequence of the -OH side groups. Since the materials prepared by this method for industrial applications such like polymeric filler in electro-conductive and electrostatic discharge composite systems, polymer compound systems, and aqueous coating systems.

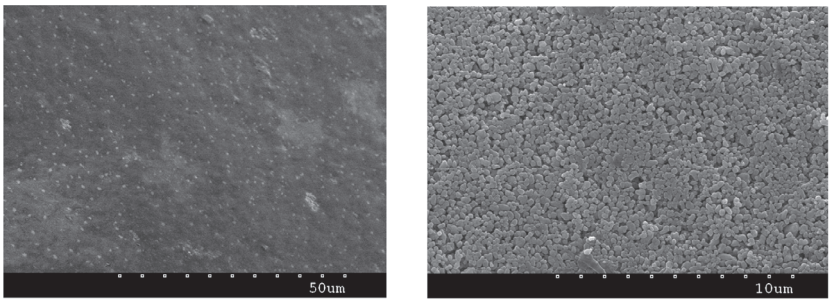

Fig. 11. SEM image of the EVOH/MWNT/ sodium silicate hybrid composites prepared from aqueous coating system (a) and EVOH coated nanofiller (b).

4. Conclusion

Current interest in nanocomposites has been generated and maintained because CNT-filled polymers exhibit unique combinations of properties not achievable with traditional composites. Some studies were carried out to investigate the properties and applicability of highly porous VOH group containing polymer/MWNT nanocomposites produced by simple saponification method. As has been shown in this study, the possible applications of highly porous MWNT nanocomposites range widely, from heating elements to polymeric filler. In addition, they can be easily processed by various techniques such as extruding, injection molding, laminating, film-casting, and printing. Since the nanocomposites prepared by this method have highly porous, good hydrophilicity, good mechanical strength and thermal properties, they can be used for various industrial applications.

Furthermore, MWNTs were subjected to electron-beam irradiation at various doses to determine the incidence of surface modification and, resultantly, deformation or destruction to the otherwise pristine graphitic structure. FTIR spectra obtained from electron-beam irradiated MWNT samples provide insight into the level of surface modification. Functional groups such like carboxyl and carbonyl groups on MWNT surface can interact with -OH group in polymer chains by hydrogen bonding and result in a better dispersion of MWNT

in EVOH matrix. Such modified MWNT could be also functionalized to introduce covalent groups onto the nanotube surface, thus aiding in the uniform dispersion into polymer composite systems. Afterward we carry out extensive studies to investigate the properties and applicability for VOH group containing polymer coated and reacted nanotube prepared by simple saponification method.

5. Acknowledgment

We are grateful to the Small and Medium Enterprises (SMEs) Technology Innovation Program, Republic of Korea, for financial support of this experimental work.

6. References

Ajayan, P.; Stephan, O.; Colliex, C.; Trauth, D. (1994). Aligned carbon nanotube arrays formed by cutting a polymer resin-nanotube composite, *Science*, Vol.265, No.5176, (1994), pp.1212-1214

Applegate, D. H., and J. D. Bryers (1991). Effects of carbon and oxygen limitations and calcium concentrations on biofilm removal processes, *Biotechnology and Bioengineering*, Vol.37, (1991), pp.17–25, DOI:10.1002/bit.260370105

Benson, J. R. (2003). Highly Porous Polymers, *American Laboratory* (April, 2003), Available from http://www.sunstorm-research.com

Balasubramanian, K.; Burghard, M. (2005). Chemically Functionalized Carbon Nanotubes, *Small*, Vol.1, No. 2, (2005), pp.180 –192, DOI:10.1002/smll.200400118

Baughman, R. H.; Cui, C.; Zakhidov, A. A.; Iqbal, Z.; Barisci, J. N.; Spinks G. M.; Wallace, G. G.; Mazzoldi, A.; Rossi, D. D.; Rinzler, A. G.; Jaschinski, O.; Roth, S.; Kertesz, M. Carbon Nanotube Actuators. *Science*, Vol.284, (1999), pp.1340–1344.

Chung, D.D.L. (2001). Electromagnetic interference shielding effectiveness of carbon, *Carbon* Vol.39, (2001), pp.279–285

Chiu, W. M.; Chang, Y. A. (2007). Chemical modification of multiwalled carbon nanotube with the liquid phase method, *Journal of Applied Polymer Science*, Vol.107, (2008), pp. 1655–1660, DOI:10.1002/app.26633

Endo, M.; Muramatsu, H.; Hayashi, T.; Kim, Y. A.; Terrones, M.; Dresselhaus, M. S. (2005).'Buckypaper' from coaxial nanotubes, *Nature*, Vol.433, (2005), pp.476

Fredrickson, J. K.; McKinley, J. P.; Bjornstad, B. N.; Long, P. E.; Ringelberg, D. B.; White, D. C.; Krumholz, L. R.; Suflita, J. M.; Colwell, F. S.; Lehman, R. M.; Phelps, T. J.; Onstott, T. C. (1997). Pore-size constraints on the activity and survival of subsurface bacteria in a Late Cretaceous shale-sandstone sequence, *Northwestern New Mexico. Geomicrobiology Journal*, Vol.14, pp.183-202

George, J. J.; Bhowmick, A. K. (2009). Influence of Matrix Polarity on the Properties of Ethylene Vinyl acetate–carbon nanofiller nanocomposites, *Nanoscale Research Letters*, Vol.4, (2009), pp.655–664, DOI:10.1007/s11671-009-9296-8

Guerra, N.; Barbani, L.; Lazzeri, L.; Lelli, L.; Palla, M.; Rizzo, C. (1995). The activation of human plasma prekallikrein as a hemocompatibility test for biomaterials. II. Contact activation by EVAL and EVAL–SMA copolymers, *Journal of Biomaterials Science,* Vol.4, (1995), pp.643–652

Harris, P. J. F. (2004). Carbon nanotube composites, *International Materials*, Vol.49, No.1, (2004), pp.31-43, DOI 10.1179/095066004225010505

Kang, S.; Herzberg, M.; Rodrigues, D. F.; Elimelech, M. (2008). Antibacterial Effects of Carbon Nanotubes: Size Does Matter!, *Langmuir*, Vol.24, (2008), pp.6409-6413, DOI: 10.1021/la800951v

Kanny, K.; Muhfuz, H.; Carlsson, L. A.; Thomas, T.; Jeelani, S. (2002). Dynamic mechanicalanalyses and flexural fatigue of PVC foams, *Composite Structures*, Vol.58, (2002), pp.175–183

Kim, G. T.; Park, E. S. (2008). Thermal Reproducibility and Voltage Stability of Carbon Black/Multiwalled Carbon Nanotube and Carbon Black/SnO_2-Sb Coated Titanium Dioxide Filled Silicone Rubber Heaters, *Journal of Applied Polymer Science*, Vol.109, (2008), pp.1381–1387, DOI:10.1002/app.28200

Kim, B. Y. A.; Muramatsu, H.; Hayashi, T.; Endo, M.; Terrones, M.; Dresselhaus, M. S. (2006).Fabrication of High Purity, Double-Walled Carbon Nanotube Buckypaper, *Chemical Vapor Deposition*, Vol.12, (2006), pp.327–330

Kumar, S.; Doshi, H.; Srinivasarao, M.; Park, J. O.; Schiraldi, D. A. 2002. Fibers from polypropylene/nano carbon fiber composites, *Polymer*, Vol.43, (2002), pp.1701-1703

Krijgsman, J. (1992). *Product Recovery in Bioprocess Technology*, Butterworth-Heinemann, ISBN: 0750615109

Lau, A. K.-T.; Hui, D. (2002). The Revolutionary Creation of New Advanced Materials: Carbon Nanotube Composites, *Composites Part B:Engineering*, Vol.33, No.2,(2002), pp.263-267

Li, Q. W.; Li, Y.; Zhang, X. F.; Chikkannanavar, S. B.; Zhao, Y. H.; Dangelewicz, A. M.; Zheng, L. X.; Doorn, S. K.; Jia, Q. X.; Peterson, D. E.; Arendt, P. N.; Zhu, Y. T. (2007). Structure-Dependent Electrical Properties of Carbon Nanotube Fibers, *Advanced Materials*, Vol.19, (2007), pp.3358–3363, DOI: 10.1002/adma.200602966

Lee, E. J.; Yoon J. S.; Park, E. S. (2011). Morphology, Resistivity, and Thermal Behavior of EVOH/Carbon Black and EVOH/Graphite Composites Prepared by Simple Saponification Method, *Polymer Composites*, 2011 (in press)

Lee, S. S.; Kim, K. R.; Han, S. H.; Jeong, Y. S.; Kim, M. N.; Park, E. S. (2011), *EVOH based Nanocomposites Prepared by Simple Saponification Method, Journal of Reinforced Plastics and Composites*, 2011 (accepted)

Lewinski, N.; Colvin, V.; Drezek, R. (2008). Cytotoxicity of Nanoparticles, *Small*, Vol.4, No.1, (January 2008), pp.26-49

Mai, Y. W.; Yu, Z. Z. (2006). *Polymer Nanocomposites*, CRC Press, ISBN: 0849392977

Mills, N. J.; Fitzgerald, C.; Gilchrist, A.; Verdejo, R. (2003). Polymer foams for personal protection: cushions, shoes and helmets, *Composites Science and Technology* Vol.63, (2003), pp.2389–2400

Okaya, T.; Ikari, K. (1997). *Polyvinylalcohol-Development*, Finch, C. A. (Ed.), John Wiley & Sons, ISBN: 978-0-471-99850-1, Chichester (Chapter 8)

Park, E. S.; Yun, S. J.; Kim, G. T.; Park, I. J.; Choi, W. H.; Jeong, J. W.; Hong, S. Y. Hong; H. W. Park; Jang, L.W.; Yoon, J. S. (2004). Preparation of Positive-Temperature Coefficient Heaters Using Platinum-Catalyzed Silicone Rubber, *Journal of Applied Polymer Science*, Vol. 92, (2004), pp. 1611–1617

Park, E. S.; Jang, L.W.; Yoon, J. S. (2005). Resistivity and Thermal Reproducibility of Carbon Black and Metallic Powder Filled Silicone Rubber Heaters, *Journal of Applied Polymer Science*, Vol. 95, (2005), pp.1122–1128, DOI:10.1002/app.21340

Park, E. S. (2005). Resistivity and Thermal Reproducibility of the Carbon Black and SnO_2/Sb Coated Titanium Dioxide Filled Silicone Rubber Heaters, *Macromol. Mater. Eng.*, Vol. 290, (2005), pp. 1213-1219, DOI:10.1002/mame.200500214

Park, E. S. (2006). Resistivity and Thermal Reproducibility of High-Density Polyethylene Heaters Filled With Carbon Black, *Macromol. Mater. Eng.*, Vol.291, (2006), pp.690–696, DOI:10.1002/mame.200500425

Park, J. S.; Kang, P. H.; Nho, Y. C.; Suh, D. H. (2003). Effects of Thermal Ageing Treatment and Antioxidants on the Positive Temperature Coefficient Characteristics of Carbon Black/Polyethylene Conductive Composites, *Journal of Applied Polymer Science*, Vol.89, (2003), pp.2316–2322

Ramanathan, T.; Stankovich, S.; Dikin, D. A.; Liu, H.; Shen, H.; Nguyen, S. T. (2007). Graphitic nanofillers in PMMA nanocomposites—An investigation of particle size and dispersion and their influence on nanocomposite properties, *Journal of Polymer Science: Part B: Polymer Physics*, 2007, Vol.45, pp. 2097–112

Ray, S. S.; Bousmina, M. (2008). *Polymer Nanocomposites and Their Applications*, American Scientific Publishers, ISBN: 158883-099-3, California, USA

Roberts, A. P.; Knackstedt, M. A. (1996). Structure-Property Correlations in Model Composite Materials, *Physical Review E*, Vol. 54, (1996), pp.2313–2328

Sears, K.; Dumée, L.; Schütz, J.; She, M.; Huynh, C.; Hawkins, S.; Mikel, M.; Gray, S. (2010). Recent Developments in Carbon Nanotube Membranes for Water Purification and Gas Separation, *Materials*, Vol.3, (2010), pp.127-149, DOI:10.3390/ma3010127

Thostenson, Erik T., Zhifeng, Ren; Tsu-Wei, Chou. (2001). Advances in the science and technology of carbon nanotubes and their composites: a review, *Composite Science and Technology*, Vol.61, (2001), pp. 1899-1912

Thostenson E. T.; Chou, T. W. (2002). Aligned multi-walled carbon nanotube-reinforced composites: processing and mechanical characterization, *Journal of Physics D: Applied Physics*, Vol.35, No.16, (2002), pp.L77-L80

Treacy, M. M. J.; Ebbesen, T. W.; Gibson, J. M. (1996). Exceptionally high Young's modulus observed for individual carbon nanotubes, *Nature*, Vol.381, No.6584, (1996), pp.678–680

Vaisman, L.; Wachtel, E.; Wagner, H. D.; Marom, G. Polymer–nanoinclusion interactions in carbon nanotube based polyacrylonitrile extruded and electrospun fibers, *Polymer*, 2007; Vol.48, (2007), pp.6843–54

Wong S. S.; Joselevich, E.; Wooley, A. T.; Cheung, C. L.; Lieber, C. M. (1998). Covalently functionalized nanotubes as nanometre-sized probes in chemistry and biology, *Nature*, Vol. 394, (1998), pp.52

Wong E. W.; Sheehan, P. E.; Lieber, C. M. (1997). Nanobeam Mechanics: Elasticity, Strength, and Toughness of Nanorods and Nanotubes, *Science*, Vol. 277, No.5334, (1997), pp.1971–1975.

Wu, H. L.; Ma, C. C. M.; Yang, Y. T.; Kuan, H. C.; Yang, C.-C.; Chiang, C. L. (2006). Morphology, Electrical Resistance, Electromagnetic Interference Shielding and Mechanical Properties of Functionalized MWNT and Poly(urea urethane) Nanocomposites, *Journal of Polymer Science: Part B: Polymer Physics*, Vol. 44, (2006), pp.1096–1105, DOI:10.1002/polb.20766

Xu, G.; Zhang, Q.; Zhou, W.; Huang, J.; Wei, F. (2008). The Feasibility of Producing MWCNT paper and strong MWCNT film from VACNT array, *Applied Physics A: Materials Science & Processing,* Vol.92, (2008), pp.531–539

Yoon, K. R.; Kim, W. J.; Choi, I. S. (2004). Functionalization of Shortened Single-Walled Carbon Nanotubes with Poly(*p*-dioxanone) by "Grafting-From" Approach, *Macromolecular Chemistry and Physics*, Vol.205, (2004), pp.1218-1221

Young, T. H.; Lai, J. Y.; You, W. M.; Cheng, L. P. (1997). Equilibrium phase behavior of the membrane forming water–DMSO–EVAL system, *Journal of Membrane Science*, Vol.128, (1997), pp.55–65

Zeleniakiene, D. (2006). The influence of microstructural stiffness changes on the stress concentration factor of porous polymer materials, *Proceedings of the Estonian Academy of Sciences Engineering*, Vol.12, No.2, (2006), pp.147–155, ISSN 1406-0175

Zhang, M.; Atkinson, K. R.; Baughman, R. H. (2004). Multifunctional Carbon Nanotube Yarns by Downsizing an Ancient Technology, *Science*, Vol.306, No. 5700, (2004), pp.1358-1361

Zhu, L.; Xu, J.; Xiu, Y; Hess, W. H.; Wong, C. P. (2006). Controlled Growth and Electrical Characterization of High-aspect ratio Carbon Nanotube Arrays, *Carbon*, Vol.4, No.2, (2006), pp.253-258

Zhu, H. W.; Xu, C. L.; Wu, D. H.; Wei, B. Q.; Vajtai, R.; Ajayan, P. M. (2002). Direct synthesis of long nanotube strands, *Science*, Vol.296, No.5569, (2002), pp.884-886

7

Reinforcement Effects of CNTs for Polymer-Based Nanocomposites

Yuan Li, Yaolu Liu and Ning Hu
Chiba University
Japan

1. Introduction

With large aspect ratio, high strength and stiffness, carbon nanotubes (CNTs) have been widely used as the reinforcement for polymer-based nanocomposites with prospective application in aerospace engineering, automotive industry, etc. Generally, there are two typical representatives: three-phase hybrid CFRP laminates (CNT/Polymer/CF) and two-phase CNT-reinforced polymer (CNT/Polymer) nanocomposites.

For **three-phase hybrid CFRP laminates** which use CNTs to improve the interlaminar mechanical properties of CFRP laminates, the fabrication methods can be categorized into the following three ways:

i. *Matrix reinforcement*, which uses the two-phase CNT/Polymer nanocomposites as the matrix for CFRP plies before lay-up [Yokozeki et al., 2007; Karapappas et al., 2009; Inam et al., 2010];
ii. *Filler reinforcement*, which employs the CNT-grafted carbon fibres as reinforcement filler for CFRP plies before lay-up [Thostenson et al., 2002; Veedu et al., 2006; He et al., 2007; Kepple et al., 2008];
iii. *Interface reinforcement*, which adds CNTs into the interface between CFRP plies during lay-up [Garcia et al., 2008; Arai et al., 2008].

Although great progress has been made for the first two ways, less work is reported on the third one.

Therefore, in the present work, a newly simple fabrication method, i.e., **Powder method** *was developed to disperse the CNTs at the interface between CFRP plies. The improvement of interlaminar mechanical properties was investigated by DCB (double cantilever bending) tests and FEM (finite element method) analysis.*

For **two-phase CNT/Polymer nanocomposites**, numerous experimental investigations have been carried out on the reinforcement effect of CNTs addition in thermosetting ones, e.g. epoxy [Schadler et al., 1998; Gojny et al., 2005; Ci & Bai, 2006], polyimide [Ogasawara et al., 2004; Jiang et al., 2005], and phenolic [Tai et al., 2004], as well as thermoplastic ones, e.g. polypropylene (PP) [Bhattacharyya et al., 2003; Chang et al., 2005], polystyrene (PS) [Thostenson & Chou, 2002; Chang et al., 2006], polymethylmethacrylate (PMMA) [Cooper et al., 2002; Lee et al., 2006] and polyether ether kentone (PEEK) [Deng et al., 2007; Bangarusampath et al., 2009]. However, the reported improvement of mechanical properties of these nanocomposites is far more less than the expectation because of poor dispersion, difficult alignment of CNTs, and weak interface between CNT and polymer matrix, which

are involved in geometrical properties of CNTs themselves, polymer properties, fabrication method of CNT/Polymer nanocomposites.

To overcome these obstacles, various efforts, such as ultrasonication [Safadi et al., 2002; Ding et al., 2003], surface treatment [Curran et al. 1999; Vigolo et al., 2000; Gojny et al., 2003], shear mixing [Andrews et al., 2002], bi/tri-axial rolling [Rosca & Hoa, 2009; Gojny et al., 2004], extrusion [Cooper et al., 2002; Wong et al., 2003], and their combination, have been firstly made to effectively achieve good dispersion of CNTs in polymer. Moreover, several techniques have been proposed to control CNTs alignment using shear [Ajayan et al., 1994], elongation [Jin et al., 1998], melt processing [Haggenmueller et al., 2000], as well as magnetic field [Kimura et al., 2003] or electrical spinning [Sen et al., 2004]. Furthermore, great progress has been made on the investigation of the interfacial properties. For example, direct CNT pull-out experiments were made in telescope electron microscopy (TEM) [Qian et al., 2000; Deng, 2008], or by atomic force microscopy (AFM) [Barber et al., 2003, 2004], Raman spectroscopy [Schadler et al., 1998], scanning probe microscope (SPM) [Cooper et al., 2002]. However, difficult manipulation in nano-scale and measurement on force/displacement makes large data scattering inevitable, which makes numerical simulation a powerful alternative approach. Continuum mechanical, molecular mechanics (MM), conventional or ab initio molecular dynamics (MD), or their combinations, have also been attempted to investigate the interfacial properties. For instance, some continuum mechanics based models (e.g. cohesive zone model [Jiang et al., 2006], shear lag model [Xiao & Zhang, 2004; Gao & Li, 2005; Tsai & Lu, 2009], and pull-out model [Lau, 2003; Natsuki et al., 2007]) were developed to investigate the interfacial properties between CNT and polymer matrix. Compared with Natsuki's suggestion [Natsuki et al., 2007] of that maximum interfacial shear stress (ISS) occurs at the pull-out end of CNT, Gao [Gao & Li, 2005] predicted that ISS approaches maximum at the two ends of CNT, but keeps zero at the middle part. On the other hand, most of MM/MD simulations [Lordi & Yao, 2000; Liao & Li, 2001; Frankland et al., 2002; Gou et al., 2004; Zheng et al., 2009; Al-Ostaz et al., 2008; Chowdhury & Okabe, 2007] assumed constant ISS during the whole pull-out process with uniform distribution along the contact surface between CNT and polymer. Obviously, the above totally different distribution forms of ISS leads to great confusion in understanding the inherent interfacial characteristics of CNT/Polymer nanocomposites. Moreover, all of the previous MM/MD simulations are limited to a specified SWCNT with a fixed length and diameter. The influences of CNTs' dimension on the pull-out behaviour have never been investigated.

Therefore, in the present work, the other focus is put on the clarification of interfacial properties between CNT and polymer matrix, in which the effects of CNTs' dimension (i.e. nanotube length, diameter and wall number) were explored for the first time. Moreover, the obtained interfacial properties were combined with the theoretical model of continuum mechanics to develop a sequential multi-scale model for predicting the overall mechanical properties of CNT/Polymer nanocomposites, which were verified using tensile tests and SENB (single-edge notched bending) tests.

Here, two commercial CNTs products, i.e. MWCNT-7 (Nano Carbon Technologies Co., Ltd. Japan) and VGCF® (Showa Denko K.K., Japan) as shown in Fig. 1, were employed as reinforcement fillers at the interface of conventional CFRP laminates to fabricate three-phase hybrid CFRP laminates, and in epoxy to fabricate two-phase CNT/Polymer nanocomposites, respectively. The average diameter of VGCF® is around two times higher than that of MWCNT-7. Moreover, wall thickness of VGCF® is larger, while the central wall is much smaller than that of MWCNT-7. The corresponding geometrical and mechanical properties of these two CNTs are listed in Table 1.

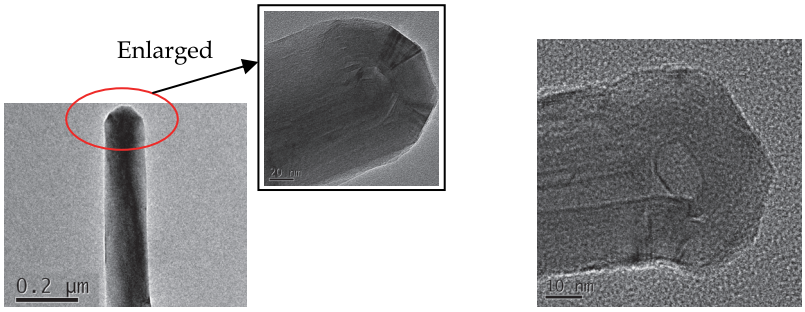

(a) VGCF® (b) MWCNT-7

Fig. 1. TEM pictures of two commercial CNTs

CFRP prepregs		Commercial CNTs	VGCF®	MWCNT-7
Matrix	#2500	Radius r_f (nm)	75	32.5
PAN-based CF	T700S	Length l_f (μm)	15 (10~20)	7.5 (5~10)
Young's modulus (GPa)		Density ρ_f (kg/m^3)	2.0	2.1
Fibre direction	116.8	Young's modulus E_f (GPa)	516.5 (273~760)	850 [Demczyk et al., 2002]
Transverse direction	8.83	Tensile strength σ_{ultf} (MPa)	3100 (2700~3500)	1.5×10^5 [Demczyk et al., 2002]

Table 1. Properties of CFRP prepregs and two commercial CNTs

2. Three-phase hybrid CFRP laminates

Powder method was developed to disperse CNTs directly at the interface between CFRP prepregs to fabricate three-phase hybrid CFRP laminates. The improvement on the interlaminar mechanical properties was confirmed by DCB tests and FEM analysis.

2.1 DCB experiments

2.1.1 Materials and specimen fabrication

The CFRP prepregs (T700S/#2500 Toray, Co. Ltd., Japan) were used, where their physical and mechanical properties are also given in Table 1.

Here, CNTs, as the reinforcement at interface, was dispersed at the mid-plane of unidirectional $[0^\circ/0^\circ]_{14}$ CFRP laminates during the hand lay-up process, where a simple fabrication method with low cost, i.e. **powder method**, was employed. The detailed process is described in Fig. 2 as below.

a. Initially, 14 pieces of CFRP plies were stacked together to form two pieces of $[0^\circ]_7$ CFRP unidirectional sublaminates, respectively;
b. CNTs powder was spread by half on the surface of lower sublaminate using a sifter with mesh size about 70μm. The zigzagged spreading path makes the distribution of CNTs at the interface as consistent as possible;
c. The left half of CNTs powder was spread after placing a 25 μm thick polyamide film (Kapton, Toray Co. Ltd., Japan) to make an initial crack;

d. The upper sublaminate was piled up;
e. Finally, it was put into an autoclave for 3 hours at the temperature of 130˚C to cure.

The obtained laminates are typed in Table 2 according to CNTs' area density ρ_A at the interface. Obviously, the measured thicknesses of formed CNTs interlayer t_I increases linearly with area density ρ_A. For reference, base CFRP laminates were also fabricated.

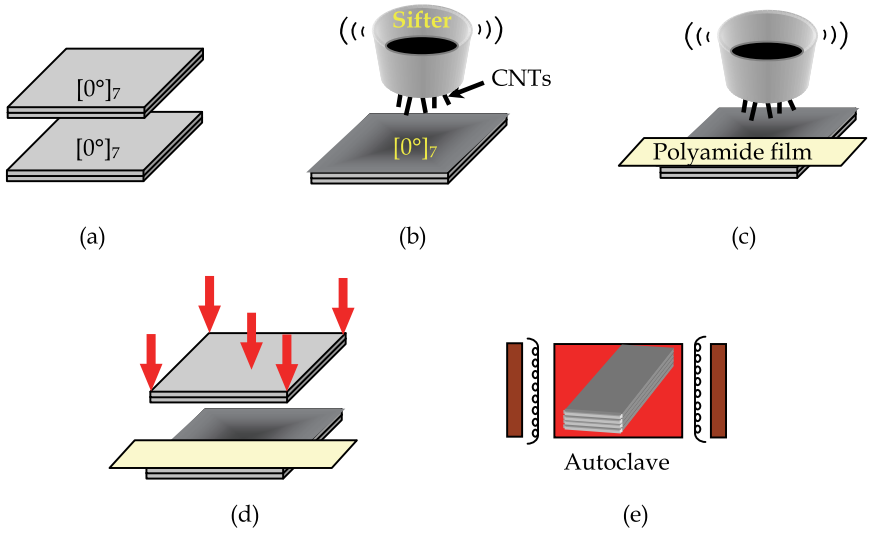

Fig. 2. Powder method

Reinforcement	ρ_A (g/m²)	Notation	t_I (μm)
VGCF®	10	CFRP/VGCF(10)	70
	20	CFRP/VGCF(20)	140
	30	CFRP/VGCF(30)	210
MWCNT-7	5	CFRP/MWCNT(5)	66
	10	CFRP/MWCNT(10)	97
	20	CFRP/MWCNT(20)	148

Table 2. Fabricated hybrid CFRP laminates

2.1.2 DCB test procedure

To evaluate Mode-I interlaminar fracture toughness, DCB tests were carried out using a universal material testing machine (AG-100kNE, Shimazu Co. Ltd, Japan) at 20˚C according to Japanese Industrial Standards (JIS K7086). Five specimens for each type were cut from the fabricated laminates, where marked lines were painted on side surface for crack length measurement. The specimens were approximately 20mm wide and 120mm long, with the initial crack of 34mm. The thickness of hybrid CFRP laminates was thicker than that of base CFRP laminates with 3.14mm due to the formed CNTs interlayer. The crosshead speed was 0.5mm/min. Tests were terminated when the increment of crack length Δa reaches 70mm.

2.1.3 Mode-I interlaminar fracture toughness

From the obtained load-COD (crack opening displacement) curves of the above various types of hybrid CFRP laminates, the average critical load at crack growth, i.e. peak load P_c, are plotted in Fig. 3a which shows the obvious increase. The highest P_c occurs at CFRP/VGCF(20) and CFRP/MWCNT(10) , which are about 41% and 17% higher than that of base CFRP laminates, respectively. Obviously, VGCF® performs better than MWCNT-7.

Since P_c is dominated by Mode-I interlaminar fracture toughness G_{IC} and interlaminar tensile strength N, it is anticipated that G_{IC} and N also increase. The average G_{IC} and fracture resistance G_{IR} are demonstrated in Fig. 3b and Fig. 3c. Note that G_{IR} is the average value when the crack length varies from 20mm to 60mm in the obtained R-curves. In Fig. 3b, there are 96% and 58% increase of G_{IC} for CFRP/VGCF(20) and CFRP/VGCF(10), respectively, which can be considered as the optimal addition. In Fig. 3c, CFRP/VGCF(20) has the highest G_{IR}, which is about 25% higher than that of base CFRP laminates. However, the effect of MWCNT on G_{IR} is unpromising. The largest value occurs at CFRP/MWCNT(5) which increases only 6%. Moreover, there is even minor negative influence for some cases on G_{IR}.

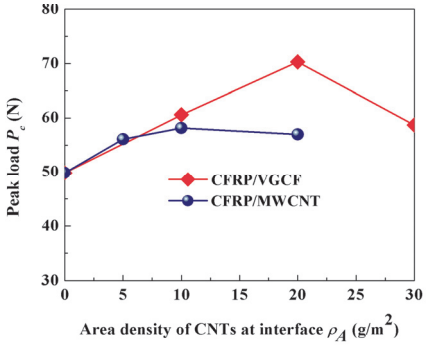

(a) Peak load

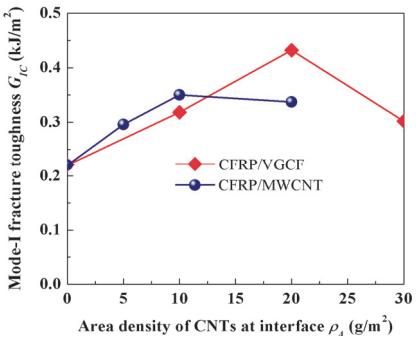

(b) Mode-I fracture toughness

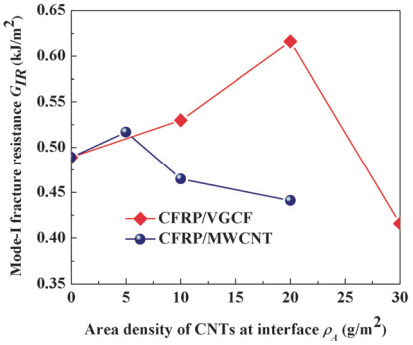

(c) Mode-I fracture resistance

Fig. 3. Reinforcement effects of two commercial CNTs in three-phase hybrid CFRP laminates

The reinforcement mechanism can be explained from crack propagation process observed by an optical microscopy. At the initial stage, crack initiates from crack tip at the CNTs interlayer for all cases (Fig. 4a), which explains the increase of G_{IC}. Moreover, for

CFRP/VGCF(10,20) and CFRP/MWCNT(5), crack extends forward in a zigzag pattern CNTs interlayer (Fig. 4a) creating much more fracture surfaces and consuming much more energy, which leads to the improved G_{IR}. However, for CFRP/VGCF(30) and CFRP/MWCNT(10,20), crack transits from toughened CNTs interlayer toward CFRP plies and propagates forward (Fig. 4c), which results in the decreased G_{IR} compared with that of base CFRP laminates.

(a) CFRP/VGCF(20) (Δa=0mm) (b) CFRP/VGCF(20) (Δa=10mm) (c) CFRP/VGCF(30) (Δa=10mm)

Fig. 4. Crack propagation process for CFRP/VGCF laminates

Moreover, fracture surfaces of DCB specimens were also investigated using scanning electron microscopy (SEM). For CFRP/VGCF(10) and CFRP/MWCNT(5), naked carbon fiber (Fig. 5a) indicates insufficient addition of CNTs at interface. On the other hand, for CFRP/VGCF(30) and CFRP/MWCNT(20), there are obvious defects (Fig. 5c) caused by the poor CNTs dispersion. It explains that CFRP/VGCF(20) and CFRP/MWCNT(10) with good dispersion of CNTs (Fig. 5b) provide best reinforcement effect, respectively.

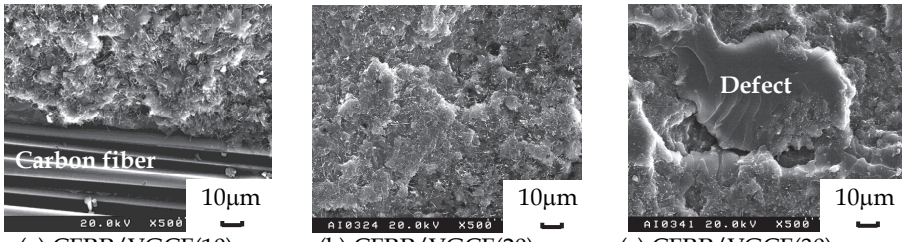

(a) CFRP/VGCF(10) (b) CFRP/VGCF(20) (c) CFRP/VGCF(30)

Fig. 5. Fracture surfaces of CFRP/VGCF laminates

2.2 Numerical simulation using FEM

Instead of experiment, such as butt-joint test under tensile load, FEM simulation on delamination propagation was employed to predict approximately Mode-I interlaminar tensile strength N.

Here, a brick element of 8 nodes [Cao et al., 2002] and a cohesive element [Camanho et al., 2002] were used to model CFRP sublaminates and CNTs interlayer, respectively. The corresponding material properties are listed in Table 3, where the latter was obtained by matching the numerical load-COD curves to experimental ones (see Fig.6). Here, experimental G_{IC} was directly adopted. Interlaminar tensile strength N and initial stiffness K were determined by matching peak load P_c and the initial slope of the numerical load-COD

curves before the peak load, respectively. In Table 3, although N increases with CNTs addition, which are about 75% and 50% higher than that of base CFRP laminates, respectively, there is no any difference among them for different CNTs addition. This can be attributed to that peak load is mainly dominated by G_{IC} while N influences it slightly.
In conclusion, the improvement of interlaminar tensile strength N was confirmed by FEM simulation, and the correctness of experimental G_{IC} was verified from good consistence between numerical and experimental results (Fig.6).

Brick element		**Cohesive element**	N (MPa)	K (N/mm^3)	G_{IC} (kJ/m^2)
E_{11} (GPa)	120	CFRP	20	3.5×10^{3}	0.221
$E_{22}=E_{33}$ (GPa)	8.8	CFRP/VGCF(10)	35	3.5×10^{3}	0.318
$G_{12}=G_{13}$ (GPa)	6.0	CFRP/VGCF(20)	35	3.5×10^{3}	0.432
G_{23} (GPa)	3.7	CFRP/VGCF(30)	35	3.5×10^{3}	0.302
$\upsilon_{12}=\upsilon_{13}$	0.25	CFFRP/MWCNT(5)	30	3.5×10^{3}	0.296
υ_{23}	0.45	CFFRP/MWCNT(10)	30	3.5×10^{3}	0.350
		CFFRP/MWCNT(20)	30	3.5×10^{3}	0.337

Table 3. Material properties for brick element and cohesive element in FEM simulation

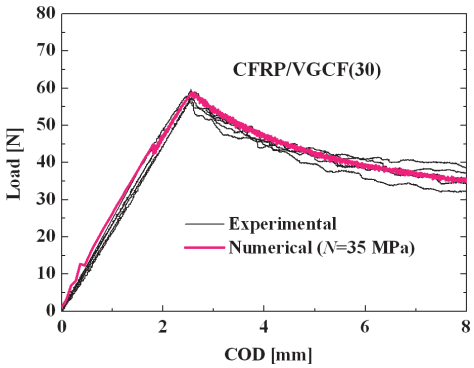

Fig. 6. Comparison of experimental and numerical load-COD curves for CFRP/VGCF(30)

3. Two-phase CNT/Polymer nanocomposites

Pull-out simulations based on MM were carried out to investigate the interfacial properties between CNT and polymer matrix, which were further incorporated into the theoretical model of continuum mechanics to develop a sequential multi-scale model for predicting the overall mechanical properties of two-phase CNT/Polymer nanocomposites. The present method is expected to be applied in CNT-reinforced nanocomposites with various matrices (e.g. metal, ceramics, etc.), which provides useful information for material design.

3.1 Pull-out simulation on Interfacial properties between CNT and polymer matrix

To investigate the interfacial properties between CNT and polymer matrix in two-phase CNT/Polymer nanocomposites only due to van der Waals (vdW) interactions, a series of CNT pull-out simulations from polyethylene (PE) matrix were carried out. Here, the

condensed phase optimization molecular potentials for atomistic simulation studies (COMPASS) force field [Sun, 1998] was employed to calculate the systematic potential energy, which has been broadly testified for CNT itself and CNT-reinforced nanocomposites because of providing reliable results as compared with more accurate tight-binding or ab initio density functional theory based methods. The PE was chosen as matrix because its structural simplicity can effectively reduce the computational cost. Moreover, PE as a representative polymer matrix can give a general picture of the possible interfacial behaviour of various CNT-reinforced polymer nanocomposites. The simulation cell was composed of a fragment of CNT totally embedded inside PE matrix. Taking SWCNT(5,5)/PE nanocomposites as a benchmark, the processes of model building and CNT pull-out are described in detail in the following.

3.1.1 Model building

The unit cell of simulation system, which was of periodic boundary conditions in *y*-*z* plane, was initialized by randomly generating 36 PE chains with initial density of 1.2g/cm^3 surrounding an open-ended SWCNT(5,5). Each PE chain had 20 repeating units of $-CH_2$. The length and diameter of the SWCNT(5,5) fragment were l=4.92nm and D=0.68nm, respectively. Note that the unsaturated boundary effect was avoided by adding hydrogen atoms at both ends of the SWCNT. The hydrogen atom had charge of +0.1268e and the connected carbon atom had charge of -0.1268e, which made the SWCNT neutral. The corresponding computational cell constructed was in the range of 2.69nm×2.69nm×4.9nm in which the volume fraction of SWCNT was V_f=9.0vol.%. Note that the size of computational cell at *x* axis (i.e. the axial direction of CNT) had to be set large enough to eliminate the interaction among polymer itself [Marietta-Tondin, 2006]. As shown in Fig. 7a, the vacuum layer was set for the CNT pull-out without extending the cell. The size of vacuum layer was about the sum of the cut-off distance of vdW interaction (0.95nm) and nanotube length.

The equilibrated structure of SWCNT/PE nanocomposites in Fig. 7 was obtained as follows:

1. While holding SWCNT as a rigid, by virtue of MD simulations, the model was first put into a constant-temperature, constant-volume (NVT) ensemble for 50ps and then a constant-temperature, constant-pressure (NPT) ensemble for another 50ps with temperature of T=298K, pressure of P=10atm, and time step of Δt=1fs after the initial minimization. The purpose of this step is to slowly compress the structure of the PE to generate an initial amorphous matrix with correct density and low residual stress.
2. The nanocomposite system was further put into NVT ensemble and equilibrated for 50ps at the same time step of Δt=1fs with releasing all rigid constraints on SWCNT. This step is to create a zero initial stress state.
3. Finally, the nanocomposite system was minimized again using MM to obtain the equilibrated configuration in vacuum.

The equilibrated separation distance h between SWCNT and PE matrix due to vdW interaction was about 0.23nm in the present work as shown in Fig. 7b, which is very close to the value of 0.18nm obtained by Han et al. [Han & Elliott, 2007] for SWCNT/PMMA nanocomposites. The difference can be attributed to the different types of polymer.

3.1.2 Pull-out process

The pull-out simulations of SWCNT from PE matrix were carried out by applying displacement-controlled load on the atoms at the right end of CNT. The displacement

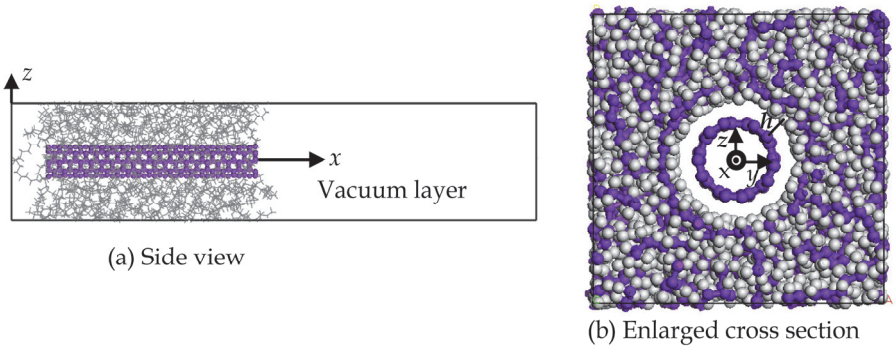

(CNT: l=4.92nm, D=0.68nm, C atoms: purple, H atoms: grey)
Fig. 7. Equilibrated structure of simulation cell for SWCNT(5,5)/PE nanocomposites

increment along the axial (x-axis) direction of CNT was Δx=0.2nm. Snap shots of the atom configurations for SWCNT/PE nanocomposites system during the pull-out process are shown in Fig. 8. Note that the deformation of PE matrix during the pull-out process was neglected by fixing the matrix to reduce the computational cost, since it was confirmed numerically that the influence of the enforced conditions on polymer was very small.
After each pull-out step, the molecular structure was relaxed to obtain the minimum systematic potential energy E by MM. The potential energies of the SWCNT/PE nanocomposites were monitored and recorded during the whole pull-out process, which will be discussed in the following.

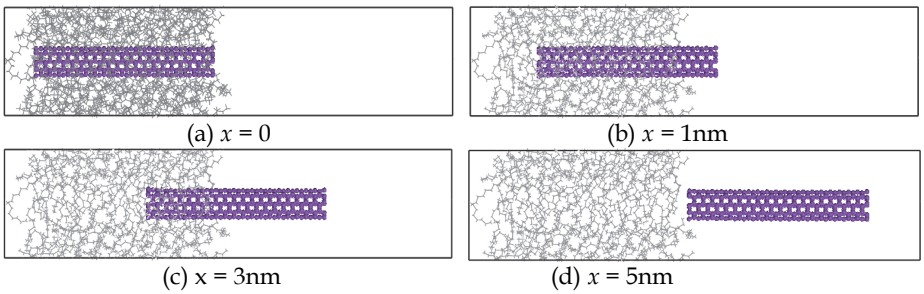

Fig. 8. Snap shots of CNT pull-out from PE matrix

3.1.3 Variation of potential energy during pull-out

In view of that the work done by the pull-out force equals energy increment of nanocomposite system at each pull-out step, the trend of potential energy variation, and the energy increment at each pull-out step becomes very important for analyzing the corresponding pull-out force, and the ISS between CNT and polymer matrix.
The obtained systematic potential energy E during the pull-out is shown in Fig. 9a, which increases gradually accompanied with the CNT pull-out. This trend is just identical to all of the previous simulation results of CNT/Polymer nanocomposites [Liao & Li, 2001; Frankland et al., 2002; Gou et al., 2004; Zheng et al., 2009].

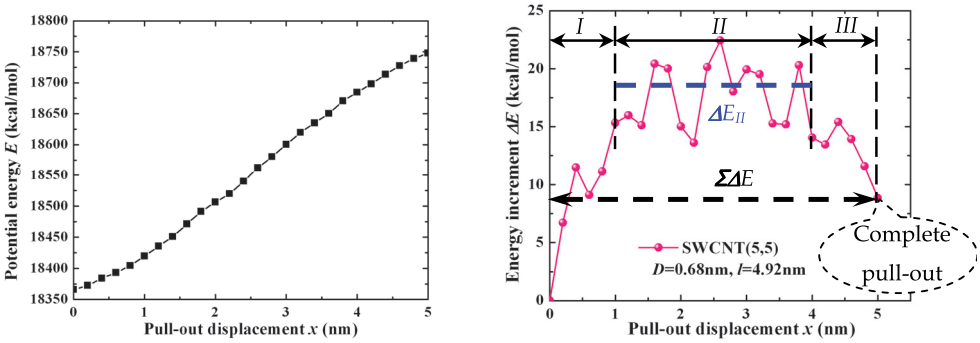

(a) Potential energy E (b) Energy increment $\Sigma\Delta E$

Fig. 9. Variation of E and ΔE during the pull-out of SWCNT(5,5)

Generally, this variation of E can be divided into four parts, i.e. the variation of potential energy in polymer matrix; the variation of potential energy of CNT; the variation of interfacial bonding energy between CNT and polymer matrix; and possible thermal dissipation. Since the polymer was fixed during the pull-out process and the potential energy change of CNT was very small as confirmed in our computations, the variation of E in the present simulation can be mainly attributed to the variation of interfacial bonding energy between CNT and polymer matrix by neglecting thermal dissipation.

Taking an example of the above SWCNT(5,5) pull-out from PE matrix, the calculated energy increment ΔE versus pull-out displacement Δx is shown by pink balls in Fig.9b, where three successive stages can be discerned: in initial stage *I*, ΔE increases sharply; after that, ΔE goes through a long and platform stage *II*, followed by final descent stage *III* until the complete pull-out. As plotted, the total energy change during the pull-out (i.e., the pull-out energy) and the average energy increment in stage *II* are referred to as $\Sigma\Delta E$ and ΔE_{II}, respectively. Moreover, stage *I* and stage *III* have the same approximate range of a=1.0nm which is very close to the cut-off distance of vdW interaction. This trend is surprisingly coincident with that observed sliding behaviour among nested walls in a MWCNT [Li et al., 2010]. The obvious severe fluctuation of energy increment may be attributed to the non-uniformity of polymer matrix in the length direction of CNT. Note that the pull-out energy may also be calculated by using the developed continuum theoretical model for short-fibre reinforced composites (e.g. [Fu & Lauke, 1997]), which plays important role in predicting the fracture toughness of the composites.

On this basis, the effects of CNTs' dimensions on interfacial properties of CNT/Polymer nanocomposites, were explored for the first time by comparing the energy increment of several CNTs with different nanotube length, diameter, or wall number.

3.1.4 Effects of CNTs' dimension

3.1.4.1 Effect of nanotube length

The variation of energy increment corresponding to the pull-out of several SWCNTs(5,5) with different lengths, are plotted in Fig. 10. Just as that in Fig. 9b, three distinct stages are clearly observed for each case. Moreover, among these three curves, there is no obvious

change in the magnitude of the platform stage *II* related to the stable CNT pull-out, which indicates that ΔE_{II} is independent of nanotube length.

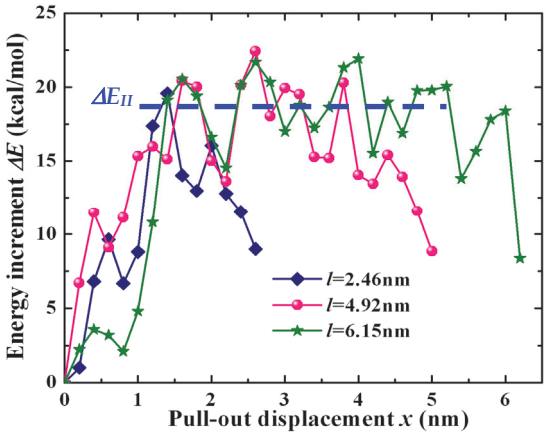

Fig. 10. Effect of nanotube length on energy increment of SWCNT(5,5)

Due to this length-independent behaviour of ΔE_{II}, the length of l_0=3.44nm was employed for all CNTs in the following simulations.

3.1.4.2 Effect of nanotube diameter

The energy increment ΔE corresponding to the pull-out of several SWCNTs with different diameters are illustrated in Fig. 11a, which increases with nanotube diameter. Both $\Sigma\Delta E$ and ΔE_{II} were found to increase linearly with nanotube diameter D as shown in Fig. 11b, which can be fitted as follows:

$$\Sigma\Delta E=277.79D+62.39 \tag{1}$$

$$\Delta E_{II}=19.29\ D+4.27 \tag{2}$$

where D has the unit of nm, $\Sigma\Delta E$ and ΔE_{II} have the unit of kcal/mol. This linear correlation can be explained by the increase of interfacial atoms accompanied with the increase of nanotube diameter. Note that the formula of Eq. (1) for calculating the pull-out energy is only applicable for the pull-out of CNT with the length of l_0=3.44nm, in contrast to the length-independent behaviour of ΔE_{II}. In view of that $\Sigma\Delta E$ increases with nanotube length, for a real SWCNT with length of l_r which is far longer than the present length l_0, $\Sigma\Delta E$ can be estimated as follows

$$\Sigma\Delta E^*=\Sigma\Delta E+\Delta E_{II}\ (l_r-l_0)/\Delta x\ (l_0<l_r) \tag{3}$$

where l_r is of the unit of nm, and the displacement increment here is Δx=0.2nm. Note that $\Sigma\Delta E$ represents the pull-out energy of SWCNT with length of l_0=3.44nm which can be calculated by Eq. (1).

In a word, the average increment in stage *II* (ΔE_{II}) during the pull-out process of the armchair SWCNT from polymer matrix, corresponding to the interfacial properties between CNT and polymer matrix, is independent of nanotube length, but proportional to nanotube

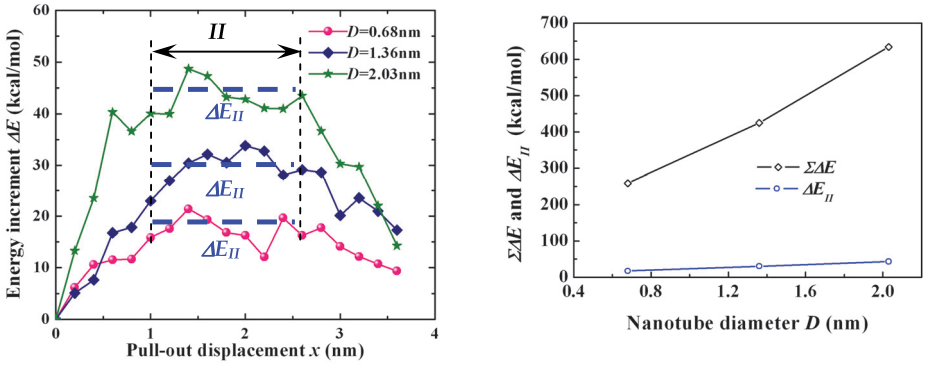

(a) Variation of energy increment (b) Dependence of energy increment on diameter

Fig. 11. Effect of nanotube diameter on energy increment of SWCNT(5,5)

diameter, which is similar to that for the sliding among nested walls in a MWCNT [Li et al., 2010]. Moreover, by using Eqs (1-3), the pull-out energy $\Sigma\Delta E$ and average energy increment in stage *II* ΔE_{II} for the pull-out of any armchair SWCNT can be predicted.

3.1.4.3 Effect of wall number

To investigate the effect of wall number n, three MWCNTs with different wall number were embedded in PE matrix: SWCNT(15,15) with n=1, DWCNT(15,15)/(10,10) with n=2, and TWCNT(15,15)/(10,10)/(5,5) with n=3. The corresponding nanocomposites are referred to as: SWCNT/PE, DWCNT/PE, TWCNT/PE, respectively. Note that the above three CNTs have the same outermost wall with diameter of D_0=2.03nm and length of l_0=3.44nm.

The corresponding energy increment ΔE are plotted in Fig. 12, whose average value in stage *II* (ΔE_{II}) are listed in Table 4. From this table, it can be found that the ΔE_{II} for DWCNT/PE is about 20% higher than that for SWCNT/PE. However, there is only a minor change of ΔE_{II} between DWCNT/PE and TWCNT/PE. The reason can be explained by the increase of distance between newly inserted inner walls and the interface. As the vdW interaction is mostly dependent on the distance, the longer the distance is, the weaker the induced vdW interaction is.

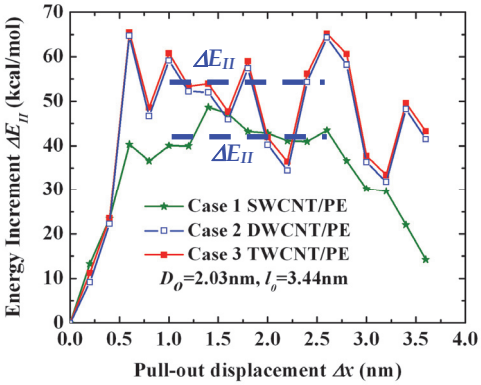

Fig. 12. Effect of n on energy increment

Therefore, ΔE_{II} for the MWCNT (n≥2) pull-out can be approximately estimated as 1.2 times of that for corresponding SWCNT, which is actually the outermost wall of the MWCNT. To some extent, this finding is consistent with the reports of Schadler [Schadler et al., 1998] who concluded that only the outer walls are loaded in tension for CNT/Epoxy nanocomposites based on the observation of Raman spectrum.
Moreover, the calculated energy increment in the present simulation on the CNT pull-out from polymer matrix is compared with the reports [Li et al., 2010] on the pull-out of outermost wall in the same MWCNT as listed in Table 4. Obviously, the former is smaller than the latter. It may indicate that even for some CNTs with fractured outer walls in the CNT/PE nanocomposites, the CNT is easier to be pulled out from matrix instead of that the fractured outer walls are pulled out against the corresponding inner walls.

	Model	ΔE_{II} (kcal/mol)
CNT Pull-out from PE	SWCNT/PE	43.07
	DWCNT/PE	51.13
	TWCNT/PE	52.71
Pull-out of the outermost wall	DWCNT	55.11
	TWCNT	59.32

Table 4. Comparison of ΔE_{II} for two types of pull-out

3.1.5 Pull-out force

In practical CNT/Polymer nanocomposites, the real pull-out force can be contributed from the following factors [Bal & Samal, 2007; Wong et al., 2003]: vdW interaction between CNT and PE matrix, possible chemical bonding between CNT and PE matrix, mechanical interlocking resulted by local non-uniformity of nanocomposites, such as waviness of CNT, mismatch in coefficient of thermal expansion, statistical atomic defects, etc. Consequently, the pull-out force can be divided into two parts, i.e., $F=F_{vdW}+F_m$. Here, F_{vdW} is the component for overcoming the vdW interaction at the interface which can be calculated by the following Eq. (4); and F_m is the frictional sliding force caused by the other factors stated. The magnitudes of these two parts strongly depend on the interfacial state and CNT dimension. For almost perfect interface, F_{vdW} dominates the pull-out force. On the other hand, for the case of chemical bonding or mechanical interlocking, which in general occurs easily for large CNTs, F_m mainly contributes to the total pull-out force. In the present study, only F_{vdW} and the related ISS for perfect interface are considered as mentioned in the beforehand work.
According to that the work done by the pull-out force at each pull-out step is equal to the energy increment of nanocomposites, the corresponding pull-out force for the stable CNT pull-out stage should be also independent of nanotube length, but proportional to nanotube diameter, just as energy increment is.
From the obtained energy increment ΔE_{II} in Eq. (2) and pull-out displacement increment of Δx=0.2nm, we can get the pull-out force as follows:

$$F_{II} = \Delta E_{II}/\Delta x = \lambda(0.67D+0.15) \quad (4)$$

where F_{II} and D have the units of nN and nm, respectively. The value of λ represents the effect of wall number, which is 1.0 for SWCNT and 1.2 for MWCNT with consideration of the contribution of the inner walls.

3.1.6 Interfacial shear stress (ISS) and surface energy density

Based on the above discussions, the corresponding ISS and surface energy density are analyzed in the following.

The pull-out force is equilibrated with the axial component of vdW interaction which induces the ISS. Conventionally, if we employ the common assumption of constant ISS with uniform distribution along the embedded CNT, the pull-out force F_{II} will vary with the embedded length of CNT, which is obviously contradict with the above length-independent reports of ΔE_{II}. For the extreme case of CNT with infinite length, the ISS tends to be zero, which is physically unreasonable. This indicates that the conventional assumption of ISS is improper for the perfect interface of CNT/PE nanocomposites. Therefore, in view of the above characteristic of the variation of energy increment ΔE_{II}, such as that the range of stage *I* or stage *III* is around 1.0nm, it is concluded that the ISS is distributed solely at each end of embedded CNT within the range of a=1.0nm at the beginning of stage *II* or the end of stage *I*. In view of the dependence of vdW force upon the distance between two atoms, the ISS at each end of the embedded CNT which is induced by the variation of vdW force, should at first increase sharply and then decrease slowly to zero after reaching the maximum. Here, by assuming its uniform distribution within two end regions for simplicity, the effective ISS can be derived as

$$\tau_{II} = F_{II}/(2\pi Da) \tag{5}$$

By using Eqs. (1-5), the pull-out energy $\Sigma\Delta E$, the average pull-out force F_{II} and the ISS τ_{II} for CNT/PE nanocomposites can be calculated. As shown in Fig. 13a, the calculated ISS is found to decrease initially with nanotube diameter and saturate at the value of 106.7MPa for SWCNT/PE nanocomposites. For MWCNT/PE, the saturated value is 128MPa, which is about 1.2 times of that for SWCNT/PE, both of which has the same outermost wall.

On the other hand, in view of that two new surface regions are generated at the two ends of CNT after each pull-out step, the corresponding surface energy should be equal to the energy increment ΔE_{II} by neglecting thermal dissipation. Therefore, the surface energy density can be calculated as

$$\gamma_{II} = \Delta E_{II}/(2\pi D\Delta x) = F_{II}/(2\pi D) \tag{6}$$

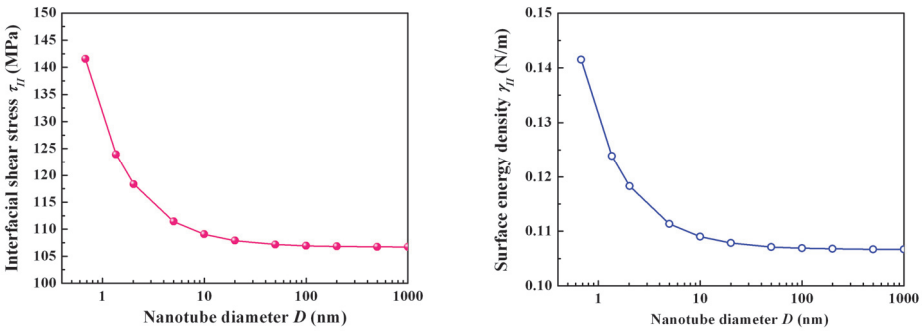

(a) Interfacial shear stress (ISS) (b) Surface energy density

Fig. 13. Dependence of ISS and surface energy density on nanotube diameter

As shown in Fig. 13b, the surface energy density has the same trend as the ISS, which initially decreases slightly as nanotube diameter increases and finally converges at the value of 0.11N/m. This value is very close to the previous reports of 6-8meV/Å^2 (i.e., 0.09-0.12N/m) [Lordi & Yao, 2000] and 0.15 kcal/molÅ^2 (i.e., 0.1 N/m) [Al-Ostaz et al., 2008] for SWCNT/PE nanocomposites, which indicates the effectiveness of the present simulation.

3.1.7 Comparison with previous reports

The predicted ISS in the present study as given in Table 5 is obviously higher than that in the previous reports [Frankland et al., 2002; Zheng et al., 2009; Al-Ostaz et al.] which is calculated from

$$\tau^*=2\Sigma\Delta E/(\pi Dl^2) \tag{7}$$

The reason of this big difference is that the assumption of the constant ISS with uniform distribution along the total embedded length of CNT employed in previous numerical simulation, which has been verified to be unreasonable here.

Ref.	SWCNT		Experimental reports		Present prediction	
	D (nm)	l (nm)	$\Sigma\Delta E^*$ (kcal/mol)	τ^* (MPa)	$\Sigma\Delta E^*$ (kcal/mol)	τ_{II} (MPa)
[Frankland et al., 2002]	1.36	5.3	×	2.7	707.4	123.9
[Zheng et al., 2009]	1.36	5.9	~500	33	798.8	123.9
[Al-Ostaz et al., 2008]	0.78	4.2	224	133	352.2	137

Table 5. Prediction in previous simulations for SWCNT/PE nanocomposites

For the pull-out force, the calculated values using the proposed formulae of Eqs.(1-4) are compared with that reported in direct CNT pull-out experiments at nano-scale from several different polymer matrices, as shown in Table 6. Obviously, the reported pull-out forces are much higher than the calculated values only when vdW interactions are considered at the interface between CNT and polymer matrix, although severe experimental data scattering has been observed which may be caused by manipulation process or force/displacement measurement. The reason can be attributed to the following factors.

Firstly, if we take into account the curvature of CNT (Fig. 14a), the necessary pull-out force will increase. Considering a special case with the highest probability where an inclined angle θ between the axial direction of CNT and the pull-out direction is 45° (Fig. 14b), the

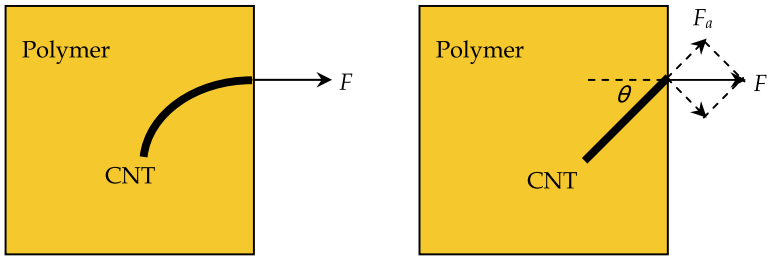

(a) Curved CNT (b) Oblique CNT

Fig. 14. Simplified model for the pull-out of curved and oblique CNT

Ref.	Matrix	MWCNT	Pull-out force (μN)	
		D (nm)	Exp.	Prediction
[Deng, 2008]	PEEK	49	1.04	0.04
		89	8.6	0.07
[Barber et al., 2003]	PE-butene	80	0.85	0.07
[Cooper et al., 2002]	Epoxy	8.2	3.8	0.01
		11	2.8	0.01
		13.4	0.6/2.3	0.01
		24	6.8/12.8	0.2

Table 6. Prediction of previous experiments for MWCNT/Polymer nanocomposites

corresponding pull-out force will increase about 40%. By observing the data in Table 6, this increase effect is still too small compared with the experimental data.

Secondly, for the effect of the pressure or residual stress in nanocomposites, a simple representative volume element (RVE) model (Fig. 15a) was constructed to perform FEM analysis. This continuum mechanics based computation is valid, at least qualitatively when the diameter of CNT is over several tens of nanometers. Assuming the symmetrical structure, the quarter part of interface region (i.e. the blue part in Fig. 15b) was employed.

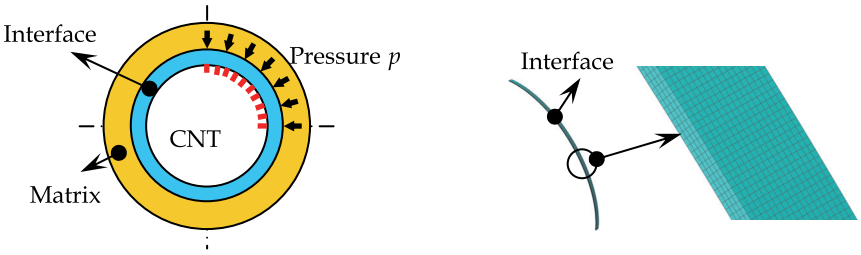

(a) Simplified composite model (b) FEM model of interface

Fig. 15. Simplified FEM model of interface between CNT and matrix

The inner wall surface of the interface region was fixed as boundary condition, which represents the rigid CNT. The uniform static pressure was applied on the outer wall of interface region. Two values of Young's modulus E_i for the interface region were considered, i.e., 1GPa and 3GPa. The corresponding FEM model is shown in Fig. 15b, where the size of element size was taken as 0.05nm for convergence and accuracy.

The relationship of strain energy density γ and the applied pressure p is shown in Fig. 16, in which strain energy increases by the power of square with p. It can be found that a large pressure p can only cause very small increase of strain energy density γ, which indicates that the effect of pressure or residual stress is not as strong as we expected. In general, the residual stress in polymer nanocomposites ranges from 25.0MPa to 40.0MPa. For instance, for the case of E_i=1GPa of interface region, by applying for the pressure of 30.0MPa, the strain energy density is around 2.85×10^{-5}N/m, which is still much smaller than the surface energy density of γ_{II}=0.11N/m caused by vdW interaction as stated previously. It means that the pressure or residual stress in polymer nanocomposite system is not a dominant factor.

The above discussion leads to an important conclusion, i.e., the interface properties between CNT and polymer matrix contributed by vdW interaction is quite minor for the real

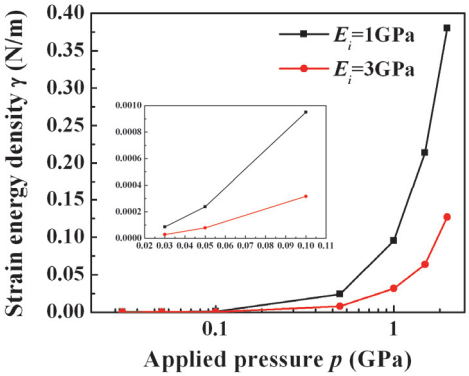

Fig. 16. Relationship between applied pressure and strain energy density

CNT pull-out from polymer matrix. Therefore, to accurately evaluate the interfacial properties for real case, it is necessary to incorporate the effects of frictional sliding caused by mechanical interlocking, atomic statistical defects, or chemical bonding. Moreover, for effectively improving the interfacial properties and therefore the mechanical properties of bulk nanocomposites, it is vital to incorporate into chemical bonding and mechanical interlocking, which will be the topic in the future.

Note that although the type of polymer will influence the value of ISS which is not discussed in the present work, the characteristics of pull-out force and the corresponding ISS will be similar to those discussed in CNT/PE nanocomposites here.

3.2 Characterization on overall mechanical properties of CNT/Polymer nanocomposites

To investigate the overall mechanical properties of CNT/Polymer nanocomposites, tensile tests and SENB tests were carried out, in which MWCNT-7 and VGCF® were used as reinforcement filler, respectively. Moreover, a sequential multi-scale model was developed by incorporating the interfacial properties between CNT and polymer matrix obtained from previous pull-out simulations into the conventional continuum theory, which connects the interfacial properties to overall mechanical properties of CNT/Polymer nanocomposites.

3.2.1 Mechanical tests for CNT/Epoxy nanocomposites

Epoxy resin jER806 (Japan Epoxy Resins Co., Ltd., Japan) and the hardener Tohmide-245LP (Fuji Kasei Kogyou Co., Ltd., Japan) were used to prepare the polymer matrix with the weight ration of 100:62. According to the weight fraction W_f of reinforcements, two groups of nanocomposites were fabricated: MWCNT/Epoxy with W_f of MWCNT-7 varying at 2, 3, 4%, and VGCF/Epoxy with W_f of VGCF® varying at 2, 4, 6%. The fabrication process as shown in Fig. 17 is described below:

1. The epoxy resin was first heated to 60˚C in an oven to decrease the viscosity for its better miscibility with MWCNTs;
2. Then the CNTs were dispersed into the epoxy resin using the planetary centrifugal mixer at 2000rpm for 10min;

3. After adding the hardener, the mixture was agitated for another 10 min at 1000rpm;
4. Subsequently, the mixture was poured into the silicon mould for a pre-curing process with 12h at room temperature, followed by a post-curing process which was performed at 80˚C in the oven for 6h.

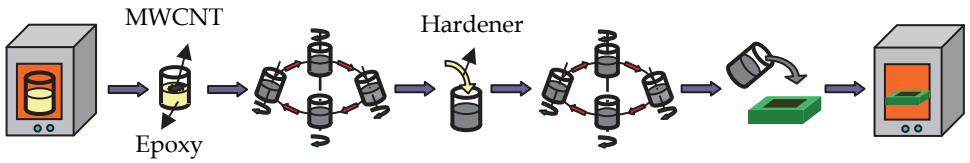

Fig. 17. Fabrication of MWCNT/Epoxy nanocomposites for mechanical tests

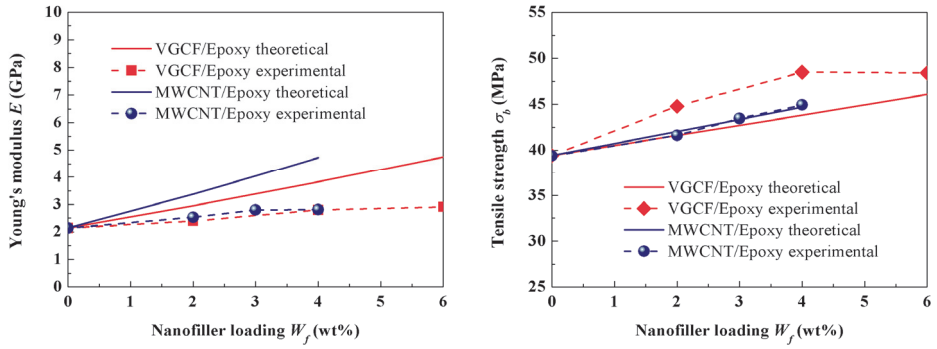

(a) Young's modulus (b) Tensile strength

Fig. 18. Comparison of theoretical and experimental Young's modulus and tensile strength

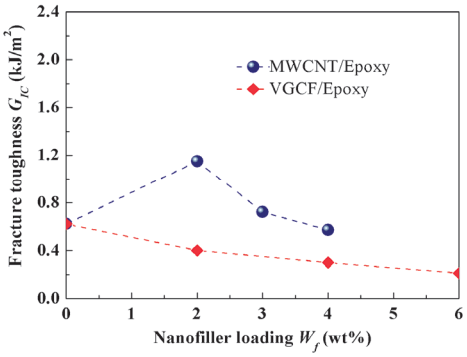

Fig. 19. Experimental fracture toughness

According to ASTM D638 (Type V) and ASTM D5045 standards, tensile tests and SENB tests were preformed. Three specimens of the above fabricated composites at a specified CNT loading were prepared. A universal materials testing machine (Instron 5567) was used with

a cross-head speed of 0.25mm/min. The Poisson's ratio of nanocomposites measured in tensile tests by using bi-axial strain gages was directly used in the evaluation of fracture toughness in SENB tests.

The obtained Young's modulus E_c, tensile strength σ_c of MWCNT/epoxy and VGCF/Epoxy nanocomposites are plotted in Fig. 18. As shown in Fig. 18a, the largest increase of 31% and 36% in E_c from 2.14GPa of neat epoxy occur at 4wt% loading for MWCNT/Epoxy and at 6wt% loading for VGCF/Epoxy, respectively. In Fig. 18b, σ_c increases obviously for nanocomposites. At 4wt% loading, the highest increases are 14.1% for MWCNT/Epoxy and

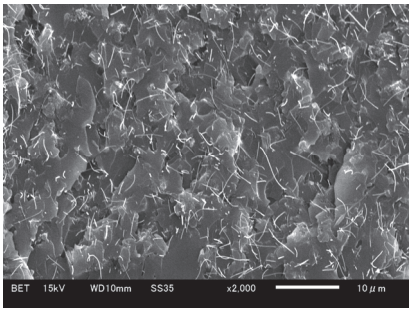

(a) MWCNT/Epoxy (3wt%)

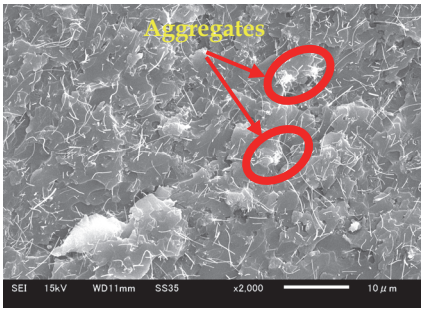

(b) MWCNT/Epoxy (4wt%)

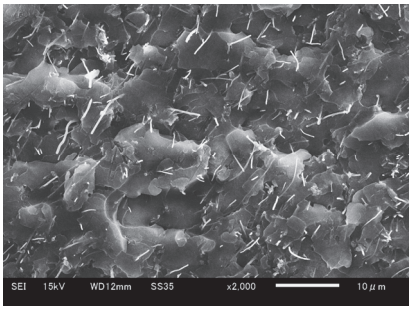

(c) VGCF/Epoxy (4wt%)

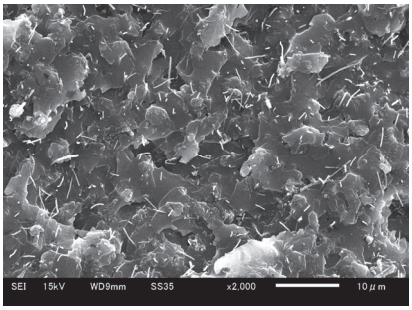

(d) VGCF/Epoxy (6wt%)

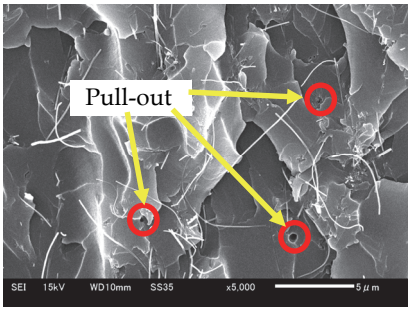

(e) MWCNT/Epoxy (2wt%)

Fig. 20. SEM pictures of SENB specimens

23.1% for VGCF/Epoxy from 39.4MPa of neat epoxy. The effect of VGCF in σ_c is slightly better than that of MWCNT. Moreover, σ_c decreases slightly when the addition is over 4wt% for VGCF/Epoxy. However, there is no obvious saturation trend in σ_c even at 4wt% loading of MWCNT, which means that σ_c may be enhanced with further addition of MWCNT. The corresponding Mode-I fracture toughness G_{IC} is given in Fig. 19, a remarkable increase, i.e. 85.5% can be identified for 2wt% MWCNT loading, although the effect of VGCF to G_{IC} is unpromising.

In order to clarify the reinforcement mechanism, SEM observations were performed on the fracture surfaces of SENB specimens as shown in Fig. 20. Even there are some small aggregates at a high loading, e.g. 4wt% in Fig. 20(b), good dispersion of MWCNT or VGCF can be identified, which leads to the increase of E and σ_b in both nanocomposites. As shown in Fig. 19, 6wt% VGCF leads to the lowest G_{IC} while 2wt% MWCNT provides the highest G_{IC}. However, it is difficult to distinguish them through the fracture surfaces from Fig. 20 (d) and (e), although the former demonstrates a clear brittle fracture feature. One possible reason for the increase of G_{IC} in 2wt% MWCNT may be there are more pull-out holes of MWCNT, which improves the fracture toughness.

3.2.2 Theoretical prediction on tensile properties of MWCNT/Polymer nanocomposites

With consideration of fibre length and fibre orientation distribution, Cox's shear-lag model [Cox, 1952; Krenchel, 1964] predicts the longitudinal modulus of short-fiber reinforced composites as

$$E=\eta_o\eta_l E_f V_f+E_m(1-V_f) \tag{8}$$

where V_f is the volume fraction of fiber, E_f and E_m are Young's moduli of nanofiller and matrix, respectively. The orientation efficiency factor η_o is 1/5 for three-dimensional random distribution, and the nanofiller length efficiency factor η_l was given in Ref. [Cox, 1952]. The predicted Young's modulus is also plotted in Fig. 18(a), which is a bit higher than experimental ones, especially for higher nanofiller loadings, which may be caused by the difficult dispersion of nanofiller in experiments.

For short-fiber reinforced composites under the assumption of iso-strain state in the fibers and matrix, Fukuda and Chou [Fukuda & Chou, 1982] developed a probabilistic theory as follows

$$\sigma_{ultc}=\begin{cases}\sigma_{ultf}V_f\left(1-\dfrac{l_c}{2l_f}\right)C_0+\sigma_m'\left(1-V_f\right) & (l>l_c)\\ \sigma_{ultf}V_f\left(\dfrac{l_f}{2l_c}\right)C_0+\sigma_m'\left(1-V_f\right) & (l\le l_c)\end{cases} \tag{9}$$

where l_f is the length of fiber, σ_{ultf} the tensile strength of fiber, σ_m' the matrix stress at the failure of composites, and C_0 the orientation factor which is 1/8 in the case of three-dimensional random array model. The critical length l_c is defined as [Kelly & Tyson, 1965]

$$l_c=\sigma_{ultf}r_f V_f/\tau_y \tag{10}$$

where r_f is the fiber radius, and τ_y is the shear strength of fiber/matrix interface.

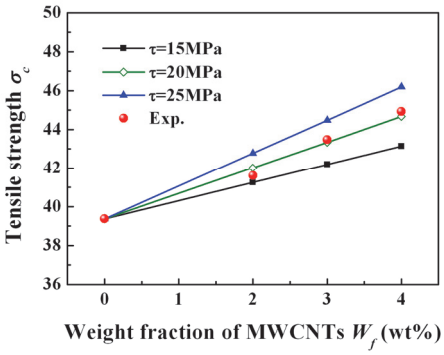

Fig. 21. Prediction of σ_c for MWCNT/Epoxy

Here, the key point is how to define the shear strength τ_y by using the previous MM simulation results. With consideration of its distribution which is only at each end of embedded CNT within 1.0nm, the shear strength should be around 106.7MPa for SWCNT, and 128.04MPa for MWCNT which is about 1.2 times of that for SWCNT. On the other hand, if we define the shear strength based on the whole embedded length of CNT (e.g., 5μm for present experiments), the corresponding shear strength can be calculated as 0.09MPa for SWCNT, and 0.1MPa for MWCNT. Naturally, these values defined from the conventional conception of shear strength seem to be very small from common sense. It further confirms the previous analysis, which indicates that the contribution from vdW interaction to the pull-out force may be comparatively small in practical nanocomposites compared with that from frictional sliding caused by possible chemical bonding or mechanical interlocking. From the above statements, no matter what kind of definition for the shear strength is used, the interfacial shear strength can be assumed to range from 0.1MPa to 128.04MPa for MWCNT. Naturally, by considering the obliqueness of CNT (Fig.14) to the direction of pull-out force, this shear strength range can modified as 0.14~179.26MPa. With consideration of the effects of residual stress in polymer systems, and especially possible chemical bonding or mechanical interlocking, the above range may be increased significantly. Taking the possible range of 0.5~200MPa, the corresponding critical length is about 9750 ~24.38μm, all of which are much longer than that of the MWCNTs used, i.e. $l_f \ll l_c$. It means that the reinforcement effect predicted theoretical in Eq. (7) is unpromising. Replacing $\sigma_m^{'}$ by the measured tensile strength of neat epoxy σ_m, the tensile strength of MWCNT/Epoxy nanocomposites can be predicted. As shown in Fig. 21, the interfacial shear strength of 15~25MPa provides good consistence between experimental measurements and theoretical prediction. Therefore, the previously stated wide range for ISS can rightly cover this narrow band, which indicates that the present multi-scale method is meaningful. Moreover, if we employ the conventional definition of interfacial shear strength which leads to a value lower than 1MPa, it is obviously lower than 15~25MPa. This indicates that the contribution from frictional sliding dominates the interfacial shear strength, which is at least 10 times higher than that from vdW interaction. Taking the value of 20MPa for interfacial shear strength, the predicted value is plotted in Fig. 18b, which indicates good consistence with experimental results.

4. Conclusion

The above research results clearly clarify the different reinforcement effects of two kinds of CNTs (i.e., MWCNT-7 and VGCF®) in two types of nanocomposites (i.e., three-phase hybrid CFRP laminates and two-phase CNT/Polymer nanocomposites).

For **three-phase hybrid CFRP laminates**, a new simple fabrication method *powder method* was developed to disperse CNTs at the interface between CFRP plies. DCB experiments and FEM analysis were carried out which verifies the significant improvement of interlaminar mechanical properties.

For **two-phase CNT/Polymer nanocomposites**, the interfacial properties between CNT and polymer matrix was clarified, where the effects of nanotube length, diameter and wall number were explored for the first time. Moreover, the obtained interfacial mechanical properties were incorporated into the continuum mechanics to develop a sequential multi-scale model, which predicts the overall mechanical properties of nanocomposites and indicates the relationship between the interfacial properties and overall mechanical properties.

5. Acknowledgment

This work is partly supported by two Grand-in-Aids for Scientific Research (No. 19360045 and No. 22360044) from the Japanese Ministry of Education, Culture, Sports, Science and Technology. The authors acknowledge Prof. C. B. Fan (Beijing Institute of Technology, China) for kindly providing the computational resources.

6. References

Ajayan, P.M.; Stephan, O.; Colliex, C. & Trauth, D. (1994) Aligned Carbon Nanotube Arrays Formed by Cutting a Polymer Resin-nanotube Composite. *Science,* Vol. 265, pp 1212.

Al-Ostaz, A.; Pal, G.; Mantena, P.R.; Cheng, A. (2008) Molecular Dynamics Simulation of SWCNT-Polymer Nanocomposite and its Constituents. *Journal of Materials Science,* Vol. 43, pp 164-173.

Andrews, R.; Jacques, D.; Minot, M. & Rantell, T. (2002) Fabrication of Carbon Multiwall Nanotube/Polymer Composites by Shear Mixing. *Macromolecular Materials and Engineering,* Vol. 287, pp 395-403.

Arai, M.; Noro, Y.; Sugimoto, K. & Endo M. (2008) Mode I and Mode II Interlaminar Fracture Toughness of CFRP Laminates Toughened by Carbon Nanofiber Interlayer. *Composites Science and Technology,* Vol. 68, pp 516-525.

Bal, S. & Samal, S.S. (2007) Carbon Nanotube Reinforced Polymer Composites - A State of Art. *Bulletin of Materials Science,* Vol. 30, No. 4, pp 379-386.

Bangarusampath, D.S.; Ruckdaschel, H.; Altstadat, V.; Sandler, J.K.W.; Garray, D.& Shaffer M.S.P. (2009) Rheology and Properties of Melt-Processed Poly (ether ether ketone)/ Multi-Wall Carbon Nanotube Composites. *Polymer,* Vol. 50, pp 5803- 5811.

Barber, A.H.; Cohen, S.R.; Kenig, S. & Wagner, H.D. (2003) Measurement of Carbon Nanotube-Polymer Interfacial Strength. *Applied Physics Letters,* Vol. 82, No. 23, pp 4140-4142.

Barber, A.H.; Cohen, S.R.; Kenig, S. & Wagner, H.D. (2004) Interfacial Fracture Energy Measurements for Multi-walled Carbon Nanotubes Pulled from a Polymer Matrix. *Composite Science and Technology,* Vol. 64, pp 2283-2289.

Bhattacharyya, A.R.; Sreekumar, T.V.; Liu, T.; Kumar, S.; Ericson, L.M.; Hauge, R.H. & Smalley, R.E. (2003) Crystallization and Orientation Studies in Polypropylene/Single Wall Carbon Nanotube Composite. *Polymer,* Vol. 44, pp 2373-2377.

Camanho, P.P. & Davila, C.G. (2002) Mixed-mode Decohesion Finite Elements for the Simulation of Delamination in Composite Materials. NASA/TM, pp. 211737.

Cao, Y.; Hu, N.; Lu, J.; Fukunaga, H. & Yao, Z. (2002) A 3D Brick Element based on Hu-Washizu Variational Principle for Mesh Distortion. *International Journal for Numerical Methods in Engineering,* Vol. 53, pp 2529-2548.

Chowdhury, S.C. & Okabe, T. (2007) Computer Simulation of Carbon Nanotube Pull-out from Polymer by the Molecular Dynamics Method. *Composites Part A,* Vol. 38, pp 747-754.

Chang, T.E.; Jensen, L.R.; Kisliuk, A.; Pipes, R.B.; Pyrz, R. & Sokolov, A.P. (2005) Microscopic Mechanism of Reinforcement in Single-Wall Carbon Nanotube/Polypropylene Nanocomposite. *Polymer,* Vol. 46, pp 439-444.

Chang, T.E.; Kisliuk, A.; Rhodes, S.M.; Brittain, W.J. & Sokolov, A.P. (2006) Conductivity and Mechanical Properties of Well-Dispersed Single-Wall Carbon Nanotube/ Polystyrene Composite. *Polymer,* Vol. 47, pp 7740-7746.

Ci, L. & Bai, J. (2006) The Reinforcement Role of Carbon Nanotues in Epoxy Composites with Different Matrix Stiffness. *Composite Science and Technology,* Vol. 66, pp 599-603.

Cooper, C.A.; Ravich, D.; Lips, D.; Mayer, J. & Wagner, H.D. (2002) Distribution and Alignment of Carbon Nanotubes and Nanofibrils in a Polymer Matrix. *Composite Science and Technology,* Vol. 62, pp 1105-1112.

Cooper, C.A.; Cohen, S.R.; Barber, A.H. & Wagner, H.D. (2002) Detachment of Nanotubes from a Polymer Matrix. *Applied Physics Letters,* Vol. 81, No. 20, pp 3873-3875.

Cox, H.L. (1952) The Elasticity and Strength of Paper and Other fibrous Materials. *British Journal of Applied Physics,* Vol. 3, pp 72-79.

Curran, S.; Davey, A.P.; Coleman, J.; Dalton, A.; McCarthy, B.; Maier, S.; Drury, A.; Gray, D.; Brennan, M.; Ryder, K.; Chapelle, M.L.; Journet, C.; Bernier, P.; Byrne, H.J.; Carroll, D.; Ajayan, P.M.; Lefrant, S.; Blau, W. (1999) Evolution and Evalution of the Polymer/Nanotube Composite. *Synthetic Metals,* Vol. 103, pp 2559-2562.

Demczyk, B.G.; Wang, Y.M.; Cumings, J.; Hetman, M.; Han, W.; Zettl, A.; Ritchie, R.O. (2002) Direct Mechanical Measurement of the Tensile Strength and Elastic Modulus of Multiwalled Carbon Nanotubes. *Materials Science and Engineering A,* Vol. 334, pp 173-178.

Deng, F.; Ogasawara, T. & Takeda, N. (2007) Experimental Characterization of Poly (Ether Ether Ketone)/Multi-Wall Carbon Nanotube Composites. *Key Engineering Materials,* Vol. 334-335, pp 721-724.

Deng, F. (2008) Investigation of the Interfacial Bonding and Deformation Mechanism of the Nano Composites Containing Carbon Nanotubes. Tokyo University. PhD Dissertation.

Ding, W.; Eitan, A.; Fisher, FT.; Chen, X.; Dikin, D.A.; Andrews, R.; Brinson, L.C.; Schadler, L.S. & Ruoff, R.S. (2003) Direct Observation of Polymer Sheathing in Carbon Nanotube-Polycarbonate Composites. *Nano Letters,* Vol. 3, No. 11, pp 1593-1597.

Frankland, S.J.V.; Caglar, A.; Brenner, D.W. & Griebel, M. (2002) Molecular Simulation of the Influence of Chemical Cross-links on the Shear Strength of Carbon Nanotube-Polymer Interfaces. *Journal of Physical Chemistry B,* Vol. 106, pp 3046-3048.

Fu, S.Y. & Lauke, B. (1997) The Fiber Pull-out Energy of Misaligned Short Fibre Composites. *Journal of Materials Science,* Vol. 32, pp 1985-1993

Gao, X.L. & Li, K. (2005) A Shear-lag Model for Carbon Nanotube-Reinforced Polymer Composites. *International Journal of Solids and Structures,* Vol. 42, pp 1649- 1667.

Garcia, E.J.; Wardle, B.L. & Hart, A.J. (2008) Joining Prepreg Composite Interfaces with Aligned Carbon Nanotubes. *Composites Part A,* Vol. 39, pp 1065-1070.

Gojny, F.H.; Nastalczyk, J.; Roslaniec, Z. & Schulte, K. (2003) Surface Modified Multi-Walled Carbon Nanotubes in CNT/Epoxy-Composites. *Chemical Physics Letters,* Vol. 370, pp 820-824.

Gojny, F.H.; Wichmann, M.H.G.; Fiedler, B. & Schulte, K. (2005) Influence of Different Carbon Nanotubes on the Mechanical Properties of Epoxy Matrix Composites - A Comparative Study. *Composite Science and Technology,* Vol. 65, pp 2300- 2313.

Gojny, F.H.; Wichmann, M.H.G.; Kopke, U.; Fiedler, B. & Schulte, K. (2004) Carbon Nanotube-Reinforced Epoxy-Composites: Enhanced Stiffness and Fracture Toughness at Low Nanotube Content. *Composite Science and Technology,* Vol. 64, pp 2363-2371.

Gou, J.; Minaie, B.; Wang, B.; Liang, Z. & Zhang, C. (2004) Computational and Experimental Study of Interfacial Bonding of Single-walled Nanotube Reinforced Composites. *Computational Materials Science,* Vol. 31, pp 225-236.

Haggenmueller, R.; Gommans, H.H.; Rinzler, A.G.; Fischer, J.E. & Winey, K.I. (2000) Aligned Single-wall Carbon Nanotubes in Composites by Melt Processing methods. *Chemical Physics Letters,* Vol. 330, No.10, pp 219-225.

Han, Y. & Elliott, J. (2007) Molecular Dynamics Simulations of the Elastic Properties of Polymer/Carbon Nanotube Composites. *Computational Materials Science,* Vol. 39, No. 2, pp 315-323.

He, X.; Zhang, F.; Wang, R. & Liu, W. (2007) Preparation of a Carbon Nanotube/Carbon Fiber Multi-Scale Reinforcement by Grafting Multi-walled Carbon Nanotubes onto the Fibers. *Carbon,* Vol. 45, pp 2559-2563.

Inam, F.; Wong, D.W.Y.; Kuwata, M. & Peijs, T. (2010) Multiscale Hybrid Micro-Nanocomposites based on Carbon Nanotubes and Carbon Fibers. *Journal of Nanomaterials.* (In press)

Jiang, X.; Bin, Y. & Matsuo M. (2005) Electrical and Mechanical Properties of Polyimide-Carbon Nanotubes Composites Fabricated by In Situ Polymerization. *Polymer,* Vol. 46, pp 7418-7424.

Jiang, L.Y.; Huang, Y.; Jiang, H.; Ravichandran, G.; Gao, H.; Hwang, K.C. & Liu, B. (2006) A Cohesive Law for Carbon Nanotube/Polymer Interfaces based on the van der Waals Force. *Journal of the Mechanics and Physics of Solids,* Vol. 54, pp 2436- 2452.

Jin, L.; Bower, C. & Zhou, O. (1998) Alignment of Carbon Nanotube in a Polymer Matrix by Mechanical Stretching. *Applied Physics Letters,* Vol. 73, No. 9, pp1197-1193.

Karapappas, P.; Vavouliotis, A.; Tsotra, P. & Kostopoulos, V. (2009) Enhanced Fracture Properties of Carbon Reinforced Composites by the Addition of Multi-Wall Carbon Nanotubes. *Journal of Composite Materials,* Vol. 43, No. 9, pp 977-985.

Kelly, A. & Tyson, W.R. (1965) Tensile Properties of Fiber-reinforced Metals: Copper/Tungsten and Copper/Molybdenum. *Journal of the Mechanics and Physics of Solids,* Vol. 13, pp 329-350.

Kepple, K.L.; Sanborn, G.P.; Lacasse, P.A.; Gruenberg, K.M. & Ready, W.J. (2008) Improved Fracture Toughness of Carbon Fiber Composite Functionalized with Multi Walled Carbon Nanotubes. *Carbon,* Vol. 46, pp 2026-2033.

Fukuda, H. & Chou, T.W. (1982) A Probabilistic Theory of the Strength of Short-fiber Composites with Variable Fiber Length and Orientation. *Journal of Materials Science,* Vol. 17, pp 1003.

Kimura, T.; Ago, H.; Tobita, M.; Ohshima, S.; Kyotani, M. & Yumura, M. (2003) Polymer Composites of Carbon Nanotubes Aligned by a Magnetic Field. *Advanced Materials,* Vol. 14, No. 19, pp 1380-1383.

Krenchel, H. (1964) Fibre Reinforcement. Akademisk Forlag. Copenhagen.

Lau, K. (2003) Interfacial Bonding Characteristics of Nanotube/Polymer Composites. *Chemical Physics Letters,* Vol. 370, pp 399-405.

Lee, W.; Lee, S. & Kim C. (2006) The Mechanical Properties of MWNT/PMMA Nanocomposites Fabricated by Modified Injection Molding. *Composite Structures,* Vol. 76, pp 406-410.

Li, Y.; Hu, N.; Yamamoto, G.; Wang, Z.; Hashida, T.; Asanuma, H.; Dong, C.; Okabe, T.; Arai, M. & Fukunaga, H. (2010) Molecular Mechanics Simulation of the Sliding Behavior between Nested Walls in a Multi-walled Carbon Nanotube. *Carbon,* Vol. 48, pp 2934-2940.

Liao, K. & Li S. (2001) Interfacial Characteristics of a Carbon Nanotube-Polystyrene Composite System. *Applied Physics Letters,* Vol. 79, No. 25, pp 4225-4227.

Lordi, V. & Yao, N. (2000) Molecular Mechanics of Binding in Carbon-Nanotube-Polymer Composites. *Journal of Materials Research,* Vol. 15, No. 12, pp 2770-2779.

Marietta-Tondin, O. (2006) Molecular Modelling of Nanotube Composite Materials: Interface Formation, Interfacial Strength, and Thermal Expansion. The Florida State University. PhD Dissertation.

Natsuki, T.; Wang, F.; Ni, Q.Q. & Endo, M. (2007) Interfacial Stress Transfer of Fiber Pullout for Carbon Nanotubes with a Composite Coating. *Journal of Materials Science,* Vol. 42, pp 4191-4196.

Ogasawara, T.; Ishida, Y.; Ishikawa, T. & Yokota, R. (2004) Characterization of Multi-walled Carbon Nanotube/Phenylethynyl Termainated Polyimide Composites. *Composite: Part A,* Vol. 35, pp 67-74.

Qian, D.; Dickey, E.C.; Andrews, R. & Rantell, T. (2000) Load Transfer and Deformation Mechanisms in Carbon Nanotube-Polystyrene Composites. *Applied Physics Letters,* Vol. 76, No. 20, pp 2868-2870.

Rosca, I.D. & Hoa, S.V. (2009) Highly Conductive Multiwall Carbon Nanotube and Epoxy Composites Produced by Three-roll Milling. *Carbon,* Vol. 47, pp 1958-1968.

Safadi, B.; Andrews, R. & Grulke, E.A. (2002) Multiwalled Carbon Nanotube Polymer Composites: Synthesis and Characterization of Thin Films. *Journal of Applied Polymer Science,* Vol. 84, pp 2660-2669.

Schadler, L.S.; Giannaris, S.C. & Ajayan, P.M. (1998) Load Transfer in Carbon Nanotube Epoxy Composites. *Applied Physics Letters,* Vol. 73, No. 26, pp 3842-3844.

Sen, R.; Zhao, B.; Perea, D.; Itkis, M.E.; Hu, H.; Love, J.; Bekyarova, E. & Haddon, R.C. (2004) Preparation of Single-walled Carbon Nanotube Reinforced Polystyrene and Polyurethane Nanofibers and Membranes by Electrospinning. *Nano Letters,* Vol. 4, No. 3, pp 459-464.

Sun, H. (1998) COMPASS: An ab Initio Force-Field Optimized for Condensed-Phase Applications - Overview with Details on Alkane and Benzene Compounds. *Journal of Physical Chemistry B,* Vol. 102, No. 38, pp 7338-7364.

Tai, N.; Yeh, M. & Liu J. (2004) Enhancement of the Mechanical Properties of Carbon Nanotube/Phenolic Composites using a Carbon Nanotube Network as the Reiforcement. *Carbon,* Vol. 42, pp 2735-2777.

Thostenson, E.T.; Li, W.Z.; Wang, D.Z.; Ren, Z.F. & Chou, T.W. (2002) Carbon Nanotube/Carbon Fiber Hybrid Multiscale Composites. *Journal of Applied Physics,* Vol. 91, No. 9, pp 6034-6037.

Thostenson, E.T. & Chou TW. (2002) Aligned Multi-walled Carbon Nanotube-Reinforced Composites: Processing and Mechanical Characterization. *Journal of Physics D,* Vol. 35, pp L77-L80.

Tsai, J. & Lu, T. (2009) Investigating the Load Transfer Efficiency in Carbon Nanotubes Reinforced Nanocomposites. *Composite Structures,* Vol. 90, pp 172-179.

Veedu, V.P.; Cao, A.; Li, X.; Ma, K.; Soldano, C.; Kar, S.; Ajayan, P.M. & Ghasemi-Nejhad, M.N. (2006) Multifunctional Composites using Reinforced Laminae with Carbon-nanotube Forests. *Nature Materials,* Vol. 5, pp 457-462.

Vigolo, B.; Penicaud, A.; Coulon, C.; Sauder, C.; Pailler, R.; Journet, C.; Bernier, P. & Poulin, P. (2000) Macroscopic Fibers and Ribbons of Oriented Carbon Nanotubes. *Science,* Vol. 290, No. 17, pp 1331-1334.

Wong, M.; Paramsothy, M.; Xu, XJ.; Ren, Y.; Li, S. & Liao, K. (2003) Physical Interactions at Carbon Nanotube-Polymer Interface. *Polymer,* Vol. 44, pp 7757-7764.

Xiao, K.Q. & Zhang, L.C. (2004) The Stress Transfer Efficiency of a Single-walled Carbon Nanotube in Epoxy Matrix. *Journal of Materials Science,* Vol. 39, pp 4481-4486.

Yokozeki, T.; Iwahori, Y. & Ishiwata, S. (2007) Matrix Cracking Behaviors in Carbon Fiber/Epoxy Laminates Filled with Cup-stacked Carbon Nanotubes (CSCNTs). *Composites Part A,* Vol. 38, pp 917-924.

Zheng, Q.; Xia, D.; Xue, Q.; Yan, K.; Gao, X. & Li Q. (2009) Computational Analysis of Effect of Modification on the Interfacial Characteristics of a Carbon Nanotube-Polyethylene Composites System. *Applied Surface Science,* Vol. 255, pp 3524-3543.

8

Characterization of Nanotube-Reinforced Polymer Composites

Wenjie Wang[1] and N. Sanjeeva Murthy[2]
[1]*Ames Laboratory, Iowa State University, Ames, IA,*
[2]*New Jersey Center for Biomaterials, Rutgers – The State University of New Jersey, NJ U.S.A.*

1. Introduction

Polymers are more readily processible than metals and ceramics, but are not as strong or as stiff. But the mechanical attributes of the polymer can be significantly improved by reinforcing polymers with high Young's modulus fibers. The resulting polymer composites are an important class of light weight materials with excellent specific mechanical properties. Unlike micron size particles and short fibers used in conventional composites, carbon nanotubes (CNTs) allow polymers to be reinforced at the molecular level and thus impart significantly greater improvement in mechanical properties. This is because for the reinforcement to be effective, it is necessary that the fibers be sufficiently long and the interface between the fiber and the matrix be strong, features that are provided by CNTs. The advantages of polymer-nanotube composites (PNCs) were discussed by Calvert (Calvert, 1999). Besides the economic advantage brought about by mixing costly CNTs and inexpensive polymer matrices, it is possible that a synergy exists between the CNTs and polymer matrices so that it is possible to go beyond the simple rule of mixture, and make full use of CNTs' exceptional mechanical properties to enhance the mechanical properties of the composite.

There are several reviews of PNCs (e.g., Breuer & Sundararaj, 2004, Moniruzzaman & Winey, 2006, and Coleman et al., 2006). The present chapter is different from these excellent reviews in that it focuses on the structure and morphology of the reinforced structures, and the consequence of these structures to their performance. The general features of the PNCs will be further illustrated using the results from our work on the study of reinforcements in polyacrylonitrile (PAN) with multi- and single-wall carbon nanotubes (CNTs).

2. Polymer nanocomposites

2.1 Carbon nanotubes and nanofibers

Carbon nanotubes (CNTs), discovered by Iijima in 1991, are seamless cylinders made of rolled up hexagonal network of carbon atoms (Iijima, 1991). Single-wall nanotubes (SWNTs) consist of a single cylindrical layer of carbon atoms. The details of the structure of multi-wall carbon nanotubes (MWNTs) are still being resolved, but can be envisioned as a tubular structure consisting of multiple walls with an inter-layer separation of 0.34 nm. The diameter for inner most tube is on the scale of nanometer, and the length of the tube can be up to ~ μm. In one model, the MWNTs are considered as a single sheet of graphene that is

rolled up like a scroll to form multiple walls (Dravid et al., 1993). In another model, MWNT is thought to be made of co-axial walls consisting of hexagons aligned in helical manner, the individual tubes forming a nested-shell structure. Ge and Sattler (Ge & Sattler, 1993) found that as the graphene sheet rolls up and matches at joint line seamlessly, different wrapping angles resulting in different helicities is necessary for tubes to be separated by a uniform spacing. It is also likely that there could be the coexistence of scroll-type (open cylinder) and perfect Russian doll (nested shell) structures (Zhou et al., 1994). These two different structure models have an impact on the mechanical as well as the optical and electronic properties of CNTs. The carbon atoms in the plane of graphene sheet are bound with strong covalent sp^2 hybridized bonds. The interaction between walls can be approximated by weak van de Waals force or π bond. Thus, the sliding of walls with respect to each other might significantly reduce axial modulus of MWNT compared to SWNT, more so in the nested shell structure than in the scroll-type structure.

Vapor-grown carbon nano-fibers (VGCNF), which are also used as reinforcements, are 50-200 nm in diameter, 20-100 μm in length, and bear resemblance to MWNT, except that graphite sheets make an angle (~15°) to the long- axis (Uchida et al., 2006). Compared to the CNTs, VGCNF is less costly to produce.

CNTs have exceptional mechanical, optical, electrical and thermal properties (Chae et al., 2009; Chae et al., 2007; Guo et al., 2005; Koganemaru et al., 2004; Sreekumar et al., 2004; Ye et al., 2004). The elastic modulus of an isolated CNT, estimated using intrinsic thermal vibrations in TEM, is 1.8 TPa. (Treacy et al., 1996), almost an order of magnitude larger than that of carbon fibers. This axial modulus is higher than the 1 Tpa in-plane modulus of a single graphene sheet due to the wrap-up of the graphene sheet into a cylinder. Bower et al. measured the fracture strain of MWNT ≥18% in polymer composites, almost one or two orders of magnitude larger than carbon fibers (Bower et al., 1999). Chae and Kumar suggested that, because the tensile strength of CNTs is 100-600 GPa, about two orders of magnitude larger than that of ordinary carbon fibers, the CNTs might be the ultimate reinforcing materials for strong fibers (Chae & Kumar, 2009).

2.2 CNT/Polymer composites

The advantages of using CNTs as reinforcements in polymer matrices can be illustrated with the following empirical relationship between the critical length (l_c), and fracture stress σ_f of the reinforcing fiber (Wang et al., 2008a):

$$l_c = \frac{\sigma_f d}{2\tau_c} \tag{1}$$

where d is the fiber diameter, and τ_c is the interfacial strength. The critical fiber length is the minimum length of the fiber such that the failure occurs within the fiber, and thus ensures that it acts as an effective reinforcement. This relationship shows that nanotubes with their smaller diameter, and greater interfacial strength when molecularly dispersed serve as effective reinforcements even at smaller lengths.

The importance of bonding between CNTs and matrices for effective load transfer without slipping of contact surfaces has been widely recognized (Calvert, 1999). It is desirable that a large fraction of the load applied to the composites is efficiently transferred to CNTs through the interaction or bonding between the outer surface of the CNTs and the surrounding polymer matrix (Ajayan et al., 1997). It is widely accepted that larger the area of interface between the matrix and nano-fillers, the better the mechanical enhancement.

Several load-transfer models have been proposed and examined using atomistic molecular dynamic simulations. Most recent molecular dynamics simulations suggest that weak van der Waals force (Srivastava et al., 2003), as well as thermal expansion mismatch can contribute to strong interfacial interaction (Wong et al., 2003; Zhang & Wang, 2005). Panhuis's model suggests that the polymer chains will adapt their conformations to wrap around a single CNT (Panhuis et al., 2003; Wong et al., 2003). Frankland's model suggests that a small fraction of chemical bonds are formed between polymers and carbon atoms of the CNTs thus cross-links are formed between the matrix and CNTs (Frankland et al., 2002). Chemical bonding between CNT and polymer is apparent in the adhesion of polymers to CNT on the fracture surface through transmission electron microscopy (TEM) (Bower et al., 1999). However, Raman spectroscopy along with the SEM images of fracture surface by Ajayan et al. showed the sliding of SWNT bundles with respect to the matrix suggesting that the actual load transfer was poor between CNT and the polymer matrix, which rules out the chemical bonding model (Ajayan et al., 2000). A number of experiments have been carried out to test these models for the interaction between polymer matrix and CNTs (SWNTs and MWNTs) through tensile tests, microscopy and x-ray scattering. Deformation of the CNTs observed by x-ray scattering measurements (see section 3.3) shows an interaction between the matrix and CNTs that is sufficient to transfer the load from the matrix to the CNTs (Wang et al.,2008b). Actual measurements of the adhesion between the matrix and CNTs were also carried out using scanning probe microscope to pull out the CNTs from the matrix (Cooper et al., 2002). Coleman et al. found that a layer of polymer attached to the CNTs after pullout was very similar to the crystalline polymer coating nucleated by the MWNTs. The presence of interfacial crystalline layers partly contributes to the mechanical properties of composites (Coleman et al., 2006). Pull-out measurement can also be carried out by atomic force microscopy (AFM). Barber et al. attached one end of a single CNT to the tip of AFM and embedded the other end into the polymer matrix. The critical force needed to pull the nanotube from the polymer matrix was then recorded (Figure 1).

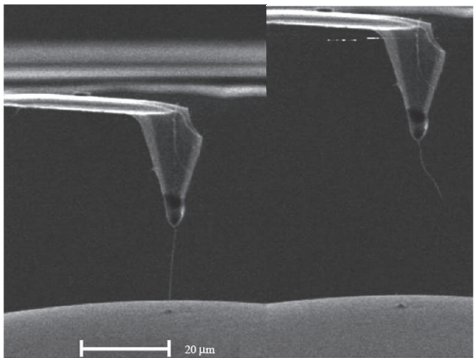

Fig. 1. Left panel shows that one end of a single CNT is attached to the AFM tip and the other is embedded in the solid polymer matrix. Right panel shows the process of pull-out of CNT. The critical force needed for pull-out can be recorded by AFM (Reprinted from Philosophical Transactions of the Royal Society A: Mathematical, Physical and Engineering Sciences, vol. 366, W. Wang, P. Ciselli, E. Kuznetsov, T. Peijs and A.H. Barber. "Effective reinforcement in carbon nanotube-polymer composites", Figure 2, Copyright 2008, with permission from the Royal Society.).

Because of the interfacial interaction between CNTs and the polymer matrix, the properties of the matrix in the interfacial regions are different from the bulk materials (Schadler, 2007). CNTs dispersed in the polymer matrix, despite the small volume fraction (usually 1-5 vol%), enhance the overall mechanical properties, also affect the structure of the matrix during conventional processing. Many observations show that the presence of CNTs can affect the crystallization behaviors of the polymers (Brosse et al., 2008; Grady et al., 2002; Liu et al., 2004) and alter the morphology of matrix (Brosse et al., 2008; Chatterjee et al., 2007). For instance, instead of the expected spherulites, crystalline lamellae were observed growing perpendicular to the surface of CNTs. (Brosse et al., 2008). Therefore, the microstructure of the polymer matrix should be taken into account when evaluating the performance of nanocomposites (Advani, 2006).
Two other factors that affect the performance of CNT-reinforced nanocomposites are the degree of dispersion and alignment of nanotubes. Poor or nonuniform dispersion causes the fillers to aggregate, acting as defect sites (Advani, 2006). Dispersion process is affected by interactions of CNT-CNT and CNT-matrix. It is controlled by several factors such as filler's size, specific surface area, and interfacial volumes (Moniruzzaman & Winey, 2006). The degree of dispersion of CNTs in polymer matrix can be assessed using small angle x-ray scattering as described in the following section. Rheological study of dispersions of MWNTs in the polymer matrix by Huang et al (Huang et al., 2006) also suggests that a satisfactory dispersion can be achieved if the mixing time exceeds a critical value (characteristic mixing time).

2.3 Processing of PNCs

CNTs are dispersed into the polymer matrix to form a polymer/CNTs composite, and there are several ways to achieve a good dispersion. Following is a condensed version of the various processing methods as discussed by Coleman et al. (Coleman et al., 2006). Solution processing is the easiest if the polymer can be dissolved in a suitable solvent. Typically, nanotubes well dispersed in a solvent is mixed with a polymer solution with energetic agitation (e.g., sonication), and the solvent is allowed to evaporate in a controlled way leaving a composite film. For insoluble thermoplastic polymers, the polymer is heated above either glass transition (if amorphous) or melt temperature (if semicrystalline) to form a viscous liquid, and the CNTs are mixed into this viscous liquid to be then processed into a fiber or a film using common production processes. For thermosetting polymers such as epoxy, the CNTs are blended when epoxy is in a liquid state, and the mixture is then allowed to cure. Chemical processing of Polymer/CNTs composites aims at formation of chemical bonds between the polymer matrix and the CNTs; this provides for stronger interaction between the polymer and CNTs and better dispersion, and thus results in better mechanical properties. Chemical methods include *in-situ* polymerization and functionalization of CNTs with polymer, also called polymer grafting.

3. Characterization of CNT/Polymer composites

Although the CNTs' high strength and stiffness as well as high aspect ratio promise significant improvement in mechanical properties of polymer nanocomposites (Treacy et al., 1996), the actual measured enhancement is below these expectations (Schaefer et al., 2003). The major reason might be the intrinsic van der Waals' attraction makes CNTs entangled agglomerates incapable of fully blending into the polymer matrix. Since the four

factors important to the reinforcement are CNTs' aspect ratio, alignment, dispersion, and interfacial interactions (Coleman et al., 2006), it is desirable to examine the morphology of CNTs in the polymer matrix. Several methods including x-ray diffraction, Raman spectroscopy, scanning and transmission electron microscopy are employed to characterize the structure, morphology and properties of carbon nanotube-reinforced polymer nanocomposites.

3.1 Electron microscopy

Transmission electron microscopy (TEM) and scanning electron microscopy (SEM) enable the visualization of the microscopic structure and morphology of CNTs in composites at resolution down to 0.1 nm (Michler, 2008; Sawyer et al., 2010). The limitations of using electron beam to probe the polymer are the low contrast (most polymers are made of light elements) and radiation damage. TEM is used to probe the bulk structure from thin sections of the material, and SEM to examine the surfaces. In addition to imaging, TEM is also used to carry out micromechanical measurements. Examples of these applications will be illustrated below.

3.1.1 Dispersion and alignment of the CNTs

One of the primary uses of microscopy is characterizing the dispersion and alignment of the nanotubes in the polymers. Figure 2a is an SEM image from a composite prepared by mixing aqueous solution poly(vinyl alcohol) with CNT dispersions followed by subsequent casting and controlled water evaporation (Shaffer & Windle, 1999). It shows homogeneous dispersion of the nanotubes even at 50 wt% loading. By examining the fracture surface using SEM, they confirmed the uniform dispersion of CNTs. Figure 2b shows the use of TEM to examine the dispersion of CNTs (Qian et al., 2000). In this experiment Qian et al. used high-energy sonication to disperse MWNTs (predispersed in toluene) into polystyrene (PS) dissolved in toluene, and the solvent was then evaporated to produce 0.4 mm thick films. Figure 2b shows 34 nm diameter MWNTs well dispersed down to the μm length scales. The inset is a plot of the loading of the CNT's at different length scale, and shows that homogeneity increases (decrease in standard deviation) with increase in the length scale. Furthermore, the TEM images also reveal defects that were present as a result of the polymer shrinkage primarily at the end of the nanotubes. Other than the quality of dispersion, both of these nanoscale images show that in PNCs, as pointed out by Fisher et al., the nanotubes are curved instead of being straight. Based on these observations, Fisher et al. illustrated that the reduction of effective modulus of CNT-reinforced materials is due to the curvature of embedded CNTs (Fisher et al., 2002).

Figure 3 illustrates the degree of alignment that can be achieved in PNC composites as seen in a TEM image (Thostenson & Chou, 2002). Unlike the two examples discussed above, in this instance, Thostenson & Chou extruded the polymer (polystyrene, PS) and a master batch of nanotube dispersed in PS using a micro-compounder. The film coming out of a rectangular die was drawn and solidified by passing over a chill roll. TEM was used to characterize the dispersion and alignment of MWNTs in polymer films. Figure 3a shows the large-scale dispersion and overall alignment of the carbon nanotubes and Figure 3b shows the alignment of the individual nanotubes. Examination of the drawn films showed that a draw ratio of five was sufficient to achieve a good nanotube alignment.

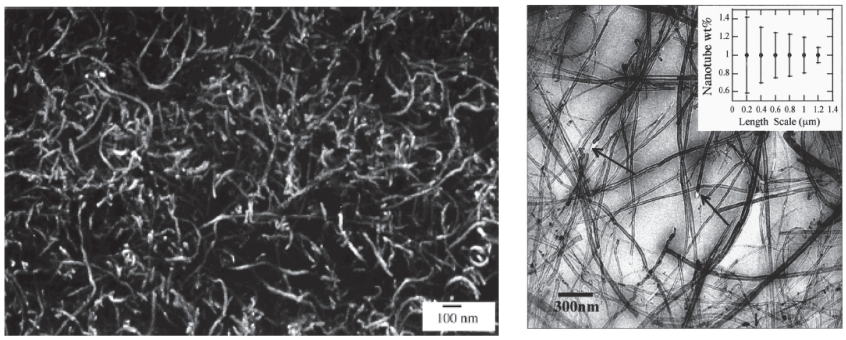

Fig. 2. Left Panel (a): A SEM image for 50 wt% CNT/ Poly(vinyl alcohol) composites (S.P. Shaffer and A.H. Windle, "Fabrication and characterization of carbon nanotube/poly(vinyl alcohol) composites". Advanced materials (1999). Vol. 11. 937-941. Copyright Wiley-VCH Verlag GmbH & Co. KGaA. Reproduced with permission.). Right panel (b): An example of TEM image at 1 μm length scale showing homogeneously dispersed MWNT in polystyrene (PS) matrix. Homogeneity of nanotube dispersion was evaluated by assessing the weight fraction of nanotubes in different areas in the TEM images for different length scale. The inset shows that homogeneity is greater at 1.2 μm length scale (small error bar) than lower length scale. An arrow in the image indicates the defects present at the nanotube ends (Reprinted with permission from D.Qian, E.C. Dickey, R. Andrews and T. Rantell., "Load transfer and deformation mechanisms in carbon nanotube-polystyrene composites", Applied Physics Letters, vol. 76, 2868-2870. Copyright 2000, American Institute of Physics.)

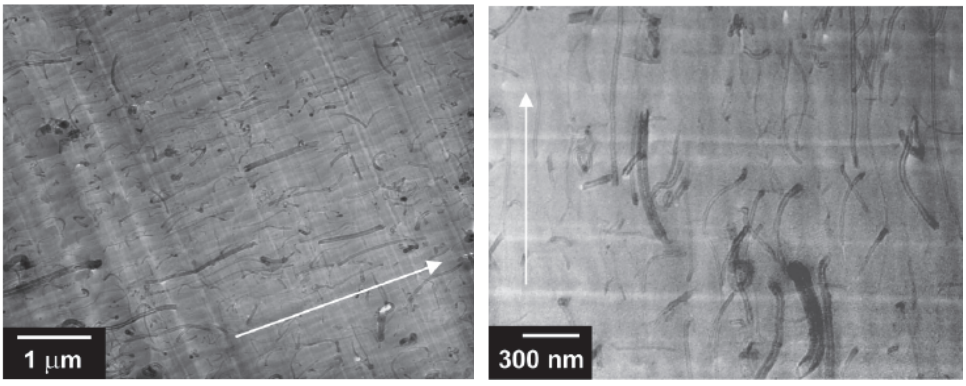

Fig. 3. TEM images of dispersion and alignment of CNTs in nanocomposites films. The arrows indicate flow/drawing direction. Left panel (a): TEM at length scale of micrometer. Right panel (b): TEM at length scale of nanometer (Reprinted with permission from E.T. Thostenson and T.W. Chou, "Aligned multi-walled carbon nanotube-reinforced composites: processing and mechanical characterization", J. Phys. D: Appl. Phys., vol. 35, L77-L80. Copyright 2002, Institute of Physics Publishing.).

3.1.2 Mechanical properties of CNTs

TEM is also used to measure the mechanical properties and to study the deformation mechanism in PNCs. In fact, the Young's modulus of CNTs, which is hard to measure by conventional means, was first directly measured using TEM from the thermal vibration amplitudes of CNTs, and thus confirming the predicted axial stiffness on the scale of terapascal (TPa) and the high axial strength due to the in-plane graphitic structure of CNTs (Treacy et al., 1996). Bower et al. (Bower et al., 1999) aligned MWNTs in the thermoplastic polymer (polyhydroxyaminoether, DowChemical Co.) films by stretching above the glass transition temperature and releasing the load at 300 K. The uniaxial alignment of MWNTs was confirmed by x-ray diffraction. The CNTs in the polymer matrix are bent (Figure 4), presumably because of the shrinkage of the polymer matrix as the composite is cooled from 100 °C to room temperature. The deformation was reversible at moderate bending, i.e. the CNTs returned to their straight cylindrical shape by heating the polymer matrix. Fracture surfaces in PNC's can be examined to ascertain the strength of the adhesion between the polymer and the nanotube. Figure 5 shows MWNT protruding from polymer matrix attached with a layer of polymer. All these observations point to the effective interactions and intimate contact between CNTs and polymer matrix. In a final example, Figure 6 shows the use of TEM to observe the nucleation and propagation of a crack induced in thin MWNT-PS film by thermal stresses in a TEM (Qian et al., 2000). The nucleation and propagation occur in regions of low CNT density and along the weak CNT-polymer interface. Also, the CNTs tend to align perpendicular to the crack and bridge the gap, and some of them are already pulled out, suggesting that the critical failure force is determined by interaction between polymer matrix and CNTs. These CNTs provide a closure force until a critical value is reached to be pulled out of the matrix.

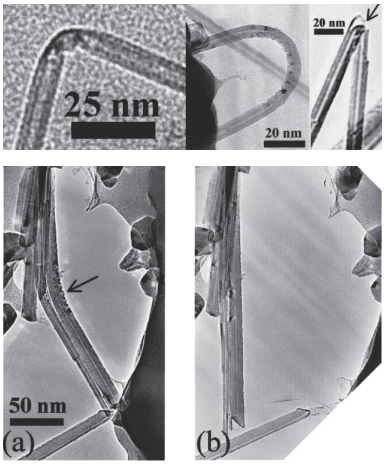

Fig. 4. Top panel: TEM images showing the buckling of in bent MWNTs in MWNT/polymer composites. Bottom panel: (a) A bent nanotube before heating; (b) the bent nanotube restored to its straight cylindrical shape after heating (Reprinted with permission from C. Bower, R. Rosen, L. Jin, J. Han and O. Zhou, "Deformation of carbon nanotubes in nanotube-polymer composites", Applied Physics Letters, vol. 74, 3317-3319. Copyright 1999, American Institute of Physics.).

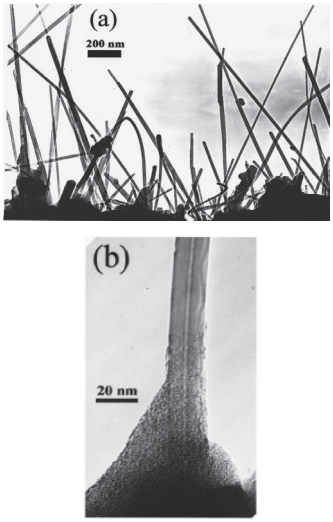

Fig. 5. TEM images of the fracture surface showing MWNT protruding from the polymer matrix suggestive of strong adhesion between the MWNT and the polymer matrix (Reprinted with permission from C. Bower, R. Rosen, L. Jin, J. Han and O. Zhou, "Deformation of carbon nanotubes in nanotube-polymer composites", Applied Physics Letters, vol. 74, 3317-3319. Copyright 1999, American Institute of Physics.).

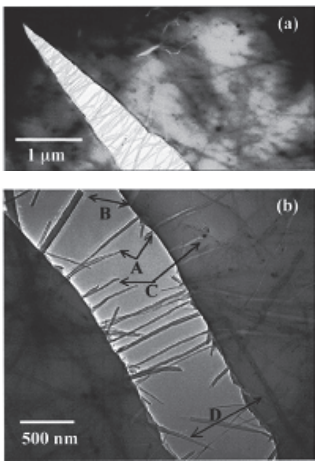

Fig. 6. Crack initiated by thermal stress. Upper panel shows the crack initiation and propagation at low CNT density areas. Lower panel shows the CNTs aligned perpendicular to the crack bridging the crack. Arrows labelled A, B, C and D point to CNTs that are broken and pulled out of matrix (Reprinted with permission from D. Qian, E.C. Dickey, R. Andrews and T. Rantell, "Load transfer and deformation mechanisms in carbon nanotube-polystyrene composites", Applied Physics Letters, vol. 76, 2868-2870. Copyright 2000, American Institute of Physics.).

3.2 Raman spectroscopy

Infrared (IR) and Raman spectroscopy (RS) are the two vibrational spectroscopic techniques widely used to obtain molecular structure information for the identification of polymers, functional groups and stereochemical structures. Both techniques measure the vibrational energies of molecules. However, for a vibrational motion to be IR active, the dipole moment of the molecule must change, and for a transition to be Raman active there must be a change in polarizability of the molecule. In most instances, IR and RS yield complementary information because IR activity suggests RS inactivity and vice versa. Sample requirements for RS are less stringent than for IR. Details of application of RS to CNTs have been discussed thoroughly in the literature (Dresselhaus et al., 2005), and a few examples of the use of RS to PNCs are provided here. For oriented specimen, the intensity of RS spectra line depends on the orientation of molecules relative to the polarization of the incident beam as well as scattering beam. This feature is used to determine the orientation distribution for CNTs in polymer matrix. Polarized RS has also been used to probe the one -dimensional nature of SWNT in the bulk materials (Gommans et al., 2000). These results show that the RS intensity has the same orientation dependence as nanotube's polarizability. A similar work on MWNT has also shown that there is a strong dependence of the graphite-like G band and the disorder-induced D band on the polarization geometry (Rao et al., 2000).

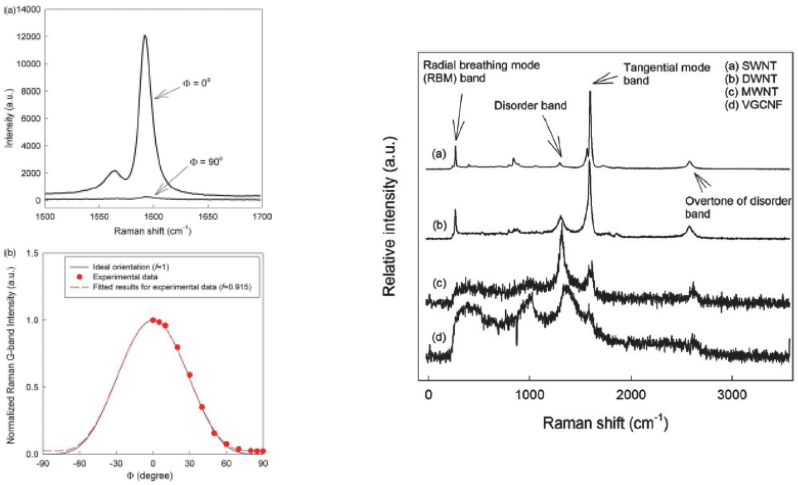

Fig. 7. Upper left panel: G-band Raman spectra for PAN/SWNT fiber. The ratio of the peak intensity at 1592 cm^{-1} are compared when the angles between polarizer and the fiber axis are 0 and 90°, respectively. Lower left panel: The normalized G-band Raman intensity as function of angles between polarizer and fiber axis. Experimental data are for PAN/SWNT (1 wt%) at draw ratio 51 (Reprinted from Polymer, Vol.47, H.G. Chae, M.L. Minus and S. Kumar, "Oriented and exfoliated single wall carbon nanotubes in polyacrylonitrile", 3494-4504. Copyright 2006, with permission from Elsevier.) Right panel: Raman spectra for pristine CNT powders (Reprinted from Polymer, Vol.46, H.G. Chae, T.V. Sreekumar, T. Uchida and S. Kumar, "A comparison of reinforcement efficiency of various types of carbon nanotubes in polyacrylonitrile fiber", 10925-10935. Copyright 2005, with permission from Elsevier.).

Mathematical description of Raman intensity distribution as a function of SWNT's orientation has been derived using Legendre polynomials by Liu et al. (Liu & Kumar, 2003). They built a relationship between 2nd and 4th orientation parameters of SWNT and Raman scattering intensity and depolarization ratio. This quantitative relation was used by Chae et al. to investigate the orientation of SWNT in polyacrylonitrile fibers (Chae et al., 2006). They measured G-band intensity ratio at about 1592 cm^{-1} for polarization parallel and perpendicular to the fiber axis (Figure 7). By comparing the G-band ratio for conventional spun and gel-spun PAN/SWNT fibers, they were able to conclude that the orientation of SWNT is only slightly improved by the gel-spinning process. They also showed that RS could be used to estimate the relative intensity of disorder band for SWNT, DWNT, MWNT, VGCNF (Chae et al., 2005) (Figure 7). They concluded that SWNT has best perfection while MWNT and VGCNF have more disorder (Chae et al., 2005).

3.3 X-ray scattering

X-ray scattering is an ideal tool to investigate the influence of CNTs on polymer morphology at multiple length scales from nm to sub μm length scales. This is achieved by using variations of the basic diffraction/scattering technique that are usually referred to as x-ray diffraction (XRD), wide-angle x-ray diffraction (WAXD), and small-angle x-ray scattering (SAXS). The scattering or diffraction intensity is expressed as a function of the scattering vector, $q(=4\pi\sin\theta/\lambda)$ or $s(=2\sin\theta/\lambda)$, 2θ being the scattering angle, and λ the x-ray wavelength. The sample preparation is far simpler than that for TEM. Whereas electron microscopy can provide information about the distribution of the CNTs and other structural information within a particular frame of an image, SAXS can provide similar data about the distribution, but averaged over lengths ~ mm in the bulk of the sample. Some of the characteristics of the PNCs that can be measured using x-ray scattering include the structural changes in the polymer due to the incorporation of the CNT, orientation of the polymer chains/crystals and the CNTs, and structure at the interface between the polymer and the CNT, and the changes in these features during deformation. The advent of synchrotron radiation, whose brilliance is ~ 10 orders of magnitude higher than that from a rotating anode tube, makes it possible to carry out *in-situ* dynamical measurements. Some of the data in this section were obtained from CNTs dispersed in polyacrylonitrile (PAN) that was then spun into a fiber. PAN fibers reinforced with CNTs are made by solution- or gel-spinning. PAN/CNTs fibers with significant enhancement in properties suggested good interactions between PAN and CNTs (Chae et al., 2006; Chae et al., 2005; Guo et al., 2005; Sreekumar et al., 2004; Uchida et al., 2006). These studies showed that the improvement in low strain is due to the interaction of PAN and CNTs, while the improvement as high strain is partly due to the CNT length.

3.3.1 Characterization of the CNTs

Before discussing the results for the PNCs, we will first discuss some of the scattering data relevant to the characterization for the CNTs. Historically, the MWNTs were observed by electron microscopy and were depicted as concentric seamless cylinders (Iijima, 1991). This model was used to interpret XRD data (Pasqualini, 1997), and further direct evidence appeared later to support this concentric cylinder model (Xu et al., 2001). However, there has been evidence that suggest that the local structure is similar to turbostratic graphite or scrolls of graphite sheets (Dravid et al., 1993; Zhou et al., 1994). More recent data suggest that while thin MWNTs could be modelled as concentric 7-15 tubules, thicker MWNTs were

found to be mixtures of both scroll-type MWNT and concentric-cylinder (nested Russian doll) MWNTs (Maniwa et al., 2001).
An individual CNT cannot be characterized using SAXS. However, due to the π-π chemical bonding and van de Waals interactions, the CNTs tend to aggregate into bundles while lacking a clear-cut rod-like morphology (Schaefer et al., 2003a), and this typical morphology can be characterized using SAXS. Schaefer et al. combined small-angle light scattering, ultra-SAXS and SAXS to measure morphology and degree of dispersion of SWNTs and MWNTs suspended in water (Schaefer, 2003a; Schaefer, 2003b). They found that the intensities over 5 decades of q are characterized by different power laws. The power-law of intensity from SWNT indicates a branched rope network with fractal characteristics. Porod's law was observed at length scale smaller than inner radius, suggesting the smoothness of interface. The nonuniform dispersion of CNTs in polymers partly explains why the reinforcement of CNTs to polymer composites falls below expectations.
In another experiment (Inada et al., 2005), two segments of different power-law behavior were observed in the intensity distribution (Figure 8). One segment conforms to Porod's law corresponding to smooth interfaces. The other follows a power-law with exponent -1, suggesting scattering is from a rod-like structure. The scattering could be modeled as those from MWNTs represented as hollow tubes with an inner diameter of about 8 nm and a wall thickness of 6 nm, which is in agreement with the reported results from direct measurement through TEM.

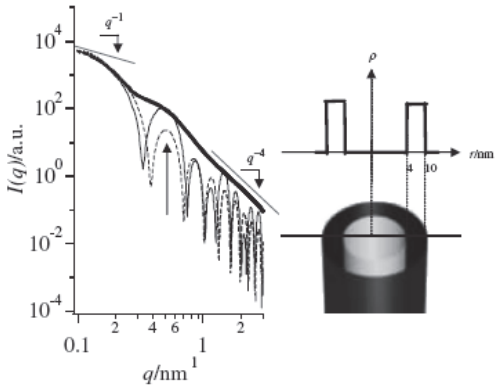

Fig. 8. Left: Measured SAXS intensity as function of scattering vector. Two power laws were presented indicating a one-dimension cylinder structure and sharp interface, respectively. Straight line and dotted line are calculated for a core-shell and hard cylinder models, respectively. Right: The best fit parameter suggest the structure of CNT is a core-shell structure (Reprinted from T. Inada et al., "Small-angle x-ray scattering from multi-wall carbon nanotubes (CNTs) dispersed in polymeric matrix", Chemistry Letters, Vol. 34, 525 (2005), with permission from The Chemical Society of Japan.)

3.3.2 SAXS characterization of the voids and the CNTs in the polymer

Voids are invariably formed in the fibers during the spinning and the drawing process, especially in the presence of reinforcements. Voids, and in general any scattering entities, give rise to SAXS that can be analyzed to obtain information about the length, diameter, and

orientation of these entities as well the information about the nature of the interface. In the work with PAN fibers, the degree of orientation of the voids measured by SAXS was found to be same as those of the crystalline domains observed in WAXS. Both increased reversibly upon stretching, indicating that the voids are integral parts of the polymer matrix and closely associated with the crystalline domains in the fibrils (Wang et al., 2009). SAXS data also showed large changes in the size distribution of the voids during elongation in the solution spun PAN fibers, but not the composite fibers. Furthermore, heating the fiber above the glass transition temperature (T_g) decreased the volume fraction of the voids considerably as indicated by a decrease in the scattered intensity. Figure 9 shows examples of the decay in equatorial scattering with scattering angle. The rate of this decay, as indicated by the slope of the log-log plot (called the exponent) provides valuable insight into the nature of the void-polymer interface. In the plot of the PAN with MWNT, we see the exponent is 4.4 (Figure 9a). An exponent of 4.0 would indicate a sharp, smooth interface. A value higher than 4 suggests that in the PAN/MWNT sample, there is a diffuse interface between the polymer and the void as indicated schematically in the figure. An exponent between 3 and 4 would indicate a rough void-polymer interface, which was observed in gel-spun fibers without any CNT's (Figure 9b). An exponent between 2 and 3 indicates that the structure within the void is similar to a mass-fractal. It is speculated that because of the nature of gel-spinning process, the voids are partially filled with polymer, and perhaps CNT, and as a result the scattering exponent falls below 3 as indicated in Figure 9c. It is possible that a similar analysis can be carried out to probe the nanotube-polymer interface provided there is a contrast between the CNTs and the matrix.

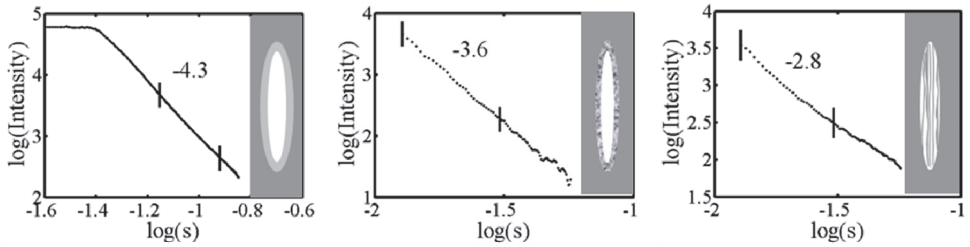

Fig. 9. Power law for equatorial intensities. (a) PAN/MWNT for a void with diffuse boundary ; (b) gel-spun PAN for a void with surface fractal; (c) gel-spun PAN/SWNT for a void with mass fractal The linear segments that are fitted to obtain the fractal dimension are shown in the figure (Wang et al., 2009).

3.3.3 WAXD analysis of the polymer and the CNTs

Figure 10 shows example of the 2D diffraction patterns and the corresponding 1D scans that can be obtained from polymer composites with CNTs. Because of the large fraction of the polymer (95%) the major features in these scans are due to the polymer, and these features can be used to follow the changes in the polymer structure in terms of the unit cell dimensions, crystallinity, crystallite size and polymer orientation (Wang et al., 2008b). For example, the data show that a monotonic decrease in PAN inter-chain spacing with the fiber strain is accompanied by a reversible change from helix to zigzag conformation, and by changes in the axial repeats of the two conformations. These changes are much larger in gel-spun fibers than in solution-spun fibers, indicating more effective load transfer between the

amorphous and crystalline segments in gel -spun fibers. In addition to the intense polymer peaks, it is also possible to see the weak features of the CNT reinforcements in the pattern, especially in the 1D scans. Note the broad feature due to MWNT in Figure 10e, and the sharp features due to VGCNF in Figure 10f. The changes in these features with stress were used to ascertain the modulus of the polymer and the CNT in the composite. Such data are potentially useful in determining the distribution of load between the two components.

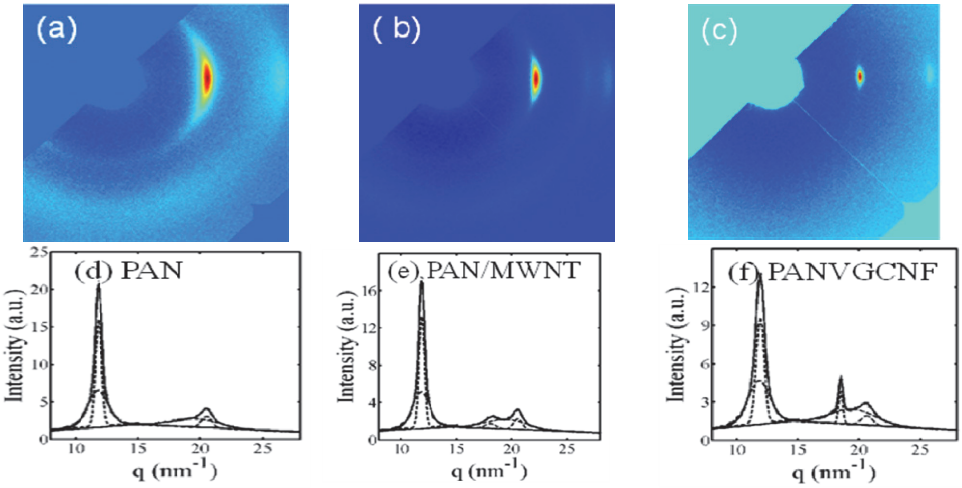

Fig. 10. Upper Panel: Two dimensional wide-angle x-ray diffraction pattern for (a) solution-spun PAN ; (b) solution-spun PAN/MWNT; (c) gel-spun PAN/SWNT fibers. Lower Panel: Profile fitted equatorial scans: (d) PAN; (e) PAN/MWNT; (f) PAN/VGCNF. The data for gel fibers are similar to that of PAN. (Reprinted from Polymer, Vol.49, W. Wang, N.S. Murthy, H.G. Chae and S. Kumar, "Structural changes during deformation in carbon nanotube-reinforced polyacrylonitrile fibers", 2133-2145. Copyright 2008, with permission from Elsevier.)

3.3.4 Alignment of the CNTs and the polymer

As indicated earlier, to a large extent, the strength, modulus and shrinkage properties of the polymer composite are determined by the distribution in orientation and alignment of both the CNT and the polymer. XRD is an appropriate tool for determining this parameter. (Wang et al., 2008b). For instance, Pichot et al. obtained the orientation of SWNT and PVA chain by azimuthal intensity distribution (Pichot et al., 2006). They related the alignment of SWNT in polyvinyl alcohol (PVA) fibers with different draw ratio and accounted for the improvement of alignment with draw ratio by applying a simplistic continuum mechanical model, i.e. the induced alignment is due to the constant volume. In the work on PAN fibers, by measuring the orientation during loading and unloading of the fibers, it was found that the orientation reversibly increases as the fiber is stressed (Wang et al., 2008b).

Chen et al. (Chen et al., 2006) employed in-situ WAXS/SAXS to investigate the deformation of nanocomposites fiber containing fluorinated MWNT (FMWNT) and fluorinated polyethylene-propylene. Orientation of FMWNT can be characterized by (002) reflection of

WAXS and quantitatively described by Hermans' orientation parameter. Similar experiments were carried out by Wang et al. (Wang et al., 2008b) on the deformation of PAN and its nanocomposites containing a variety of CNTs (MWNT,VGCNF,SWNT). The effect of CNT reinforcement could be ascertained by monitoring the structural change in PAN crystals. In this work, it was found that CNTs facilitate the orientation of the PAN crystals during deformation (Figure 11) and increase the load-transferred to PAN crystals as evidenced by their increased lateral and axial strain at 75 °C.

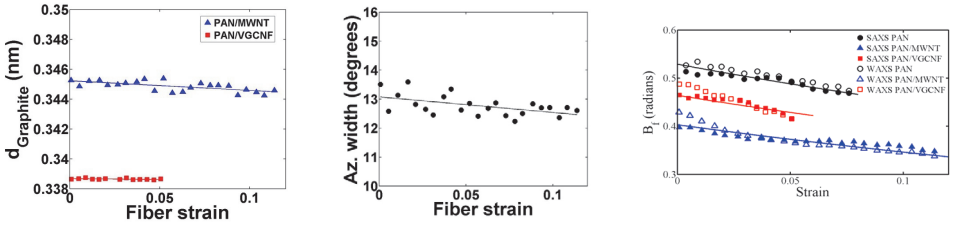

Fig. 11. (a)-(c) from left to right. Changes in the *d*-spacing of carbon as a function of strain derived from the Bragg's peak of nanotubes at room temperature; (b) Degree of orientation of MWNT in the form of the azimuthal breadth.(Reprinted from Polymer, Vol.49, W. Wang, N.S. Murthy, H.G. Chae and S. Kumar, "Structural changes during deformation in carbon nanotube-reinforced polyacrylonitrile fibers", 2133-2145. Copyright 2008, with permission from Elsevier.) (c) Changes in the extent of misorientation (B_f) for scattering entities at room temperature. Black circle, blue triangle and red square represent PAN, PAN/MWNT, and PAN/VGCNF, respectively. Filled and empty symbols represent SAXS and WAXS results, respectively. Straight line segments are calculated based on affine deformation model. (Wang et al.,. 2009).

3.3.5 Deformation of the CNTs in the composite

The diffraction patterns shown in Figure 10 can be used to characterize the deformation of CNTs under stress by monitoring the changes in the (002) peak of CNTs. This interlayer distance d_{002} is used to ascertain the changes in the lattice dimension under strain (Figure 11). This figure also shows the changes in the azimuthal width of these reflections with strain as well as the crystallite size corresponding to this reflection. The changes in these parameters show that CNTs deform under load and thus contributes to the increased modulus, and also alter the response of the PAN matrix to stress, thus enhancing the performance of the composite.

4. Conclusions

Among the many techniques that are currently available, electron microscopy, Raman spectroscopy and x-ray scattering have proved to be most valuable to study the structure in polymer nanocomposites. These techniques complement each other by covering overlapping length scales from sub nm to μm. These techniques are valuable in assessing the dispersion, alignment of the nanotubes in the matrix, to probe the adhesion and the interface between the nanotube and the polymer, and to study the structural changes that occur due to the interaction between the two components as well as during deformation.

5. References

Advani, S. G. (2006). Processing and Properties of Nanocomposites: World Scientific.

Ajayan, P. M., Redlich, P., & Ruhle, M. (1997). Structure of carbon nanotube-based nanocomposites. Journal of Microscopy, 185, 275-282.

Ajayan, P. M., Schadler, L. S., Giannaris, C., & Rubio, A. (2000). Single-Walled Carbon Nanotube-Polymer Composites: Strength and Weakness. Advanced Materials, 12(10), 750-753.

Bower, C., Rosen, R., Jin, L., Han, J., & Zhou, O. (1999). Deformation of carbon nanotubes in nanotube-polymer composites. Applied Physics Letters, 74(22), 3317-3319.

Breuer, O., & Sundararaj, U. (2004). Big Return From Small Fibers: A Review of Polymer/Carbon Nanotube Composites. Polymer Composites, 25(6), 630-645.

Brosse, A.-C., Tence-Girault, S., Piccione, P. M., & Leibler, L. (2008). Effect of multi-walled carbon nanotubes on the lamellae morphology of polyamide-6. Polymer, 49, 4680-4686.

Calvert, P. (1999). Nanotube composites: A recipe for strength. Nature, 399, 210-211.

Chae, H. G., Choi, Y. H., Minus, M. L., & Kumar, S. (2009). Carbon nanotube reinforced small diameter polyacrylonitrile based carbon fiber. Composites Science and Technology, 69, 406-413.

Chae, H. G., & Kumar, S. (2009). Making Strong Fibers. Science, 319(5865), 908-909.

Chae, H. G., Minus, M. L., & Kumar, S. (2006). Oriented and exfoliated single wall nanotubes in polyacrylonitrile. Polymer, 47(10), 3494-3504.

Chae, H. G., Minus, M. L., Rasheed, A., & Kumar, S. (2007). Stabilization and Carbonization of gel spun polyacrylonitrile/single Wall nanotube Composite Fibers. Polymer, 48, 3781-3789.

Chae, H. G., Sreekumar, T. V., Uchida, T., & Kumar, S. (2005). A comparison of reinforcement efficiency of various types of carbon nanotubes in polyacrylonitrile fiber. Polymer, 46, 10925-10935.

Chatterjee, T., Mitchell, C. A., Hadjiev, V. G., & Krishnamoorti, R. (2007). Hierarchical Polymer-Nanotube Composites. Advanced Materials, 19, 3850-3853.

Chen, X., Burger, C., Fang, D., Sics, I., Wang, X., He, W., et al. (2006). In-Situ X-ray Deformation Study of Fluorinated Multiwalled Carbon Nanotube and Fluorinated Ethylene-Propylene Nanocomposite Fibers. Macromolecules, 39, 5427-5437.

Coleman, J. N., Khan, U., & Gun'ko, Y. K. (2006). Mechanical Reinforcement of Polymers Using Carbon Nanotubes. Advanced Materials, 18, 689-705.

Cooper, C. A., Cohen, S. R., Barber, A. H., & Wagner, H. D. (2002). Detachment of nanotubes from a polymer matrix. Applied Physics Letters, 81(20), 3873-3875.

Dravid, V. P., Lin, X., Wang, Y., Wang, X. K., Yee, A., Ketterson, J. B., et al. (1993). Buckytubes and Derivatives: Their Growth and Implications for Buckyball Formation. Science, 259(5101), 1601-1604.

Dresselhaus, M. S., Dresselhaus, G., Saito, R., & Jorio, A. (2005). Raman spectroscopy of carbon nanotubes. Physics Reports, 409, 47-99.

Fisher, F. T., Bradshaw, R. D., & Brinson, L. C. (2002). Effects of nanotube waviness on the modulus of nanotube-rein. Applied Physics Letters, 80, 4647--4649.

Frankland, S. J. V., Caglar, A., Brenner, D. W., & Griebel, M. (2002). Molecular Simulation of the Influence of Chemical Cross-Links on the Shear Strength of Carbon Nanotube-Polymer Interfaces. J. Phys. Chem. B, 106, 3046-3048.

Ge, M., & Sattler, K. (1993). Vapor-Condensation Generation and STM Analysis of Fullerene Tubes. Science, 260(5107), 515-518.

Gommans, H. H., Alldredge, J. W., Tashiro, H., Park, J., Magnuson, J., & Rinzler, A. G. (2000). Fibers of aligned single-walled carbon nanotubes: Polarized Raman spectroscopy. Journal of Appied Physics, 88, 2509-2514.

Grady, B. P., Pompeo, F., Shambaugh, R. L., & Resasco, D. E. (2002). Nucleation of Polypropylene Crystallization by Single-Walled Carbon Nanotubes. Journal of Physical Chemistry B, 106, 5852-5858.

Guo, H., Sreekumar, T. V., Liu, T., Minus, M., & Kumar, S. (2005). Structure and Properties of Polyacrylonitrile/single wall carbon nanotube composite films. Polymer, 46, 3001-3005.

Huang, Y. Y., Ahir, S. V., & Terentev, E. M. (2006). Dispersion rheology of carbon nanotubes in a polymer matrix. Physical Review B, 73, 125422.

Iijima, S. (1991). Helical microtubules of graphitic carbon. Nature, 354, 56-58.

Inada, T., Masunaga, H., Kawasaki, S., Yamada, M., Kobori, K., & Sakurai, K. (2005). Small-angle X-ray Scattering from Multi-walled Carbon Nanotubes (CNTs) Dispersed in Polymeric Matrix. Chemistry Letters, 34(4), 524-525.

Koganemaru, A., Bin, Y., Agari, Y., & Matsuo, M. (2004). Composites of Polyacrylonitrile and Multiwalled Carbon Nanotubes Prepared by Gelation/Crystallization from solution. Advanced Functional Materials, 14(9), 842-850.

Liu, T., & Kumar, S. (2003). Quantitative characterization of SWNT orientation by polarized Raman spectroscopy. Chemical Physics Letters, 378, 257-262.

Liu, T., Phang, I. Y., Shen, L., Chow, S. Y., & Zhang, W.-D. (2004). Morphology and Mechanical Properties of Multiwalled Carbon Nanotubes Reinforced Nylon-6 Composites. Macromolecules, 37, 7214-7222.

Maniwa, Y., Fujiwara, R., Kira, H., Tou, H., Nishibori, E., Takata, M., et al. (2001). Multiwall carbon nanotubes grown in hydrogen atmosphere: An X-ray study. Physical Review B, 64, 073105-073104.

Michler, G. H. (2008). Electron Microscopy of Polymers (1st ed.): Springer.

Moniruzzaman, M., & Winey, K. I. (2006). Polymer Nanocomposites Containing Carbon Nanotubes. Macromolecules, 39, 5194-5205.

Panhuis, M. i. h., Maiti, A., Dalton, A. B., Noort, A. v. d., Coleman, J. N., McCarthy, B., et al. (2003). Selective Interaction in a Polymer-Single-Wall Carbon Nanotube Composite. J. Phys. Chem. B, 107, 478-482.

Pasqualini, E. (1997). Concentric carbon structure. Physical Review B, 56(13), 7751-7754.

Pichot, V., Badaire, S., Albouy, P. A., Zakri, C., Poulin, P., & Launois, P. (2006). Structural and mechanical properties of single-wall carbon nanotube fibers. Physical Review B, 74(245416), 245416.

Qian, D., Dickey, E. C., Andrews, R., & Rantell, T. (2000). Load Transfer and deformation mechanisms in carbon nanotube-polystyrene composites. Applied Physics Letters, 76(20), 2868-2870.

Rao, A. M., Jorio, A., Pimenta, M. A., Dantas, M. S. S., Saito, R., Dresselhaus, G., et al. (2000). Polarized Raman Study of Aligned Multiwalled Carbon Nanotubes. Physical Review Letters, 84, 1820-1823.

Sawyer, L., Grubb, D. T., & Meyers, G. F. (2010). Polymer Microscopy (3rd ed.): Springer.

Schadler, L. (2007). Nanocomposites: Model Interface. Nature Materials, 6, 257-258.

Schaefer, D. W., Brown, J. M., Anderson, D. P., Zhao, J., Chokalingam, K., Tomlin, D., et al. (2003a). Structure and dispersion of carbon nanotubes. J. Appl. Cryst., 36, 553-557.

Schaefer, D. W., Zhao, J., Brown, J. M., Anderson, D. P., & Tomlin, D. W. (2003b). Morphology of dispersed carbon single-walled nanotubes. Chemical Physics Letters, 375, 369-375.

Shaffer, M. S. P., & Windle, A. H. (1999). Fabrication and characterization of carbon nanotube/poly(vinyl alcohol) composites. Advanced Materials, 11, 937-941.

Sreekumar, T. V., Liu, T., Min, B. G., Guo, H., Kumar, S., Hauge, R. H., et al. (2004). Polyacrylonitrile Single-Walled Carbon Nanotube Composite Fibers. Advanced Materials, 16(1), 58-61.

Srivastava, D., Wei, C., & Cho, K. (2003). Nanomechanics of carbon nanotube and composite. Appl. Mech. Rev 56(2), 215-230.

Thostenson, E. T., & Chou, T.-W. (2002). Aligned multi-walled carbon nanotube-reinforced composites: processing and mechanical characterization. J. Phys. D: Appl. Phys., 35, L77-L80.

Treacy, M. M. J., Ebbesen, T. W., & Gibson, J. M. (1996). Exceptionally high Young's modulus observed for individual carbon nanotubes. Nature, 381, 678-680.

Uchida, T., Anderson, D., Minus, M., & Kumar, S. (2006). Morphology and modulus of vapor grown carbon nano fibers Journal of Materials Science, 41(18), 5851-5856.

Wang, W., Ciselli, P., Kuznetsov, E., Peijs, T., & Barber, A. H. (2008a). Effective reinforcement in carbon nanotube-polymer composites. Philosophical Transactions of the Royal Society A: Mathematical, Physical and Engineering Sciences, 366, 1613-1626.

Wang, W., Murthy, N. S., Chae, H. G., & Kumar, S. (2008b). Structural changes during deformation in carbon nanotube-reinforced polyacrylonitrile fibers. Polymer, 49(8), 2133-2145.

Wang, W., Murthy, N. S., Chae, H. G., & Kumar, S. (2009). Small-Angle X-ray Scattering Investigation of Carbon Nanotube-Reinforced Polyacrylonitrile Fibers During Deformation. Journal of Polymer Science: Part B: Polymer Physics.

Wong, M., Paramsothy, M., Xu, X. J., Ren, Y., Li, S., & Liao, K. (2003). Physical interactions at carbon nanotube-polymer interface. Polymer, 44, 7757-7764.

Xu, G., Feng, Z.-c., Popovic, Z., Lin, J.-y., & Vittal, J. J. (2001). Nanotube structure Revealed by High-resolution X-ray Diffraction. Advanced Materials, 13(4), 264-267.

Ye, H., Lam, H., Nick, T., Gogotsi, Y., & Frank, K. (2004). Reinforcement and rupture behavior of carbon nanotubes-polymer nanofibers. Applied Physics Letters, 85(10), 1775-1777.

Zhang, Y. C., & Wang, X. (2005). Thermal effects on interfacial stress transfer characteristics of carbon nanotubes/polymer composites. International journal of solids and structures, 42, 5399-5412.

Zhou, O., Fleming, R. M., Murphy, D. W., Chen, C. H., Haddon, R. C., Ramirez, A. P., et al. (1994). Defects in Carbon Nanostructure. Science, 263, 1744-1747.

9

Carbon Nanotubes as Conductive Filler in Segregated Polymer Composites - Electrical Properties

Yevgen Mamunya
Institute of Macromolecular Chemistry, National Academy of Sciences of Ukraine
Ukraine

1. Introduction

Carbon nanotubes are of great interest as a filler for polymer composites due to their unique properties such as high electrical and thermal conductivity, ultrahigh mechanical strength, high ratio length/diameter (~1000) at nanosized value of diameter. Several recent reviews summarizing different aspects of the composite investigations display a broad spectrum of properties useful for production of sensitive electrodes, sensors for chemical vapours, electromagnetic radiation shielding materials, electrical heaters, as well as pressure, deformation and temperature sensors and photovoltaic cells (Thostenson et al., 2001; Popov, 2004; Breuer & Sundararaj, 2004; Ramirez, 2005; Moniruzzaman & Winey, 2006; Baibarac & Gomez-Romero, 2006; Rajesh et al., 2009; Spitalsky et al., 2010). More substantially the methods of preparation and properties of CNT based polymer composites are described in new book (Mittal, 2010). Specials interest is represented by electrical properties of the composites because of the variety of potential applications.

Such systems are represented in a form of the polymer matrix containing conductive filler creating the conductive network. It seems promising to prepare composite materials with small conductive filler content, which preserves mechanical properties of a polymer along with high electrical conductivity. Random filler distribution typically shows the value of percolation threshold (i.e. critical filler concentration at which a conversion from nonconductive to conductive state occurs) within 10–30% for dispersed metals and 5-15 % for carbon black , for example (Foulger, 1999; Mamunya et al., 2002a). Selectively localized conductive particles in a polymer matrix can form the ordered network of conductive phase creating so-called segregated systems. Considerably lower value of percolation threshold φ_c compared to usual filled polymers can be attained due to this effect, for example (Chan et al., 1997; Bouchet et al., 2000; Mamunya et al., 2002b). On the other hand, high ratio of carbon nanotubes causes lower value of percolation threshold compared to the isotropic filler particles (Simien et al., 2008). Combination of these two factors can lead to the existence of conductivity in the polymer composite at extremely low content of carbon nanotubes.

Segregated polymer composites can be formed either by technological methods in the composites processed by hot compacting or in the polymer blends by filler localization inside one polymer component and on the interface. In this chapter the conditions of creation of the ordered distribution of conductive filler (namely carbon nanotubes) in

polymer matrix and electrical/physical properties of the segregated composites prepared by hot compacting method have been considered and analyzed.

2. Development of the segregated system approaches

First such a term "segregated distribution" was proposed in ref. (Malliaris & Turner, 1971) where the authors investigated electrical conductivity of the system based on PE powder and metal (Ni) powder. The scheme of processing of the polymer-metal composite with ordered, segregated distribution of conductive filler is presented in Fig.1. On the first stage of processing the "shells" of small metal particles around randomly distributed large polymer particles are created in the initial mechanical mixture at condition $D>>d$.

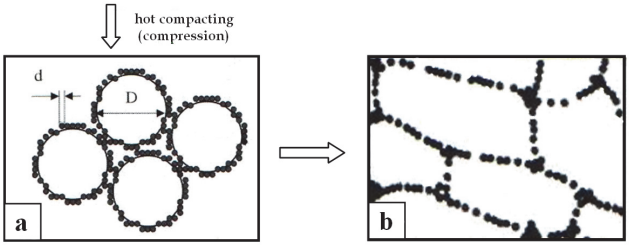

Fig. 1. Scheme of a segregated polymer-filler system processed by hot compacting: a – mechanical mixture of polymer and metal powders, $D>>d$; b – structure of composite as a result of hot compacting (after Malliaris & Turner, 1971).

After hot compacting (compression at temperature of the polymer softening) the initial distribution of metal particles remains essentially unchanged on the boundaries between polymer grains and forms observed pattern of the segregated structure. While the polymer particles are deformed under pressure and conglomerated creating solid polymer matrix. The Malliaris & Turner model predicts appearance of conductivity (percolation threshold) due to formation of continuous chains of the metallic particle contacts in a monolayer at a volume percent of V_a. Then further excess of filler leads to the sharp drop of resistivity up to completion of the double layer at $V_b=2V_a$. The D/d ratio plays a principal role in a structure of conductive phase and a value of percolation threshold. The authors obtained the values of percolation threshold V_a equal to 14 and 6 % at D/d ratio 7.5 and 16, respectively, whereas at random distribution of Ni in PE matrix the value of percolation threshold was about 30 %. Decreasing of the polymer particles size D from 150 to 30 μm (at conductive particles size d=0.8 μm) resulted in increase of φ_c from 5 to 25 % (Bouchet et al., 2000). In composites polytetrafluorethylene/carbon black the value of φ_c was equal to 5 % in case of size of PTFE particles D=1 μm while φ_c =1 % if D=100 μm (Youngs, 2003).

Evolution of the conductive phase structure as a result of growth of the filler content is shown in Fig. 2. At very low volume filler content $\varphi << \varphi_c$ the condition $B>D$ takes place and distribution of filler can be considered as random in this case (Fig. 2-a). The Fig. 2-b demonstrates noticeable ordered filler structure in the region below percolation threshold, $\varphi<\varphi_c$. The pattern of conductive particles which create the infinite conductive cluster at $\varphi=\varphi_c$ is shown in Fig. 2-c. Further growth of the filler content increases a number of layers of the conductive particles on the interface between polymer particles and forms a conductive skeleton (Fig. 2-d).

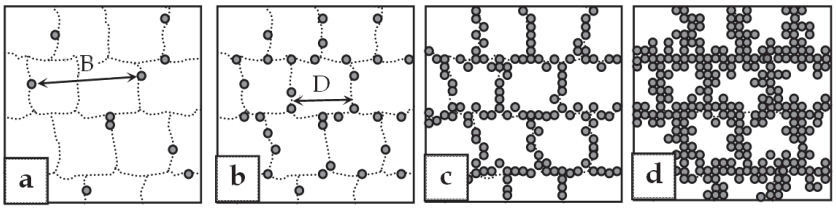

Fig. 2. Scheme of transformation of the segregated structure consisting of conductive particles at volume filler content: a – $\varphi << \varphi_c$, b - $\varphi < \varphi_c$, c – $\varphi = \varphi_c$, d – $\varphi > \varphi_c$. *B* is average distance between filler particles, *D* is size of polymer grain.

Such a type of system can be characterized by two values of filler concentration, the average concentration φ related to whole volume of composite and the local concentration of particles φ_{loc} in the wall of formed skeleton. It is clear that $\varphi_{loc} > \varphi$. The properties which can be related to the distance between particles and existence of contacts between them, such as electrical and thermal conductivity, dielectric characteristics, certain mechanical parameters are mostly defined by local concentration of filler and shifted to the lower values if the average concentration of filler is used. Thus, in ref. (Kusy and Corneliussen, 1975) it has been found that thermal conductivity in polyvinyl chloride/copper (PVC/Cu) segregated composites more than twice the value was achieved over epoxy/metal composites with only a fraction of loading. The power-law equation, describing the concentration dependence of PVC/Ni segregated system, contains the variable value of exponent in opposite to usual form of this equation with constant value of exponent in case of random filler distribution (Mamunya et al, 2002c). Moreover, it is a reason of low value of percolation threshold φ_c in the segregated systems (average value $\varphi = \varphi_c$ is lower than true value of φ_{loc} at φ_c).

Very important for attainable electrical parameters of segregated composites are the conditions of processing. Increasing of mixing time of the powders mixture from 25 to 100 min gives a value of the composites resistivity four orders of magnitude lower due to better distribution of small conductive particles on the surface of polymer particles and breakdown of their aggregates. Increasing of time and pressure of hot compacting promotes the lower values of resistivity as well (Bouchet et al., 2000). In contrast of this, in PE/carbon black composites the pressure did not influence on the composites morphology whereas higher temperature and longer time of pressing led to the penetration of particles of carbon black into polymer grains and increased resistivity of composites (Chan et al., 1997). Mechanical and rheological properties of polymer matrix influence on segregated structure as well. In composites based on methylmethacrylate, buthylacrylate and carbon black the value of φ_c =1.5 % for Young modulus of polymer E'=640 MPa and φ_c =4.9 % in case of E'=3.6 MPa (Kim et al., 2008). The high viscosity of polymer melt minimizes the migration of carbon black particles into PE matrix and deformation of the polymer particles during hot compacting that reduces the value of percolation threshold. From this point of view ultrahigh molecular weight polyethylene (UHMWPE) is a preferred matrix (Zhang et al., 2005).

Since first detailed study of Malliaris & Turner, 1971 many investigations of segregated systems based on metal (and ceramic) particles as conductive filler were fulfilled, for example (Boushet et al., 2000; Bridget et al., 1990; Kusy, 1977; Kusy & Corneliussen, 1975; Lebovka et al., 2006; Mamunya et al., 2002b, 2002c; Privalko et al., 2000; Yacubowicz et al., 1990b). Extensive study of segregated polymer/metal systems and their possible

applications were presented elsewhere (Kusy, 1986) where the prominent achievements in this area have been summarized. The polymer/carbon black composites were thoroughly studied as well (Chan et al., 1997; Chiteme & Mclachlan, 2000; Yacubowicz et al., 1990a; Youngs, 2003; Zhang et al., 2005). Segregated structure of conductive filler was also obtained in emulsions where the particles of conductive filler surround the particles of emulsified polymer (Bridge et al., 1990; Grunlan et al., 2001; Kim et al., 2008; Miriyala et al., 2008). The values of percolation threshold in poly(vinyl acetate)/carbon black composites prepared with using a solution (random distribution of filler) or an emulsion (latex) were 8.18 and 1.2 %, respectively (Miriyala et al., 2008).

A variety of models have been proposed to describe the electrical properties of segregated polymer systems. First model that represented the segregated structure of metal particles in a form of planar hexagonal, square and triangular lattices was not agreed well with experimental values of φ_c and resistivity (Malliaris & Turner, 1971). In ref. (Kusy and Corneliussen, 1975) heightened thermal conductivity in PVC/Ni and PVC/Cu segregated composites was explained by the model of interpenetrating metal/polymer network. Kusy, 1977, has proposed the developed model of distribution of conductive particles on the surface of polymer grains which defined the conditions of continuity of segregated structure created by dispersed metal. Several different models of segregated systems has been analyzed and compared in detail by Lux, 1993, in the extensive review. The parameters of percolation depending on segregated structure and chemical nature as well as size and shape of conductive particles were studied elsewhere (Chiteme & Mclachlan, 2000). Using an approach of non-spherical excluded volume (ellipsoidal shape of the polymer particles after compacting) Youngs, 2003, proposed the equation based on the Bhattacharya model (Bhattacharya et al., 1978). The Bridge et al., 1990, model allows to calculate the number (weight fraction) of colloidal metal particles at maximum latex particle coverage that provides the appearance of conductivity above percolation threshold. Geometrical model of segregated system as 3D shell structure is shown in Fig. 3 and stipulates introduction of the structural coefficient $K_s = \varphi_{loc}/\varphi$.

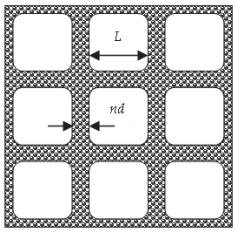

Fig. 3. Geometrical shell structure model. Parameters of the model: $D=L+nd$, L is size of the excluded volume, n is the number of layers of conductive particles in the shell.

The geometry of the shell structure model implies:

$$1/K_s = 1-(1-nd/D)^3 \quad (1)$$

From this the following expression can be obtained for the percolation threshold φ_{cs} of the shell structure:

$$\varphi_{cs} = \varphi_c[1-(1-nd/D)^3] \quad (2)$$

where φ_c is the value of percolation threshold for the randomly distributed filler. This model gives the value of φ_{cs} coincident with the experimental results for PVC/Ni composite at the number of layers of conductive particles n=2, i.e. every polymer particle is covered with a monolayer of conductive particles. Computer simulation on the base of similar model with the linear size of the system $N \leq 2048$ in 2D case and $N \leq 200$ of calculated units in 3D case allowed estimation the value of percolation threshold x_c in such a manner (Lebovka et al., 2006):

$$x_c = p_c^{\infty}[1-(1+n_{eff}/\lambda)^{-\delta}] \quad (3)$$

where p_c^{∞} is a percolation concentration for the random percolation problem in the infinite system, n_{eff} is an effective number of the conductive layers ($n_{eff}/n=1+cn^{-k}$, the c and k parameters are different for 2D or 3D systems, i.e. when δ is 2 or 3, respectively), $\lambda=D/d$, δ is the dimension of system. The equations (2) and (3) give close values of the percolation threshold and satisfactory agreement with the experimental data in PVC/Cu composites.

3. Carbon nanotubes in segregated systems

The investigations of segregated systems have got a new impulse with expansion of the carbon nanotubes area, namely as conductive filler in polymer composites. It is caused by possibility to reach still lower value of percolation threshold than for carbon nanotubes and segregated systems separately. Authors (Mierczynska et al., 2004) formed a segregated structure using UHMWPE and single-walled carbon nanotubes (SWCNT) and obtained the value of the percolation threshold equal to 0.5-1.5% depending on type of SWCNT. In next extensive paper the authors (Mierczynska et al., 2007) have shown the influence of CNTs type on the value of φ_c, for example, they found low value of φ_c=0.095 % in case of MWCNT and 0.3-0.7 % for single-walled nanotubes. Big variation of the percolation threshold values was observed for different methods of the segregated systems preparation, thus previous dispersion of CNTs in solvents gave ten times lower value of percolation threshold for the dispersion of SWCNT in DMF versus dry SWCNT. Interesting to note that influence of the processing parameters is similar to that in the segregated systems based on carbon black and metals, namely insignificant influence of pressure and temperature of compacting, and the rise of conductivity with increasing of mixing time of the polymer powder/CNTs mixture. The comparison of CB/UHMWPE and MWCNT/UHMWPE segregated systems has shown that the values of percolation thresholds were less than 0.5 % in both of cases (Hao et al., 2008). Investigation of conductivity of the MWCNT/UHMWPE composites (Gao et al., 2008) has revealed two-dimensional character of the MWCNT structure and low value of percolation threshold (φ_c=0.072 %). In this study the value of critical parameter t in the scaling relation that describes the conductivity above φ_c

$$\sigma = \sigma_0 (\varphi - \varphi_c)^t \quad (4)$$

was equal to 1.15 whereas a theory predicts the value of t=1.6-2 for 3D conductive structure that is evidence of two-dimensional structure of conductive phase. In ref. (Du et al., 2011) two types of segregated structures based on MWCNT and graphite nanosheets (GNS) formed in HDPE matrix were compared. Lower value of percolation threshold (φ_c=0.15 %) and higher conductivity was revealed in the MWCNT/HDPE composites in comparison with the GNS/HDPE composites (φ_c=1 %).

Introduction of CNTs into polymer emulsions is of benefit to creation of the conductive segregated structure with low value of percolation threshold, for example φ_c=0.2 % in styrene-isoprene emulsion with SWCNT (Ha et al., 2007). The iPP-g-MA nanocomposites, initially artificially brought into a latex form after polymerization, displayed extremely low electrical percolation threshold values of the order of 0.05 % and 0.1 % for SWCNT- and MWCNT-based systems, respectively (Grossiord et al., 2010). The PVA-functionalized CNTs were dispersed in the acrylic latex matrix and obtained nanocomposite films exhibited low optical absorption coefficients. It is expected that this type of nanocomposite coating will potentially exhibit high thermal and electrical conductivity along with high wear-resistance (Vandervorst et al., 2006). A percolation threshold below 0.04% of SWCNT was achieved when an emulsion polymer (i.e., latex) has been used as the polymer matrix (Grunlan et al., 2004). Formation of the segregated SWCNT structure in PVA emulsion allows achievement of high electrical conductivity (48 S/cm) and acceptable thermopower at low thermal conductivity in solid state of the composite that indicates the promising applications of such a type of materials in thermoelectric systems for collection and generation of energy (Yu et al., 2008).

4. Segregated PVC/MWCNT and UHMWPE/MWCNT systems

An excursus in a history of development of the segregated systems indicates that polyvinyl chloride is the most acceptable polymer for creation of segregated composites processed by hot compacting due to its high viscosity, a variety of the powdered PVC types with different size of particles manufactured by industry, wide temperature range of softening (as a result of its amorphous structure) that facilitates a processing (Kusy, 1986). Second attractive polymer is UHWMPE which has very high viscosity, acceptable temperature range of the processing and good mechanical properties.

4.1 The processing features of segregated PVC/MWCNT composites

Electrical, thermal conductivity and dielectric properties of the PVC/MWCNT segregated system depending on concentration of the nanotubes in wide temperature and frequency range have been studied.

Polyvinyl chloride was used in the powder form with average size of particles of 100 μm and density of 1.37 g/cm^3. Ultrahigh molecular weight polyethylene Hostalen GUR, type GHR 8110, in a powdered form with average size of particles about 100 μm and density of 0.95 g/cm^3 was used. The multiwalled nanotubes were produced by TMSpetsmash (Ukraine) using CVD-method. The MWCNT typically had diameter b about 12-20 nm and their length l was about tens of microns (μm) that results in the value of aspect ratio l/b about 1000. Value of the nanotubes density has been taken 2.045 g/cm^3 (Lisunova et. al., 2007). The TEM image of the MWCNT is shown in Fig. 4.

Fig. 5 represents a transformation of PVC/MWCNT structure from mechanical mixture of PVC powder and CNTs (a) to hot compacted segregated composite (c). There is only one distinction compared to Fig.1, namely the presence of intermediate stage (b) that provides the even distribution of tangled CNTs on the surface of polymer grains. It is indispensable condition of the hot compacted system having perfect conductive network without aggregates. In this case one can expect to obtain the conductive composite with low value of the percolation threshold. This has been reached by preliminary solution of MWCNT in ethanol

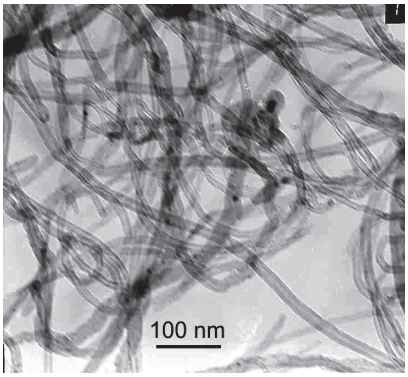

Fig. 4. TEM image of multiwalled carbon nanotubes used for preparation of the composites.

with following exposition during 20 min under ultrasonic action with frequency of 22 kHz. The sonicated MWCNT and PVC powder were homogenized by thorough grinding in a porcelain mortar to the visually homogeneous state. Homogenized composite was placed into a hot steel mold heated to 145 °C and then pressed (hot compacted) during 5 min at 20 MPa with subsequent cooling of the mold in the air flow to room temperature. The samples of pressed composites used for dielectric and electrical measurements were produced as discs with 30 mm diameter and 1-1.5 mm height.

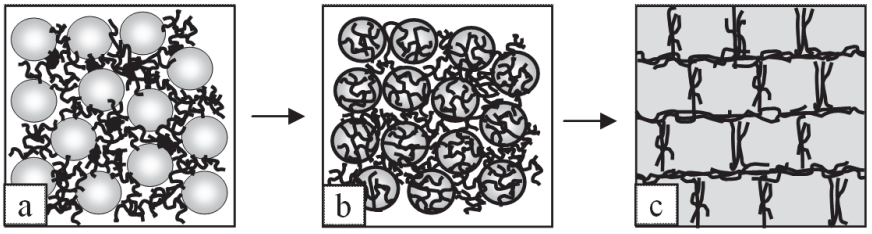

Fig. 5. A model of evolution of the PVC/MWCNT structure along a process of its forming by hot compacting method

The DC electrical conductivity was measured using a two-contact scheme. The values of DC conductivity σ_{DC} (S/cm) were estimated using the following equation:

$$\sigma = \frac{h}{R \cdot S} \tag{5}$$

where R (Ohm) is an electrical resistance measured experimentally using E6-13 teraohmmeter, and h (cm) and S (cm^2) are the thickness and area of the sample, respectively. The characterization of the dielectric parameters of the samples, such as real ε' part of the dielectric permittivity and AC conductivity σ_{AC}, were determined by means of the Novocontrol system in the frequency range from 10^{-1} Hz to 10^6 Hz at room temperature. Thermal conductivity was measured by method described in (Boudenne et al., 2004). The structure of nanotubes was examined using transmission electron microscope (TEM) Philips

CM120. The investigations of structure of the PVC/MWCNT composites were fulfilled using the scanning electron microscope (SEM) Hitachi S800 and the optical microscope Carl Zeiss Primo Star.

4.2 Structure of segregated PVC/MWCNT system

The structure of hot compacted PVC/MWCNT system was studied by optical and electron (SEM) microscopy. Figs. 6 and 7 display the segregated structure of composites. Optical microscope images of the segregated PVC/MWCNT structure are presented in Fig. 6. It shows the evolution of the composite structure along increase of the MWCNT concentration from 0.02 % that is below percolation threshold φ_c (Fig. 6-a) through 0.04 % (close to φ_c) (Fig. 6-b) to 0.07 % (above φ_c) (Fig. 6-c). One can see more pronounced boundaries between polymer grains, blackened by nanotubes, with increase of the MWCNT content that reflects a creation of the nanotubes framework.

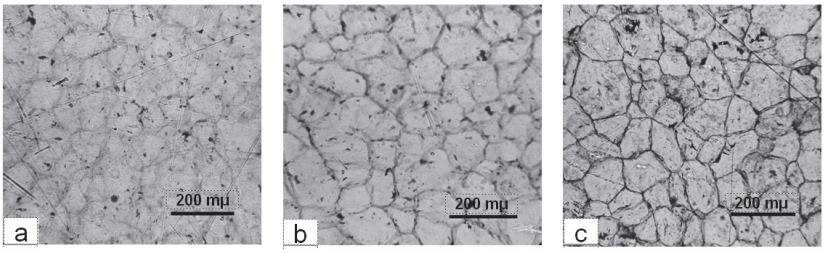

Fig. 6. Optical microscope images of segregated PVC/MWCNT composites with the MCWNT content: a - below (0.02%), b - close (0.04%) and c - above (0.07%) percolation threshold.

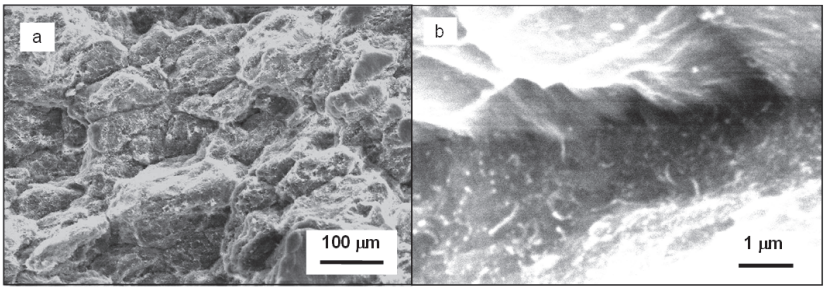

Fig. 7. SEM image of the PVC/MWCNT composite after cryogenic fracture: a – hot compacted composite, b – intergrain surface in the composite.

Hot pressing deforms polymer particles and results in formation of compacted continuous polymer phase, where conductive paths of CNTs are located on the boundaries between particles. Fig. 7 demonstrates the SEM images of PVC/MWCNT composite prepared by the fracture in liquid nitrogen. It is seen a granular structure of the polymer matrix with granules covered by nanotubes (Fig. 7-a). The presence of nanotubes on the surface between grains displays Fig. 7-b.

4.3 Electrical properties of segregated PVC/MWCNT composites

The concentration dependence of DC conductivity σ of the PVC/MWCNT composites is represented in Fig. 8. The electrical conductivity of composites abruptly increases by many orders of magnitude when the filler content φ exceeds the threshold concentration φ_c. It can be seen that the non-conducting - conducting state transition takes place at a rather small volume content of MWCNT, approximately equal to 0.05 vol. %. The electrical conductivity behavior above the percolation threshold can be described by the equation (4). In this equation the critical exponent t reflects dimensionality of the system and universality class of the problem (Stauffer & Aharony, 1992), σ_0 is an adjustable parameter. The theoretical random percolation value t is close to 2.0 for the three-dimensional system.

Insertion to Fig. 8 shows scaling of σ versus $\varphi-\varphi_c$ in the double logarithmic presentation. Line corresponds to the least square fitting of the experimental data with φ_c=0.00047. The slope of this line gives t=3.3; this values exceeds the theoretically predicted value t≈2.0. This effect can be explained by non-statistical ordered distribution of conductive phase in the polymer matrix since value t≈2 is provided by random (statistical) distribution of conductive particles in non-conductive medium (Stauffer & Aharony, 1992). As it is seen in Fig. 8, dependence of electrical conductivity on the content of nanotubes in PVC/MWCNT composites demonstrates very low value of the percolation threshold φ_c=0.00047 (≈0.05 vol. %). The high anisotropy of the MWCNT with aspect ratio $l/b \approx 1000$ is one of the reasons of such effect. Higher aspect ratio of the filler particles leads to lower value of the percolation threshold (He & Ekere, 2004).

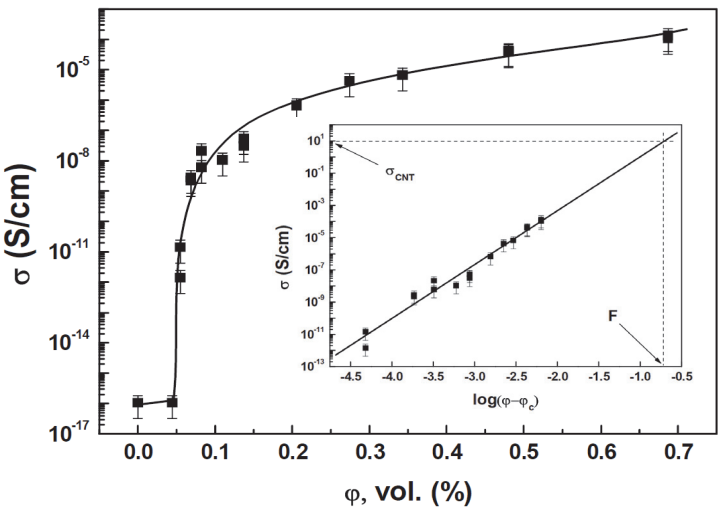

Fig. 8. Electrical conductivity σ versus volume content φ of nanotubes. The insertion presents the scaling relation $\log\sigma \sim \log(\varphi - \varphi_c)$ to fit the values of φ_c, t and σ_0.

The $\log\sigma \sim \log(\varphi - \varphi_c)$ function, used for calculation of t value enables to define the value of the packing-factor F or a limit of the composite filling for the given type of the filler. Extrapolation of this function to σ_f equal to 10.0 S/cm (*i.e.* to the conductivity of MWCNT) gives us the value of $\varphi = F$ (insertion in Fig. 8). The value of σ_f =10.0 S/cm was obtained

using a method of the fillers conductivity measurement described in ref. (Mamunya et al, 2004). The F parameter is a limit of the system filling and it is equal to the highest possible volume fraction of the filler:

$$F = \frac{V_f}{V_f + V_p} \tag{6}$$

where V_f is the volume occupied by the filler particles at the highest possible filler fraction, V_p is the volume occupied by the polymer (space among filler particles). The value of F depends on the shape of particles and their type of spatial distribution. For statistically packed monodispersed spherical particles of any size, the F value is equal to 0.64. In case of deviation of the shape of particles from the spherical one or presence of nonstatistical ordered (shell or skeleton) structure, the F value decreases with V_p increasing. The use of polydispersed filler particles results in increase of F (Kusy, 1977). Thus, F value characterizes the filler phase topology taking into account the shape, fractional size and spatial distribution of particles. The volume fraction F value, defined in such a way, is equal to 0.20 (insertion in Fig. 8). It means that the volume fraction of the MWCNT filler in a polymer can not exceed 0.20, and at φ=0.20 the composite has conductivity equal to the conductivity of the filler: $\sigma_f = \sigma_{CNT}$.

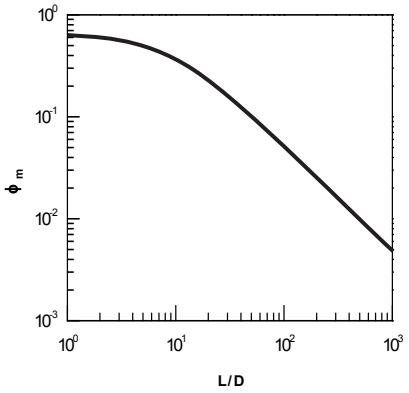

Fig. 9. The values of packing-factor versus a filler aspect ratio for its random distribution (after Bigg, 1995). Here $\phi_m = F$, $L/D = l/b$.

The value of F for nanotubes is essentially lower than 0.64 because of anisotropic shape of the MWCNT particles, as far as their high aspect ratio l/b causes their loose packing. For aligned MWCNT particles, the value of $l/b \approx 1000$. However, as MWCNT are tangled, the value of l/b has to be lower. It can be estimated from the computer simulation of the packing-factor F versus l/b, given in (Big, 1995) (Fig. 9). This plot can be described by empirical equation which relates the values of F and l/b (Lisunova et al., 2007):

$$F = \frac{5}{\frac{75}{10 + a} + a} \tag{7}$$

where $a=l/b$ (in case of very high aspect ratio a (a>>1) this relation can be rewritten as $F\approx 5/a$). Using the value of F=0.20, the eq. (7) gives a=22. Taking into account that the value of b for the MWCNT used is in the range of 10-20 nm, we can accept the average b value equal to 15 nm, which gives l = 330 nm. This value may be defined as an effective nanotube size $l = l_e$ and may be associated with the average distance between linkages of crossing nanotubes; i.e. l_e means the length of a nanotube between adjacent contact linkages with other nanotubes. Fig 4 demonstrates that this value is quite realistic.

Described above models (see section 2) predict decrease of the percolation threshold φ_{cs} in a segregated system compared with the value of φ_c for random distribution of conductive filler in the polymer matrix. The value of φ_{cs} depends on the D/d ratio under condition of D>>d, where D is size of the polymer grains (D=100 μm for the PVC used) and d is size of the filler particles. It can be determined that the value of d is equivalent to the effective size of a nanotube, *i.e.* $d = l_e$. In a segregated polymer/MWCNT system, the value of the percolation threshold can be calculated as (Lisunova et al., 2007):

$$\varphi_{cs} \approx \frac{3n}{\frac{l}{b}\cdot\frac{D}{d}} \tag{8}$$

where n is the number of layers of the filler on the boundary between polymer grains, and it is rather small: n~1. Taking into account that $l = l_e$ and $d = l_e$. (l_e = 330 nm), the value of φ_{cs} can be estimated by eq. (8). Such a calculation gives $\varphi_{cs} \approx 4.5\cdot10^{-4}$. The experimentally measured value of φ_c in the PVC/MWCNT composites is $4.7\cdot10^{-4}$, which is in excellent agreement with the theoretically estimated value of φ_{cs}. It follows from the said data that the observed ultra-low value of the percolation threshold φ_c in the PVC/MWCNT composites can be explained by both very high aspect ratio of the nanotubes and segregation of MWCNT inside the PVC matrix.

Temperature dependencies of conductivity of the PVC/MCWNT composites are shown in Fig. 10. The increase of filler content changes the form of the curves. In pure PVC and composite with 0.04 % MCWNT the conductivity increases with rise of temperature (curves 1, 2). Therefore it is possible to assume ionic character of conductivity in these systems as a growing of conductivity with temperature is the feature of ionic conductivity and is caused by rise of the ionic mobility (Margolis, 1989; Blythe & Bloor, 2005;). The temperature dependence is found to be composed of two linear regions with a bend at temperature of glass transition T_g. The transition from glassy state to high-elastic state leads to stronger dependence of conductivity on temperature that can be related to lightened ionic mobility in the polymer state with heightened molecular mobility. These dependencies are represented by Arrhenius plot in Fig. 11:

$$\sigma = \sigma_0 \exp\left(-\frac{E}{kT}\right) \tag{9}$$

where E is an activation energy, k is a Boltzmann constant. Calculation of the activation energy values for the both parts of curve gives the E values in the temperature regions higher and lower of T_g respectively: 23.0 and 2.1 kcal/mole for the pure PVC and 19.0 and 0.9 kcal/mole for the PVC/MWCNT composite with 0.04 % MWCNT.

Crossing glass transition temperature the value of activation energy sharply increases as a result of rise of the charge carrier mobility at temperature higher of T_g. Such values of the

activation energy are typical for ionic conductivity, for example the close values of E (22.0 and 3.6 kcal/mole) were found in the PVA/H_3PO_4 system (Margolis, 1989). Influence of temperature (temperature higher or lower of T_g) on the value of activation energy enables to include the segmental mobility in the charge transport process. This approach takes into consideration the change of viscosity of the polymer matrix under temperature action that, in turn, influences on the charge carriers mobility (Seanor, 1982).

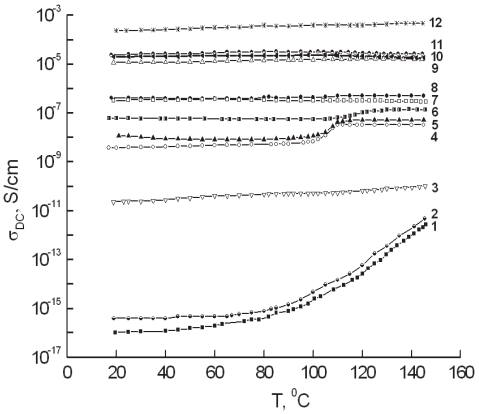

Fig. 10. Temperature dependencies of conductivity for composites with different content of filler. Content of MWCNT in the composites (vol. %): 1 – 0, 2 – 0.044, 3 – 0.054, 4 – 0.08, 5 – 0.107, 6 – 0.134, 7 – 0.201, 8 – 0.268, 9 – 0.336, 10 – 0.470, 11 – 0.672, 12 – MWCNT.

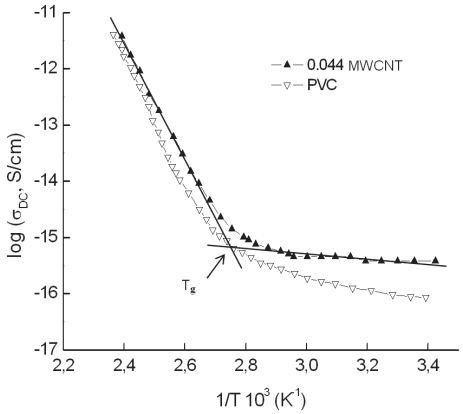

Fig. 11. Arrhenius plots for the conductivity of the pure PVC and composite with 0.044 % of MWCNT.

Even insignificant excess of the filler concentration over percolation threshold leads to the change of the conductivity character, thus at MWCNT content equal to 0.054 % the conductivity σ increases essentially and becomes almost independent on temperature (Fig. 10, curve 3). It indicates a conversion from ionic conductivity through the matrix to electronic

type of conductivity through the filler phase. Further growth of filler content causes the increase of the conductivity value and it becomes independent on temperature in the region of 20-150 °C (curves 4-11). Only the composites with MWCNT content from 0.08 to 0.134 % (curves 4-6) show weak shift of conductivity in the region 100-120 °C that is essentially higher of T_g. Measurement of the nanotubes conductivity demonstrates independence of σ on temperature (curve 12), accordingly temperature dependence of conductivity of PVC/MWNT composites has the same character since it is provided by conductivity of the filler phase.

4.4 Dielectric properties of PVC/MWCNT and UHMWPE/MWCNT systems

Fig. 12 represents dielectric constant ε' and AC conductivity σ_{AC} versus frequency. The value of ε' in the PVC/MWCNT composites with the MCWNT content 0–0.04 vol. % (i.e. lower than percolation threshold) are close and independent on frequency. This value of ε' increases and reveals a negative slope if the filler content exceeds the percolation threshold.
The frequency dependence of dielectric parameters in two-phase conductive-insulating system can be considered with two models, such as intercluster polarization (IP) that implies polarization effects between clusters inside percolation system or anomalous diffusion (AD) within cluster (Song et al., 1986; Yoon & Lee, 1990; Youm & Lee, 1991). The IP model predicts the power-law dependence of ε' and σ_{AC} on the frequency that may be written as follows:

$$\varepsilon'(\omega) \propto \omega^{-y} \tag{10}$$

$$\sigma(\omega) \propto \omega^{x} \tag{11}$$

$$x + y = 1 \tag{12}$$

where $y = s/(t + s)$ and $x = t/(t + s)$. The critical exponents, x and y, have to satisfy the condition (12). In the case of three-dimensional lattice the critical exponents t and s are: $t \approx 2$, $s \approx 0.8$ (Stauffer & Aharony, 1992) that gives the values of x and y equal to 0.72 and 0.28 respectively.

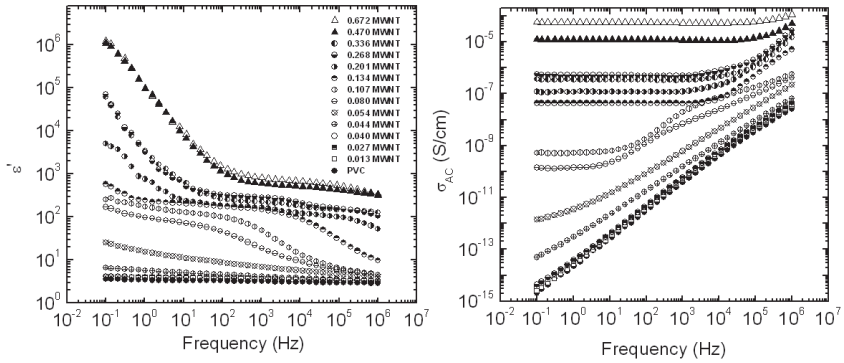

Fig. 12. Frequency dependencies of dielectric constant ε', and AC conductivity σ_{AC} for the composites with different MWNT content.

In the AD model the values of x and y are equal to 0.58 and 0.42 respectively for three dimensions. For the conductive PVC/MWCNT composites with MWCNT content in the range of 0.08–0.134 % the average value of y (calculated for the 10^{-1}–10^{2} Hz frequency range) is found to be 0.18, which is lower than the theoretically predicted value.

Plot of conductivity versus frequency in a double logarithmic scale (Fig. 12) shows two cases of the frequency dependence of AC conductivity σ_{AC}: (a) below percolation threshold the values of σ_{AC} of the composites are overlapping and the curves have average slope close to 1, which indicates the highly insulating material (McLachlan et al., 2005); (b) above φ_c the conductivity is constant at low frequency due to contribution of DC conductivity. The average slope of curves at higher frequencies is 0.91 that exceeds the theoretically predicted value of critical exponent x=0.72. One can consider satisfactory fulfilling the general scaling relation (10), the measured values are $x+y$=1.09. Thus the experimental results are closer to the IP model than to the AD model. Note that in (Song et al., 1986; Yoon & Lee, 1990; Youm & Lee, 1991) the critical exponents x and y do not agree separately with the theoretical predictions but general scaling law (10) is satisfactorily fulfilled. For PE/MWCNT composites the authors (Liang & Tjong, 2006) have found an agreement of the experimental values of critical exponents with the theoretical prediction by power low relations (10)-(12).

For higher concentration of the filler in the composites (in the range of 0.201–0.672%) the values of ε' grow drastically. The reason of such an effect can be an electrode polarization that leads to a separation of charges which gives an additional contribution to the polarization. It occurs for moderately to highly conductive systems and results in extremely high values of the real and imaginary part of the complex dielectric permittivity (Kremer & Schonhals, 2003). In fact Fig. 12 demonstrates the presence of very high ε' values equal to 10^{5}-10^{6} in the range of low frequencies 10^{-1}-10^{0} Hz for the samples with filler concentration above 0.201%.

The comparison of conductivity and dielectric parameters (ε' and tan δ) versus MWCNT content in PVC/MWCNT and UHMWPE/MWCNT segregated systems is presented in Fig. 13. Dependence of electrical conductivity on the nanotubes content in the PVC/MWCNT and UHMWPE/MWCNT composites demonstrates very low values of the percolation threshold, equal to 0.00047 (≈0.05 vol. %) and 0.00036 (≈0.04 vol. %), respectively. It is a result both, of high anisotropy of MWCNT with aspect ratio length/diameter ≈1000 and of segregated distribution of CNT in the polymer matrix. It is interesting that the φ_c value is lower for UHMWPE/MWCNT composite although the geometrical parameters for both of composites are identical.

Dielectric characteristics, measured at fixed frequency 1 kHz, demonstrate the percolation behaviour as well (Fig. 13). In the region above percolation threshold φ_c the sharp increase of ε' and tan δ takes place, after that the values of dielectric parameters rich the plateau. Such behavior is predicted by model for two-phase insulating/conducting systems and was observed in polymer/dispersed metal composites (Mamunya et al., 2002c). Rise of ε' in the region above percolation threshold was observed for the LDPE/MWCNT composites in (Liang & Tjong, 2006). It is necessary to note that some differences for PVC/MWCNT and UHMWPE/MWCNT composites exist. The value of ε' on the plateau is an order of magnitude higher for UHMWPE/MWCNT than for PVC/MWCNT. Probably it is caused by heightened conductivity of UHMWPE/MWCNT composite which is ten times higher than in PVC/MWCNT composite for samples with maximal content of MWCNT. The reason of such features is not clear since the geometry of conductive phase (the values of D and ratio D/d) is the same for both of composites.

It is seen from Fig. 13 that the interval of tan δ alteration with change of MWCNT content is much wider for UHMWPE/MWCNT composites. The maximal values of tan δ are approximately equal for both of composites while initial value of tan δ for UHMWPE is two orders of magnitude lower than for PVC. It is known that polyethylene is a polymer with one of lowest values of dielectric losses. Very small content of carbon nanotubes that is slightly higher of the φ_c value leads to sharp increase of dielectric losses. Probably it can be caused by creation of segregated structure of CNT in the volume of hot compacted composite that forms "shielding framework" of conductive phase for the electromagnetic flow. Such ability is promising for creation of shielding materials for electromagnetic irradiation.

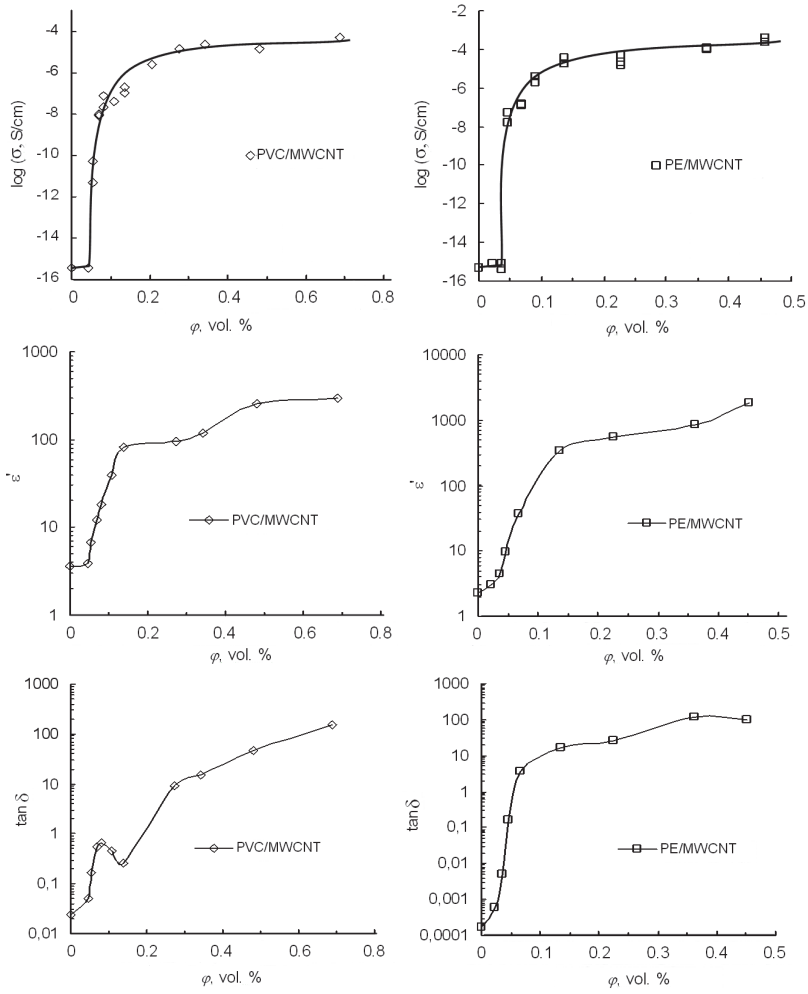

Fig. 13. Dependence of conductivity σ, dielectric constant ε' and loss-factor tan δ on MWCNT content for the PVC/MWCNT and UHMWPE/MWCNT composites.

A very low concentration of MWCNT in the composites and a specific type of their distribution as the segregated nanotube shell structure remains most part of the polymer in the neat state within framework. Consequently, one could expect the dielectric properties of polymer/MWCNT composites close to those ones in the unfilled polymer. However, the experimental data reveal very high contribution of conductive phase in the dielectric response. We can assume that majority of nanotubes creating the framework takes part in conductivity due to their high local concentration φ_{loc} in the shell whereas in usual statistical conductive clusters only small part of particles creates a conductive skeleton (Feder, 1988), and the rest ones are dead ends and non-conductive side branches.

4.5 Thermal conductivity of PVC/MWCNT composites

The thermal conductivity values of PVC/MWCNT composites and their associated uncertainties are plotted in Fig. 13 versus MWCNT volume content φ. The variation of k can be separated into three regions. For very low concentrations (φ < 0.05 vol. %), we observe a drop of the thermal conductivity. This decrease of k represents about 6 % of the thermal conductivity of the PVC matrix. Then, for concentrations 0.05 < φ< 0.14 vol. %, a rapid increase of the thermal conductivity is observed. Finally, for the highest concentrations (φ > 0.14 vol. %), the thermal conductivity increases linearly upon the MWCNT volume fraction. Dependence of the thermal conductivity k on the volume content of filler is not monotonous and reaches a minimum at $\varphi \approx 0.05$ vol. %, which coincides with the percolation threshold value φ_c. However, in our opinion, creation of an infinite conductive cluster of fillers at $\varphi = \varphi_c$ can not be a reason for decrease of the thermal conductivity values. The progressive introduction of filler into the polymer matrix is accompanied by two opposite effects influencing heat transport in the composite. First is appearance of a surface of a new phase and, correspondingly, of an interfacial layer, in which the phonon scattering tends to reduce

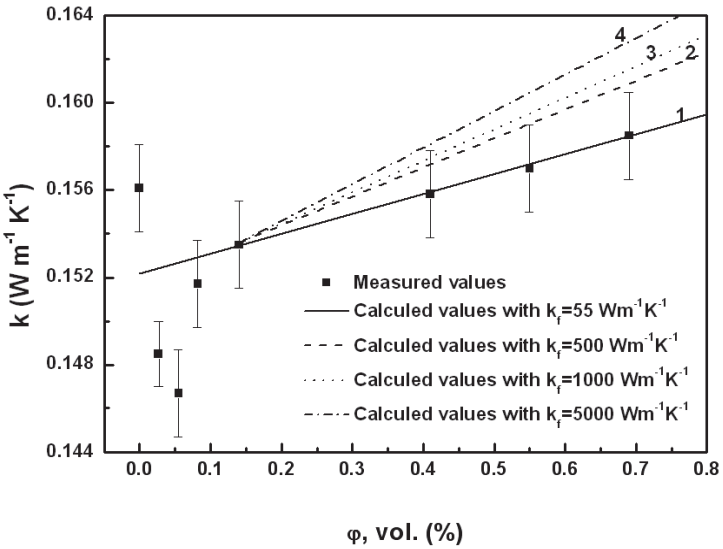

Fig. 13. Thermal conductivity of composites as a function of MWCNT concentration. Lines are calculated in accordance with eq. (13).

the heat flow transport, thus resulting in the interfacial resistance. Second effect is the presence of the volume of a new phase with high thermal conductivity, which results in increase of the heat flow. Our results (Fig. 13) demonstrate that the first effect is predominant at low filler concentrations ($\varphi < \varphi_c$). Then, increase of the MWCNT content at $\varphi > \varphi_c$ leads to prevalence of the second effect, and we can observe increase of the thermal conductivity due to additional heat transfer through the filler phase (Mamunya et al., 2008).
Indeed, in spite of a small content of filler in the polymer matrix at $\varphi < \varphi_c$, the presence of the filler can noticeable influence the heat transport owing to high specific surface of the CNTs (~ 190 m^2/g). As it was shown in (Mamunya et al.., 2002b; Lebovka et al., 2006), conductive behaviour appears at $\varphi = \varphi_c$ in the segregated system, where each polymer particle is covered by one layer of filler particles and even not full covering is possible (Kusy, 1977). In this model, the filler creates a shell inside the polymer matrix with thickness of one filler particle. In our case, according to this model, the MWCNT are forming, a "shielding framework" with developed surface for the heat flow at $\varphi < \varphi_c$, which transforms into "conductive framework" at $\varphi = \varphi_c$. Thus, the presence of a segregated structure of MWCNT in the polymer matrix is most probable for coincidence of the minimum of k variation with φ_c value. It is necessary to note that decrease of k at low filler content was also observed by Moisala et al., 2006 and Grunlan et al.., 2006, respectively, for epoxy resin and poly(vinyl acetate) latex filled with SWCNT. These authors explained this phenomenon by the presence of very high interfacial resistance to the heat flow, associated with poor phonon coupling between nanotubes and the polymeric matrix.
Comparison of dependencies of the PVC/MWCNT electrical conductivity σ and thermal conductivity k against MWCNT concentration demonstrates their different character. Particular feature of electrical conductivity is the presence of a percolation threshold φ_c. Formation of an infinite conductive cluster leads to sharp increase of the conductivity by many orders of magnitude starting from $\varphi = \varphi_c$. The thermal conductivity k exhibits no percolation behaviour. The $k = f(\varphi)$ is a monotonous function, with the exception of minimum, which was discussed above. The reasons for such a difference were analyzed in (Shenogina et al., 2005), where it was found that large difference between thermal conductivity ratio k_f/k_p and electrical conductivity ratio σ_f/σ_p (where k_f, σ_f are conductivities of the filler and k_p, σ_p are conductivities of the polymer matrix) might explain this effect. In fact, transport of electrical charges takes place only along the filler phase without contribution of the polymer matrix. Therefore, such transport critically depends on the presence of percolation and formation of the conductive clusters. By contrast, thermal conductivity always involves the polymer matrix in the heat transport. As far as thermal conductivities of the filler and polymer phases are comparable, it leads to insensitivity of the thermal conductivity to formation of the conductive cluster. Besides, the authors (Shenogina et al., 2005) considered the presence of a large interfacial thermal resistance in the filled systems as a one more reason for the lack of percolation in the thermal conductivity behaviour.
Experimental results presented in Fig. 13 show that starting from 0.14 vol. % of MWCNT, the thermal conductivity slowly rises with increase of the filler content. For two-phase systems, the concentration dependence of the thermal conductivity can be described by a large number of equations (Progerlhof et al., 1976). All of them lie within the interval between the largest thermal conductivity $k_\parallel$ (when the system is represented by a parallel set of plates extended in direction of the heat flow):

$$k_{//} = k_f \varphi + k_P (1 - \varphi) \tag{13}$$

to the smallest thermal conductivity $k_\perp$ (when the plates are stacked in series in a plane perpendicular to direction of the heat flow):

$$\frac{1}{k_\perp} = \frac{\varphi}{k_f} + \frac{(1-\varphi)}{k_P} \tag{14}$$

The thermal conductivity of real two-phase systems lies within the interval between functions (13) and (14) and can not be higher than $k_{//}$ or lower than $k_\perp$. In our computations, we have taken $k_P = k$ (φ = 0.14 %) as the thermal conductivity value of the matrix. Using of eq. (13) for calculation of the concentration dependence of k for PVC/MWCNT composites gives good agreement with experimental results if we choose k_f = 1.07 Wm^{-1} K^{-1}; however, this value is unacceptable for thermal conductivity of the MWCNT. The values of k calculated using eq. (14) lie lower than experimental points whatever values of k_f. Hence, these boundary relations are not suitable for prediction of the value of thermal conductivity k_f of MWCNT.

Some authors (Nan et al., 2003) have proposed a simple equation for description of $k = f(\varphi)$ in the case of oil suspension/CNT systems with low content of CNTs ($\varphi \leq 1\%$):

$$k = k_p + \frac{\varphi \cdot k_f}{3} \tag{15}$$

Eq. (15) fits our experimental data quite well if the value of k_f is equal to 2.7 $Wm^{-1}K^{-1}$; this value is also too low. In ref. (Mamunya et al., 2002b) it has been shown that the Lichtenecker's equation is suitable for description of the thermal conductivity of the filled systems:

$$\log k = (1 - \varphi) \log k_p + \varphi \log k_f \tag{16}$$

The thermal conductivity of PVC/MWCNT composites, calculated according to eq. (16), is plotted in Fig. 13 for several k_f values. Line 1 was computed using k_f = 55 $Wm^{-1}K^{-1}$. It can be seen that this function is in quite good agreement with experimental data. Such value of the filler conductivity k_f is lower than the one predicted for carbon nanotubes as k_f = 3000 $Wm^{-1}K^{-1}$ for MWCNT and 6000 $Wm^{-1}K^{-1}$ for SWCNT (Berber et al., 2000), and even lower than the thermal conductivity of bulk graphite k_g = 209 $Wm^{-1}K^{-1}$ (Agari et al., 1985, 1987).

Lines 2, 3 and 4 in Fig. 13 represent data calculated according to eq. (14) for k_f = 500 $Wm^{-1}K^{-1}$, used for the oil suspension/CNT systems (Nan et al., 2003; Xue, 2005) and for higher values of k_f (1000 and 5000 $Wm^{-1}K^{-1}$), which were predicted for carbon nanotubes. In the last three cases, a big divergence between predictions and experimental data is observed. It is necessary to note that experimental measurements were carried out within the range of low concentrations of MWCNT (less than 1 vol.%) and we extrapolated the calculated values to φ = 100 vol. %, in order to predict the value of k_f; so such prediction is rather approximate. Moreover, it was shown in (Huang et al., 2005), that when MWCNT within the polymer matrix are aligned in direction of the heat flow, the thermal conductivity of such a composite is essentially higher than for the system with dispersed MWCNT. The value of

the thermal conductivity of aligned MWCNT array was determined as $k_f \geq 160$ $Wm^{-1}K^{-1}$, which is close to conductivity of the graphite.

5. Conclusion

Investigation of electrical conductivity σ_{DC} of the PVC/MWCNT and UHMWPE/MWCNT composites depending on MWCNT content revealed the ultralow values of percolation threshold, φ_c = 0.00047 (≈0.05 vol. %) and φ_c = 0.00036 (≈0.04 vol. %), respectively. It is caused by two reasons: high anisotropy of MWCNT with aspect ratio length/diameter ~1000 and the presence of segregated structure of MWCNT within polymer matrix with distribution of nanotubes on the boundaries between polymer grains. The geometrical shell structure model predicts the value of percolation threshold which is in excellent agreement with the experimental values.

Frequency dependence of the dielectric parameters ε' and conductivity σ_{AC} demonstrates different behavior below and above percolation threshold. Interfacial polarization gives a contribution to the complex dielectric permittivity $\varepsilon=\varepsilon'-i\varepsilon''$ that is resulted in the increasing of ε' with the decreasing of frequency ω. Power law dependencies $\varepsilon' \propto \omega^{y}$ and $\sigma \propto \omega^{x}$ were observed in the range of low frequencies that corresponds to an approach of the intercluster polarization (IP) model. At fixed frequency the values of the dielectric parameters ε' and tan δ revealed the percolation behavior with identical value of the percolation threshold to φ_c obtained by measurements of DC conductivity.

The thermal conductivity k does not reveal any percolation behaviour in the vicinity of electrical percolation concentration $\varphi = \varphi_c$ but exhibits minimum in this region. This effect can be explained by running of two opposite processes: first, the presence of interfacial resistance to heat flow on the polymer-MWCNT boundary that decreases the values of k; and a subsequent increase of the heat flow due to appearance of a noticeable concentration of the filler phase with high thermal conductivity. Lichtenecker's equation allowed to predict the value of the thermal conductivity of MWCNT, k_f = 55 $Wm^{-1}K^{-1}$. This value is much lower than the theoretically predicted one for nanotubes $k_f = 10^3 - 10^4$ $Wm^{-1}K^{-1}$. In the polymer materials filled with conductive particles, both polymeric and filler phases always take part in the heat transport. So, the thermal conductivity value of such a system depends on relative concentrations of the polymer and filler.

6. Acknowledgment

My deep gratitude to doctorant V.V. Levchenko for his help in preparation of the manuscript.

7. References

Agari, Y. & Uno, T. (1985). Thermal conductivity of polymer filled with carbon materials: effect of conductive particle chains on thermal conductivity. *J. Appl. Polym. Sci.*, Vol. 30, pp. 2225-2335.

Agari, Y.; Tanaka, M. & Nagai, S. (1987). Thermal conductivity of a polymer composite filled with mixtures of particles. *J. Appl. Polym. Sci.*, Vol. 34, pp. 1429-1437.

Baibarac, M. & Gomez-Romero, P. (2006). Nanocomposites based on conducting polymers and carbon nanotubes from fancy materials to functional applications. *J. Nanosci. Nanotechn.*, Vol. 6, No 1, pp. 1–14, ISSN 1533-4880.

Berber, S.; Kwon, Y.K. & Tomanek, D. (2000). Universally high thermal conductivity of carbon nanotubes. *Phys. Rev. Lett.*, Vol. 84, No 20, pp. 4613-4616.

Bhattacharya, S.K., Basu, S. & De, S.K. (1978). Effect of size, shape and oxide content of metal particles on the formation of segregated networks in PVC composites. *Composites*, Vol. 9, No 3, pp. 177-183.

Big, D.M. (1995). Thermal conductivity of heterophase polymer compositions. In *Thermal and electrical conductivity of polymer materials*. Y.K. Godovsky & V.P. Privalko, (Eds.), Springer, *Adv. Polym. Sci.*, Vol. 119, pp.1-30.

Blythe, T. & Bloor, D. (2005). *Electrical properties of polymers*. Cambridge University Press, ISBN 0-521-55219-2, Cambridge, GB.

Boudenne, A.; Ibos, L.; Gehin, E. & Candau, Y. (2004). A simultaneous characterization of thermal conductivity and diffusivity of polymer materials by a periodic method. *J. Phys. D: Appl. Phys.*, Vol. 37, pp.132–139.

Boushet, J.; Carrot, C.; Guillet, J.; Boiteux, G.; Seytre, G. & Pinneri, M. (2000). Conductive composites of UHMWPE and ceramics based on the segregated network concept. *Polym. Eng. Sci.*, Vol. 40, No 1, pp. 36-46.

Breuer, O. & Sundararaj, U. (2004). Big returns from small fibers: A review of polymer/carbon nanotube composites. *Polym. Compos.*, Vol. 25, No 6, pp. 630-645.

Bridge, B., Folkes, M.J. & Wood, B.R. (1990). Investigation into the DC conductivity of colloidally dispersed gold/polymer composites. *J. Phys. D: Appl. Phys.*, Vol. 23, pp. 890-898, ISSN 0022-3727/90/070890.

Chan, C.-M.; Cheng, C.-L. & Yuen M.M.F. (1997). Electrical properties of polymer composites prepared by sintering a mixture of carbon black and ultra-high molecular weight polyethylene powder. *Polym. Eng. Sci.*, Vol. 37, No 7, pp. 1127-1136.

Chiteme, C. & Mclachlan, D.S. (2000). Measurements of universal and non-universal percolation exponents in macroscopically similar systems. *Physics,* Vol. B279, pp. 69-71, ISSN 0921-4526/00.

Du, J.; Zhao, L.; Zeng, Y.; Zhang, L.; Li, F.; Liu, P. & Liu, C. (2011). Comparison of electrical properties between multi-walled carbon nanotube and graphene nanosheet/high density polyethylene composites with a segregated network structure. *Carbon*, Vol. 49, No 4, pp. 1094-1100.

Feder, J. (1988). *Fractals*. Plenum Press, ISBN 0-306-42851-2, New York.

Foulger, S.H. (1999). Electrical properties of composites in the vicinity of the percolation threshold. *J. Appl. Polym. Sci.*, Vol. 72, pp. 1573-1582.

Gao, J.-F.; Li, Z.-M.; Meng, Q. & Yang, Q. (2008). CNTs/ UHMWPE composites with a two-dimensional conductive network. *Mater. Lett.*, Vol. 62, pp. 3530–3532, ISSN 0167-577X.

Grossiord, N.; Wouters, M.E.L.; Miltner, H.E.; Lu, K.; Loos, J.; Van Mele, B. & Koning, C.E. (2010). Isotactic polypropylene/carbon nanotube composites prepared by latex

technology: Electrical conductivity study. *Europ. Polym. J.*, Vol. 46, pp. 1833–1843, ISSN 0014-3057.

Grunlan, J.C.; Gerberich, W.W. & Francis L.F. (2001). Lowering the percolation threshold of conductive composites using particulate polymer microstructure. *J. Appl. Polym. Sci.,* Vol. 80, pp. 692-705.

Grunlan, J.C.; Mehrabi, A.R.; Bannon, M.V. & Bahr, J.L. (2004). Water-based single-walled-nanotube –filled polymer composite with an exceptionally low percolation threshold. *Adv. Mater.* Vol. 16, No 2, pp. 150–153.

Grunlan, J.C.; Kim, Y-S; Ziaee, S.; Wei, X.; Abdel-Magid, B. & Tao, K. (2006). Thermal and mechanical behavior of carbon-nanotube-filled latex. *Macromol. Mater. Eng.,* Vol. 291, pp. 1035–1043.

Ha, M.L.P.; Grady, B.P.; Lolli, G.; Resasco, D.E. & Ford, W.T. (2007). Composites of single-walled carbon nanotubes and styrene-isoprene copolymer latices. *Macromol. Chem. Phys.*,Vol. 208, pp. 446–456.

Hao, X.; Gai, G.; Yang, Y.; Zhang, Y. & Nan, C. (2008). Development of the conductive polymer matrix composite with low concentration of the conductive filler. *Mater. Chem. & Phys.*, Vol.109, pp. 15–19, ISSN 0254-0584.

He, D. & Ekere, N.N. (2004). Effect of particle size ratio on the conducting percolation threshold of granular conductive-insulating composites. *J. Phys. D: Appl. Phys.*, Vol. 37, pp. 1848-1852.

Huang, H.; Liu, C.; Wu, Y. & Fan, S. (2005). Aligned carbon nanotube composite films for thermal management. *Adv. Mater.*, Vol. 17, pp. 1652-1656.

Kim, Y. S.; Wright, J. B. & Grunlan J. C. (2008). Influence of polymer modulus on the percolation threshold of latex-based composites. *Polymer*, Vol. 49, pp. 570-578.

Kremer, F. & Schonhals, A. (Eds.). (2003). *Broadband dielectric spectroscopy*.: Springer-Verlag, ISBN 3-540-43407-0, Berlin-Heidelberg, Germany.

Kusy, R.P. (1977). Influence of particle size ratio on the continuity of aggregates. *J. Appl. Phys.*, Vol. 48, No 12, pp. 5301-5305.

Kusy R.P. (1986). Applications. In: *Metal-filled polymers. Properties and applications.* S.K. Bhattacharya, (Ed.), 1–143, Marcel Dekker Inc., New York and Basel.

Kusy, R.P. & Corneliussen R.D. (1975). The thermal conductivity of nickel and copper dispersed in poly(vinyl chloride). *Polym. Eng. Sci.*, Vol. 15, No 2, pp. 107-112.

Lebovka, N.; Lisunova, M.; Mamunya, Ye.P. & Vygornitskii N. (2006). Scaling in percolation behaviour in conductive-insulating composites with particles of different size. *J. Phys. D: Appl. Phys.*, Vol. 39, No 1, pp. 1-8, ISSN 0022-3727/06/010001.

Liang, G.D. & Tjong S.C. (2006). Electrical properties of low-density polyethylene/multiwalled carbon nanotube composites. *Mater. Chem. Phys.*, Vol. 100, pp. 132-137.

Lisunova, M.O.; Mamunya, Ye.P.; Lebovka, N.I. & Melezhyk, A.V. (2007). Percolation behaviour of ultrahigh molecular weight polyethylene/multi-walled carbon nanotubes composites. *Europ. Polym. J.*, Vol. 43, pp. 949-958.

Lux, F. (1993). Review. Models proposed to explain the electrical conductivity of mixtures made of conductive and insulating materials. *J. Mater. Sci.*, Vol. 28, pp. 285-301, ISSN 0022-2461.

Malliaris, A. & Turner, D.T. (1971). Influence of particle size on the electrical resistivity of compacted mixtures of polymeric and metallic powders. *J. Appl. Phys.*, Vol. 42, No 2, pp. 614-618.

Mamunya, Ye.P.; Muzychenko, Yu.V.; Pissis, P.; Lebedev, E.V. & Shut, M.I. (2002a). Percolation phenomena in polymers containing dispersed iron. *Polym. Eng. Sci.*, Vol. 42, No 1, pp. 90-100.

Mamunya, Ye.P.; Davydenko, V.V.; Pissis, P. & Lebedev E.V. (2002b). Electrical and thermal conductivity of polymers filled with metal powders. *Europ. Polym. J.*, Vol. 38, pp.1887-1897, ISSN 0014-3057.

Mamunya, Ye.P.; Davydenko, V.V.; Zois, H.; Apekis, L.; Snarskii, A.A. & Slipchenko, K.V. (2002c). Dielectric properties of polymers filled with dispersed metals. *Polym. & Polym. Compos.*, Vol. 10, No 3, pp. 219-228.

Mamunya, Ye.P.; Zois, H.; Apekis, L. & Lebedev, E.V. (2004). Influence of pressure on the electrical conductivity of metal powders used as fillers in polymer composites, *Powd. Technol.*, Vol. 140, pp. 49-55.

Mamunya, Ye.; Boudenne, A.; Lebovka, N.; Ibos, L.; Candau, Y. & Lisunova, M. (2008). Electrical and thermophysical behaviour of PVC-MWCNT nanocomposites. *Compos. Sci. Techn.*, Vol. 68, pp. 1981–1988, ISSN 0266-3538.

Margolis, J.M. (Ed.). (1989). *Conductive polymers and plastics*. Chapman and Hall, ISBN 0-412-01431-9, NewY ork.

McLachlan, D.S.; Chiteme, C.; Park, C.; Wise, K.E.; Lowther, S.E.; Lillehel, P.T.; Sioshi, E.J. & Harrison, J.S. (2005). AC and DC percolative conductivity of single wall carbon nanotube polymer composites. *J. Polym. Sci.: Part B: Polym. Phys.*, Vol. 43, pp. 3273-3287.

Mierczynska, A.; Friedrich, J.; Maneck, H. E.; Boiteux, G. & Jeszka, J. K. (2004). Segregated network polymer/carbon nanotubes composites. *Centr. Europ. J. Chem.*,,Vol. 2, No 2, pp. 363-370.

Mierczynska, A.; Mayne-L'Hermite, M.; Boiteux. G. & Jeszka, J. K. (2007). Electrical and mechanical properties of carbon nanotube/ultrahigh-molecular-weight polyethylene composites prepared by a filler prelocalization method. *J. Appl. Polym. Sci.*, Vol. 105, pp. 158–168.

Miriyala, S.M.; Kim, Y.S.; Liu, L. & Grunlan, J. C. (2008). Segregated networks of carbon black in poly(vinyl acetate) latex: influence of clay on the electrical and mechanical behavior. *Macromol. Chem. Phys.*, Vol. 209, pp. 2399–2409.

Mittal, V. (Ed.). (2010). *Polymer nanotube composites. Synthesis, properties, and applications*. Wiley & Scrivener Publishing, ISBN 978-0-470-62592-7, New Jersey & Massachusetts.

Moisala, A.; Li, Q.; Kinloch, I.A. & Windle A.H. (2006). Thermal and electrical conductivity of single- and multi-walled carbon nanotube-epoxy composites. *Comp. Sci. Tech.*, Vol. 66, pp. 1285–1288.

Moniruzzaman, M. & Winey, K.I. (2006). Polymer nanocomposites containing carbon nanotubes, *Macromolecules*, Vol. 39, pp. 5194-5205.

Progerlhof, R.C.; Throne, J.L. & Ruetch, R.R. (1976). Methods for predicting the thermal conductivity of composite systems: a review. *Pol. Eng. Sci.*, Vol. 16, pp. 615-625.

Nan, C-W.; Shi, Z. & Lin, Y. (2003). A simple model for thermal conductivity of carbonanotube-based composites. *Chem. Phys. Lett*., Vol. 375, pp. 666–669.

Popov, V.N. (2004). Carbon nanotubes: properties and application. *Mater. Sci. Eng*., Vol. 43R, pp. 61-102.

Privalko, E.G., Mamunya, E.P., Lebedev, E.V., Privalko, V.P., Balta Calleja, F.J. & Pissis P. (2000). Structure-dependent microhardness of metal-filled polyvinyl chloride composites. *Dopovidi of National Academy of Sciences of Ukraine*, No 5, pp. 159-162.

Rajesh; Ahuja,T. & Kumar, D. (2009). Recent progress in the development of nano-structured conducting polymers/nanocomposites for sensor applications. *Sensors and Actuators,* Vol. B136, pp. 275–286, ISSN 0925-4005.

Ramirez A.P. (2005). Carbon nanotubes for science and technology. *Bell Labs Techn. J*., Vol. 10, No 3, pp. 171-185.

Seanor, D.A. (Ed.) (1982). *Electrical properties of polymers.* Academic Press, ISBN 0-12-633680-6, New York.

Shenogina, N.; Shenogin, S.; Xue, L. & Keblinski, P. (2005). On the lack of thermal percolation in carbon nanotube composites. *Appl. Phys. Lett.,* Vol. 87, pp. 133106/1-133106/3.

Simien D.; Fagan, J.A.; Luo, W.; Douglas, J.F.; Migler, K. & Obrzut J. (2008). Influence of nanotube length on the optical and conductivity properties of thin single-wall carbon nanotube networks. *ACS Nano*, Vol. 2, No 9, pp.1879-1884.

Song, Y.; Noh, T.W.; Lee, S-I. & Gaines, J.R. (1986). Experimental study of three-dimensional ac conductivity and dielectric constant of a conductor-insulator composite near the percolation threshold. *Phys. Rev*., Vol. B33, pp. 904-908.

Spitalsky, Z.; Tasis, D.; Papagelis, K. & Galiotis, C. (2010). Carbon nanotube–polymer composites: Chemistry, processing, mechanical and electrical properties. *Progr. Polym. Sci.,* Vol. 35, No 3, pp. 357-401, ISSN 0079-6700.

Stauffer, D. & Aharony, A. (1992). *Introduction to Percolation Theory*. Taylor and Francis, London, GB.

Thostenson, E.T.; Ren, Z. & Chou, T-W. (2001). Advances in the science and technology of carbon nanotubes and their composites: a review. *Compos. Sci. Techn.,* Vol. 61, pp. 1899-1912.

Vandervorst, P.; Lei, C.-H.; Lin, Y.; Dupont, O.; Dalton, A.B.; Sun, Y.-P. & Keddie, J.L. (2006). The fine dispersion of functionalized carbon nanotubes in acrylic latex coatings. *Progr. in Org. Coat.,* Vol. 57, pp. 91–97, ISSN 0300-9440.

Xue, Q.Z.(2005). Model for thermal conductivity of carbon nanotube-based composites. *Physica, B*, Vol. 368, pp. 302–307.

Yacubowicz, J.; Narkis, M. & Benguigui, L. (1990a). Electrical and dielectric properties of segregated carbon black-polyethylene systems. *Polym. Eng. Sci*., Vol. 30, No 8, pp. 459-468.

Yacubowicz, J.; Narkis, M. & Kenig, S. (1990b). Dielectric and magmetic properties of random and segregated ferrite polystyrene composites. *Polym. Eng. Sci*., Vol. 30, No 8, pp. 469-475.

Yoon, C.S. & Lee, S-I. (1990). Measurement of the ac conductivity and dielectric constant in a two-dimensional lattice percolation system. *Phys. Rev*., Vol. B42, pp. 4594-4597.

Youm, K.H. & Lee, S-I. (1991). AC conductivity and dielectric constant in a two-dimensional swiss cheese percolation system. *Solid State Comm.*, Vol. 79, pp. 1069-1072.

Youngs, I. J. (2003). A geometric percolation model for non-spherical excluded volumes. *J. Phys. D: Appl. Phys.* Vol. 36, pp. 738–747, ISSN 0022-3727/03/060738.

Yu, C.; Kim, Y.S.; Kim, D. & Grunlan, J.C. (2008). Thermoelectric behavior of segregated-network polymer nanocomposites. *Nano Lett.*, Vol. 8, No 12, pp. 4428-32.

Zhang, C; Ma, C-A; Wang, P. & Sumita, M. (2005). Temperature dependence of electrical resistivity for carbon black filled ultra-high molecular weight polyethylene composites prepared by hot compaction. *Carbon*, Vol. 43, pp. 2544-2553, ISSN 0008-6223.

10

Conductivity Percolation of Carbon Nanotubes in Polyacrylamide Gels

Önder Pekcan and Gülşen Akın Evingür
Kadir Has University,
İstanbul Technical University,
Turkey

1. Introduction

Polymer composites can be used in many different forms in various areas ranging from structural units in the construction industry to the composites of the aerospace applications. The extraordinary properties of carbon nanotubes make them very promising and favorable as fillers for fabrication of a new class of polymeric heterostructures. Polymer matrices have been widely exploited as a medium for carbonnanotubes (CNTs) which have been described as effective conducting fillers for polymers. Nanotubes can be described as long and slender fullerenes, in which the walls of the tubes are hexagonal carbon (graphite structure). There are two main types of carbon nanotubes (CNT) known as single (SWCNT) and multiwalled (MWCNT). Since the discovery of carbon nanotubes (CNT) in 1991 by lijima (lijima, 1991), single- wall carbon nanotubes (SWNT) and multiwalled carbon nanotubes (MWNT) have attracted great interests throughout the academic and industrial applications. Therefore, many researchers are focused on the development of CNT-based polymer materials that utilize the carbon nanotubes characteristics and properties, such as the high strength and stiffness of the CNTs are used for developing superior polymer composites for structural applications which are lighter, stronger, and tougher than any polymer-based material. There are several important requirements for an effective improvement of CNT-based composites' properties, such as: a large aspect ratio of a filler, good exfoliation and dispersion of nanotubes, and good nanotube-nanotube and nanotube-polymer interfacial bonding. Numerous studies have shown already, that an effective performance of the carbon nanotubes in composites for a variety of applications strongly depends on the ability to disperse the CNTs homogenously throughout the matrix. Good interfacial bonding and interactions between nanotubes and polymers are also necessary conditions for improving mechanical properties of the composites. Because of their high mechanical strength, high aspect ratio, small diameter, light weight, high electrical and thermal conductivities, and high thermal and air stabilities, CNT have been found many applications in the industrial world (Chang, 2006; Hu, 2006). Polymer composites with carbon nanotube addition are one of the research subjects which attract huge attention in recent years (Lau, 2002& Thostenson, 2001). Thermoplastic polymers are usually used as an insulating material because of their low electrical conductivity properties ($\approx 10^{-15}$ S/m). Dispersing the conducting filler such as carbon black and CNT in polymer phase forms conductive polymer composites. Electrical

resistivities of polymer-MWCNT composites which are strongly dependent on the volume or mass fractions of the CNTs may vary between 10^{16} to several ohms. At low volume or mass fractions, the resistivity remains very close to the resistivity of pure polymer. Insulating polymers are transformed to conductive composites by addition of CNTs above a critical concentration threshold (known as percolation threshold). When the positions of CNTs in the polymer matrix form a conducting network, the conductivity of composite sharply increases. This phenomenon is known as percolation and can be well explained by percolation theory (Stauffer, 1994). Percolation threshold can be determined by measuring the resistivity variations in composites. Electrical percolation thresholds for some MWCNT and SWCNT polymer-composites were reported as ranging from 0.0021 to 15 wt% (Bauhofer, 2009). Studies on polymer-CNT composites show that their electrical, mechanical and thermal properties are improved by addition of CNTs (Chang, 2006; Choi, 2007; Du, 2004; Gao, 2007; Park, 2007). The first polymer nanocomposites using carbon nanotubes as filler were reported in 1994 by Ajayan (Ajayan, 1994). Earlier nanocomposites were used nanoscale fillers such as carbon blacks, silicas, clays, and carbon nanofibers (CNF) to improve the mechanical, electrical, and thermal properties of polymers. In recent years, carbon nanotubes have been used to improve electrical and mechanical properties of polymers (Anazawa, 2002; Choi, 2007; Du, 2004; Gao, 2007; Park, 2007; Moniruzzaman, 2006). However, by some reason of the advantage, provided by surface morphology, the literature focused on polymer composite thin films (Andrews, 2002; Bin, 2006; Blanchet, 2003; Hill, 2002; Kymakis, 2002; Shaffer, 1999; Qian, 2000) while there are no detailed studies on tri-dimensional composite gels with carbon nanotube content. Recently, carbon nanotubes and their polymer composites are used in various industrial areas such as flat panel screens, electron microscope guns, gas discharge tubes, microwave amplifiers, fuel cells, batteries, hydrogen storing media, nano probes, sensors and body-parts of aircrafts and spacecrafts (Ajayan, 2001). Some CNTs are stronger than steel and lighter than aluminum and more conductive than copper (Ajayan, 2001). Thus, studies on polymer-CNT composites have been accelerated at last decade.

Composite gels appear during a random linking process of monomers to larger and larger molecules. Even though the sol-gel transition is not a phase transition in thermodynamic sense, being a geometrical one, as a subject of critical phenomenon, it behaves like a second order phase transition and constitutes a universal class by itself (Tanaka, 1981). Experimental techniques used for monitoring sol-gel transition must be very sensitive to the structural changes, and should not disturb the system mechanically. Fluorescence technique is of particularly useful for elucidation of detailed structural aspects of the gels. This technique is based on the interpretation of the change in anisotropy, emission and/or excitation spectra, emission intensity, and viewing the lifetimes of injected aromatic molecules to monitor the change in their microenvironment (Barrow, 1962; Birks, 1970; Herculus, 1965; Galanin, 1995).

Electrical measurements are an unambiguous criterion of the existence of a percolated network in the case of conductive fillers in an isolating matrix. Dielectric measurements performed with varying frequency can lead to additional information about the percolation network as it was shown for percolation structures of carbon black in polymeric matrices. Recently, results on percolated structures of carbon nanotubes in disc sheet dry gels were presented (Pötschke, 2004). Similarly, the AC and DC conductivities of carbon nanotubes-polyepoxy composites have been investigated from 20 to 110 ^{0}C in the frequency range 10^{-2}-

10^6 Hz as a function of the conductive weight fraction, p ranging from 0.04 to 2.5 wt% (Barrau, 2003). The ability of existing theories to predict electrical properties of conductive fiber composites have been examined (Weber, 1997). Complex permittivity and related AC conductivity measurements in the frequency range between 10^{-4}- 10^7 Hz are presented for composites of polycarbonates (PC) filled with different amounts of multiwalled carbon nanotubes (MWNTs) varying in the range between 0.5 and 5 wt% (Pötschke, 2003). In addition, the conductivity of dry gel composites such as polystyrene (Chang, 2006) and polypropylene (Seo, 2004) has been enhanced significantly with the addition of CNTs. On the other hand, the PAM –CNTs composite thin films was characterized by the instruments of Fourier transform infrared spectroscopy, UV absorbance spectra, fluorescence spectra and transmission electron microscope (Li, 2004) Dielectric spectroscopy represents a method which has been successfully applied to investigate the percolation structure of CNTs in polymer (see, e.g.(Chang, 2006; Hu, 2006; Seo, 2004)). Therefore, we expect that this method can lead to new insights in MWNTs doped systems.

This work initially aims to study the influence of MWNTs dispersion on gelation (occurring composite gels) and conductivity properties of composites. In this work, when polymer systems which are initially of isolator character doped with carbon nanotubes of nano dimensions and when amount of such addition exceeds a critical value known as percolation threshold, composite gel systems with carbon nanotube addition capable of electrically converting into conductor structure are obtained. Composite gels are analyzed using the steady state fluorescence and dielectric spectroscopy. Here the total monomer concentration is kept 2M and very small amount of pyranine added to the pre-polymerization solution presented a spectral shift to the shorter wavelengths upon the initiation of polymerization. This spectral shift is due to the binding of pyranine to the polymer chains during the formation of PAM-MWNTs composite gels. The pyranine, thus, becomes an intrinsic fluoroprobe while it is extrinsic at the beginning of the reaction. The fluorescence intensity of the pyranine bonded to the strands of the polymers allows one to measure directly the gel fraction near the sol-gel phase transition, and thus the corresponding critical exponent, β.

Finally this work is designed to investigate the percolation structure of conductivity, and the state of dispersion of MWNTs in polyacrylamide using dielectric spectroscopy. Here critical conductivity exponent, around the conductivity percolation threshold where a material shifts to a conductor from an insulator character, is determined and found to be about 2.0 in agreement with random resistor network.

2. Theoretical considerations

2.1 Conductivity percolation

It has been established the percolation theory has been used to interpret the behavior in a mixture of conducting and non conducting components (Weber, 1997). Schematic representation of electrical percolation threshold (before and after) is shown Figure 1. Direct connection and overlapping of the CNT is not necessary i.e. nanotubes do not need to physically touch each other for conductivity. Nanotubes can just be close enough to allow for a hopping/ tunneling electron effect; these mechanisms require the CNT- CNT distance to be less than 5nm. As a result, a higher volume fraction of CNTs filler is needed to achieve electrical percolation threshold (Hu, 2006). Two classes of models have been developed for the description of the frequency dependence of the complex conductivity

$$\sigma^{*}(w) = \sigma'(w) - i\sigma''(w) \tag{1}$$

where $\sigma`(w)$ real part, $\sigma``(w)$ imaginary part of the complex conductivity, i imaginary unit, and w, angular frequency in percolating systems:

- the equivalent circuit model which treats a percolation system as a random mixture of resistors and capacitors(Bergman, 1977; Stauffer, 1994) and *(ii)* model based on charge carrier diffusion on percolating clusters (Sahimi, 1994; Stauffer 1994) For two-component systems- percolation cluster of high conductivity (σ_1) embedded in a matrix of considerable lower conductivity (σ_2, $\sigma_2 \ll \sigma_1$)
- macroscopic effective conductivity near the percolation threshold p_c can be written in the scaling form (Bergman, 1977; Stauffer, 1994; Straley, 1977).

$$\sigma(p,w) \alpha \sigma_1 \left| p^{'} - p_c^{'} \right|^{r} \Phi_{\pm} \left(\frac{\sigma_2}{\sigma_1} \left| p' - p_c^{'} \right|^{-(r+s)} \right) \tag{2}$$

where $p`$ is the concentration of conducting filler, Φ_{+} and Φ_{-} denote scaling functions for $p^{'} > p_c^{'}$ and $p^{'} < p_c^{'}$ respectively, s and r are the critical exponents.

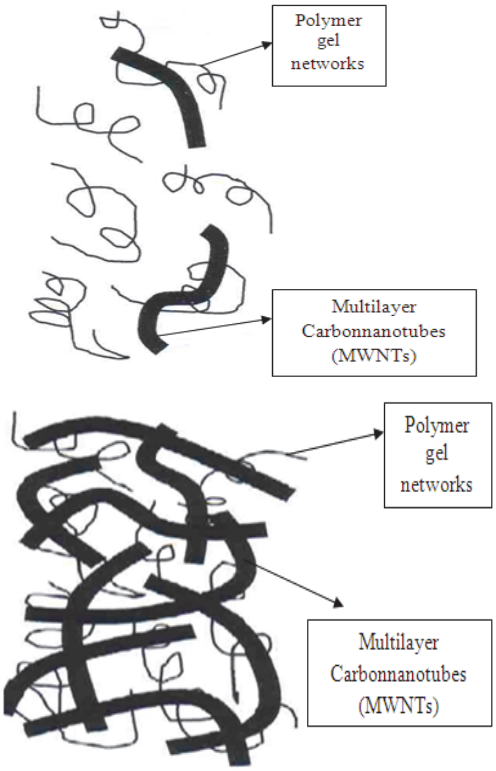

Fig. 1. Schematic of MWNTs/gel composite, before and after the gel formation with isotropic orientation of nanotubes.

These models treat a percolation system as a random mixture of resistors, R and capacitors C having a characteristic relaxation time $\tau = \frac{1}{w_0} = RC$, scaling law Eq. 2 for the complex conductivity near the percolation threshold takes the form (Bergman, 1977; Pearson, 1978; Seo, 2004)

$$\sigma^*(p,w)\alpha\frac{1}{R}\left|p^{'}-p_c^{'}\right|^r \Phi_{\pm}\left(\frac{iw}{w_0}\left|p^{'}-p_c^{'}\right|^{-(r+s)}\right) \tag{3}$$

One of the main physical content of this key scaling law is the existence of a time scale

$$\tau_c\left(p^{'}\right)\alpha\frac{1}{\omega_p\left(p^{'}\right)}\alpha\frac{1}{\omega_0}\left|p^{'}-p_c^{'}\right|^{-(r+s)} \tag{4}$$

that diverges as the percolation threshold is approached from both sides.
For the frequency dependence of AC conductivity at the percolation threshold Bergman and Imry (Bergman, 1977) derived the following law:

$$\sigma^{'}(w)\alpha w^{\frac{r}{r+s}} \tag{5}$$

where σ', the real part of Eq.1; w, angular frequency; r and s critical exponents for conductivity. A wide variety of approaches have been applied to the determination of these exponents as given in Table 1 for 3D with references (Adler, 1990; Bergman, 1977; Derrida, 1983; Fisch, 1978; Gingold, 1990; Herrman, 1984; Sahimi, 1994; Straley, 1977).

System	r	s	References
Resistor lattice	1.70 ± 0.05	0.70 ± 0.05	Straley, 1977
Random resistor network	1.95 ± 0.03	-	Fish and Harris, 1978
Random resistor network	2.02 ± 0.05	-	Adler,1990
Random resistor lattices	2.003 ± 0.047	-	Gingold and Lobb, 1990
Random resistor network	1.9 ± 0.1	0.75 ± 0.04	Herrman, 1984 Derrida, 1983

Table 1. Critical exponents for electrical percolation threshold in three dimension (3D).

2.2 Sol-gel phase transition

In the past half century various models have been developed to describe gel formation, among which Flory-Stockmayer theory and percolation theory provide bases for modeling the sol-gel phase transition (Flory, 1941; de Gennes, 1988; Hermann, 1986; Stauffer, 1982, 1985; Stockmayer, 1943). Statistical theories based on tree-like structure (Bethe lattice) uses mean field approximation, originate from Flory (Flory, 1941) and Stockmayer (Stockmayer, 1943), and assume equal reactivities of functional groups and the absence of cyclization reactions. Most statistical theories derived in the following decades are fully equivalent, differing only in mathematical language (Durand, 1979; Gordon, 1962; Macosko, 1976; Pearson, 1978).

Percolation offers a particularly simple and yet detailed picture in terms of which one may seek to understand gelation (de Gennes, 1988; Stauffer, 1985, 1994). In the language of percolation, one may think of monomers as occupying the vertices of a periodic lattice, and the chemical bonds as corresponding to the edges joining these vertices at any given moment, with some probability, p. Then, the gel point can be identified with the percolation threshold p_c, where, in the thermodynamic limit, the incipient infinite cluster starts to form. Identifying the weight average degree of polymerization DP_w with the average cluster size S_{av} and the gel fraction G with the probability P_∞ of an occupied site to belong to the incipient infinite cluster, one can predict the scaling behavior of these and related quantities near the gel point, as a function of $|p - p_c|$,

$$DP_w \propto \left(p_c - p\right)^{-\gamma} \qquad p \to p_c^- \tag{6}$$

$$G \propto \left(p - p_c\right)^{\beta} \qquad p \to p_c^+ \tag{7}$$

If p approaches p_c from below it is denoted as $p \to p_c^-$, in contrast, $p \to p_c^+$ denotes when p approaches p_c from above. Here, β and γ are the critical exponents, respectively. The critical exponents in percolation theory, β=0.41 and γ=1.70, differ from those found in Flory-Stockmayer, β=1 and γ=1.

3. Experimental

PAM- MWNT composites were prepared from various amounts of AAm and MWNTs. The solution is composed of MWNTs (Cheap Tubes Inc.), Polyvinyl pyrolidone (PVP), and water. The AAm and MWNTs concentrations are given in (Table 2). BIS (Merck) dissolving in $40x10^{-6}m^3$ of water in which 10^{-4}lt of TEMED (tetramethylethylenediamine) was added as an accelerator. The initiator, Ammonium persulfate (APS, Merck) was used and the initiator and pyranine concentrations were kept constant at $7x10^{-3}$ M and $4x10^{-4}$ M, respectively, for all samples. All samples were deoxygenated by bubbling nitrogen for 10 minutes, just before gelation process has started.

The Model LS-50 spectrometer of Perkin-Elmer was used for the fluorescence intensity measurements. All measurements were made at 90^o position and slit widths were kept at 5 nm. Pyranine was excited at 340 nm during *in situ* gelation experiments and variation in the fluorescence spectra and emission intensity of the pyranine were monitored as a function of gelation time.

The AC conductivity measurements were carried out by means of an HP- 4192 A impedance analyzer controlling a computer at room temperature. The dielectric cell was a parallel capacitor with sample thickness of 2mm.

4. Results and discussion

4.1 Conductivity exponents

The conductivity as a function of alternative current frequency is shown in Figure 2 for the gels with different content of PAM and/or MWNTs. It is observed that conductivity

behavior of the composite gels increased exponentially by increasing AC frequency. The results show that the critical conductivity behavior of the composite system occurs at 4 kHz for lower MWNTs content while this behavior occurs nearly 0 kHz for higher MWNTs contents. PAM doped by lower MWNTs composite system converts into conductive character at higher frequency than the frequency value needed for PAM doped by higher MWNTs composite system. From figure 2, one can seen that the conductivity, (σ) of 0.3 % MWNT gel was stable up to 4 kHz then suddenly increased to some point, and become stable. On the other hand, the conductivity, (σ) for 1.0 and 3.0 % MWNT gels increased suddenly at very low frequency, then become stable after 4 kHz.

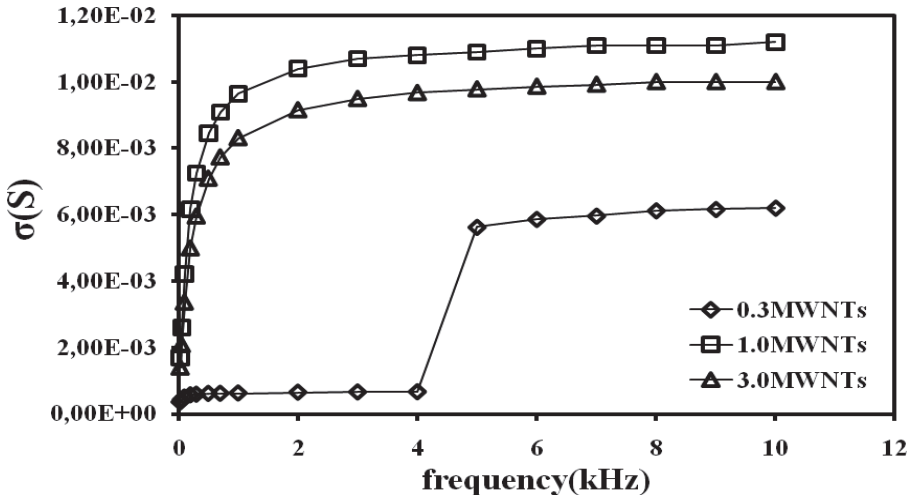

Fig. 2. Conductivity of PAM- MWNTs composites versus alternatively current (AC) frequency at room temperature for 0.3 %MWNTs, 1.0 %MWNTs and 3.0 %MWNTs contents, respectively.

The effect of MWNTs content on conductivity of PAM- MWNTs composite gels is presented in Figure 3 for 5kHz. At very low content of MWNTs (0.3%), the conductivity is quite low, however, after 0.3 %, a definite increase in conductivity is observed. This stepwise change in conductivity is a result of the formation of an interconnected structure of MWNTs and can be regarded as an electrical percolation threshold which simply means that at contents between 0.3 and 1.0 % MWNTs, some percentage of electrons are permitted to flow through the specimen due to the creation of an interconnecting conductive pathway. At contents above 1.0 %MWNTs, the conductivities are stable by increasing MWNTs content (Seo, 2004).

The value of the fitting exponent r in Eq. 7 was estimated from the slope of the linear relation between log σ and log$w$ as shown in Figure 4. s is the critical exponent which taken from literature by s≈0.7±0.05(Straley, 1977). The produce r values are listed in Table 2 where it is seen that the electrical percolation occurs above 0.3 % MWNTs with a critical exponent around r≈2 which is close to the theoretical prediction of this value in 3D percolated system as known random resistor network (Derrida, 1983; Straley, 1977).

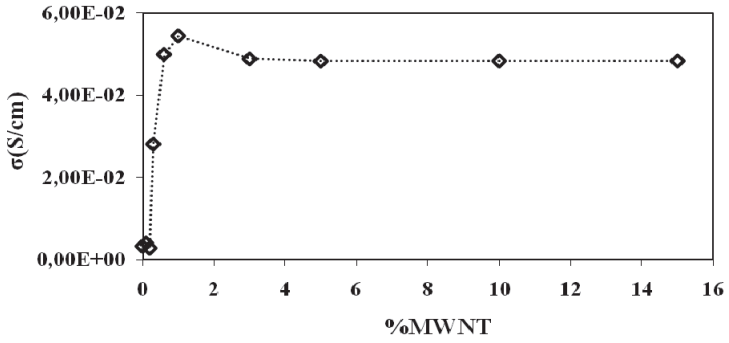

Fig. 3. Conductivity as a function MWNTs content at 5 kHz.

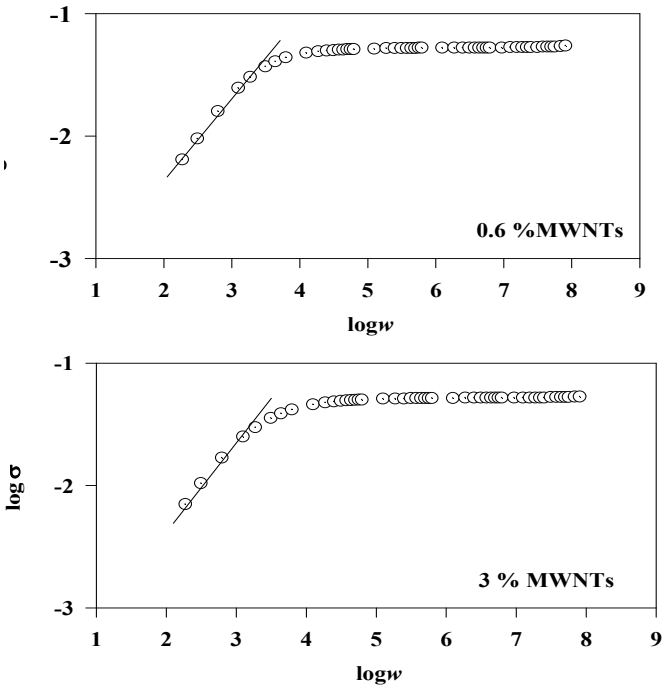

Fig. 4. Logarithmic plot of the conductivity versus frequency curves of 0.6 %MWNTs and 3 % MWNTs, respectively.

4.2 Sol-gel exponents

Figure 5 shows the typical fluorescence spectra of pyranine at two different stages of gelation for PAM-MWNTs composite. Beginning of the reaction only the 512nm peak exists, and then the intensity of the new peak around 380 nm started to increase as the intensity of the 512nm peak decreased during the course of gelation of PAM-MWNTs composite gels.

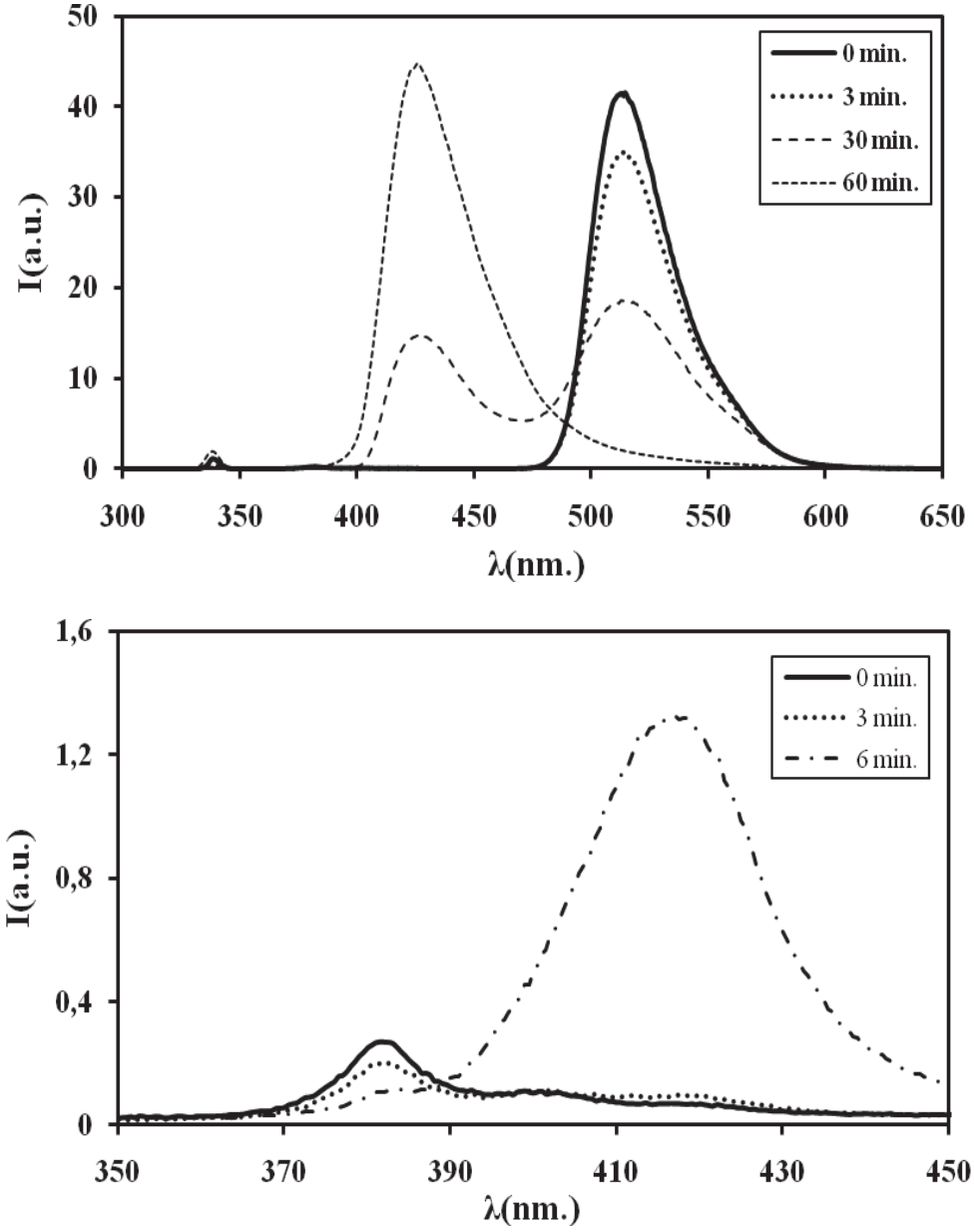

Fig. 5. Typical fluorescence spectra of pyranine at different stages of gelation for PAM-MWNTs composite during the whole course of gelation presenting the binding of pyranines and at the early stage of gelation, presenting the spectral shift from 380nm toward 427nm, respectively.

AAm (%)	MWNTs(%)	t_{gel} (s)	C^-/C^+	β	r
			1.0	0.92	
			0.37	0.50	
100	0	300±5	0.28	0.55	-
			0.23	0.52	
			0.1	0.52	
			1.0	0.75	
			0.37	0.50	
99.9	0.1	300±5	0.28	0.56	0.10±0.02
			0.23	0.48	
			0.1	0.50	
			1.0	1.05	
			0.37	0.50	
99.8	0.2	300±5	0.28	0.65	0.57±0.02
			0.23	0.60	
			0.1	0.50	
			1.0	0.75	
			0.37	0.66	
99.7	0.3	300±5	0.28	0.58	0.34±0.02
			0.23	0.55	
			0.1	0.50	
			1.0	0.96	
			0.37	0.67	
99.4	0.6	360±5	0.28	0.60	1.80±0.02
			0.23	0.55	
			0.1	0.55	
			1.0	0.90	
			0.37	0.65	
99	1	420±5	0.28	0.57	1.90±0.02
			0.23	0.65	
			0.1	0.60	
			1.0	0.83	
			0.37	0.51	
97	3	420±5	0.28	0.48	1.90±0.02
			0.23	0.50	
			0.1	0.50	
			1.0	1.10	
			0.37	0.70	
95	5	480±5	0.28	0.63	2.30±0.08
			0.23	0.68	
			0.1	0.65	

AAm (%)	MWNTs(%)	t_{gel} (s)	C^-/C^+	β	r
			1.0	0.88	
			0.37	0.72	
90	10	540±5	0.28	0.57	1.80±0.05
			0.23	0.60	
			0.1	0.56	
			1.0	1.10	
			0.37	0.45	
85	15	660±5	0.28	0.40	1.90±0.02
			0.23	0.41	
			0.1	0.40	

Table 2. Experimentally measured parameters for PAM-MWNTs composite gels.

As one can see from Figure 6 the intensity of the short-wavelength peak (380 nm-peak) increases during the course of polymerization, meanwhile as the polymerization progresses the maxima of the short wavelength-peak shifts to some higher wavelengths from 380 nm to 427nm (Kaya et al., 2004). Here at first the shift from 512 nm to 380 nm in the emission spectra due to a C- O ether bond formation between the hydroxyl oxygen of 3sPyOH and a terminal C-atom of the growing AAm chain.

Then the shift in the short-wavelength peak between 380 and 427 nm is probably due to the complexation of SO_3^- groups with protonated amide groups whether on the same polymer molecule or on the other polymer strands (Yılmaz et al., 2009). The reason for the shift in the isoemissive (isostilbic) point is the change in the internal morphology of the system: at the beginning of the polymerization the system is in the "sol" state (all pyranine are free) and above a certain time it turns into the "gel" state (most of pyranine are bonded).

Figure 6 presents the fluorescence intensity, I_{512} of the free pyranine (512nm.) from the reaction mixture as a function of the gelation time for 1 and 5 % MWNTs concentrations. As seen in Figure 6 that the fluorescence intensity increased up to some point (gelation stage), and then decreased to zero at the end of the reaction (final stage) for different MWNTs concentration.

Figure 7 presents the fluorescence intensities, I_{em} from the bonded pyranine (427nm) against the gelation time for 1 and 5 %MWNTs concentrations. The maxima of the spectra shift from 380nm to 427nm as the gelation progresses. Therefore, we monitored the fluorescence spectra in relatively large periods of time and plotted the intensity I_{em} corresponding to the maxima of the spectra as a function of time. These data were used to evaluate the critical behavior of the sol- gel phase transition (Kaya et al., 2004).

For the determination of the gel points, t_{gel}, each experiment was repeated at the same experimental conditions, and the gel points were produced by dilatometric technique (Okay et al., 1999). A steel sphere of 4.8 mm diameter was moved in the sample up and down slowly by means of a piece of magnet applied from the outer face of the sample cell. The time at which the motion of the sphere is stopped was evaluated the onset of the gel point, t_{gel}. The t_{gel} values are summarized in Table 2 together with the other parameters.

Now, it can be argued that the total fluorescence intensity from the bonded pyranines monitors the weight average degree of polymerization and the growing gel fraction for below and above the gel point, respectively. This proportionality can easily be proven by

using a Stauffer type argument under the assumption that the monomers occupy the sites of an imaginary periodic lattice (Stauffer et al., 1982; 1985; 1994).

Gelation theory often makes the assumption that the conversion factor, p, alone determines the behavior of the gelation process, though p may depend on temperature, concentration of monomers, and time (Stauffer et al. 1982; 1994). If the temperature and concentration are kept fixed, then p will be directly proportional to the reaction time, t. This proportionality is not linear over the whole range of reaction time, but it can be assumed that in the critical region, i.e. around the critical point $|p - p_c|$ is linearly proportional to the $|t - t_{gel}|$ (Yılmaz et al., 1998, 2002). Therefore, below the gel point, i.e., for $t < t_{gel}$ the maximum fluorescence intensity, $I^{'}$, measures the weight average degree of polymers (or average cluster size). Above t_{gel}, if the intensity from finite clusters distributed through the infinite network I_{ct} is subtracted from the maximum fluorescence intensity, then, the corrected intensity $I^{'}$- I_{ct} measures solely the gel fraction G, the fraction of the monomers that belong to the macroscopic network. In summary, we have the following relations, (Kaya et al., 2004)

$$I^{'} \propto DP_w = C^{+}\left(t_{gel} - t\right)^{-\gamma} \qquad t \to t_{gel}^{-} \tag{8a}$$

$$I_{ct} \propto DP_w = C^{-}\left(t_{gel} - t\right)^{-\gamma'} \qquad t \to t_{gel}^{+} \tag{8b}$$

$$I^{'} - I_{ct} \propto G = B\left(t - t_{gel}\right)^{\beta} \qquad t \to t_{gel}^{+} \tag{9}$$

where C^{+}, C^{-} and B are the critical amplitude, respectively.

It has been well established that the average cluster size of the finite clusters (distributed through the infinite network) above the gel point decreases with the same, but negative slope of the increasing cluster size before the gel point. This means that the exponents γ and γ', defined for the cluster sizes below and above the gel point, have the same values (de Gennes, 1988; Hermann, 1986; Stauffer et al., 1982, 1985, 1994). But, the critical amplitudes for the average cluster size defined below (C^{+} in Eq. 8a) and above (C^{-} in Eq. 8b) the gel point are different, and there exist a universal value for the ratio C^{+}/C^{-}. This ratio is different for mean-field versus percolation as discussed by Aharony (Aharony, 1980) and Stauffer (Stauffer, 1982). The estimated values for C^{+}/C^{-} (Stauffer, 1982, Aharony, 1980) is given in Table 3. In order to determine the intensity I_{ct} in Eqs.(8b) and (9), we first choose the parts of the intensity-time curves up to the gel points, then the mirror symmetry I_{ms} of this parts according to the axis perpendicular to time axis at the gel point were multiplied by the ratio C^{-}/C^{+}, so that $I_{ct} = \frac{C^{-}}{C^{+}} I_{ms}$. Thus, I_{ct} measures solely the intensity from the cluster above the gel point, and I'-I_{ct} measures the intensity from the gel fraction. This process is clarified explicitly in Figure 8.

Using the Eq. (9), and the values for t_{gel} summarized in Table 2 we calculated β exponents as a function of AAm and/or MWNTs contents. Figure 9 represents the log-log plots of the typical intensity- time data above the gel point, for 0.6 %MWNTs and 1% MWNTs concentration, respectively, where the slope produced β values which are listed in Table 2 for various PAM-MWNTs.

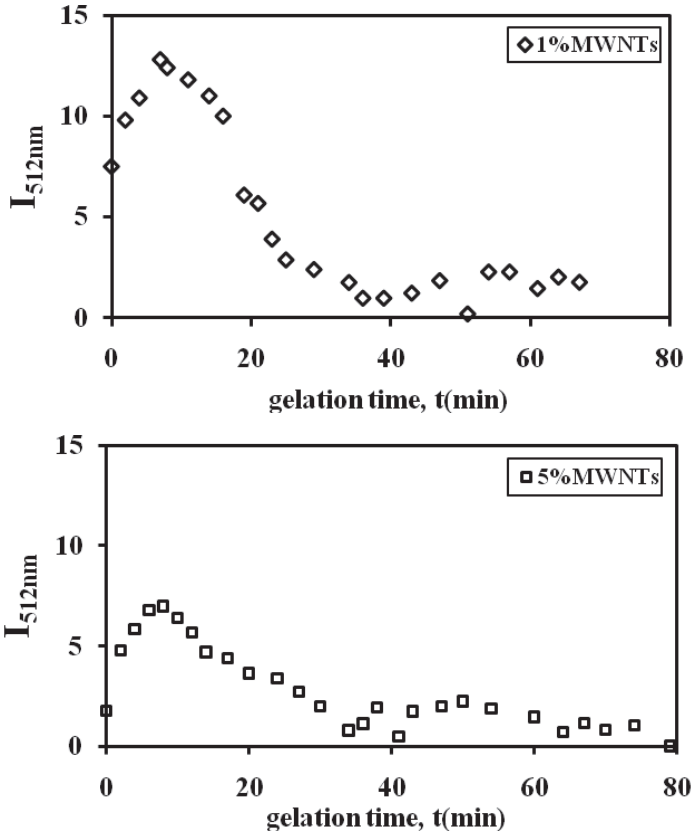

Fig. 6. Fluorescence intensity of the free pyranine at 512nm, I_{512nm}, versus reaction time for 1 %MWNTs and 5 %MWNTs contents.

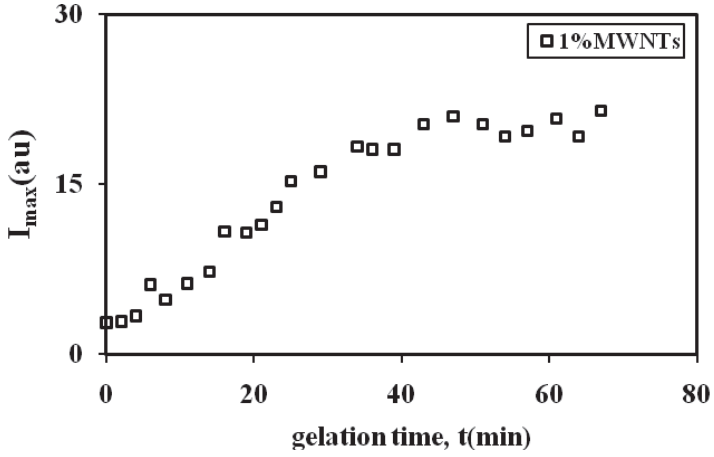

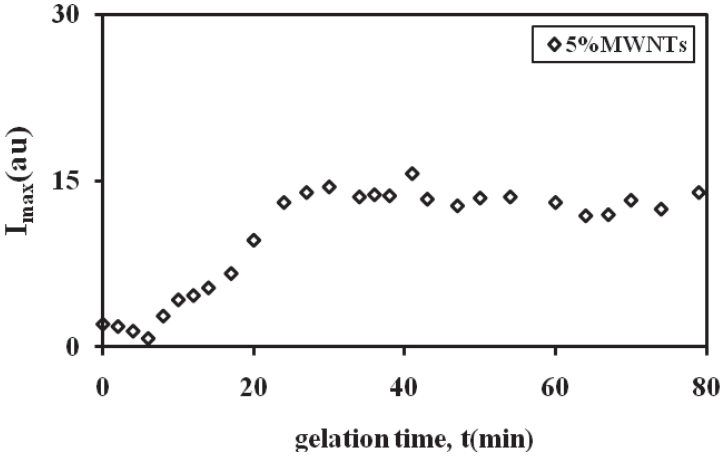

Fig. 7. Fluorescence intensity 427nm. variation of the pyranine, bonded to the PAM for different MWNTs concentrations, versus reaction time for 1 %MWNTs and 5 %MWNTs contents, respectively.

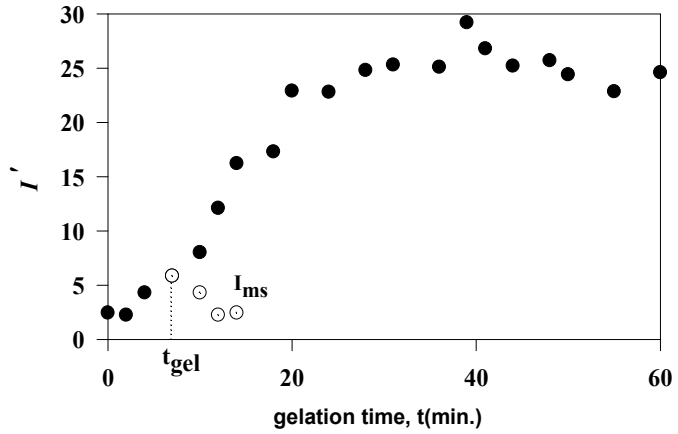

Fig. 8. Intensity- time curve during occurring of PAM- 0.6 %MWNTs composite gels. The curve depicted by dots represents the mirror symmetry I_{ms} of the intensity according to the axis perpendicular to time axis at $t=t_{gel.}$ The intensity from the clusters above the gel point is calculated as $I_{ct}=\frac{C^-}{C^+} I_{ms}$. Thus, $I^- - I_{ct}$ monitors the growing gel fraction for $t>t_{gel}$. The intensity from the below part of the symmetry axis monitor the average cluster size for $t<t_{gel}$.

	Classical	Percolation			
		Direct ε expansion	$\gamma_{\varepsilon exp}$=1.840 and $\beta_{\varepsilon exp}$ = 0.52	γ =1.7 and β = 0.4	Series and Montecarlo
C^- / C^+	1	1/2.7	1/3.5	1/4.3	1/10

Table 3. The estimated values for the ratio C^- / C^+ (Aharony, 1980)

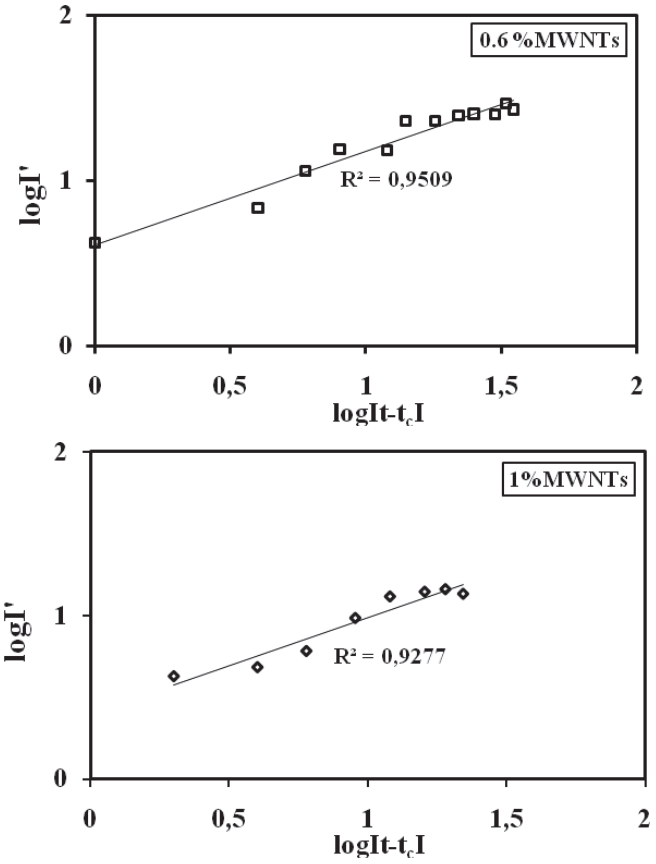

Fig. 9. Double logarithmic plot of the intensity I` versus time curves above t_{gel} for 0.6 %MWNTs and 1% MWNTs concentrations, respectively. The β exponents were determined from the slope of the straight lines.

5. Conclusion

In conclusion, PAM- MWNTs composites were prepared by the free-radical crosslinking copolymerization. The gelation and conductivity measurement of PAM- MWNTs composites were characterized by steady state fluorescence spectroscopy and dielectric spectroscopy, respectively. Here the critical phenomena of the gelation and conductivity were tested as a function of MWNTs concentration.

It is found that the electrical percolation threshold occurs above 0.3% MWNTs with critical exponent of r=1.8 - 2.3 which is quite close to the theoretical prediction of this value in 3D percolated system (r=2). The percolation critical exponent, r obtained from fitting the composition dependence of the AC conductivity above the percolation threshold is consistent with the suggestions of percolation for a random resistor network. It is observed that if polymer systems which are initially of isolator character doped with carbon nanotubes of nano dimensions and when amount of such addition exceeds a critical value known as percolation threshold, then composite gel systems with carbon nanotube addition became capable of electrically converting into conductor structure are obtained.
It is understood that the gel fraction exponent β obeyed the percolation theory for PAM-MWNTs composite gels. We were, thus, able to measure the copolymerization kinetics obeying the percolation picture without disturbing the system mechanically. In the mean time the universality of the sol-gel transition was tested as a function of parameters like MWNTs concentration ratios.

6. References

Adler, J.; Meir, Y.; Aharony, A.; Harris, A. B. & Klein, L. (1990). Low concentration series in general dimension. *Journal of Statistical Physics*, Vol. 58, pp. 511- 538.

Aharony, A. (1980). Universal critical amplitude ratios for percolation, *Physical Review B.* Vol. 22, pp. 400-414.

Ajayan, P. M. (1994). Aligned Carbon Nanotube Arrays Formed by Cutting a Polymer Resin-Nanotube Composite, *Science*, Vol. 265, pp. 1212- 1214.

Ajayan, P. M. & Zhou, O. Z. (2001). Applications of carbon nanotubes. *Carbon Nanotubes* (Topics in Applied Physics), ed Dresselhaus, M.S.; Avouris, Ph. Vol. 80, pp. 391-425, Berlin: Springer Verlag.

Anazawa, K.; Shimotani, K.; Manabe, C.; Watanabe, H. & Shimizu, M. (2002). High- purity carbon nanotubes synthesis method by an arc discharhing in magnetic field. *Applied Physics Lett*ers, Vol. 81, pp. 739–741.

Andrews, R.; Jacques, D.; Qian, D. & Rantell, T. (2002) Multiwall Carbon Nanotubes: Synthesis and Application, *Accounts of Chemical Research*, Vol.35, pp.1008–1017.

Barrau, S.; Demont, P.; Peigney, A.; Laurent, C. & Lacabanne, C. (2003). DC and AC Conductivity of Carbon Nanotubes- polyepoxy Composites. *Macromolecules,* Vol. 36, pp. 5187- 5194.

Barrow, G. M. (1962). *Introduction to Molecular Spectroscopy*, McGraw-Hill, New York.

Bauhofer, W. & Kovacs, J. Z. (2009). *Composite Science and Technology*, Vol. 69, pp. 1486- 1498.

Bergman, D. J. & Imry, Y. (1977).Critical Behavior of the Complex Dielectric Constant near the percolation threshold of a heterogeneous material. *Physical Review Letters*, Vol. 39(19), pp.1222- 1225.

Bin, Y.; Mine, M.; Koganemaru; A.; Jiang, X.; Matsuo, M. (2006).Morphology and mechanical and electrical properties of oriented PVA- VGCF and PVA- MWNT composites, *Polymer*, Vol.47, pp.1308–1317.

Birks, J. B. (1970). *Photophysics of Aromatic Molecules*, Wiley Interscience, London.

Blanchet, G. B.; Fincher, C. R. & Gao, F. (2003). Polyaniline nanotube composites: A high-resolution printable conductor, *Applied Physics Letters,* Vol. 82(8), pp.1290–1292.

Chang, T.-E.; Kisliuk, A.; Rhodes, S. M.; Britain, W. J.; Sokolov, A. P. (2006).Conductivity and mechanical properties of well- dispersed single wall carbon nanotube/polystyrene composite. *Polymer*, Vol. 47, pp. 7740- 7746.

Choi, C. S.; Park, B.J. & Choi, H.J. (2007). Electrical and rheological characteristics of poly (vinyl acetate)/multi-walled carbon nanotube nanocomposites, *Diamond and Related Materials* Vol. 16, pp. 1170- 1173.

de Gennes, P. G. (1988). *Scaling Concepts in Polymer Physics,* Cornell University Press, Ithaca.

Derrida, B.; Stauffer, D.; Herrman, H. J. & Vannimenus J. (1983).Transfer matrix calculation of conductivity in three- dimensional random resistor networks at percolation threshold. *Le Journal de Physics Letters,* Vol. 44, pp. L701-L706.

Du, F.; Scogna, R.C.; Zhou, W.; Brand, S.; Fischer, J. E. & Winey, K. I. (2004). Nanotube networks in polymer nanocomposites: rheology and electrical conductivity, *Macromolecules*, Vol. 37, pp. 9048- 9055.

Durand, D. & Bruneau, C. -M. (1979). Reactivity and Gelation. I. Intrinsic Reactivity. *Journal of Polymer Science: Polymer Physics Education*, Vol. 17, pp. 273- 294.

Fisch, R. & Harris, A. B. (1978). Critical behavior of random resistor networks near the percolation threshold. *Physical Review B*, Vol. 18, pp. 416- 420.

Flory, P. J. (1941). Molecular Size Distribution in Three Dimensional Polymers. I. Gelation. *Journal of American Chemical Society*, Vol. 63, pp. 3083- 3090.

Galanin, M. D. (1995). *Luminescence of Molecules and Crystals,* Cambridge International Science Publishing.

Gao, L.; Zhaou, X. & Ding, Y. (2007). Effective thermal and electrical conductivity of carbon nanotube composites. *Chemical Physics Letters* Vol. 434, pp. 297- 300.

Gingold, D. B. & Lobb, C. J. (1990). Percolative conduction in three dimensions. *Physical Review B*, Vol. 42, pp. 8220- 8224.

Gordon, M. (1962). Good's theory of cascade processes applied to the statistics of polymer distributions. *Proceeding Royal Society A*, Vol. 268, pp. 240-256.

Herculus, D. M. (1965). *Fluorescence and Phosphorescence Analysis*, Wiley Interscience, New York.

Herrman, H. J.; Derrida, B. & Vannimenus, J. (1984). Superconductivity exponents in two and three dimensional percolation. *Physical Review B*, Vol. 30, pp. 4080- 4082.

Hermann, H. J. (1986). Geometrical cluster growth models and kinetic gelation. *Physics Report*, Vol.136, pp.153-224.

Hill D. E.; Lin, Y.; Rao, A. M.; Allard, L. F. & Sun, Y.-P. (2002). Functionalization of Carbon nanotubes with Polystyrene, *Macromolecules,* Vol.35, pp.9466–9471.

Hu, G.; Zhao, C.; Zhangi, S.; Yang, M.; Wang, Z. (2006). Low percolation thresholds of electrical conductivity and rheology in poly (ethylene terephthalate) through the networks of multi- walled carbon nanotubes. *Polymer*, Vol. 47, pp. 480- 488.

Kaya, D.; Pekcan, Ö. & Yılmaz, Y. (2004). Direct test of the critical exponents at the sol- gel transition. *Physical Review E*. Vol. 69, pp. 16117(1-10).

Kymakis, E.; Alexandou, I. & Amaratunga, G. A. J. (2002). Single-walled carbon nanotube–polymer composites: electrical, optical and structural investigation, *Synthetic Metals*, Vol. 127, pp. 59- 62.

Lau, K. T. & Hui, D. (2002). The revolutionary creation of new advanced materials- carbon nanotube composites. *Composites Part B, Engineering*, Vol. 33, pp. 263–277.

lijima, S. (1991). Helical microtubules of graphitic carbon. *Nature,* Vol. 354, pp.56.

Li, X.; Guan, W.; Yan, H. & Huang, L. (2004). Fabrication and atomic force microscopy/ friction force microscopy studies of polyacrylamide-carbon nanotubes copolymer thin films. *Materials Chemistry and Physics*, Vol. 88, pp. 53- 58.

Macosko, C. W. & Miller, D. R. (1976). *A new derivation of Average Molecular Weights of Nonlinear Polymers,* Macromolecules, Vol. 9, pp. 199- 206.

Moniruzzaman, M. & Winey, K. I. (2006). Polymer nanocomposites containing carbon nanotubes, *Macromolecules*, Vol. 39, pp. 5194- 5205.

Park, S. J.; Lim, S. T.; Cho, M. S.; Kim, H. M.; Joo, J. & Choi, H.J. (2007). Electrical properties of multi-walled carbon-nanotube/poly (methyl methacrylate) nanocomposites, *Current Applied Physics* Vol. 5, pp. 302-304.

Pearson, D. S. & Graessley, W. W. (1978). *The structure of Rubber Networks with Multifunctional Junctions. Macromolecules*, Vol. 11, pp. 528- 533.

Pötschke, P., Dudkin, S. M. & Alig, I. (2003). Dielectric spectroscopy on melt processed polycarbonate- multiwalled carbon nanotube composites. *Polymer*, Vol. 44, pp.5023-5030.

Pötschke, P.; Abdel-Goad, M.; Alig, I.; Dudkin, S. & Lellinger, D. (2004). Rheological and dielectrical characterization of melt mixed polycarbonate-multiwalled carbon nanotube composites. *Polymer*, Vol. 45, pp. 8863- 8870.

Okay, O.; Kaya D. & Pekcan, Ö. (1999). Free- radical crosslinking copolymerization of styrene and divinylbenzene: real time monitoring of the gel effect using fluorescence probe. *Polymer*, Vol. 40, pp. 6179- 6187.

Qian, D.; Dickey, E. C.; Andrews, R. & Rantell, T. (2000). Load transfer and deformation mechanisms in carbon nanotube- polystyrene composites. *Applied Physics Letters*, *Vol.* 76, pp.2868–2870.

Sahimi, M. (1994). *Application of Percolation Theory*, Taylor and Francis, London.

Seo, M. - K., Park, S.-J. (2004). Electrical resistivity and rheological behaviors of carbon nanotubes- filled polypropylene composites. *Chemical Physics Letters*, Vol. 395, pp.44- 48.

Shaffer, M. S. P. & Windle, A. H. (1999). Fabrication and Characterization of Carbon Nanotube/ Poly (vinyl alcohol) Composites. *Advanced Materials*, Vol. 11, pp. 937–941.

Stauffer, D.; Coniglio, A. & M. Adam. (1982). Gelation and Critical Phenomena. *Advances Polymer Science*. Vol. 44, pp.103- 158.

Stauffer, D. (1985). *Introduction to Percolation Theory,* Taylor and Francis, London.

Stauffer, D. & Aharony, A. (1994). *Introduction to Percolation Theory*, 2nd ed. Taylor&Francis, London.

Straley, J. P. (1977).Critical exponents of conductivity of random resistor lattices. *Physical Review B*, Vol. 15(12), pp. 5733- 5737.

Stockmayer, W. H. (1943). Theory of Molecular Size Distribution and Gel Formation in Branched- Chain Polymers. *Journal of Chemical Physics*, Vol. 11, pp. 45-54.

Thostenson, E. T.; Ren, Z. F. & Chou, T. W. (2001). Advances in the science and technology of carbon nanotubes and their composites: a review. *Composition of Science and Technology*, Vol. 61, pp. 1899–1912.

Tanaka, T. (1981). Gels. *Scientific American,* Vol.244, pp.124- 136.

Weber, M. & Kamal, M. R. (1997). Estimation of the Volume Resistivity of Electrically Conductive Composites. *Polymer Composites*, Vol. 18, pp. 711- 725.

Yılmaz, Y.; Erzan, A. & Pekcan, Ö. (1998). Critical exponents and fractal dimension at the sol- gel phase transition via in situ fluorescence experiments. *Physical Review E*, Vol. 58, pp. 7487- 7491.

Yılmaz Y.; Erzan A. & Pekcan, Ö. (2002). Slow Release percolate near glass transition. *European Physical Journal E*, Vol. 9, pp. 135- 141.

Yılmaz, Y.; Uysal, N.; Güney, O.; Gelir, A.; Aktaş, D. K.; Göğebakan, S.& Öner. A. (2009). Elucidation of multiple- point interactions of pyranine fluoroprobe during the gelation. *Spectrochimica Acta Part A: Molecular and Biomolecular Spectroscopy Part A,* Vol. 72, pp. 332- 338.

11

Electrical Properties of CNT-Based Polymeric Matrix Nanocomposites

Alessandro Chiolerio[1], Micaela Castellino[1], Pravin Jagdale[2], Mauro Giorcelli[2], Stefano Bianco[3] and Alberto Tagliaferro[2]
[1]*Physics Department, Politecnico di Torino*
[2]*Materials Science and Chemical Engineering Department, Politecnico di Torino*
[3]*Fondazione IIT (Istituto Italiano di Tecnologia), Centre for Space Human Robotics Torino*
Italy

1. Introduction

NanoComposites (NCs) are a class of materials widely investigated in the last decade. The term NC material has broadened significantly to encompass a large variety of systems such as one-dimensional, two-dimensional, three-dimensional and amorphous materials, made of distinctly dissimilar components and mixed at the nanometer scale. The general class of organic/inorganic NC materials is a fast growing area of research. The properties of NCs depend not only on the properties of their individual elements but also on their morphology and interfacial characteristics. Large interface area between the matrix and the nano filler is a key issue for NCs.
NCs' fillers include Carbon nanomaterials. They are a large family of materials carbon based that include: fibers, nanotubes, fullerene, nano-diamonds, etc. Carbon Nanotubes (CNTs) are one of the most popular and intensively studied Carbon nanomaterials.
Since their discovery in 1991 by Iijima (Iijima, 1991), they have attracted great interest as an innovative material in most fields of science and engineering. CNTs can be thought of as sheets of graphite rolled up to make a tube. They are divided in two large classes: Multi wall CNTs (MWCNTs) and Single wall CNTs (SWCNTs). This classification depends on the number of graphite walls: several in the case of MWCNTs and only one for SWCNTs. The dimensions are variable, from few nanometers for SWCNTs to tenths of nanometers for MWCNTs. CNTs have outstanding mechanical, thermal and electrical properties.
For example as shown by Collins et al. (Collins et al., 2000) CNTs have electrical properties and electric-current-carrying capacity 1000 times higher than a copper wire. Young's module for a single-walled carbon nanotube (SWCNTs) has been estimated by Yu et al. (Yu et al., 2000) in a range of 0.32-1.47 TPa and strengths between 10 and 52 GPa with a toughness of ~ 770 Jg^{-1}. A room-temperature thermal conductivity of 1750–5800 $Wm^{-1}K^{-1}$ has been estimated by Hone et al. (Hone et al., 1999).
These remarkable properties make them excellent candidates for a range of possible new classes of materials.
Several studies demonstrate how just a small percentage of CNTs loading can improve the material properties (Breuer, 2004), while still maintaining the plasticity of the polymers.

The most accessible near-term application for CNTs-polymer composite involves their electrical properties. The intrinsic high conductivity of CNTs makes them a logical choice for tuning the conductive properties of polymers. As demonstrated by MacDiarmid (MacDiarmid, 2002) CNT-added polymers are ideal candidate because they can increase the electrical conductivity by many orders of magnitude from 10^{-10} – 10^{-5} up to 10^{3} – 10^{5} Scm^{-1}.
CNTs production cost depends upon several parameters, one of them is the type of CNTs. In general the production of SWCNTs is more expensive than MWCNTs due to low quantity production. Purification, surface modification treatments and functionalisation also increase the cost of CNTs production. For commercialization of process it is important to use cost effective and easily reproducible CNTs i.e. MWCNTs, whose diffusion, in the last years, seems to be greater.
Depending on the specific application of CNT-based NCs, it is possible to create either an isotropic material or an anisotropic one, by orienting preferentially the CNTs: its physical properties will be in the first case independent of sample positioning and geometry, in the second case strongly geometry-dependent (Chiolerio et al., 2008). In the case of NCs prepared for electrical applications, it is desirable to create a homogeneous polymer composite.
Carboxylic functionalized CNTs (-COOH groups) for their well known easy dispersion in polymers (Gao et al., 2009) are the ideal candidate in polymer composites. In fact the modification of their surface decreases their hydrophobic nature and improves interfacial adhesion to a bulk polymer through chemical attachment. Easy and good dispersion of CNTs in the polymer matrix is essential to obtain a homogeneous final product. Small diameter CNTs, providing a uniform dispersion, means more CNTs per volume unit and as a consequence a more capillary distribution in the polymer matrix at the same weight percentage. Following these reasoning the choice of CNTs has been done on a commercial product (Nanocyl™ NC3101) ready to our purposes (see all details in experimental section).
The choice of the polymers has focused on low cost materials, commercial products featuring good affinity with selected CNTs. A thermoplastic polyolefine: polyvinyl butyral (PVB) normally used in the area of glass gluing. A syloxane, Polydimethylsiloxane (PDMS) the most widely silicon-based organic polymer used. Two thermoset commercial epoxy resins: Epilox™ used in the automotive field (E) and Henkel Resin Hysol EA-9360 leader in the aerospace field (H1).
In this chapter a detailed study is presented, on the experimental conductivity and scaling laws thereof, for each of the four polymeric matrices above mentioned, as a function of the CNTs volume fraction. It will be shown that, depending on the polymer choice, it is possible to obtain NCs having a DC conductivity either showing a huge dependence on the volume fraction of CNTs or a less marked one. We also found that in one case there is no typical conductivity kink in correspondence of the percolation threshold, for the PVB matrix.

2. Experimental

2.1 Composite processing

The effective utilization of CNT materials in composite applications depends strongly on their ability to be dispersed individually and homogeneously within a matrix. To maximize the advantage of CNTs as effective reinforcement for high strength polymer composites, the CNTs should not form aggregates, and must be well dispersed to enhance the interfacial interaction with the matrix. Several processing methods are available for fabricating

CNT/polymer composites. Some of them include solution mixing, in situ polymerization, melt blending and chemical modification processes.
The general protocol for solution processing method includes the dispersion of CNTs in a liquid medium by vigorous stirring and sonication, mixing the CNTs dispersion solvents in a polymer solution and controlled evaporation of the solvent with or without vacuum conditions.
In experimental part, solution processing method was adopted for making polymer NCs.
PVB and MWCNTs were treated with solvent like ethanol and butanol. Commercial thermosetting resins E, H1 and PDMS with MWCNTs followed the same method without solvent due to their liquid/viscous nature. In this way, a satisfactory level of dispersion of CNTs into the polymer matrix was obtained. Different weight % (wt.-%) concentrations of MWCNTs in polymer resin were tried to study the electrical behavior of the polymer NC.

2.2 Characterization of functionalized MWCNTs

Commercial NC3101 MWCNTs (NANOCYL™) are produced via the catalytic carbon vapour deposition (CCVD) process with average diameter 9.5 nm and average length ~ 1.5 µm (Figure 1, Field Effect Secondary Electron Microscope, FESEM).

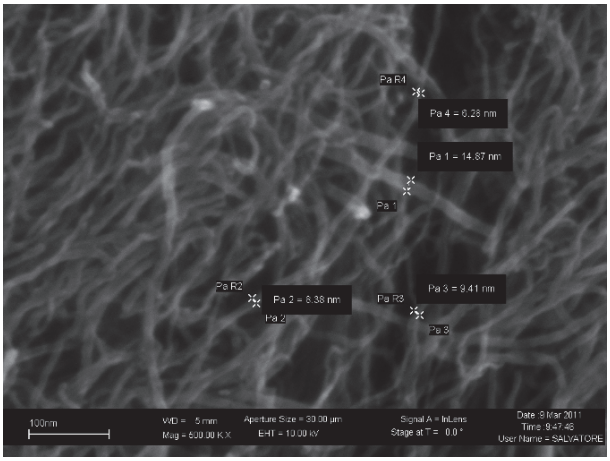

Fig. 1. FESEM image of Nanocyl™ (NC3101) Functionalized MWCNTs.

MWCNTs are then purified to greater than 95% carbon to produce the 3100 grade. This product is then functionalized with a carboxylic group (-COOH) to produce the 3101 grade. This functionalization is useful to avoid the clumps and agglomeration of MWCNTs in Polymer resin.

2.3 Thermoset epoxy resin (E)

2.3.1 Resin (T 19-36/700)

It is a commercially modified, colorless, low viscosity (650-750 mPa·s at 25 °C) epoxy resin with reduced crystallization tendency having density 1.14 gcm^{-3}. Cross linking with suitable curing agents is preferably performed at room temperature. The chemical composition of Epilox resin T19-36/700 is mainly Bisphenol A (30 – 60 wt.-%), added by crystalline silica (quartz) (1 – 10 wt.-%), glycidyl ether (1 – 10 wt.-%), inert fillers (10 –60 wt.-%).

2.3.2 Hardener (H 10-31)

It is a liquid, colourless, low viscosity (400-600 mPa.s) modified cycloaliphatic polyamine epoxide adduct having density 1 gcm^{-3}. Modified cycloaliphatic amine adducts.

2.3.3 Samples preparation

Resin T 19-36/700, MWCNTs and hardener H 10-31 were mixed with vigorous stirring followed by sonication. The mixture was degassed in vacuum. The mixture was poured in a mold to acquire desired shape for electrical measurements and subsequently kept in an oven at 70 °C for 4 hours for curing purposes. Electron microscopy images show the dispersion of MWCNTs in E (Figure 2).

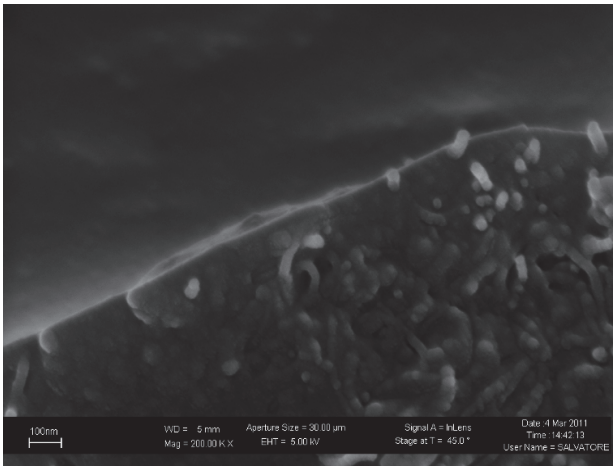

Fig. 2. FESEM of E + 5 wt.-% of MWCNTs.

2.4 Thermoset henkel resin (H1)

2.4.1 Hysol EA-9360 Part A

Henkel (Hysol EA-9360 Part A) is a white viscous paste having density 1.18 gml^{-1}. It has some interesting properties like high peel strength, excellent static stress durability, room temperature curability.

2.4.2 Hysol EA-9360 part B

Henkel (Hysol EA-9360 Part B) is a blue paste having density 1 gml^{-1}. The mixing ratio of Part A and Part B is 100:43 by weight. The chemical composition of the Henkel Part A and Part B is given below (Table 1).

2.4.3 Sample preparation

Combining Part A, Part B and MWCNTs in the correct ratio and mixing thoroughly with stirring was performed. Subsequently: degassing the mixture in vacuum, mixing of Part A and Part B which resulted in exothermic reaction (mixing smaller quantities would minimize the heat build up). The bonded parts were held in contact until the adhesive was set. Handling strength for this adhesive occurs in 24 hours (>25°C) and complete curing achieves after

Henkel Resin Hysol (EA-9360) Chemical Composition (wt.-%)			
Part A		Part B	
Epoxy resin Proprietary	30-60	Piperazine derivative Proprietary	30-60
Polyfunctional epoxy resin Proprietary	10-30	Butadiene-acrylonitrile copolymer	10-30
Synthetic rubber Proprietary	10-30	Silica amorphous (fumed)	5-10
Glass spheres Proprietary	5-10	Benzyl alcohol	5-10
Filler Proprietary	1-5	Cycloaliphatic amine Proprietary	5-10
Substituted silane Proprietary	1-5	Phenol	1-5
		Diethylene glycol Di-(3-aminopropyl)ether	1-5
		Substituted Piperazine Proprietary	1-5

Table 1. Chemical composition of Henkel Part A and Part B.

5-7 days keeping at 25 °C , for faster curing the molds were kept in the oven at 82 °C for 1 hour. Electron microscopy image shows the dispersion of MWCNTs in H1 (Figure 3).

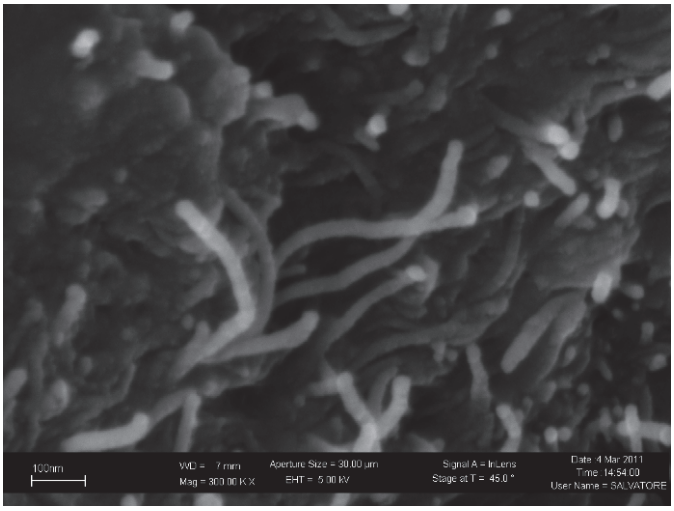

Fig. 3. FESEM of H1+ 5 wt.-% of MWCNTs.

2.5 Poly (dimethylsiloxane) (PDMS)

2.5.1 Base (Silicon Elastomer Sylgard 184 (Dow corning))

It is a Silicon based clear colourless low viscous liquid having specific gravity 1.11 gcm^{-3}. It is chemically stable and not forming hazardous polymerization.

2.5.2 Curing Agent (Silicon Elastomer Sylgard 184 (Dow corning))

It is silicon resin clear colourless low viscous liquid having specific gravity 1.03 gcm^{-3}.It is also chemically stable and not forming hazardous polymerization like base. The mixing ratio of base and curing agent is 1:1 by weight and curing time for the composite is 48 hours at 25 °C. Chemical formula of PDMS is CH_3 $[Si\ (CH_3)_2O]_n$ $Si(CH_3)_3$. After polymerization and cross-linking, PDMS samples present an external hydrophobic surface.

2.5.3 Method for sample preparation

To ensure uniform distribution of MWCNTs, Base and Curing agent must be thoroughly mixed prior to their combination in a 1:1 ratio. The mixture was stirred and sonicated well followed by degassing in vacuum. The base and curing agent liquid mixture should have a uniform appearance. The presence of light-colored streaks or marbling indicates inadequate mixing and will result in incomplete cure. Electron microscopy image shows the dispersion of MWCNTs in PDMS resin (Figure 4).

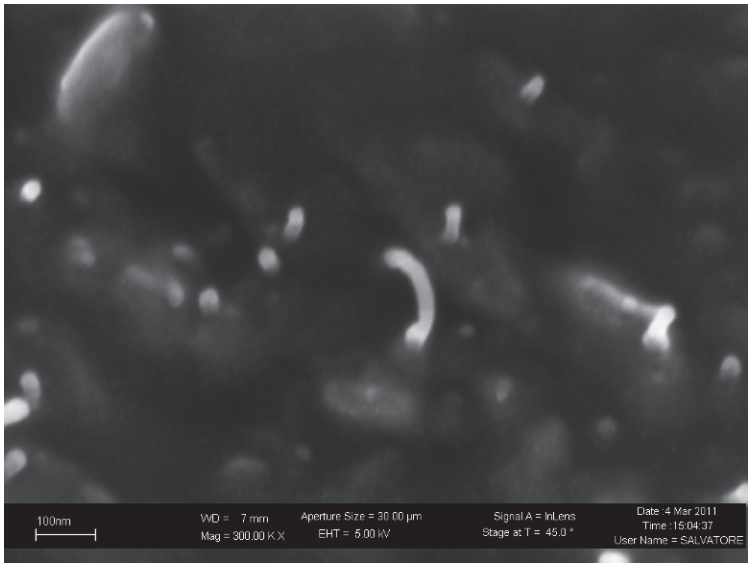

Fig. 4. FESEM of PDMS and 5 wt.-% MWCNTs.

2.6 Poly (vinyl butyral) (PVB)

PVB is a resin usually used for applications that require strong binding, optical clarity, adhesion to many surfaces, toughness and flexibility. It is prepared from polyvinyl alcohol by reaction with butyraldehyde. The IUPAC name of the polymer is Poly[(2-propyl-1,3-dioxane-4,6-diyl) methylene] with chemical structure as mentioned below (Figure 5). It is in white powder form with specific gravity 1.083 gcm^{-3}.

2.6.1 Method of preparation of PVB/MWCNTs NCs by solution processing

In preparation of CNTs–PVB (Butvar B-98, Sigma Aldrich) polymer composites, Ethanol (Carlo Erba) and 1-Butanol (Sigma-Aldrich) solvents were used with vigorous stirring and

sonication. Degassing was important for eliminating the entrapped solvent gas bubbles under vacuum. The composite was treated in oven at 70 °C for curing. Electron microscopy images show the dispersion of MWCNTs in PVB (Figure 5).

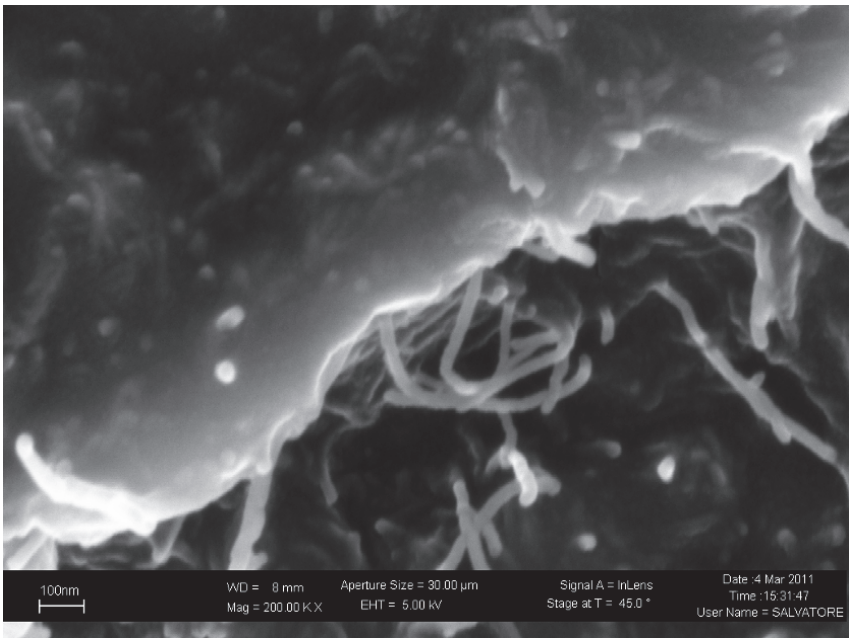

Fig. 5. PVB with 5 wt.-% of MWCNTs.

2.7 Electrical characterization

Electrical measurements were performed for each sample of the four polymer series using the so called "*Two Point Probe (TPP) method*" (Schroder, 1990)(Grove, 1993). Since we have dealt with, in principle, highly non conductive matrices, we have decided not to use the in-line "*Four Point Probes (FPP) technique*" (Smith, 1958), which is typically used for highly conductive materials, where the contact resistance between sample and connection wires could play an important role, leading to a wrong estimate of the real material resistance (Chiolerio et al., 2007).

In order to perform I-V measurements a setup already tested was chosen and used for the estimate of CNTs bundles resistivity at room temperature (Castellino et al., 2010).

In this case it was adjusted to fit our samples' dimensions. As it is possible to see from the scheme in Figure 6 a square sample was placed onto an insulating board with tin islands to place electrical connections for the Voltage supplier. To create the connections directly onto our samples surface, in an easy, fast and reproducible way, the silver conductive paste was chosen (Hu et al., 2008), which does not require any particular equipment (such as metals sputtering or thermal evaporators devices) (Coleman et al., 1998), just several minutes in order to let the solvent to evaporate. In this way it was also prevented any kind of warming of NCs or metals infiltrations during the metal contacts creation, which could have changed their properties.

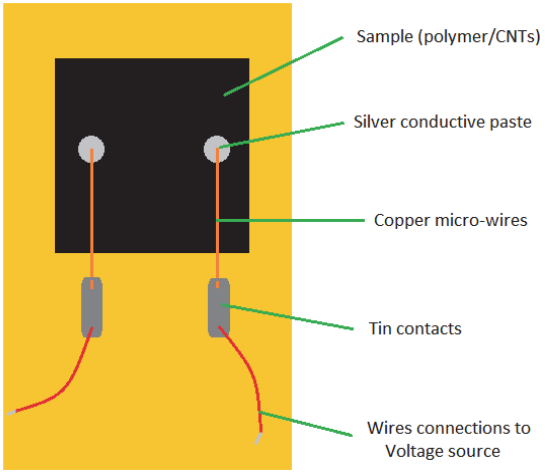

Fig. 6. Scheme of the electrical circuit device used for I-V measurements.

Insulated copper micro-wires were used to connect the Ag paste onto the sample and the tin islands on the board, since they are very thin and can be easily attached with this conductive paste. Their ends were previously exposed by means of a scalpel under an optical microscope.

A Keithley-238 High Current Source Measure Unit was used as high voltage source and nano-amperometer. It can supply up to ± 110 V and measure up to ±1 A (at ±15 V) and down to 10 fA.

Each sample was measured three times to have a statistical average value for the resistance and to see if the behavior observed was reproducible. For this purpose electrical connections between the voltage supplier and the board were removed every time before each measure.

For samples with 0 wt.-% CNTs the I-V measurements were performed in the range between ±110 V with a voltage step of 1 V, in order to observe a sort of trade in the very noisy curve where the current was $I \sim 10^{-11} - 10^{-10}$ A (see Figure 7 upper panel) to obtain a sort of "*zero value*" for the conduction (σ_0), which will be used further in the results and discussion section for the percolation theory fit.

Instead a narrower range (±10 V or ± 20V, with a step of 0.1 V) was chosen for samples with wt.-% CNTs ≥ 1 mainly for two reasons:

- to avoid samples warming due to high current flow;
- since the voltage supplier possesses a threshold cut-off for currents higher than 1 A.

The first phenomenon has been observed especially with samples with a CNTs load equal or higher than 4 wt.-%. For this reason the range was moreover reduced between ±7 or ± 3 V for some highly conductive samples (see Table 2 and Figure 7 lower panel).

In fact for E and PDMS composites a huge warming of the samples was observed, especially for PDMS + 5 wt.-% CNTs, which produced fumes from the silver paste.

On the other hand H1 NCs showed quite standard behaviors, showing an increase in the conductivity due to the increase in the CNTs amount, with no remarkable aspects to be noticed.

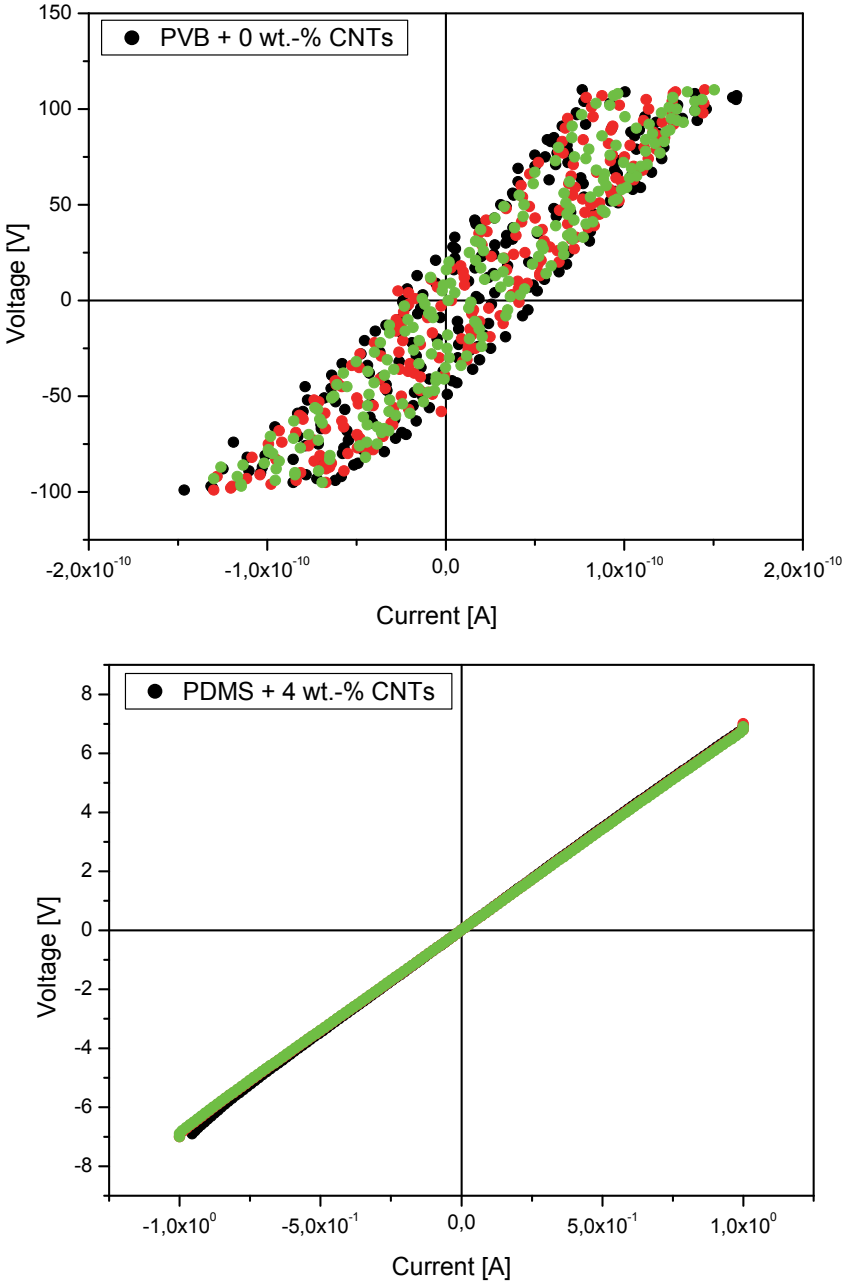

Fig. 7. Noise curves of samples PVB + 0 wt.-% CNTs (upper panel) and reduced voltage range measurements for sample PDMS + 4 wt.-% CNTs (lower panel).

Polymer	wt.-% CNTs	Voltage range (± V)	Voltage step (V)	Current range (± A)
E	0	110	1	1×10^{-10}
	1	10	0.1	2×10^{-4}
	2	10	0.1	3×10^{-2}
	3	10	0.1	3×10^{-1}
	4	10	0.1	8×10^{-1}
	5	7	0.1	8×10^{-1}
H1	0	110	1	2×10^{-10}
	1	110	1	1×10^{-10}
	2	10	0.1	1.5×10^{-6}
	3	10	0.1	3×10^{-4}
	4	10	0.1	1.5×10^{-2}
	5	10	0.1	4×10^{-2}
PDMS	0	110	1	1×10^{-10}
	1	10	0.1	1×10^{-3}
	2	10	0.1	1×10^{-1}
	3	10	0.1	5×10^{-1}
	4	7	0.1	1×10^{0}
	5	3	0.1	4×10^{-1}
PVB	0	110	1	1.5×10^{-10}
	1	10	0.1	2.5×10^{-10}
	2	10	0.1	8×10^{-5}
	3	20	0.1	6×10^{-5}
	4	10	0.1	2×10^{-3}
	5	10	0.1	6×10^{-3}

Table 2. Voltage (supplied) and current (registered) ranges for each sample.

3. Results and discussion

3.1 Finite element method simulation

Electrical resistivity measures were performed on the samples produced as described in the previous section. Figure 8 shows the sample geometry and the layout of the silver electrodes, placed in the 2-point configuration.

A Finite Element Method simulation was performed, using the commercial code Comsol Multiphysics™, of a composite material slab characterized by different resistivities, having the same dimensions of real samples, with the aim of evaluating the volume interested by the higher fraction of current density and estimating the penetration depth of DC currents into the sample thickness. An example of the simulation control volume is given in Figure 9, where the tetrahedral mesh of Lagrangian cubic elements is shown. The complexity of the system was quite high, having 162 k degrees of freedom and 111 k elements composing the

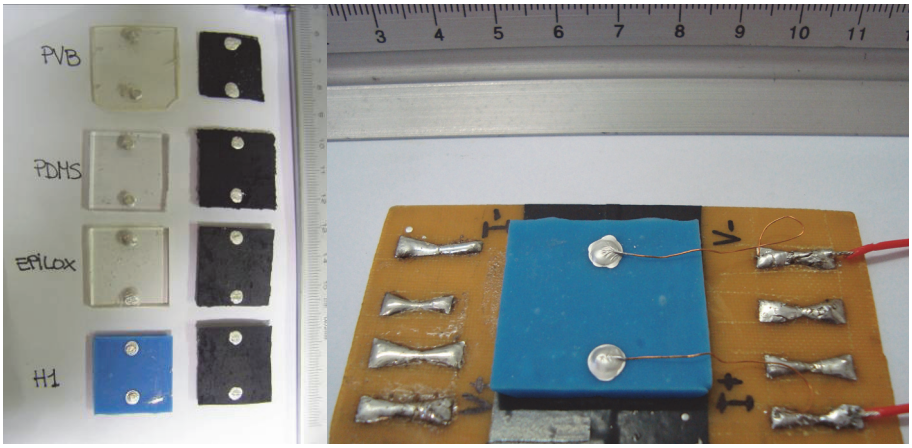

Fig. 8. Samples ready for electrical measurements; left panel: left column, pure matrices; right column, composites containing 5 wt.-% of CNTs. Right panel: sample placed in the fixture used for DC measurements.

mesh, with a solution time of more than 315 s (Intel™ Core® 2 Quad Q9550 2.83 GHz 4 GB DDR3).

As it can be seen in Figure 10, the current density is distributed almost in the whole sample, with the exception of the portions close to the electrodes, where the effective path avoids the sample bottom and edges. Based on these simulations, the effective electrical path was estimated to be: 3 mm thick (same thickness of the sample), 3 cm width (same width of the sample) and 1 cm long (sample length reduced by the electrode size and dead ends).

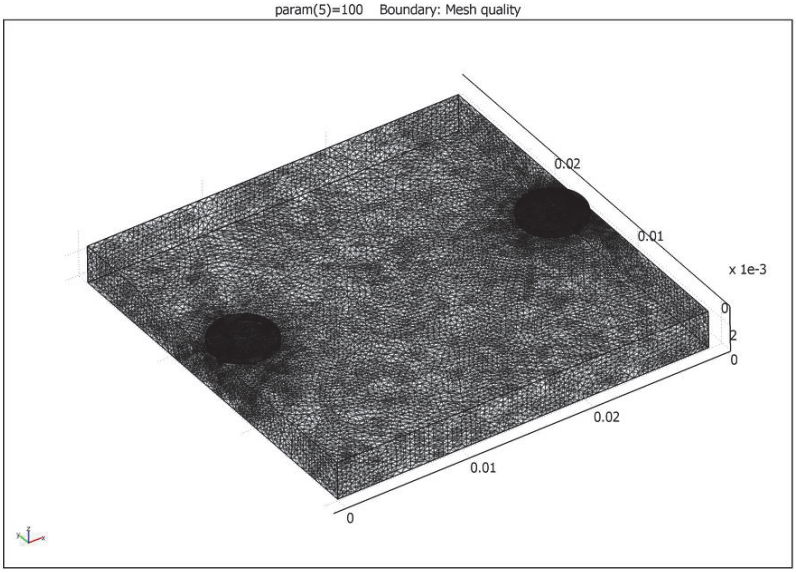

Fig. 9. Mesh distribution on the control volume of the FEM simulation.

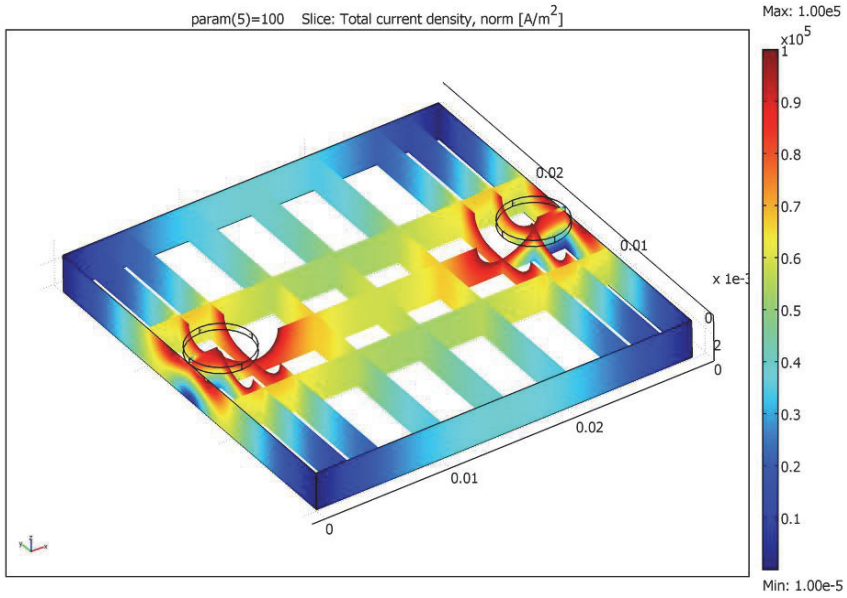

Fig. 10. Current density distribution in a composite volume.

3.2 DC conductivity and scaling laws thereof

NCs samples showed two different electrical behaviors: linear response and non-linear response, in the voltage range ±10 V. In particular, samples characterized by the PDMS, PVB and E matrices, at low dispersoid concentrations, resulted in a symmetric nonlinear response, as shown in Figure 11. In particular, at least two regimes were observed, that typical of PDMS composites, having higher conductivities (mA range under 10 V) and that typical of PVB composites, having much lower conductivities (μA range under 10 V). The same samples, by increasing the amount of CNTs, resulted in a perfect linear response (Figure 12), as well as H1 samples.

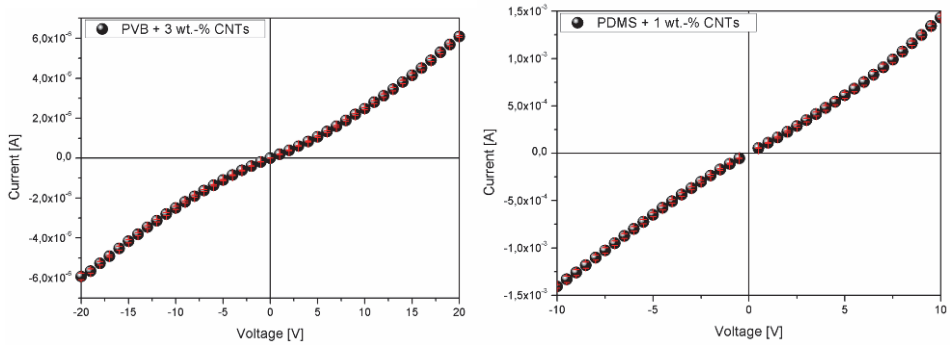

Fig. 11. Nonlinear response of samples PVB + 3 wt.-% CNTs (left panel) and PDMS + 1 wt.-% CNTs (right panel). For clarity, only 1 experimental point every 5 is shown.

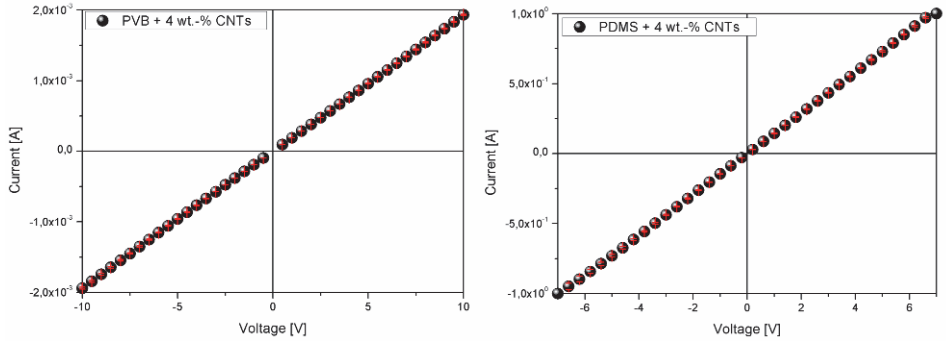

Fig. 12. Linear response of samples PVB + 4 wt.-% CNTs (left panel) and PDMS + 4 wt.-% CNTs (right panel). For clarity, only 1 experimental point every 5 is shown.

In literature, a nonlinear behavior was observed in composites based on MWCNTs networks dispersed in PDMS rubber even though the authors report no transition towards a linear response by increasing the amount of dispersoid (Liu and Fan 2007).
A possible explanation is given by the fluctuation-induced tunnelling mechanism acting in correspondence of CNTs' intersections. Some intersections, occurring between a metallic and a semiconductive CNTs, result in a Schottky barrier; when the dispersoid amount is low enough that no percolative random walks are formed going through point contact intersections, Schottky-like intersections play a major role and influence the macroscopic behavior of the NC. The energy necessary for the carriers to tunnel across the potential barrier consistent with a certain amount of polymer spacer placed between two CNTs is given by local temperature oscillations (Sheng, 1978).
In order to model the results obtained for conductivity for the different NCs as a function of the dispersoid amount, percolation theory was used as universal framework to describe physical properties of disordered systems (Stauffer & Aharony, 1994). Conductivity was computed by fitting the experimental data at high field values, thus neglecting eventual nonlinear effects which appear in the low voltage region. The idea behind the theory is that, given a lattice of a certain dimensionality and coordination, representing the dissipative or insulating matrix, a certain concentration of conductive nodes is randomly added to the system. By increasing the number of conductive nodes beyond a certain limit, said percolation threshold, a complete random walk across the lattice is made available to the carriers and a conductive behavior is observed.

$$\sigma \propto (p-p_c)^t \tag{1}$$

Equation (1) indicates that conductivity σ is proportional to a quantity depending on the volume fraction p of conductive dispersoid, on the percolation threshold p_c and on a universal scaling exponent t. Figure 13 shows the fit to experimental data, relative to our samples. The extrapolated parameters are expressed in Table 3. Generally the model seems unsuitable to fit experimental data relative to the PVB NCs: no clear transition between insulating and conductive behavior is seen and the trend of conductivity versus CNTs volume fraction is linear, in semi-logarithmic scale (Figure 13, left panel). Remarkable is the case of matrix H1, showing an insulating state even when added by more than 1 v.-% of CNTs. E and PDMS matrices, for comparison, present a clear transition. Referring to Table 3 data, we can see that the lowest percolation threshold was found for E resin (0.2±0.1 v.-%),

followed by PDMS (0.7±0.2 v.-%). The critical exponent t is always close to 2.0, which is the expected value for a 3-dimensional sample (Kilbride et al., 2002).

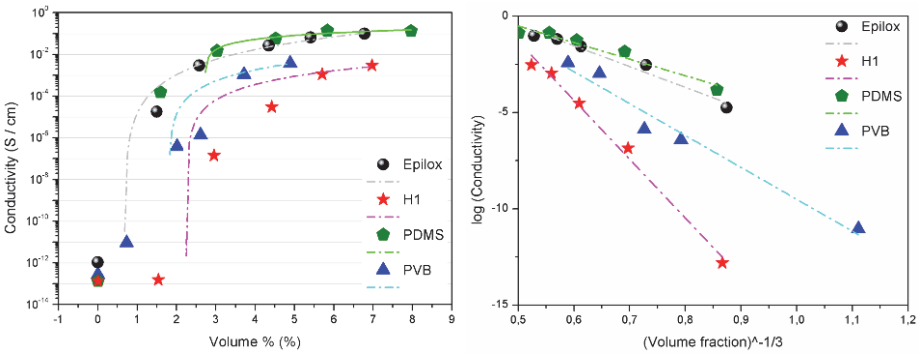

Fig. 13. Left panel: DC conductivity as a function of dispersoid volume fraction fitted by percolation model of Equation (1). Right panel: fit to experimental data according to the fluctuation-assisted tunnelling model of Equation (2).

Considering the real geometry of practical samples, physical models must be modified to take into account in particular the probability and nature of a contact between dispersoids. For example both computations and experiments show that the aspect ratio of the dispersoid plays an important role for the resulting composite properties: in particular, high aspect ratio materials (Balberg, 1987) result in a lower percolation threshold with respect to spherical particle ones (Chiolerio et al., 2010). An interesting simplification of the fluctuation-induced tunnelling for constant temperature (Kilbride et al., 2002), assuming that the CNT content is homogeneously dispersed, results in a scaling of the conductivity according to Equation 2:

$$\ln \sigma = -Ap^{-1/3} \tag{2}$$

This means that, under constant temperature, the electrical behavior is described by fluctuations depending on the mean distance between CNTs, which determines the potential barrier height. A fit to experimental data according to Equation (2) is presented in Figure 13, right panel. The model provides a very good and universal framework to predict data for every sample considered in this chapter. Parameters extrapolated from the equation are presented in Table 3. In particular, it is possible to see from the R^2 values that the fit according to this model is more accurate. It appears that PDMS has the lowest effect on affinity, the lowest the probability that the matrix affects the dispersion geometry. When the affinity, on the contrary, is not so high, CNTs may be detached from the matrix and increasing their concentration may have a smoother effect.

Matrix	p_c [v.-%]	T	R^2	A	R^2
E	0.2±0.1	2.0±0.2	0.97	11±1	0.96
H1	2.0±0.1	2±1	0.90	31±2	0.99
PDMS	0.7±0.2	2.7±0.5	0.91	9±1	0.93
PVB	2.0±0.1	2±1	0.84	17±2	0.97

Table 3. Properties of the PMNCs as extrapolated from models in Equation (1) and (2).

4. Conclusions

In conclusion we prepared four sets of NCs, using four commercial polymeric matrices (E, H1, PDMS and PVB), by dispersing an increasing amount of functionalized MWCNTs. Aim of our work was the easy preparation of cost-effective materials for electrical applications. A detailed characterization, made making use of sophisticated FEM simulations and a careful realization of a measurement setup, allowed to collect confident estimates for the resistivities and to apply physical models such as the percolation theory and the fluctuation-mediated tunneling theory. Parameters extracted from the model fitting allowed us to conclude that the lowest percolation threshold may be found for resin E; the PDMS resin shows the lowest variation of electrical properties by addition of CNTs, even though the matrix conductivity is quite high even with a very low amount of CNTs. On the contrary, resin H1 shows the higher variation of electrical resistance by addition of CNTs. Finally, PVB NCs show an interesting threshold-free behavior, consisting in a linear variation of logarithmic conductivity versus CNTs volume fraction.

5. Acknowledments

The Authors would like to acknowledge Dr. Salvatore Guastella and Mr. Edoardo Benassi for their precious help.

6. References

Ajayan PM, Stephan O, Colliex C, Trauth D (1994). Aligned carbon nanotube arrays formed by cutting a polymer resin–nanotube composite, Science Vol. 265, (1994), pp.1212-4

Balberg, I. (1987). Tunneling and nonuniversal conductivity in composite materials. Physical Review Letters, Vol.59, No.12, (1987), pp. 1305-1308

Breuer O., Sundararaj U. (2004). Big returns from small fibers: a review of polymer/carbon nanotube composites, Polymer Composite Vol. 25, (2004), pp.630-645

Castellino, M.; M. Tortello, S. Bianco, S. Musso, M. Giorcelli, M. Pavese, R. S. Gonnelli, A. Tagliaferro (2010). Thermal and Electronic Properties of Macroscopic Multi-Walled Carbon Nanotubes Blocks, Journal of Nanoscience and Nanotechnology, Vol. 10 (2010), p. 3828-3833, ISSN: 1533-4880

Chiolerio, A., Allia P., Chiodoni A., Pirri F., Celegato F. and Coisson M. (2007). Thermally evaporated Cu-Co top spin valve with random exchange bias. Journal of Applied Physics, Vol.101, (2007), pp. 123915-1-123915-6

Chiolerio, A., Musso S., Sangermano M., Giorcelli M., Bianco S., Coisson M., Priola A., Allia P. and Tagliaferro A. (2010). Preparation of polymer-based composite with magnetic anisotropy by oriented carbon nanotube dispersion. Diamond and Related Materials, Vol.17, (2008), pp. 1590-1595

Chiolerio, A., Vescovo, L. and Sangermano, M. (2010). Conductive UV-cured acrylic inks for resistor fabrication: models for their electrical properties. Macromolecular Chemistry and Physics, Vol.211, (2010), pp. 2008-2016

Coleman, J. N. ; S. Curran, A. B. Dalton, A. P. Davey, B. McCarthy, W. Blau, and R. C. Barklie (1998). Percolation-dominated conductivity in a conjugated-polymer-carbon-nanotube composite, Physical Review B, Vol. 58 (1998), pp. R7492-7495

Coleman JN, Khan U, Blau WJ & Gun'ko YK. (2006). Small but strong: a review of the mechanical properties of carbon nanotube polymer composites, Carbon Vol. 44, (2006), pp.1624-52

Collins P.G., P.Avouris, Scientific American, Vol.283, (2000), 62

Gao Guan-hui, Chen Shou-gang, Xue Rui-ting, Yin Yan-sheng (2009), Study on the surface modification and dispersion of multi-walled carbon nanotubes, Advanced Material Research, Vols. 79-82, (2009), pp. 609-612

Grove, A. S. (1993). Physics and Technology of Semiconductor Devices, Wiley & Sons, 1993

Hone J, Piskoti C, Zettl A. Thermal conductivity of single-walled carbon nanotubes. Physics Review B, Vol.59(4), (1999), R2514–6

Hu, N. ; Yoshifumi Karube, Cheng Yan, Zen Masuda, Hisao Fukunaga (2008). Tunneling effect in a polymer/carbon nanotube nano composite strain sensor, Acta Materialia, Vol. 56, (2008), pp. 2929–2936

Iijima S., (1991). Helical microtubules of graphitic carbon, Nature, Vol.354, p. 56–8

Kilbride B.E., Coleman J.N., Fournet P., Cadek M., Drury A., Hutzler S., Roth S. and Blau W.J. (2002), Experimental observation of scaling laws for alternating current and direct current conductivity in polymer-carbon nanotube composite thin films, Journal of Applied Physics, Vol. 92, (2002), pp. 4024-4030

Liu, C.H. & Fan S.S. (2007). Nonlinear electrical conducting behaviour of carbon nanotube networks in silicone elastomer. Applied Physics Letters, Vol.90, (2007), pp. 041905-1-041905-3

MacDiarmid, A.G. (2002). Synthetic metals: a novel role for organic polymers. Synth. Metals, Vol. 125, pp. 11-22, ISSN: 0379-6779

Moniruzzaman M, Winey KI. (2006). Polymer nanocomposites containing carbon nanotubes, Macromolecules Vol. 39, (2006), pp.5194-205

Schroder, D. K. (1990). Semiconductor Material and Device Characterization, Wiley Inter-Science Publications, 1990

Sheng, P. (1980). Fluctuation-induced tunnelling conduction in disordered materials. Physical Review B, Vol.21, No.6, (1980), pp. 2180-2195

Smits F.M. , "Measurement of sheet resistivities with the four-point probe", Bell Syst. Tech. J., (1958), pp. 711-718

Stauffer, D. & Aharony A. (1994). Introduction to percolation theory. Taylor and Francis, London, 1994

Yu M.-F., B.S. Files, S. Arepalli, R.S. Ruoff, Tensile Loading of Ropes of Single Wall Carbon Nanotubes and their Mechanical Properties Physical Review Letters, Vol.84, (2000),5552

http://www.nanocyl.com/en/Products-Solutions/Products/Research-Grades/Thin-Multi-Wall-Carbon-Nanotubes

http://www.leuna-harze.de/eindex.html

http://www.leuna-harze.de/eindex.html

http://www.dowcorning.com/applications/search/products/Details.aspx?prod=01064291&type=PROD

http://www3.dowcorning.com/DataFiles/090007b2815a650e.pdf

http://www3.dowcorning.com/DataFiles/090007b28147aa39.pdf

http://www.sigmaaldrich.com/catalog/DisplayMSDSContent.do

12

Polymer Composites with Carbon Nanotubes in Alignment

Huisheng Peng, Xuemei Sun and Tao Chen
Key Laboratory of Molecular Engineering of Polymers of Ministry of Education, Department of Macromolecular Science, and Laboratory of Advanced Materials, Fudan University, China

1. Introduction

Carbon nanotubes are typically considered as molecular-scale tubes of graphitic carbon. Depending on numbers of carbon layers, they are categorized as single-walled and multi-walled nanotubes (Zhao & Stoddart, 2009). The unique structure provides nanotubes with extraordinary mechanical and electrical properties, e.g., tensile strength up to 63 Gpa (Harris, 2004) and theoretically carrying electrical current density of 1,000 times higher than copper (Hong & Myung, 2007). Nanotubes have been extensively investigated with publication over 50,000 (searched from Web of Science) in recent ten years, and have been proposed for various applications in the fields of chemistry, physics, and engineering (Feldman et al., 2008; Guldi et al., 2005; Liu et al., 2009; Peng et al., 2008a; Shi, 2009).

Although nanotubes are very promising in a wide variety of fields, the large-scale applications of individual nanotubes remain challenging due to the difficulty in structure control, existence of impurities, and poor processability (Karousis et al., 2010). In order to improve their practical applications, bulk nanotube materials have recently attracted increasing attentions, particularly, by formation of composites with polymers (Moniruzzaman & Winey, 2006; Peng, 2008b). Here nanotubes may provide good mechanical, electrical, and thermal properties, while polymers enable them with high flexibility, low cost, and easy fabrication. Three typical methods, i.e., solution blending, melt blending, and in situ polymerization, have been widely explored (Moniruzzaman & Winey, 2006). Unfortunately, a common and critical challenge is yet to be solved, i.e., randomly dispersed nanotubes in polymer matrices (see Figure 1) (Peng, 2008b). As a result, the prepared composites could not fully take advantage of the exceptional properties of individual nanotubes. For instance, we found that a nanotube/poly(methyl methacrylate) composite showed low tensile strength and electrical conductivity of 10–100 MPa and 10^{-6}–10^{-1} S/cm, respectively.

Several groups have done extensive research in trying to solve the above challenge (Feldman et al., 2008; Guldi et al., 2005; Karousis et al., 2010; Liu et al., 2009; Moniruzzaman & Winey, 2006; Peng, 2008b). Various approaches such as the use of external field (Kimura et al., 2002), mechanical stretching (Jin et al., 1998), spin-casting (Safadi et al., 2002), melt fiber spinning (Haggenmueller et al., 2003), and electrospinning (Ge et al., 2004), have been

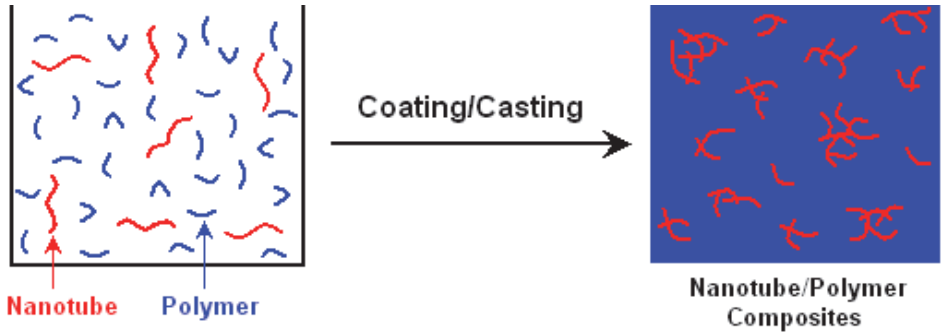

Fig. 1. Schematic illustration for the random aggregation of nanotubes in nanotube/polymer composites synthesized by traditional approaches. Reproduced with permission from Reference (Peng, 2008b). Copyright 2008, American Chemical Society.

investigated. However, alignment of nanotubes still needs to be improved, and properties of composites are not as good as expected. Recently, an effective approach has been developed by the use of nanotube arrays, sheets, and fibers with highly aligned nanotubes as building blocks to synthesize composite materials. Successful systems have been extensively reported by us and other groups. This chapter describes recent progress in aligned nanotube/polymer materials with excellent mechanical, electrical, and sensing properties.
For the convenience of readers, the basic synthesis and characterization of nanotube arrays, sheets, and fibers which are crucial to fabricate high-quality composites are first discussed in this chapter. Then the main efforts are paid to the preparation of aligned nanotube/polymer arrays, films, and fibers with emphasis on the improved mechanical, electrical, and sensing properties.

2. Aligned carbon nanotubes in forms of arrays, sheets, and fibers

2.1 Carbon nanotube arrays

Nanotube arrays are typically synthesized through a chemical vapor deposition process in which the catalytic metal (e.g., Fe, Co, or Ni) film on SiO_2/Si wafer form nanoparticles at high temperature to assist nanotube growth. High-efficiency catalysts are critical to grow high-quality aligned nanotube arrays. Iron possibly represents the most studied catalyst system (Fan et al., 1999). For the traditional direct coating of iron film on SiO_2/Si wafer, the iron layer generally becomes inactive within several minutes of nanotube growth due to its inter-diffusion with the substrate and accumulation of amorphous carbon. In order to grow longer nanotube arrays, catalyst precursors were continuously added to the system to nucleate new catalyst nanoparticles during the growth, however, the arrays were often composed of several stacked layers of nanotubes. In addition, the nanotubes grown in this way were often accompanied by excessive catalyst particles and amorphous carbon.
Recently, a new approach was reported, in which a thin Al_2O_3 layer was introduced between the catalyst and substrate to efficiently improve the growth of nanotubes (Li et al., 2006). The dense buffer layer enhances the Fe wettability during the preparation of catalyst. In addition, the Al_2O_3 layer functions as a buffer to prevent the inter-diffusion between Fe and substrate, and further improves the formation of stable catalyst nanoparticles during the nanotube growth.

For the Fe/Al_2O_3 catalyst system, the thickness uniformity of the Fe film is critical to grow good nanotube arrays. As compared in Figure 2, for the catalyst of Fe (thickness of 1 nm)/Al_2O_3 (thickness of 10 nm) under the same experimental conditions, the non-uniform Fe film melted to form polydisperse nanoparticles from which no nanotube array was grown (Figure 2a), while the uniform Fe film produced monodisperse nanoparticles which assisted the growth of long nanotube array (Figure 2b). The sizes of nanoparticles may be qualitatively controlled by the thickness of Fe film, which typically ranges from 0.2 to 1 nm. The resulting nanotubes are mainly multi-walled with diameters from 7 to 50 nm.

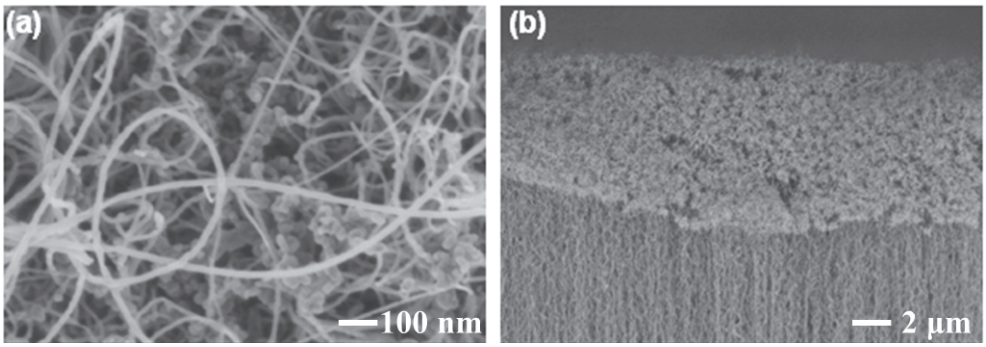

Fig. 2. The influence of the uniformity of Fe film on growth of aligned nanotube arrays. (a) Scanning electron microscopy (SEM) image of grown nanotubes by the use of non-uniform Fe film. (b) SEM image of grown nanotubes by the use of uniform Fe film. The thickness of the used Fe film was the same of 1 nm.

In a typical synthesis, the growth is fast (e.g., ~ 60 μm/min) in the first 20 min; afterwards, the growth gradually slows down and was normally terminated at 90 min. The growing rate also depends on the synthetic temperature. Zhu et al. had investigated a temperature range of 730–780 °C, and found that the growing rates increased with increasing temperatures, e.g., 46 μm/min at 730 °C, 64 μm/min at 750 °C, and 74 μm/min at 780 °C (Li, Q. et al., 2006). Water vapor, a weak oxidant, also greatly affected the growth of nanotubes in a more complex behavior. Introduction of water vapor did not obviously promote the growth of nanotubes at a lower temperature range of 730 to 750 °C. In contrast, it significantly increased the growing rates of nanotubes at a higher temperature range from 750 to 780 °C. In addition, water vapor had been found to prolong the growth time from 90 to 120 min, which produced longer nanotubes.

In order to further improve the production of nanotube arrays, an approach based on continuously moving substrates has been developed during chemical vapor deposition processes. As shown in Figure 3, the Fe/Al_2O_3 catalyst on Si substrate was fed continuously into the growth zone of the furnace through a moving stage driven by external motor, and nanotube arrays were then realized to be produced at large scale (de Villoria et al. 2009). Currently, the nanotube arrays could be grown at moving speeds of substrates up to 2.4 mm/s. No obvious differences had been observed for the resulting nanotube arrays between static and moving growth models.

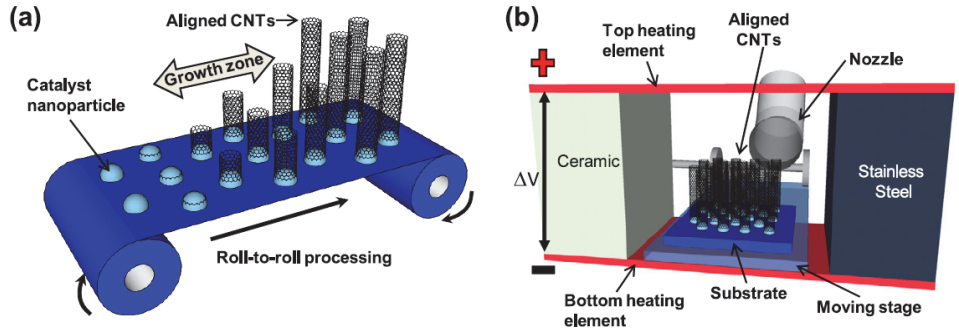

Fig. 3. (a) Schematic illustration of the continuous feeding of the catalyst. (b) Schematic construction of the synthetic system. Reproduced with permission from Reference (de Villoria et al., 2009). Copyright 2009, IOP Publishing.

2.2 Carbon nanotube sheets

A general and efficient route of preparing aligned nanotube sheets is to directly spin them out of the above array. Figure 4a schematically shows the formation of nanotube sheet spun from an array. Figure 4b and 4c further show scanning electron microscopy images of nanotube sheets in which nanotubes are highly aligned along the spinning direction as required. The measured areal sheet density was 2.7 $\mu g/cm^2$ and the volumetric density was 1.5 $\mu g/cm^3$. The density of nanotube sheet can be further improved, e.g., 0.5 g/cm^3, simply by immersing them into a liquid along the nanotube-aligned direction and then taking them out (Zhang, M. et al., 2005).

It should be noted that most nanotube arrays are not spinnable. In order to investigate their spinnability, nanotube arrays grown with increasing growth times from 10 to 180 min were first compared as model materials (Huynh & Hawkins, 2010; Sun & Peng, unpublished results). It was found that the prolonged growth time dramatically decreased the spinnability of the arrays, and the arrays grown longer than 30 min did not show good spinnability. For instance, long sheets up to meters were spun from the arrays grown in 15 min; sheets with length of centimeters were spun from the arrays grown in 40 min as the sheets easily broke during the spinning process; even worse, only short clumps were pulled out of the arrays grown in 180 min. The morphologies of the arrays were studied by scanning electron microscopy (Sun & Peng, unpublished results). The nanotube array shows very clean surfaces at growth times below 30 min. With the increase of growth time, a disordered layer was observed at the top of the arrays. The thickness of this layer increased with increasing growth time. Figure 5 compares the top and side views of arrays synthesized with different growth times of 15 and 90 min. The array grown in 15 min is clean without aggregates, while a lot of flake-like carbon aggregates are found at the top of the nanotube array grown in 90 min. These flakes are randomly piled, and their sizes decrease with increasing growth times. The flakes severely hinder the spinnability of synthesized arrays.

Besides growth time, the other experimental conditions including substrate, temperature, gas flow rate, and catalyst as well as its pre-treatment are also critical for synthesis of spinnable nanotubes. Huynh et al. and Zhang et al. had systematically investigated the effects of above variables that influence the spinnability of nanotubes, respectively (Huynh,

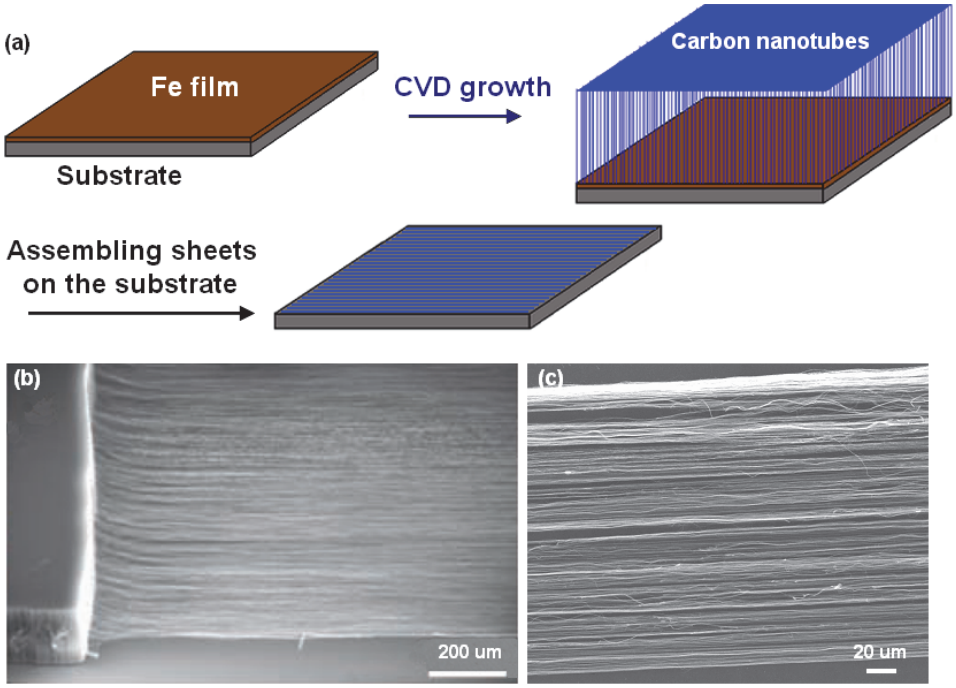

Fig. 4. Fabrication of nanotube sheets by a direct spinning method. (a) A schematic illustration. (b) SEM image for the formation of nanotube sheet from an array. Reproduced with permission from Reference 21. Copyright 2005, American Association for the Advancement of Science. (c) SEM image of a nanotube sheet. Reproduced with permission from Reference (Peng, 2008b). Copyright 2008, American Chemical Society.

2010; Zhang, Y. et al.; 2010). However, there is no simple reason or key factor for nanotube spinnability. In addition, although the surface morphology and alignment of nanotube arrays had been demonstrated to be very important for their spinnability, no unique characteristic is found to obviously distinguish a spinnable from a non-spinnable array. It was shown that nanotube arrays could be spinnable or not for a wide variety of height (80-900 μm) with nanotube diameters ranging from 7 to 11 nm and areal densities across an order of magnitude. Although it is difficult to fully understand the mechanism of nanotube spinnability currently, two possible models had been suggested by Fan et al. and Baughman et al., respectively (Zhang, M. et al., 2004; Zhang, X. et al., 2006). Fan and co-workers proposed that the unique features of spinnable nanotube arrays lied in that the nanotubes had very clean surfaces, and consequently there were strong van der Waals interactions among them (Zhang, X. et al., 2006). When nanotubes were pulled out of the arrays, it was the van der Waals force that made the nanotubes to join end to end to form a continuous sheet. Baughman and co-workers claimed that the spinnability was due to the disordered region at the top and bottom of the nanotube array, which entangled together forming a loop (Zhang, M. et al., 2004, 2005). The above mechanisms had been demonstrated to work for specific arrays. However, as spinnable nanotube arrays greatly vary for different systems or even for the same systems, it remains challenging to draw general conclusions.

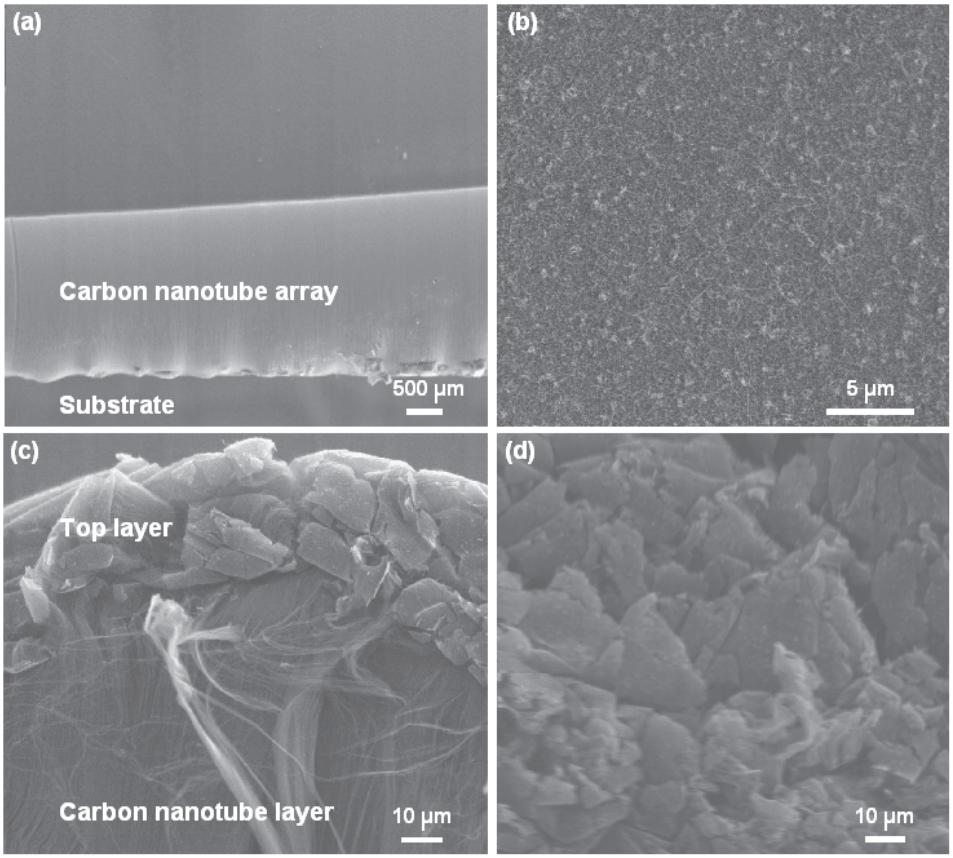

Fig. 5. Typical SEM images of (a) the spinnable nanotube array by side view, (b) the spinnable nanotube array by top view, (c) the non-spinnable nanotube array by side view, and (d) the non-spinnable nanotube array by top view.

2.3 Carbon nanotube fibers

Similar to nanotube sheets, nanotube fibers are mainly spun from nanotube arrays (Zhang, M. et al., 2004). Figures 6a and 6b show the formation of a fiber by twisting the nanotube sheet pulled out of an array. This spinning process can be easily scaled up to produce long nanotube fibers. The diameters of nanotube fibers can be controlled from 2 to 30 μm by tuning the initial ribbon width which is defined as a bunch of nanotubes pulled out of an array at the beginning of the spinning.

Although nanotube fibers are generally spun from aligned nanotube arrays, they had been also fabricated from nanotube cottons in which nanotubes were randomly arranged on substrates (Zheng et al., 2007). The cotton was composed of low-density nanotubes with length of centimeters and diameter of 100-380 nm, and these ultra-long nanotubes were entangled to form continuous fibers. The other methods, e.g., wet spinning of nanotube dispersions (Zhang, M. et al., 2004) and direct spinning from chemical vapor deposition reactions(Ericson et al.; 2004), had been also developed to fabricate nanotube fibers. Figure 6c shows a spool of 30-m

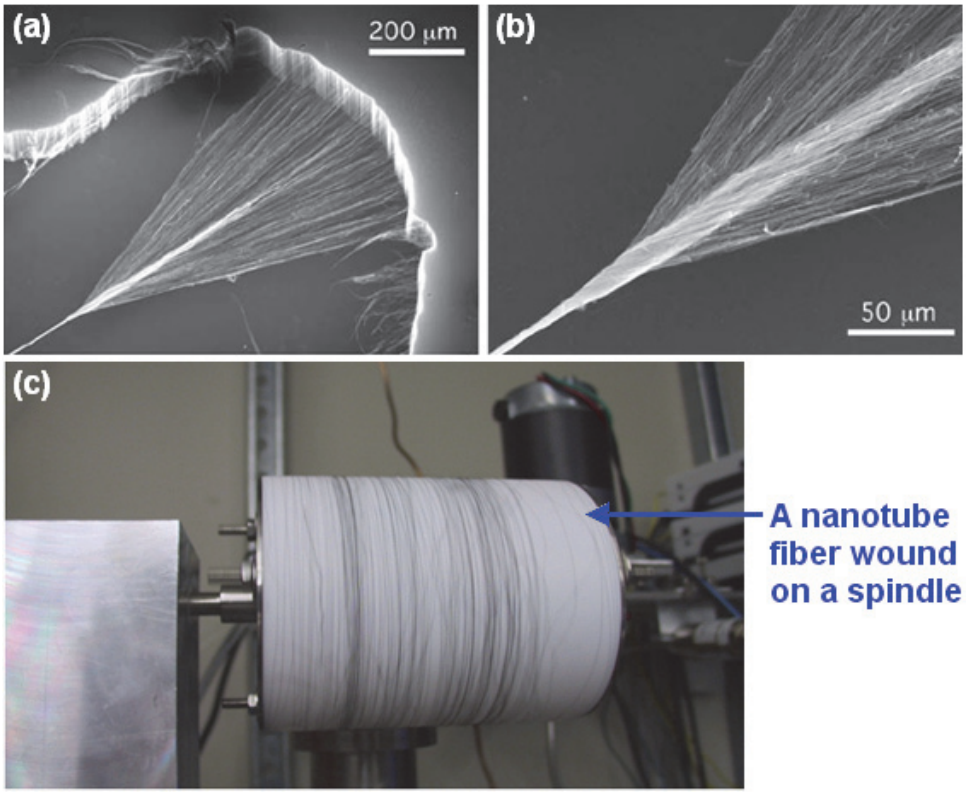

Fig. 6. (a) and (b) SEM images of a nanotube fiber spun out of an array. Reproduced with permission from Reference (Zhang, M. et al., 2004). Copyright 2004, American Association for the Advancement of Science. (c) A 30-m spool of nanotube fiber fabricated by a solution spinning process. Reproduced with permission from Reference (Ericson et al., 2004). Copyright 2004, American Association for the Advancement of Science.

nanotube fiber wound on a spindle via a solution spinning process (Ericson et al.; 2004). Nanotube fibers showed much higher density of ~ 0.8 g/cm^3 compared with nanotube sheets (Zhang, M. et al., 2004). The linear density is typically 10 μg/m compared with 10 mg/m and 20-100 mg/m for cotton and wool yarns, respectively. That is, about a million of nanotubes pass through the cross section of a fiber with diameter of 5 μm. As nanotubes are tightly bundled together inside, nanotube fibers had shown excellent mechanical and electrical properties, e.g., high tensile strengths and electrical conductivities.

In general, the tensile strength of a twisted fiber can be described by the equation of $\delta_f/\delta_{nanotube} \approx \cos\alpha[1 - (k\cos\alpha)]$, where δ_f and $\delta_{nanotube}$ are the tensile strengths of the fiber and the nanotube, respectively; α is the twist angle; and $k = (dQ/\mu)^{1/2}/3L$ with d of the nanotube diameter, L of the nanotube length, μ of the friction coefficient among nanotubes, and Q of the nanotube migration length (Li, Y. L. et al., 2004). Therefore, the fiber strength increases with increasing nanotube length and decreasing nanotube diameter. For instance, the nanotube fibers spun from arrays of 300, 500, and 650 μm in thickness showed tensile

strengths of 0.32, 0.56, and 0.85 GPa, respectively (Li, Y. L. et al., 2004); the diameter of spinnable nanotubes typically ranges from 7 to 11 nm. Post-spin twisting can also improve their tensile strengths with larger twist angle and higher density of building nanotubes. For instance, the twist angle of outer nanotubes increased from 10° to 21°; the density of nanotubes increased two times with decreasing fiber diameter from 10 to 7 μm, and the closer contact among nanotubes enhanced their van der Waals forces and frictions with better load transfers. Similarly, a solution treatment can also increase the fiber densities with improved tensile strengths. Zhu and co-workers reported that the specific strength of nanotube fiber could be 5.3 times the specific strength of the strongest commercial carbon fiber (T1000), and the specific stiffness of nanotube fiber could be 4.3 times the specific stiffness of the stiffest commercial carbon fiber (M70J) (Zhang, X. et al., 2007). Windle and co-workers further increased the tensile strength of nanotube fiber to ~9.6 GPa (Koziol et al., 2007). Figure 7 compares the specific strength and specific stiffness of the above nanotube fibers (the elliptical area at the top left corner of the graph) with other high-performance engineering fibers.

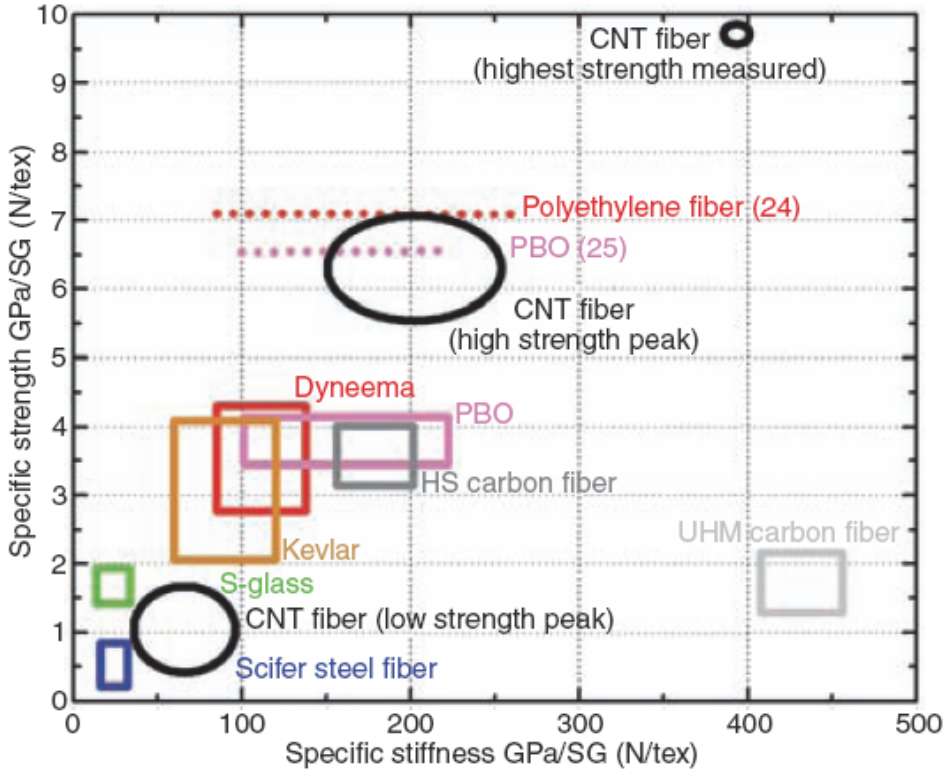

Fig. 7. Comparison of the specific strength and specific stiffness of nanotube fibers versus the properties of other commercially available high-performance fibers. Reproduced with permission from Reference (Koziol et al., 2007). Copyright 2007, American Association for the Advancement of Science.

Nanotube fibers showed excellent electrical conductivities up to 10^3 S/cm at room temperature. Figure 8a further indicates the temperature dependence of a nanotube fiber's conductivities measured by a four-probe method. The conductivity increases with the increase of the temperature, suggesting a semiconducting behavior. For the temperature dependence of conductivity, two main mechanisms had been suggested, i.e. variable range hopping mechanism and tunneling conduction mechanism (Li, Q. et al., 2007; Peng et al., 2008c). A systematic comparing study showed that the conduction in nanotube fibers was mainly controlled by the hopping mechanism. In more detail, the relationship between conductivity and temperature in hopping model can be also expressed as $\sigma \propto \exp(-A/T^{[1/(d+1)]})$, where A is a constant and d is the dimensionality. The plots of $\ln\sigma$ *vs.* $T^{-1/4}$ (for d=3), $T^{-1/3}$ (for d=2) and $T^{-1/2}$ (for d=1) show decreasing linear fitting coefficients (Figures 8b, 8c, and 8d), which suggests that the electron transport is more consistent with a three-dimensional hopping mechanism. This behavior is most likely due to the defect structures of nanotubes and a lot of contacting points among neighboring short nanotubes in fibers. Therefore, electrons cannot be confined in the one-dimensional channel along the nanotube-aligned direction. Instead, electrons hop from one localized site to another, or possibly from a nanotube to another.

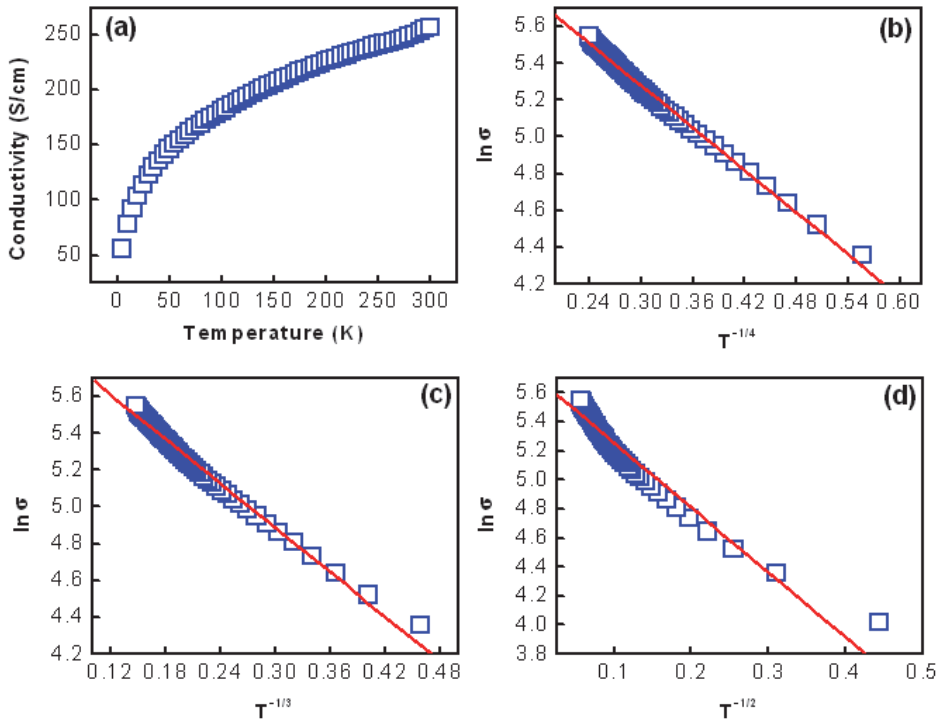

Fig. 8. Electrical properties of a nanotube fiber. (a) Temperature dependence of the conductivity measured by a four-probe method. (b) Three-dimensional hopping conduction model by plot of $\ln\sigma$ vs. $T^{-1/4}$. (c) Two-dimensional hopping conduction model by plot of $\ln\sigma$ vs. $T^{-1/3}$. (d) One-dimensional hopping conduction model by plot of $\ln\sigma$ vs. $T^{-1/2}$.

The electrical properties of nanotube fibers largely depend on structural changes of nanotubes. Therefore, their conductivities can be tuned by different chemical treatments. Oxidization on their surfaces increased the fiber's conductivities by introduction of acceptor dopant groups. The covalent link of metal nanoparticles onto nanotubes also enhanced the fiber's conductivities through an increase of carrier density. However, annealing of nanotube fiber in forming gas (94% Ar and 6% H_2) significantly lowered their conductivity due to the formation of sp^3 carbon bonds (Li, Q. et al., 2007).

3. Aligned carbon nanotube/polymer composites

3.1 Preparation of aligned carbon nanotube/polymer composites

The structures of aligned nanotube/polymer composites in the forms of arrays, films, and fibers have been schematically shown in Figure 9. Polymers are incorporated into nanotubes which maintain the high alignments. These composites are mainly synthesized through the use of above pure nanotube arrays, sheets, and fibers, and the other fabrication methods will be also compared later.

Aligned nanotube/polymer arrays are typically prepared by immersing a pure nanotube array into polymer solution, followed by evaporation of solvent (Peng & Sun, 2009). For this approach, a wide variety of polymers (either plastic or conjugated polymers) may be used to fabricate composite arrays. Figure 10 compares a nanotube array before and after incorporation with polystyrene. Obviously, nanotubes maintained the high alignment in polymer matrix. Similarly, aligned nanotube/polymer composites could be also synthesized by first immersing pure nanotube arrays into monomers, followed by polymerization of monomers (Feng et al., 2003; Raravikar et al., 2005; Yang et al., 2008). Recently, porous nanotube arrays were fabricated after heating treatment of as-synthesized dense nanotube arrays or through the use of polystyrene beads (Das et al., 2009; Dionigi et al., 2007), and polymers could be incorporated into the pores to form aligned nanotube composites.

The aligned nanotube/polymer films are produced by spin-coating or casting polymer solutions onto nanotube sheets, followed by evaporation of solvents. Film thickness may be controlled by varying concentrations of polymer solutions and coating times. After incorporation of designed polymers such as polystyrene, poly(methyl methacrylate), or sulfonated poly(ether ether ketones), the derived composite films were transparent and showed optical transparencies of higher than 80% (thickness of ~5 μm) (Peng, 2008b).

Alignment of nanotubes in both composite arrays and films had been also realized through the use of external stimuli such as mechanical force, magnetic field, and electrical field (Ahir et al., 2006; Ajayan et al., 1994; Jin et al., 1998; Kimura et al., 2002; Zhu et al., 2009). As to

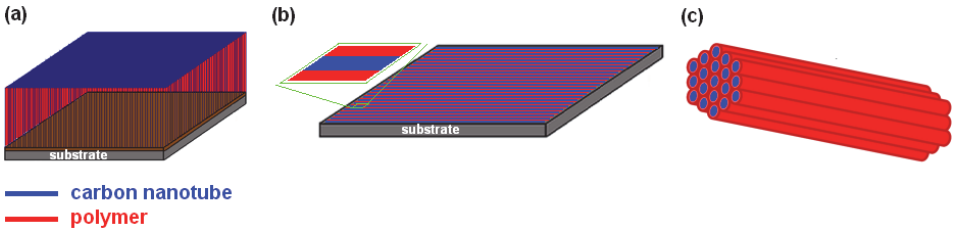

Fig. 9. Schematic illustration of the aligned nanotube/polymer composites in the forms of (a) array, (b) film, and (c) fiber.

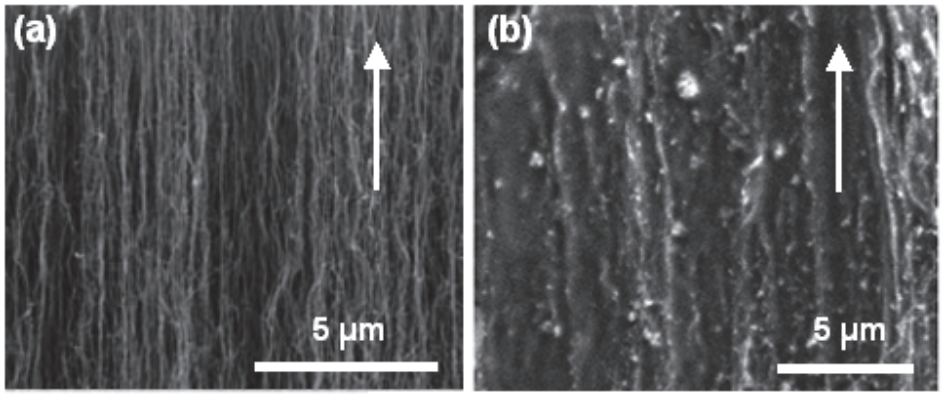

Fig. 10. SEM images of the aligned nanotubes (a) before and (b) after formation of composite with polystyrene. The white arrows show the aligned directions of nanotubes. Reproduced with permission from Reference (Peng & Sun, 2009). Copyright 2009, Elsevier.

mechanical force, cutting nanotube/resin composites induced nanotubes on the surface to align along the cutting direction (Kimura et al., 2002), or mechanical stretching of nanotube/polyhydroxyaminoether composites at high temperature aligned nanotubes in polymer matrix (Kimura et al., 2002). For the synthesis of aligned nanotube/polymer composites by magnetic field, monomers in nanotube solutions were polymerized in a mold under magnetic field (Kimura et al., 2002). Alignment of nanotubes was based on their anisotropic nature. Alignment of nanotubes in bulk epoxy matrix was available by application of electrical field, where nanotube/epoxy composites were prepared by a layer-by-layer method (Zhu et al., 2009). Alignment of nanotubes was due to polarization of their high aspect ratios under electrical field. However, composites by these methods show relatively low alignments of nanotubes compared to the use of nanotube arrays or sheets. The alignment of nanotubes may be assessed by microscopy technology, X-ray diffraction, and polarized Raman spectroscopy.

Aligned nanotube/polymer fibers can be directly prepared by physical attachment or chemical reaction of polymers onto nanotubes in pure nanotube fibers. To improve the uniformity of polymers, monomers may be first incorporated into nanotube fibers followed by polymerization as monomers can penetrate into much smaller voids in nanotube fibers and form more uniform composites through solution processes. For instance, high-quality nanotube/polydiacetylene composite fibers were produced by the physical attachment of diacetylenic monomers followed by topochemical polymerization of diacetylenic moieties under UV light (Peng et al., 2009).

Another widely explored method to aligned nanotube/polymer fibers is electrospinning, an electrostatically induced self-assembly process where nanoscale fibers were typically produced (Baji et al., 2010; Ge et al., 2004; Go et al., 2004; Kang et al., 2009). The surface tension, jet elongation, and slow relaxation of nanotubes contribute to orientation of nanotubes. Some other approaches including coagulation-based spinning (Razal et al., 2007; Vigolo et al., 2000 & 2002), melting spinning (Haggenmueller et al., 2003), dip coating method through microfluidic phenomena (Jang et al., 2009), and orientation by external stimuli such as mechanical interaction (Ji et al., 2009) had been also developed to synthesize

aligned nanotube/polymer fibers. However, similar to the composite arrays and films, the nanotube alignments in the resulting composite fibers are much lower compared to the direct use of pure nanotube fibers.

3.2 Improved mechanical, electrical, and sensing properties of aligned carbon nanotube/polymer composites

The alignment of nanotubes has greatly improved the mechanical properties of their polymer composites. Figure 11 compares the tensile strengths of less aligned nanotube/polymer fibers and aligned nanotube/polymer fibers. The nanotube/polymer fibers at Figure 11a were fabricated through a melting spinning process, i.e., the melting nanotube/nylon 6 mixtures were pressurized through a spinneret to form composite fibers (Gao et al., 2005). The nanotube/nylon 6 fibers showed relatively low strengths of less than 100 MPa. In contrast, the aligned nanotube/polymer fibers exhibited the strength of higher than 1000 MPa (Figure 11b).

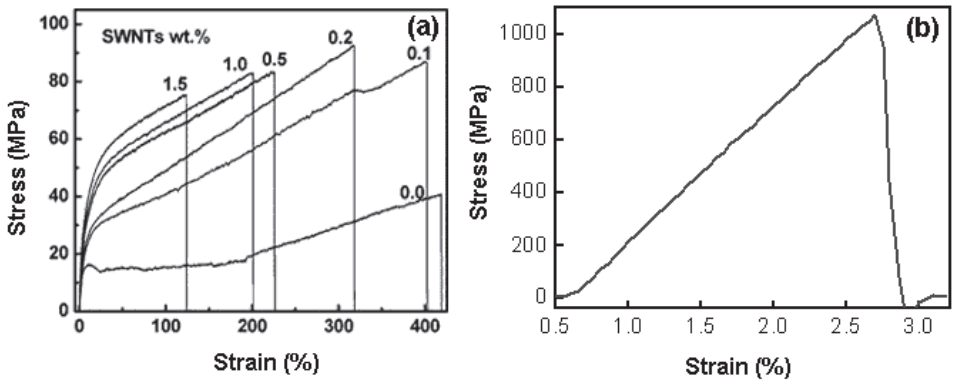

Fig. 11. Comparison of the mechanical strengths for (a) non-aligned nanotube/polymer fibers and (b) aligned nanotube/polymer fibers. Reproduced with permission from Reference (Gao et al., 2005). Copyright 2005, American Chemical Society.

The alignment of nanotubes has also greatly improved the electrical properties of their polymer composites. Figure 12 summarizes and compares the conductivities of randomly dispersed nanotube/polymer composites and aligned nanotube/polymer composites in forms of arrays, films, and fibers (Peng et al., 2008a, 2008b, 2008c; Peng & Sun, 2009). The non-aligned nanotube/polymer composites (including arrays, films, and fibers) fabricated through traditional solution blending or melt blending generally show conductivities lower than 10^{-1} S/cm at room temperature. As a comparison, the aligned nanotube/polymer arrays, films, and fibers show conductivities of 1-100 S/cm, 10-200 S/cm, and 10^2-10^3 S/cm at room temperature, respectively. The aligned nanotube/polymer composites followed a three-dimensional hopping conduction mechanism, which can be important for some optoelectronic applications (Peng et al., 2009).

The improved mechanical and electrical properties of above aligned nanotube/polymer composite have been realized through the direct use of nanotube arrays, sheets, and fibers. In the case of other approaches to align nanotubes (Baji et al., 2010; Ge et al., 2004; Go et al.,

2004; Haggenmueller et al., 2003; Jang et al., 2009; Ji et al., 2009; Kang et al., 2009; Razal et al., 2007; Vigolo et al., 2000, 2002), similar improvements were also observed. For instance, aligned nanotube/polyacrylonitrile fibers after hot-stretching treatment showed a significant enhancement of tensile strength by 320.7% (Ji et al., 2009), while aligned nanotube/epoxy arrays induced by electric field could improve electrical conductivities by four orders of magnitude in the direction of alignment (Zhu, Y. et al., 2009). However, possibly due to the relatively low degree of alignment, both strengths and conductivities were much lower compared with the direct use of aligned nanotube materials, e.g., strength below 325 MPa and conductivity of 10^{-10}–10^{-8} S/cm at room temperature for the discussed nanotube/polyacrylonitrile fibers and nanotube/epoxy arrays, respectively.

Orientation factor had been already used to quantitatively characterize the alignment degree of nanotubes through Herman's equation of $f = (3\langle\cos^2\theta\rangle - 1)/2$, where θ is the average angle between the nanotube and the aligned direction determined by Raman spectroscopy (Ge et al., 2004). However, the orientation factors were only available in very limited studies. Therefore, it remains difficult to quantitatively compare the experimental results (e.g., strengths and conductivities) of nanotube/polymer composites among different methods or different lab.

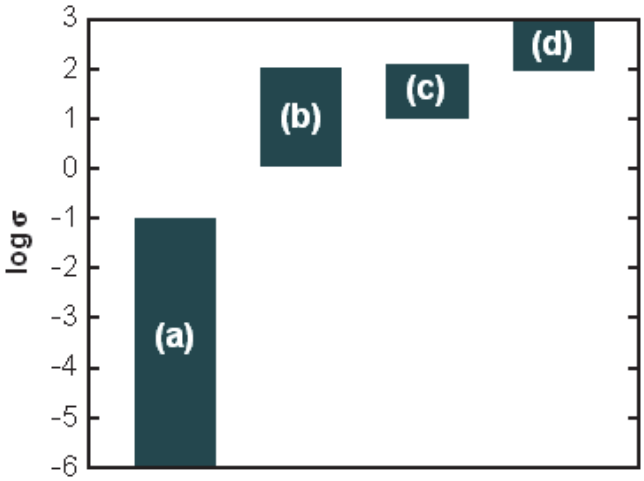

Fig. 12. Comparison of the electrical conductivities for (a) non-aligned nanotube/polymer composites, (b) aligned nanotube/polymer arrays, (c) aligned nanotube/polymer films, and (d) aligned nanotube/polymer fibers.

Nanotubes show the gas sensing capabilities through the changes of resistances after gas sorption. However, the use of non-aligned nanotubes for the sensing detection often needs tedious fabrication processes to integrate single nanotubes into sensors, and the number of analytes is also largely limited. In contrast, aligned nanotubes do not need direct manipulation of individual nanotubes. Particularly, the resistance changes of individual nanotubes could be greatly amplified as millions of nanotubes were collectively addressed through a common electrode (Lin et al., 2003; Wei et al., 2006; Zhu, Z. et al., 2010). For instance, Wei et al. reported that aligned nanotube/poly(vinyl acetate)

arrays showed high sensitivity and good selectivity to a wide variety of chemical vapors such as tetrahydrofuran, ethanol, and cyclohexane (Wei et al., 2006). The similar improvements at sensing capabilities after the nanotube alignment had been also observed for detections of the glucose and other biosensing applications (Lin et al., 2003; Zhu, Z. et al., 2010).

As previously discussed, the aligned nanotube/polymer composites show a semiconducting behavior with three-dimensional hopping conduction mechanism. This electrical property provides composites with other unexpected sensing properties. For instance, polydiacetylene is well known to change colors under external stimuli such as temperature, pH, solvent, and mechanical stress, mainly due to the conformation change of the conjugated backbone (Peng et al., 2007; Sun et al., 2010a, 2010b). By incorporation of polydiacetylene into aligned nanotube fibers, polydiacetylene was first realized to rapidly and reversibly change colors under electrical current, typically from blue to red (Figure 13) (Peng et al., 2009). The capability of forming strong electrical fields among aligned nanotubes was believed to induce the conformation change of incorporated polydiacetylene with the chromatic transition.

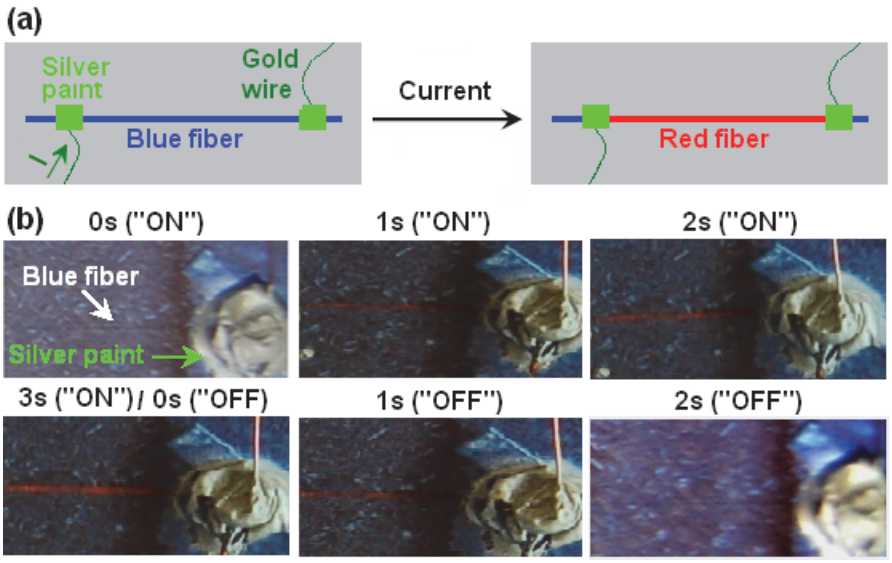

Fig. 13. Chromatic transitions of nanotube/polydiacetylene fibers in response to electric current. (a) Schematic illustration of experimental setups for current-induced chromatism. (b) Rapid and reversible electrochromatism. Reproduced with permission from Reference (Peng et al., 2009). Copyright 2009, Nature Publishing Group.

4. Conclusion

This chapter has mainly described the realization and importance of alignment of nanotubes in their polymer composites. Three typical forms of composites including arrays, films, and fibers are fabricated through the use of nanotube arrays, sheets, and fibers, respectively. The aligned nanotube composites have exhibited much improved mechanical, electrical, and sensing properties compared with those without alignment of nanotubes. The aligned nanotube/polymer composites may show promising applications in a wide variety of fields, particularly as high-end components for aerospace, energy, and other structural and optoelectronic materials.

Despite the great progresses having been made on fabrications, characterizations, and properties of aligned nanotube/polymer composites, here we also hope to call attention to a few key unmet challenges on further developing this new family of functional materials in the future.

Firstly, increasing attentions should be paid to establishing quantitative relationships between the alignment degrees of nanotubes and the properties (e.g., strengths and conductivities) of the composites. Therefore, it becomes available to accurately compare different fabrication approaches and different composite systems, which may provide important and general clues to improve the composite properties.

Secondly, most nanotube arrays are not spinnable, and more efforts are required to understand and control the spinnability of nanotube arrays to fabricate high-performance composite films and fibers. For instance, the mechanical and electrical properties of aligned nanotube/polymer composites strongly depend on the length of nanotubes. The longer the nanotubes, the better are the properties of composites. However, spinnable nanotube arrays range from 80 to 900 μm in height, and higher arrays are typically not spinnable. For the spinnability of nanotube arrays, another crucial issue is related to the nanotube alignment. It had been qualitatively shown that a high alignment of nanotubes was required for their spinnability (Sun & Peng, Unpublished results; Zhang, M. et al., 2005). However, as no quantitative characterizations have been made for the alignment degrees of nanotubes in arrays, it remains unclear for an accurate relationship between the alignment and spinnability of nanotube arrays.

Thirdly, polymers are mainly incorporated into aligned nanotubes through non-covalent interactions, and very few studies can be found to connect polymers and nanotubes by chemical bonds. Nevertheless, compared to physical attachment, polymers can be more uniformly incorporated into nanotubes by chemical modifications, and the resulting composites show more excellent properties, e.g., improved mechanical strengths as polymers cross-link neighboring nanotubes. Of course, some other issues such as uniformity in the composite and repeatability of the fabrication are also important for the development of aligned nanotube/polymer composites, particularly for their practical applications.

5. Acknowledgement

This work was supported by Natural National Science Foundation of China (20904006, 91027025), Science and Technology Commission of Shanghai Municipality (1052nm01600,

09PJ1401100), Program for New Century Excellent Talents in University (NCET-09-0318), Ministry of Education of China, and Program for Key Discipline Creativity Talents at Fudan University.

6. References

Ahir, S. V.; Squires, A. M.; Tajbakhsh, A. R. & Terentjev, E. M. (2006). Infrared actuation in aligned polymer-nanotube composites. Phys. Rev. B, Vol. 73, No. 8, (February 2006), pp. 085420(12).

Ajayan, P. M. & Tour, J. M. (2007). Nanotube composites. Nature, Vol. 447, (June 2007), pp. 1066-1068.

Ajayan, P. M.; Stephan, O.; Colliex, C. & Trauth, D. (1994). Aligned Carbon Nanotubes Arrays Formed by Cutting a Polymer Resin-Nanotube Composite. Science, Vol. 265, No. 5176, (August 1994), pp. 1212-1214.

Baji, A.; Mai, Y.; Wong, S.; Abtahi, M. & Du, X. (2010). Mechanical Behavior of Self-Assembled Carbon Nanotube Reinforced Nylon 6,6 Fibers. Compos. Sci. Technol., Vol. 70, No. 9, (September 2010), pp. 1401-1409.

Das, R. K.; Liu, B.; Reynolds, J. R. & Rinzler, A. G. (2009). Engineered Macroporosity in Single-Wall Carbon Nanotube Films. Nano Lett., Vol. 9, No. 2, (February 2009), pp. 677-683.

de Villoria, R. G.; Figueredo, S. L.; Hart, A. J.; Steiner III, S. A.; Slocum, A. H. & Wardle, B. L. (2009). High-yield growth of vertically aligned carbon nanotubes on a continuously moving substrate. Nanotechnology, Vol. 20, No. 40, (October 2009), pp. 405611(8).

Dionigi, C.; Stoliar, P.; Ruani, G.; Quiroga, S. D.; Facchini, M. & Biscarini, F. (2007). Carbon nanotube networks patterned from aqueous solutions of latex bead carriers. J. Mater. Chem., Vol. 17, No. 35, (September 2007), pp. 3681-3686.

Ericson, L. M. et al. (2004). Macroscopic, Neat, Single-Walled Carbon Nanotube Fibers. Science, Vol. 305, No. 5689, (September 2004), pp. 1447-1450.

Fan, S.; Chapline, M. G.; Franklin, N. R.; Tombler, T. W.; Cassell, A. M. & Dai, H. (1999). Self-Oriented Regular Arrays of Carbon Nanotubes and Their Field Emission Properties. Science, Vol. 283, No. 5401, (January 1999), pp. 512-514.

Feldman, A. K.; Steigerwald, M. L.; Guo, X. F. & Nuckolls, C. (2008). Molecular Electronic Devices Based on Single-Walled Carbon Nanotube Electrodes. Acc. Chem. Res., Vol. 41, No. 12, (August 2008), pp. 1731-1741.

Feng, W.; Bai, X. D.; Lian, Y. Q.; Liang, J.; Wang, X. G. & Yoshino, K. (2003). Well-aligned polyaniline /carbon-nanotube composite films grown by in-situ aniline polymerization. Carbon, Vol. 41, No. 8, (2003), pp. 1551-1557.

Gao, J.; Itkis, M. E.; Yu, A.; Bekyarova, E.; Zhao, B. & Haddon, R. C. (2005). Continuous Spinning of a Single-Walled Carbon Nanotube−Nylon Composite Fiber. J. Am. Chem. Soc., Vol. 127, No. 11, (March 2005), pp. 3847-3854.

Ge, J. J.; Hou, H. Q.; Li, Q.; Graham, M. J.; Greiner, A.; Reneker, D. H.; Harris, F. W. & Cheng, S. Z. D. (2004). Assembly of Well-Aligned Multiwalled Carbon Nanotubes in Confined Polyacrylonitrile Environments: Electrospun Composite Nanofiber Sheets. J. Am. Chem. Soc., Vol. 126, No. 48, (November 2004), pp. 15754-15761.

Go, J. B.; Yu, A. P.; Itkis, M. E.; Bekyarova, E.; Zhou, B.; Niyogi, S. & Haddon, R. C. (2004). Large-Scale Fabrication of Aligned Single-Walled Carbon Nanotube Array and Hierarchical Single-Walled Carbon Nanotube Assembly. J. Am. Chem. Soc., Vol. 126, No. 51 (December 2004), pp. 16698-16699.

Guldi, D. M.; Rahman, G. M. A.; Zerbetto, F. & Prato, M. (2005). Carbon Nanotubes in Electron Donor-Acceptor Nanocomposites. Acc. Chem. Res., Vol. 38, No. 11, (September 2005), pp. 871-878.

Haggenmueller, R.; Zhou, W.; Fischer, J. E. & Winey, K. I. (2003). Production and Characterization of Polymer Nanocomposites with Highly Aligned Single-Walled Carbon Nanotubes. J. Nanosci. Nanotech., Vol. 3, No. 1-2, (February 2003), pp. 105-110.

Harris, P. J. F. (2004). Carbon nanotube composites. International Materials Reviews, Vol. 49, No. 1, (February 2004), pp. 31-43.

Hong, S. & Myung, S. (2007). Nanotube Electronics: A flexible approach to mobility. Nature Nanotechnology, Vol. 2, (April 2007), pp. 207–208.

Huynh, C. P. & Hawkins, S. C. (2010). Understanding the synthesis of directly spinnable carbon nanotube forests. Carbon, Vol. 48, No.4, (April 2010), pp. 1105-1115.

Jang, E. Y.; Kang, T. J.; Im, H.; Baek, S. J.; Kim, S.; Jeong, D. H.; Park, Y. W. & Kim, Y. H. (2009). Macroscopic Single-Walled-Carbon-Nanotube Fiber Self-Assembled by Dip-Coating Method. Adv. Mater., Vol. 21, No. 43, (November 2009), pp. 4357-4361.

Ji, J.; Sui, G.; Yu, Y.; Liu, Y.; Lin, Y.; Du, Z.; Ryu, S. & Yang, X. (2009). Significant Improvement of Mechanical Properties Observed in Highly Aligned Carbon-Nanotube-Reinforced Nanofibers. J. Phys. Chem. C, Vol. 113, No. 12, (March 2009), pp. 4779-4785.

Jin, L.; Bower, C. & Zhou, O. (1998). Alignment of carbon nanotubes in a polymer matrix by mechanical stretching. Appl. Phys. Lett., Vol. 73, No. 9, (August 1998), pp. 1197-1199.

Kang, M. S.; Shin, M. K.; Ismail, Y. A.; Shin, S. R.; Kim, S. I.; Kim, H.; Lee, H. & Kim, S. J. (2009). The fabrication of polyaniline/singlewalled carbon nanotube fibers containing a highly-oriented filler. Nanotechnology, Vol. 20, No.8, (February 2009), pp. 085701(5).

Karousis, N.; Tagmatarchris, N. & Tasis, D. (2010). Current Progress on the Chemical Modification of Carbon Nanotubes. Chem. Rev., Vol. 110, No. 9, (June 2010), pp. 5366–5397.

Kimura, T.; Ago, H.; Tobita, M.; Ohshima, S.; Kyotani, M. & Yumura, M. (2002). Polymer Composites of Carbon Nanotubes aligned by a Magnetic Field. Adv. Mater., Vol. 14, No. 19, (October 2002), pp. 1380-1383.

Koziol, K.; Vilatela, J.; Moisala, A.; Motta, M.; Cunniff, P.; Sennett, M. & Windle, A. (2007). High-Performance Carbon Nanotube Fiber. Science, Vol. 318, No. 5858, (December 2007), pp. 1892-1895.

Li, Q.; Li, Y.; Zhang, X.; Zheng, L.; Doorn, S. K.; Zhao, Y.; Dangelewicz, A. M.; Zheng, L.; Doorn, S. K.; Jia, Q.; Peterson, D. E. ; Arendt, P. N. & Zhu, Y. T. (2007). Structure-Dependent Electrical Properties of Carbon Nanotube Fibers. Adv. Mater., Vol. 19, No. 20, (October 2007), pp. 3358-3363.

Li, Q.; Zhang, X.; DePaula, R. F.; Zheng, L.; Zhao, Y.; Stan, L.; Holesinger, T. G.; Arendt, P. N.; Peterson, D. E. & Zhu, Y. T. (2006). Sustained Growth of Ultralong Carbon Nanotube Arrays for Fiber Spinning. Adv. Mater., Vol. 18, No. 23, (December 2006), pp. 3160-3163.

Li, Y. L.; Kinloch, I. A. & Windle, A. H. (2004). Direct Spinning of Carbon Nanotube Fibers from Chemical Vapor Deposition Synthesis. Science, Vol. 304, No. 5668, (April 2004), pp. 276-278.

Lin, Y.; Lu, F.; Tu, Y. & Ren, Z. (2003). Glucose Biosensors Based on Carbon Nanotube Nanoelectrode Ensembles. Nano. Lett., Vol. 4, No. 2, (February 2004), pp. 191-195.

Liu, Z.; Tabakman, S. M.; Chen, Z. & Dai, H. J. (2009). Preparation of carbon nanotube bioconjugates for biomedical applications. Nature Protocols, Vol.4, No.9, (September 2009), pp. 1372-1382.

Moniruzzaman, M. & Winey, K. I. (2006). Polymer Nanocomposites Containing Carbon Nanotubes. Macromolecules, Vol. 39, No. 16, (July 2006), pp. 5194-5205.

Peng, H. & Sun, X. (2009). Macroporous carbon nanotube arrays with tunable pore sizes and their template applications. Chem. Commun., No. 9, pp. 1058-1060.

Peng, H. & Sun, X. (2009). Highly aligned carbon nanotube/polymer composites with much improved electrical conductivities. Chem. Phys. Lett., Vol. 471, No. 1-3, (March 2009), pp. 103-105.

Peng, H. (2007). Unusual Assembly of Small Organic Building Molecules in Common Solvent. J. Phys. Chem. B, Vol. 111, No. 30, (August 2007), pp. 8885-8890.

Peng, H. (2008). Aligned Carbon Nanotube/Polymer Composite Films with Robust Flexibility, High Transparency, and Excellent Conductivity. J. Am. Chem. Soc., Vol. 130, No. 1, (January 2008), pp. 42-43.

Peng, H.; Chen, D.; Huang, J.; Chikkannanavar, S. B.; Hanisch, J.; Peterson, D. E.; Doorn, S. K.; Lu, Y.; Zhu, Y. & Jia, Q. (2008). Strong and Ductile Colossal Carbon Tubes with Walls of Rectangular Macropores. Phys. Rev. Lett., Vol. 101, No. 14, (October 2008), pp. 145501(4).

Peng, H.; Jain, M.; Li, Q.; Peterson, D. E.; Zhu, Y. & Jia, Q. (2008). Vertically Aligned Pearl-like Carbon Nanotube Arrays for Fiber Spinning. J. Am. Chem. Soc., Vol. 130, No. 4, (January 2008), pp. 1130-1131.

Peng, H.; Sun, X.; Cai, F.; Chen, X.; Zhu, Y.; Liao, G.; Chen, D.; Li, Q.; Lu, Y.; Zhu, Y. & Jia, Q. (2009). Electrochromatic carbon nanotube/polydiacetylene nanocomposite fibres. Nat. Nanotechnol., Vol. 4, No. 11, (November 2009), pp. 738-741.

Raravikar, N. R.; Schadler, L. S.; Vijayaraghavan, A.; Zhao, Y. P.; Wei, B. Q. & Ajayan, P. M. (2005). Synthesis and Characterization of Thickness-Aligned Carbon Nanotube-Polymer Composite Films. Chem. Mater., Vol. 17, No. 5, (March 2005), pp. 974-983.

Razal, J. M.; Coleman, J. N.; Munoz, E.; Lund, B.; Gogotsi, Y.; Ye, H. H.; Collins, S.; Dalton, A. B.; Baughman, R. H. (2007). Arbitrarily Shaped Fiber Assemblies from Spun Carbon Nanotube Gel Fibers. Adv. Funct. Mater., Vol. 17, No. 15, (October 2007), pp. 2918-2924.

Safadi, B.; Andres, R. & Grulke, E. A. (2002). Multiwalled Carbon Nanotube Polymer Composites: Synthesis and Characterization of Thin Films. J. Appl. Polym. Sci., Vol. 84, No. 14, (June 2002), pp. 2660-2669.

Shi, D. (2009). Integrated Multifunctional Nanosystems for Medical Diagnosis and Treatment. Adv. Funct. Mater., Vol. 19, No. 23, (December 2009), pp. 3356-3373.

Sun, X. ; Peng, H. Unpublished results.

Sun, X.; Chen, T.; Huang, S.; Cai, F.; Chen, X.; Yang, Z.; Li, L.; Lu, Y. & Peng, H. (2010). UV-Induced Chromatism of Polydiacetylenic Assemblies. J. Phys. Chem. B, Vol. 114, No. 7, (February 2010), pp. 2379-2382.

Sun, X.; Chen, T.; Huang, S.; Li, L. & Peng, H. (2010). Chromatic polydiacetylene with novel sensitivity. Chem. Soc. Rev., Vol. 39, No. 11, (April 2010), pp. 4244-4257.

Vigolo, B.; Penicaud, A.; Coulon, C.; Sauder, C.; Pailler, R.; Journet, C.; Bernier, P. & Poulin, P. (2000). Macroscopic Fibers and Ribbons of Oriented Carbon Nanotubes. Science, Vol. 290, No. 5945, (November 2000), pp. 1331-1334.

Vigolo, B.; Poulin, P.; Lucas, M.; Launois, P. & Bernier, P. (2002). Improved structure and properties of single-wall carbon nanotube spun fibers. Appl. Phys. Lett., Vol. 81, No. 7, (August 2002), pp. 1210-1212.

Wei, C.; Dai, L.; Roy, A. & Tolle, T. B. (2006). Multifunctional Chemical Vapor Sensors of Aligned Carbon Nanotube and Polymer Composites. J. Am. Chem. Soc., Vol. 128, No. 5, (February 2006), pp. 1412-1413.

Yang, Z. H.; Gao, Z.; Sun, H. & Li, Y. (2008). Composite Films Based on Aligned Carbon Nanotube Arrays and a Poly(N-Isopropyl Acrylamide) Hydrogel. Adv. Mater., Vol. 20, No. 11, (June 2008), pp. 2201-2205.

Zhang, M.; Atkinson, K. R. & Baughman, R. H. (2004). Multifunctional Carbon Nanotube Yarns by Downsizing an Ancient Technology. Science, Vol. 306, No. 5700, (November 2004), pp. 1358-1361.

Zhang, M.; Fang, S. L.; Zakhidov, A. A.; Lee, S. B.; Aliev, A. E.; Williams, C. D.; Atkinson, K. R. & Baughman, R. H. (2005). Strong, Transparent, Multifunctional, Carbon Nanotube Sheets. Science, Vol. 309, No. 5738, (August 2005), pp. 1215-1219.

Zhang, X. B.; Jiang, K. L.; Feng, C.; Liu, P.; Zhang, L. N.; Kong, J.; Zhang, T. H.; Li, Q. Q. & Fan, S. S. (2006). Spinning and Processing Continuous Yarns from 4-Inch Wafer Scale Super-Aligned Carbon Nanotube Arrays. Adv. Mater., Vol. 18, No. 12, (June 2006), pp. 1505-1510.

Zhang, X.; Li, Q.; Tu, Y.; Li, Y.; Coulter, J. Y.; Zheng, L.; Zhao, Y.; Jia, Q. Peterson, D. E. & Zhu, Y. (2007). Strong Carbon-Nanotube Fibers Spun from Long Carbon-Nanotube Arrays. Small, Vol. 3, No. 2, (February 2007), pp. 244-248.

Zhang, Y.; Zou, G.; Doorn, S. K.; Htoon, H.; Stan, L.; Hawley, M. E.; Sheehan, C. J.; Zhu, Y. & Jia, Q. (2009). Tailoring the Morphology of Carbon Nanotube Arrays: From Spinnable Forests to Undulating Foams. ACS Nano, Vol. 3, No. 8, (July 2009), pp. 2157-2162.

Zhao, Y. L. & Stoddart, J. F. (2009). Noncovalent Functionalization of Single-Walled Carbon Nanotubes. Acc. Chem. Res., Vol. 42, No. 8, (August 2009), pp. 1161-1171.

Zheng, L.; Zhang, X.; Li, Q.; Chikkannanavar, S. B.; Li, Y.; Zhao, Y.; Liao, X.; Jia, Q.; Doorn, S. K.; Peterson, D. E. & Zhu, Y. (2007). Carbon-Nanotube Cotton for Large-Scale Fibers. Adv. Mater., Vol. 19, No. 18, (September 2007), pp. 2567-2570.

Zhu, Y. F.; Ma, C.; Zhang, W.; Zhang, R. P. & Koratkar, N.; Liang, J. (2009). Alignment of multiwalled carbon nanotubes in bulk epoxy composites via electric field. J. Appl. Phys., Vol. 105, No. 5, (March 2009), pp. 054319(6).

Zhu, Z.; Song, W.; Burugapalli, K.; Moussy, F.; Li, Y. & Zhong, X. (2010). Nano-yarn carbon nanotube fiber based enzymatic glucose biosensor. Nanotechnology, Vol. 21, No. 16, (April 2010), pp. 165501.

13

Silanization of Carbon Nanotubes: Surface Modification and Polymer Nanocomposites

C. Velasco-Santos[1], A.L. Martínez-Hernández[1] and V.M. Castaño[2]
[1]*Departamento de Metal-Mecánica Instituto Tecnológico de Queretaro, Av. Tecnológico s/n esq. Gral Mariano Escobedo,*
[2]*Centro de Fisica Aplicada y Tecnologia Avanzada, Universidad Nacional Autonoma de Mexico, Campus Juriquilla, Queretaro, Mexico*

1. Introduction

Since the first publication of successful silanization in carbon nanotubes (Velasco-Santos 2002) different research groups have opted for modify carbon nanotubes using various organosilanes. Silanization offer to carbon nanotubes (CNTs) the possibility to diversify their surface features depending on the organic part in organosilane inserted to nanotube surface. Silanized nanotubes show different features related with the silane used in functionalization. Dispersion of CNTs in organic solvents is modified by the organosilane type applied in silanization of nanotubes.

Silanization have been achieved in CNTs taking advantage of the carboxyl and hydroxyl groups produced during the oxidation process of nanotubes. Also, silylation achieved without previous oxidation and by hydroxylation have been developed. In addition, silanized CNTs (s-CNTs) are used to attach to nanotube surface other nanoparticles and molecules. This later is useful to create alternatives to functionalize or accomplish CNTs to other inorganic or organic nanometric structures. Due to the alternatives that the silanization offer to carbon materials, recently the successful approaches used to silanize CNTs have been applied to other carbon materials such as nanofibers and graphene.

In spite of silanization is a successful method to change nanotube surface behavior, to attach other molecules or chains to nanotubes, or linking CNTs with other nanostructures; this route with organosilanes is an established approach in polymer composites. In this type of chemical functionalization, silanes are used as coupling agents of glass and carbon fiber with polymer matrices in order to improve interface. In this context, silanization in CNTs, also have been proposed as nanometric coupling agent (Velasco-Santos 2002) of CNTs with polymer matrices and thus, recently silanized carbon nanotubes have been incorporated to develop polymer nanocomposites.

Thus, in the first part of this chapter are described the principles of silanization reaction achieved in CNTs and the characterization obtained in the first report. The second part of the chapter describes diverse researches of silanization reactions achieved in nanotube

surface, including silanization after oxidation, silylation and hydroxylation. Arrangement of some nanostructures attached to CNTs surface via silanization and functionalization of other carbon nanomaterials with organosilanes are also reviewed and discussed in this section. Finally, advances related with silanized carbon nanotubes as reinforced in polymer nanocomposites are analyzed. Hence, silanization is shown as important chemical route in order to attach different organic moieties, diversify carbon nanotube properties, develop new nanoarrangements and improve compatibility between CNTs and polymer matrices.

2. Principles of silanization in CNTs

As it was mentioned, carbon nanotubes exhibit amazing mechanical properties, such as exceptionally high Young's modulus, stiffness and flexibility (Lourie et al 1998; Yu et al 2000). Also the CNTs density is very low and their sp^2 carbon-carbon bond in the plane of the graphene lattice is among the strongest of all chemical bonds (Jin et al. 2001; Velasco-Santos et al. 2003). Therefore, one of the most proposed possible uses to CNTs is their incorporation to other materials with the aim to produce engineering composite materials in order to truly take advantage of their outstanding mechanical properties. Related with this, the functionalization has taken part in order to employ these materials as effective reinforcements in advanced composites, inasmuch as a good chemical bond to the matrix must exist, to effectively transfer mechanical loads from the matrix to the nanotubes and thus take advantage of their mechanical features. Accordingly, the addition of diverse chemical groups to the surface of functionalized CNTs has been proposed extensively (Velasco-Santos et al. 2004, Tasis et al. 2006, Karousis et al. 2010;) with the target to reach the compatibility between polymer matrix and CNTs and diversify their inclusion with different matrices. In this context the functionalization of CNTs with organosilanes inserted to oxidized Multiwalled Carbon Nanotubes (f-MWNTs) was proposed (Velasco-Santos 2002). Silanization provide a single approach in order to add different organic molecules to CNTs surface and in this way not only diversifying their surface behavior of these nanomaterials, but incorporate to nanotubes, a variety of chemical moieties depending on the coupled organosilanes; and thus open the opportunities to the silane function as coupling agent of different organic compounds, polymer matrices, nanomaterials and nanostructures. Principles and details of silanization reaction on CNTs and characterization of these materials are described next.

Organofunctional silanes coupling agents have been attached to CNTs follow diverse approaches. However, the first silanization on CNTs reported took as base the typical silanization reaction achieved in different fibers such as: glass, carbon and naturals. Organosilanes are substances that allow us to chemically join two materials. This "link" can be accomplished through chemical bonds or physical interactions. The organosilanes are chemically described as:

$$R\text{-}Si\text{-}R'_3$$

where R is an organo-functional group attached to silicon. In the silanization on CNTs have been proposed that the R group can be chosen to be reactive depending on the organic matrix being used. Silane also could be selected depending on the nature of the material to be attached to CNTs surface. In the other hand the R' group reacts through silicon-oxygen fiber bonds and is generally trimethoxy 3(OCH_3) which is easily hydrolyzed to form a trisilanol. This group reacts readily with the hydroxyl groups (produced through oxidation)

on the nanotube surface. The sequence is schematically shown in Figure 1, where the chemical structure of the organosilane is again represented (Figure 1a), along with the reaction scheme (Figure 1b) and a representation of silane chemical interactions on the nanotube surface (Figure 1c). Also, in this scheme are represented two R groups as R1 and R2 with two different organosilane moieties that have been attached to functionalized CNTs (f-CNTs) with the same approach; 3-mercaptopropyl trimethoxysilane (3-MPT) and 3-methacryloxypropyl-trimethoxysilane (3-MAT). As it was mentioned, silanization have allowed adding new chains to the open end cap and to the walls of the MWNTs oxidized before, aiming to improve their compatibility to polymer chains. Besides, the method is useful to link CNTs with other chemical groups depending on R terminal group.

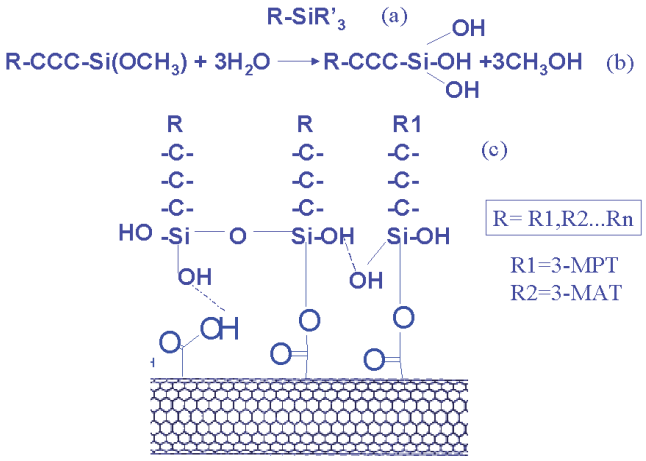

Fig. 1. Sequence of silanization reactions on nanotubes surfaces.

As it was mentioned before, oxidation is the first step in some researches focus to subsequent silanization of CNTs. Nowadays there are several methods in order to oxidize the CNTs surface (Velasco-Santos et al. 2004, Wiltshire et al 2004, Datsyuk et al. 2008). For the first silanization on CNTs the method to achieve the oxidation of CNTs involves $KMnO_4$ as oxidant in acid media. In this report MWNTs obtained by the arc-discharge method were employed. Oxidation was developed according to the report of Hiura 1995, but with slight variations in the quantity of $KMnO_4$ and reflux time. The chemical nature of the purification and functionalization of CNTs is due to the other carbon forms presents are oxidized almost completely, and new groups are produced on the tube surface, mainly in the nanotubes tips, which in turn increases the reactivity and allows us to attach either organic and inorganic moieties as has been done in other carbonaceous materials.

After the oxidation, funtionalized Multiwalled Carbon Nanotubes (f-MWNTs) were reacted with the organofunctional silane 3-mercaptopropyl trimethoxysilane (3-MPT) and 3-methacryl trimethoxysilane (3-MAT), in both cases the reaction was performed with 25 mg of f-MWNT; the silanes were used in liquid form, and were diluted in ethanol prior to the reaction, in order to make an alcoholic solution. In these solutions f-MWNTs were added slowly to ensure an even distribution. The amount of used organosilane was 1:1 in weight with respect to the f-MWNTs. The mixes were refluxed for 3 h, maintaining the temperature

around 65-70ºC and under constant stirring. The silanized functionalizated multiwalled carbon nanotubes (identified as fs-MWNT) were dried at 100ºC for around 12 h to allow a complete evaporation of ethanol, followed by washing with hot water and acetone to eliminate any non-reacted organosilane.

Figures 2a and 2b show a comparison between MWNT and f-MWNT FTIR spectra. The bands in both spectra at 840 and 1587 cm^{-1} are due to the A_2u and E_1u IR phonon modes present in carbon nanotubes (Kastnert 1994, Saito 1998); the f-MWNTs were terminated with carboxylic acid groups and carboxylate. This is seen in low intensities of the band around 1740 cm^{-1} which correspond to v(C=O) typical of carboxyl moieties. Other evidence of carboxyl group is a slight increase in 1346 cm^{-1} δ(O-H) in plane and 960 cm^{-1} δ(O-H) out of plane bands (Coates 2000). Also, a higher intensity is seen in the band around 1495 cm^{-1} and in the peaks between 1600 cm^{-1} and 1680 cm^{-1} in comparison with the zone above 1700 cm^{-1}, these corroborate that quinone and carboxylate groups exist in these oxidized nanotubes (Coates 2000, Zhang 2003, Chen 2001, Ma 2006). The peak at 1576 cm^{-1}, assigned to -C=C in spectrum a), is notably weaker than that in spectrum b); this indicates changes in CNTs surface due to oxidation (Zhang 2003) , inasmuch as, it is known that some damage is produced in CNTs walls. In figure 2c) are found results of successful silanization process; the bands at 794 cm^{-1} and 919 cm^{-1} are typical for v(Si-OH) and δ(OH) out of plane. These bands appear when trimethoxy groups are broken in order to form silanol groups. The silanol groups provide interactions between oxygen of carboxylates and hydroxyl moieties of oxidized nanotubes and the organosilane. In addition spectrum 2c) does not show bands between 815 cm^{-1} and 845 cm^{-1}, characteristic signals of nonreacted SiOR groups in organosilane compound (Velasco-Santos 2002, Bourgeat-Lami 2002). The bands at 1045 cm^{-1} and 1111 cm^{-1} are due to Si-O-Si and Si-O-C vibrations (Bourgeat-Lami 2002, Coates 2000) and correspond to siloxane units formed during silanization process. The high intensity band at 1740 cm^{-1} becomes stronger due to the ester group v(C=O) vibration which corresponds to methacrylate moiety in this case of the organosilane attached to CNTs.

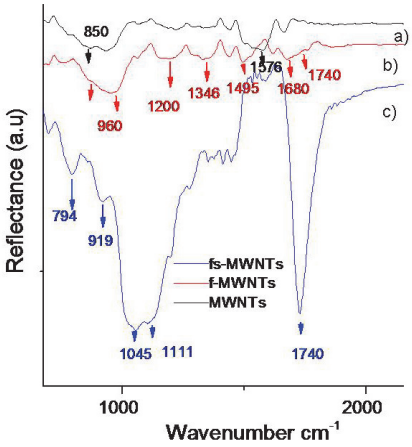

Fig. 2. Infrared Spectra of a) MWNTs, b) f-MWNTs, c) fs-MWNTs (3-MAT).

Figures 3a and 3b show the MWNT and f-MWNT Raman spectra. In both cases, two bands at 1576 cm^{-1} (G line) and 1328 cm^{-1} (D line) appear. The first peak corresponds to the E_2g modes, which has been assigned to the movement of two neighboring carbon atoms in opposite directions, characteristic of highly oriented pyrolitic graphite (HOPG). The second signal is due to the disorder present in the MWNTs, a feature related to the region near the K-point phonon of the graphite´s Brillouin zone (Zhao 1998, Wang 2002, Dresselhaus 2002). It is clear that in this case the ratio of intensities between D and G peaks changes in the f-MWNT spectrum (figure 3b) with respect to the MWNT spectrum (figure 3a), this is due to the formation of sp^3 hybridized carbon "defect" sites on the carbon nanotubes walls due to the addition of the functional groups (COOH), which supports the results obtained in the FTIR analysis. The Raman spectrum of fs-MWNTs is shown in figure 3c, where no changes with respect to the f-MWNT RAMAN spectrum are observed in this case; since the bands in this spectrum represent details of the carbon nanotubes crystalline structure, in which silanization does not take place. The changes are observed when the functionalization is performed through oxidation directly in the end cap and sidewall carbon nanotubes due to the insertion of carboxylic groups such as it have been indicated before. Also, silanization analysis are completed in this research by elemental analysis obtained by Energy Dispersion Spectroscopy (EDS); in this case of CNTs silanized with 3-MPT. A clear 12% of Si is obtained to fs-MWNTs.

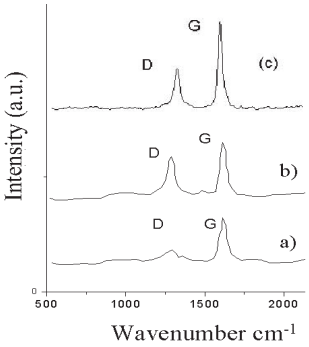

Fig. 3. a) Raman spectra of a) MWNTs b) f-MWNTs, c) fs-MWNTs.

The oxidation and silanization in CNTs yields functionalized moieties, which contain R groups bonded to the nanotubes by silanol groups. Thus the approach in this research allows modifying oxidized nanotubes with many different materials chemically-bonding to f-MWNTs in this case, inasmuch as the R group (methacryl, glycidoxy, etc) in the organofunctional silanes have been changed in different researches depending on the specific polymeric matrix employed for a particular use. The behavior of fs-MWNTs changes when the R terminal changes also, consequently it have found that fs-MWNTs (3-MAT silanization) produce soluble MWNTs (s-MWNTs) in organic solvent such as acetone or ethanol (Velasco-Santos 2004), inasmuch as the methacryl chain attached as R group in the fs-MWNTs surface changes the character of this material which allow their solubility, this does not occur when 3-MPT is attached in fs-MWNT due to the thiol group produces different properties in f-MWNTs surface. The figure 4 shows three kinds of CNTs: MWNTs, f-MWNT and fs-MWNTs (3-MAT), the samples were dissolved in acetone by 5 minutes in

ultrasonic bath in order to disperse the CNTs, then, the samples were kept on repose 5 minutes. The image shows that the sample "c" which correspond to fs-MWNTs (3MAT) presents the most black color intensity due to these fs-MWNTs stay disperse more time in the solution in comparation with MWNTs and f-MWNTs which stay disperse by some minutes and after precipitate. The fs-MNWTs stays in solution during days forming a homogeneous solution.

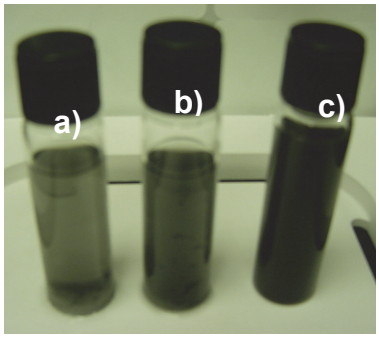

Fig. 4. Samples of carbon nanotubes dissolving in acetone, a) Multiwalled carbon nanotubes (MWNTs) , b) oxidized functionalized multiwalled carbon nanotubes (f-MWNTs), c) silanized functionalized multiwalled carbon nanotubes (fs-MWNTs). (Velasco-Santos 2003).

3. Silanization of carbon nanotubes

Once that silanization was reported as single and efficient approach in order to modified CNTs with several organic molecules, different researches have been focus to attach diverse organosilanes. Next are reviewed the silanization routes employed and the silanes linked to nanotube surface.

Bag et al. 2004, silanized CNTs also with 3-MAT. In this research the previous oxidation is achieved by $KMnO_4$ as oxidant along with a phase transfer catalyst (Aliquat-336 in acetic acid media). Authors mention clearly that the aim of silanization is as well to get a modified CNTs linked with the coupling agent having a functional group such as a double bond which can be utilized further for copolymerization with other vinyl monomers and also improve interface of CNTs with polymer matrices. For the silanization 0.024 g of oxidized CNTs are mixed by sonication for 15 min with 2 ml of 3-MAT in toluene solution. Reaction is achieved at 100 ◦C for 6 h with stirring .The product is washing with deionized water and acetone. The resulting material (fs-MWNTs) was separated by a centrifugation and drying in a vacuum oven at 80◦C.

Silanization is confirmed in this research by IR spectroscopy and EDS. Results show similar evidence that those found by previous reports of silanization on CNTs (Velasco-Santos 2002, 2003). IR signals in 1090 cm^{-1} due to Si–O vibration, at 798 and 960 cm^{-1} due to Si–OH and other bands related with alkyl chains to the organosilanes corroborate successful silanization. Also, the quantity of Si measure by EDS in fs-MWNTs completes the information.

Vast et al 2004 modified MWNTs using ((tridecafluoro-1,1,2,2-tetrahydrooctyl)trichlorosilane) (FTCS). In this research carboxyl and hydroxyl groups of the previously oxidized MWNTs

are taking in advance in order to link the silane to CNTs surface. For the oxidation of CNTs in this research is used a acids mixture. 5 g of MWNTs are dispersed in a solution of 400 ml of H2SO4/HNO3 (3:1 v:v) at 50 ◦C and stirred for 20 h. However in this research the carboxyl groups produced during oxidation process are also reduced. Both systems; Oxidized CNTs and reduced CNTs after oxidation are silanized. For the reduction of the carboxylic acid of CNTs; 0.6 g of oxidized nanotubes are dispersed in dry tetrahydrofuran (THF) at 0 ◦C, under argon atmosphere. 14 ml of diisobutylaluminium hydride (DIBAL-H) are added and the solution is stirred for 3 h at room temperature. The solution is filtered, washed with dry THF and reprotonated by stirring the nanotubes with ethyl alcohol. Solvent is eliminated by filtration and the powder is dried at 60 ◦C for 12 h. For the silanization of both materials (oxidized MWNTs and reduced MWNTs); 0.2 g of activated nanotubes are dispersed in 40 ml of dry toluene by ultrasonic head under argon atmosphere. Then 0.25 g of triethylamine are added and stirring in order to deprotonate carboxylic acid or alcohol groups. 25 ml of a 10^{-2} M toluene solution of FTCS are added to the nanotube mixture and stirred for 20 h. The filtration of nanotubes is followed by three successive sonications in toluene to eliminate unreacted silane. Finally, the powder is dried in an oven at 90 ◦C for 20 h.

The silanized nanotubes obtained by this process show different bonds related with those found in the previously silanization. The links between CNTs and FTCS are corroborated by X-Ray electron spectroscopy (XPS) and shown that both kinds of CNTs are successfully silanized. The covalent bonds that prevail in both silanization are Si-O-C_{NTS} and Si-O-Si. Thermogravimetric Analysis (TGA) of both kinds of silanized CNTs and the analysis of the residual mass by XPS shown a slight appear of Si-O bonds in the reduced CNTs. However the authors mention that reduction after oxidation does not induce major differences on the silanization level on CNTs.

Ma et al. 2006 silanized CNTs with 3-glycidoxypropyltrimethoxy (3-GPTMS), also using oxidized CNTs. The oxidation method employed in this research involves UV/O_3 treatment in a chamber and reduction of carboxyl groups on CNTs as was proposed by Vast el al 2004. However the approach used to reduction of oxidized CNTs is different to the reported for Vast et al. The reduction of the oxidized MWNTs is realized using lithium aluminum hydride (LiAlH4). 20.0 mg of f-MWNTs are dispersed in toluene by ultrasonication for 30 min. Then 5.0 mg of LiAlH4 are added. The solution is stirred for 1 h at room temperature. Next 2.0 ml of 2.0 N hydrochloric acid are added into the solution in order to remove the lithium and aluminum. The reduced MWNTs are obtained after filtration of the solution and washing with toluene, absolute ethanol and acetone and drying in a vacuum oven at 80 ◦C overnight.

For Silanization 20.0 mg of reduced MWNTs with 50.0 ml toluene are sonicated for 30 min. Then 7.5 ml of 1.0 wt% toluene solution of GPTMS are added and stirred for 6 h at 60–65 ◦C. After the reaction, 30 ml of methanol are added to dilute the unreacted GPTMS. The fs-MWNTs are obtained by filtration and washing with methanol, water and acetone sequentially. fs-MWNTs are dried in a vacuum oven at 80 ◦C for 12 h.

fs-MWNTs are characterized by IR, EDS and Transmission Electron Microscopy (TEM). Infrared analysis of nanotubes shown typical bands after oxidation related with COOH which are converted to OH after reduction. After silanization the analysis of IR spectrum only is focus to the bands related with epoxy alkyl groups of GPTMS. XPS show similar bonds in fs-MWNTs that those found by Vast et al. Si-O-C_{NTs} and Si-O-Si are found by this

technique. Also, the possibility of the damage to the MWNT surface after silanization is studied by TEM. Fs-MWNTs are heated at 400 ◦C in atmosphere of nitrogen for 1 h in order to remove silane groups and observe the structure of these materials after silanization. TEM image of this process is shown in the figure 5. This micrograph suggests that the silane molecules on the MWNT surface can be removed, zone A and B in Fig. 5 shown typical damages after light oxidation but there are not extra damage in the walls. The layered structure of the MWNTs remained largely intact during the silanization process. These results are agreed with the Raman analysis reported by Velasco-Santos et al 2002. Raman spectra of f-MWNTs and fs-MWNTs are practically similar showing not extra damage after silanization.

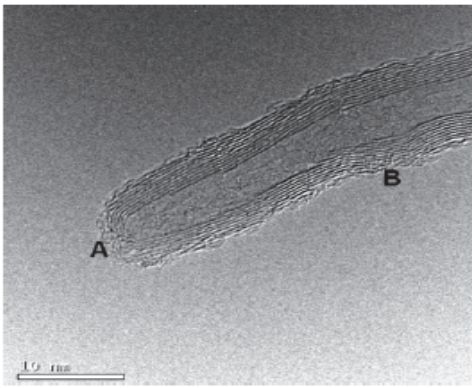

Fig. 5. Surface of fs-MWNTs, after decomposition of organosilanes. Copyright Elsevier Science

Recently, other researches have followed the tendency of attaching organosilanes to carbon nanotubes via carboxyl and hydroxyl groups produced during oxidation. With the same propose of improve interface of CNTs with different organic polymer matrices, amino silanes have been incorporated to MWNTs after oxidation. Kathi and Ree 2008, Scheibe et al 2009, silanized CNTs with 3-aminopropyltriethoxysilane (3-APTS). In the first research oxidation of MWNTs is achieved with acids mixture using H2SO4/HNO3 (3:2 v/v) at 50 ◦C and stirred for 20 h. For silanization .050 g of f-MWNTs are dispersed in 50 ml of ethanol via ultrasonication for 30 min. Silanization is realized with 3-APTS at 70 ◦C for 4 h and stirring. The fs-MWNTs are washing with water and acetone. Fs-MWNTs are separated by filtration and dried under vacuum at 80 ◦C for 12 h.

fs-MWNTs produced by Kathi and Ree are characterized by IR, EDS, TEM and Scanning Electron Microscopy (SEM). Microscopy images of silanized CNTs in this investigation allow concluding to authors that some amorphous material is deposited in tip and walls of these carbon materials. Also weak bands of absorption are observed to 1,070 cm^{-1}, attributed to a Si–O vibration and 803 cm^{-1}, related with Si–OH. Elemental Analysis of fs-MWNTs shows a 2.34 atomic % of Si.

In the other research about silanization of CNTs with 3-APTS (Scheibe et al 2009), acid mixture of HNO3/H2SO4 (v/v = 1:3) at 175 ◦C for 18 h is used to oxidize MWNTs. The acidic solution with f-MWNTs is diluted with purified water obtained of reversed osmosis process (RO H_2O) and filtrated through a polycarbonate filter. Then, the sample is washed

with RO H2O and acetone. f-MWNTs are dried under vacuum conditions at 180 ◦C for 1 h in order to eliminate adsorbed CO2 and H2O.

Then, two kind of silanization are developed for f-MWNTs, the different of the processes is basically the solvent used to rinse and to disperse the f-CNTs (acetone or RO H_2O). This and other conditions in the process according with the solvent used, produce notable differences in the silanized CNTs. Before to the silanization process f-MWNTs are divided in two parts and dispersed in RO H_2O, under vacuum in ultra-sonication bath at 60 ◦C for 20 min. Then silanization is achieved for each sample. Next both processes used are described: For the first sample, f-MWNTs are filtrated through a polycarbonate filter and washing with acetone in order to eliminate adsorbed water molecules and this way avoid hydrolysis. Then, the obtained sample is re-dispersed in acetone in a test tube and placed onto the magnetic stirrer. Next APTS solution is added slowly to the dispersed f-MWNTs solution, until the silane concentration reaches the 2%., the mixture is stirred under vacuum conditions for 15 min. Next, the pressure is elevated until the atmospheric pressure and the mixture was left for 30 min at room temperature. The final product obtained in the experiment I is well dispersed solution.

For the second silanization process, the solution is filtrated through the polycarbonate filter and rinsed in this time with RO H_2O. The obtained sample is re-dispersed in RO H_2O in the test tube in the ultra-sonication bath under vacuum conditions at 40 ◦C for 20 min. Then, pH of f-MWNTs solution is adjusted to 4.0 with glacial acetic acid. Next, APTS solution is added slowly to the dispersed f-MWNTs solution, until the silane concentration reaches the 2%. Subsequently, the mixture is sonicated under vacuum for 15 min and after the sample reaches the atmospheric pressure. The mixture is left for 3 h in a closed tube at 40 ◦C. The final product obtained in the experiment II gives weakly solubility.

After each silanization procedure, the mixtures are filtered through a polycarbonate filter, and rinsed with acetone in order to remove excess of the aminosilane molecules and dried. The most outstanding results in this research are obtained by the techniques IR, TGA and HRTEM (High Resolution Transmission Electron Microscopy) for both kind of fs-CNTs and the samples used as comparison, such as purified MWNTs and f-MWNTs. Besides of corroborated oxidation by the typical bands in f-MWNTs; IR spectra of silanized CNTs show typical bands of successful silanization. The presence of weak signals at 1110 cm^{-1} related with Si-O-C and 875 cm^{-1} which correspond with Si-OH found also in other researches confirm silanization in both kinds of fs-MWNTs. However other weak signal is found at 1161 cm^{-1} only for the silanization achieved in the experiment II, and is related with Si-O-Si. Authors associate this band with the APTS hydrolysis and its self-condensation which occurred by the conditions employed in the experiment II. This fact is also link due to the aminosilane layer found in TEM fs-MWNTs (experiment II) is thicker than the layer of the fs-MWNTs (experiment I). In addition TGA confirm better thermal stability for CNTs silanized by the conditions of experiment II than CNTs silanized in the experiment I. Thus the second process is favorable in order to obtain thicker aminosilane layer and a system thermally more stable.

Hemraj-Benny and Wong 2006 functionalized CNTs with trimethoxysilane and hexaphenyldisilane. However their silylation protocol does not require previous oxidative methods. The study is focus to explore the photochemical silylation of SWNTs, taking in count an analogous reaction to that involving fullerenes. Authors assume that the reaction scheme of the silylation of SWNTs is similar to that of fullerenes due to the nature of both materials.

For the silylation of SWNTs adducts, they use two reference samples: purified SWMTs and control SWNTs. In order to prepare control SWNTs a sample of purified CNTs is placed in

2-propanol and stirring for 48 h with exposure to the UV lamp. Authors confirm by HRTEM and that there is not visible damage occurring on tube sidewalls. Before to the silylation, SWNTs are dissolved in the presence of dry 2-propanol and flushed continuously with argon. For the reaction with hexaphenyldisilane, 50 mg of the silane precursor are placed into a Schlenk flask with 20 ml of dry 2-propanol, this solution is combined with the SWNT dispersion. The mixture is irradiated with a 500 W mercury xenon lamp for 48 h. The functionalized adduct was isolated by filtering over a 0.2 μm polycarbonate membrane. Then sample is washed with 2-propanol and distilled water to eliminate unreacted silane. For the sylilation with trimethoxysilane, hydrogen hexachloroplatinate(IV) hexahydrate (38-40% Pt) is used as catalyst and represent the main difference with respect to hexaphenyldisilane reaction . In this case, the catalyst solution is initially added to a solution of SWNTs, and then 0.016 mol of the organosilane is incorporated. The process is performed under Schlenk conditions to ensure the absence of moisture. Sample is irradiated for 48 h and filtered and washed.

Results of both sylilation processes show important variations. Data obtained of AFM (Atomic Force Microscopy) for both samples indicate an average height of 6.99 ± 1.53 nm for the SWNTs adducts modified with trymethoxysilane and 7.03 ± 2.56 nm for the SWNTs adducts functionalized with hexaphenyldisilane. The average height for the SWNTs control adduct is 3.92 ± 1.58 nm. This indicates a coating produced in adducts due to the silane in the CNTs surface. Raman spectra analyses of both silanized samples are examined considerer two zones. The first zone is related with the signals D and G typical bands in carbon nanotubes. The intensity of these bands is related with the purity but also defects of CNTs and therefore some changes in the D/G ratio several times are related with structural modifications. In this case authors compare the values obtained by 1-D/G at different excitation wavelengths to verify structural changes; the results indicate similar trends found for all utilized laser. The expression values decreases upon chemical functionalization. The functionalized SWNTs show lower values of the expression 1-D/G than SWNTs and control SWNT. However, trimethoxysilane-SWNT adduct shows the smallest value of this expression. These results suggest a more effective sidewall functionalization of SWNTs with trimethoxysilane as compared with hexaphenyldisilane. Raman analyses are completed with the estimated atomic concentrations obtained by XPS; control SWNT adduct does not contain Si and the values obtained for trimethoxysilane-SWNTs and hexaphenyldisilane SWNTs are 7.99 and 1.55 respectively. The highest Si contain for the first sample also is related with effective functionalization and is agree with Raman results.

The second zone analyzed in Raman spectra is related with Radial Breathing Mode (RBM). This signal for CNTs is related with the nanotube diameter and some values of wavelength for this band have been assigned to metallic or semiconducting CNTs. The bands assigned to metallic nanotubes show more intensity for trimethoxysilane-SWNTs than the signals related with semiconducting behavior which decrease in intensity as compared with non modified SWNTs. The same signals (related with metallic and semiconducting tubes) show different behavior for the hexaphenyldisilane SWNTs, inasmuch as, signals related with both features decrease in intensity as compared with pristine SWNTs. Thus, authors conclude that trimethoxysilane has less reactivity with metallic nanotubes and this reaction has preferential selectivity for semiconducting CNTs. However, hexaphenyldisilane reaction is less selective to the diameter and the structural features of CNTs. This suggestion is also corroborated by UV-Visible-NIR spectroscopy; the absorption bands obtained by this technique which correspond with electronic transitions (metallic and semiconducting) are

presented in control SWNTs adducts. However, in adducts modified with hexaphenyldisilane the bands of all electronic transitions disappear indicating that sp^2 hybridized structure is changed. For trimethoxysilane-SWNT adducts prevail the absorption bands related with metallic features and semiconducting electronic transitions disappear. This confirms the reaction tendency of each silylation process.

IR analysis of these adducts corroborated that silylation is achieved by covalent bonds Si-O-C and Si-C, but silanol groups are not produced in the reaction. In the IR spectra the signals for adducts are compare with silane precursor. For trimethoxysilane-SWNT adduct, the bands related with Si-O-C stretching and bending are found at 1037 and 737 cm^{-1} respectively; these peaks are presented in the precursor at 1074 and 787 cm^{-1}. The shifts are related with the link between silane and CNTs. For the spectrum of hexaphenyldisilane SWNTs adduct the signals detected are related with the silane precursor attached to CNTs; bands of Si-C stretching vibration are found at 1257 and 1099 cm^{-1}. In both spectra of functionalized CNTs are not found signals at 798 and 956 cm^{-1} which are related with Si-OH groups. This corroborates that bonds between silane and CNTs are produced directly. A proposal of link in SWNTs surface for each silane is shown in the figure 6.

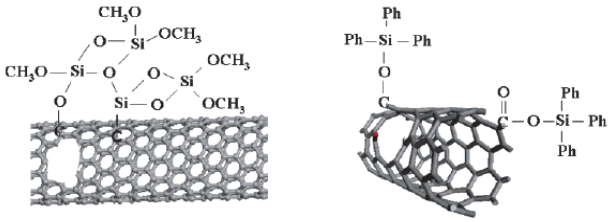

Fig. 6. Schematic representation of SWNTs modified with silane precursors. Copyright ACS.

Lee et al 2009 develop silanization without previous oxidation using spontaneous hydrosilylation reaction that induces direct C–Si covalent bonds. They use triethylsilane (TES) due to the molecule contain a neutral Si–Hx moiety. Hydrosilylation is used in this research because of is efficient catalytic reaction useful for the insertion of silicon-based functional moieties into unsaturated hydrocarbons, such as alkenes or alkynes. Thus, the sp^2 hybridized structure could be modified in similar way. However the main purpose of authors is focus to use the hydrosilylation reaction in order to silencing metallic SWNTs from mixtures. The silencing of metallic SWNTs would allow fabrication of network-type SWNT field-effect transistor (FET) devices showing high on/off ratio.

The Hydrosilylation reaction is performed in an N2-filled glove bag. Diluted TES solutions are prepared in hexane at various concentrations. Substrates previously prepared containing SWNTs are immersed in TES solution for 1 h at room temperature. The sample are washed with hexane and isopropyl alcohol, and dried with N2.

Successfully hydrosilylation is corroborated by Raman analysis by the changes in D/G ratio of the band areas of SWNTs spectrum after reaction as compared SWNTs spectrum before reaction. Substantial increase of the D band and therefore changes in the values of D/G ratios are related with the breakdown of sp2 conjugations by hydrosilylation reaction. Authors also probe the silencing metallic by hydrosilylation verifying the changes in the current–gate voltage (I–Vg) curves of SWNT-FET (Field Effect Transistor) devices before and

after the hydrosilylation reaction. Results show dramatic increases in on/off ratio observed when the original devices react with 1mM and neat TES for 1 h. These results imply that the hydrosilylation reaction is indeed effective for silencing metallic SWNTs to give semiconducting nanotubes at wide ranges of silane concentration.

The two latter reviewed researches, give important evidence related with the silanization process is an important route not only to compatibilize molecules with CNTs; also, selective electronic behavior can be induced. Thus, silanization using previous oxidation or produced directly on CNTs surface is a versatile functionalization approach that opens different alternatives to diversify CNTs research and applications. Next are reviewed some silanization process in order to attached nanoparticles.

4. Nanoparticles attached on carbon nanotube via silanization

Recently silanization also have emerged as important route to diversify nanoarchitectures derived of CNTs. Lin et al 2009 use organosilane chemistry in order to attached magnetically iron oxide- in-silica nanoparticles and also polyethylene glycol to CNTs surface by similar protocols. Silanization is achieved taking advantage of the carboxyl and hydroxyl groups produced by oxidation; trimethylchlorosilane is used as coupling agent. Next is described the modification of silanized SWNTs with nanoparticles. For this propose a solution containing a dispersion of 3 mg of encapsulated magnetic iron oxide silica nanoparticles (prepared previously) and 1 ml of triethylamine is combined with 3 mg of the silanized SWNTs. The mixture is ultrasonicated for 15 min and stirred for 12 h. The resulting product is rinsed by benzene and distilled water, respectively, in order to remove the residual nanoparticles. Then fs-SWNT is filtered and dried at 60 ^{o}C overnight. TEM images of the nanoparticles attached to CNTs are shown in the figure 7.

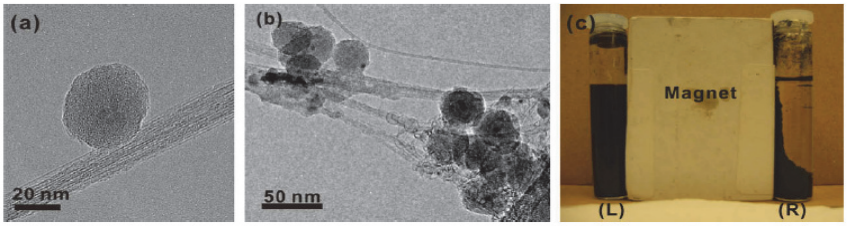

Fig. 7. TEM images of fs-SWNTs-(Fe_3O_4@SiO_2) nanoparticles; a) Interaction between nanoparticles and fs-SWNTs adduct, b) Different nanoparticles attached to fs-SWNTs adduct , c) Dispersion of (L) oxidized SWNTs mixed with Fe_3O_4@SiO_2 nanoparticles in ethanol exposure to a magnetic field, (R) fs-SWNTs-(Fe_3O_4@SiO_2) nanoparticles in ethanol exposure to a magnetic field. Copyright Elsevier Science.

Liu et al. 2008 as well modified CNTs with nanoparticles using silane as part of the coupling agents in their reaction procedures to develop nanoarchitectures based on MWNTs. They synthesize a silica–polymer–CNT hybrid. The nanotubes are encapsulated by poly(3-acrylaminopropylsiloxane) with silica nanospheres on the polymer surface. Reactions are sequence are next : 1) reactive poly(acryloyl chloride) (PAC) is grafted on the CNTs through the reaction of side acyl chloride groups taking advantage of the hydroxyl groups produced after oxidation. 2) 3-aminopropyltriethoxysilane (3-APTS) react with grafted PAC through

the reaction between amino and acyl chloride, siloxane-containing sub-grafts are introduced onto the primary PAC grafts. 3) silica nanospheres are covalently attached to the sub-grafts by condensation. The intermediate structures in this research are confirmed by authors by IR spectroscopy and XPS. Figure 8 shown the reactions sequence on CNTs surface including organosilane insertion. Figure 9 shown TEM images of silica nanoparticles and the hybrid nanostructures based on CNTs.

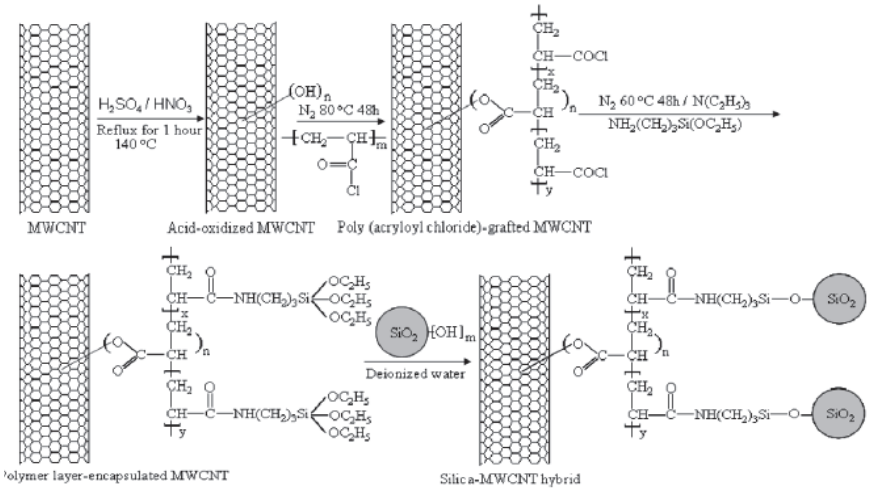

Fig. 8. Schematic representation of the reaction sequence to develop MWNT-polymer-silica nanoparticles hybrids. Copyright Elsevier Science.

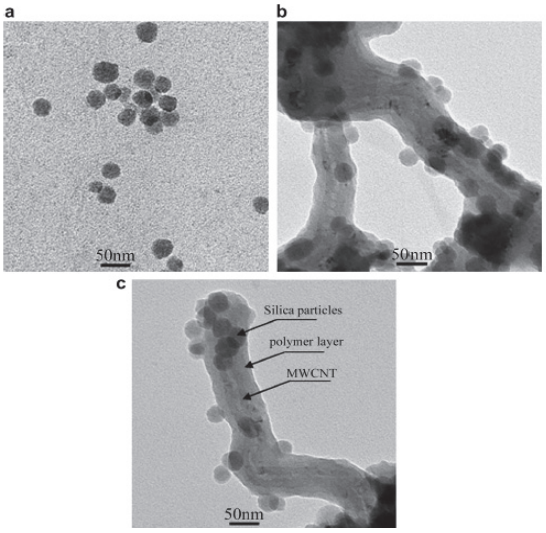

Fig. 9. TEM images; a) silica nanoparticles, b-c) MWNTs-polymer-silica nanoparticles hybrid. Copyright Elsevier Science.

5. Silanization of carbon nanomaterials

Due to the silanization is relatively a single reaction, and recently advances in research on CNTs have shown that is an effective method not only to insert organic chains such as been reached in microscopic fibers, but also to produce important progress in diversify CNTs properties and possible applications. Nowadays, some groups have used silanization in order to modify other carbon nanoforms. Carbon nanofibers (CNF) and graphene oxide (GO) are two carbon nanostructures modified by silanization effectively. Palencia et al, 2009, developed a complete study related with silanization conditions of CNF. Time, Temperature, silane type and concentration are the parameters studied in this research. 3-APTS is used in order to study the influence of temperature and reaction time on silanization process. For the study of the concentration and the silane structure influence, different silanes are probed such as: 3-APTS, 3-GPTMS, 2-AE-3-APTS (N-(2-aminoethyl)-3-(aminopropyltrimethoxysilane)) and 3-APMS (3-aminopropyltrimetoxysilane).

Thermal analysis and surface area measurements reveal that silane is not absorbed in CNFs surface with reaction times higher than 1 min. and reaction temperature higher than 25ºC. Also, the silane adsorption is related with silane structure. Aminosilanes such as: 3- APTS and 3-APMS show similar behavior due to these silanes include the same functional group. However, the diaminosilane (2-AE-3-APTS) shows lower interaction with CNFs surface due to the length of the diamine chain, that avoid further silane adsorption on the coated CNFs surface. 3-GPTMS shows a similar behavior to other silanes at low concentrations, while for high concentrations multilayers are produced. Recently the same group (Nistal et al. 2011) reported other studies related with CNFs modified with vinyltryethoxy silane (VTS) and 3-MAT. The interactions between CNFs and silanes are analyzed by different techniques such as: TGA, FTIR, TEM, HRTEM, SEM and nitrogen adsorption. The TGA results indicate that similar silane concentration of VTS and 3-MAT form one and three silane monolayers, respectively. Authors also have shown that each silane produce different interactions with CNF. Thus, while in low silane concentrations, the vinyl group of VTS is bonded to the graphene CNF surface mainly through π–π interactions; 3-MAT link to CNFs through the carbonyl group with hydroxyl groups of graphene defect sheets; Silanol–CNF hydroxyl interactions are also expected at these silane concentrations. Silica layers also are detected by IR at 1250 cm^{-1} assigned to Si-O-Si vibrations. However, for high silane concentration, when the silica layer is formed, both silanes shown vinyl free and carbonyl free groups. This later is detected by the signals at 1370 and 1686 cm^{-1} in IR analysis, respectively. TEM and HRTEM images of these silanized carbon structures with 5% (w/w) of silane shown clear differences between CNFs and the same materials after silanization. TEM images are shown in the figure 10, there pristine CNFs present smooth surface (figure 10a) and the silane coating appears clearly for silanized CNF in the figures b–d. The 3-MAT coating seems less homogeneous, with localized increased thickness. HRTEM images of pristine and silane coated CNFs are also shown in Figure 11. Graphene layers of CNFs are observed in the case of pristine material. However, silane coated CNFs show thicker surfaces with low inner channels, mainly for the samples that are coated with 3-MAT (Figure 11b). It is clear that graphene layers are not observed at higher magnifications, showing that the silanes are coating the CNF surface. In addition, using Nitrogen adsorption, authors give evidence that each silane depend on the nature is adsorbed in different mode, inasmuch as, VTS is adsorbed essentially on graphene surface (defect free) and 3-MAT on the micropores with hydroxyl groups (defects zone).

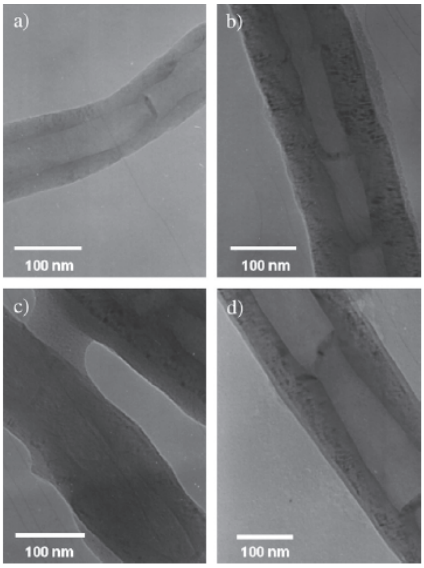

Fig. 10. TEM images; a) CNFs b-c) 3- MAT Silanized CNFs, d) VTS Silanized CNFs. Copyright Elsevier Science.

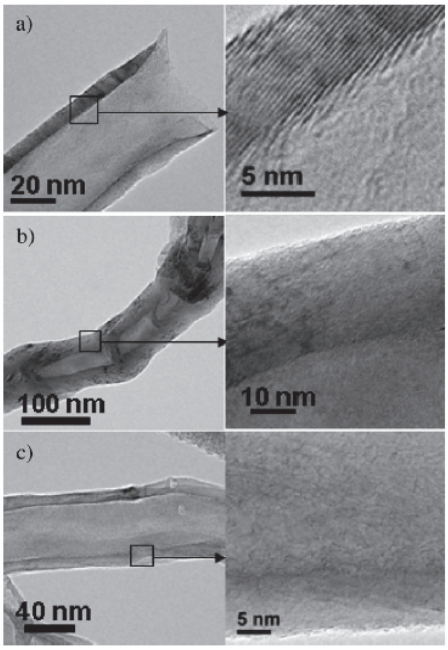

Fig. 11. HRTEM images; a) CNFs b) 3- MAT Silanized CNFs, c) VTS Silanized CNFs. Copyright Elsevier Science.

Silanization have also been used to attach optically active quaterthiophene molecules (T4) to graphene oxide sheets (Melucci et al. 2010). The procedure is achieved using a novel microwave-assisted silanization reaction. The method is useful to perform GO functionalization in one-step, under soft conditions in few minutes. The T4 molecules are linked to 3-APTS in order to form silane T4 moieties (T4-Si). The GO previously exfoliated in dimethylformamide (DMF) and T4-Si are introduced in a microwave oven reactor and irradiated at 80 °C (100 W) for 40 min. The hybrid GOT4 can be synthesized in either H2O or apolar organic solvents and deposited as single sheets, microplatelets or macroscopic membranes. Authors probe the properties of the new hybrid and the successful chemical functionalization considering a combined test of solubility and fluorescence. The hybrid properties for GOT4 are compared with its precursors: a mixture of GO and T4-Si without silanization reaction, and only GO. All suspensions are prepared in polar (DMF-H_2O 1:5 in volume) and apolar (DMF-CH_2-Cl_2 1:5 in volume) solvents. Suspensions are probed either normal light and under UV lamp showing different properties of the GOT4 hybrid as compared with GO and the mixture of T4-Si and GO. The figure 12 shows the GO-T4 membrane, the membrane observed with fluorescence microscopy and the suspensions under the two light types.

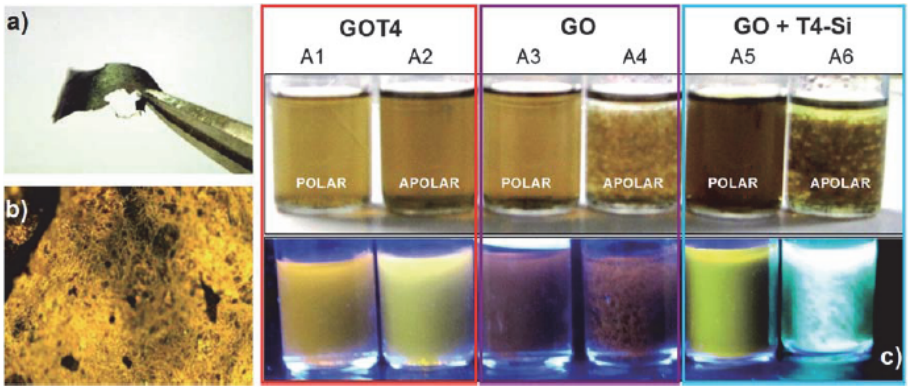

Fig. 12. GOT4 hybrids; a) membrane, b) image of GOT4 hybrid by fluorescence microscopy, c) Suspensions of GOT4, GO and GO + T4-Si in polar and apolar solvents under normal light (top) and UV lamp (bottom). . Copyright RSC.

Thus, silanization has started to establish it, as important protocol in order to attach organic moieties, biomolecules, polymers and other organic and inorganic groups that allow diversify carbon nanomaterials properties and possible uses. In this context, one of the first proposals to use silanization in CNTs is the specific and compatible interface in polymer nanocomposites. Next are reviewed the first results related with the silanization of CNTs and their incorporation in polymer matrices.

In spite of, there exist only few researches focus to use silanes as coupling agents in CNTs polymer nanocomposites (CNTPN), due to the versatility of silanization and the moieties that could be attached to CNTs and other carbon nanomaterials in the next years silanization follow being used as important chemical reaction in order to diversify carbon nanomaterials and improve their interaction with other materials.

6. Properties of polymer nanocomposites reinforced with silanized-carbon nanotubes

Recently, research focus to silanized CNTs has beginning to include these carbon nanomaterials in polymer matrices. As it has been mentioned one of the first propose of silanizing CNTs is improve the interface between carbon nanomaterials and the polymer matrices. The fact of incorporate different organic groups included in organosilanes to CNT surface is attractive to enhance the interactions at molecular level of nanomaterials with polymer. In addition, silanization could diversify properties of CNTs and therefore the features and possible applications of polymer nanocomposites. The selectivity of electronic properties and the behavior of CNTs depend on silane used, are some of the additional characteristics that also could be take in advantage in order to produce novel nanocomposites based on silanized CNTs. The easy application of silanization reactions to other carbon nanomaterials is an extra boon to considerer with a view to applied silanization to functionalize, diversify the properties and applications of different carbon

Polymer	Carbon nanomaterial type	Silane	Composites characterization	Reference
Epoxi	MWNT	3-Glycidoxypropyltrimethoxysilane (GPTMS)	TGA, DMA, three-point flexure test, compact tension test, dispersion and morphology, bulk electrical conductivity	Ma et al, 2007
Polyimide	MWNT	3-Isocyanatopropyltriethoxysilane (IPTES)	Dispersion and morphology, CP/MAS solid state ^{29}Si NMR spectroscopy, surface and volume electrical resistivity	Yuen et al, 2008 a
Polypropilene	MWNT	3-methacryloxypropyltrimethoxysilane (3-MAT)	Tensile test, morphology.	Zhou et al, 2008
Polyimide	MWNT	Vinyltriethoxysilane (PVTES)	Morphology, CP/MAS solid state ^{29}Si NMR spectroscopy, surface and volume electrical resistivities, tensile test.	Yuen et al, 2008 b
Silicone rubber (Sylgard®184)	MWNT	7-Octenyltrichlorosilane (7-OTCS) n-octyltrichlorosilane (*n*-OTCS)	Dispersion and morphology, indentation test,	Vast et al, 2009
High Density Polyethylene	Carbon nanofiber	Octadecyltrimethoxysilane	DMA, DSC	Wood et al, 2010
Ultra high molecular weight polyethylene	MWNT	3-Aminopropyltriethoxysilane (3-APTS)	Dispersion and surface morphology, wear test	Lee et al, 2010

Table 1. Polymer nanocomposites reinforced with silanized-carbon nanomaterials

materials including the nanocomposites field. Next are reviewed the advantages of silanized CNTs and CNFs on the development of polymer nanocomposites. Table 1 shows a resume of carbon nanomaterials silanized, the silane type, the polymer matrix used and the analyzed properties of polymer nanocomposites.

6.1 Electrical conductivity

One of the most outstanding properties of carbon nanomaterials is their electrical behavior. Carbon nanotubes or nanofibers posses π-bonds (C=C) that transfer electrical charges allowing a high electrical conductivity. Therefore adding small quantities of carbon nanomaterials to polymer matrix will reduce dramatically their surface and volume resistivity. This has been used in order to diversify the applications of polymer nanocomposites that could be since electronic devices to automotive and aerospace purposes. An extensive research with different kind of polymers has been done, giving many different conclusions about conductivity in nanocomposites that generate discrepancies between authors that have studied this phenomenon by years. In spite of divergence on results it is possible conclude that polymer matrix is not really a decisive factor in the electric response, in fact even when the nanocomposites are made with the same matrix the processing method can affect their electrical performance.

Research has shown that diverse factors can influence electrical behavior of nanocomposites, among the most important it is possible to mention the kind of nanomaterial structure: nanotubes (SWNT or MWNT), graphene sheets or nanofibers, their production method, dispersion technique, alignment inside the matrix, adhesion between nanomaterial and polymer, purification or chemical modification.

Regarding chemical modification, silane functionalization, as technique to improve dispersion and adhesion, also has important consequences in electrical conductivity of nanocomposites as was demonstrated by several authors.

Ma et al, 2007, evaluated the effects of silane functionalization of MWNTs on electrical properties of CNTs/epoxy nanocomposites. These authors utilize GPTMS as the functionalization agent; this silane is compatible with diglycidyl ether of bisphenol A (DGEBA), used as precursor of epoxy. The curing agent for this matrix was m-phenylenediamine. Nanocomposites with different weight fractions (0.05%, 0.10%, 0.25% and 0.50%) of the untreated CNTS (untreated-CNTs) and silane functionalized CNTs (silane-

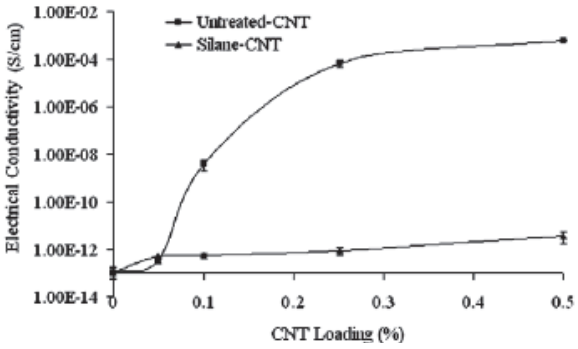

Fig. 13. Electrical conductivity for GPTMS-MWNTs epoxy nanocomposites. Copyright Elsevier Science.

CNTs) were evaluated. Figure 13 shows that percolation threshold for untreated-CNTs nanocomposite is around 0.1%, achieving the maximum electrical conductivity value (5.9 X 10^{-4} S/cm) with 0.50 %, whereas silane-CNTs nanocomposites only exhibit a very small increasing in conductivity. This behavior is explained taking into account that GPTMS molecules and epoxy endgroups are covalently bonded to the CNTs surface, these could react easily with the curing agent and produce wrapping of CNTs by the epoxy. This wrapping affects π-bonds and consequently charge transfer is also perturbed. The authors also conclude that a better dispersion of CNTs in polymer matrix is unfavorable to the creation of electrical networks.

On the other hand, Yuen et al, 2008, showed that chemical modification of MWNTs with silane improves electrical behavior of polymer nanocomposites. In this research, the authors use acid-modified MWNTs and IPTES-modified MWNTs, for these last also acid-modified MWNTs were prepared as base material. Three ratios in weight of IPTES to acid-modified MWNTs were used: 1:1 (IPTES-MWCNT-1[1]), 2:1 (IPTES-MWCNT-2) and 3:1 (IPTES-MWCNT-3). All these were included in polyamic acid, which acts as polyimide precursor. Mixture of modified-MWNTs (with acid and with IPTES) and polyamic acid was heated to 300 °C, temperature for imidation reaction; at this point the IPTES molecules attached to MWNTs surface react and connect other MWNTs, thus an IPTES-MWNTs network is achieved, as is shown in figure 14. This network reduces the electrical resistivity and provides desired effective electrical pathways. Figure 15 a-b shows surface and volume electrical resistivity of the IPTES-MWNT/polyimide composites. As can be observed the acid-MWNTs nanocomposites exhibit the highest values for both surface and volume resistivity when 6.98 wt% concentration was used, whereas at the same concentration IPTES-MWCNT-3 nanocomposites have the low resistivity value. These results show that silanization could be a useful technique to improve conductivity of CNTs polymer nanocomposites if a MWNTs network is formed. In contrast to when IPTES content was low and no more than 2.44 wt% of MWNTs was used, the network was not produced and MWNTs may be isolated, this means well dispersed, this fact causes higher values in volume resistivity.

Similar results with polyimide matrix were obtained using PVTES-modified MWNTs (Yuen et al, 2008 b). In this study three ratios in weight of VTES to unmodified MWNTs were used: 1:1 (VTES-MWCNT-1[2]), 2:1 (VTES-MWCNT-2) and 3:1 (VTES-MWCNT-3). The nanocomposites were synthesized using polyamic acid as polyimide precursor. Electrical behavior, depicted in figure 16, shows that unmodified MWNTs nanocomposites need high concentrations of CNTs in order to achieve low volume resistivity, however VTES-modified nanocomposites reach the percolation threshold with only 2.44 wt% of CNTs. These results were attributed to connections between VTES-MWNTs that can occur during imidization reaction.

Accordingly with these results, electrical conductive properties of polymer nanocomposites reinforced with silanized-carbon nanotubes depend on network formation; consequently increase in the dispersion does not improve conductivity nor decrease the percolation threshold. However other important properties, such as thermal stability or thermo-mechanical behavior, are closely dependent on dispersion features.

---

[1] The original nomenclature in the figure given by Yuen et al, 2008a is maintained in order to avoid confusions if the article is consulted. MWNCT appear instead of MWNTs

[2] The original nomenclature in the figure given by Yuen et al, 2008b is maintained in order to avoid confusions if the article is consulted. MWNCT appear instead of MWNTs

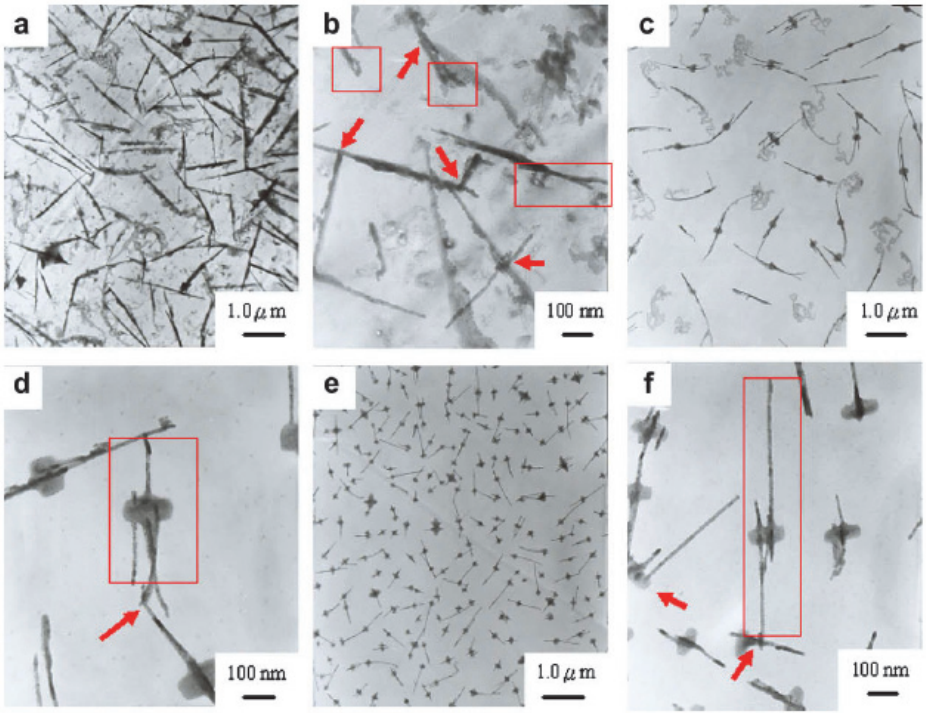

Fig. 14. TEM images of 6.98 wt% IPTES-MWNT polyimide nanocomposites, a) IPTES:MWCNT-1 (10,000X), b) IPTES:MWCNT-1 (50,000X), c) IPTES:MWCNT-2 (10,000X), d) IPTES:MWCNT-2 (50,000X), e) IPTES:MWCNT-3 (10,000X), f) IPTES:MWCNT-3 (50,000X). The arrows show connected MWNTs by IPTES molecules. Copyright Elsevier Science.

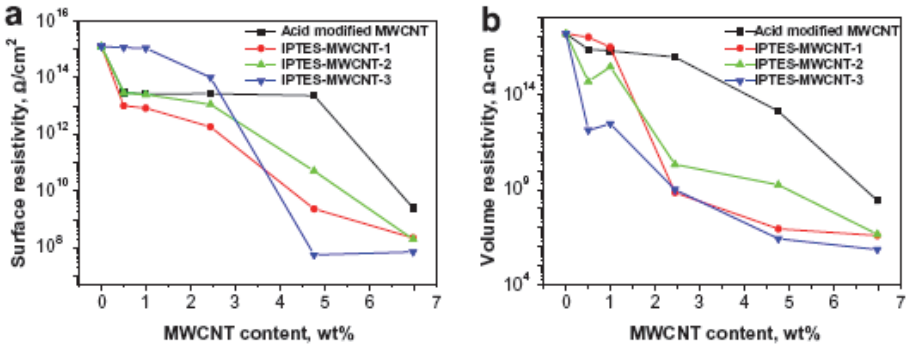

Fig. 15. Electrical behavior of acid and IPTES modified MWNTs poyimide nanocomposites, a) Surface resistivity, b) Volume resistivity. Copyright Elsevier Science

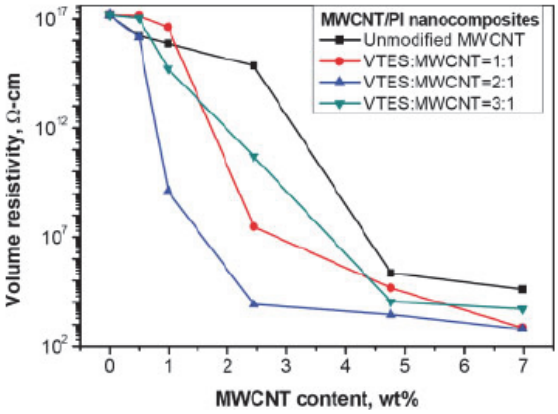

Fig. 16. Volume resistivity of VTES-MWNTs polyimide nanocomposites. Copyright Wiley Periodicals Inc.

6.2 Mechanical properties

It is well known that CNTs have outstanding mechanical properties, however as well as in other kind of composites good interfaces and dispersion of reinforcements are needed to take full advantage of this feature. Nanometric reinforcements have interactions at molecular level, increasing synergic effects between matrix and nanostructures, thus only small quantities of CNTs can increase drastically the mechanical properties of nanocomposites when interfacial contacts and good dispersion are achieved. In fact, reinforcement properties in CNTs polymer nanocomposites involve optimal transfer of strain between matrix and CNTs. This implies a strong interfacial bonding at nanometric level. A useful procedure to get this challenge is to cause that CNTs form covalent bonds during the polymerization process and have them chemically integrated in the cross-linked matrix. Silanization provides functional chemical interactions to CNTs in order to reach these conditions, this have been probed by several authors.

GPTMS-MWNTs in epoxy matrix cause higher elastic modulus than the untreated-CNTs epoxy nanocomposite, over the entire range of CNTs content studied (from 0 to 0.5 wt %). Also the flexural strength of these nanocomposites has a similar tendency (Ma et al, 2008). Compact tension tests provide interesting results for these GPTMS-MWNTs nanocomposites. The quasi-static fracture toughness (K_{IC}) evaluated with this study show a continuous decrease when untreated-CNTs were used, in contrast to nanocomposites with GPTMS-MWNTs. The use of silanized-MWNTs increases K_{IC} values with CNTs content. Ma et al, 2008, explained this behavior considering that untreated-CNTs have poor dispersion in the epoxy matrix, in addition to few interfacial interactions. After silane functionalization, both conditions were improved by the attachment of silane molecules onto CNTs surface.

Vast et al, 2009, used two types of silane: 7-OTS and *n*-OTCS, which differ only by the nature of their end groups. These were used in order to compare dispersion of purified and silanized MWNTs in a thermally curable silicone rubber: Sylgard®184 and the effect on the Young's modulus. The authors considered that silane act by two ways simultaneously, they graft on the MWNTs and also they form siloxane networks on MWNTs surface through condensation with nearby silane molecules. In addition the chemical structure of the

siloxane network on the silanized-MWNTs is very similar to vinyl-terminated PDMS chains and methylhydrosiloxane copolymer chains (both are precursors of silicone rubber), this fact is favorable to achieve well silanized-MWNTs dispersion. The results in this research show that chemical structure of silane has a strong influence in dispersion and mechanical performance. Rubber nanocomposites with n-OTCS-MWNTs exhibit poor dispersion that is reflected by reduced mechanical properties, since pristine silicone rubber itself has a better Young's modulus. In effect, increasing the n-OTCS-MWNTs content gives even poor mechanical behavior, this is due to growth of big aggregates causes Young's modulus to decrease significantly. In contrast to this effect, 7-OTCS-MWNTs rubber composites show an important increasing in Young's modulus, since it increases from 6.7 MPa for pristine rubber to 9.9 MPa only with 0.2 wt% of silanized-MWNTs. This fact is attributed to silane interactions because of purified-MWNTs modulus increases slightly, reaching only 7.7 MPa with 0.5 wt% content of MWNTs.

Yuen et al, 2008, also have studied the effect of silanized MWNT's in the polymer crosslinking process. In this case they used VTES that is covalently attached to MWNT's surface by free radical reaction.VTES-MWCNTs[3] were added to the polyamic acid (imide precursor) and then the mixture was heated until 300 °C was reached. Tensile test results show that when unmodified MWNTs were used, the tensile strength of the MWCNT polyimide composite was increased 19% compared to neat polyimide. However, as can be observed in figure 17, VTES-MWCNT's polimide nanocomposites show better mechanical behavior, since all the samples have higher values in tensile strength, with exception of 7 wt % of VTES:MWCNT=3:1. The highest tensile strength (165 MPa) was reached with two VTES:MWCNT nanocomposites: 1:1 and 2:1, both with only 0.5 wt % of modified CNTs content, but beyond this concentration tensile strength decreases gradually. On the other hand Young's modulus for pure polyimide is around 2.3 GPa and increases gradually with unmodified-MWNTs content until reach 3 GPa with 7 wt%, whereas with VTES-MWNTs the Young's modulus increases considerably, reaching a maximum value of 5.5 GPa with VTES:MWCNT=1:1. In accordance with these authors, VTES:MWCNTs ratio has an important effect in nanocomposite performance. VTES was grafted on MWNTs most effectively with 2:1 ratio. However, 3:1 ratio allows grafting but leaves VTES free to interact during cross linking polymerization. Therefore, for Young's modulus, VTES-MWNTs=3:1 shows the highest values over all range of contents, and with 7 wt % has the second better one. This occurs due to free VTES groups connect VTES-MWCNTs with Si-O-Si bonding, causing evident increasing in Young's modulus and brittleness of the composites.

Nanocomposites are made with an extensive variety of polymers, such as epoxi, polyimide or rubber, mentioned before, where it is possible to take advantage of polymerization reaction in order to achieve an adequate dispersion of MWNTs. But also other processing techniques can be used with interesting results. For instance, Zhou et al, 2008, prepared blends of polypropylene and silanized-MWNTs by using a rheometer at 190 °C for 10 min and a rotor speed of 75 rpm. The contents of MWNTs in these blends were: 0.25 wt%, 0.5 wt%, 1 wt% and 2 wt%. Once mixed, the silanized-MWNTs–polypropylene blends were molded by compression at 190 °C to form nanocomposite sheets. Before mixing, the MWNTs were silanized using 3-MPTS. The effects of silanization treatment and CNTs content on the tensile properties of polypropylene nanocomposites were studied. Tensile

[3]The original nomenclature given by Yuen et al, 2008b is maintained in order to avoid confusions if the article is consulted. MWNCT appear instead of MWNTs.

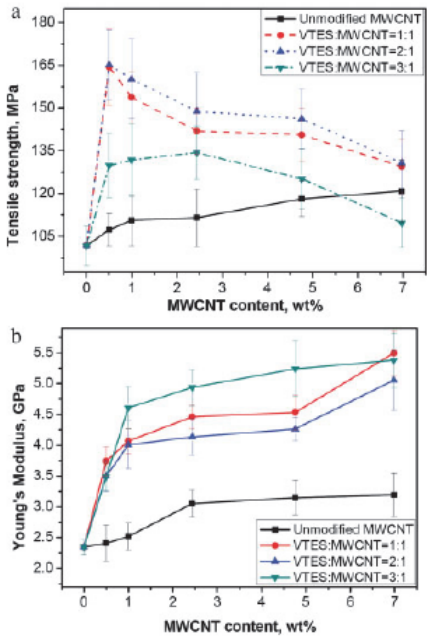

Fig. 17. Effect of VTES:MWCNT ratio and MWCNT content on the mechanical properties of polyimide nanocomposites, a) Tensile strength, b) Young's Modulus. Copyright Wiley Periodicals Inc.

strengths for all percentages of CNTs content were high when 3-MPTS-MWNTs were used. The highest value was around 39.5 MPa with 1 wt%, this means and increasing of 10% with respect to pure polypropylene. Unmodified MWNTs only increase the tensile strength in almost 6% for the same content of MWNTs. Homogeneous dispersion is severely influenced by concentration of CNTs, low quantities of 3-MPTS-MWNTs or unmodified-MWNTs allow that partial tensile strain can be transferred to CNTs, producing increments in tensile strength until 1 wt% of MWNTs content is reached. Furthermore, if higher quantities of CNTs are used the tensile strength of polypropilene nanocomposites decreases due to agglomerates of MWNTs are formed.

Tribology deserves a special mention among the mechanical properties. The tribological properties of polymers are usually improved if some reinforcements are used, likewise mechanical properties. However, there is a lack of information regarding this theme. In fact, understanding the tribology of polymers is not easy, since these have complicated multiphase structures with multiple domains and subdomains in which their mechanical behavior varies significantly, in addition polymers are viscoelastic, and this implies that their properties change with time, as was described by Brostow et al, 2006 and 2008. In spite of these difficulties, Dasari et al, 2009, published a complete and interesting review with important results on wear and scratch damage in polymer nanocomposites, however they do not mention any functionalization treatment, not even silanization. To the date, almost all authors in silanized-CNTs polymer nanocomposites deal with mechanical properties, but they do not include tribological data among their results.

One of the few results on this area was reported by Lee et al, 2010, they studied specifically friction coefficient and wear rate of 3-APTS-MWNTs in ultra high molecular weight polyethylene (UHMWPE). These authors demonstrated that silanized CNT/UHMWPE nanocomposites have better dispersion and stronger interfacial bonding than oxidized-MWNTs, this fact is reflected in an evident lower friction coefficient for silanized-MWNTs nanocomposites. Besides, as figure 18a shows, the maximum values for depth profile were those corresponding to raw UHMWPE and oxidized-CNT for all sliding speed range, these results are in agreement with wear rate, which confirm that silanized CNT/UHMWPE nanocomposites have a better performance. The wear rate of these nanocomposites decreased around 83, 53 and 59 %, respectively at sliding speeds of 0.12, 0.18 and 0.24 m/s, compared with the raw UHMWPE.

SEM images in figure 18 shows wear tracks (indicated by arrows) in raw polymer and nanoreinforced composites. There are severe damages in raw polymer, such as wear debris, cracks and exfoliation, but these diminish evidently for oxidized CNT/UHMWPE nanocomposite, and even more for silanized CNT/UHMWPE, corroborating thus an improvement in CNT dispersion and interfacial interactions between CNTs and polymer matrix because of silane treatment of CNTS.

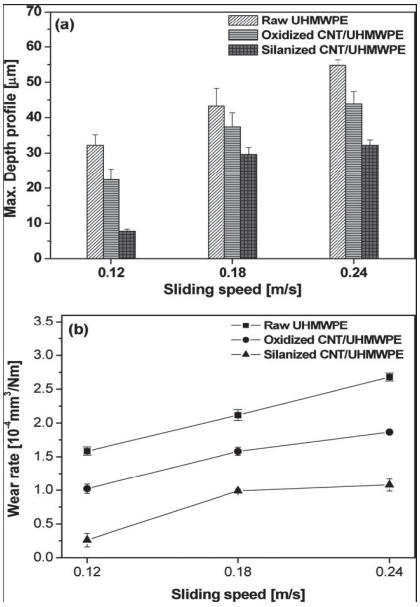

Fig. 18. Tribological behavior of raw UHMWPE, oxidized CNT/UHMWPE and silanized CNT/UHMWPE nanocomposites, a) Maximum depth profile, b) Wear rate. Copyright Wiley InterScience.

Certainly, it is evident that, as well as other mechanical properties, tribological behavior needs to be exhaustively studied, since results until now are not conclusive, as was described by Dasari et al, 2009. In addition to their concern, also it is worthy to take into account that different kinds of functionalization, such as silanization, play an essential role

to take advantage of dispersion and interfacial interactions and thus to improve polymer nanocomposite performance.

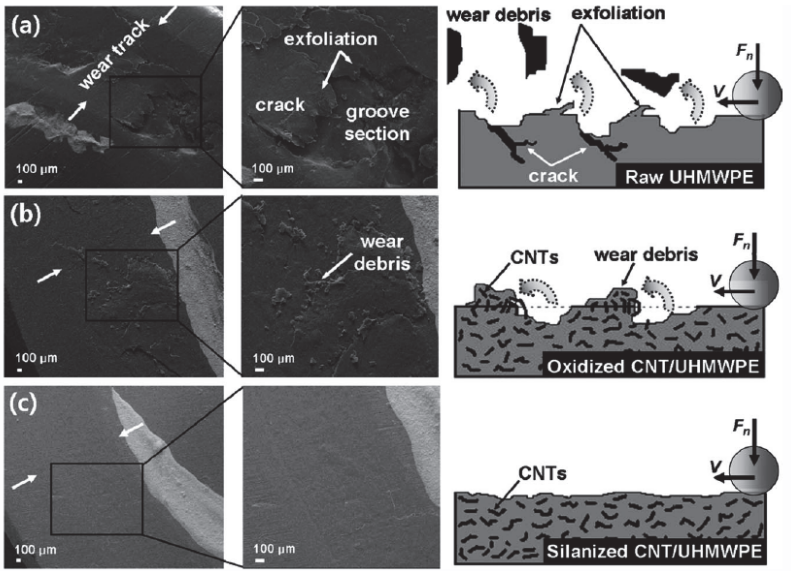

Fig. 19. SEM images and schematic illustration of worn surface, a) raw UHMWPE, b) oxidized CNT/HMWPE nanocomposite, and c) silanized CNT/UHMWPE nanocomposite. Copyright Wiley InterScience.

6.3 Dynamical mechanical analysis

The evaluation of thermomechanical properties in polymer nanocomposites is an important parameter in order to estimate the performance of these kinds of materials. The elastic behavior and the movement of chains related with thermal transition can be evaluated by Dynamical Mechanical Analysis (DMA). The interactions produced between CNTs and polymer matrix also can be evidenced by the results obtained by this technique indicating if functionalization produces some changes as compared with not functionalized materials.

In spite of, the relevance of DMA in Carbon Nanotube Polymer Nanocomposites CNPNs, only few researches that involve polymer matrix reinforcement with silanized CNTs or silanized carbon nanomaterials, have reported this behavior. Ma et al. 2007 evaluate thermomechanical properties of Epoxy composites reinforced with MWNTs silanized with 3-GPTMS. Epoxy is reinforced with silanized CNTs at different concentrations. Figure 20 show the results of polymer nanocomposites including silanized CNTs. Nanocomposites with untreated CNTs present lower storage modulus that epoxy matrix at 30 ^{o}C. However at the same temperature, nanocomposites reinforced with silanized CNTs show a slight increment in storage modulus as compared with the modulus of Epoxy. Authors, indicate this behavior as better dispersion of silanized CNTs than untreated CNTs in polymer matrix. At high temperature both nanocomposites with silanized and untreated CNTs improve notably the storage modulus; but, the values in tang delta indicate more slippages

between CNTs and polymer in nanocomposites with untreated CNTs than those containing silanized CNTs (figures 20 b, d). This effect is attributed cross-linking reactions of epoxy and hardener promoted by silanized CNTs. Thus, the link between the silane-treated CNT and epoxy effectively change the movement of molecular chains reflected in Tan Delta.

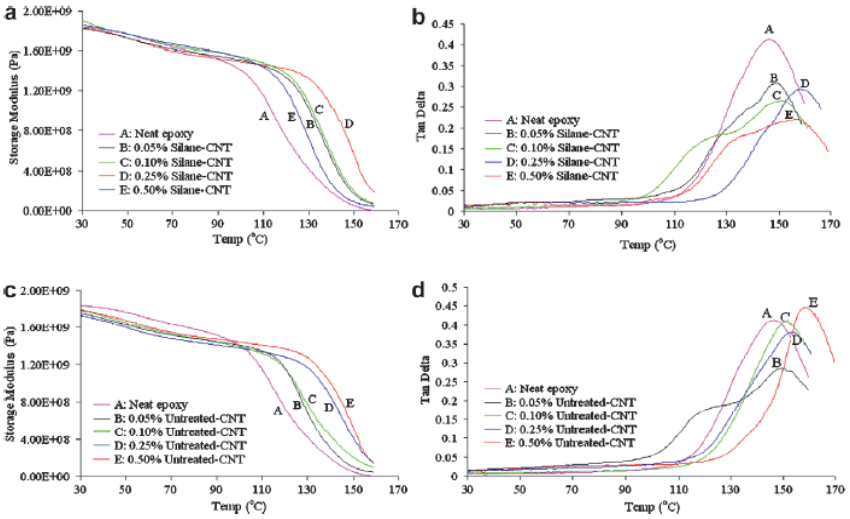

Fig. 20. Dynamical Mechanical Analysis of polymer nanocomposites reinforced with CNTs and silanized CNTs (3-GPTMS). a,c) Storage Modulus; b,d) Tan Delta. Copyright Elsevier Science

Other researches (Wood et al. 2010) that involve DMA of Polymer Nanocomposites containing silanized CNFs with different silane treatments have found that silane reaction assisted by NaOH improve the interactions at interface level more than only silanization. Therefore, the storage modulus at -70 ºC of polymer nanocomposites reinforced with silanized CNFs increase 39 % with respect to polymer matrix (HDPE High Density Poly ethylene) . Storage modulus at 25 ºC also increase in 20% for the CNPNs reinforced with silanized CNTs assisted by NaOH as compared with HDPE. Nanocomposites containing silanized CNTs but, where the reaction is not assisted by NaOH, only increase the storage modulus at 70 ºC in 6 % with respect to HDPE and storage modulus for these composites is not increased at 25 ºC.

Recently, in our group (Velasco-Santos et al. 2011) DMA have been used to evaluate CNPNs reinforced with 1 wt% of silanized CNTs (3-MAT) in Poly (methyl methacrylate) (PMMA) matrix. Storage modulus of CNPNs with modified CNTs (1 wt%) at 30 ºC increases 150 % with respect to PMMA and CNPNs synthesized with untreated CNTs (1 wt %) only increase 82 %. In addition, the storage modulus at 90 ºC is almost three times for composite with silanized CNTs as compared with composite reinforced with untreated CNTs. Thus, in spite of there are some reports that involve the evaluation of CNPNs reinforced with CNTs functionalized by silanization; a lot research that evaluates thermomechanical properties of CNPNs modified with CNTs functionalized with different organosilanes is needed. Successful silanization provide to CNTs diverse properties including compatibility and

undoubtedly DMA is very important technique to evaluate interface, chains movement, transitions and storage and loss modulus. DMA have been employed for other systems than involve the evaluation of CNPNs modified with organosilane but do not involve interaction of organic moieties of the silane with polymer matrix. For instance, Silica-coated multi-walled carbon nanotubes (MWCNT@SiO2) were synthesized by a sol–gel method and then incorporated into an epoxy matrix (1 wt%) by Cui et al 2011. The storage modulus of CNPN with modified CNTs improves slightly with respect to CNPN with unmodified CNTs and epoxy. However the increase is maintained constantly since 30 ^{o}C until 140 ^{o}C

7. Conclusion

Silanization is a single chemical functionalization process that is effective to modify CNTs surface and properties. The reaction could be achieved after oxidation or directly on CNT surface by sylilation and hydrosilylation. Silanization type and oxidation process play an important role in the final properties of silanized- CNTs. Taking in count previously results of silanization, it is possible that the combination of soft oxidation and redox or initiation reactions also could yield silanized carbon nanotubes.

The control of this kind of chemical modifications on CNTs, depending on the organosilane used; is useful to manage electronic features of CNTs, and therefore diversify the electrical conductivity and related properties of silanized CNTs. The field of silanizing carbon nanomaterials in order to diversify their properties is a new open gate with interesting opportunities.

Moreover, silanization is functional method to modify chemically other carbon nanostructures such as graphene oxide and carbon nanofibers and could be applied to other carbon nanoforms with sp^2 graphitization. The opportunity to use organosilanes to diversify carbon nanomaterial characteristics and properties is other field that could be exploited.

Results reviewed here show that successful silanization change the surface behavior of CNTs and depending on the organic moieties in the organosilane used, the interaction of CNTs with different polymer matrices can be improved, as was suggested by our group some years ago. Recently, silanized CNTs incorporated to diverse polymers have shown interesting, electrical, mechanical, thermal and thermomechanical properties that can be improved or diversifying in the CNPNs synthesized.

Thus, silanization is shown as single chemical reaction that is useful to modified and diversify carbon nanomaterials properties, and work as effective coupling agent to develop polymer composites. However, the versatility of the silane moieties could be effective to diversify even more the applications of organosilanes in other systems or composite types. Chemical of carbon nanomaterials provide other possibilities that not are possible in macroscopic materials.

8. References

Bag, D. S.; Dubey, R.; Zhang, N.; Xie, J.; Varadan, V. K.; Lal, D. & Mathur, G. N. (2004). Chemical functionalization of carbon nanotubes with 3-methacryloxypropyltrimethoxysilane (3-MPTS). *Smart Materials and Structures*, Vol.13, No.5, (October 2004), pp. 1263-1267, ISSN 0964-1726

Bourgeat-Lami, E.; Tissot, I. & Lefebvre, F. (2002). Synthesis and Characterization of SiOH-Functionalized Polymer Latexes Using Methacryloxy Propyl Trimethoxysilane in

Emulsion Polymerization. *Macromolecules*, Vol.35, No.16, (June 2002), pp. 6185-6191, ISSN 0024-9297

Brostow, W. & Hagg-Lobland, H.E. (2006). Sliding Wear, Viscoelasticity, and Brittleness of Polymers. *Journal Materials Research,* Vol.21, No.9, (September 2006), pp.2422-2428, ISSN 0884-2914

Brostow, W. & Hagg-Lobland, H.E. (2008). Predicting Wear from Mechanical Properties of Thermoplastic Polymers. *Polymer Engineering and Science,* Vol.48, No.10, (October 2008), pp.1982-1985, ISSN 1548-2634

Chen, J.; Rao, A. M.; Lyuksyutov, S.; Itkis, M. E.; Hamon, M. A.; Hu, H.; Cohn, R. W.; Eklund, P. C.; Colbert, D. T.; Smalley, R. E. & Haddon, R. C. (2001). Dissolution of Full-Length Single-Walled Carbon Nanotubes. *Journal of Physical Chemistry B*, Vol.105, No.13, (March 2001), pp. 2525-2528, ISSN 1089-5647

Coates, J. P. (2000). Interpretation of Infrared Spectra, A Practical Approach, In: *Encyclopedia of analytical chemistry: applications, theory and instrumentation,* Meyers, R. A., pp. 10815, John Wiley & Sons Ltd, ISBN 978-0-471-97670-7, Chichester

Cui, W.; Du, F.; Zhao, J.; Zhang, W.; Yang, Y.; Xie, X. & Mai, Y.-W. (2011). Improving thermal conductivity while retaining high electrical resistivity of epoxy composites by incorporating silica-coated multi-walled carbon nanotubes. *Carbon*, Vol.49, No.2, (February 2011), pp. 495–500, ISSN 0008-6223

Dasari, A.; Yu, Z.-Z. & Mai, Y.-W. (2009). Fundamental aspects and recent progress on wear/scratch damage in polymer nanocomposites. *Materials Science and Engineering R,* Vol.63, No. 2 (January 2009), pp. 31-80, ISSN 0927-796X

Datsyuk V., Kalyva M., Papagelis K., Parthenios J., Tasis D., Siokou A., Kallitsis I., Galiotis C., (2008). Chemical oxidation of multiwalled carbon nanotubes. *Carbon*, Vol. 46, No. 6 (May 2008), pp.833-840, ISSN 0008-6223

Dresselhaus, M. S.; Dresselhaus, G.; Jorio, A.; Souza Filho, A. G.; Saito, R. (2002). Raman spectroscopy on isolated single wall carbon nanotubes. *Carbon*, Vol.40, No.12, pp. 2043-2061, ISSN 0008-6223

Hemraj-Benny, T. & Wong, S. S. (2006). Silylation of Single-Walled Carbon Nanotubes. *Chemistry of materials,* Vol.18, No.20, (October 2006), pp. 4827-4839, ISSN 0897-4756

Hiura, H.; Ebbesen, T. W.; Tanigaki, K. (1995). Opening and purification of carbon nanotubes in high yields. *Advanced Materials*, Vol.7, No.3, (March 1995), pp. 275-276, ISSN 1521-4095

Jin, Z.; Pramoda, K. P.; Xu, G.; Goh S. H. (2001). Dynamic mechanical behavior of melt-processed multi-walled carbon nanotube/poly(methyl methacrylate) composites. *Chemical Physics Letters,* Vol.337, No.1-3, (March 2001), pp. 43-47, ISSN 0009-2614

Karousis N.; Tagmatarchis, N.; Tasis D., (2010) Current progress on the chemical modification of carbon nanotubes. *Chemistry Reviews,* Vol. 110 No. 9, (June 2010), pp. 5366-5397, ISSN 0009-2665

Kastner, J.; Pichler, T.; Kuzmany, H.; Curran, S.; Blau, W.; Weldo, D. N.; Delamesier, M.; Draper, S.; Zandbergen, H. (1994). Resonance Raman and infrared spectroscopy of carbon nanotubes. *Chemical Physics Letters*, Vol.221, No.1-2, (April 1994), pp. 53-58, ISSN 0009-2614

Kathi, J. & Rhee, K. Y. (2008). Surface modification of multi-walled carbon nanotubes using 3-aminopropyltriethoxysilane. *Journal Material Science*, Vol.43, No.1, (January 2008), pp. 33–37, ISSN 0022-2461

Lee, Y.; Jeon, K.-S.; , Lim, H.; Shin, H. S.; , Jin, S. M.; Byon, H. R.; Suh, Y. D. & Choi, H. C. (2009). Silencing of Metallic Single-Walled Carbon Nanotubes via Spontaneous

Hydrosilylation. (2009). *Small*, Vol.5, No.12, (June 2009), pp. 1398-1402, ISSN 1613-6810

Lee, J.-H.; Kathi, J.; Rhee, K. Y. & Lee, J. H. (2010). Wear Properties of 3-Aminopropyltriethoxysilane-Functionalized Carbon Nanotubes Reinforced Ultra High Molecular Weight Polyethylene Nanocomposites. *Polymer Engineering and Science,* Vol.50, No.7, (July 2010), pp. 1433-1439, ISSN 0032-3888

Lin, T.-W.; Salzmann, C. G.; Shao, L.-D.; Yu, C.-H.; Green, M. L. H. & Tsang, S.-C. (2009). Polyethylene glycol grafting and attachment of encapsulated magnetic iron oxide silica nanoparticles onto chlorosilanized single-wall carbon nanotubes. *Carbon*, Vol. 47, No.6, (May 2009), pp. 1415-1420, ISSN 0008-6223

Liu, Y.; Zhang, C.; Du, Z.; Li, C.; Li, Y.; Li, H. & Yang, X. (2008). The preparation of multi-walled carbon nanotubes encapsulated by poly(3-acrylaminopropylsiloxane) with silica nanospheres on the polymer surface. *Carbon*, Vol.46, No.13, (November 2008), pp. 1670-1677, ISSN 0008-6223

Lourie, O.; Cox, D. M. & Wagner, H. D. (1998). Buckling and Collapse of Embedded Carbon Nanotubes. *Physical Review Letters*, Vol.81, No.8, (August 1998), pp. 1638-1641, ISSN 0031-9007

Ma, P. C.; Kim J.-K. & Tang B. Z. (2006). Functionalization of carbon nanotubes using a silane coupling agent. *Carbon*, Vol.44, No.15, (December 2006), pp. 3232–3238, ISSN 0008-6223

Ma, P. C.; Kim, J.-K. & Tang, B. Z. (2007). Effects of silane functionalization on the properties of carbon nanotube/epoxy nanocompositos. *Composites Science and Technology,* Vol.67, No.14, (November 2007), pp. 2965–2972, ISSN 0266-3538

Melucci, M.; Treossi, E.; Ortolani, L.; Giambastiani, G.; Morandi, V.; Klar, P.; Casiraghi, C.; Samorì, P. & Palermo, V. (2010). Facile covalent functionalization of graphene oxide using microwaves: bottom-up development of functional graphitic materials. *Journal of Materials Chemistry*, Vol.20, No.41, (November 2010), pp. 9052-9060, ISSN 0959-9428

Nistal, A.; Palencia, C.; Mazo, M. A.; Rubio, F.; Rubio, J. & Oteo, J. L. (2011). Analysis of the interaction of vinyl and carbonyl silanes with carbon nanofiber surfaces. *Carbon,* Vol.49, No.5, (April 2011), pp. 1635-1645**,** ISSN 0008-6223

Palencia, C.; Rubio, F.; Merino, C.; Rubio, J.; & Oteo, J. L. (2009). Study of the Silanization Process in CNFs: Time, Temperature, Silane Type and Concentration Influence. *Journal of Nano Research*, Vol.4, (January 2009), pp. 33-43, ISSN 1662-5250

Saito, R.; Dresselhaus, G. & Dresselhaus, M. S. (1998). *Physical Properties of Carbon Nanotubes*, Imperal College Press, ISBN 978-1-86094-093-4, London

Scheibe, B.; Borowiak-Palen, E. & Kalenczuk, R. J. (2009). Effect of the Silanization Processes on the Properties of Oxidized Multiwalled Carbon Nanotubes. *Acta Physica Polonica A*, Vol.116, No. SUPPL, pp. S150-S155, ISSN 0587-4246

Tasis, D., Tagmatarchis, N. , Bianco, A. and Prato, M.,(2006) Chemistry of carbon nanotubes, *Chemistry Reviews*. Vol. 106, No. 3, (February 2006) p.p. 1105-1136, ISSN 0009-2665.

Vast, L.; Philippin, G.; Destrée, A.; Moreau, N.; Fonseca, A.; Nagy, J. B.; Delhalle, J. & Mekhalif, Z. (2004). Chemical functionalization by a fluorinated trichlorosilane of multi-walled carbon nanotubes. *Nanotechnology*, Vol.15, No.7, (July 2004), pp. 781–785, ISSN 09574484

Vast, L.; Lallemand, F.; Colomer, J.-F.; Van Tendeloo, G.; Fonseca, A.; Mekhalif, Z. & Delhalle, J. (2009). Multiwalled carbon nanotubes functionalized with 7-octenyltrichlorosilane and n-octyltrichlorosilane: Dispersion in Sylgard®184 silicone and Young's modulus. *Journal of Materials Science*, Vol.44, No.13, (July 2009), pp. 3476-3482, ISSN 0022-2461

Velasco-Santos, C.; Martínez-Hernández, A.L.; Lozada-Cassou, M.; Alvarez-Castillo, A.; Castaño, V.M. (2002). Chemical funtionalization of carbon nanotubes through an organosilane. *Nanotechnology,* Vol. 13, No. 4, (August 2002), pp 495-498, ISSN 09574484

Velasco-Santos, C.; Martínez-Hernández, A. L.; Fisher, F.; Rouff, R. S. & Castaño, V. M. (2003). Dynamical-mechanical and thermal analysis of carbon nanotube-methyl-ethyl methacrylate nanocomposites. *Journal of Physics D: Applied Physics*, Vol.36, No.12, (June 2003), pp. 1423-1428, ISSN 0022-3727

Velasco-Santos C., Martínez-Hernández A.L. and Castaño V.M., (2004), Chemical functionalization on carbon nanotubes: Principles and applications. In *Trends in Nanotechnology Research*, Edited E. V. Dirote, Nova Science Publishers Inc. Vol. I, p.51. New York, USA.

Velasco-Santos, C.; Martínez-Hernández, A.L.; Brostow, W. & Castaño, V. M. (2011). Influence of silanization treatment on thermo-mechanical properties of multiwalled carbon nanotubes-poly(methylmethacrylate) nanocomposites. Submitted to *Journal of Nanomaterials*, ISSN 1687-4129

Wang, X. J.; Lu, J.; Xie, Y.; Du, G.; Guo, Q. & Zhang, S. (2002). A Novel Route to Multiwalled Carbon Nanotubes and Carbon Nanorods at Low Temperature. *Journal of Physical Chemistry B*, Vol.106, No.5, (January 2002), pp. 933-937, ISSN 1089-5647

Wiltshire J.G., Khlobystov A.N.; Li, L.J.; Lyapin, S.G.; Briggs, G.A. D.; Nichola R.J., (2004). Comparative studies on acid and thermal based selective purification of HiPCO produced single-walled carbon nanotubes. Chemical Physics Letters, Vol. 386, No.4-6 (March 2004) pp. 239-243, ISSN 0009-2614.

Wood, W. Kumar, S. & Zhong, W.-H. (2010). Synthesis of Organosilane-Modified Carbon Nanofibers and Influence of Silane Coating Thickness on the Performance of Polyethylene Nanocomposites. *Macromolecular Materials and Engineering*, Vol.295, No.12, (December 2010), pp. 1125-1135, ISSN 1438-7492

Yu, M.-F.; Lourie, O.; Dyer, M. J.; Moloni, K.; Kelly, T. F. & Ruoff , R. S. (2000). Strength and breaking mechanism of multiwalled carbon nanotubes under tensile load. *Science*, Vol.287, No.5453, (January 2000), pp. 637-640, ISSN 0036-8075

Yuen, S.-M.; Ma, C.-C. M. & Chiang C.-L. (2008). Silane grafted MWCNT/polyimide composites – Preparation,morphological and electrical properties. *Composites Science and Technology*, Vol.68, No.14, (November 2008), pp. 2842–2848, ISSN 0266-3538

Yuen, S.-M.; Ma, C.-C. M.; Chiang, C.-L.; Teng, C.-C. & Yu, Y.-H. (2008). Poly(vinyltriethoxysilane) Modified MWCNT/Polyimide Nanocomposites—Preparation, Morphological, Mechanical, and Electrical Properties. *Journal of Polymer Science: Part A: Polymer Chemistry*, Vol.46, No.3, (February 2008), pp. 803–816, ISSN 0887-624X

Zhang, J.; Zou, H.; Qing, Q.; Yang, Y.; Li, Q.; Liu, Z.; Guo, X. & Du, Z. (2003). Effect of Chemical Oxidation on the Structure of Single-Walled Carbon Nanotubes. *Journal of Physical Chemistry B*, Vol.107, No.16, (March 2003), pp. 3712-3718, ISSN 1089-5647

Zhao, X. & Ando, Y. (1998). Raman Spectra and X-Ray Diffraction Patterns of Carbon Nanotubes Prepared by Hydrogen Arc Discharge. *Japanese Journal of Applied Physics*, Vol.37, No. 9A, (September 1998), pp. 4846-4849, ISSN 0021-4922

Zhou, Z.; Wang, S.; Lu, L; Zhang, Y & Zhang Y. (2008). Functionalization of multi-wall carbon nanotubes with silane and its reinforcement on polypropylene composites. *Composites Science and Technology*, Vol.68, No.7-8, (June 2008), pp. 1727–1733, ISSN 0266-3538

14

Prediction of the Elastic Properties of Single Walled Carbon Nanotube Reinforced Polymers: A Comparative Study of Several Micromechanical Models

Selmi Abdellatif and Hassis Hédi
Ecole Nationale d'Ingénieurs de Tunis,
Civil Engineering Laboratory
Tunisia

1. Introduction

The exceptional mechanical properties: Young's modulus, tensile strength, toughness, flexibility, etc. (Desprès et al., 1995) of carbon nanotubes (CNT) are due to their molecular structure consisting of tiny concentric graphene cylinders (Tijima, 1991). In order to determine the mechanical properties of this nano-structured material some theoretical and experimental methods were applied. Theoretical investigations yielded a widespread range of elastic property predictions, the predicted Young's modulus scatters in an interval of 0.5-5.5TPa (Lusti & Gusev, 2004). The first experimental investigations of multi-walled nanotubes (MWNT) were based on the measurement of their intrinsic thermal vibration using a transmission electron microscope. Direct mechanical measurements of the Young's modulus were done using an atomic force microscope. Experimentally determined Young's modulus of single-walled carbon nanotubes (SWNT) scatter in a relatively large interval of 2.8 to 3.6TPa (Lourie & Wagner, 1998). Their stiffness, strength, high aspect ratio, high Young's modulus and high flexibility, make CNT the best reinforcements of a polymer matrix.
Many parameters influence the overall effective properties of SWNT/Polymer composites, e.g. CNT structure, orientation, dispersion, diameter and matrix stiffness (Bai, 2006).
It was found (Lopez et al., 2005) by using a combined finite-element micromechanics approach that the degree of CNT waviness has a significant effect on the elastic properties of (NRP). The influence of the interaction at the CNT-polymer interface on the overall effective stiffness of NRP is investigated by linking molecular dynamics (MD) simulations with a micromechanical model (Odegard et al., 2003).
In this work, we develop and compare several micromechanical models. First, using a homogenization method based on energy equivalence, the nanotube's elastic properties are characterized.
Second, a direct finite element (FE) based numerical approach is used, which allows to model fully aligned, long and homogeneously dispersed SWNT in a SWNT/Polyimide composite.
Third, several mean-field homogenization schemes are investigated, namely: sequential, two-level (Mori-Tanaka/Mori-Tanaka): (M-T/M-T), two-step (M-T/M-T) and two-step (M-T/Voigt) models.

This is the main contribution of the paper. Indeed, while most papers dealing with the prediction of elastic properties of SWNT/Polymer composites study only one micromechanical model, in the present work we investigate 4 homogenization schemes and validate them against a fifth micromechanical approach: FE analysis of unit cells or representative volume elements (RVEs). Some predictions are also compared to experimental data or other micromechanical schemes.
The paper has the following outline. In section 2, the graphene sheet's elastic properties are characterized. In section 3, the investigated mean-field homogenization schemes are summarized. In section 4, several numerical predictions are presented. Conclusions are discussed in section 5.

2. Homogeneous elastic properties of graphene sheet

A fundamental issue that needs to be solved in modelling macroscopic mechanical behaviour of nano-structured materials based on molecular structure is the large difference in length scales. The lengths associated to computational chemistry and solid mechanics are on the opposite ends of the length scale spectrum. Computational chemistry models predict molecular properties based on known quantum interaction and solid mechanics models predict the macroscopic mechanical behavior of materials idealized as continuous media based on known bulk material properties. To adress this issue, (Odegard et al., 2002) proposed a method for developing structure-property relationships of nano-structured materials. This method serves as a link between computational chemistry and solid mechanics by substituting discrete molecular structures with equivalent continuum models. It has been shown that this substitution may be accomplished by equating the molecular potential energy of the nano-structured material with the strain energies of the representative truss and continuum models. The technique developed by (Odegard et al., 2002) is applied here to the determination of the homogenous nanotube elastic properties. To reduce the computational time associated with modelling the graphene sheet, a representative volume element (RVE) for graphene was used. The RVE of the graphene's chemical structure has been substituted with equivalent truss and equivalent continuum models (Fig. 1).

2.1 Chemical model

The energy associated with the chemical structure which is formed by chemical bonds is given by:

$$E^{\rho} + E^{\theta} = \sum_{m} \frac{k_m^{\rho}}{2} \left(\rho_m - P_m \right)^2 + \sum_{m} \frac{k_m^{\theta}}{2} \left(\theta_m - \Theta_m \right)^2 \tag{1}$$

where the terms P_m and Θ_m refer to the undeformed interatomic distance of bond m and the undeformed bond-angle m, respectively.
The quantities ρ_m and θ_m are the bond length and angle after stretching, respectively (Fig. 1). k_m^{ρ} and k_m^{θ} are the force constants associated with the stretching and angle variation of bond and bond-angle m, respectively. Using the parameters for the AMBER force field (Cornell et al., 1995), the force constants used are:

$$k_m^{\rho} = k^{\rho} = 6.5210^{-7} \frac{nJ}{bond.nm^2}$$

and

$$k_m^{\theta} = k^{\theta} = 6.5210^{-7} \frac{nJ}{angle.rad^2}$$

2.2 Truss model

The truss model is formed by rods (Fig. 1) whose Young's moduli are given by (Odegard et al., 2002):

$$E_m^a = \frac{R_m^a k_m^{\rho}}{A_m^a}, \quad E_m^b = \frac{12 k_m^{\theta}}{R_m^b A_m^b} \tag{2}$$

where m is the rod number and a and b are types of rods. R^a is the distance between two successive carbon atoms taken equal to 0.14nm, $\theta = 2\pi/3$ and $R^b = \sqrt{3}R^a = 0.2424nm$. A_m^a and A_m^b are the cross sectional areas of the mth rod of type a and b, respectively (Odegard et al., 2002).

2.3 Continuum model

Knowing the characteristics of the two rod types, to determine the properties of the continuum model, the homogenization method based on energy equivalence is used. So it is assumed that the truss and continuum models are equivalent when the elastic strain energies stored in the two models are equal under identical displacement boundary conditions. The strain energies associated to the truss model for the two loading cases are calculated by the finite element method: **CASTEM** (CASTEM, 2000) program.

The area of the RVE is known and the homogeneous model-thickness (0.34nm) is taken equal to the graphite interlayer distance (Krishnan et al., 1998). The mechanical properties of the truss elements have been determined as described above.

Knowing that the distance between two successive carbon atoms is the same, the nanotube structure is isotropic. So only two parameters (Young's modulus (E) and Poisson's ratio (ν) are needed to characterize the continuum model. Thus both the truss and continuum models were subjected to two sets of loading conditions. For each set, we get an equation which relates E and ν.

For a pure shear strain in the x_1-x_2 plane (Fig. 2), the RVE is subjected to the following boundary conditions:

$$\begin{cases} u_1 = 0 \\ u_2 = \gamma x_1 \\ u_3 = 0 \end{cases} \tag{3}$$

The continuum model associated energy is:

$$U = \frac{V}{4} \frac{E}{(1+\nu)} \gamma^2 \tag{4}$$

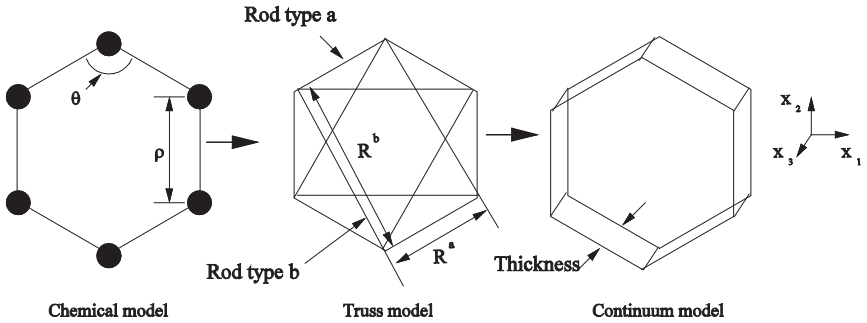

Fig. 1. Representative volume elements of the graphene sheet. Transition between chemical (bond distance ρ and bond-angle θ), truss (two rod types R^a, R^b) and continuum models, after (Odegard et al., 2002).

where V is the volume of the RVE which is given by:

$$V = St = \frac{3\sqrt{3}\left(R^a\right)^2 t}{2} \tag{5}$$

Where S is the hexagon's area and t is the homogeneous model-thickness.
For a uniaxial deformation along the x_1 direction, the RVE is subjected to the following boundary conditions (Fig. 2):

$$\begin{cases} u_1 = \gamma x_1 \\ u_2 = 0 \\ u_3 = 0 \end{cases} \tag{6}$$

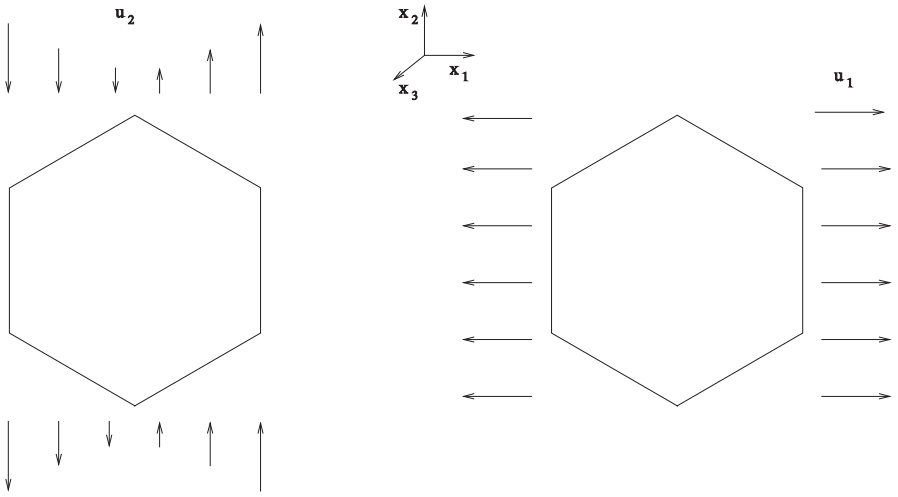

Fig. 2. Graphene RVE subjected to pure shear loading in the x_1-x_2 plane (left) and to extension in the x_1 direction (right).

The continuum model associated energy is:

$$U = \frac{VE}{2(1+\nu)}\left[\frac{\nu}{(1-2\nu)}+1\right]\gamma^2 \tag{7}$$

By equating the two strain energies for the truss and continuum model, we retrieve E and ν:

$$\begin{cases} E = 2.52\ TPa \\ \nu = 0.25 \end{cases}$$

These elastic properties are entirely based on the strong intratube valence forces of the carbon-carbon bonds. The obtained Young's modulus value is retrieved close to the minimum value measured by (Lourie & Wagner, 1998) with a micro-Raman spectroscopy (2.8-3.6TPa). It is also higher than the value measured by (Krishnan et al., 1998) with vibration method using a transmission electron microscope (1.45-2.25TPa).

3. Overall elastic properties of SWNT composites

SWNT composites can be seen as reinforced materials made up of three phases: polymer matrix, cylindrical cavities and carbon coatings. In this section, different ways to predict their overall elastic properties are explored: mean-field homogenization procedures, namely: the sequential method (Ben Hamida & Dumontet, 2003), the two-step (Friebel et al., 2006) and the two-level (Friebel et al., 2006) procedures, and two dimensional unit-cell finite element calculations. The main ideas of these methods are summarised hereafter. Earmarks are underlined for each of them in the framework of CNT composites.

3.1 The sequential method

Many homogenization schemes are applicable only for low inclusion percentage, while in some cases it is needed to predict the influence of higher concentrations. Hence some homogenization schemes are improved with the iterative method (Ben Hamida & Dumontet, 2003) which consists in the homogenization of the heterogeneous material in steps by adding the inclusions little by little. First, we have a homogeneous isotropic material, to it we add a volume δV of isotropic inclusions (Fig. 3). The problem is solved by a given homogenization scheme. Then, this procedure is repeated iteratively by taking at step (i+1), the effective homogeneous material obtained at step (i). The end is detected when the inclusion percentage is reached.

For aligned long SWNT/Polymer composite, the considered RVE is formed by a unidirectional SWNT (void+continuum graphene) embedded in the matrix. In each homogenization step the problem is solved analytically for different elementary boundary conditions, and the overall macroscopic properties are thus computed.

3.2 The two-step procedure

The principle of the two-step procedure is depicted on Fig. 4 (bottom) for composites with aligned CNT. The coating phase (the carbon) is actually treated as a separate reinforcement phase. Carbon and void inclusions (both having the same shape and orientation) are thus

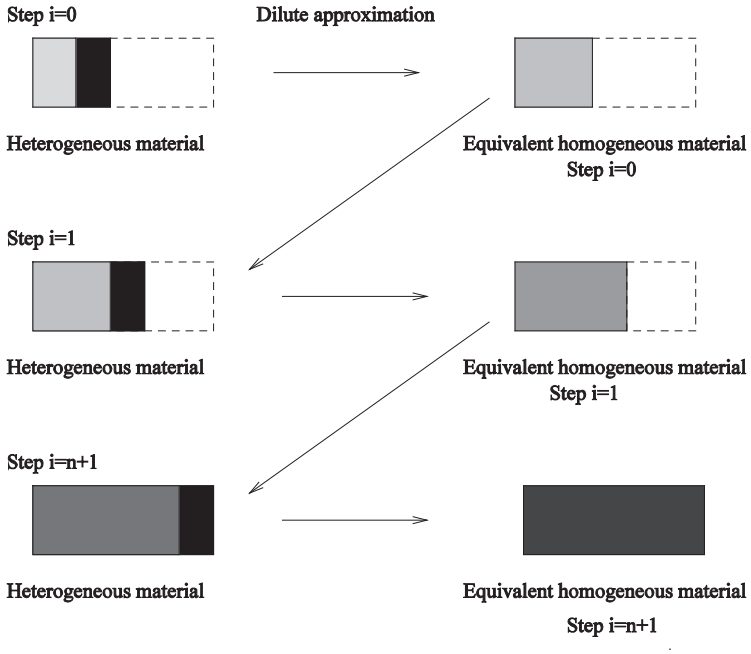

Fig. 3. Schematic illustration of the sequential method. The reinforcing material is added little by little; each addition is followed by a homogenization of the resulting composite; the procedure ends when the desired volume fraction is reached.

lying in the matrix. This three phase composite is virtually decomposed into an aggregate of two pseudo-grains: "matrix+voids" and "matrix+carbon". Each two-phase pseudo grain is homogenized (first step) and then the effective properties of the aggregate are computed (second step).

For the first step almost any homogenization scheme valid for two-phase composites with aligned inclusions can be used, e.g. Mori-Tanaka (M-T). Care must be taken when one of the phases consists actually of voids.

A way to achieve the second step is to assume the same deformation -- Voigt-like hypothesis -- inside both pseudo-grains. Other choices can be made (Friebel et al., 2006). One of them assumes the same strains in both matrix phases of the two pseudo-grains. Combined with M-T at first step, the two-step approach degenerates then into the classical direct extension of the M-T scheme to multi-phase composites.

We draw attention to the fact that this two-step procedure can handle CNT composites with long nanotubes as well as short ones, aligned or not in the matrix. For composites with misaligned CNT extra pseudo-grains (in addition to the preexisting ones) are required, one for each orientation (Friebel et al., 2006).

The models used in the numerical simulations (section 4) are identified by the homogenization schemes used for the steps. They are labeled "two-step (M-T/Voigt)" and "two-step (M-T/M-T)". The latter is the direct extension of the M-T scheme to multi-phase composites.

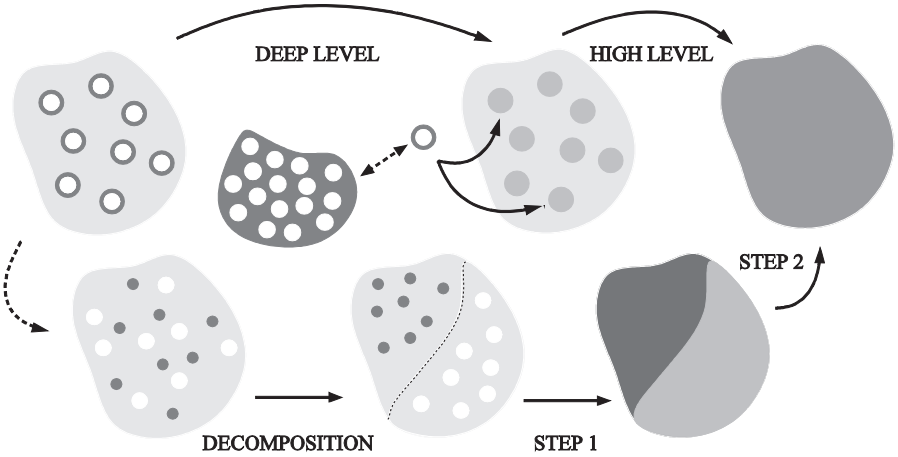

Fig. 4. Schematic view of the two-step (bottom) and two-level (top) homogenization procedures for the effective properties of SWNT composites. For each step/level a two-phase homogenization model is required.

3.3 The two-level procedure

The two-level procedure was proposed by (Friebel et al., 2006) for coated inclusion-reinforced materials. It is based on the idea that the matrix sees reinforcements (CNT) which are themselves composites (carbon+void). The methodology is illustrated on Fig. 4 (top) for composites with aligned CNT. Each CNT is seen (deep level) as a two-phase composite (carbon matrix with cavities) which, once homogenized, plays the role of a homogeneous reinforcement for the matrix material (high level).

A two-level recursive application of two-phase homogenization schemes (e.g. M-T) is thus proposed. As far as the choice of the two-phase models is concerned, the same remarks as for the first step of the two-step approach hold for the deep level. In addition, the inclusion phase is no more isotropic at high level.

Like the two-step approach, the two-level procedure is able to handle long as well as short CNT. The two-level procedure cannot be used stand-alone for composites with misaligned CNT. For this kind of materials, a combined two-step/two-level method is designed: the virtual decomposition is based only on the orientations; the pseudo-grains are homogenized (first step) using the two-level procedure; the second step is performed with the Voigt assumption.

A particular scheme is identified by the schemes used to perform the levels. In section 4, choosing M-T for both levels is labeled "two-level (M-T/M-T)". The same label is abusively used for composites with misaligned CNT , keeping in mind that it is indeed a combination of the two-level and two-steps procedures, as described above.

3.4 2D FE for hexagonal array arrangement

The following FE procedure is only valid for composites with long and aligned CNT. We suppose a hexagonal array arrangement (Fig. 5) of the CNT in the matrix. As a result, the overall behavior is transversely isotropic. The macroscopic stiffness tensor is (partially) filled-in with help of only two generalized plane strain (2D) simulations.

The unit-cell is shown on Fig. 5. It is reduced to a quarter of its size by exploiting two symmetry planes. Knowing the dimensions of the CNT (radii R_v and R_c on Fig. 5) and their volume fraction, one can compute the half tube inter-distance d. The height and width of the reduced unit-cell are h=d and l=d $\sqrt{3}$, respectively.

	Axial tension	Transverse tension
x_1=0	u_1=0	u_1=0
x_2=0	u_2=0	u_2=0
x_1=1	u_1=constant	u_1=u
x_2=h	u_2=constant	u_2=constant
Reference node	u_3=u	u_3=0

Table 1. Displacement boundary conditions for the transverse and axial tension tests. The unit-cell (Fig. 5) is in the x_1-x_2 plane, the symmetry planes are x_1=0 and x_2=0.

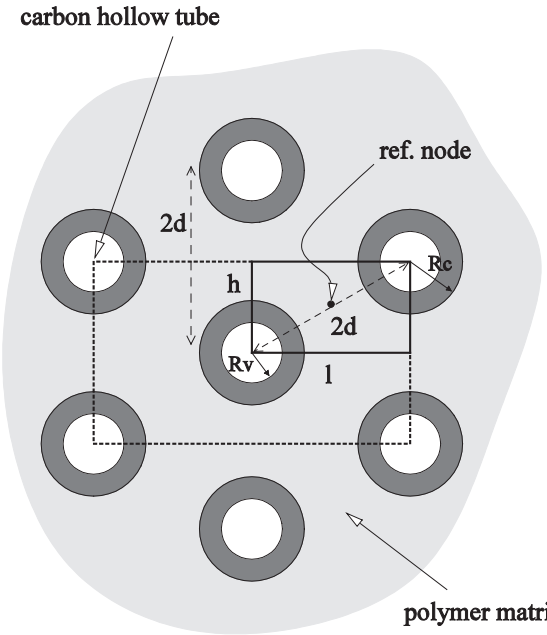

Fig. 5. Periodic hexagonal array arrangement of long carbon nanotubes inside the composite. Generalized plane strain (the reference node is shown) FE simulations are conducted on the two dimensional rectangular unit cell reduced to its quarter by symmetry.

Two tension tests are needed to obtain 4 among the 5 independent effective elastic moduli: a plane strain transverse tension followed by an axial tension under generalized plane strain conditions. Assuming the CNT are aligned along the third direction, the appropriate boundary conditions are summarized in Table 1. With this method, only the effective longitudianl shear modulus remains unknown.

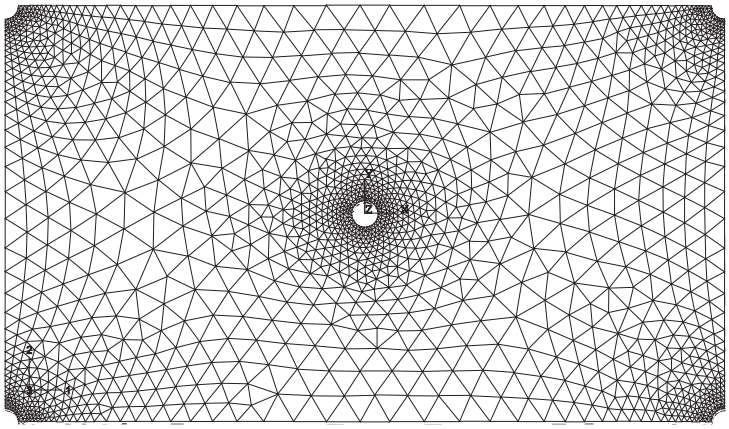

Fig. 6. Unit cell with periodic boundary conditions: 2D view of FE mesh corresponding to 10% of SWNT.

3.5 3D FE with periodic boundary conditions

Again we consider composites with long and aligned SWNT and assume a hexagonal array arrangement. However, both the unit cell and the boundary conditions are different from those of section 3.4. Here, the unit cell is the large rectangle with dotted sides of Fig. 5, i.e. with one tube at its center and a quarter of a tube at each corner. Actually, a 3D cell with unit thickness is considered. Periodic boundary conditions are applied, as in (Segurado & Llorca, 2002) for other micro-structures.

Periodic boundary conditions are written in a form representing periodic deformation and antiperiodic tractions on the boundary of the cell. The boundary conditions applied on an initially periodic cell perserve the periodicity of the cell in the deformed state. This model allows us to compute the whole mechanical properties of the transversely isotropic composite.

The selected cell is meshed using NETGEN (NETGEN, 2004) mesher, with which periodic boundary conditions can be applied. The FE meshes consisted of linear tetrahedral elements, Figs. 6 and 7 show respectively, a 2D and 3D view of the FE mesh corresponding to 10 % of SWNT.

4. Numerical predictions

The models described above are used to predict the overall mechanical properties of various SWNT reinforced polymers. Our analytical schemes (sequential, two-step and two-level) are compared to FE calculations in section 4.1 for polyimide (LaRC-SI) and epoxy systems. Confrontation to experimental data is made in section 4.2 for a polypropylene matrix composite. Through all these composites, different orientations (fully aligned, random in space or in plane) and shapes (aspect ratio) of the CNT are simulated. In all figures, R_v and R_c represent the cylindrical cavity radius and the carbon coating radius, respectively (see Fig. 5). In all following figures, the nanotube volume fraction is the sum of cavities and carbon coating volume fractions.

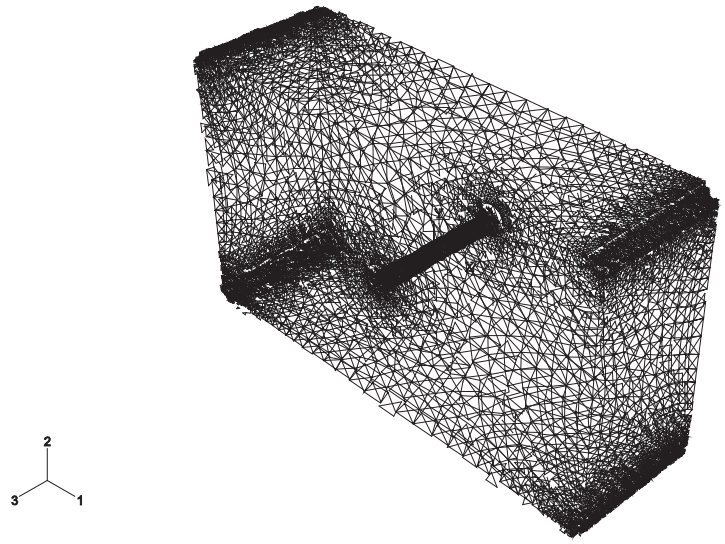

Fig. 7. Unit cell with periodic boundary conditions: 3D view of FE mesh corresponding to 10% of SWNT.

4.1 Comparison between FE predictions and micromechanical models

4.1.1 Long SWNT/polyimide composite

A polyimide (LaRC-SI) is reinforced with fully aligned, long homogeneously dispersed SWNT; see Table 2 for the properties. The predicted mechanical response of the composite relative to the mechanical properties of LaRC-SI is reported in Figs. 8a-8d.

	Young's modulus (GPa)	Poisson's ratio
LaRC-SI	3.8	0.4
Continuumgraphene	2520	0.25

Table 2. Elastic constants of LaRC-SI and Continuum graphene, Young's modulus and

Poisson's ratio of Continuum graphene are calculated in section 2, those of LaRC-SI were found in (Odegard et al., 2003).

Interpretation

Comparing the two FE results, it is found that, the 3D FE calculations with periodic boundary conditions coincide with the 2D FE ones for all the long SWNT/Polyimide composite mechanical properties. The transverse shear modulus of the composite is found by the 3D FE simulations. As one can expect, all models give the same prediction of the longitudinal elastic modulus which indeed obeys to the rule of mixture. However for the transverse Young's modulus E_T (Fig. 8a), the longitudinal shear modulus G_L (Fig. 8a) and the transverse shear modulus G_T (Fig. 8c), the sequential and the two-level (M-T/M-T)

predictions are close to FE results, while the other models fail in a spectacular way. For the longitudinal Poisson's ratio ν_{LT} (Fig. 8d) -- for tension in the L-direction, $\nu_{LT} = \frac{\varepsilon_T}{\varepsilon_L}$, it is the two-level (M-T/M-T) model which gives the best predictions compared to the FE results. The "knee" in the transverse Young's modulus (Fig. 8a) shown by all homogenization methods at approximately 1% SWNT volume fraction is a-priori surprising. Thankfully it is confirmed by the FE model. This behavior is actually due to the high contrast between the moduli of the phases. From a homogenization scheme point of view the dependence of the transverse Young's modulus on the volume fraction of fillers is indeed typical to a Mori-Tanaka scheme for two-phase fibrous composites when the contrast between the rigidities becomes important.

Figs. 8a-8c exhibit a behavior of the two-step approach that has already been observed for viscoelastic coated fiber composites by (Friebel et al., 2006). Their numerical simulations show that using a two-step model for these composites may lead to erroneous estimates (compared to FE results) depending on the repartition of the materials between the phases. Our SWNT composite here modeled as a three phase material of this kind seems to fall into this category for which the two-step approach is completely inefficient.

The pretty good behavior of two-level already observed in (Friebel et al., 2006) is once again illustrated here (Figs. 8a-8d). Surprisingly, the sequential method which is alway close to the two-level (M-T,M-T) scheme on Figs. 8a-8c fails in the prediction of the longitudinal Poisson's ratio (Fig. 8). We don't have any explanation for this yet. This issue requires further investigations.

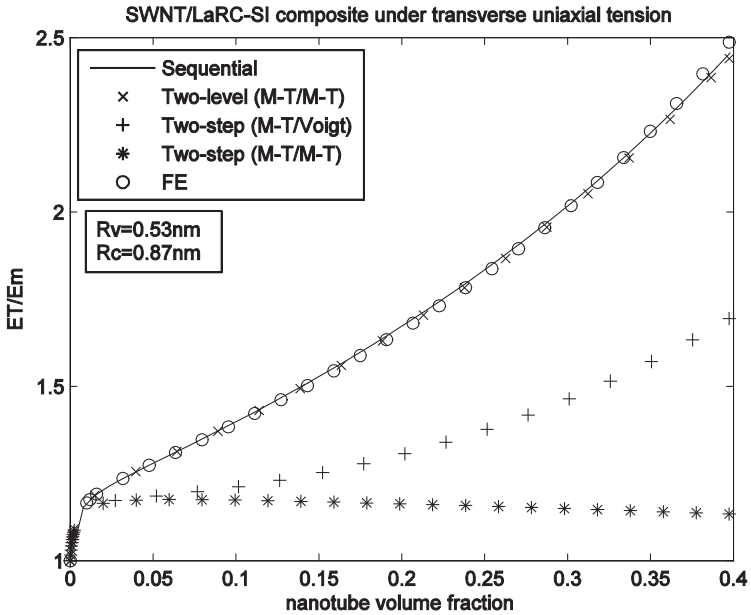

Fig. 8a. SWNT/LaRC-SI composite with long and aligned reinforcements. Normalized properties: comparison between the predictions of unit cell FE and micromechanical models. Transverse Young's modulus.

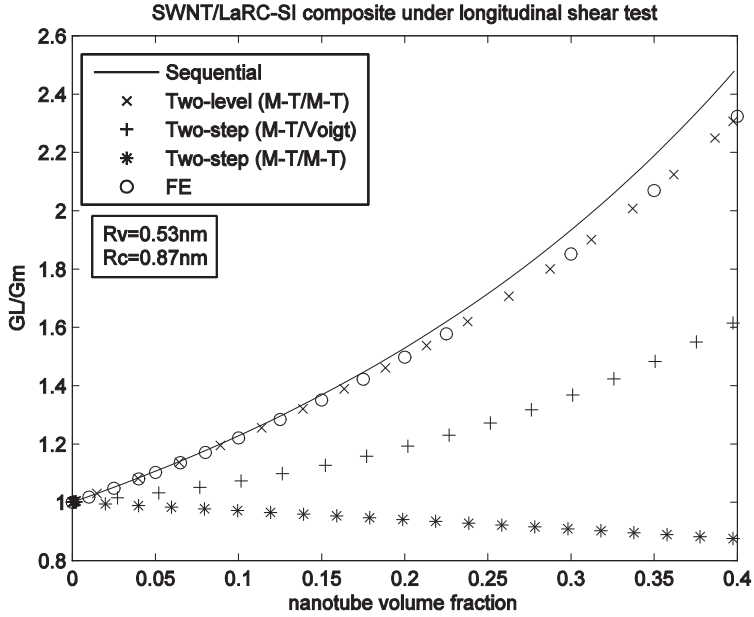

Fig. 8b. Same as Fig. 8a. Longitudinal shear modulus.

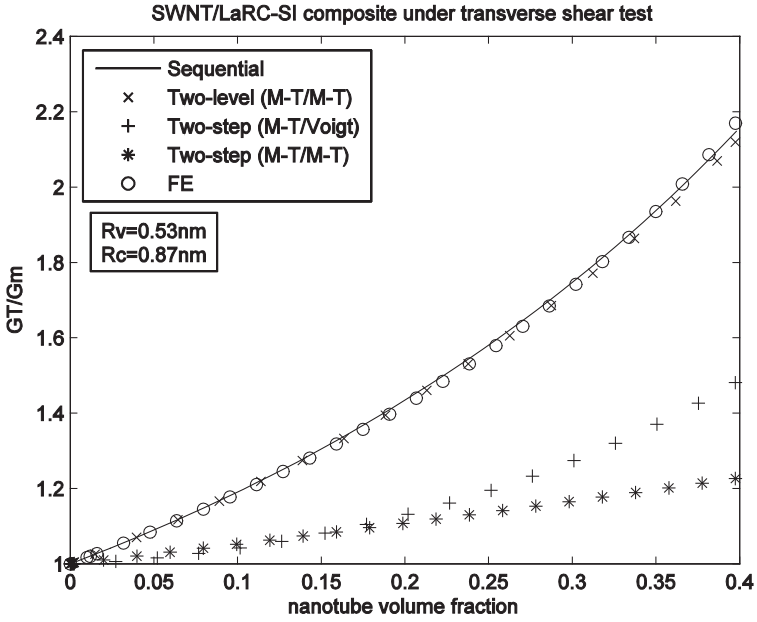

Fig. 8c. Same as Fig. 8a. Transverse shear modulus.

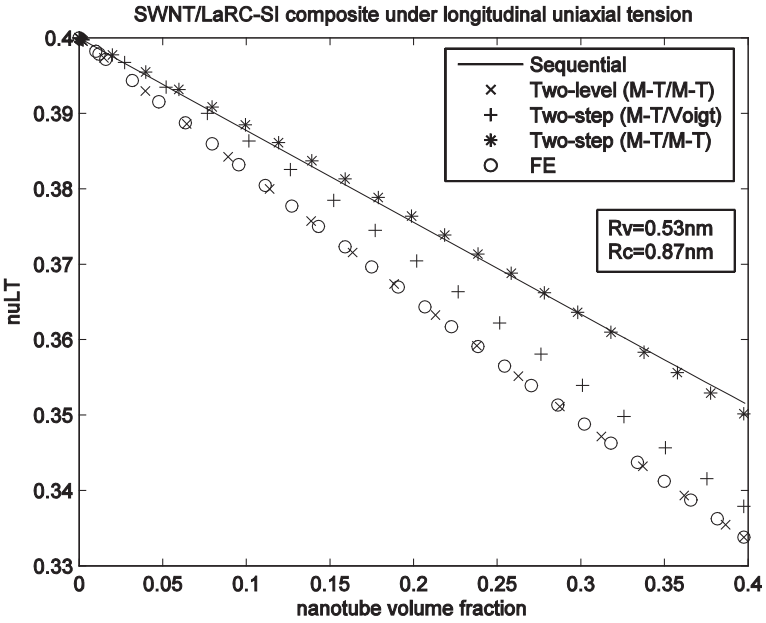

Fig. 8d. Same as Fig. 8a. Poisson's ratio ν_{LT}

4.1.2 SWNT/Epoxy composite

The stiffness enhancement of an epoxy matrix comprising SWNTs is investigated here for three morpholigies namely 3D randomly oriented (Fig. 9a), 2D in-plane randomly oriented (Fig. 9b) and fully aligned reinforcements (Fig. 9c). On these figures our estimates of effective elastic moduli are compared with FE calculations after (Lusti & Gusev, 2004).

The authors designed orthorhombic cells containing 50 equally sized and fully aligned nanotubes as well as cubics cells with 350 randomly oriented (3D or 2D planar) nanotubes distributed by employing a Monte Carlo algorithm. All geometries were meshed with tetrahedral elements - up to several millions elements were necessary in some cases - and periodic boundary conditions were applied. They conducted both direct calculations on the cubic cells with misaligned CNTs and orientation averaging of the moduli coming from orthorhombic cells. It is not clear which method was chosen to obtain their results given on Figs. 9b and 9c. But the authors report that a perfect match is obtained between both approaches for the 3D random orientation while deviations of up to 8% can be observed in the 2D case.

(Lusti & Gusev, 2004) modeled the nanotubes as massive cylinders with hemispherical caps at both ends. The elastic properties they used in their two-phase modeling of the SWNT/Epoxy composites are reported in Table 3. We used the same material parameters but added a void phase, affecting the cylinders properties to the graphene coating phase. The volume ratio between void and graphene was obtained from the chirality of the SWNT reported in (Lusti & Gusev, 2004) using a formula after (Toshiaki et al., 2004).

	Young's modulus (GPa)	Poisson's ratio
Epoxy	3	0.35
SWNT	1220	0.275

Table 3. Elastic constants of epoxy and SWNT (modeled as massive cylinders), after (Lusti & Gusev, 2004).

Interpretation

We conclude that all three composite morphologies have one property in common, namely that the overall effective Young's modulus increases linearly with the nanotube volume fraction for any aspect ratio in $[100,\infty[$.
For all three composite morphologies and for the two aspect ratios, the predictions given by the two-level (M-T/M-T), two-step (M-T/Voigt) and two-step (M-T/M-T) models are quite close to the FE data.
Furthermore, it appears that the stiffness enhancement that can be achieved with fully aligned, 2D random in-plane and 3D random orientation states differ considerably. For a composite comprising 12% fully aligned SWNT (Fig. 9c) one can expect an enhancement by a factor 30-45 for the longitudinal Young's modulus E_L. A composite comprising 12% 2D randomly oriented SWNT (Fig. 9b) the in-plane Young's modulus is increased by a factor of 11-15 whereas with 3D randomly oriented SWNT (Fig. 9a) the Young's modulus E is only raised by a factor of 6-9.

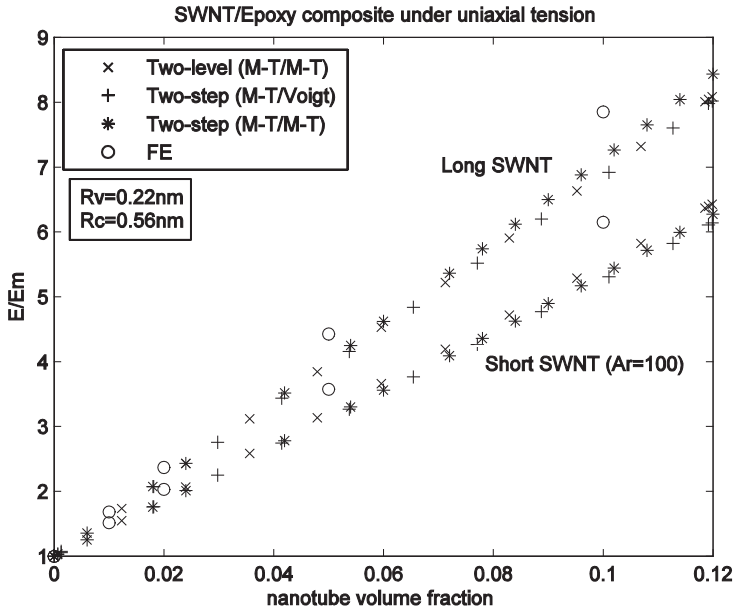

Fig. 9a. Epoxy composite with 3D randomly oriented reinforcements. Normalized Young's modulus: comparison between FE (Lusti & Gusev, 2004) predictions and micromechanical models.

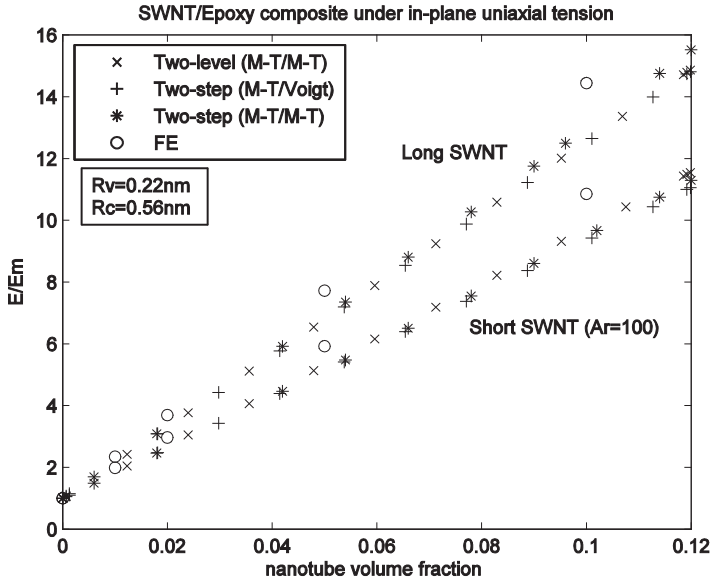

Fig. 9b. SWNT/Epoxy composite with 2D randomly oriented reinforcements. Normalized in-plane Young's modulus: comparison between FE (Lusti & Gusev, 2004) predictions and micromechanical models.

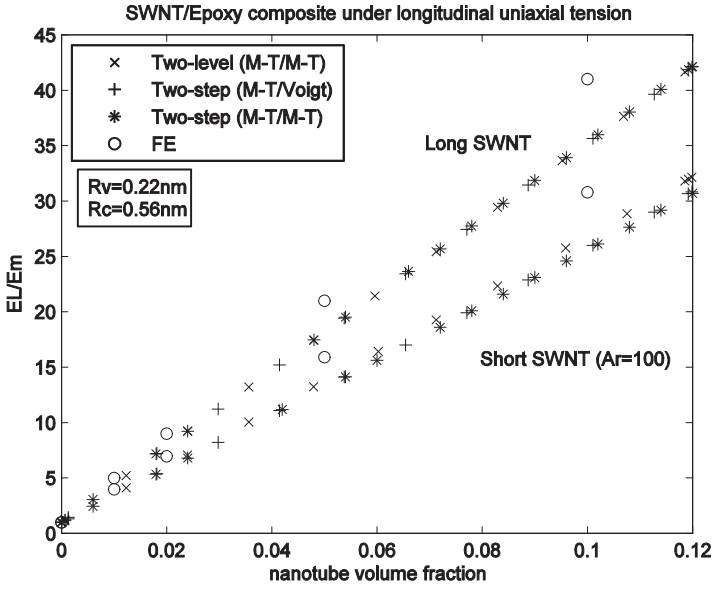

Fig. 9c. SWNT/Epoxy composite with fully aligned reinforcements. Normalized longitudinal Young's modulus: comparison between FE (Lusti & Gusev, 2004) predictions and micromechanical models.

4.2 Comparisons between experimental data and micromechanical models

The exceptional mechanical properties of SWNT make them good reinforcements even at very low concentrations. The reinforcement of polymers and other matrix systems with SWNT has previously been demonstrated to increase the physical properties of the matrix materials. Such studies include SWNT/Polypropylene (Valentini et al., 2003).

4.2.1 SWNT/Polypropylene composite

In our study a SWNT concentration ranging from 0% to 0.48% as SWNT volume fractions incorporated in the polypropylene is investigated; see Table 4 for the properties. Young's modulus and Poisson's ratio of 3D randomly oriented SWNT/Polypropylene composite with various SWNT volume fractions and for an aspect ratio equal to 100 are reported in Figs. 10a and 10b.

	Young's modulus (GPa)	Poisson's ratio
Polypropylene	0.855	0.43
Continuum graphene	2550	0.25

Table 4. Elastic constants of polypropylene and Continuum graphene. Young's modulus and Poisson's ratio of Continuum graphene are calculated in section 2, those of polypropylene were found in (Lopez et al., 2005).

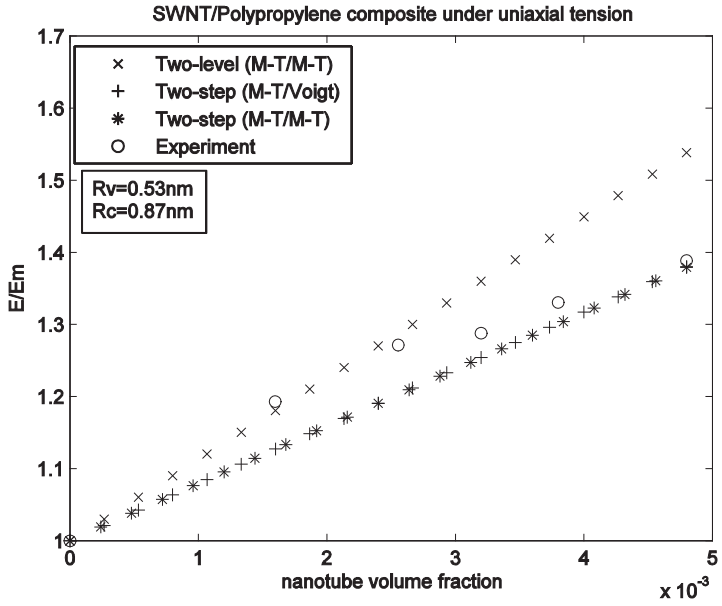

Fig. 10a. SWNT/Polypropylene composite with 3D randomly oriented reinforcements for an aspect ratio Ar=100. A comparison between experimental data after (Lopez et al., 2005) and micromechanical models. Normalized Young's modulus.

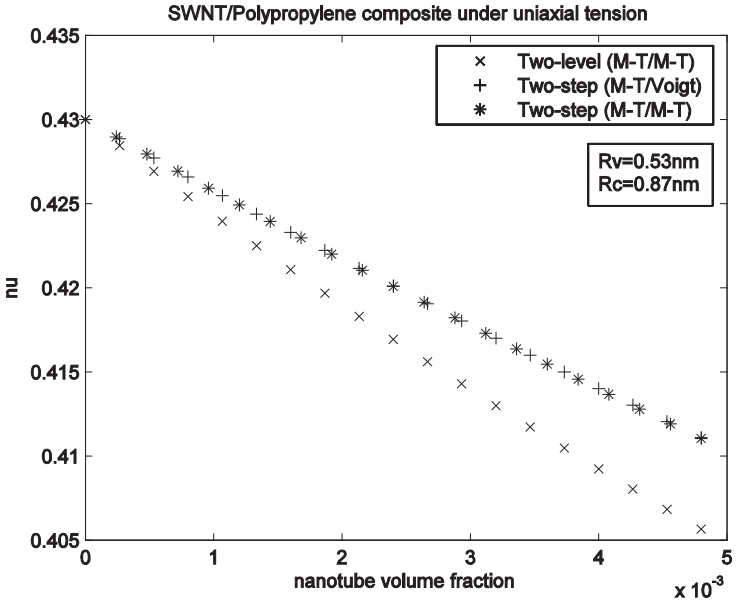

Fig. 10b. Same as Fig. 10a. Poisson's ratio.

Interpretation

From these results, it is deduced that the reinforcing effect of SWNT is very important and as the SWNT content in the polymer increases, the Young's modulus increases rapidly. For a polypropylene comprising 0.48% of SWNT, the Young's modulus E is increased by a factor of 1.4 but the Poisson's ratio decreases by a factor of 1.06.

Our results are compared with experimental results given by (Lopez et al., 2005). The nonlinear behavior in the experimental data (Fig. 10a) may be due to a change in the microstructure with respect to the concentration of SWNTs. This is observed experimentally (Lopez et al., 2005) and characterized by the forming of nanotubes aggregates and a modification of the matrix' crystallinity. Neither the clustering nor the modification of the constituents' material properties is taken into account in our models. It is thus not surprising to see differences in the behavior of measurements and numerical predictions as the volume fraction of SWNTs increases. All numerical models however give estimates of Young's modulus with the right order of magnitude over the whole range of concentrations. For low content of SWNT, where the modeling assumptions on the microstructure are valid, the two-level method performs better that the two-step one.

The Poisson's ratio predictions delivered by the two-level (M-T/M-T), the two-step (M-T/M-T) and the two-step (M-T/Voigt) models are reported in Fig. 10b. We remark that the two-step (M-T/M-T) and the two-step (M-T/Voigt) models deliver the same prediction for the Poisson's ratio.

4.2.2 SWNT/PVA composite

In this section a 2.89% SWNT (R_v=0.33nm, R_c=0.67nm) volume fraction incorporated in the polyvinyl alcohol (PVA) is investigated; see Table 5 for the properties. Young's modulus and

Poisson's ratio of 3D randomly oriented SWNT/PVA composite with long reinforcements are reported in Table 6.

	Young's modulus (GPa)	Poisson's ratio
PVA	25.6	0.4
SWNT	2550	0.25

Table 5. Elastic constants of PVA and Continuum graphene. Young's modulus and Poisson's ratio of Continuum graphene are calculated in section 2, those of PVA were found in (Zhang et al., 2004).

	Young's modulus (GPa)	Poisson's ratio
Experiment	35.8	--
Two-level (M-T/M-T)	36.13	0.378
Two-step (M-T/Voigt)	35.51	0.376
Two-step (M-T/M-T)	35.76	0.375

Table 6. SWNT/PVA composite with 3D randomly oriented and long reinforcements. A comparison between experimental data after (Zhang et al., 2004) and micromechanical models for 2.89% SWNT volume fraction.

Interpretation

From Table 6, it is seen that the modulus of the composite is 40% higher than that of PVA which is it self 8 times stiffer than that of the other studied matrix materials.
Our results were compared with experimental results given by (Zhang et al., 2004).
For 2.89% SWNT volume fraction, Young's modulus predictions delivered by all models are consistent with the experiment data.
The same Table 6 shows that the Poisson's ratio predictions delivered by all schemes are also very close.

5. Conclusion

After the characterization of the discrete nanotube structure using a homogenization method based on energy equivalence, the sequential, the two-step (M-T/M-T), the two-step (M-T/Voigt), the two-level (M-T/M-T) and finite element models were used to predict the elastic properties of SWNT/Polymer composites. The data delivered by the micromechanical models are compared against those obtained by finite element analyzes or experiments. For fully aligned, long nanotube polymer composite, it is the sequential and the two-level (M-T/M-T) models which delivered good predictions. For all composite morphologies (fully aligned, two-dimensional in-plane random orientation, and three-dimensional random orientations), it is the two-level (M-T/M-T) model which gave good predictions compared to finite element and experimental results in most situations. There are cases where other micromechanical models failed in a spectacular way.

6. References

Bai, JB. & Ci, L. (2006). The reinforcement role of carbon nanotubes in epoxy composites with different matrix stiffness. Composite Science and Technology Vol. 66, pp. 599-603.

Ben Hamida, A. & Dumontet, H. (2003). Etude micromécanique du comportement de matériaux hétérogènes par une approche itérative. Proceedings of 6ème Colloque National en Calcul des Structures, Giens (France).

CASTEM 2000. A finite element software.\hfill\mbox{} www.cines.fr/textes/cal-parallele/castem.html.

Cornell, W.D.; Cieplak, P.; Bayly, C.I.; Gould, I.R.; Merz, K.M.; Ferguson, D.M.; Spellmeyer, D.C.; Fox, T.; Caldell, J.W. & Kollmann, P.A. (1995). A second generation force field for the simulation of proteins, nucleic acids, and organic molecules. Journal of the American Chemical Society Vol. 117, pp. 5179-5197.

Desprès, J.F., Daguerre, E. & Lafdi, K. (1995). Flexibility of graphene layers in carbon nanotubes. Carbon Vol. 33, No. 1, pp. 87-92.

Fisher, F.T.; Bradshaw, R.D. & Brinson, L.C. (2002). Effect of nanotube waviness on the modulus of nanotube-reinforced polymers. Applied Physics Letters Vol. 80, No. 24, pp. 4647.

Friebel, C.; Doghri, I. & Legat, V., (2006). General mean-field homogenization schemes for viscoelastic composites containing multiple phases of coated inclusions. International Journal of Solids and Structures Vol. 43, No. 9, pp. 2513-2541.

Krishnan, A.; Dujardin, E.; Ebbesen, T.W.; Yianilos, P.N. & Treacy, M.M.J. (1998). Measurement of the young's modulus of single-shell nanotubes using TEM. Physical Review B Vol. 58, No. 20, pp. 14013-14019.

Lopez Manchado, M.A.; Valentini, L.; Biagiotti, J. & kenny, J.M. (2005). Thermal and mechanical properties of single-walled carbon nanotubes-polypropylene composites prepared by melt processing. Carbon Vol. 43, No. 7, pp. 1499-1505.

Lourie, O. & Wagner, H.D. (1998). Evaluation of Young's modulus of carbone nanotubes by micro-Raman spectroscopy. Journal of Material Research Vol. 13, No. 9, pp. 2418-2422.

Lusti, H.R. & Gusev, A.A. (2004). Finite element predictions for the thermoelastic properties of nanotube reinforced polymers. Modelling and Simulation in Materials Science and Engineering Vol. 12, No. 3, pp. 107-119.

NETGEN. An automatic three-dimensional tetrahedral mesh generator.\hfill\mbox{} Joachim Schaberl, Johannes Kepler University, Linz, Austria, 2004.

Odegard, G.M.; Gates, T.S.; Wise, K.E. & Nicholson, L.M. (2002). Equivalent-continuum modeling of nano-structured materials. Composite Science and Technology Vol. 62, pp. 1869-1880.

Odegard, G.M.; Gates, T.S.; Wise, K.E.; Park, C. & Siochi, E.J. (2003). Constitutive modeling of nanotube-reinforced polymer composites. Composite Science and Technology Vol. 63, pp. 1671-1681.

Segurado, J. & Llorca, J. (2002). A numerical approximation to the elastic properties of shpere-reinforced composites. Journal of the Mechanics and Physics of Solids, Vol. 50, No. 10, pp. 2107-2121.

Tijima, S. 1991. Helical Microtubules of Graphitic Carbon. Nature (London) 354, 56-58.

Toshiaki, N., Kriengkamol T. & Morinobu E., (2004). Prediction of elastic properties for single-walled carbon nanotubes. Carbon Vol. 42, pp. 39-45.

Zhang, X.; Liu, T.; Sreekumar, T.V.; Kumar, S.; Hu, X. & Smith, K. (2004). Gel spinning of PVA/SWNT composite fiber. Polymer Vol. 45, pp. 8801-8807.

Valentini, L.; Biagiotti, J.; kenny, J.M. & Santucci, S. (2003). Morphological characterization of single-wall carbon nanotube/polypropylene composites. Composites Science and Technology Vol. 63, No. 8, pp. 1149-1153.

15

About Grafting of Single-Walled Carbon Nanotubes on the Oligo-N-Vinyl Carbazole and Copolymer Involving N-Vinylcarbazole and Hexylthiophene

K. Alimi, B. Zaidi and M. Chemek
Université de Monastir, Unité de recherche Matériaux Nouveaux et Dispositifs Electroniques Organiques, Faculté des Sciences de Monastir
Tunisia

1. Introduction

In recent years the use of Single-Walled Carbon Nanotubes (SWNTs) at the macroscopic scale by embedding them into a polymer matrix as well as the transfer of their physical properties to a polymer have attracted considerable interest (Andrés & Blau, 2008; Canestraro et al., 2006; Zheng et al., 2009). Due to their excellent structural, mechanical and electronic properties, SWNTs could significantly improve the mechanical and optoelectronic properties of the polymer (Chen et al., 2009; Popov, 2004; Ryabenko et al., 2004). Consequently, reinforcing polymer with SWNTs can form high-performance polymer composites or nanocomposites, which could be used in manufacturing electronic organic devices such as nano-electronic displays (Bondavall et al., 2009; Capek, 2009; Fantini et al., 2009; Meng et al, 2009; Saunders & Turner, 2008), chemical sensors (Ahuja & Kumar, 2009), biosensors (Tam et al. 2009; Tripisciano et al., 2009). However, SWNTs are hardly soluble in common solvents and poor compatible with the polymer. Thus the uniformity of the dispersion process is not optimized and the resulting nanocomposite is often inhomogeneous and has undesirable properties. Among the factors innhibing the dispersion process is the shearing cohesiveness between SWNTs, which is governed by van der Waals interactions (Byron et al., 2006; Schroder et al., 2003). Different procedures have been applied in order to obtain more dispersed SWNTs. These procedures are essentially based on the centrifugation (Cathcart et al., 2009), sonification (Park et al., 2002; Brown et al., 2005) and the choice of solvent (Lau et al., 2005; Ganter, et al., 2009). Therefore, the quality of resulting composite is directly bound to the amount of SWNTs and the choice of the reactionnal medium and method.

In parallel, it was shown that Poly(N-vinylcarbazole) (PVK) is an attractive polymer owing to its photoconductive properties (Caste et al., 2003; Tang et al., 2008) and it has be used in xerographic systems (Moisan et al., 1991). This non-conjugated polymer is currently used as a good hole transporting material in photovoltaic devices (Barlier et al., 2009) or as a luminescent polymer emitting in the blue part when prepared in nanoparticles (Yoon et al., 2008). Otherwise, it can be easily doped with various dopant species (Safoula et al., 1998), which seems to be a good candidate for SWNTs functionalization. In the other hand, PVK

has been mixed with inorganic or organic compounds to achieve emitting layers for new promising optoelectronics devices strongly improving the luminescence efficiency (Yap et al., 2009; Qiu et al., 2001).

Furthermore, recent works have shown that the use of both electron donating materials (polyparaphenylene, poly(3-alkylthiophene), carbazole based polymers…) and electron acceptor materials (fullurenes, carbon nanotubes) in heterojunctions can yield highly efficient photovoltaic conversion (Zhu et al., 2009; Cai et al., 2009). Poly (3-alkylthiophene) presents an interesting family of conjugated polymer regarding its optical, transport and electronic properties (McCulloug, 1998; Akcecelrud et al., 2003; On Chan et al., 1998). Moreover, the most promising hetero-junction was obtained by mixing poly(3-hexylthiophene) (P3HT) as a donor polymer with phenyl C_{61}-butyric acid methyl ester (PCBM) as an acceptor compound and the obtained materials exhibit a conversion efficiency of ~ 5% (Kawano et al., 2009). Otherwise, it has been demonstrated that grafting of PVK to the thiophene (Th) based polymers exhibits a better optoelectronic properties (Chemek et al., 2010) compared to PVK or thiophene alone. In this context, it seems to be of interest to marry the properties of PVK/Th based copolymer with those of SWNTs.

In this chapter, we present in a first part a study of the evolution of the structural and optical properties of composites based on oligo-N-Vinyl carbazole (scheme 1a) mixed with SWNTs (scheme 1b), as a function of the solvent nature and temperature annealing (Wu et al., 2002). Our aim is firstly to reach a better functionalization process, which is directly bound to the amount of SWNTs allowed to a specific percolation threshold. Secondly, we tray to describe the grafting process between carbon nanotubes and the OVK molecules for which we report theoretical studies based on Density Functional Theory (DFT). From this systematic study, some other effects, such the solvent nature and annealing treatment effects on the SWNTs dispersion process can be also envisaged.

The second part of this chapter is however aimed on the investigation of a dependant concentration study of a novel polymer/SWNTs blend. The used polymer (scheme 1c) is based on Poly(N-vinylcarbazole) (PVK) and Poly(3-hexylthiophene) (P3HeT) named PVK-3HT, synthesized by chemical oxidative way, using $FeCl_3$ as an oxidant. The chemical synthesis way is similar to that used for the synthesis of the graft copolymer based on

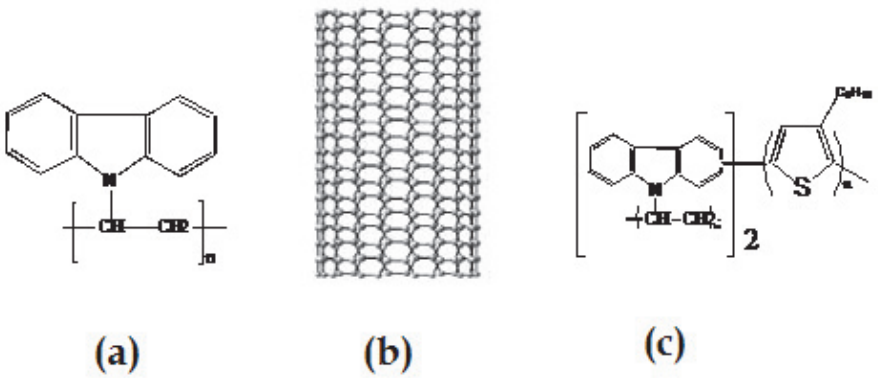

Scheme 1. Chemical structures of OVK (a), of the SWNTs (b) and of the PVK-3HT graft copolymer (c).

Poly(N-vinylcarbazole) (PVK) and Poly(3-methylthiophene) (PMeT) named PVK-MeT (Chemek et al., 2010).
As our works is mainly focused on the relationship between the structure and the optoelectronic properties of the SWNTs/polymer, the obtained composites (oligo-N-Vinyl carbazole or copolymer involving Poly(N-Vinylcarbazole)-hexylthiophene mixed with SWNTs) have been studied by infrared absorption, Raman scattering, UV–visible absorption and photoluminescence spectroscopy.

2. Functionalization of SWNTs with polymers

SWNTs used to prepare the composite were purchased from Sigma-Aldrich. SWNTs were produced by electric arc technique, having a diameter between 1.2 and 1.5 nm and a length varying from 2 to 5 µm as it is described elsewhere (Chapelle et al., 1998; Journet et al., 1999).
As the processing of SWNTs is generally blocked by their insolubility in most common solvents (Fantini et al., 2009), only the lower concentrations in weight can achieve a good dispersion process of carbon nanotube in the case of OVK polymer. In fact, the composite OVK/SWNTs have been obtained using either chloroform or chlorobenzene solvent at different SWNTs concentrations (Zaidi et al., 2010, Zaidi et al., 2011). In this chapitre, we give only resuts of the optimal concentration reashing a good functionalization process wihin intreactif character. In fact, it has been demonstrated that the maximum concentration reashing the above subject is 1.5% and 1.1 % in SWNTs weight respectively when using chloroform and chlorobenzene solvents. These SWNTs weight concentrations are emphaziazed firstly by a homogenous SWNTs dispersion and secondly by a full dependant concentration study (Zaidi et al., 2011). When using (PVK- hexylthiophene), it is however found that we resahes 60% in the SWNTs weight, within a homogenous phase for which the obtained solution is progressively blacked with SWNTs contents. Therefore, it is of importance to give a dependant concentration study.
The composite obtention is based on the mixing procedure of SWNTs with the oligo-N-vinyl carbazole or with the polymer involving carbazole and hexyl-thiophene unit (figure 1), similarly to that described in some reports (Arab et al., 2005; Wu et al., 2002). All these composites are obtained by the use of either chloroform or chlorobenzene solvents. The polymers or the oligomer are firstly dissolved in the solvent. Then, a quantified ammount of already, dispersed SWNTs is added. In order to increase SWNTs weight concentration, the ammount of SWNTs are doubled from the one solution another ($C_i=2(C_{i-1})$). This functionnalization process consists of two major steps, the dispersion and the sonication process.

2.1 Dispersion of SWNTs

The dispersion process consists to isolate the bundled SWNTs in order to facilate the functionnalisation process for eventual reactionnal intraction. For that, some appropriate weights of SWNTs relative to the desired concentrations are manually crushed. Then, each amount is introduced in a recipient and maintained under energetic agitation (figure 1a) by the use of a classical finger, qualified by a different rotational velocity varying from 6000 to 24000 tr/min, for the time of 75 min. Our optimal velocity of the classical finger is in the range of 14000 to 18000 tr/min. At this stage, constituing the dispersion process, the solution is progressively blacked and the corresponding volume shows a continious decreaese.

2.2 Sonication of the melange polymer/SWNTs

For all desired SWNTs concentrations, the appropriate soluble fraction of either OVK or PVK –3HT must be alreaday prepared. After the dispersion process, the two components reperesenting the solution of both SWNTs or of the corresponding targets (OVK and PVK-3HT) must be mixed as soon as possible in order to exploit the dispersed state of the SWNTs. This task leads to some solutions with different SWNTs weight fractions. For a better homogenity of the SWNTs in the polymer matrix, this mixing procedure is followed by a sonication process using an ultrasonically bath for 30 min. The quality of the obtained homogenty can be preliminarly evidenced by the nature of the resulting solution. In fact, for lower SWNTs concentrations, generally we obtain a homogenous, visqous and light gray colored phase. However, highter SWNTs concentrations genrally show a bundled form, floating on the surface of the solution.

Experimental analyses can be made in solution or in thin film. In the case of OVK, composites (OVK and SWNTs) are deposited at room temperature with nearly uniform thickness on glass substrate for photoluminescence and Raman measurements. Silica and silicon were used respectively for optical absorption and infrared analysis. Before all hand, all substrates were cleaned in ultrasonically bath with deionized water and ethanol. In the case of PVK-3HT, as it is known, the processing in solution is easyer by referring to that in thin films state, all the measurement are done in solution using chloroform solvent. This choice is done to conserv the homogeniety of the SWNTs dispersion in order to carry out the effect of higher concentration in the lumminescent properties of the resulting composite.

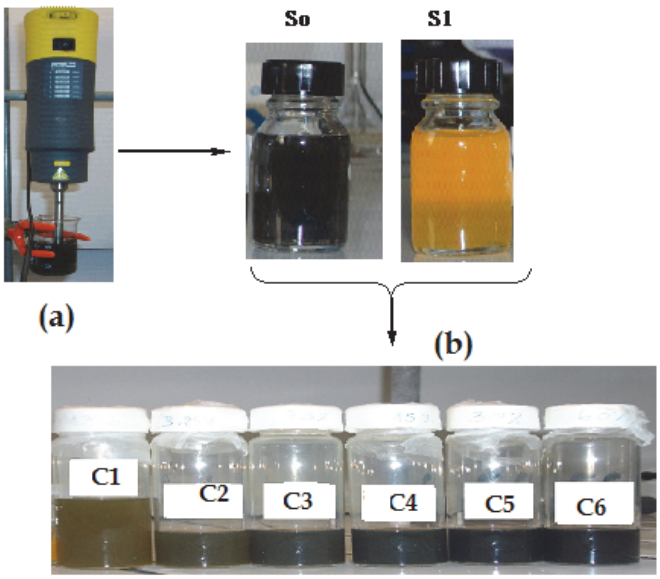

Fig. 1. Procedure used for the composite preparation: (a) SWNTs dispersion, S0: dispersed SWNTs, S1: solution of OVK or PVK-Het in the appropriate solvent and (b) the obtained polymer/SWNTs at different SWNTs weight concentrations.

3. Properties of SWNTs functionalized with short oligo-N-vinyl-carbazole

Optical absorption, photoluminescence, infrared and Raman analyses were performed to argue the grafting of OVK on SWNTs in chloroform or chlorobenzene medium. Then, the effect of the nature of the solvent in the dispersion process and the eventual differences in the optical and vibrationnal properrties are carried out.

3.1 Vibrational properties

Figure 2, shows infrared spectra of OVK, and OVK/SWNTs composites at both chloroform and chlorobenzene solvent. Adding SWNTs leads to some changes in infrared vibrationnal features of the OVK. Peaks assignments are based on the previousely published results on the PVK or PVK/ SWNTs composites prepared by other procedure (Dobruchowska et al., 2008). However, the band intensitie variations relative to the present composite is recently described in our previous paper, aimed to the grafting reaction between OVK and SWNTs (Zaidi et al., 2010). In the case of chloroform, new bands appear at 1048, 1064, 1076, 1133, 1174, 1297, 1369, 1718, 1763 and 2873 cm^{-1}. As already reported in the literature (Baibarac et al. 2007), bands peaked at 1048, 1064, 1076, 1174 and 1718, 1763 cm^{-1} are the consequence of SWNTs insertion. The two peaks at 1133 and 2873 cm^{-1} are assigned to aliphatic CH_2 in plane twist, and aliphatic CH_2 stretching, respectively. However, the band at 1297 cm^{-1} are assigned to new C-C vibration, showing that SWNTs are successfully bonded with OVK. Moreover, some other bands centered at 418, 840, 1324, 1402, 1481, 1596, 1624 and 3047 cm^{-1} disappear in the case of OVK/SWNTs composite. These bands are respectively attributed to the following vibrations: ring breathing, aliphatic C-C stretch, C-H deformation of vinylidene groups, CH_2 deformation of vinylidene groups, CH_2 rocking, CH_2 stretching, C-C stretching of benzene groups and symmetric CH-CH_2 vibration. On the other hand, bands at 717 and 742 cm^{-1}, associated to the deformation and rocking modes of CH groups respectively, are severely diminished.

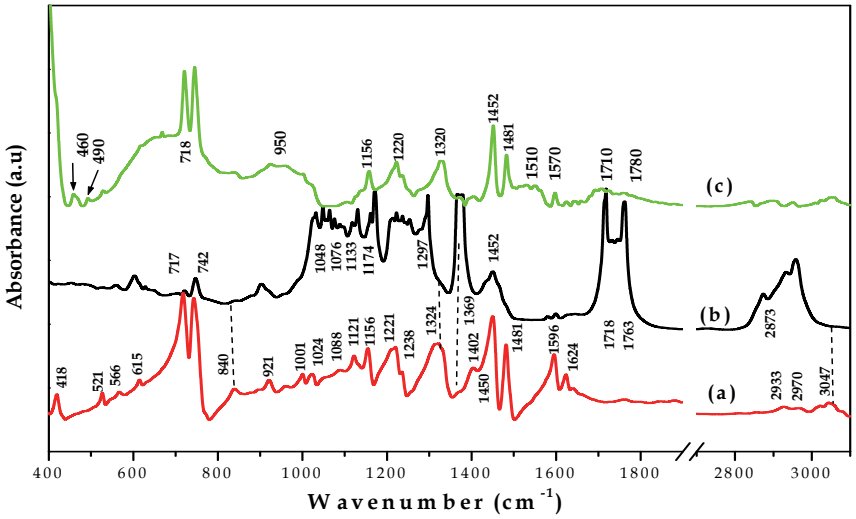

Fig. 2. Infrared spectra of: (a) OVK, and of OVK/SWNTs composite obtained using chloroform (b) and chlorobenzene (c) solvents.

In the chlorobenzene solvent, the spectrum reveals clear differences by referring to that obtained with chloroform. The introduction of SWNTs leads to some modifications in the infrared band positions and intensities of OVK. In the spectral region varying from 1100 to 1650, bands located at 1156, 1220, 1320, 1452, 1481, 1596 and 1624 cm^{-1}, attributed to the diffrent stretching modes of vinylidene groups (Bertoncello et al., 2006; Dobruchowska et al., 2008; Wu et al., 2007), are decreased. Furthermore, two additional features, ranging from 1510-1570 and 1680-1780 cm^{-1}, constituting habitually the vibration mode characteristics of C-C relative to SWNTs appeared. We suggest therefore that the nanoscopic structure of vinylidene groups is affected by adding SWNTs, without covalent attachment of both components. As we show band which appears at the 1297 cm^{-1} in the case of chloroform solvent is not present. At the same time, bands relative to the SWNTs are very low in intensity, impliying that the functionnlaization process do not leads to a reactionnal effects.
In figure 3, we present Raman spectra of OVK, SWNTs and OVK/SWNTs composites obtained at both medium (chlorobenzene or chloroform). For SWNTs and OVK/SWNTs composites spectra, the data are normalized to the main peak of the nanotube spectrum around 1590 cm^{-1} (G band). Assignments of the full spectrum are strictly based on those of PVK, SWNTs and the composite PVK/SWNTs prepared by other procedure (Pei et al., 1999). The band intensity is however recently described (Zaidi et al., 2010, Zaidi et al., 2011).

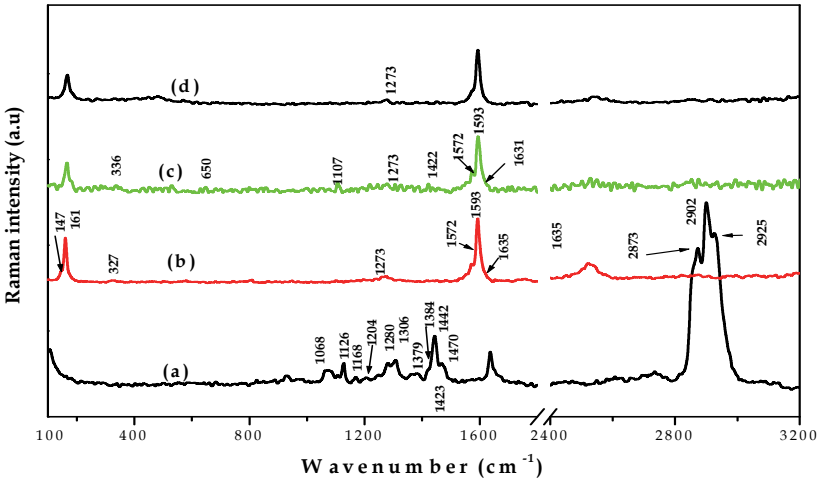

Fig. 3. Raman spectra of: (a) SWNTs, (b) OVK, and of OVK/SWNTs composite obtained using chloroform (c) and chlorobenzene (d) solvents.

In both chloroform or chlorobenzene mediums, significant changes are clearly shown by adding SWNTs on the OVK spectrum. First, we note that the most intense vibrations of OVK (1126, 1306, 1423, 1635 cm^{-1}), and of SWNTs (161, 327, 1572, 1273 and 1593 cm^{-1}) are found in the OVK/SWNTs composite spectrum. However, the Raman bands of SWNTs are clearly observed, but those of OVK have severely diminished, due to their lower intensity. Secondly, some bands with relatively higher intensity (1168, 1204, 1379, 1384, 1442, 1470, 2873, 2902 and 2925 cm^{-1}) in the case of OVK disappear. These bands are respectively ascribed to the following vibration modes: C-H deformation in benzene rings, rocking of

methylene in polyvinyl, ring vibration, quinoid C-C stretching, C-H in hetero-five member ring vibration, C-N stretch, symmetric CH_2 stretch, asymmetric CH_2 stretch and CH-H_2 stretching.

Althought the composites spectra present a global shape similarity in full range frequencies, some interesting differences (figure 4) can be checked from both radial breathing and tangential modes (RBM and TM) when they are presented separately.

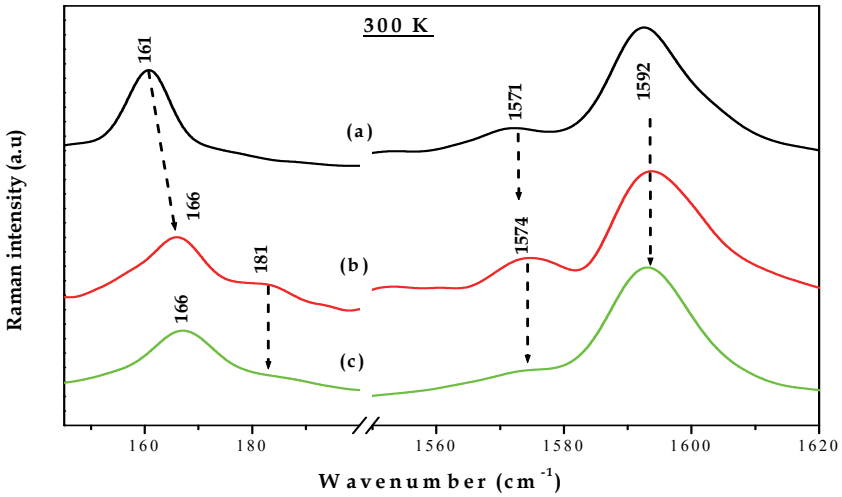

Fig. 4. Change on the rdaial breathing and tangentiel modes from SWNTs to the composite preapared using chloroform (b) and the chlorobenzene (c) solvents.

In fact, the band of SWNTs situated at 161 cm^{-1} is associated to the RBM of isolated SWNTs. The appearance of an intense peak at 181 cm^{-1} is attributed to the RBM of bundled SWNTs (Wang et al., 2004; Yang et al., 2006). The up-shift of 20 cm^{-1} is related to the tube-tube interaction (Rao et al., 2001) and could be considered also as signature of SWNTs' aggregates. The peak position (ν) of this band is related to the tube diameter (d) through the relation: ν(cm^{-1}) = 223.75/d (nm). This band indicates that, for SWNTs, the resonance occurs at the mean diameter of 1.38 nm. Modifications from SWNTs to the resulting composites are firstly limited to the up-shifting of the band at 161 cm^{-1} towards 166 c cm^{-1}. This shift can be related to the intercalation of the OVK oligomers into bundled SWNTs.

The band at 181 cm^{-1} is severely diminished by the use of chlorobenzene solvent. We conclude therefore that the intercalation of the OVK molecules is homogenous in the case of the composite obtained using chlorobenzene solvent for which SWNTs have a mean diameter of 1.34 nm. This result supports potential role of the latter solvent in the dispersion process as the case of aromatic halogenated solvent (Ganter, et al., 2009).

These changes are related to the intercalation of the polymer into bundled SWNTs. For the TM (1500-1650 cm^{-1}), by referring to that of SWNTs, except the narrowing effect, there is no significant changes, except the intensity decrease of the peak at 1571 cm^{-1} which illustrates a more change from 2D to 3D symmetry (Eklund et al., 1995).. In fact, all these changes observed either in the chloroform or chlorobenzene solvents can be related to the charge transfer complex formation (Bendiab et al., 2002; Claye et al., 2001; Wise et al., 2004).

3.2 Optical properties

Optical absorption spectra of OVK and OVK/SWNTs composites preapared by using either chloroform or chlorobenzene solvent are shown in figure 5. All mesaurements are collected at room temperature.

The main absorption bands of OVK are peaked at 232, 260, 294, 330 and 343 nm, as it is previously described in the case of PVK (Bertoncello et al., 2006). For the chloroform solvent and for wavelengths longer than 350 nm, OVK is transparent. Then, by referring to the OVK spectrum, the two bands at 232 and 343 nm sudden a slight red shift to 237 and 352 nm respectively. This red shift can be attributed to the interaction between SWNTs and OVK as it is reported in the case of multiwalled carbon nanotubes (MWCNs) (Wu et al., 2007). It is interesting to note that in the spectral region varying from 400 to 2000 nm (Zaidi et al., 2010), the OVK/SWNTs composite's absorbance decreases gradually similarly to those of halogen-doped PVK (Safoula et al., 1998). Similar effect has been also demonstrated in the case of SWNTs/Polyaniline obtained by an electro-synthesis process (Huang et al., 2003). This spectral region (λ>400 nm), presents three Lorentzian line-shapes of maximum absorbance centered at 450, 943 and 1246 nm. These bands are situated at 720, 976 and 1823 nm in the SWNTs optical spectrum from which the last band (1823 nm) is the most intense and is attributed to the inter-band optical transition in the semi conducting SWNTs. Therefore, adding OVK to SWNTs leads to a blue shifting, showing that OVK is functionalized with SWNTs.

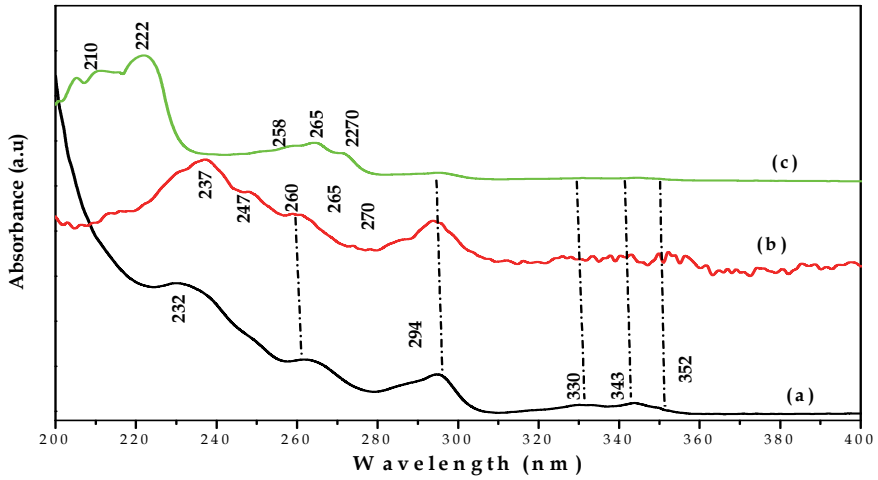

Fig. 5. Optical absorption spectra of OVK (a) and of OVK/SWNTs composites obtained either in chloroform (b) or in the chlorobenzene (c) solvents.

In the case of chlorobenzene and compared to the pristine OVK, (Bertoncello et al., 2006; Nam et al., 2002; Wu et al., 2007), new peaks appear around 210, 258, and 270 nm respectively, suggesting the formation of a charge transfer complex (Nam et al., 2002). Moreover, the three bands at 295, 331 and 344 nm are severely decreased, implying that SWNTs interacts with OVK (Wang et al., 2004; Wu et al., 2007). The main band in the blue side is blue-shifted, traducing the shorteness of the effective chain length of OVK (Yuna et al., 2008).

Figure 6 shows photoluminescence (PL) spectra of OVK and OVK/SWNTs composites. First, we note that PL spectrum of OVK is characterized by a broad emission situated in the spectral range 350-550 nm, which is constituted of three peaks. The pronounced peak located at 397 nm (3.12 eV) has been formerly assigned to lower-energy excimer, while the two lower intensity peaks are centered at 376 (3.29 eV) and 428 nm (2.90 eV), as recently described in literature (Upadhyay et al., 2008). In comparison with OVK, dramatic reduction of PL intensity is observed for OVK/SWNTs. The strength of PL quenching effect due to the SWNTs addition is more illustrated by the ratio (ΦF/Φ'F) of photoluminescence intensities related to pristine OVK (ΦF) and OVK functionalized SWNTs ((Φ'F), equal to 1.3 and 1.2 for the composite obtained by the use of chloroform and chlorobenzene respectively. Also, by inserting SWNTs, a slight red shift of the emission band at 392 nm (3.16 eV) to 404 nm (3.06 eV) has been observed in both cases. This quenching effect is caused by the scattering due to nanotubes presence (Wu et al., 2002). It is also noted that an energy tranfer has been occured, as shown by the mutual change of both Pl components situated at lower wavelength.

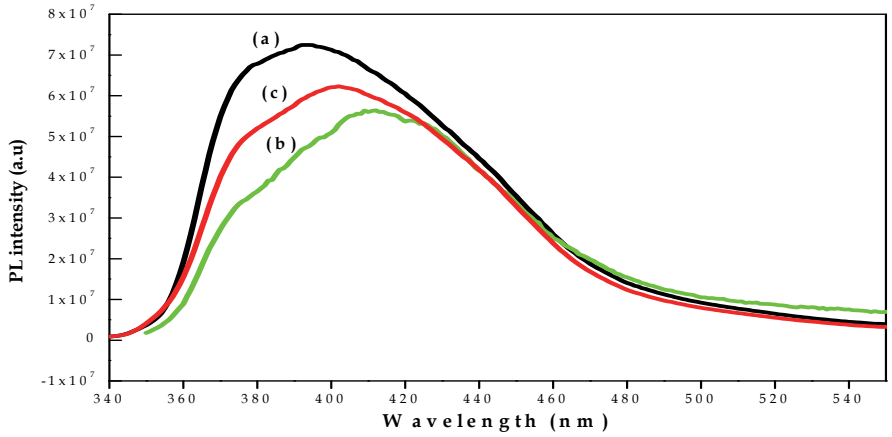

Fig. 6. PL spectra of OVK (a) and those of OVK/SWNTs composites obtained in chloroform (b) and in the chlorobenzene (c) solvents.

3.3 Grafting mechanism

From the above presented results, it appears that vibrationnal and optical properties of the resulting composite are derived from those of both OVK and SWNTs, as the case of PVK/SWNTs composites obtained by different experimental processes (Nam et al., 2002; Upadhyay et al., 2008; Wu et al., 2007). Thus, we can say that OVK is successfully functionalized with SWNTs but only in the case of chloroform solvent. In this context, infrared and Raman analysis show that the main perturbations induced in the chemical structure of OVK by adding SWNTs are limited to the vinylidene groups. Also a new C-C infrared band is created at 1297 cm^{-1}.

All experimental results let to conclude that a covalent bonding of OVK takes place in the vinylidene groups as indicated in figure 7. The obtained structure in the case of chloroform solvent is a grafting of OVK on the nanotube side wall. This hypothesis is also supported by the changes observed in infrared spectrum of OVK, especially by the disappearance of peaks

at 1402, 1481, 1596, 3047 cm^{-1} characteristic of vinylidene groups and the apparition of two C-H_2 features at 1133 and 2873 cm^{-1}. Similar grafting reaction has been proposed for PVK/MWCNs (Eklund et al., 1995) and for PVK/C60 (Wang et al., 2004) composites. It is now difficult to confirm that all (n=P) or a few number (P<n) of vinylidene groups are grafted to the SWNTs. Also, if it is the case of a partial reaction, the reactive or unreactive units can be arranged or not.

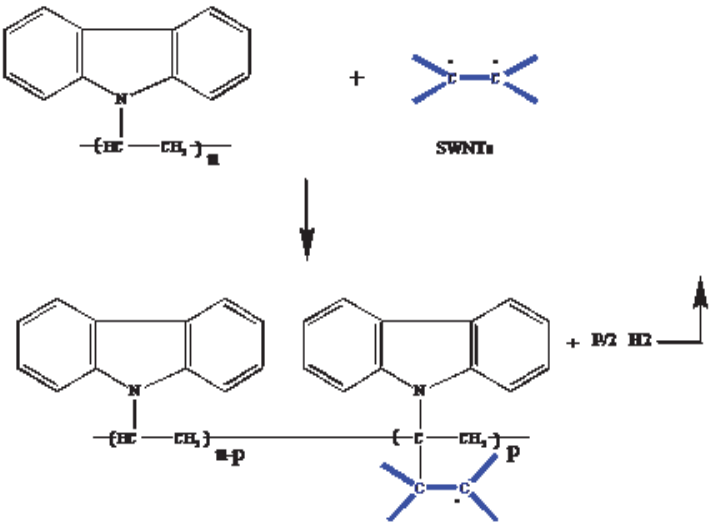

Fig. 7. Covalent bonding of OVK on the SWNTs side wall.

4. Effect of annealing treatments

The composite film obtained after solvent-evaporation is introduced in an oven and is subsequently heated under dynamic secondary vacuum (10^{-7} bar) at the temperature of 333 K for about 1 h as it is previously described (Wu et al., 2002). The choice of this temperature is strictly based on the PVK thermal properties (Alimi et al., 1998).

4.1 Vibrational properties

For infrared analysis and after annealing at 333 K (figure 8), no changes are observed in the case of chloroform solvent. However, in the case of chlorobenzene, the shape of infrared spectrum is strongly affected. More resolved spectra for which new bands appear at 1133, 1174, 1297, 1369, 1718, 1763 and 2873 cm^{-1}. The obtained spectra are closed to that obtained with chloroform solvent. According to the literature (Wang et al., 2004), bands peaked at 1174, 1369, 1718 and 1763 cm^{-1} are the signature of SWNTs. The others (1133, 1297 and 2873 cm^{-1}) are respectively assigned to aliphatic CH_2 in plane twist, new C-C vibration and aliphatic CH_2 stretching respectively. The new band at 1297 cm^{-1}, shows that SWNTs are successfully bonded with OVK. Moreover, some others bands centred at 418, 840, 1324, 1402, 1481, 1596, 1624, 3047 cm^{-1}, in the case of OVK already presented in figure 2, disappear in the case OVK/SWNTs composites. These bands are mainly attributed to the different stretching mode of vinylidene groups. We think therefore that for such SWNTs weight

concentrations, a covalent attachment of OVK to the SWNTs takes place, via vinylidene groups as it is said before in the case of chloroform solvent in both annealed and not annealed states.

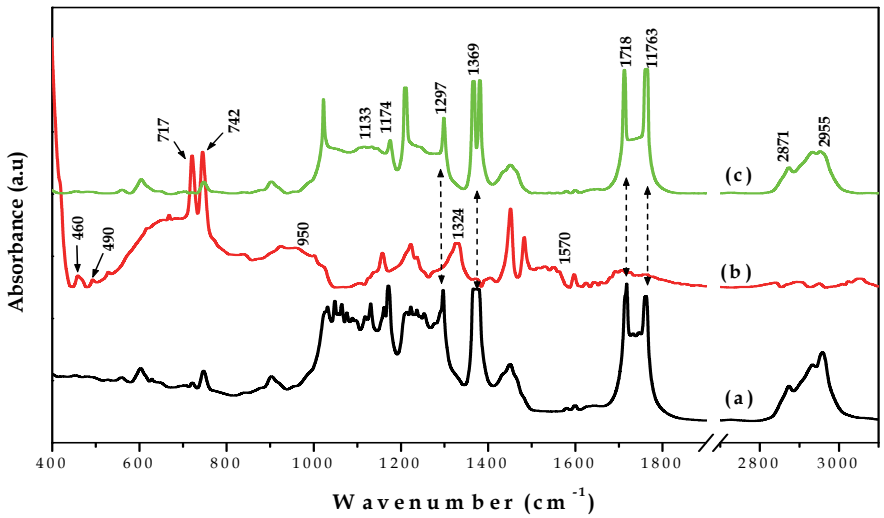

Fig. 8. Infrared spectra of OVK/SWNTs composite obtained by using chloroform (a) and chlorobenzene (b) solvents in the not annealed states and that of OVK/SWNTs obtained using chlobenzene and annealed at 333 K.

In the full spectrum of Raman frequencies, the shape of the spectrum is conserved in both cases. However, some differences are previously observed (Zaidi et al., 2010). It is recognized that annealing induces removal of solvent effect and more establishes the SWNTs functionalization. Then, it is also mentioned as the case of SWNTs produced either by an arc discharge or pulsed lasers (Coopera et al., 2001), that a new weak band appears at 1745 cm^{-1}. This latter can be related to the presence of oxygen in surface, probably originating from carbonyl groups or SWNTs deformation. In the other hand, the D band at 1273 cm^{-1} and the second order corresponding increase in intensity and undergo a slight up-shift after annealing, supporting an indication of disorder in the graphite lattice or defects in nanotubes.

While the radial breathing and tangential vibration modes are apparently the same, the annealing treatment induces some differences in position and intensity which is strictly related to a better functionalization process (Figure 9).

It is shown that after annealing in both cases only the band at 166 c cm^{-1} persists. Thus, SWNTs are in the isolated form and have a mean diameter of 1.34 nm. This indicates a more dispersion of the SWNTs into OVK matrix. For the tangential mode, we notice a slight up-shift and a narrowing of the band at 1592 cm^{-1} by the introduction of nanotubes. In fact, for lower OVK concentrations (higher SWNTs concentrations), the quantity of OVK intercalated between nanotubes could not lead to a destruction of bundled SWNTs. The introduction of OVK into bundled (decrease of the SWNTs concentration) increases the distance between

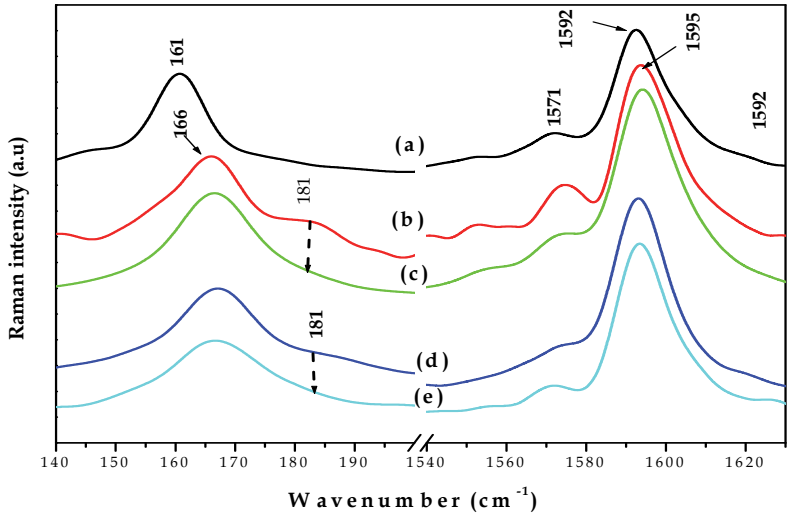

Fig. 9. Radial breathing and tangential modes in Raman spectra of: only SWNTS (a), composite OVK/SWNTs in chloroform: not heated (b) and heated at 333 K (c), composite OVK/SWNTs obtained in chlorobenzene: not heated (d) and heated at 333 K (d).

nanotubes and therefore interaction between them is decreased, explaining why width of peaks is weaker when nanotubes are introduced in the OVK Matrix. Then, as it is previously described (Claye et al., 2001; Rao et al., 1997) that doping SWNTs with either electron donors or acceptors resulted in noticeable shift in certain characteristic vibrational modes, especially removing charge from SWNTs (oxidizing) results in up-shift in the G band peak around 1590 c cm^{-1}. This up shift is explained as the addition of some SP3 character to the SP2 hybridized orbitals. Removing electron density from these orbitals reduces the repulsion resulting in stronger net bonding and higher G band frequency. Moreover, the intensity of the peak at 1571 cm^{-1} decreases after annealing at 333 K illustrating a change from 2D to 3D symmetry (Eklund et al., 1995). For more details, all these results are previousely described (Zaidi, et al., 2010)

4.2 Optical properties

After annealing both composites, as shown in figure 10, the strength of PL quenching effect became more prounonced. The ratio (ΦF/Φ'F) of photoluminescence intensities related to pristine OVK (ΦF) and OVK functionalized SWNTs ((′F) reashes 2.7 and 1.5 respectively for both composites. Moreover, a new vibronic structure apperas at lower energy side of the emission spectrum centered at 499 nm (2.48 eV) is observed in the case of the chloroform solvent.

In fact, in both cases an energy transfer is occured as depicted by the mutual change of PL intensity between the two PL bands situated at lower wavelengths as it is reported for PPV/SWNTs (Mulazzi et al., 2006). This change implies the formation of new luminescent centre which corresponds probably to the defect related to the covalent bonding of SWNTs

In fact, the band observed at 499 nm can be the consequence of annealing treatment or of the SWNTs addition. A more clarification can be illustrated by the PL spectra of both annealed OVK and OVK/SWNTs composite recorded at 87 K (Figure 11).

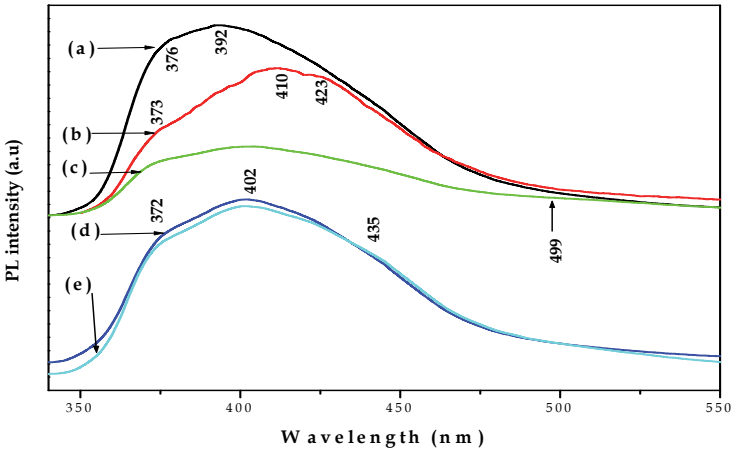

Fig. 10. PL spectra of: (a) only OVK, composite OVK/SWNTs in chloroform: not heated (b) and heated at 333K (c); composite OVK/SWNTs in chlobenzene: not heated (d) and heated at 333 K (e).

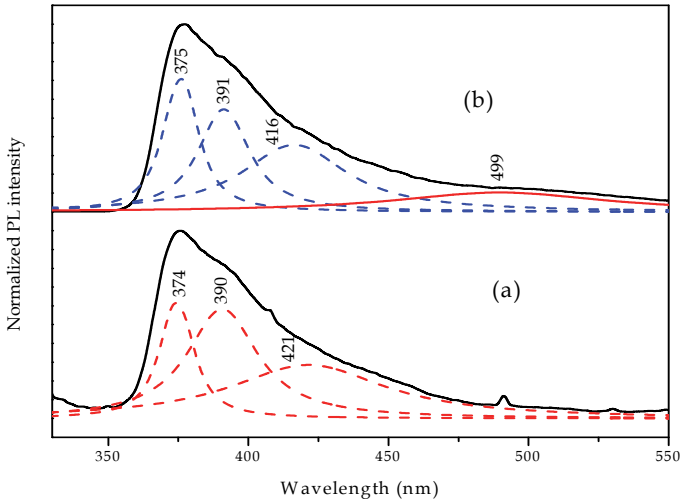

Fig. 11. PL spectra recorded at 87 K of annealed OVK (a) and annealed OVK/SWNTs (b).

As the new band appears only in the case of annealed OVK/SWNTs composite, it is, however, the consequence of SWNTs insertion. From figure 11, other modifications are also clearly seen. In fact, by referring to the OVK spectrum recorded at room temperature, peaks at 397 and 428 nm in the annealed OVK undergo a blue shift of 7 nm toward 390 and 421 nm respectively. Otherwise, the energy transfer induced by annealing is more pronounced for measurements at 87 K.

At present, SWNTs insertion leads to additional bands in the optical absorption and photoluminescence spectra which results from an electronic interaction between OVK and

SWNTs. A possible quenching mechanism originating from transfer of electron-hole pair (excitons) generated in OVK chain to SWNTs was already proposed (Baibarac et al. 2007b). In fact, the two PL maximums observed at 379 and 404 nm are considered originating from excimers formed in the partially and fully eclipsed configurations (Baibarac et al. 2007). Therefore, the variation of the PL spectra, traducing the energy transfer allows to conclude that adding SWNTs leads to the formation of fully eclipsed structure rather than partially eclipsed-one, showing that the resulting composite is homogenous and SWNTs are more dispersed in the OVK matrix.

5. Theoretical aspect

The structures of OVK oligomer or SWNTs either in the neutral or in the oxidized states have been fully optimized with the most popular Becke's three-parameter hybrid, B3 (Becke, 1993) with non local correlation of Lee-Yang-Parr, LYP (B3LYP) method (Lee et al., 1998). This method is based on density functional theory (DFT) for uniform electron gas and is used with the basis set such as 3-21G* (Pietro et al., 1982). This basis is applied to other systems based polymers (Ayachi et al., 2006; DiCesare et al., 1998; Pickholz and Santos, 1999). For the resulting composite, it has been reported that the semi-empirical Austin Model (AM1) method is an effective tool for qualitative study of functionalized nanotubes (Wongchoosuk et al., 2009). For this reason, geometry structure optimization of OVK/SWNTs composite is carried out using AM1 method (Dewar et al., 1985). On both fully geometry-optimized structures of OVK and OVK/SWNTs composite, infrared vibrationnal frequencies are carried out using respectively ab-initio Hartree-Fock (HF) and Austin (AM1) semi-empirical calculations. All these methods (AM1, ab-initio: HF and DFT) are implemented in Gaussian 98 program (Frisch et al., 1998). In the other hand, force constants of both OVK and SWNTs in the neutral and oxidized states are carried out using Mopac 2000 program (Stewart, 1999).

5.1 OVK and SWNTs modelling structures

In general, the vibrationnal and electronic properties of polymers can be reproduced theoretically using a typical modeling structure of maximum seven to eight units (Ayachi et al., 2006; Wang et al., 2004). For OVK, our calculations are limited to four VK units (figure 12-a). For the SWNTs, in order to obtain the real diameter of the tube (1.3 nm), the modeling structure is the rolling up of a graphene's sheet, having each 14 rings (figure 12-b).

5.2 Prediction of reactive sites by the mean of force constants variation from neutral to oxidized states

First, to rationalize the reactive sites either in OVK or SWNTs, involving the grafting reaction, force constants between neighboring atoms in both neutral and oxidized states are made on the fully optimized structures for both OVK and SWNTs (figure 13). These force constants are the mean taken from the equivalent sites in both modeling structures. As shown, only a large shift is observed for F_9, F_{10} and F_{11} in the case of OVK. These force constants are between neighboring carbon atoms in the vinylidene groups. However, in the case of nanotube the most significant variations are restricted to F_1, F_2 and F_3 which traduce the bonding between carbon atoms, located in the side of SWNTs. These results indicate that the grafting process take place in the nanotube side wall.

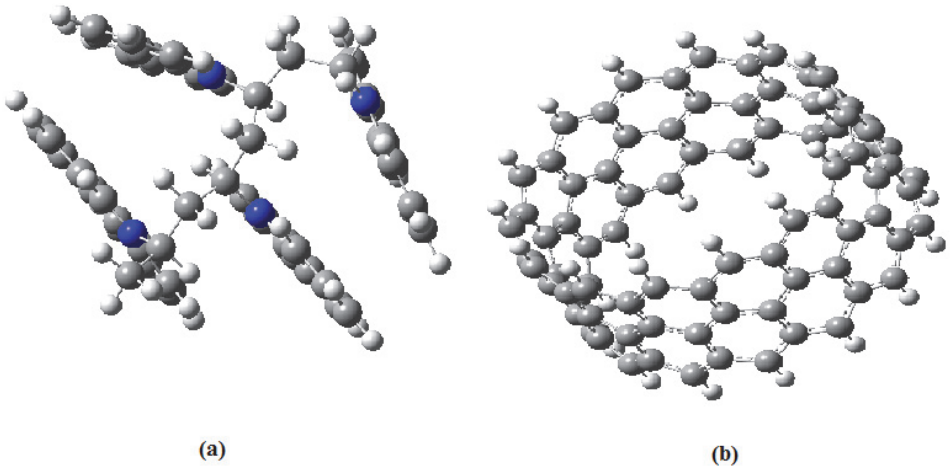

Fig. 12. OVK (a) and SWNTs (b) modelling structures optimized using DFT/B3LYP/3-21G*.

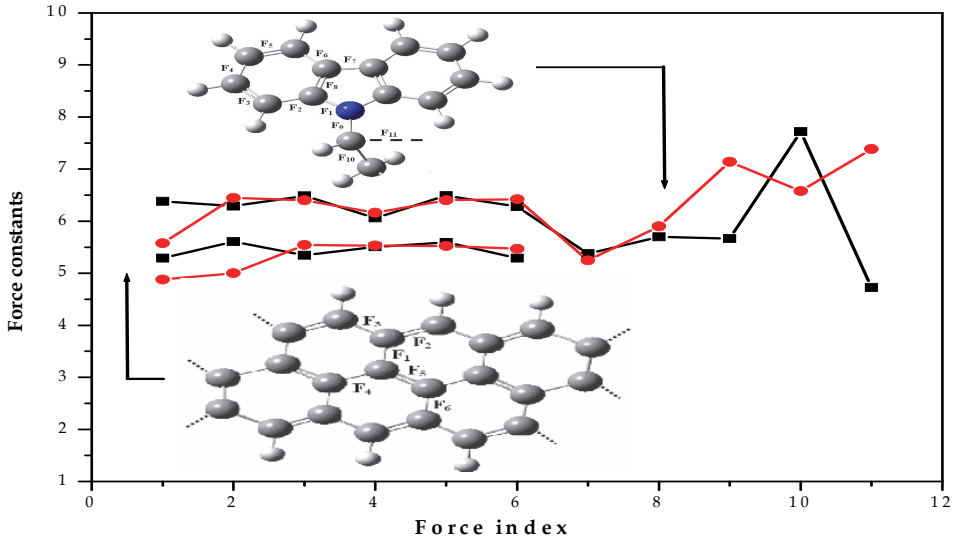

Fig. 13. Main force constants of equivalent sites in the neutral (square symbol) or oxidized (circle symbol) states of OVK and of SWNTs.

5.3 Composite modelling structure

Based on the above changes in force constants, we suggest a grafting reaction between vinylidene groups and the nanotube side wall. If we consider that only a few number of VK monomers are effectively bonded with SWNTs, we propose a one VK unit grafted to the nanotube as a typical modeling structure (figure 14).

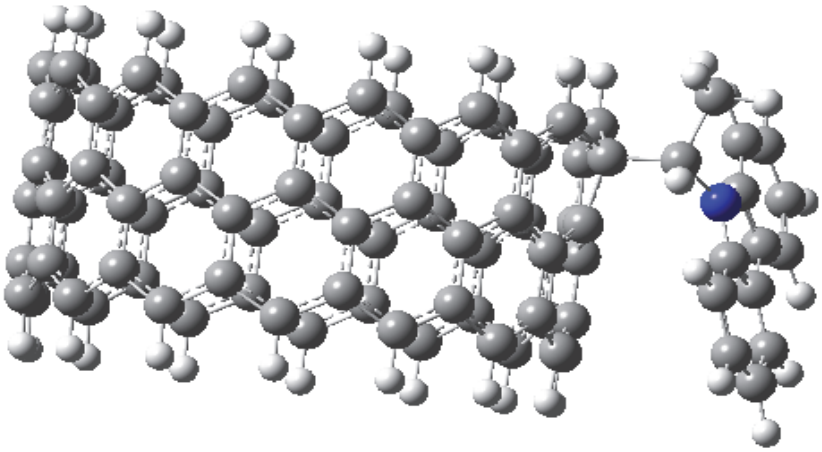

Fig. 14. OVK/SWNTs modelling structure.

5.4 Validity of the grafting process

To argue the above presented grafting mechanismm, our work is extended to a comparative study between experimental and theoritical vibrationnal frequencioes obtained either for OVK or OVK/SWNTs composite. Results are fully presented in our previous paper (Zaidi et al., 2010). It is demonstrated that a maximum typical shift of 40 cm^{-1} is observed (Zaidi et al., 2010). For OVK, both spectra exhibit nearly the same shape in band positions and intensities, except both features at 1034 and 1625 cm^{-1}. In fact, these two bands which are respectively attributed to aromatic C-C in plane deformation and C-C benzene stretching are strongly enhanced. This enhancement may be probably due to the absence of the steric effect. For the OVK/SWNTs, a partially accordance between experimental and theoretical band intensities is observed which might be principally due to the weight ratio (W_{SWNTs}/W_{OVK}) that is strongly shifted from the experimental-one. In fact, two SWNTs vibrationnal modes at 1048 and 1064 cm^{-1} and another feature ascribed to C-C in plane deformation centered at 1118 cm^{-1} are absent in the theoretical spectra. This behavior is probably related to the SWNTs length which is not taken into account in our modeling structure.

A similar computational study describing the functionalization of carbon nanocones by free radicals (Trzaskowsk et al., 2007), predicts that single-wall graphene nanocones can be selectively functionalized by methyl radicals, as well as by other free radicals. Such functionalization has been supported by infrared spectra of these compounds as a new intense C-C bond at 1171 cm^{-1}.

5.5 Electronic structure

The effect of SWNTs insertion on the electronic structure has been elucidated by geometrical optimization using DFT/B3LYP/3-21G* method. Adding SWNTs induces the modification of the electronic transitions in the absorption diagram as indicated in figure 15.

Through this energetic diagram, the most relevant transitions observed in the experimental spectra are reproduced. For OVK, the optical gap is around 3.3 eV which is 0.2 eV lower than that determined experimentally. In fact, this difference (LUMO-HOMO) has been

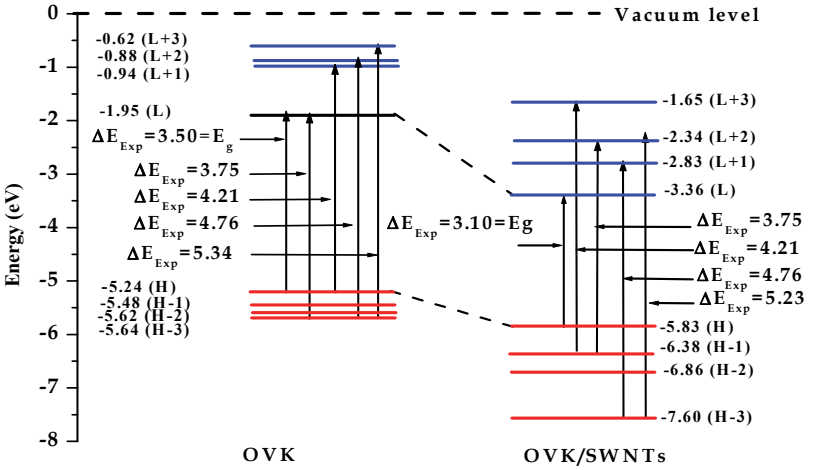

Fig. 15. Change of the electronic structure from OVK to OVK/SWNTs: (H: HOMO, L: LUMO).

calculated as a function of VK units number, using DFT/B3LYP/6-31G* method (Pana et al., 2005; Yang et al., 2006) where results are nearly the same in our case. For SWNTs modeling structure, the optical gap is 1.38 eV. The calculated gap of the resulting nanocomposite is 2.5 eV which is 0.6 eV lower than that deduced from optical density measurements. This relatively large difference might be firstly due to the fact that calculations are done in gas phase. Secondly, the weight ratio (W_{SWNTs}/W_{OVK}) of the model structure is largely higher than the experimental-one.

6. Properties of SWNTs functionalized with PVK-3HT

6.1 Vibrational properties

The Raman spectra of SWNTs and composite PVK-3HT/SWNTs, shown in Figure 16, contain two main features, a radial breathing mode (RBM) at low frequencies (~ 160 cm^{-1}) and tangential G-band at high frequencies (1595 cm^{-1}). In addition, an intermediate feature related to the disorder or defects on SWNTS with weaker intensity is also shown at 1250 cm^{-1}.
Qualitatively, the two bands occurring at 1250 (D-band) and 1595 cm^{-1} (G-band) are nearly the same in all cases of composite samples as well as in the case of purified nanotubes. Qualitatively, a part the band shapes of RBM for composites sensitive to the added SWNTs, a similar up-shift of around 5 cm^{-1} of the band at 161cm^{-1}, associated to the isolated SWNTs is observed. However, the significant second band appears in composites at 179 cm^{-1} is attributed to the bundled SWNTS. Note that pure PVK-3HT hardly diffuses light and its spectrum has not shown.
It is well known that close examination of the radial breathing modes of the dispersed nanotubes can gives information about degrees of diameter selectivity when increasing weight of nanotubes (Dresselhaus et al., 2004). In order to appreciate the interaction within the PVK-3HT/SWNTs composites, here, we examine the radial breathing mode (RBM) features (in the first range: 145-200 cm^{-1}) in SWNTs and the composites. Using the inverse

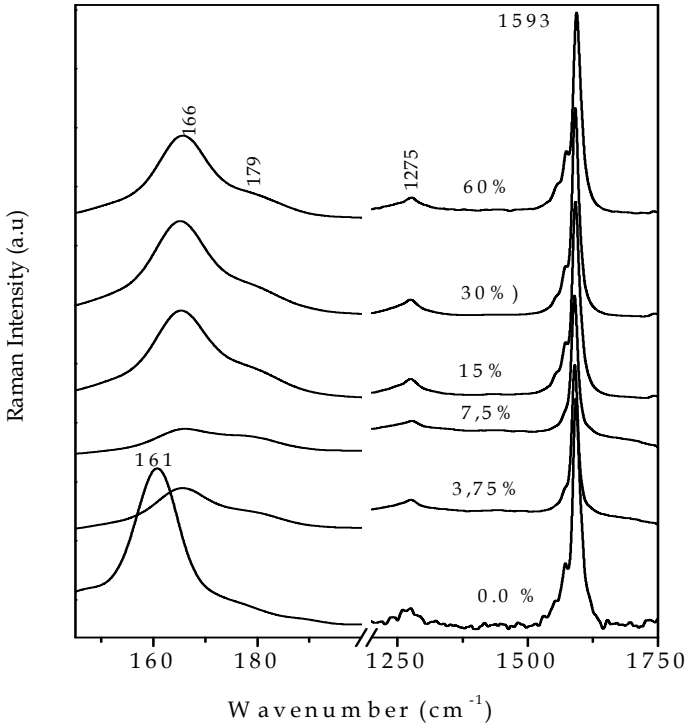

Fig. 16. Raman spectra of PVK-3HT/SWNTs composites at different weight ratio of SWNTs (0%, 3.75%, 7.5%, 15%, 30% and 60%).

relationship between RBM mode frequency and the tube diameter (d) proposed by Rao et all (Rao et al., 1997), the two bands located at about 166 and 179 cm^{-1}, respectively, attributed to the RBM of SWNTs activated in isolated and bundled nanotubes, indicate that the resonance Raman occurs at the diameter varying from ~1.34 to 1.25 nm, taking into account that SWNTs have diameter around 1.39 nm.

Figure 17 displays normalized optical infrared spectra of PVK-3HT, SWNTs and their corresponding PVK-3HT/SWNTs composite at weight ratio of 60%. The room temperature infrared spectra of PVK-3HT/SWNTs composite shown in Figure 17c exhibits seven characteristic modes of PVK, at 746 cm-1 (C-H rocking), at 921 cm^{-1} (C–C ring vibration), at 1022 cm^{-1} (aliphatic C–C rocking), at 1220 cm^{-1} (C–N stretching), at 1330 cm^{-1} (C–H deformation of vinylidene groups), at 1483 cm^{-1} (CH2 rocking) and at 1676 cm^{-1} (C–C benzene stretching). For the characteristic modes of 3-hexylthiophene (Figure 17a), the 723 cm^{-1} is ascribed to C-H out-of-plane bending, the 798 cm^{-1} is assigned to C-H out-of-plane deformation of thiophene), the 1095 cm^{-1} mode is from C-H in-plane bending of the thiophene rings, the 1261 cm^{-1} mode corresponds to C-C stretching of the carbon which connect the thiophene rings and 1452 and 1598 cm^{-1} are typical ring stretch modes. The observed results support the chemical structure of copolymer under study.

According to Ref (Kim et al., 2005), infrared absorbance bands for the SWNTs are observed at 1170, 1456, 1540, and 1734 cm^{-1}. In our case, these bands appear at 1174, 1440, 1579 and

1710 cm^{-1}, respectively. Compared to the pure PVK-3HT, for the composite sample, two new pronounced features at 1049 and 1384 cm^{-1} appear and retain their oscillator strength. These features are assigned to C–C vibration of SWNTs and CH_3 deformation in 3HT, respectively. Significant changes in intensity are clearly shown by adding SWNTs. Then, some bonds were loosened, whereas other vibrations were hindered when passing from pristine copolymer to the composite. Besides, we note that the most intense vibrations of PVK-3HT and those of SWNTs are found in the PVK-3HT composite spectrum. Accordingly and combined to the Raman analysis, the whole vibrational results supported a strong PVK-3HT/SWNTs interaction.

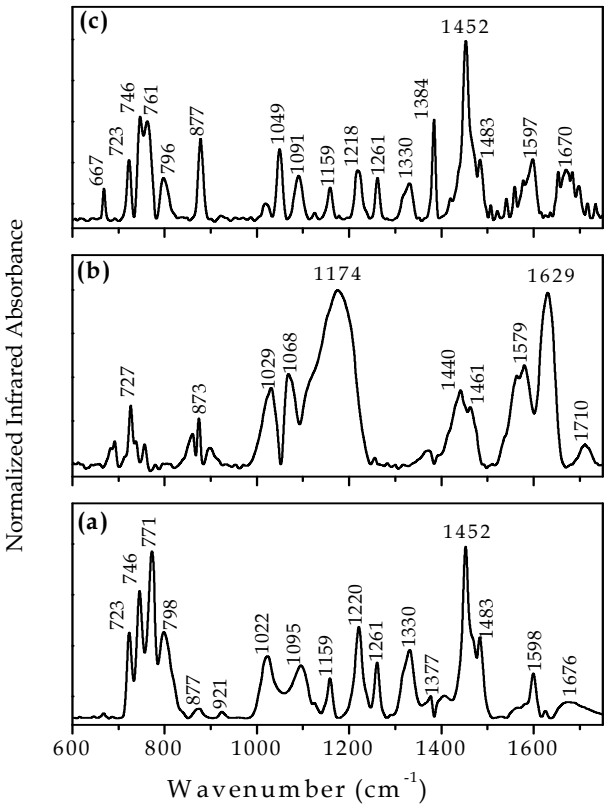

Fig. 17. Normalized infrared spectra of: PVK-3HT (a), SWNTs (b) and PVK-3HT/SWNTs composite (60%) (c).

6.2 Optical properties

As it is noted; from vibrational propertries of the resulting composite when using the PVK-3HT polymer, SWNTs exists as isolated or bundled SWNTs. However, infrared, results supports the hypothesis that there is a grafting process which takes place in the hexylthiophenes rings. From optical absorption spectra presented in figure 18, we see that PVK-H3T absorbs in two separate spectral regions. The first range is situated the UV part at

around 240 and 300 nm and corresponds to the presence of bicarbazole units in the formed graft copolymer (Chemek et al., 2010). The second domain is situated in the visible part at around 430 nm and traduce to the presence of an extended conjugated main chain of Poly(3-hexylthiophene) in the obtained copolymer (Carley et al., 2009; McCullough, 1998). In fact; from optical spectra, it appears that there is a net difference between the pristine state of the polymer and the corresponding functionalized form with SWNTs, especially for the 1.85 SWNts weight content. Thus, at the blue side of the spectrum (wavelength lower than 400) relative to the PVK polymers, bands are nearly the same. However, the band at 430 nm shows a sudden decrease when adding SWNTs and undergoes a continuously blue-shiftwing, reflecting that there is a shortness of the effective conjugation length of these blocks (Wéry et al., 2003).

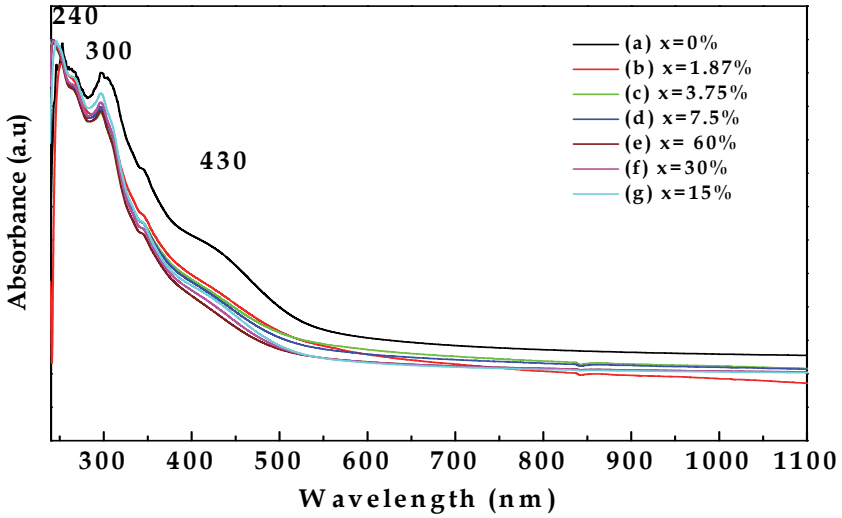

Fig. 18. Optical absorption at room temperature of pristine PVK-3HT (a) and those of PVK-3HT/SWNTs composites for different SWNTs weight concentrations (x): (a) Standard PVK-3HT, (b) x=1.87%, (c) x=3.75%, (d) x=7.5%, (e) x=60%, (f) x=30%, and (g) x=15%.

Although, there is no significant changes observed in optical absorption spectra when increasing SWNTs weight concentration due to the already reached percolation threshold, the large amount of SWNTs either in grafted or not, or in isolated or bundled forms can influences the excitated states of the resulting composite (Massuyeau et al., 2007). Therefore, the luminescent properties must logically undergo a dependent evolution versus the SWNTs weight concentrations. In fact, as it is previously described, carbon nanotubes can present a good network for charge migration from short to long conjugation. Particularly, at higher SWNTs concentrations, it has been demonstrated that the PL originates globally from the recombination of excitons on a majority of short conjugated segments. In this limit, statistically, the portion of long conjugated segments becomes negligible. These hot excitons can easily migrate due to their mobility (Chu et al., 2008) and then a separation process can be take place when reaching the SWNTs network. This assumption is consistent with the PL quenching, reflecting a decrease in quantum yield efficiency and the rise of the conductivity

and the photoconductivity when x increases. Based on these assymptions, and for better understanding of the excited state dynamics of the prepared composites, time-resolved photoluminescence (TRPL) technique at room temperature (RT) is recorded (figure 19).

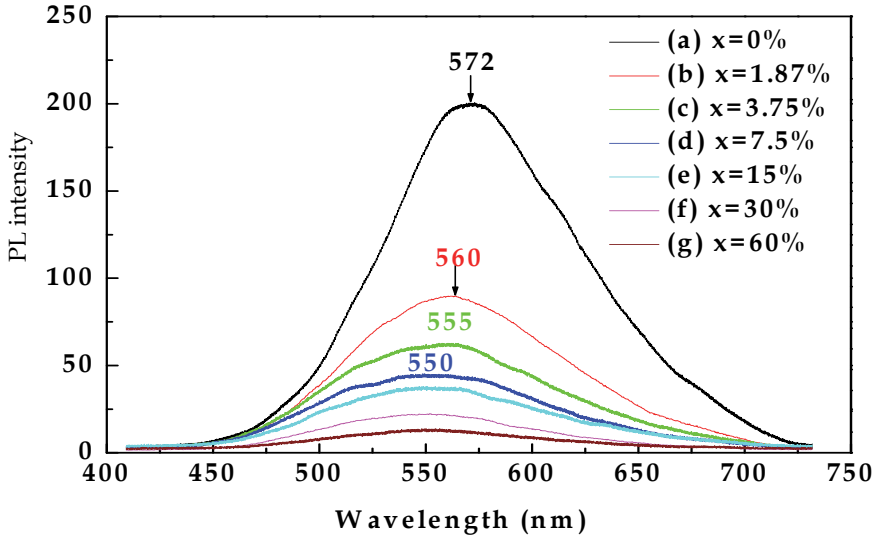

Fig. 19. Transient photoluminescence (TRPL) spectra in chloroform solution of pristine PVK-3HT (a) and those of PVK-3HT/SWNT composites for different SWNTs weight concentrations (x) of SWNT: (b) x= 1.87%, (c) x=3.75%, (d) x= 7.5%, (e) x=15%, (f) x= 30%, (g) x=60%.

All the spectra relative to all SWNTs weight concentrations are collected with excitation of 400 nm using seep range of 1 ns. First, it is shown that the hexylthiophene influences the maximum emission to reach 572 nm rather than 300 nm for OVK/SWNTs. The quenching of luminescence intensity is observed with a continuous blue shiftwing of the maximum emission. The latter is detected at 572 nm for the pristine PVK-3HT rashes 550 nm for higher SWNTs contents. The blue shift observed in the TRPL spectra is in quite agreement with the observation in the optical absorption spectra, and supporting the gradual decrease of the conjugation length in PVK-3HT, backbone consequently on the lifetime of the resulting excitons.

3D-maps TRPL obtained with energy emission versus time (range 0-1 ns) and intensity in false color of PVK-3HeT and PVK-3HT/SWNTs prepared composite for different weight concentration x (0%, 1.87%, 7.5%,15%, 30% and 60%) are presented in figure 20. In this case, 3D-maps colors going from blue to red represent the increasing of the PL intensity.

To obtain a better understanding on how the SWNTs influence the excited states dynamics on the PVK-3HT, we analyzed the TRPL decays on the different prepared composites. Figure 21 shows the normalized TRPL decay dynamics on a logarithmic scale in the range of 0-1ns. Compared to the pristine PVK-3HT, the increase of SWNTs weight concentration progressively induces a faster decays time. A comparable behavior has been observed on the transient decays time of the prepared composite of PPV and SWNTs (Massuyeau et al., 2007).

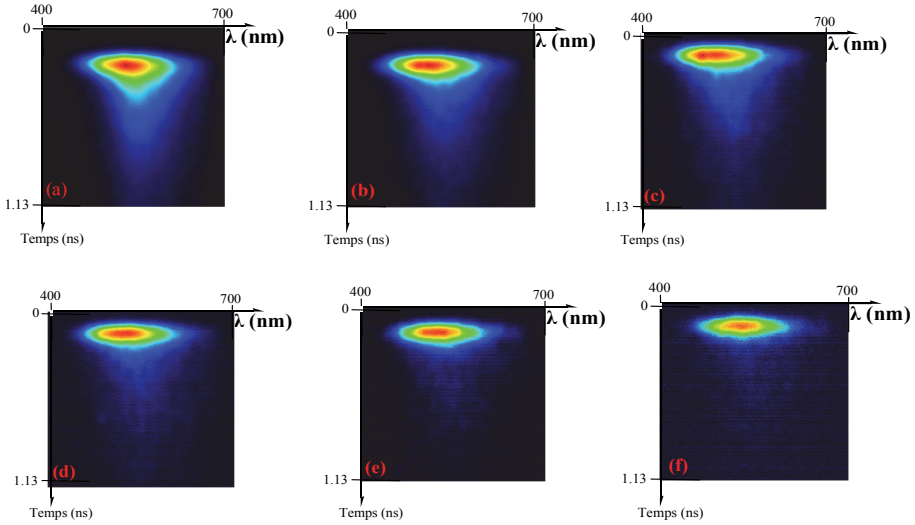

Fig. 20. Transient photoluminescence contour maps in false color of standard PVK-H3T (a) and thoseof PVK-3HT/SWNTs composites for different mass concentrations x of SWNT. (a) Standard PVK-3HT, (b) x= 1.87%, (c) x=7.5%, (d) x= 15%, (e) x=30%, (f) x=60%.

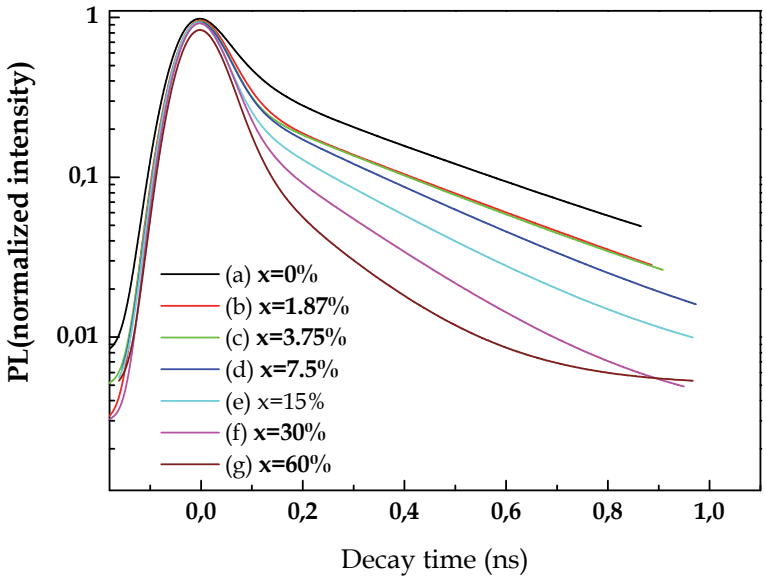

Fig. 21. Transient photoluminescence decays spectra of pristine PVK-3HT (a) and those of PVK-3HT/SWNT composites for different weight concentrations (x): (b) x= 1.87%, (c) x=3.75%, (d) x= 7.5%, (e) x=15%, (f) x= 30% and (g) x=60%.

This behavior supports the hypothesis that SWNTs in the composite present a good network for the charge migration from and their presence facilate also the separation process. Thus, as x increase, exciton migration under light excitation is favored, resulting in carrier transport on SWNTs and PL quenching. These hot excitons can easily migrate due to their mobility (Chu et al., 2008) and then separate when reaching the SWNT network. This assumption is consistent with the PL quenching, a decrease in quantum yield efficiency and the rise of the conductivity and the photoconductivity when x increases.

7. Conclusion

The spontaneous covalent functionalization of SWNTs at the appropriate SWNTs weight concentrations with OVK has been demonstrated in a chloroform or chlorobenzene mediums, using optical absorption, photoluminescence, infrared and Raman spectroscopies. More dispersed SWNTs in the OVK matrix is obtained after annealing the resulting structure at the temperature of 333 K. In comparison with chloroform solvent, the chlorobenzene reveals a more SWNTs dispersion process but its potential to the eventual interaction between both components is limited. Otherwice, a homogenous dispersion process is achieved for SWNTs weight concentration lower than 1.10 %, but without covalent attachment between both components. However, annealing the resulting composites at the moderate temperature of 333 K induces strong modifications on their infrared and Raman vibrational modes, involving a covalent bonding between both components. Such a covalent bonding either using chlorobenzene or chloroform is a grafting of OVK oligomers from their vinylidene groups to the nanotubes side wall. To confirm the validity of the grafting mechanism, theoretical calculations including force constants, vibrational infrared frequencies and modification of electronic structure based on the DFT methods are accomplished.

In the case of PVK-3HT, the introduction of carbon nanotube induces a great effect in the optical properties. In particular, a decrease in the absorption, blue-shift of the emission and strong PL quenching with a fast recombination of electron-hole pairs was observed for high carbon nanotube weight concentration. These behaviors are doing to the strong interaction of SWNTs with copolymer backbone, which improve exciton dissociation and better carrier transport on SWNTs and polymer backbone. Finally, the presence of nanotubes as a filler network in polymer matrix may be of importance in view of applications for solar cell development.

8. References

Ahuja, R.T. & Kumar, D. (2009). Recent progress in the development of nano-structured conducting polymers/nanocomposites for sensor applications. *Sens. Actuators,* Vol. 136, No. 1, (February 2009), pp. (275-286). ISNN 0925-4005.

Akcelrud, L. (2003). Electroluminescent polymers, Prog. Polym. Sci. Vol. 28, No. 6, (June 2003), pp (875–962). ISNN 0079-6700/03.

Alimi, K., Safoula. G., Bernede, J. C., Rabiller, C. (1998), Degradation of poly(N-vinylcarbazole) by annealing under iodine pressure. J. Polym. Sci. Part B: Polymer Phys.; Vol. 34, No. 15,Issue 5, (April 1996), pp. (845–851),). ISNN 7 DEC 1998.

Andrés, J.A. & Blau, W.J. (2008). Enhanced device performance using different carbon nanotube types in polymer photovoltaic devices. *Carbon,* Vol. 46, No. 15, (December 2008), pp. (2067-2075). ISSN 0008-6223

Arab, H., Baitoul, M., Wery, J., Almairac, R., Lefrant, S., Faulques, E., Duvail, J. L., & Hamedoun, M. (2005). Electrical and optical properties of PPV and single-walled carbon nanotubes composites films. *Synt. Met.,*Vol. 155, No.1, (October 2005), pp. (63-67). ISSN 0379-6779.

Ayachi, S., Alimi, K., Bouachrine, M., Hamidi, M., Mevellec, J.Y, & Porte, J.P.L. (2006). Spectroscopic investigations of copolymers incorporating various thiophene and phenylene Monomers. *Synt. Met.*, Vol. 156, No. 2-4, (February 2006), pp. (318-326). ISSN 0379-6779.

Baibarac, M., Baltog, I., Lefrant, S. & Romero, P.G. (2007). Spectroscopic evidence for the bulk polymerization of N-vinyl carbazole in the presence of single-walled carbon nanotubes. *Polym.,* Vol. 48, No. 18, (August 2007) ,pp. (5279-5288). ISSN 0032-3861.

Barlier, V., Bounor-Legaré, V., Boiteux, G., Davenas, J., Slazak, A., Rybak. A & Jung, J. (2009). Photogeneration and photovoltaic effect in poly(N-vinylcarbazole): TiO2 bulk-heterojunction elaborated by hydrolysis–condensation reactions of TiO2 precursors. *Synth. Met.* Vol. 159, No. 5-6, (March 2009), pp. (508-512). ISNN 0379-6779.

Becke, A.D. (1993). Density-functional thermochemistry. III. The role of exact exchange. *J. Chem. Phys.,* Vol. 98, No. 7, (1993), pp. (5648-2652). ISSN 0021-9606.

Bendiab, N., Anglaret, E., Bantignies, J.-L., Sauvajol, J.L., Petit, P., & Mathis, C. (2002). Stoichiometry dependence of the Raman spectrum of Li-doped single-wall carbon nanotubes. *Physica B,* Vol. 323, No. 1-4, (October 2002), pp. (259-261). ISSN 0921-4526.

Bertoncello, P., Notargiacomo, A., Erokhin, V., & Nicolini, C. (2006). Functionalization and photoelectrochemical characterization of poly[3-3-(vinylcarbazole)] multi-walled carbon nanotube (PVK-MWNT) Langmuir–Schaefer films. *Nanotechnol.,* Vol. 17, No. 3, (February2006), pp. (699-705). ISSN 0957-4484.

Bondavalli, P., Legagneux, P., & Pribat, D. (2009). Carbon nanotubes based transistors as gas sensors: State of the art and critical Review. *Sens. Actuators,* Vol. 140, No. 1, (June 2009), pp. (304-318). ISSN 0925-4005.

Brown, M. J., Anderson, D. P., Justice, R. S., Lafdi, K.., Belfor, M., Strong, L. K., Schaefe, W. D., (2005). Hierarchical morphology of carbon single-walled nanotubes during sonication in an aliphatic diamine, *Polym*. Vol. 46, No. 24 (November 2005), pp.(10854–10865). ISSN 0032-3861.

Byron, P. R., Hubert, P., Salvetat J.-P., Zalamea, L., (2006). Flexural deflection as a measure of van der Waals interaction forces in the CNT array. *Compos. Sci. and Tech.* 66, No 9 (July 2006) pp. (1125–1131). ISSN 266-3538.

Cai, W., Gong, X. & Cao, Y. (2010). Polymer solar cells: Recent development and possible routes for improvement in the performance. Sol. Energy Mater. *Sol. Cells*, Vol. 94, No.2, (Febrary 2010), pp 114–127. ISNN 0927-0248.

Canestraro, C.D., Schnitzler, M.C., Zarbin, A.J.G., da Luz, M.G.E., & Roman, L.S. (2006).Carbon nanotubes based nanocomposites for Photocurrent improvement. *Appl. Surf. Sci.,* Vol 252, No. 15, (May 2006), pp. (5575-5578). ISSN 0169-4332.

Capek, I. (2009). Dispersions, novel nanomaterial sensors and nanoconjugates based on carbon nanotubes. *Adv. Colloid Interface Sci.,*Vol. 150, No. 2, (September 2009), pp. (63-89). ISSN 0001-8686.

Caste, C., Castelvetro, V., Ciardelli, F., Colligiani, A., Mazzotta. A., Michelotti, D., Ruggeri, G., Veracini, C.A; (2003). Photoconductive films of poly-N-vinylindole-based blends for high-voltage photorefractive electrooptic cells. *Synth. Met.,* 138, No 1-2 (June 2003), pp. (341–345). ISSN 0379-6779.

Cathcart, H., Coleman J. N.; (2009) Quantitative comparison of ultracentrifuged and diluted single walled nanotube dispersions: differences in dispersion quality. *Chem. Phy. Lett.* Vol. 474, No 1-3 (May 2009), pp. 122–126. ISSN 0009-2614.

Chapelle, M.L., Lefrant, S., Journet, C., Mase, W., Bernier, P., & Loiseau, A. (1998). Raman Studies on single Walled carbon nanotubes produced by the electric arc technique. *Carbon,* Vol. 36, No. 5-6, (1998), pp. (705-708). ISSN 0008-6223.

Chemek , M., Wéry, J., Bouachrine, M., Paris, M., Lefrant, S. & Alimi, K. (2010). Synthesis and characterization of novel graft copolymers of Poly(N-vinylcarbazole) and Poly(3-methylthiophene) for optoelectronic applications . *Synth. Met.* Vol.160, No. 21-22, (November 2010), pp (2306-2314). ISNN 0379-6779.

Chen, B., Inoue, S., & Ando, Y. (2009). Raman spectroscopic and thermogravimetric studies of high-crystallinity SWNTs synthesized by FH-arc discharge method. *Diamond Relat. Mater.,*Vol. 18, No. 5-8, (May-August 2009), pp. (975-978). ISSN 0925-9635.

Chu, W., Wang, Y., S., Li, F., Feng, L. W. & Gong, Q., (2008). Steady-state and transient-state optical properties of a charge-transfer composite material MO-PPV/SWNTs. *Chem. Phys. Lett.* Vol. 451, (Jannary 2008), pp. (116-120). ISNN 0009-2614.

Claye, A., Rahman, S., Fischer, J.E., Sirenko, A., Sumanasekera, G.U. & Eklund, P.C. (2001). Insitu Raman scattering studies of alkali-doped single wall carbon nanotubes. *Chem. Phys. Lett.,* Vol. 333, No. 1-2, (January 2001), pp. (16-22). ISSN 0009-2614.

Coopera, C.A., Younga, R.J., & Halsallb, M. (2001). Investigation into the deformation of carbon nanotubes and their composites through the use of Raman spectroscopy. *Compos. PartA,* Vol. 32, No. 3-4, (March, April 2001), pp. (401-411). ISSN 1359-835X.

Craley, C. R., Zhang, R., Kowalewski, T., McCullough, R. D. & Stefan, M, C. (2009). Regioregular Poly(3-exylthiophene) in a Novel Conducting Amphiphilic Block Copolymer. *Macromol. Rapid Commun*. Vol. 30, No. 2, (Jannary 2009) pp (11-16). ISNN 200800487.

Dewar, M.J.S., Zoebish, E.G., Healy, E.F., & Stewart, J.J.P. (1985). Development and use of quantum mechanical molecular models. 76. AM1: a new general purpose quantum mechanicalmolecular model. *J. Am. Chem. Soc.,* Vol. 107, No. 13, (1985) ,pp. (3902-3909).

DiCesare, N., Belletete, M., Marrano, C., Leclerc, M., & Durocher, G. (1998). Conformational Analysis (ab initio HF/3-21G*) and Optical Properties of Symmetrically Disubstituted Terthiophenes. *J. Phys. Chem. A.,* Vol. 102, No. 26, pp. (5142-5149). ISSN 1089-5639.

Dobruchowska, E., Glowacki, I., Ulanski, J., Sanetra, J. & Pielichowski, J. (2008). Thermoluminescence of poly(9-vinylcarbazole) modified by substitution with halogens. *J.Chem. Phys.,* Vol. 348, No. 1-3, (June 2008), pp. (249-253). ISSN 0301-0104.

Dresselhaus, M.S., Dresselhaus, G., Saito, R., & Jorio, A. (2005). Raman spectroscopy of carbone naotubes. Phys. Rep., Vol. 409, No. 2, (March 2005), pp. (47-99). ISSN 0370-1573.

Eklund, P.C., Holden, J.M. & Jishi, R.A. (1995). Vibrational modes of carbon nanotubes; spectroscopy and theory. *Carbon,* Vol. 33, No. 7, (1995), pp. (959-972). ISSN 0008-6223.

Fantini, C., Cassimiro, J., Peressinotto, V.S.T., Plentz, F., Filho, A.G.S., Furtado, C.A., &Santos, A.P. (2009). Investigation of the light emission efficiency of single-wall carbon nanotubes wrapped with different surfactants. *Chem. Phys. Lett.,* Vol. 473, No. 1-3, (April 2009), pp. (96-101). ISSN 0009-2614.

Frisch, M.J., Trucks, G.W., Schlegel, H.B., Scuseria, G.E., Robb, M.A., Cheeseman, J.R., Zakrzewski, V.G.Jr., Montgomery J.A., Stratmann, R.E., Burant, J.C., Dapprich, S., Millam, J.M., Daniels, A.D., Kudin, K.N., Strain, M.C., Farkas, O., Tomasi, J., Barone, V., Cossi, M., Cammi, R., Mennucci, B., Pomelli, C., Adamo, C., Clifford, S., Ochterski, J., Petersson, G.A., Ayala, P.Y., Cui, Q., Morokuma, K., Malick, D.K., Rabuck, A.D., Raghavachari, K., Foresman, J.B., Cioslowki, J., Ortiz, J.V., Stefanov, B.B., Liu, G., Liashenko, A., Piskorz, P., Komaromi, I., Gomperts, R., Martin, R.L., Fox, D.J., Keith, T., Al-Laham, M.A., Peng, C.Y., Nanayakkara, A., Gonzalez, C., Challacombe, M., Gill, P.M.W., Johnson, B., Chen, W., Wong, M.W., Andres, J.L., Head-Gordon, M., Replogle, E.S., Pople, J.A., GAUSSIAN 98, Gaussian Inc., Pittsburgh, PA (1998).

Ganter, M.J., Landi, B.J., Worman, J.J., Schauerman, C.M., Cress, C.D., & Raffaelle, R.P. (2009). Variation of single wall carbon nanotube dispersion properties with alkyl amide and halogenated aromatic solvents. *Mater. Chem. Phys.* Vol. 116, No. 1, (July 2009), pp. (235-241). ISSN 0254-0584.

Huang, J. E., Li, X.H., Xu, J.C. & Li, H.L. (2003). Well-dispersed single-walled carbon nanotube/polyaniline composite films. *Carbon,* Vol. 41, No. 14, (2003), pp. (2731-2736). ISSN 0008-6223.

Journet, C., Alvarez, L., Micholet, V., Guillard, T., Chapelle, M. L., Anglaret, E., Sauvajol, J.L., Lefrant, S., Bernier, P., Laplaze, D., Flamant, G., & Loiseau, A. (1999). Single walled carbon nanotubes: two ways of production. *Synt. Met.,*Vol. 103, No. 1-3, (June 1999), pp. (2488-2489).ISSN 0379-6779.

Kawano, K., Sakai, J., Yahiro, M. & Adachi, C. (2009). Effect of solvent on fabrication of active layers in organic solar cells based on poly(3-hexylthiophene) and fullerene derivatives. *Sol. Energy Mater. Sol. Cells*, Vol. 93, No. 4, (April 2009), pp. (514–518). ISNN 0927-0248.

Kim, U. J.; Liu, X. M.; Furtado, C. A.; Chen, G.; Saito, R.; Jiang, J.; Dresselhaus, M. S, Eklund, P. C. (2005). Infrared-Active Vibrational Modes of Single-Walled Carbon Nanotubes. *Phys. Rev. Lett.,* Vol. 95, No. 15, (October 2005), pp. (157402). ISSN 10-1103.

Lau, K.-t.; Lu, M.; Lam C.-k., Cheung H.-y., Sheng; F.-L, Li, H.-L., (2005). Thermal and mechanical properties of single-walled carbon nanotube bundle-reinforced epoxy nanocomposites: the role of solvent for nanotube dispersion. *Compos. Sci. and Tech.* Vol. 65, No. 5 (April 2005) pp. (719–725). ISSN 0266-3538.

Lee, C., Yang, W., & Parr, R.G. (1998). Development of the Colle-Salvetti correlation-energy formula into a functional of the electron density. *Phys. Rev. B.,* Vol. 37, No. 2, (January 1988), pp. (785-789).

Li, C., Liu, C. , Li, F. & Gong, Q. (2003). Optical limiting performance of two soluble multi-walled carbon nanotubes. *Chem. Phys. Lett.,* Vol. 380, No 1-2, (October 2003), pp. (201-205). ISSN 0009-2614.

Massuyeau, F., Aarab, H., Mihut, L., Lefrant, S., Faulques, E. & Wéry. J., (2007). Optical Properties of Poly(para-phenylenevinylene) and single-walled Carbon Nanotube composite films : effects of conversion temperature, prucursor dilution and nanotube concentrations. *Phys.Chem.C.* Vol. 111, (September 2007), pp. (15111-15118). ISNN jp074635x CCC.

McCullough, R. (1998). The Chemistry of Conducting Polythiophenes. *Adv. Mater*, Vol. 10, No. 2, (Jannary 1998), pp. (93-116). ISNN 0201-0093.

Meng, L., Fu, C., & Lu, Q. (2009). Advanced technology for functionalization of carbonNanotubes. *Prog. Nat. Sci.,* Vol. 19, No. 7, (July 2009), pp. (801-810). ISSN 1002-0071.

Moisan ,J.-Y; Andre, B; Lever, R; (1991) Xerographic dark discharge of PVK-TNF photoconductive. *Mater. Chem. Phys*., Vol. 153, No. 1-2, (May 1991) pp. 305-312. ISSN 0301-0104.

Mulazzi, E., Perogo, R., Wery, J., Mihut, L., Lefrant, S., & Faulques, E. (2006). Evidence of temperature dependant charge migration on conjugated segment in poly-p-phenylene vinylene and single-walled carbon nanotubes. *J. chem. phys.,* Vol. 125, No. 1, (July 2006), pp. (1-014703.6). ISSN 0021-9606.

Nam, N.P.H., Cha, S.W., Kim, B.S., Choi, S.H., Choi, D.S. & Jin, J. I. (2002).Photoluminescence and electroluminescence properties of poly(9-vinylcarbarzole) doped with Anthracence derivatives containing bis(ethynylphenyl oxadiazole) or bis(vinylphenyl oxadiazole) substituents. *Synt. Met.,* Vol. 130, No. 3, (October 2002), pp. (271-277). ISSN 0379-6779.

On chan, H. S. & Ng, S. C. (1998). Synthesis, characterization and applications of thiophene-Based functional polymers. *Prog. Polym. Sci.* Vol. 23, No.7, (Novembre 1998), pp. (1167–1231). ISNN 0079–6700.

Pana, J.-H., Chiub, H.-L., & Wang, B.-C. (2005). Theoretical investigation of carbazole derivatives as hole-transporting materials in OLEDs. *J. Mol. Struct.: THEOCHEM,* Vol. 725, No. 1-3, (July 2005), pp. (89-95). ISSN 0166-1280.

Park, C., Ounaies, Z.,Watson, A. K., Crooks, E. R., Smith, J. J., Lowther, E.S., Connell, W.J., Siochi, J. E., Harrison, S J., Clair, L.S. T., (2002). Dispersion of single wall carbon nanotubes by in situ polymerization under sonication. Chem. Phys. Lett. Vol. 364, N.o 3-4, (October 2002), pp. (303–308). ISSN 0009-2614.

Pei, N., Zhang, X.T., Li, Y.C., Huang, Y.B. & Mo, Y.J. (1999). A study of poly (vinylcarbazole) adsorbed on silver surface by SERS. *Vibra. Spectro.,* Vol. 21, No. 1-2, (December 1999), pp. (39-43). ISSN 0924-2031.

Pickholz, M., & dos Santos, M.C. (1999). Interchain and correlation effects in oligothiophenes. *Synt. Met.,* Vol. 101, No. 1-3, (May 1999), pp. (528-529). ISSN 0379-6779.

Pietro, W.J., Francl, M.M., Hehre, W.J., Defrees, D.J., Pople, J.A. & Binkley, J.S. (1982). Self-consistent molecular orbital methods. 24. Supplemented small split-valence basis

sets for second-row elements. *J. Am. Chem. Soc.,* Vol. 104, No. 19, (1982), pp. (5039-5048).

Popov, V.N. (2003). Carbon nanotubes : properties and application. *Mater. Sci. Eng.,* Vol. 43, No. 3, (January 2004), pp. (61-102). ISSN 0927-796X.

Qui, Y., Duan, L., Hu, Xiaoming, Zhang, D., Zheng, M. & Bai, F. (2001). Electroluminescence enhancement by blending PVK with an alternating copolymer containing triphenylamine and phenylene units. *Synth. Met.*,Vol.123, No. 1, (August 2001), pp (39-42). ISNN) 0379-6779.

Rao, A. M., Richter, E., Bandow, S., Chase, B., Eklund, P. C., Williams, K. A., Fang, S., Subaswamy, K., Menon, M., Thess, A., Smalley, R. E., & Dresslhaus, G. (1996). Diameter-Selective Raman Scattering from Vibrational Modes in Carbon Nanotubes. *Sci.,* Vol. 275, No. 5297, (January 1997), pp. (187-191). ISSN 0036-8075.

Rao, A.M., Eklund, P.C., Bandow, S., Thess, A. & Smalley, R.E. (1997). Evidence for chargetransfer in doped carbon nanotube bundles from Raman scattering. *Nature,* Vol. 388, No. (July 1997), pp. (257-259). ISSN 0028-0836.

Rao, A.M. , Chen, J. , Richter, E. , Schlecht, U. , Eklund, P.C. , Haddon, R.C., Venkateswaran, U.D., Kwon, Y. K. & Tomanek, D. (2001). Effect of van der Waals Interactions on the Raman Modes in Single Walled Carbon Nanotubes. *Phys. Rev. Lett.,* Vol. 86, No. 17, (April 2001), pp. (3895-3898). ISSN 0031-9007.

Ryabenko, A.G., Dorofeeva, T.V., & Zvereva, G.I. (2004). UV–VIS–NIR spectroscopy study of sensitivity of single-wall carbon nanotubes to chemical processing and Van-der-Waals SWNT/SWNT interaction. Verification of the SWNT content measurements by absorption Spectroscopy. *Carbon,*Vol. 42, No. 8-9, (2004), pp. (1523-1535). ISSN 0008-6223

Safoula, G., Touihri, S., Bernede, J.C., Jamali, M., Rabiller, C., Molinie, P., & Napo, K. (1998). Properties of the complex salt obtained by doping the poly(N-vinylcarbazole) with bromine. *Polym.,* Vol. 40, No. 2, (1999), pp. (531-539). ISSN 0032-3861.

Saunders, B.R., Turner, M.L. (2007). Nanoparticle–polymer photovoltaic cells. *Adv. Colloid Interface Sci.,*Vol. 138, No. 1, (April 2008), pp. (1-23). ISSN 0001-8686.

Schroder, E.; Hyldgaard, P. (2003) Van der Waals interactions of parallel and concentric nanotubes, *Mat. Sci. Eng*., C 23, No 6-8 (December 2003), pp. (721–725). ISSN 0928-4931.

Stewart, J.J.P., Quantum chemistry program exchange, No. 455, Mopac 2000 © Fujitsu limited, Tokyo, Japan (1999).

Tam, P.D., Hieu, N.V., Chien, N.D., Le, A.-T., & Tuan, M.A. (2009). DNA sensor development based on multi-wall carbon nanotubes for label-free influenza virus (type A) detection. *J. Immunol. Methods,* Vol. 350, No.1-2, (October 2009), pp. (118-124). ISSN 0022-1759.

Tang, A.; Teng, F., Xiong; S., Hou, Y.; (2008). Spectral studies of thin films based on poly(N-vinylcarzole) and red dopant (January 2008), *Appl. Surf. Sci*. 254 (January 2008), issue 7 pp. (2043-2047). ISSN 0169-4332.

Touhri, S., Safoula, G., Leny, R., Bernede, J.C., (1997). Comparison of the properties of iodine-doped poly(N-vinylcarbazole)(PVK) thin films obtained by evaporation of pure powder followed byiodine post-deposition doping and iodine pre-doped powder. *Thin Solid films*, vol 304, No (April 1997), pp. (16-23).ISSN 0040-6090.

Tripisciano, C., Kraemer, K., Taylor, A., & Palen, E.B. (2009). Single-wall carbon nanotubes based anticancer drug delivery system. *Chem. Phys. Lett.,* Vol. 478, No. 4-6, (August 2009), pp.(200-205). ISSN 0009-2614.

Trzaskowski, B., Jalbout, A.F. & Adamowicz, L. (2007). Functionalization of carbon nanocones by free radicals: A theoretical study. *Chem. Phys. Lett.,* Vol. 444, No. 4-6, (August2007), pp. (314-318). ISSN 0009-2614.

Upadhyay, P., Ramrakhiani, M., & Bisen, D.P. (2008). Photoluminescence and electroluminescence studies of polyvinylcarbazole films. *J. Lumines.,* Vol. 128, No. 10, (October 2008), pp. (1595-1600). ISSN 0022-2313.

Wang, C., Guo, Z.X., Fu, S., Wu, W. & Zhu, D. (2004). Polymers containing fullerene or carbon nanotube structures. *Prog. Polym. Sci.,* Vol. 29. No. 11, (November 2004), pp. (1079-1141). ISSN 0079-6700.

Wéry, J., Aarab, H., Lefrant, S., Faulques, E., Mulazzi, E. & Perego, R. (2003). Photoexcitations in compositrs of poly(paraphenylene vinylene) and single–walled carbon nanotubes. *Phys. Rev. B*. Vol. 67, (March 2003), pp. (115202-115207). ISNN 115202(6).

Wise, K.E., Park, C., Siochi, E.J., & Harrison, J.S. (2004). Stable dispersion of single wall carbon nanotubes in polyimide: The role of non covalent interactions. *Chem. Phys. Lett.* Vol.391, No. 4-6, (June 2004). pp. (207-211). ISSN 0009-2614.

Wongchoosuk, C., Udomvech, A., & Kerdcharoen, T. (2009). The geometrical and electronic structures of open-end fully functionalized single-walled carbon nanotubes. *Curr. App. Phys.,* Vol. 9, No. 2, (March 2009), pp. (352-358). ISSN 1567-1739.

Wu, W., Li, J., Liu, L., Yanga, L., Guo, Z.-X., Dai, L., & Zhu, D. (2002). The photoconductivity of PVK-carbon nanotube blends. *Chem. Phys. Lett.*,Vol. 364, No.1-2, (September 2002), pp. (196-199). ISSN 0009-2614.

Wu, H.X., Qiu, X.Q., Cai, R.F. & Qian, S.X. (2007). Poly(N-vinyl carbazole)-grafted multiwalled carbon nanotubes: Synthesis via direct free radical reaction and optical limiting properties. *App. Surf. Sci.,* Vol. 253, No. 11, (March 2007), pp. (5122-5128). ISSN 0169-4332.

Yang, L., Feng, J.-K. , Ren, A.-M. , Sun, J.-Z. (2006). The electronic structure and optical properties of carbazole-based conjugated oligomers and polymers, a theoretical investigation. *Polym.* Vol. 47, No. 4, (February 2006), pp. (1397-1404). ISSN 0032-3861.

Yap, C.C., Yahaya, M. & Salleh, M.M. (2009). Influence of tetrabutylammonium hexafluorophosphate (TBAPF6) doping level on the performance of organic light emitting diodes based on PVK:PBD blend films. *Curr. App. Phys*., Vol. 9, No. 4, pp. (Jully 2009), (722–726). ISNN 0379-6779.

Yoon, S. J., Chun, H., Lee, M. S. & Kim. N. (2008). Preparation of poly(*N*-vinylcarbazole) (PVK) nanoparticles by emulsion polymerization and PVK hollow particles. *Synth. Met*. Vol. 159, No.5-6, (March 2009) pp. (518-522). ISNN 0254-0584.

Yuna, D., Feng, W., Wu, H., Li, B. , Liu, X., Yi, W., Qiang, J., Gao, S., & Yan, (2008) Controllable functionalization of single-wall carbon nanotubes by in situ polymerization method for organic photovoltaic devices. *Syn. Met.* Vol. 158, No. 21-24, (December 2008), pp. (977-983). ISSN 0379-6779.S.

Zaidi, B., Bouzayen, N., Wéry, J., Alimi, K., (2010). Grafting of oligo-N-vinyl carbazole on single walled carbon nanotubes. *J. Mol. Struc*., vol. 971, No. 1-3 (May 2010), pp. (71-80). ISSN 0022-2860.

Zaidi, B., Bouzayen, N., Wéry, J., Alimi, K., (2011). Annealing treatment and carbon nanotubes concentration effects on the optical and vibrational properties of single walled carbon nanotubes functionalized with short oligo-N-vinyl carbazole. *Mter. Chem.phys*., vol. 126, No. 1-2 (March 2011), pp. (417-423). ISSN 0254-0584.

Zheng, Q., Xia, D., Xue, Q., Yan, K., Gao, X., & Li, Q. (2008). Computational analysis of effect of modification on the interfacial characteristics of a carbon nanotube–polyethylene composite system. *Appl. Surf. Sci.,* Vol. 255, No. 6, (January 2009), pp. (3534-3543). ISSN 0169-4332.

Zhu, H., Wei, J., Wang, K. & Wu, D. (2009). Applications of carbon materials in photovoltaic solar cells. *Sol. Energy Mater*. Sol. Cells, Vol. 93, No. 9, (Septembre 2009), pp 1461–1470. ISNN 0927-0248.

16

Giant Moment Enhancement of Magnetic Nanoparticles Embedded in Multi-Walled Carbon Nanotubes: Consistent with Ultrahigh Temperature Superconductivity

Guo-meng Zhao[1,2], JunWang[2], Yang Ren[3] and Pieder Beeli[1]
[1] *Department of Physics and Astronomy, California State University at Los Angeles, Los Angeles*
[2]*Department of Physics, Faculty of Science, Ningbo University, Ningbo*
[3]*X-Ray Science Division, Advance Photon Source, Argonne National Laboratory, Argonne*
[1,3]*USA*
[1,2]*P. R. China*

1. Introduction

There are reports of intrinsic weak ferromagnetism in graphite and carbon-based materials well above room temperature Cervenka et al. (2009); Esquinazi et al. (2003); Kopelevich et al. (2000); Mendoza et al. (1999); Moehlecke et al. (2002); Mombru et al. (2005), as well as a theoretical prediction of a ferromagnetic instability in graphene sheets Bas & Jafari (2002). On the other hand, Dzwilewski *et al.* Talyzin et al. (2007) show that the observed high-temperature ferromagnetism in rhombohedral C_{60} Makarova et al. (2001) is not intrinsic but caused by contamination of magnetic impurities. In addition to the observation of unusual high-temperature ferromagnetism in the carbon-based materials, there was a report of extra magnetic moment induced in graphite due to a large magnetic proximity effect between graphite and magnetic nanoparticles Coey et al. (2002). Similarly, high-temperature magnetic data of multi-walled carbon nanotube (MWCNT) mat samples embedded with Fe and Fe_3O_4 nanoparticles Zhao et al. (2008) indicated that the room-temperature saturation magnetizations of the magnetic nanoparticles embedded in the MWCNTs are enhanced by a factor of about 3 as compared with what they would be expected to have for free magnetic nanoparticles. Recently, the study has been extended to nickel nanoparticles embedded in MWCNTs Wang et al. (2010) and shown a similar enhancement factor.

More intriguringly, there were reports of ultrahigh temperature superconducting behaviors in carbon films Antonowicz (1974); Lebedev (2004), carbon nanotubes Zhao & Wang (2001); Zhao (2004; 2006), graphite Kopelevich et al. (2000), and graphite-sulfur composites Da Silva et al. (2001); Moehlecke et al (2004). Highly oriented pyrolithic graphite (HOPG) was shown to display either a partial superconducting or a ferromagnetic-like response to an applied magnetic field up to 400 K Kopelevich et al. (2000).

The existence of ultrahigh temperature superconductivity in the carbon-based materials is not accidental. The unique electronic structures of the carbon-based materials make them

ideal for high-temperature superconductivity. Several theoretical models based on different types of interactions predict high-temperature superconductivity in quasi-one-dimensional (quasi-1D) and/or quasi-two-dimensional (quasi-2D) electronic systems. Alexandrov and Mott Alexandrov & Mott (1995) demonstrated that strong electron-phonon coupling can lead to the formation of intersite bipolarons and that the Bose-Einstein condensation of the bipolarons can explain high-temperature superconductivity in cuprates. Little Little (1964) proposed that high-temperature or room-temperature superconductivity could be realized by exchanging high-energy excitons in quasi-1D systems. Lee and Mendoza showed that superconductivity as high as 500 K can be achieved through a pairing interaction mediated by undamped acoustic plasmon modes in quasi-1D systems Lee & Mendoza (1989). High-temperature superconductivity can also occur in a multi-layer electronic system due to an attraction of charge carriers in the same conducting layer via exchange of virtual plasmons in neighboring layers Cui & Tsai (1991). If the plasmon-mediated pairing mechanisms are relevant, one should be able to find high-temperature superconductivity in quasi-one-dimensional and/or multi-layer systems such as cuprates, carbon nanotubes (CNTs), and graphites. In contrast to the mechanisms based on the attractive interactions between electrons by virtually exchanging phonons, excitons, and/or plasmons, an exotic model based on resonating-valence-bond (RVB) theory originally proposed by Anderson Anderson (1987) even predicts ultrahigh temperature *d*-wave superconductivity in heavily doped graphene Black-Schaffer & Doniach (2007). Gonzalez *et al.* Gonzalez et al. (2001) showed that both high-temperature ferromagnetic and *p*-wave superconducting instabilities can occur in defective regions of graphite, where topological disorder enhances the density of states. Schrieffer Schrieffer (2004) predicted ultrahigh temperature superconductivity at a quantum critical point where ferromagnetic fluctuations are the strongest.

In this article, we will present the detailed magnetic properties of multi-walled carbon nanotubes embedded with Ni Wang et al. (2010), Fe Zhao et al. (2008; 2011), Fe_3O_4 Zhao et al. (2008; 2011), and Fe_3C magnetic nanoparticles. Magnetic measurements were carried out using Quantum Design vibrating sample magnetometer (VSM). Inductively coupled plasma mass spectrometer and high energy synchrotron x-ray diffractometer were used to accurately determine the impurity concentrations. Scanning electron microscope and/or transmission electron microscopy were used to characterize MWCNTs and magnetic nanoparticles embedded. In sections 2,3, and 4, we will present the detailed experimental results for multi-walled carbon nanotubes embedded with Fe_3C, Ni, Fe, and Fe_3O_4 magnetic nanoparticles. We found that the saturation magnetizations of Fe, Fe_3O_4, and Ni magnetic nanoparticles are enhanced by a factor of about 3 as compared with what they would be expected to have for free magnetic nanoparticles. In contrast, a smaller enhancement factor (1.6) is found for Fe_3C nanoparticles. In section 5, we will provide possible theoretical interpretations to the giant moment enhancements. The results cannot be explained by a magnetic-proximity model but can be naturally explained in terms of ultrahigh temperature superconductivity in MWCNTs. In section 6, we will identify the diamagnetic Meissner effect in the magnetic field parallel to the tube axis up to room temperature for aligned MWCNTs that are physically separated and have negligibly small magnetic impurities. The magnitude of the Meissner effect is in quantitative agreement with the predicted penetration depth expected from the measured carrier density. In section 7, we will give concluding remarks and discuss possible microscopic mechanisms for high-temperature superconductivity in carbon nanotubes.

2. Magnetic properties of Fe_3C nanoparticles embedded in MWCNTs

Purified MWCNT mat samples (Catalog No. PD15L520) from Nanolab were synthesized by chemical vapor deposition under catalyzation of Fe nanoparticles. The average outer diameter is about 15 nm and the average inner diameter is about 10 nm. The morphology of the mat sample can be seen from scanning electron microscopy (SEM) image shown in Fig. 1a. The SEM image was taken by a field emission scanning electron microcopy (FE-SEM, Hitachi S-4800) using an accelerating voltage of 2 kV. One can see that the outer diameters of these MWCNTs are in the range of 10-20 nm and centered around 15 nm, in agreement with the product specification from Nanolab. Fig. 1b shows a transmission electron microscopic (TEM) image of the mat sample, which was provided by Nanolab. The image reveals the multiwall nature of the carbon nanotubes with a mean inner diameter of about 10 nm.

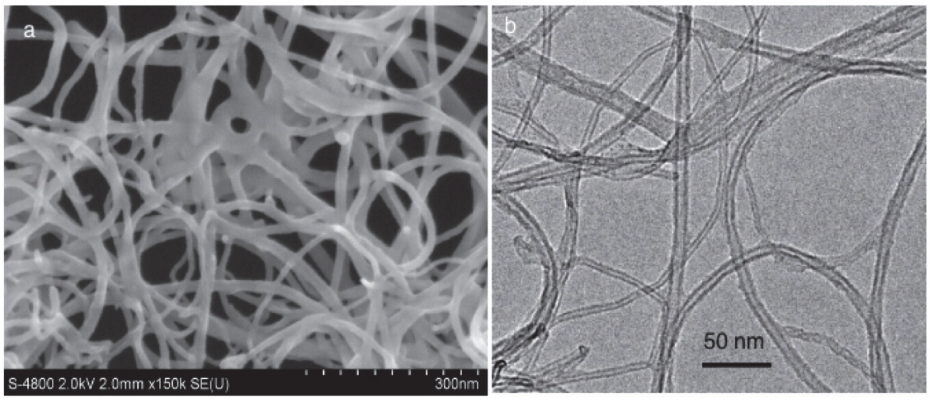

Fig. 1. a) SEM image of a MWCNT mat sample of PD15L520. b) TEM image of the MWCNT mat sample.

The total metal-based impurity concentrations of the mat sample can be determined from the composition analysis of the residual of the sample, which was obtained by burning off carbon-based materials in air. A Perkin-Elmer Elan-DRCe inductively coupled plasma mass spectrometer (ICP-MS) was used to analyze the composition of the residual. From the weight (3.6%) of the residual and the ICP-MS analysis, we obtain the metal-based magnetic impurity concentrations in weight: Ni = 0.01936%, Fe = 1.001%, and Co = 0.00102%. The Fe concentration determined from our ICP-MS is in excellent agreement with the product specification (Fe = 0.94%) from Nanolab.

Since the magnetic impurity phases are so minor, it is impossible to identify the minor phases from a normal low-energy x-ray diffraction (XRD) spectrum. But we can achieve this goal by performing high-energy synchrotron x-ray diffraction experiment. Fig. 2 shows synchrotron XRD spectrum for the mat sample along with the standard spectrum of Fe_3C. The XRD spectrum was taken on a high-energy synchrotron x-ray beam-line 11-ID-C at the Advanced Photon Source, Argonne National Laboratory, using monochromatic radiation with a wavelength of λ = 0.1078 Å. The major peaks in the spectrum of Fig. 2 correspond to the diffraction peaks of the MWCNTs Reznik et al. (1995) and Fe_3C. In particular, the (002) diffraction peak of the MWCNTs is seen at $2\theta = 1.786^\circ$.

Figure 3a shows XRD intensity as a function of the wave-vector transfer Q for the (002) peak of a pure MWCNT sample. The data are digitized from Reznik et al. (1995). The solid red

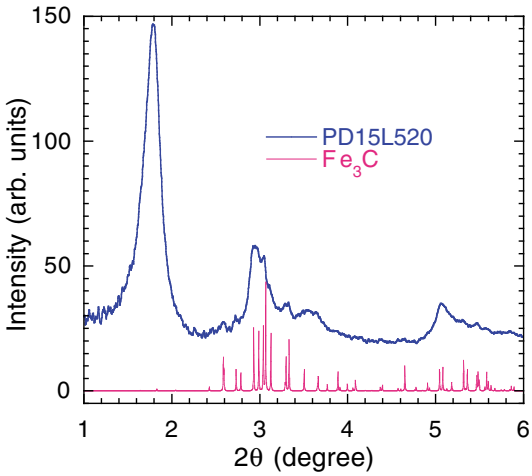

Fig. 2. High-energy synchrotron x-ray diffraction (XRD) spectrum for a virgin MWCNT sample of PD15L520 and the standard spectrum of Fe_3C.

line in Fig. 3a is the fitted curve by the sum of a Gaussian and a cut-off Lorentzian function, which takes into account both domain size broadening and strain broadening Reznik et al. (1995). The Lorentzian function is cut off to zero when $|Q - Q_\circ| \geq 3.65\gamma$, where $Q_\circ$ is the peak position and γ is the full width at half maximum (FWHM). The integrated intensity of the cut-off Lorentzian is 91.4% of the intensity of the corresponding full Lorentzian. In Fig. 3b, we display the expanded view of the (002) peak of our mat sample. We also fit the data with the sum of a Gaussian and a cut-off Lorentzian function (solid red line). It is apparent that the fit is excellent. In Fig. 3c and Fig 3d, we show the expanded views at 2θ around 2.6° and 3.3°, respectively. At 2θ around 2.6°, there are closely spaced double peaks, corresponding to the (121) and (210) diffraction peaks of the Fe_3C phase. The intensity of the (121) peak is higher than that of the (210) peak by a factor 1.52. The solid red line in Fig. 3c is the best fitted curve by the sum of two Gaussian functions with the intensity ratio of 1.52 and peak separation of 0.008°, which are consistent with the standard spectrum of the Fe_3C phase. The Gaussian function is consistent with particle-size broadening Reznik et al. (1995). From the best fit, we obtain γ = 0.0589° for both peaks. The integrated intensity of the two Gaussian peaks is calculated to be 0.501±0.035% of the intensity of the MWCNT (002) peak. Using the standard intensities of graphite's (002) peak and Fe_3C's (121) and (210) peaks and assuming that the intensity of MWCNT (002) peak is the same as that of graphite (002) peak, we find that the Fe_3C concentration is 0.935±0.065% (in weight). This corresponds to the Fe concentration of 0.874±0.061%, which is in good agreement the total Fe concentration (1.00%) determined from the ICP-MS above and also close to the product specification for the Fe concentration (0.94%). This implies that the dominant Fe-based phase is Fe_3C and the minor phases may also contain Fe and/or Fe oxides, which are not visible from the XRD spectrum.

Similarly, at 2θ around 3.3°, there are also closely spaced double peaks, corresponding to the (131) and (221) diffraction peaks of the FeC_3 phase. The intensity for the (131) peak is 2/3 of that for the (221) peak. The solid red line in Fig. 3d is the best fitted curve by the sum of two Gaussian functions with the intensity ratio of 2/3 and peak separation of 0.038°. The peak widths are kept the same as those of the (121) and (210) peaks. The integrated intensity of the double Gaussian peaks is calculated to be 0.811±0.024% of the intensity of the MWCNT (002)

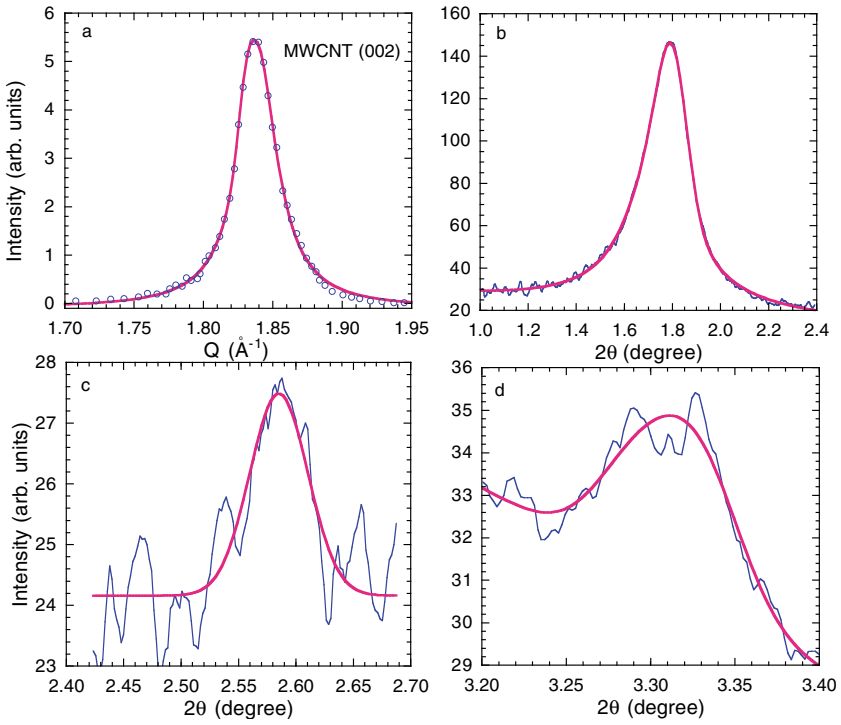

Fig. 3. a) The XRD intensity as a function of the wave-vector transfer Q for the (002) peak of a pure MWCNT sample. The data are digitized from Reznik et al. (1995). b) The expanded view of the MWCNT (002) peak of sample PD15L520. c) The expanded view at 2θ around 2.6° of sample PD15L520. There are closely spaced double peaks, corresponding to the (121) and (210) diffraction peaks of the Fe_3C phase. d) The expanded view at 2θ around 3.3°. There are also closely spaced double peaks, corresponding to the (131) and (221) diffraction peaks of the FeC_3 phase.

peak. The intensity ratio implies that the Fe_3C concentration is 0.947±0.028% (in weight), in excellent agreement with that (0.935±0.065%) inferred from the (121) and (210) peaks above. It is important to determine the average diameter d of the ferromagnetic Fe_3C nanoparticles embedded in MWCNTs. We can determine d from the peak width of the XRD spectrum. The full width at half maximum has been found to be 0.0589°. Using the Scherrer equation: $d = 0.89\lambda/(\gamma_b \cos\theta)$ and the width $\gamma_b = 0.0546°$ (after correcting for the instrumental broadening), we calculate d = 10.0 nm, in good agreement with the average inner diameter of the tubes (see Fig. 1b).

Fig. 4a shows magnetization versus magnetic field for the MWCNT mat sample at 310 K. The magnetization was measured using a Quantum Design vibrating sample magnetometer. The linear field dependence of the magnetization with a negative slope at $H > 20$ kOe is due to the diamagnetic contribution. The linear extrapolation to $H = 0$ yields $M_s = 1.53$ emu/g. In Fig. 4b, we present temperature dependence of the saturation magnetization M_s for the mat sample. It is clear that the M_s value is small (0.05 emu/g) above the Curie temperature (about 470 K) of the Fe_3C phase. Therefore, the saturation magnetization for the Fe_3C phase is 1.47 emu/g.

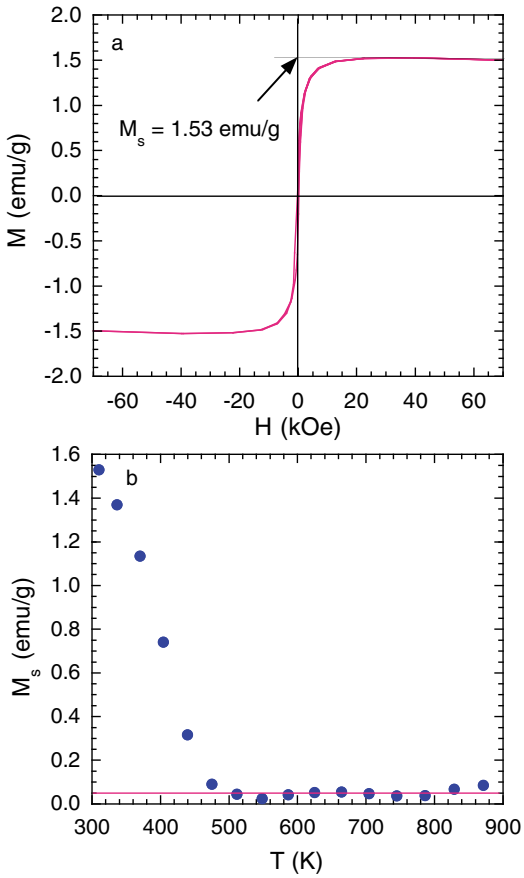

Fig. 4. a) The magnetization versus magnetic field for sample PD15L520 at 310 K. b) The temperature dependence of the saturation magnetization M_s for the mat sample.

With the Fe_3C concentration of 0.94±0.07%, we calculate the saturation magnetization to be 156±11 emu per gram of Fe_3C.

For 11-nm Fe_3C nanoparticles embedded in carbon matrix and prepared at 900 °C, M_s was found to be 89-97 emu per gram of Fe_3C and the reduced remanence is 0.16-25 [see Sajitha et al. (2007)]. The reduced remanence in our 10-nm Fe_3C nanoparticles embedded in MWCNTs is about 0.18, very close to those of the samples prepared at 900 °C. Therefore, M_s of our 10-nm Fe_3C nanoparticles embedded in MWCNTs is enhanced by a factor of 1.6±0.2, compared with that (93±4 emu/g) of free Fe_3C particles. This enhancement factor is significantly lower than those for Ni, Fe, and Fe_3O_4 nanoparticles (see below). It is interesting to note that sample CFe05980 of Sajitha et al. (2007), prepared at 980 °C, has a large M_s value of 169 emu per gram of Fe_3C. These authors tentatively attributed this large value to the proximity of the nanoparticles to carbon nanotubes, which may have been formed at this higher temperature. Our current results support this interpretation.

3. Magnetic properties of nickel nanoparticles embedded in MWCNTs

MWCNT mat samples embedded with nickel nanoparticles were obtained from SES Research of Houston (Catalog No. TS0636). The mat samples were synthesized by chemical vapor deposition under catalyzation of nickel nanoparticles. The morphology of the mat sample can be seen from scanning electron microscopy images shown in Fig. 5a and Fig. 5b. One can see that the mean outer diameter of these MWCNTs is around 35 nm. The mean inner diameter of the MWCNTs is about 15±5 nm, as seen from the transmission electron microscopy image (Fig. 5c) recorded by FEI Tecnai F20 with an accelerating voltage of 200 kV. The nickel nanoparticles sit inside the innermost shells near the ends of the tubes, as labeled by A, B, C, and D in Fig. 5d. Some nickel nanoparticles are connected to form a continuous chain (see a location labeled by D in Fig. 5d).

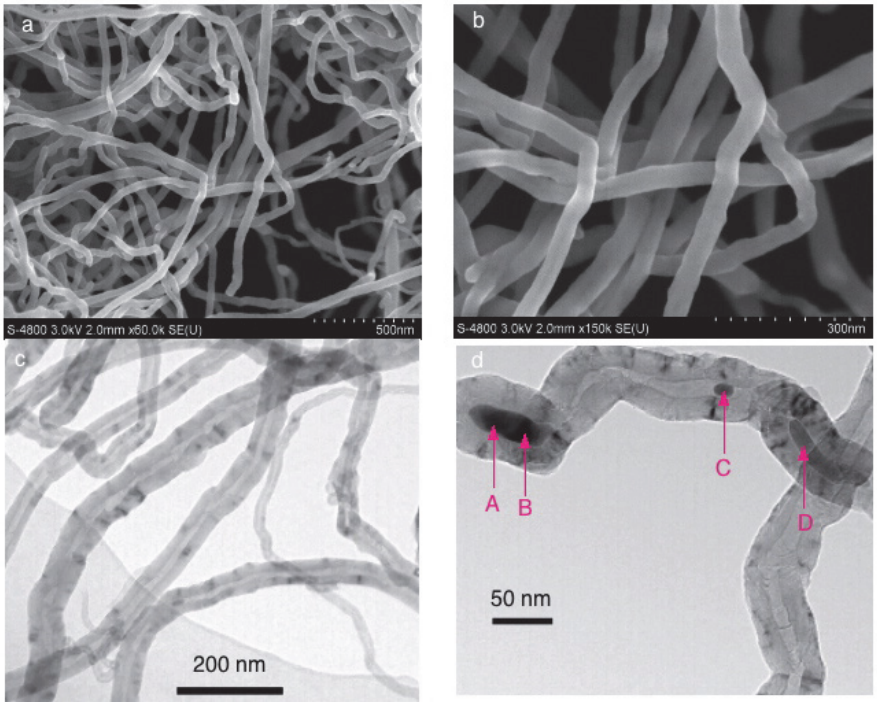

Fig. 5. a) SEM image of a MWCNT mat sample of TS0636. b) SEM image of the MWCNT mat sample with a higher magnification. c) TEM image of the MWCNT mat sample. c) TEM image of a selected MWCNT filled with nickel nanoparticles labeled by A, B, C, and D. After Wang et al. (2010).

The metal-based impurity concentrations of the mat sample were also determined from ICP-MS, which yielded the metal-based magnetic impurity concentrations in weight: Ni = 0.476%, Fe = 0.00907%, and Co = 0.0133%. The major impurity phase is nickel, in agreement with the sample preparation condition.

We also determined the concentration of the ferromagnetic phase of nickel from the high-energy synchrotron x-ray diffraction spectrum. Fig. 6a shows synchrotron XRD spectrum for a MWCNT sample of TS0636 along with the standard spectrum of the

face-centered cubic (fcc) phase of Ni. The major peaks in the spectrum of Fig. 6a correspond to the diffraction peaks of MWCNTs and the fcc phase of Ni. The Ni (311) peak is clearly seen at $2\theta = 5.815^{\circ}$.

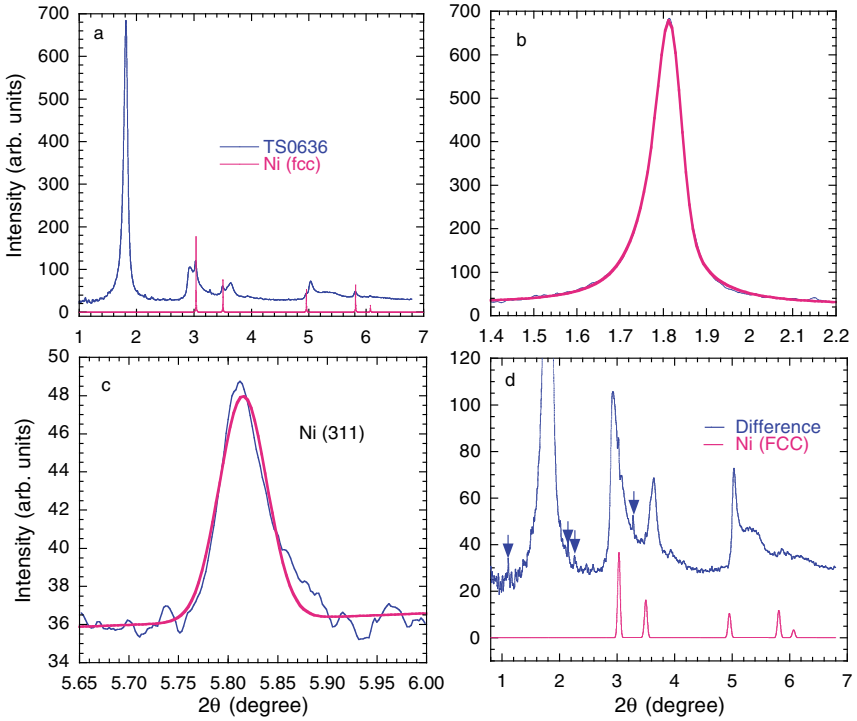

Fig. 6. a) High-energy synchrotron x-ray diffraction spectrum of sample TS0636 along with the standard spectrum of the face-centered cubic (fcc) phase of Ni. b) The expanded view of of the MWCNT (002) peak. c) The expanded view of of the Ni (311) peak. d) The expected XRD spectrum of the fcc Ni (red line) based on the nickel concentration (0.45%) and the difference spectrum (blue line), which is obtained by subtracting the Ni spectrum from the spectrum of TS0636 in Fig. 6a. After Wang et al. (2010).

Figure 6b and Fig. 6c display the expanded views of the MWCNT (002) and Ni (311) peaks, respectively. The solid red line in Fig. 6b is the fitted curve by the sum of a Gaussian and a cut-off Lorentzian function. The solid red line in Fig. 6c is the fitted curve by a Gaussian function. The integrated intensity of the Ni (311) peak is found to be $0.882\pm0.020\%$ of the intensity of the MWCNT (002) peak. From the intensity ratio, we find that the ferromagnetic fcc nickel concentration is $0.451\pm0.010\%$ (in weight), which is slightly lower than the total Ni concentration (0.476%) inferred from ICP-MS. This implies that the ferromagnetic fcc nickel is the dominant phase while the concentrations of other nonmagnetic nickel-based phases are too small to be seen in the XRD spectrum.

In order to check the reliability of our inferred ferromagnetic nickel concentration based on the Ni (311) peak, we show, in Fig. 6d, the expected XRD spectrum of the fcc Ni with the concentration of 0.451% (lower curve in Fig. 6d) and the difference spectrum (upper curve in Fig. 6d), which is obtained by subtracting the Ni spectrum from the spectrum of sample

TS0636 in Fig. 6a. The difference spectrum shows no observable residual of any peaks of the fcc nickel, implying that the inferred Ni concentration is indeed reliable. Furthermore, all the peaks except for some peaks indicated by arrows in the difference spectrum agree with the peaks observed in pure MWCNTs Reznik et al. (1995). The extra peaks indicated by the arrows should be associated with other impurity phases.
It is also essential to determine the average diameter d of the ferromagnetic Ni nanoparticles embedded in MWCNTs. The full width at half maximum of the Ni (311) peak is found to be 0.0556° from the Gaussian fit in Fig. 6c. Using the Scherrer equation: $d = 0.89\lambda/(\gamma_b \cos\theta)$ and the width $\gamma_b = 0.0511^\circ$ (after correcting for the instrumental broadening), we calculate d = 11 nm, close to the average inner diameter of the tubes (see Fig. 5c).

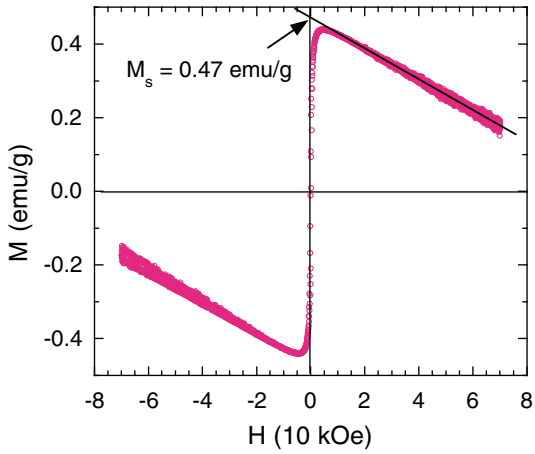

Fig. 7. Magnetic hysteresis loop of sample TS0636 at 320 K. After Wang et al. (2010).

Figure 7 shows magnetization versus magnetic field for the Ni-filled MWCNT mat sample at 320 K. The linear extrapolation to $H = 0$ yields $|\chi_{dia}| = 4.2\times10^{-6}$ emu/g and $M_s = 0.47$ emu/g. With the ferromagnetic nickel concentration of 0.451% in the Ni-filled MWCNT sample, we calculate the M_s value to be 104 emu per gram of nickel. The saturation magnetization of the 11-nm nickel nanoparticles embedded in MWCNTs is a factor of 3.4 larger than the known M_s = 30-32 emu/g for pure fcc Ni nanoparticles with d = 11-12 nm Chen &Hsieh (2002); Gong et al. (1991). It is also a factor of 1.9 larger than that (55 emu/g) for the bulk nickel. Thus, there is a giant magnetic moment enhancement of the Ni nanoparticles when they are embedded inside the MWCNTs, in contrast to the case for Fe_3C nanoparticles, where the enhancement factor is much smaller.

4. Magnetic properties of Fe and Fe_3O_4 nanoparticles embedded in MWCNTs

MWCNT mat samples embedded with Fe and Fe_3O_4 nanoparticles were obtained from SES Research of Houston (Catalog No. RS0657). The mat samples were synthesized by chemical vapor deposition under catalyzation of Fe nanoparticles. During purification process, some Fe nanoparticles were oxidized into the Fe_3O_4 and α-Fe_2O_3 phases and were removed by HCl. Nevertheless, some fractions of Fe, Fe_3O_4, and α-Fe_2O_3 nanoparticles may still remain inside and/or outside the tubes due to incomplete purification, in agreement with high-energy synchrotron x-ray diffraction data Zhao et al. (2011).

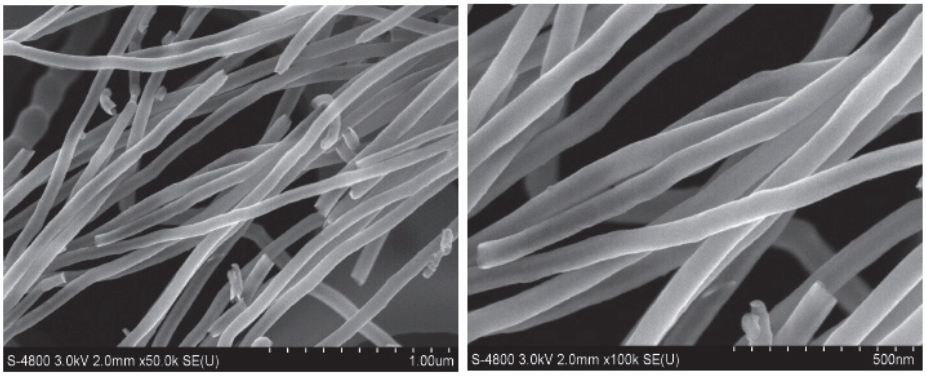

Fig. 8. SEM images of a MWCNT mat sample of RS0637.

The morphology of the mat sample can be seen from scanning electron microscopy images shown in Fig. 8. It is clear that the tubes are quite uniform and the mean outer diameter of these MWCNTs is about 70 nm. The mean inner diameter of the MWCNTs is estimated to be about 50 nm from the mean outer diameter and the mean wall thickness of the MWCNTs (about 10 nm) determined from the width of the XRD (002) peak Zhao et al. (2011).

The total metal-based impurity concentrations of the mat sample were determined from the ICP-MS analysis of the residual of the mat sample (1.73±0.05%), which was obtained by burning off carbon-based materials in air at 550 °C for about 10 minutes. The metal-based magnetic impurity concentrations in weight were found to be: Fe = 0.69±0.02%, Co = 0.0036±0.0001%, and Ni = 0.0021%. The major impurity phase is Fe, in agreement with the sample preparation condition.

Quantitative analyses on the high-energy XRD data Zhao et al. (2011) have shown that the mat sample contains (in weight): Fe = 0.241±0.004%; α-Fe_2O_3 = 0.216±0.015%, and Fe_3O_4 = 0.250±0.010%. The Fe concentration contributed from the α-Fe, α-Fe_2O_3, and Fe_3O_4 phases is calculated to be 0.58±0.02%, which is about 0.11±0.04% lower than the total Fe concentration (0.69±0.02%) determined from the ICP-MS. The mean diameters of Fe, α-Fe_2O_3, and Fe_3O_4 nanoparticles are 46 nm, 23 nm, and 18 nm, respectively.

The total Fe concentration determined from the ICP-MS is also in quantitative agreement with the magnetization data of the residual where α-Fe_2O_3 is the only possible Fe-based phase. We have shown Wang et al. (2011) that α-Fe_2O_3 nanoparticles can be completely reduced to the magnetic Fe_3O_4 phase after the sample was heated up to 1000 K during the magnetic measurement (due to a high vacuum environment inside the VSM system). In Fig. 9a, we plot the high-field (10 kOe) magnetization versus temperature (up to 1000 K) for the α-Fe_2O_3 nanoparticles. The mean diameter of the nanoparticles is about 60 nm, as determined from the width of the XRD (104) peak (see Fig. 9b). Upon heating the magnetization shows a rapid rise above 650 K, which is the onset temperature of the reduction of the weak ferromagnetic α-Fe_2O_3 to the ferrimagnetic Fe_3O_4 phase. Upon cooling, the magnetization data indicate a magnetic transition at about 850 K (see Fig. 9a), which is the same as the Curie temperature of the Fe_3O_4 phase. The XRD spectrum shown in Fig. 9c, which was taken right after the sample was removed from the magnetometer, confirms this. All the peaks can be indexed by the Fe_3O_4 phase except for the peaks indicated by stars, which represent a minor phase of FeO (less than 10%). From the magnetic hysteresis loop at 330 K (Fig. 9d), we obtain the coercive field H_C to be 87 Oe. After correction for about 10% of FeO and the small difference

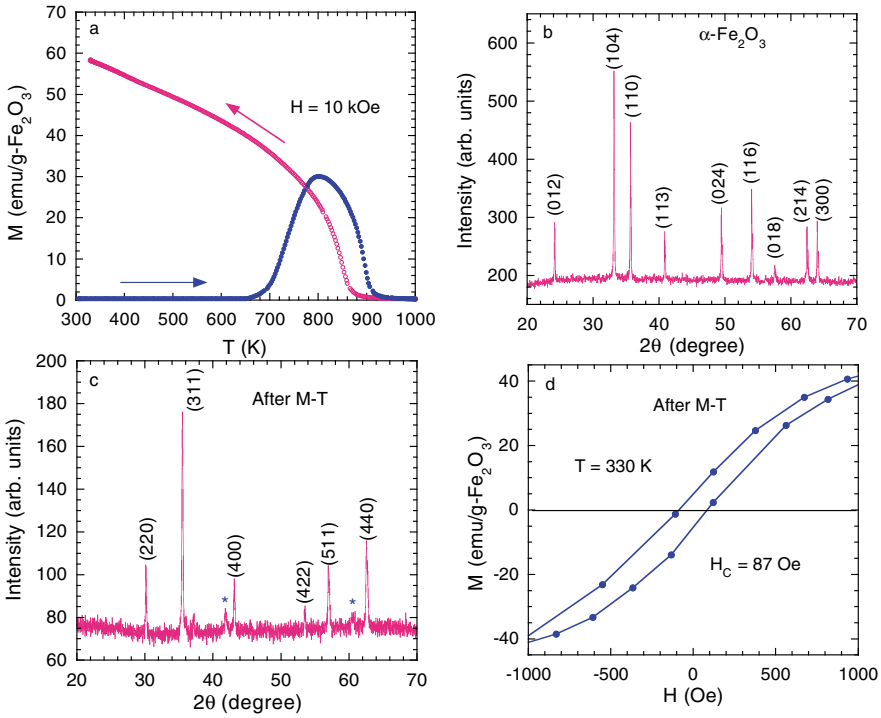

Fig. 9. a) High-field (10 kOe) magnetization versus temperature for α-Fe_2O_3 nanoparticles. b) X-ray diffraction spectrum of the α-Fe_2O_3 nanoparticles. c) XRD spectrum taken right after the sample was removed from the magnetometer. All the peaks can be indexed by the Fe_3O_4 phase except for the peaks indicated by stars, which represent a minor phase of FeO (less than 10%). d) Magnetic hysteresis loop taken at 330 K after the sample was cooled from 1000 K. After Wang et al. (2011).

in the atomic weights of Fe_3O_4 and Fe_2O_3, the saturation magnetization of the converted Fe_3O_4 phase is found to be about 68 emu/g-Fe_3O_4. Since the mean diameter of the converted Fe_3O_4 phase is about 45 nm, as determined from the (311) peak width, the inferred M_s for the 45-nm Fe_3O_4 nanoparticles is in quantitative agreement with the reported value (e.g., M_s = 65 emu/g-Fe_3O_4 and H_C = 156 Oe for d = 55 nm) Goya et al. (2003).

Figure 10a shows temperature dependence of the high-field magnetization for the residual of the mat sample. The magnetization was calculated according to the content of the α-Fe_2O_3 phase in the residual, which was determined by the ICP-MS. For the first run, the sample was heated up to 920 K and measured in a field of 20 kOe. For the second run, it was heated up to 1000 K and measured in a field of 10 kOe. The magnetization data suggest that the α-Fe_2O_3 phase in the residual was not completely reduced to the Fe_3O_4 phase after the first run possibly because the temperature of 920 K is not high enough. After the second run up to 1000 K, the remaining α-Fe_2O_3 phase should be completely reduced to Fe_3O_4 and the magnetization increases by about 34%. The final saturation magnetization at 320 K is about 67 emu/g-Fe_2O_3 or 69 emu/g-Fe_3O_4, which is about 10% larger than that (60 emu/g-Fe_2O_3) for the 60-nm α-Fe_2O_3 nanoparticles (see Fig. 9). The discrepancy should arise from larger

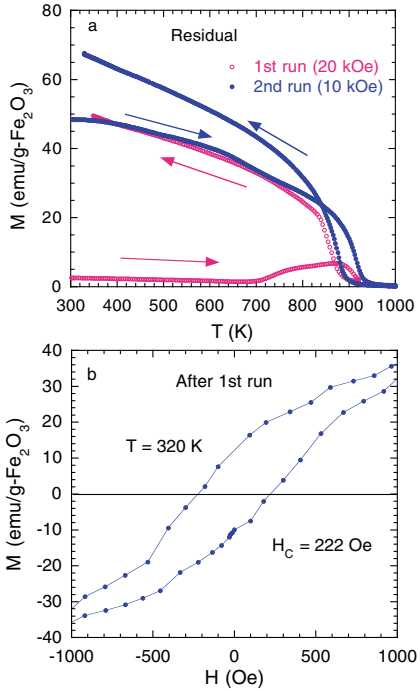

Fig. 10. a) High-field magnetization versus temperature for the residual of the mat sample. In the first run, the applied magnetic field is 20 kOe while in the second run the field is 10 kOe. b) Magnetic hysteresis loop taken at 320 K after the sample was cooled from 920 K in the first run.

particle sizes and higher coercive field of the converted Fe_3O_4 nanoparticles in the residual. The magnetic hysteresis loop shown in Fig. 10b yields H_C = 222 Oe, which is a factor of 2.5 larger than that for the 45-nm Fe_3O_4. By comparing the measured H_C = 222 Oe for the residual with the size dependence of H_C for Fe_3O_4 nanoparticles Goya et al. (2003), we estimate d = 100 nm and M_s = 70 emu/g-Fe_3O_4 for the converted Fe_3O_4 nanoparticles in the residual. Therefore, the magnetization data of the residual are in quantitative agreement with the Fe concentration determined by the ICP-MS.

Figure 11 shows zero-field-cooled (ZFC) and field-cooled (FC) susceptibility for sample RS0657. The sample was first heated up to 1000 K and cooled down to 320 K in a "zero" field. A magnetic field of 2.0 Oe was applied at 320 K and the ZFC susceptibility was measured upon warming up to 1000 K. The FC susceptibility was taken when the temperature is lowered from 1000 K to 320 K. The FC and ZFC susceptibilities clearly show a large thermal hysteresis up to the Curie temperature of about 850 K, which should be associated with the ferrimagnetic transition of the Fe_3O_4 impurity phase. Our previous data Zhao et al. (2008) showed a similar magnetic transition, but the transition temperature was around 1000 K, about 18% higher than that reported here. We have found that the systematically higher Curie temperatures reported in Zhao et al. (2008) arise from an undesirable thermal contact between the sample and the radiation shield (copper foil) of the heat stick. The current ZFC and FC susceptibility data were obtained when the sample was thermally insulated from the radiation shield. Incomplete

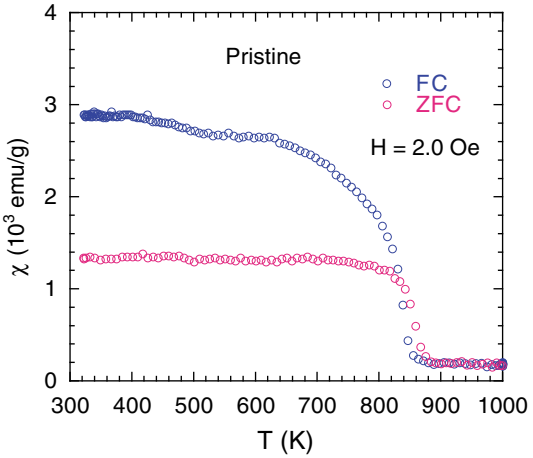

Fig. 11. Temperature dependencies of the zero-field-cooled (ZFC) and field-cooled (FC) susceptibility for a mat sample of RS0657.

thermal insulation always causes a thermal gradient between the sample and thermometer and special attention to this problem must be paid for sample mounting. Fortunately, this thermal gradient is found to be linearly proportional to $T-$ 300 K and can be corrected easily.

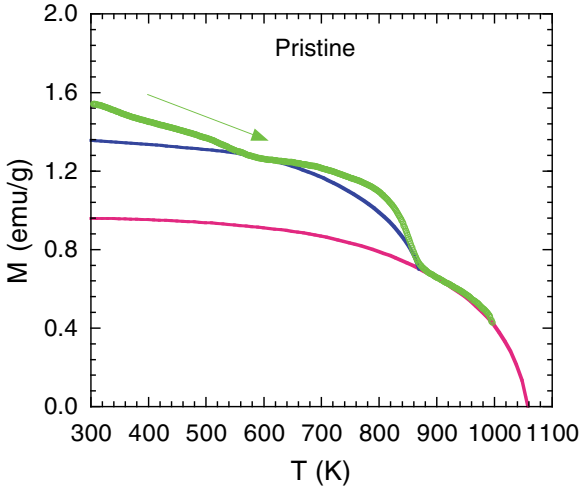

Fig. 12. Temperature dependence of the high-field (20 kOe) magnetization for a virgin sample of RS0657. The data are reproduced from Zhao et al. (2008) and the temperatures are corrected by matching the Curie temperature of the Fe_3O_4 impurity phase. The solid red line is a simulated curve for the Fe impurity phase with $M_s(300K)$ = 0.96 emu/g and T_C = 1056 K and the solid blue line fit is a simulated curve for the Fe_3O_4 impurity phase with $M_s(300K)$ = 0.40 emu/g and T_C = 870 K.

Figure 12 shows temperature dependence of the magnetization for a pristine sample of RS0657, which was measured upon heating in a magnetic field of 20 kOe. The data are

reproduced from Zhao et al. (2008) and the temperatures are corrected by matching the Curie temperature of the Fe_3O_4 impurity phase. Since the magnetization in 20 kOe is close to the saturation magnetization Zhao et al. (2008), the temperature dependence of the saturation magnetization is approximated by the temperature dependence of the magnetization in 20 kOe. It is clear that there are two major magnetic transitions associated with the ferrimagnetic Fe_3O_4 impurity phase and the ferromagnetic α-Fe impurity phase. We can identify the magnetic contributions of the Fe and Fe_3O_4 impurity phases by simulation of their magnetizations with the measured curve of $M_s(T)/M_s(0)$ versus T/T_C for ferromagnetic nickel. The solid red line is a simulated curve for the Fe impurity phase with $M_s(300K)$ = 0.96 emu/g and T_C = 1056 K and the solid blue line is a simulated curve for the Fe_3O_4 impurity phase with $M_s(300K)$ = 0.40 emu/g and T_C = 870 K. There is a significant difference between the data and simulated curve for Fe_3O_4 at temperatures above 640 K. This is caused by the reduction of the α-Fe_2O_3 phase to the Fe_3O_4 phase, as seen in Fig. 9. The remaining $M_s(300K)$ = 0.18 emu/g should contribute from the Fe_3C impurity phase with a Curie temperature of about 476 K, which is clearly seen in the FC susceptibility shown in Fig. 11.

With $M_s(300K)$ = 0.96 emu/g for the α-Fe phase with the concentration of 0.24% and mean diameter of 46 nm, we calculate the saturation magnetization to be 400 emu per gram of Fe. For free Fe nanoparticles with a mean diameter of 46 nm, the saturation magnetization can be extrapolated to be 160 emu per gram of Fe from the measured diameter dependence of $M_s(300K)$ Gong et al. (1991). It is apparent that the saturation magnetization of the 46-nm Fe nanoparticles embedded in MWCNTs is enhanced by a factor of about 2.5 compared with that of free Fe nanoparticles.

With $M_s(300K)$ = 0.40 emu/g for the Fe_3O_4 phase with the concentration of 0.25% and mean diameter of 18 nm, we calculate the saturation magnetization to be 160 emu per gram of Fe_3O_4. For free Fe_3O_4 nanoparticles with a mean diameter of 18 nm, the $M_s(300K)$ value can be inferred to be about 62 emu per gram of Fe_3O_4 from the measured diameter dependence of $M_s(300K)$ Goya et al. (2003). Then, the $M_s(300K)$ value of the 18-nm Fe nanoparticles embedded in MWCNTs is enhanced by a factor of about 2.6 compared with that of free Fe_3O_4 nanoparticles. This enhancement is almost the same as that for the 46-nm Fe nanoparticles embedded in MWCNTs within the experimental uncertainty.

For the Fe_3C impurity phase, the impurity concentration is $0.11\pm0.04\%$ and $M_s(300K)$ = 0.18 emu/g, so the saturation magnetization is calculated to be 165 ± 75 emu per gram of Fe_3C. The enhancement factor is difficult to estimate because the mean diameter of the Fe_3C nanoparticles is unknown and the concentration has a large uncertainty.

The moment enhancement factor of Fe_3O_4 nanoparticles can be also determined independently from the magnetization data of an annealed sample of RS0657. After annealing a pristine sample of RS0657 in air at 480 °C for about 5 minutes, most Fe and Fe_3O_4 nanoparticles have been oxidized into α-Fe_2O_3, as clearly demonstrated from Fig. 13a. The magnetic hysteresis loop at 305 K shows a saturation magnetization of 0.25 emu/g, which is dramatically reduced compared with that (1.54 emu/g) of the pristine sample. Fig. 13b shows the temperature dependence of the high-field magnetization for the annealed sample. After the sample was heated to 990 K, the α-Fe_2O_3 phase in the annealed sample was converted to the Fe_3O_4 phase, similar to the results shown in Figs. 9 and 10. At 980 K, the saturation magnetization is about 0.06 emu/g, which is reduced by a factor of about 8 compared with that of the pristine sample. This implies that only about 0.03% Fe impurity phase is left in the annealed sample. Therefore, after the annealed sample was cooled to 320 K, the total Fe_3O_4 concentration should be 0.91%. This implies that the room-temperature saturation magnetization of the converted Fe_3O_4 is 180 emu per gram of Fe_3O_4. Since the H_C value

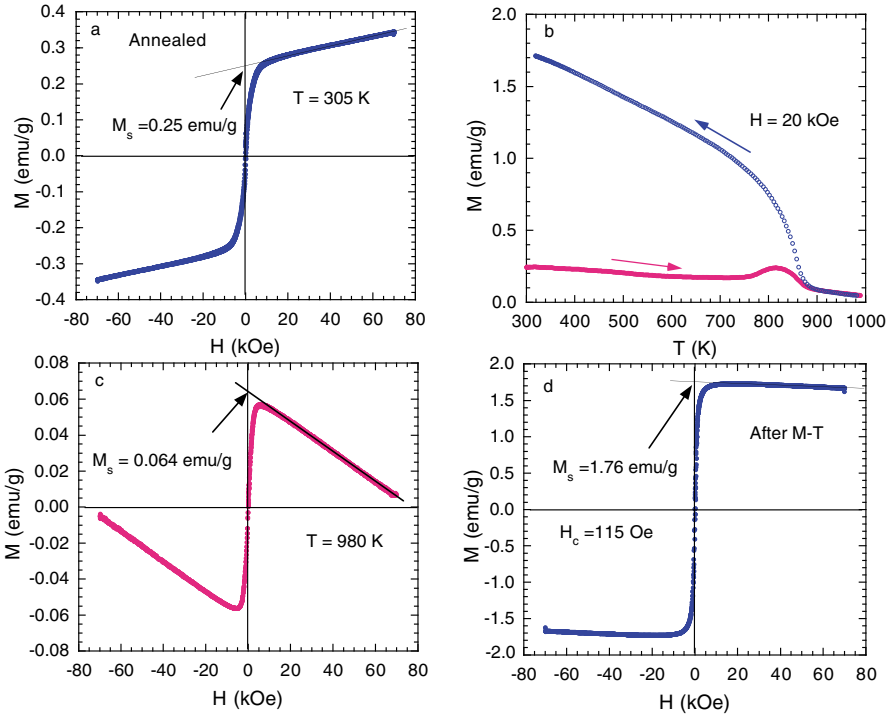

Fig. 13. a) Magnetic hysteresis loop at 305 K for an annealed sample of RS0657. b) Temperature dependence of the high-field (20 kOe) magnetization for the annealed sample. c) Magnetic hysteresis loop at 980 K for the annealed sample. d) Magnetic hysteresis loop taken at 320 K after the sample was cooled from 990 K.

of the converted Fe_3O_4 is 115 Oe, similar to that of the 55 nm Fe_3O_4 nanoparticles Goya et al. (2003), the $M_s(300K)$ value for the converted Fe_3O_4 nanoparticles would be about 65 emu per gram of Fe_3O_4 if they would be isolated from MWCNTs. This implies that the moment enhancement factor is 2.8, very close to the value deduced above.
Above results clearly demonstrate that the moment enhancement factor is nearly independent of the particle size. Furthermore, the moment enhancement factors for Ni, Fe, and Fe_3O_4 nanoparticles are all close to 3, independent of the mean particle diameters that are varied from 11 nm to 46 nm.

5. Plausible interpretations of the giant moment enhancements

We have precisely determined the magnetic impurity concentrations from the high-energy x-ray diffraction spectra, which are all in quantitative agreement with those determined independently from ICP-MS. These analyses along with the magnetic data allow us to precisely determine the saturation magnetizations for various magnetic nanoparticles embedded in MWCNTs. It turns out that the saturation magnetizations for all the nanoparticles embedded in MWCNTs are greatly enhanced compared with those of free (unembedded) nanoparticles. For 10-nm Fe_3C, the saturation magnetization M_s is 156 emu/g-Fe_3C, which is enhanced by ΔM_s = 60 emu/g-Fe_3C or 473 emu/cc-Fe_3C, compared

with the value (93 emu/g) for free particles. Similarly, from the measured results above, we find that ΔM_s = 653 emu/cc-Ni for 11-nm Ni nanoparticles, ΔM_s = 1891 emu/cc-Fe for 46-nm Fe nanoparticles, and ΔM_s = 506 emu/cc-Fe_3O_4 for 18-nm Fe_3O_4 nanoparticles, and 595 emu/cc-Fe_3O_4 for 55-nm Fe_3O_4 nanoparticles.

Now we turn to discuss the origin of the giant magnetization enhancement of the magnetic nanoparticles embedded in MWCNTs. One possibility is that this enhancement arises from a large magnetic proximity effect Cespedes et al. (2004); Coey et al. (2002). We consider a simple case where our ferromagnetic nanoparticles have a cylindrical shape with both length and diameter equal to d and the curved surface of the cylinder contacts with the innermost shell of a MWCNT (this is the most favorable case for the proximity effect). The curved surface area is equal to πd^2 and the total number of the contact carbon is $\pi N_c d^2$, where N_c is the number of carbon per unit area and equal to $3.82\times10^{15}/\text{cm}^2$ Wallace (1947). If the induced magnetic moment is $m\mu_B$ per contact carbon atom, then the induced saturation magnetization normalized to the volume of the ferromagnetic nanoparticle is $\Delta M_s = 4N_c m\mu_B/d = 1420(m/d)$ emu/cc (here d is in units of nm). Using the measured ΔM_s = 653 emu/cc and d = 11 nm for ferromagnetic nickel nanoparticles, we find that m = 5.1, which is a factor of 51 larger than the value ($\sim$0.1) calculated using density function theory Cespedes et al. (2004). For ferromagnetic iron nanoparticles with d = 46 nm, the measured ΔM_s = 1891 emu/cc. This implies m = 61, which is about three orders of magnitude larger than the value predicted from the magnetic proximity effect. For Fe_3C, ΔM_s = 473 emu/cc and d = 10 nm, we find m = 3.3. For Fe_3O_4 with ΔM_s = 506 emu/cc and d = 18 nm, we calculate m = 6.4. For Fe_3O_4 with ΔM_s = 595 emu/cc and d = 55 nm, we calculate m = 23. For the same type (Fe_3O_4) of magnetic nanoparticles and the same MWCNTs, it is hard to imagine the enhanced moment per carbon atom would be so different within the magnetic proximity effect. Further, the magnetic proximity model also predicts two distinctive magnetic transitions Coey et al. (2002), which are not seen in our magnetic data. Therefore, the magnetic proximity model is unlikely to explain our magnetic data.

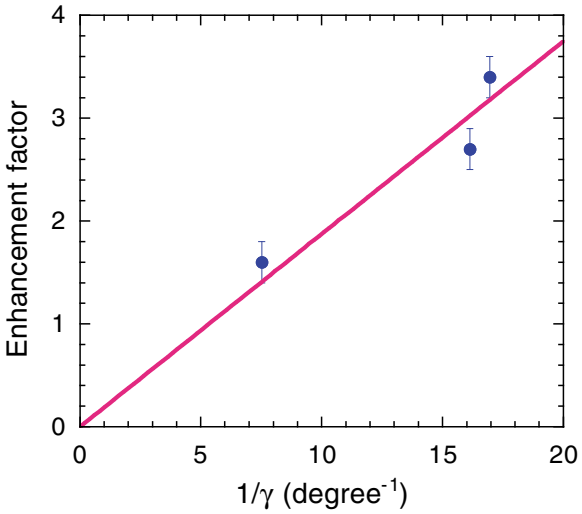

Fig. 14. The moment enhancement factor as a function of the reciprocal of the full width at half maximum of the Gaussian function, fitted for the MWCNT (002) peak.

Alternatively, it is possible that a strong diamagnetic tube could enhance the extrinsic magnetic moment of a (single-domain) magnet embedded inside it. If the tube were a perfect diamagnet, the "poles" of the magnet would be extended further apart (to the length of the tube) without changing their strength, thus giving an extrinsic enhancement to the magnetic moment. This is because the perfect diamagnetism of the tube prevents the magnetic field lines of the magnet from leaking out through the wall of the tube. With this picture, one should expect that the moment enhancement factor should increase with increasing the diamagnetism for the magnetic field parallel to the tube axes. This scenario can naturally explain why the enhancement factors are similar in samples TS0636 and RS0657 with similar numbers of shells while a smaller enhancement factor is found for sample PD15L520 with a much smaller number of shells. In fact, the enhancement factor is inversely proportional to the width of the Gaussian function, fitted for the (002) peak of MWCNTs, as shown in Fig. 14. Since the wall thickness is inversely proportional to the width, the enhancement factor is simply proportional to the thickness of the nanotube wall.

The plausibility of this interpretation depends on whether MWCNTs show strong diamagnetism when the magnetic field is applied in the tube-axis direction in which the orbital diamagnetism is negligibly small Lu (1995). If MWCNTs are ultrahigh temperature superconductors, they will exhibit strong diamagnetism. The observation of superconducting-like hysteresis loops in HOPG at 400 K should be a good indication of local superconductivity well above room temperature Kopelevich et al. (2000). Similarly, there is also compelling evidence for ultrahigh temperature superconductivity in MWCNTs [see a review article Zhao (2004)]. A recent theoretical work Black-Schaffer & Doniach (2007) predicts ultrahigh temperature d-wave superconductivity in well-doped graphene based on RVB theory originally proposed by Anderson Anderson (1987). A similar model for layered cuprates Lee et al. (2006) predicts that an optimal superconducting transition temperature $T_c \simeq 0.14J/k_B$ (where J is the antiferromagnetic exchange energy and k_B is the Boltzmann constant). In graphene, $J \simeq t \simeq 3.0$ eV Black-Schaffer & Doniach (2007), so the optimal T_c should be about 0.42 eV$/k_B \simeq 5000$ K, in quantitative agreement with the numerical calculation Black-Schaffer & Doniach (2007). Very recent large-scale quantum Monte Carlo simulations of correlated Dirac fermions on a honeycomb lattice (realized in graphene) have confirmed the existence of a short-range RVB liquid Meng et al. (2010). If the RVB theory for superconductivity is relevant, ultrahigh temperature superconductivity can be realized in the MWCNTs where sufficient doping is realized by charge-transfer between ferromagnetic nanoparticles and MWCNTs. The special morphology (granular nature) in the mat samples, and the presence of magnetic nanoparticles can also promote the paramagnetic Meissner effect, which could also explain our magnetic data.

6. Identification of the diamagnetic Meissner effect in pure MWCNTs

One of the most important signatures of superconductivity is the existence of the diamagnetic Meissner effect. Therefore, it is essential to provide evidence for the existence of the diamagnetic Meissner effect to prove ultrahigh temperature superconductivity. However, the diamagnetic Meissner effect may be less visible because the outer diameters of the tubes may be much smaller than the magnetic penetration depth. Further, the orbital diamagnetic susceptibility in the magnetic field perpendicular to the graphite sheet is large, making it difficult to separate the diamagnetic Meissner effect from the large orbital diamagnetic susceptibility. Fortunately, the orbital diamagnetic susceptibility of carbon nanotubes in the magnetic field parallel to the tube axes is predicted to be very small at room temperature Lu

(1995). This makes it possible to extract the diamagnetic Meissner effect from the measured susceptibility in the parallel field.

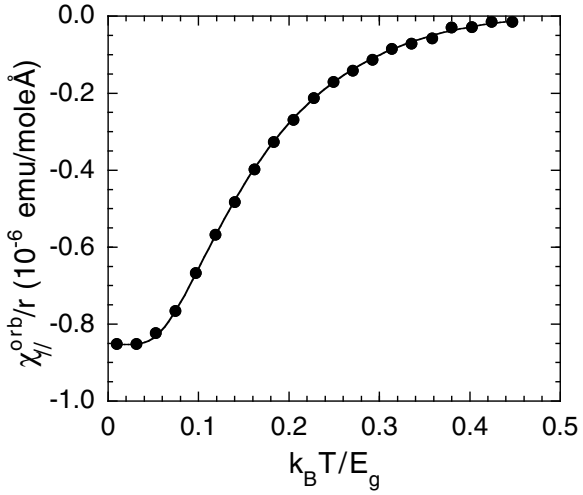

Fig. 15. The calculated temperature dependence of the orbital diamagnetic susceptibility of a single-walled carbon nanotube in the parallel magnetic field. The calculation is based on the tight-binding approximation Lu (1995).

Figure 15 shows the temperature dependence of the orbital diamagnetic susceptibility of a single-walled carbon nanotube in the parallel magnetic field (solid circles), which was calculated based on the tight-binding approximation Lu (1995). Here $E_g = \gamma_\circ a_{C-C}/r$, a_{C-C} (= 0.142 nm) is the bonding length, r is the radius of the tube, and $\gamma_\circ$ (= 2.6 eV) is the tight-binding transfer matrix element Lu (1995). What is remarkable is that the temperature dependence of the orbital susceptibility can be perfectly fitted by an equation (solid line):

$$\frac{\chi_{\parallel}^{orb}(T)}{r} = \frac{\chi_{\parallel}^{orb}(0)}{r}[1 - 1.242\sqrt{E_g/k_BT}\exp(-0.283E_g/k_BT)]. \quad (1)$$

From Eq. 1, we can determine the orbital diamagnetic contribution for a tube or shell. To calculate the orbital diamagnetic susceptibility for a multi-walled carbon nanotube comprising several concentric shells, one needs to replace E_g and r in Eq. 1 by the averaged $< E_g >$ and $< r >$. Since both $\chi_{\parallel}^{orb}$ and the mass of each shell are proportional to r, the average $< r >$ should be $(2/3)r_{out}$ (where r_{out} is the outer radius of a MWCNT). Considering the fact that $\chi_{\parallel}^{orb}$ is proportional to $\gamma_\circ^2$ Kotosonov & Kuvshinnikov (1997), we finally have

$$\chi_{\parallel}^{orb}(T) = -7.0 \times 10^{-9}\gamma_\circ^2 r_{out}[1 - 1.52\sqrt{\frac{a_{C-C}\gamma_\circ}{r_{out}k_BT}}\exp(-\frac{0.425a_{C-C}\gamma_\circ}{r_{out}k_BT})], \quad (2)$$

where $\chi_{\parallel}^{orb}$, $\gamma_\circ$, and r_{out} are in units of emu/g, eV, and Å, respectively.

Now we consider the diamagnetic Meissner effect for a superconducting MWCNT in the magnetic field parallel to the tube axis. We are particularly interested in the case where the magnetic penetration depth is larger than the outer radius of the tube. In this case, the

diamagnetic susceptibility due to the Meissner effect is given by

$$\chi_{\parallel}^{S}(T) = -\frac{r_{out}^2}{32\pi\lambda_{\theta}^2(T)}, \tag{3}$$

where $\lambda_{\theta}(T)$ is the penetration depth when carriers move along the circumferential direction (or the field is parallel to the tube axis). For a macroscopic sample consisting of a macroscopic number of MWCNTs, the r_{out}^2 in the above equation should be replaced by $< r_{out}^2 >$, the average of r_{out}^2. In the low temperature limit: $k_B T \leq 0.2\Delta_{min}(0)$ [where $\Delta_{min}(0)$ is the minimum value of the superconducting gap at zero temperature], the penetration depth follows the following expression:

$$\lambda_{\theta}(T) = \lambda_{\theta}(0) + \lambda_{\theta}(0)\sqrt{\pi\Delta_{min}(0)/2k_B T}\exp[-\Delta_{min}(0)/k_B T]. \tag{4}$$

Combining Eqs. 3 and 4, we can readily show that

$$\chi_{\parallel}^{S}(T) = \chi_{\parallel}^{S}(0)(1 - 2\sqrt{\pi\Delta_{min}(0)/2k_B T}\exp[-\Delta_{min}(0)/k_B T]). \tag{5}$$

The total diamagnetic contribution of a superconducting MWCNT is the sum of $\chi_{\parallel}^{S}(T)$ and $\chi_{\parallel}^{orb}(T)$, that is,

$$\begin{aligned}\chi_{\parallel}(T) = {} & \chi_{\parallel}^{S}(0)(1 - 2\sqrt{\pi\Delta_{min}(0)/2k_B T}\exp[-\Delta_{min}(0)/k_B T]) \\ & -7.0\times 10^{-9}\gamma_{\circ}^2 r_{out}[1 - 1.52\sqrt{\frac{a_{C-C}\gamma_{\circ}}{r_{out}k_B T}}\exp(-\frac{0.425 a_{C-C}\gamma_{\circ}}{r_{out}k_B T})].\end{aligned} \tag{6}$$

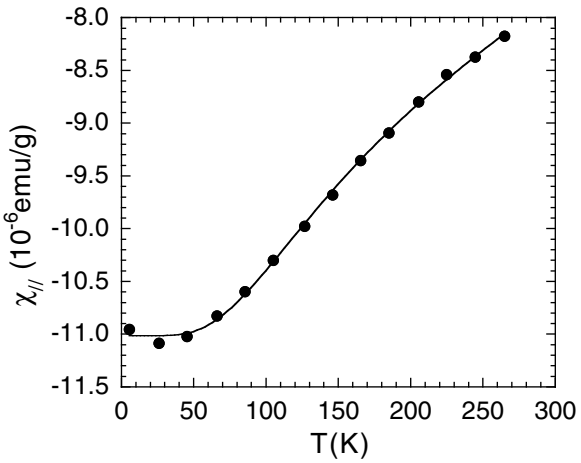

Fig. 16. Temperature dependence of the susceptibility for physically separated and aligned MWCNTs in a magnetic field parallel to the tube axes. The data are extracted from Chauvet et al. (1995).

Figure 16 shows the temperature dependence of the parallel-field susceptibility for pure MWCNTs, which are physically separated and aligned Chauvet et al. (1995). The outer diameters of the tubes are 10±5 nm and the lengths are on the order of 1 μm Chauvet et al. (1995). It is apparent that the diamagnetic susceptibility is significant up to 265 K. If these MWCNTs are ultrahigh-temperature superconductors with $\Delta_{min} \geq 100$ meV, the data should be consistent with Eq. 6. The solid line in Fig. 16 is the best fitted curve by Eq. 6. It is striking that the fit is excellent. The fitting parameters are the following: $\chi_{\parallel}^{S}(0) = -(7.6\pm0.2)\times10^{-6}$ emu/g, Δ_{min} = 124±14 meV, $\gamma_{\circ}$ = 2.80±0.09 eV, and r_{out} = 62.9±0.7 Å. The value of Δ_{min} = 124 meV justifies the temperature range for the fitting. If we use the BCS relation between the gap and superconducting transition temperature: $T_c = \Delta(0)/1.76k_B$, we find that $T_c \geq 800$ K. The value of r_{out} = 62.9 Å is consistent with the average outer radius of 50±25 Å, which was directly measured by TEM Chauvet et al. (1995). The value of $\gamma_{\circ}$ = 2.80 eV is in quantitative agreement with both theory and experiment.

Now we would like to check if the fitted parameter $\chi_{\parallel}^{S}(0) = -(7.6\pm0.2)\times10^{-6}$ emu/g is consistent with the expected Meissner effect. If we assume that the outer radii of MWCNTs are equally distributed from 23 to 103 Å with $< r_{out} >$ = 63 Å (in agreement with that inferred from the best fit above), we find $< r_{out}^2 >$ = 4502 Å^2. With the weight density of 2.17 g/cm^3 Qian et al. (2000) and $\chi_{\parallel}^{S}(0) = -7.6\times10^{-6}$ emu/g, we calculate $\lambda_{\theta}(0) \simeq 1648$ Å using Eq. 3. This value of the penetration depth corresponds to $n/m_{\theta}^{*} = 1.04\times10^{21}/\mathrm{cm}^3 m_e$, where n is the carrier density, m_{θ}^{*} is the effective mass of carriers along the circumferential direction. If we take $m_{\theta}^{*} = 0.012 m_e$, typical for graphite Bayot et al. (1989), we estimate $n = 1.25\times10^{19}/\mathrm{cm}^3$, in quantitative agreement with the Hall effect measurement Baumgartner et al. (1997) which gives $n = 1.6\times10^{19}/\mathrm{cm}^3$. It is worthy of noting that the inferred magnetic penetration depth is far larger than the outer radii of MWCNTs, which justifies Eq. 3. This also ensures that the Hall effect in the superconducting state is the same as that in the normal state.

A carbon nanotube should behave like graphene when the electron mean free path is shorter than the circumference of the tube Schönenberger et al. (1999). In graphene, the effective mass of carriers is given by $m^{*} = \sqrt{\pi n_{2D}}\hbar/v_F$ Novoselov et al. (2005), where n_{2D} is the sheet carrier density and v_F is the Fermi velocity. Using $\hbar v_F = 1.5 a_{C-C}\gamma_{\circ} = 5.96$ eVÅ and taking $n = 1.6\times10^{19}/\mathrm{cm}^3$, we find that $m^{*} = 0.018\ m_e$. This leads to $n/m^{*} = 0.89\times10^{21}/\mathrm{cm}^3 m_e$, very close to what we have inferred from the susceptibility data. Therefore, the susceptibility data of the aligned MWCNTs are in quantitative agreement with ultrahigh temperature superconductivity.

7. Concluding remarks

It is well known that copper-based perovskite oxides rightly enjoy consensus as high-temperature superconductors on the basis of two signatures: the resistive transition and the Meissner effect. Here we have provided magnetic evidence for ultrahigh temperature superconductivity in carbon nanotubes. The giant magnetic moment enhancement found for the magnetic nanoparticles embedded in MWCNTs cannot be explained by the magnetic proximity effect. But rather the result can be naturally explained in terms of the interplay between magnetism of the magnetic nanoparticles and ultrahigh temperature superconductivity in multi-walled carbon nanotubes. The diamagnetic susceptibility of pure MWCNTs for the field parallel to the tube axes agrees quantitatively with the predicted penetration depth from the measured carrier density. Furthermore, bundling of individual MWCNTs into closely packed bundles leads to a large enhancement in the

diamagnetic susceptibility, which can be naturally explained by the Josephson coupling among the tubes in the bundles Zhao et al. (2008). Because of a finite number of transverse conduction channels, both quantum and thermally activated phase slips are important and the on-tube resistance will never go to zero below the mean-field superconducting transition temperature. Nonetheless, the room-temperature on-tube resistance has been found to be indistinguishable from zero for many individual MWCNTs De Pablo et al. (1999); Frank et al. (1998); Poncharal et al. (2002); Urbina et al. (2003).

There are also other independent evidences for ultrahigh temperature superconductivity in both SWCNTs and MWCNTs Zhao & Wang (2001); Zhao (2004; 2006). Some resistivity data of MWCNTs and SWCNTs show quite broad superconducting transitions above room temperature and can be well explained Zhao (2006) in terms of thermally activated phase slip theory developed by Langer, Ambegaokar, McCumber, and Halperin. Raman data and tunneling spectra of SWCNTs consistently show single particle excitation gaps in the range of 100-200 meV Zhao (2006). This would imply that T_{c0} = 600-1200 K. The tunneling spectra of some MWCNTs also indicate a gap of about 200 meV, which is too large to be consistent with the expected semiconducting gap for semiconducting-chirality tubes Zhao (2006).

Although electron-phonon coupling in graphite and related materials is strong and the phonon energy is high ($>$ 100 meV), the calculated electron-phonon coupling constants for various carbon-based materials Barnett et al. (2005); Park et al. (2008) are small due to low density of states. This implies that electron-phonon interaction alone would be insufficient to explain ultrahigh temperature superconductivity in carbon nanotubes, graphite, and carbon films. Although the RVB theory Anderson (1987); Black-Schaffer & Doniach (2007) might be able to explain ultrahigh temperature superconductivity in heavily-doped graphene and MWCNTs, it does not predict ultrahigh temperature superconductivity at low doping. We speculate that strong electron-electron correlation of the relativistic Dirac fermions may lead to a huge enhancement of electron-phonon coupling. Indeed, the electron-phonon coupling constant has been calculated to be about 0.04 for graphene and graphite Park et al. (2008) while the coupling constant determined by angle-resolved photoemission spectroscopy is about 1.0 Sugawara et al. (2007). The enhancement factor is over one order of magnitude, similar to the case in strongly correlated cuprates. The strongly enhanced electron-phonon coupling along with strong coupling to the high-energy acoustic plasmons inherent in quasi-1D and 2D electronic systems Cui & Tsai (1991); Lee & Mendoza (1989) may be the key to achieve ultrahigh temperature superconductivity. In order to take further advantage of strong electron-electron correlation, the order parameters in doubly-degenerate bands near K and K' points might be of opposite signs (nodelss d-wave). Another important factor to influence superconductivity in carbon nanotubes is the strong long-range Coulomb interaction, which can completely destroy superconductivity if it is not well screened by substrates and/or electrodes De Martino & Egger (2004); Zhao (2006). More extensive experimental and theoretical investigations are required to understand the pairing mechanism of ultrahigh temperature superconductivity in carbon-related materials.

Acknowledgment: We thank M. Du and F. M. Zhou for the elemental analyses using ICP-MS. Use of the Advanced Photon Source was supported by the U.S. Department of Energy, Office of Science, Office of Basic Energy Sciences, under Contract No. DE-AC02-06CH11357. This work was partly supported by the National Natural Science Foundation of China (10874095) and Y. G. Bao's Foundation.

8. References

Alexandrov, A. S. & Mott, N. F. (1995). *Polarons and Bipolarons*, World Scientific, ISBN-981022298X, Singapore.

Anderson, P. W. (1987). The Resonating Valence Bond State in La_2CuO_4 and Superconductivity. *Science*, 235, 4793, (March 1987) 1196-1198.

Antonowicz, K. (1974). Possible superconductivity at room temperature. *Nature (London)*, 247, 5440, (February 1974) 358-360.

Barnett, R.; Demler, E. & Kaxiras, E. (2005). Electron-phonon interaction in ultrasmall-radius carbon nanotubes. *Phys. Rev. B*, 71, 3, (January 2005) 035429-035450.

Baskaran, G. & Jafari, S. A. (2002). Gapless Spin-1 Neutral Collective Mode Branch for Graphite. *Phys. Rev. Lett.* 89, 1, (June 2002) 016402-016405.

Baumgartner, G.; Carrard, M.; Zuppiroli, L.; Bacsa, W.; De Heer, W. A. & Forro, L. (1997). Hall effect and magnetoresistance of carbon nanotube films. *Phys. Rev. B*, 55, 11, (March 1997) 6704-6707.

Bayot, V.; Piraux, L.; Michenaud, J.-P. & Issi, J. -P. (1989). Weak localization in pregraphitic carbon fibers. *Phys. Rev. B*, 40, 6, (August 1989) 3514-3523.

Black-Schaffer, A. M. & Doniach, S. (2007). Resonating valence bonds and mean-field d-wave superconductivity in graphite. *Phys. Rev. B*, 75, 13, (April 2007) 134512-134521.

Chauvet, O; Forro, L.; Bacsa, W.; Ugarte, D.; Doudin, B. & de Heer, W. A. (1995). Magnetic anisotropies of aligned carbon nanotubes. *Phys. Rev. B*, 52, 10, (September 1995) R6963-6966.

Chen, D. H.& Hsieh, C. H. (2002). Synthesis of nickel nanoparticles in aqueous cationic surfactant solutions. *J. Mater. Chem.*, 12, 8, (June 2002) 2412-2415.

Cervenka, J.; Katsnelson, M. I. & Flipse, C. F. J. (2009). Room-temperature ferromagnetism in graphite driven by two-dimensional networks of point defects. *Nature Physics*, 5, 11, (October 2009) 840-844.

Cespedes, O.; Ferreira, M. S.; Sanvito, S.; Kociak, M. & Coey, J. M. D. (2004). Contact induced magnetism in carbon nanotubes. *J. Phys.: Condens. Matter*, 16, 10, (February 2004) L155-162.

Coey, J. M. D.; Venkatesan, M.; Fitzgerald, C. B.; Douvalis, A. P.& Sanders, I. S. (2002). Ferromagnetism of a graphite nodule from the Canyon Diablo meteorite. *Nature (London)*, 420, 6912, (November 2002) 156-159.

Cui, S. M. & Tsai, C. H. (1991). Plasmon theory of high-Tc superconductivity. *Phys. Rev. B*, 44, 22, (December 1991) 12500-12510.

Da Silva, R. R.; Torres, J. H. S. & Kopelevich, Y. (2001). Indication of Superconductivity at 35 K in Graphite-Sulfur Composites. *Phys. Rev. Lett.* 87, 14, (September 2001) 147001-147003.

De Martino, A. & Egger, R. (2004). Effective low-energy theory of superconductivity in carbon nanotube ropes. *Phys. Rev. B* 70, 1, (July 2004) 014508-014517.

De Pablo, P. J.; Graugnard, E.; Walsh, B.; Andres, R. P.; Datta, S. & Reifenbergera, R. (1999). A simple, reliable technique for making electrical contact to multiwalled carbon nanotubes. *Appl. Phys. Lett.*, 74, 2, (January 1999) 323-325.

Esquinazi, P.; Spemann, D.; Hohne, R.; Setzer, A.; Han, K. H. & Butz, T. (2003). Induced Magnetic Ordering by Proton Irradiation in Graphite. *Phys. Rev. Lett.*, 91, 22, (November 2003) 227201-227204.

Frank, S.; Poncharal, P.; Wang, Z. L.& de Heer, W. A. (1998). Carbon Nanotube Quantum Resistors. *Science*, 280, 5370 (June 1998) 1744-1746.

Ginzburg, V. L. (1982). *High-Temperature Superconductivity*, Plenum Publishing Corporation, ISBN-0306109700, New York.

Gonzalez, J.; Guinea, F. & Vozmediano, M. A. H. (2001). Electron-electron interactions in graphene sheets. *Phys. Rev. B*, 63, 13, (March 2001) 134421-134428.

Gong, W.; Li, H.; Zhao, Z. & Chen, J. (1991). Ultrafine particles of Fe, Co, and Ni ferromagnetic metals. *J. Appl. Phys.*, 69, 8, (April 1991) 5119-5121.

Goya, G. F.; Berquo, T. S.; Fonseca, F. C. & Morales, M. P. (2003). Static and dynamic magnetic properties of spherical magnetite nanoparticles. *J. Appl. Phys.*, 94, 5, (September 2003) 3520-3528.

Kopelevich, Y.; Esquinazi, P.; Torres, J. H. S. & Moehlecke, S. (2000). Ferromagnetic- and Superconducting-Like Behavior of Graphite. *J. Low Temp. Phys.*, 119, 5, (April 2000) 691-702.

Kotosonov, A. S. & Kuvshinnikov, S. V. (1997). Diamagnetism of some quasi-two-dimensional graphites and multiwall carbon nanotubes. *Phys. Lett. A*, 229, 5 (June 1997) 377-380.

Lebedev, S. G. (2004). Particle irradiation for verification of superconducting-like behavior in carbon arc films. *Nucl. Instr. Meth.*, A521, 1, (March 2004) 22-29.

Lee, P. A.; Nagaosa, N. & Wen, X.-G. (2006). Doping a Mott insulator: Physics of high-temperature superconductivity *Rev. Mod. Phys.*, 78, 1, (January 2006) 17-85.

Lee, Y. C. & Mendoza, B. S. (1989). Possible high-Tc superconductivity in thin wires. *Phys. Rev. B*, 39, 7, (March 1989) 4776-4779.

Little, W. A. (1964). *Phys. Rev.*, 164, 6A, (June 1964) A1416-1424.

Lu, J. P. (1995). Novel Magnetic Properties of Carbon Nanotubes. *Phys. Rev. Lett.*, 74, 7, (February 1995) 1123-1126.

Makarova, T. *et al*. (2001). Magnetic carbon. *Nature (London)*, 413, 6857, (October 2001) 716-718.

Mendoza, D.; Morales, F.; Escudero, R. & Walter, J. (1999). Magnetization studies in quasi two-dimensional palladium nanoparticles encapsulated in a graphite host. *J. Phys.: Condens. Matter*, 11, 28, (July 1999) L317-320.

Meng, Z. Y.; Lang, T. C.; Wessel, S.; Assaad, F. F. & Muramatsu, A. (2010). Quantum spin liquid emerging in two-dimensional correlated Dirac fermions. *Nature (London)*, 464, 7290, (April 2010) 847-851

Moehlecke, S.; Ho, C.; & Maple, M. B. (2002). Coexistence of superconductivity and ferromagnetism in the graphite-sulphur system. *Phil. Mag. B*, 82, 12, (August 2002) 1335-1347.

Moehlecke, S.; Kopelevich, Y. & Maple, M. B. (2004). Interaction between superconducting and ferromagnetic order parameters in graphite-sulfur composites. *Phys. Rev. B*, 69, 13, (April 2004) 134519-134523.

Mombru, A. W.; Pardo, H.; Faccio, R.; de Lima, O. F.; Leite, E. R.; Zanelatto, G.; Lanfredi, A. J. C.; Cardoso, C. A. & Araujo-Moreira, F. M. (2005). Multilevel ferromagnetic behavior of room-temperature bulk magnetic graphite. *Phys. Rev. B*, 71, 10, (March 2005) 100404-100407(R).

Novoselov, K. S.; Geim, A. K.; Morozov, S. V.; Jiang, D.; Katsnelson, M. I.; Grigorieva, I. V.; Dubonos, S. V. & Firsov, A. A. (2005). Two-dimensional gas of massless Dirac fermions in graphene. *Nature (London)*, 438, 7065, (November 2005) 197-200.

Park, C.-H.; Giustino, F.; Cohen, M. L. & Louie, S. G. (2008). Electron-Phonon Interactions in Graphene, Bilayer Graphene, and Graphite. *Nano Lett.*, 8, 12, (November 2008) 4229-4233.

Poncharal, P.; Berger, C.; Yi, Y.; Wang, Z. L. & de Heer, W. A. (2002). Room Temperature Ballistic Conduction in Carbon Nanotubes. *J. Phys. Chem. B*, 106, 47, (November 2002) 12104-12118.

Qian, D.; Dickeya, E. C.; Andrews, R. & Rantell, T. (2000). Load transfer and deformation mechanisms in carbon nanotube-polystyrene composites. *Appl. Phys. Lett.*, 76, 20, (May 2000) 2868-2870.

Reznik, D.; Olk, C. H.; Neumann, D. A. & Copley, J. R. D. (1995). X-ray powder diffraction from carbon nanotubes and nanoparticles. *Phys. Rev. B*, 52, 1, (July 1995) 116-124.

Sajitha, E. P.; Prasad, V.; Subramanyam, S. V.; Mishra, A. K.; Sarkar, S. & Bansal, C. (2007). Size-dependent magnetic properties of iron carbide nanoparticles embedded in a carbon matrix. *J. Phys.: Condens. Matter*, 19, 4, (January 2007) 046214(1-13).

Schönenberger, C.; Bachtold, A.; Strunk, C.; Salvetat, J.-P. & Forro, L. (1999). Interference and Interaction in multi-wall carbon nanotubes. *Appl. Phys. A*, 69, 3, (August 1999) 283-295.

Schrieffer, J. R. (2004). Gauge Theory Pairing and Spin Fluctuations Near the Quantum Critical Point. *Low Temp. Phys.*, 32, 4, (April 2006) 359-362.

Sugawara, K.; Sato, T.; Souma, S.; Takahashi, T. & Suematsu, H. (2007). Anomalous Quasiparticle Lifetime and Strong Electron-Phonon Coupling in Graphite. *Phys. Rev. Lett.*, 98, 3, (January 2007) 036801-036804.

Talyzin, A.; Dzwilewski, A.; Dubrovinsky, L.; Setzer, A. & Esquinazi, P. (2007). Structural and magnetic properties of polymerized C60 with Fe. *Eur. Phys. J. B*, 55, 1, (February 2007) 57-62.

Urbina, A.; Echeverrõa, I.; Perez-Garrido, A.; Dõaz-Sanchez, A. & Abellan, J. (2003). Quantum Conductance Steps in Solutions of Multiwalled Carbon Nanotubes. *Phys. Rev. Lett.*, 90, 10, (March 2003) 106603-106606.

Wallace, P. R. (1947). The Band Theory of Graphite. *Phys. Rev.*, 71, 9, (May 1947) 622-634.

Wang, J.; Beeli, P.; Ren, Y. & Zhao, G. M. (2010). Giant magnetic moment enhancement of nickel nanoparticles embedded in multiwalled carbon nanotubes. *Phys. Rev. B*, 82, 19, (November 2010) 193410-193413.

Wang, J.; Wu, W.; Zhao, F. & Zhao, G. M. (2011). Suppression of the Néel temperature in hydrothermally synthesized α-Fe_2O_3 nanoparticles. *J. Appl. Phys.*, 109, 5, (March 2011) 056101-056103.

Zhao, G. M. & Wang, Y. S. (2001). Possible superconductivity above 400 K in carbon-based multiwall nanotubes. arXiv:cond-mat/0111268v2

Zhao, G. M. (2004). Arguments for quasi-one-dimensional room-temperature superconductivity in carbon nanotubes, In: *Molecular Nanowires and Other Quantum Objects*, Alexandrov, A. S.; Demsar, J. & Yanson, I. K. (Ed.), 95-106, Nato Science Series, Kluwer Academic Publishers, ISBN-978-1-4020-2068-1, Netherlands.

Zhao, G. M. (2006). Compelling Evidence of High-Temperature Superconductivity in Carbon Nanotubes, In: *Trends in Nanotubes Research*, Delores A. Martin, D. A., (Ed.), 39-75, Nova Science Publishers, ISBN-1-59454-791-2, New York.

Zhao, G. M. & Beeli, P. (2008). Observation of an ultrahigh-temperature ferromagnetic-like transition in iron-contaminated multiwalled carbon nanotube mats. *Phys. Rev. B*, 77, 24, (June 2008) 245433-245438.

Zhao, G. M.; Wang, J.; Ren, Y. & Beeli, P. (2011). Anomalous thermal hysteresis in the high-field magnetizations of magnetic nanoparticles embedded in multi-walled carbon nanotubes: Consistent with ultrahigh temperature superconductivity. submitted to Nature.

17

Carbon Nanotubes Influence on Balk and Surface Properties of the Optical Materials

Natalia V. Kamanina
Vavilov State Optical Institute,
Russia

1. Introduction

After discovery of the fullerenes, carbon nanotubes and quantum dots, many scientific and research groups have found different area of applications of these nano-objects. The main reason to use the fullerenes and quantum dots is connected with their unique energy levels and high value of electron affinity energy. The basic features of carbon nanotubes are regarded to their high conductivity, strong hardness of their C—C bonds as well as complicated and unique mechanisms of charge carrier moving. These peculiarities of carbon nanotubes and their possible optoelectronics applications will be under consideration in this topic with good new advantage.
In this section of the book the features of some nano-objects have been considered in order to apply and to recommend them in the extended area of laser, display, telecommunications, medicine, etc. technique.

1.1 Homeotropic alignment of nematic liquid crystals elements using carbon nanotubes

It is well known that mostly liquid crystal (LC) cells, which can be considered as display pixel, operate in *S* and *T* configurations that realize a planar orientation of the LC mesophase on the aligning substrate surface. However, the solution of some problems, where the initial black field is necessary for the regime of light transmission through the cell structure, requires a homeotropic alignment of LC molecules on the substrate. Homeotropic alignment is frequently obtained using surfactants, such as lecithin, fused quartz, etc. [1,2]. A new alternative method for obtaining a surface nanorelief that favors the homeotropic alignment of an LC mesophase is offered by the so-called nanoimprinting technology [3]. Realization of this method, while making possible the formation of a surface relief with a good optical quality, requires the use of toxic substances, in particular, acids.
Recently a new method for the homeotropic alignment of LC molecules has been proposed [4]. It is based on a contactless technique of relief formation on the surface of a glass (quartz) substrate using the deposition of carbon nanotubes (CNTs) and their additional orientation in an electric field. The procedure can be briefly shown as follows. This treatment has been made when glass or quartz substrates have been used. These substrates have been covered with ITO contact and then with CNTs using laser deposition technique. As an additional, CNTs have been oriented at the electric field close to 100-250 $V \times cm^{-1}$. To decrease the

rougness of the relief the surface electromagnetic wave (SEW) treatment has been used. SEW source was a quasi-CW gap CO_2 laser generating *p*-polarized radiation with a wavelength of 10.6 micrometers and a power of 30 W. The skin layer thickness was ~0.05 micrometers. The relief obtained before and after SEW treatment of the CNTs layers is shown in figure 1 *a* and *b*.

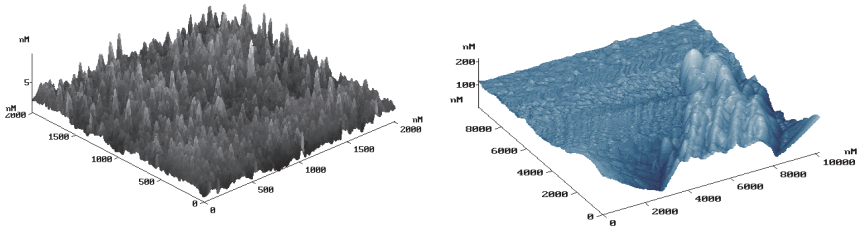

Fig. 1. New orientation relief obtained after laser deposition oriented CNTs: before (*a*) and after (*b*) SEW treatment

The homeotropic alignment of LC molecules was studied using two sandwich type cells with an nematic LC mesophase confined between two glass plates. The reference cell represented a classical nematic LC structure, in which the alignment surfaces were prepared by rubbing of polyimide layers. In the experimental cell, both alignment surfaces were prepared using CNTs as described above. Experiments with the second cell confirmed that a homeotropic alignment of the LC molecules was achieved. The results of these experiments are presented in the table 1. The spectral data in a 400–860 wavelength range were obtained using an SF-26 spectrophotometer. Reference samples with planar alignments and homeotropically aligned samples prepared using the new nanotechnology of substrate surface processing were mounted in a holder and the transmission of both cells was simultaneously measured at every wavelength in the indicated range. It should be noted that the two cells had the same thickness of 10 μm and contained the same nematic LC composition belonging to the class of cyanobiphenyls. The experimental data were reproduced in several sets of cells. The spectral results are shown in table 1.
Thus, the new features of CNTs have been demonstrated in order to obtain the initial black field of LC cells using a homeotropic orientation of LC molecules on CNTs relief.
The results of this investigation can be used both to develop optical elements for displays with vertical orientation of NLC molecules (for example, in MVA-display technology) and to use as laser switcher.

1.2 Polarization elements for visible spectral range with nanostructured surface modified with carbon nanotubes

The functioning of various optoelectronic devices implies the use of polarization elements. As it is known, the operation of polarization elements is based on the transverse orientation of fields in electromagnetic waves. Polarization devices transmit one component of the natural light, which is parallel to the polarizer axis, and retard the other (orthogonal) component. There are two main approaches to create thin film polarizers. The first method employs metal stripes deposited onto a polymer base. The metal layer reflects the incident light, while the polymer film transmits and partly absorbs the light, so that only the light of a certain polarization is transmitted. Another method is based on the creation of

Wave-length, nm	Transmission, %		Wave-length, nm	Transmission, %	
	reference cell (planar)	experimental cell (homeotropic)		reference cell (planar)	experimental cell (homeotropic)
400	0	0	620	24.1	0.4
410	2.8	0	630	23.8	0.4
420	11.1	0	640	23.3	0.4
430	19	0	650	22.5	0.3
440	23.2	0	660	22.1	0.3
450	25.6	0.5	670	21.7	0.3
460	26.7	0.5	680	21.4	0.3
470	27.3	0.5	690	21.0	0.3
480	27.6	0.5	700	20.6	0.3
490	27.5	0.5	710	20.2	0.3
500	27.4	0.5	720	20.0	0.3
510	27.2	0.5	730	19.3	0.3
520	27.0	0.5	740	19.0	0.3
530	26.8	0.5	750	18.6	0.3
540	26.6	0.5	760	18.2	0.3
550	26.3	0.4	770	17.9	0.3
560	26.1	0.4	780	17.4	0.3
570	25.8	0.4	790	17.1	0.3
580	25.6	0.4	800	16.7	0.3
590	25.2	0.4	820	16.1	0.3
600	24.9	0.4	840	15.5	0.3
610	24.5	0.4	860	14.8	0.3

Table 1. Optical transmission of LC cells prepared using different methods of alignment at the substrate–LC interface

polymer-dispersed compositions, e.g., iodinated poly(vinyl alcohol) (PVA) films, which transmit the parallel component of the incident light and absorb the orthogonal component. Thus, the principle of operation of the iodinated PVA film polarizer is based on the dichroism of light absorption in PVA–iodine complexes.

This paragraph briefly considers the possibility of improving the optical and mechanical properties of iodine–PVA thin film polarizers by the application of modern nano-objects - carbon nanotubes (CNTs). The polarizers structures comprising iodinated PVA films with a thickness of 60–80 μm, which were coated from both sides by ~0.05 μ thick layers of single walled CNTs have been studied. The polarizers contained polarization films with either parallel or mutually perpendicular (crossed) orientations, depending on the need to obtain the initial bright or dark field. It was found that the modification (nanostructuring) of the surface of polarization films by CNTs led to some increase in the optical transmission for the parallel component of incident light (see. curves *1* and *2* in the figure 2), while retaining minimum transmission for the orthogonal component (cf. curves *3* and *4*).

It should be mentioned that CNTs were laser deposited onto the surface of polarization films in vacuum using *p*-polarized radiation of a quasi-CW CO_2 laser. During the deposition, the CNTs were oriented by applying an electric field with a strength of 50–150 $V \times cm^{-1}$. For the first time the method of laser deposition of CNTs onto iodine-PVA structures has been descried in paper [5]. The optical transmission measurements were performed using an SF-26 spectrophotometer operating in a 200–1200 nm wavelength range. The results of spectral measurements were checked using calibrated optical filters. The error of transmission measurements did not exceed 0.2%.

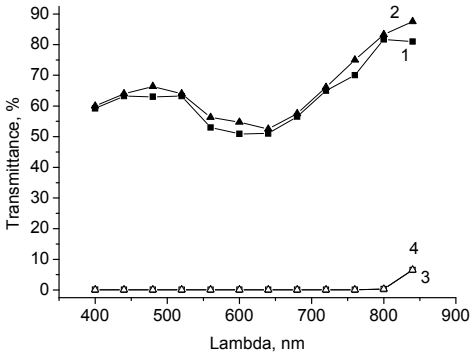

Fig. 2. Dependence of percentage transmission versus wavelength of (*1*,*2*) parallel and (*3*, *4*) orthogonal polarized light for iodinated PVA film polarizers without (*1*, *3*) and with (*2*, *4*) CNTs modified nanostructured surfaces.

The nanostructuring of the surface of polarization films by CNTs led to a 2–5% increase in the optical transmission in the visible spectral range for the parallel component of incident light, while retaining minimum transmission for the orthogonal component. This result is evidently related to the fact that the deposition of CNTs onto the surface of iodinated PVA films modifies the properties of air–film interface and reduces the reflection losses. The losses are decreased due to the Fresnel effect, which is related to a small refractive index of CNTs ($n \sim 1.1$). In a spectral interval of 400–750 nm, the CNT-modified iodinated PVA films ensured the transmission of the parallel component on a level of 55–80%.

As an additional feature of a new method to deposit the CNTs onto both surfaces of polarization films are based on the improved mechanical protection of the films. Really, the standard approach to mechanical protection of polymeric polarization films against scratching and bending consists in gluing polarizers between plates of K8 silica glass or pressing them into triacetatecellulose. The proposed method of surface nanostructuring increases the surface hardness, while retaining the initial film shape that is especially important in optoelectronic devices for reducing aberrations in optical channels and obtaining undistorted signals in display pixels. The increase in the surface hardness is apparently related to the covalent binding of carbon nano-objects to the substrate surface, which ensures strengthening due to the formation of a large number of strong C–C bonds of the CNTs, which are difficult to destroy.

The CNT-modified thin film polarizers can be employed in optical instrumentation, laser, telecommunication, and display technologies, and medicine. These polarizers can also be

used in devices protecting the eyes of welders and pilots against optical damage and in crossed polaroids (polarization films) based on liquid crystals.

1.3 Carbon nanotubes influence on the photorefractive features of the organics materials

In the present paragraph the emphasis is made on the improving of the photorefractive characteristics of conjugated organic materials doped by fullerenes, CNTs, and quantum dots. The possible mechanism to increase the laser-induced change in the refractive index, nonlinear refractive index and cubic nonlinearity has been explained in the papers [6-8]. Regarding CNTs it was necessary to take into account the variety of charge transfer pathways, including those along and across a CNT, between CNTs, inside a multiwall CNT, between organic molecules and CNTs, and between the donor and acceptor moieties of an organic matrix molecule. The possible schemes of charge transfer are schematically depicted in figure 3 (middle part).

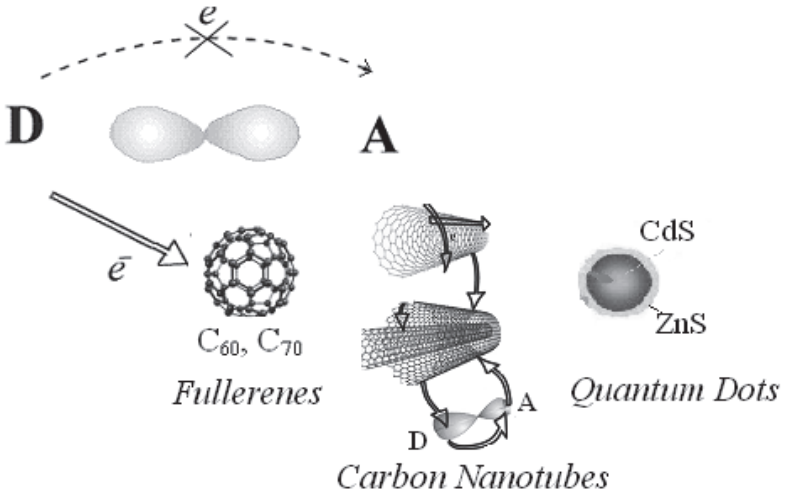

Fig. 3. Schematic diagram of possible charge transfer pathways in the organic molecule–nano-objects

The systems have been studied using a four-wave mixing scheme analogous to that described previously [9]. By monitoring the diffraction response manifested in this laser scheme, it is possible to study the dynamics of a photoinduced change in the refractive index of a sample and to calculate the nonlinear refraction and nonlinear third order optical susceptibility (cubic nonlinearity). An increase in the latter parameter characterizes a change in the specific (per unit volume) local polarizability and, hence, in the macroscopic polarization of the entire system. The experiments were performed under the Raman–Nath diffraction conditions in thin gratings with spatial frequencies of 100 and 150 cm^{-1} recorded at an energy density varied within 0.1–0.5 J/cm^2.

The organic compositions were based on polyimide (PI), prolinols, and pyridines, including N-(4_nitrophenyl)-*L*-prolinol) (NPP), 2-(N-prolinol)-5-nitropyridine (PNP), and 2-cyclooctylamine-5-nitropyridine (COANP). The thicknesses of thin film samples were

within 2–4 μm. The organic matrices were sensitized by doping with commercially available fullerenes (C_{60} and C_{70}) and CNTs (purchased from Alfa Aesar Company, Karlsruhe, Germany). The concentration of dopants was varied within 0.1–5 wt % for fullerenes and below 0.1 wt % for CNTs.

The main results of this study are summarized in the table 2 in comparison to the data of some previous investigations. An analysis of data presented in the table 2 for various organic systems shows that the introduction of fullerenes as active acceptors of electrons significantly influences the charge transfer under conditions where the intermolecular interaction predominates over the intramolecular donor–acceptor contacts. Indeed, the electron affinity of the acceptor fragments (which is close to 1.1–1.4 eV in PI-based composites and 0.4–0.5 eV in pyridine-based systems) is 2.5–5 times that of fullerenes (2.6–2.7 eV). Redistribution of the electron density during the recording of gratings in nanostructured materials changes the refractive index by at least an order of magnitude as compared to that in the initial matrix. This results in the formation of a clear interference pattern with a distribution of diffraction orders shown in figure 4. The diffusion of carriers from the bright to dark region during the laser recording of the interference pattern proceeds in three (rather than two) dimensions, which is manifested by a difference in the distribution of diffraction orders along the horizontal and vertical axes. Thus, the grating displacement takes place in a three dimensional (3D) medium formed as a result of the nanostructirization (rather than in a 2D medium).

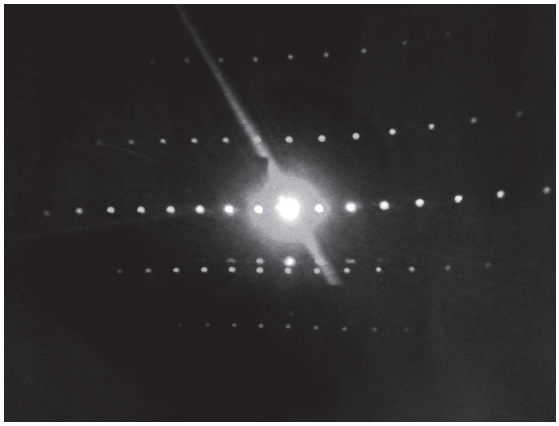

Fig. 4. The visualization of the diffraction response in the organics doped with nano-objects

In addition, data in the table 2 show that the introduced CNTs produce almost the same change in the refractive properties as do fullerenes, at a much lower percentage content of the CNTs as compared to that of C_{60} and C_{70} and for the irradiation at higher spatial frequencies (150 mm^{-1} for CNTs versus 90–100 mm^{-1} for fullerenes). This implies that the possibility of various charge transfer mechanisms in the systems with CNTs is quite acceptable and may correspond to that depicted in figure 3. Using the obtained results, we have calculated the nonlinear refraction n_2 and nonlinear third order optical susceptibility (cubic nonlinearity) $\chi^{(3)}$ for all systems using a method described in [10]. It was found that these parameters fall within $n_2 = 10^{-10}$–10^{-9} cm^2/W and $\chi^{(3)} = 10^{-10}$–10^{-9} cm^3/erg.

It should be noted that classical inorganic nonlinear volume media (including lithium niobate) exhibit significantly lower nonlinearity, while bulk silicon based materials have

nonlinear characteristics analogous to those of the organic nano-objects-doped materials under consideration.

Structure	Content of dopants, wt.%	Wavelength, nm	Energy density, $J \times cm^{-2}$	Spatial frequency, mm^{-1}	Laser pulse duration, ns	Laser-induced change in the refractive index, Δn
NPP	0	532	0.3	100	20	0.65×10^{-3}
NPP+C_{60}	1	532	0.3	100	20	1.65×10^{-3}
NPP+C_{70}	1	532	0.3	100	20	1.2×10^{-3}
PNP*	0	532	0.3	100	20	*
PNP+C_{60}	1	532	0.3	100	20	0.8×10^{-3}
PI	0	532	0.6	90-100	10-20	10^{-4}-10^{-5}
PI+malachite green dye	0.2	532	0.5-0.6	90-100	10-20	2.87×10^{-4}
PI+C_{60}	0.2	532	0.5-0.6	90-100	10-20	4.2×10^{-3}
PI+C_{70}	0.2	532	0.6	90-100	10-20	4.68×10^{-3}
PI+C_{70}	0.5	532	0.6	90-100	10-20	4.87×10^{-3}
PI+CNTs	0.1	532	0.5-0.8	90-100	10-20	5.7×10^{-3}
PI+ CNTs	0.05	532	0.3	150	20	4.5×10^{-3}
PI+ CNTs	0.07	532	0.3	150	20	5.0×10^{-3}
PI+ CNTs	0.1	532	0.3	150	20	5.5×10^{-3}
PI +quantum dots based on CdSe(ZnS)	0.003	532	0.2-0.3	100	20	2.0×10^{-3}
COANP	0	532	0.9	90-100	10-20	10^{-5}
COANP+ TCNQ**	0.1	676	2.2 $W \times cm^{-2}$			2×10^{-5}
COANP+C_{60}	5	532	0.9	90-100	10-20	6.21×10^{-3}
COANP+C_{70}	5	532	0.9	90-100	10-20	6.89×10^{-3}

* The diffraction efficiency has not detected in pure PNP system at this energy density
** Dye TCNQ - 7,7,8,8,-tetracyanoquinodimethane – has been used in the paper [11]

Table 2. Laser-induced change in the refractive index in some organic structures doped with nano-objects

1.4 Carbon nanotubes use to modify the surface properties of the inorganic materials

It is the complicated complex task to modify the optical materials operated as output window in the UV lamp and laser resonators, as polarizer in the telecommunications, display and medicine systems. Many scientific and technological groups have made some steps to reveal the improved characteristics of optical materials to obtain good mechanical hardness, laser strength, and wide spectral range. Our own steps in this direction have been firstly shown in paper [12]. In order to reveal the efficient nano-objects influence on the materials surface it is necessary to choose the model system.

It should be noticed that magnesium fluoride has been considered as good model system. For this structure the spectral characteristics, atomic force microscopy data, measurements to

estimate the hardness and roughness have been found in good connection. The main aspect has been made on interaction between nanotubes (their C—C bonds) placed at the MgF_2 surface via covalent bonding [13]. Table 3 presents the results of surface mechanical hardness of MgF_2 structure after nanotubes placement; Table 4 shows the decrease of MgF_2 roughness.

Structures	Abrasive surface hardness (number of cycles before visualization of the powder from surface)	Remarks
MgF_2	1000 cycles	CM-55 instrument has been used. The test has been made using silicon glass K8 as etalon. This etalon permits to obtain abrasive hardness close to zero at 3000 cycle with forces on indenter close to 100 g.
MgF_2+nanotubes	3000 cycles	
MgF_2+vertically oriented CNTs	more than zero hardness	

Table 3. Abrasive surface hardness of the MgF_2 structure before and after CNTs modifications

One can see from Table 3 that the nanostructured samples reveal the better surface hardness. For example, after nanotubes placement at the MgF_2 surface, the surface hardness has been better up to 3 times in comparison with sample without nano-objects. It should be noticed that for the organic glasses this parameter can be increased up to one order of magnitude. Moreover, the roughness of the MgF_2 covered with nanotubes and treated with surface electromagnetic waves has been improved essentially. Really, R_a and S_q roughness characteristics have been decreased up to three times. One can see from Table 4 that the deposition of the oriented nanotubes on the materials surface and surface electromagnetic waves treatment decreases the roughness dramatically. Indeed this process is connected with the nature of the pure materials; it depends on the crystalline axis and the defects in the volume of the materials.

In order to explain observed increase of mechanical hardness we compared the forces and energy to bend and to remove the nanotubes, which can be connected with magnesium fluoride via covalent bond MgC. Thus, the full energy responsible for destruction of the surface with nanotubes should be equal to the sum of W_{rem} (energy to remove the layer of nanotubes) and of W_{destr} (energy to destroy the magnesium fluoride surface).

Parameters	Materials	Roughness before nanotreatment	Roughness after nanotreatment	Remarks
R_a	MgF_2	6.2	2.7	The area of 5000×5000 nm has been studied via AFM method
S_q	MgF_2	8.4	3.6	

Table 4. Roughness of the MgF_2 structure before and after CNTs modifications

Due to the experimental fact that nanotubes covering increases drastically the surface hardness of MgF_2 [13], the values of W_{rem} and W_{destr} can be close to each other. Under the conditions of the applied forces parallel to the surface, in order to remove the nanotibes from MgF_2 surface, firstly, one should bend these nanotubes, and secondly, remove these nanotubes. In this case W_{rem} are consisted of W_{elast} (elasticity energy of nanotube) plus W_{MgC} (energy to destroy the covalent MgC binding). The energy of elasticity can be estimated as follow [14]:

$$W_{elast} = F^2_{rem} \times L^3 / 6E \times I \quad (1)$$

where E=1.5 TPa [15] is the modulus of elasticity, $I = \pi \cdot r^3 \cdot \Delta r$ – is the inertion moment of the nanotube cross section at its wall thickness Δr=0.34 nm, r=4 nm; and L=50 nm is the nanotube length. The force F_{rem} can be estimated as follows:

$$F_{rem} = F_{MgC} \times 2r / L, \quad (2)$$

where F_{MgC} is close to 2 nN.

Based on our calculation we should say that in order to broke the relief with nanotubes, we should firstly bend the nanotubes with energy that is 5 times more than the one, which can be applied to simply remove the nanotubes from surface after the destroying MgC binding. This fact is in good connection with the experimental results.

This calculation can be used to explain the results of dramatically increased mechanical surface hardness of the MgF_2 covered with nanotubes. The experimental data testified that the surface mechanical hardness of MgF_2 materials covered with nanotubes can be compared with the hardness of etalon based on silicon glass K8. As a result of this process, the refractive index can be modified which explains the increase in transparency in the UV. Moreover, the spectral range saving or increasing in the IR range can be explained based on the fact that the imaginary part of dielectric constant of carbon nanotubes, which is responsible for the absorption of the nano-objects, is minimum (close to zero) in the IR range. The UV-VIS and near IR-spectra of the magnesium fluoride is shown in Fig. 5.

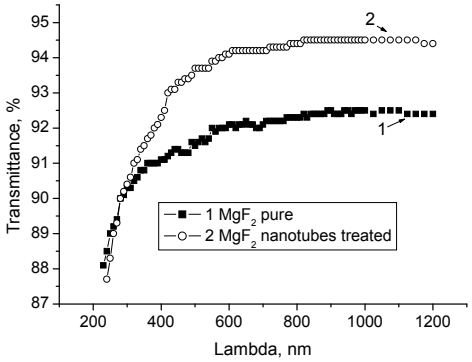

Fig. 5. UV-VIS-near IR spectra of MgF_2 before (curve 1) and after single wall nanotubes deposition (curve 2). The thickness of the sample close to 2 mm.

It should be noticed that the drastic increase in the transparency at wavelength of 126 nm has been observed. Really, for the 5 units of MgF_2 sample, the transparency T has been changed after nanotubes deposition as follows: sample №1. T= 61.8% → T=66.6%1 №2. T=63.6% → T=69%; №3. T=54.5% → T=65.8%; №4. T=58.1% → T=67.5%; №5. T=50.9% →T=65%.

It should be mentioned that the CNTs are the good candidate to modify the surface properties of the materials in order to obtain the good advantage in the hardness and spectra.

1.5 Conclusion

In conclusion, the influence of the nano-objects, *such as carbon nanotubes*, on alignment ability, polarization features, dynamic, photoconductive and photorefractive characteristics

as well as on mechanical hardness and spectral parameters has been shown. CNTs can modify balk and surface properties of the materials with good advantage.
As the result of this discussion and investigation, new area of applications of the nanostructured materials can be found in the optoelectronics and laser optics, medicine, telecommunications, display, microscopy technique, etc. Moreover, the nanostructured materials can be used for example, for development of transparent UV and IR window, for gas storage and solar energy accumulation, as well as in airspace and atomic industry.

2. Acknowledgments

The authors would like to thank their Russian colleagues: Prof. N. M. Shmidt (Ioffe Physical-Technical Institute, St.-Petersburg, Russia), Prof. E.F.Sheka (University of Peoples' Friendship, Moscow, Russia), Dr.K.Yu.Bogdanov (Lyceum # 1586, Moscow, Russia), Dr.A.I.Plekhanov (Institute of Automation and Electrometry SB RAS, Novosibirsk, Russia), Dr.V.I.Studeonov and Dr.P.Ya.Vasilyev (Vavilov State Optical Institute, St.-Petersburg, Russia), as well as foreign colleagues: Prof. Francois Kajzar (Université d'Angers, Angers, France), Prof. D.P. Uskokovic (Institute of Technical Sciences of the Serbian Academy of Sciences and Arts, Belgrade, Serbia) for their help in discussion and study at different their steps. The presented results are correlated with the work supported by Russian Foundation for Basic Researches (grant 10-03-00916, 2010-2012 and by Vavilov State Optical Institute (grant "Perspectiva", 2009-2011).

3. References

[1] R. S. McEwen, J. Phys. E: Sci. Instrum. 20, 364 (1987).
[2] A. A. Vasil'ev, D. Kasasent, I. N. Kompanets, A. V. Parfenov, *Spatial Light Modulators* (Radio I Svyaz', Moscow, 1987) [in Russian].
[3] Jin Seog Gwag, Masahito Oh_e, Kwang_Ryul Kim, Sung_Hak Cho, Makoto Yoneya, Hiroshi Yokoyama, Hiroyuki Satou, and Setsuo Itami, Nanotechnology 19, 395301 (2008).
[4] N. V. Kamanina, P. Ya. Vasilyev, Tech. Phys. Lett., 35 (No. 6), 501 (2009).
[5] N.V. Kamanina, P.Ya. Vasilyev, V.I. Studenov, Tech. Phys. Lett., 36 No.8, 727 (2010).
[6] N.V. Kamanina, Physics-Uspekhi 48 (4), 419 (2005).
[7] N. V. Kamanina, D. P. Uskokovic, Materials and Manufacturing Processes, 23, 552 (2008).
[8] N. V. Kamanina, A. Emandi, F. Kajzar, Andre´-Jean Attias, Mol. Cryst. Liq. Cryst., 486, p. 1=[1043] (2008).
[9] N.V. Kamanina, N.A. Vasilenko, Opt. Quantum Electron., 29 (No. 1), p. 1 (1997).
[10] S. A. Akhmanov and S. F. Nikitin, *Physical Optics* (Izdat. Mos. Gos. Univ., Moscow, 1998) [in Russian].
[11] K. Sutter, J. Hulliger, P. Gunter, Solid State Commun. 74, 867 (1990).
[12] N.V. Kamanina, P.Ya. Vasilyev, V.I. Studeonov, Yu.E. Usanov, Optical Zhournal, 75 No.1, 83 (2008) – in Russian.
[13] N.V. Kamanina, P.Ya. Vasilyev, V.I. Studeonov, Optical Zhournal 75 No.12, 57 (2008) - in Russian.
[14] N.V. Kamanina, P.Ya. Vasilyev, S.V. Serov, V.P. Savinov, K.Yu. Bogdanov, D.P. Uskokovic, Acta Physica Polonica A, 117, 786 (2010).
[15] *Introduction to Nanotechnology*, Ed. by Ch. P. Poole, Jr.and F. J. Owens (Wiley Interscience, New York, 2003).

Part 3

Applications

18

The Application of Carbon Nanotube to Bone Cement

Yu-Hsun Nien
Department of Chemical and Materials Engineering
National Yunlin University of Science and Technology
Taiwan

1. Introduction

Bone cement is used as a grouting agent between the prosthesis and the bone as well as a method to anchor prosthesis in orthopedic implants such as total hip replacement. Basically, bone cement consists of two portions: (1) powder portion including pre-polymerized methylmethacrylate (PMMA) and initiator (benzoyl peroxide) and (2) liquid portion including methylmethacrylate (MMA) monomer and promoter (N, N-dimethyl-p-toluidine). When two portions are mixed, the initiation is activated by promoters that make the free radicals (initiators). The free radicals react with monomers for polymerization (Park & Lakes, 1992). Some disadvantages of PMMA bone cement are found such as significant poor mechanical properties which may cause failure of the cement. For instance, PMMA bone cement is considerably weaker than bone (Saha & Pal, 1984) and the tensile stresses of PMMA bone cement are comparatively low (Saha & Pal, 1986). Vallo et al. used cross-linked PMMA beads to prepare cements by replacing 30% of the PMMA powder and showed an increase in the flexural strength value of 22.4%. The cross-linked beads resulted in more effective reinforcing filler than plain PMMA beads (Vallo et al., 2004). Basgorenay et al. modified acrylic bone cement by addition of hydroxyapatite and ammonium nitrate. A linear relation was observed in compression strength (from 98 to 111 MPa) and in tensile strength (from 27 to 21 MPa) upon HA addition, and in the compression strength (from 103 to 85 MPa) and in the tensile strength (from 22 to 17 MPa) with NA addition (Basgorenay et al., 2006). Kwon et al. prepared bone cements incorporated with montmorillonite (MMT) to improve their mechanical properties. The measured compressive strength of the bone cement with 1 wt % MMT was 113.6 ± 3.9 MPa, which is higher than that of the bone cement without MMT (110.1 ± 2.0 MPa). The measured tensile strength of the control bone cement with 1 wt % MMT was 27.2 ± 4.4 MPa, which is higher than that of the bone cement without MMT (22.3 ± 3.8 MPa) (Kwon et al., 2007).

Carbon nanotube is known for a larger aspect ratio and higher modulus (Iijima, 1991). Kearns and Shambaugh found that the tensile strength of polypropylene fibers reinforced with carbon nanotube could increase 40% (Kearns & Shambaugh, 2002). There are several studies related to the preparation and characterization of carbon nanotube/poly(methyl methacrylate) composites. For example, Jin et al. studied muti-walled carbon nanotube/poly(methyl methacrylate) composites fabricated by melting blending and found that the nanotube was well dispersed in the polymer matrix and the storage modulus of the

composites was significantly increased (Jin et al., 2001). Stephan et al. prepared poly(methyl methacrylate)-singlewalled carbon nanotube composites by solution mixing (Stephan et al., 2000). Cooper et al. used a polymer extrusion technique to prepare carbon nanotube mixed in a poly(methyl methacrylate) matrix and found that the impact strength was significantly improved by even small amounts of single-wall nanotube (Cooper et al., 2002). Jia et al. prepared poly(methyl methacrylate)/carbon nanotube composites by an in-situ process. Their studies show that carbon nanotube could participate in the polymerization of PMMA initiated by AIBN and form a strong combining interface between the carbon nanotube and the PMMA matrix (Jia et al., 1999).

The purpose of this study is to enhance the mechanical properties of bone cement with carbon nanotube. In this study, the various systems of bone cement reinforced with carbon nanotube were fabricated. The mechanical properties of bone cement were characterized using tensile as well as compressive analysis and dynamic mechanical analysis (DMA). The results show that introduction of carbon nanotube is able to enhance the mechanical properties of bone cement.

2. Materials and Methods

Multiwall carbon nanotube was able to purify by nitric acid solution. The 0.5 g of multiwall carbon nanotube and 100 ml of 3 M of nitric acid solution were mixed in round-bottom flask by ultrasonication for 30 minutes, followed by reflux at 120°C for 12 hours. Then the mixture was cooled down to room temperature. The nitric acid solution of the mixture was taken out and the multiwall carbon nanotube was washed by distilled water until pH 7 of the filtrate. The multiwall carbon nanotube was dried in oven at 120°C for 12 hours.

2.1 Preparation of PMMA/carbon nanotube powder

Multiwall carbon nanotube (CNT) (40 ~ 60 nm in diameter, 0.5 ~ 40 mm in length) was purchased from Desunnano Co., Ltd and used as received without further treatment in this study. MMA monomer was supplied from Kanto Chemical Co., Inc. The composition of PMMA/CNT composites manufactured by in-situ process is listed in Table 1. Benzoyl peroxide (BPO) was used as initiator. The procedure for fabrication of PMMA/carbon nanotube composites was first dissolution of BPO in MMA monomer by stirring at room temperature. After well mixture of BPO and MMA monomer, carbon nanotube was added into the mixture followed by sonication and polymerized at 50°C. When the mixture became viscous, it was poured into mold for further reaction by the process of baking as following steps: (1) 60°C for 2 hours, (2) 80°C for 2 hours, and (3) 100°C for 3 hours. PMMA/CNT powder was prepared from PMMA/CNT composites ground by grinder.

MMA (g)	CNT (g)	BPO (g)	Note
100	0.1	2	(100/0.1)
100	0.2	2	(100/0.2)
100	0.27	2	(100/0.27)
100	0.43	2	(100/0.43)
100	0.59	2	(100/0.59)
100	0.75	2	(100/0.75)

Table 1. The composition of PMMA/CNT composites manufactured by in-situ process

2.2 Preparation of bone cement reinforced with carbon nanotube

The commercial cement, OSTEOBOND, was used as well in this study. The OSTEOBOND was purchased from Zimmer (Warsaw, Indiana. USA). Several systems of bone cement reinforced with carbon nanotube were prepared. The composition of liquid portion of the bone cement was the same in each system. The compositions of the bone cement in each system are shown in Table 2. The specimens of bone cement were prepared by mixing at the ratio of 1/2 at the liquid portion to the powder portion and left to solidify in a designed shape.

	Powder portion (g)		Commercial Liquid portion (ml)
	Commercial powder	PMMA/CNT powder (pmma/cnt)*	
System 1	20	0	10
System 2	17	3 (100/0.1)	10
System 3	17	3 (100/0.2)	10
System 4	17	3 (100/0.27)	10
System 5	17	3 (100/0.43)	10
System 6	17	3 (100/0.59)	10
System 7	17	3 (100/0.75)	10

*(pmma/cnt) indicates the ratio of PMMA/CNT by weight in pre-polymeric composites.

Table 2. The composition of the bone cement in each system

2.3 Analysis

The tensile and compressive strength of bone cement was characterized using INSTRON 5582. The specimens for tensile analysis are referred to the work of Harper and Bonfield (Harper & Bonfield, 2000). The specimens have the dimensions: 75 mm in length, 5 mm in width, approximately 3.5 mm in thickness, with a gauge length of 25 mm. The crosshead speed employed was 5 mm/min. The compressive analysis of bone cement corresponded to ASTM F451. The crosshead speed was 25 mm/min. The diameter and length of the specimens were 6.0 mm and 12.5 mm, respectively.

The dynamic mechanical properties of bone cements were measured using dynamic mechanical analysis (DMA 2980, TA Instruments), with the clamp of single cantilever. The dimensions of the rectangular specimens for DMA were 35mm×11mm×2.7mm. The measuring temperatures ranged from 25 to 150°C at 3°C/min, and the frequencies swept at 1 Hz, 3 Hz, 5 Hz, and 10 Hz. The glass transition temperature of a sample was labelled using the tan δ peak, which occurs at the highest temperature.

The surface of the gold-coated test specimens was observed using Scanning Electron Microscope (SEM) (JEOL, JSM-6700F) at an accelerating voltage of 10 kV.

Thermogravimetric analysis (TGA) experiment was performed with Thermogravimetric analyzer (TGA-2050, TA Instruments Inc) under air flow at a heating rate of 10°C/min. The

temperature of the curing acrylic bone cement was measured using a thermocouple. The measuring probe was situated in the bone cement.

3. Results and discussion

Table 3 shows the tensile and compressive strength of the bone cements tested in this study. System 1 is a commercial product which has tensile strength and compressive strength of 40.49 MPa and 105.33 MPa, respectively. Harper and Bonfield report that the tensile strength of Osteobond bone cement is 38.2 ± 2.65 MPa (Harper & Bonfield, 2000). Compressive strength of bone cement usually varies from 44 to 103 MPa (Saha & Pal, 1984). Systems 2 to 7 are the bone cements containing carbon nanotube. Both tensile and compressive strength of System 2 are about 18% and 23%, respectively higher than that of System 1. It indicates that the introduction of PMMA/CNT pre-polymeric composites is able to enhance mechanical properties of bone cement. Compared with Kwon's study of MMT modified bone cement showed in introduction section, the compressive strength of carbon nanotube modified bone cement exhibited significant increase (23%) than that of MMT modified bone cement (2.7 % increasing in compressive strength). Figure 1 shows the stress-strain curves of System 1 and System 2 tested in tensile strength. It indicates that the toughness of System 2 is better than that of System 1. Therefore, CNT modified bone cement should be able to block crack propagation.

	Tensile strength (MPa)	SD	Compressive strength (MPa)	SD
System 1	40.49	1.79	105.33	21.92
System 2	48.03	1.55	130	4.16
System 3	48.36	1	130.16	3.83
System 4	48.01	3.09	127.25	2.44
System 5	45.55	1.65	130.02	7.41
System 6	45.86	4.23	129.06	3.37
System 7	46.58	4.65	127.83	3.54

Table 3. The tensile and compressive strength of the bone cements tested in this study

Figure 2 illustrates the storage moduli of the bone cement systems as a function of temperature at the frequency of 3 Hz. A storage modulus in DMA can be seen as the stiffness of material. At low temperatures, the storage moduli of the all samples do not show significant difference. Since only strength of the powder portion of bone cement was increased, the liquid portion of bone cement was remained the same as commercial product. However, when the temperature increases to more than 100 °C, System 1 exhibits higher storage modulus than the others. Figure 3 is the tan δ values of the cement systems as a function of temperature at the frequency of 3 Hz. The glass transition temperature of a sample was labeled using the tan δ peak. Figure 4 is the glass transition temperatures of the

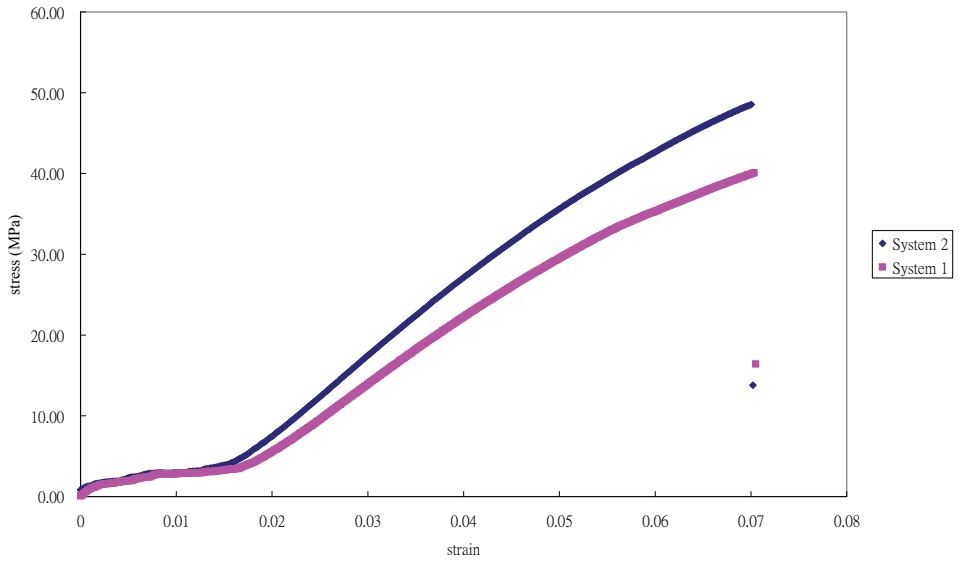

Fig. 1. The stress-strain curves of System 1 and System 2 tested in tensile strength

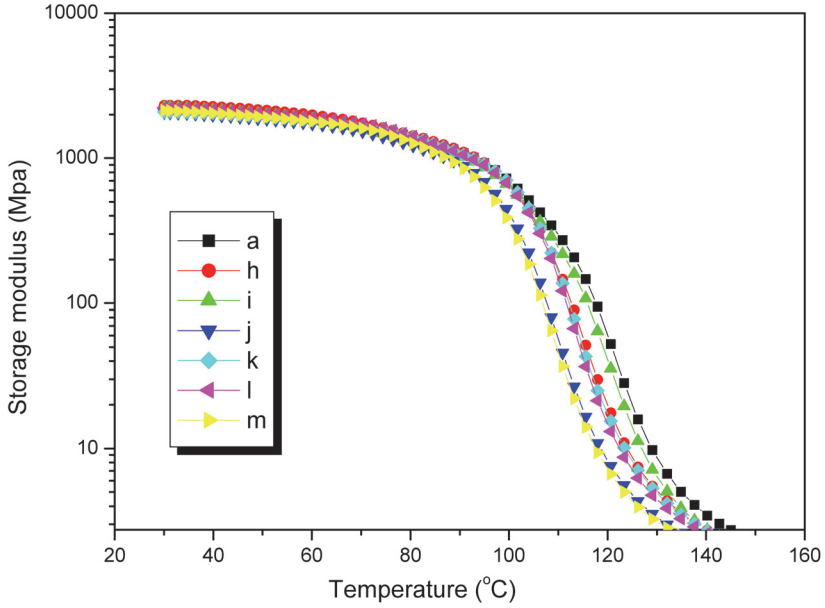

Fig. 2. The storage moduli of the bone cement systems as a function of temperature at the frequency of 3 Hz (a: System1, h: System 2, i: System 3, j: System 4, k: System 5, l: System 6, m: System 7)

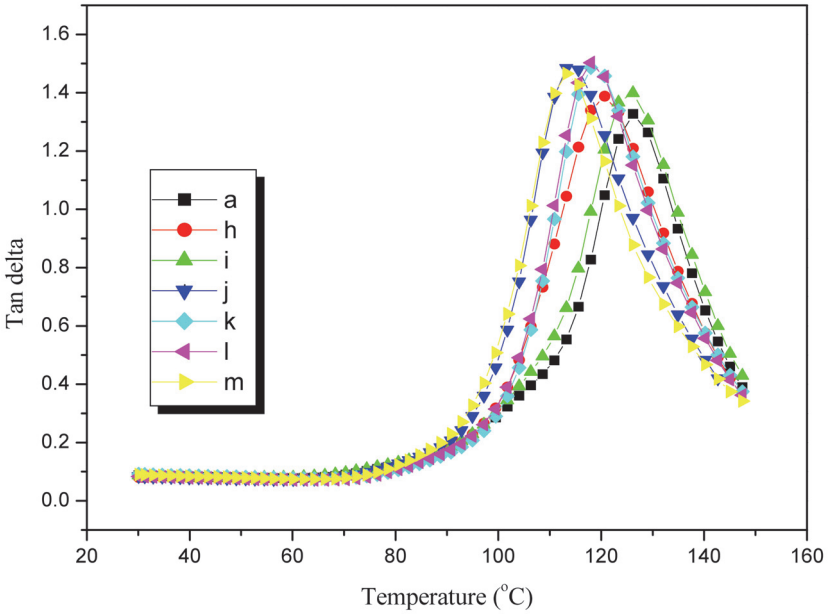

Fig. 3. The tan δ values of the cement systems as a function of temperature at the frequency of 3 Hz. (a: System1, h: System 2, i: System 3, j: System 4, k: System 5, l: System 6, m: System 7)

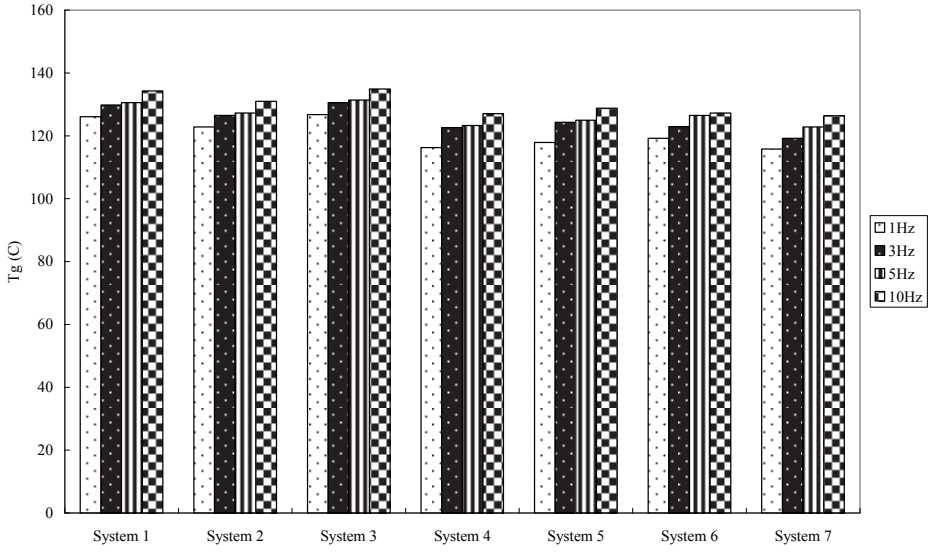

Fig. 4. The glass transition temperatures of the bone cements measured using DMA at the frequencies of 1 Hz, 3 Hz, 5 Hz, and 10 Hz

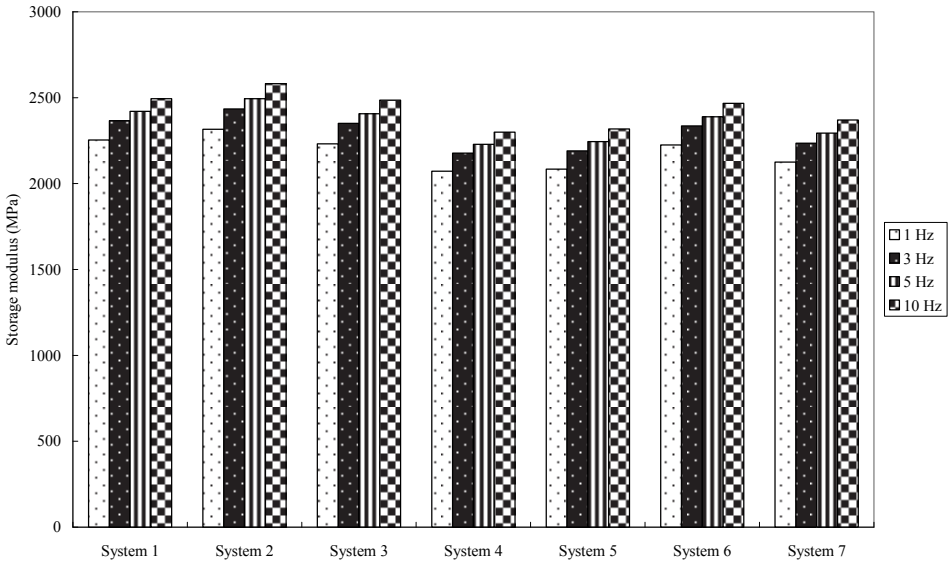

Fig. 5. The storage moduli of the bone cements measured using DMA at the frequencies of 1 Hz, 3 Hz, 5 Hz, and 10 Hz

bone cements measured using DMA at the frequencies of 1 Hz, 3 Hz, 5 Hz, and 10 Hz. System 1 (commercial product) has the highest Tg among the bone cement. The lower Tg of the modified bone cement may be due to carbon nanotube acted as plasticizer. The dynamic mechanical properties of viscoelastic materials, such as polymeric composites, are time dependent. When sweep frequency increases, the glass transition temperatures of the bone cements exhibit higher. Figure 4 is the storage moduli of the bone cements measured using DMA at the frequencies of 1 Hz, 3 Hz, 5 Hz, and 10 Hz. The storage modulus of bone cement also increases, when sweep frequency increases. Figure 6 is the surface of the CNT modified bone cement observed using SEM. It is obvious that carbon nanotube existed in bone cement. Usui et al. uses CNTs to promote bone regeneration (Usui et al., 2008). Therefore, it is expected for CNT modified bone cement in promoting bone regeneration.

Figure 7 is the SEM image of the multiwall carbon nanotube without purification. Figure 8 is the SEM image of the multiwall carbon nanotube after purification. The multiwall carbon nanotubes after purification still retained fibrous structure without damage. Figure 9 and Figure 10 are TGA curves of the multiwall carbon nanotube samples without purification and after purification, respectively. It is obvious that the multiwall carbon nanotube without purification contained impurities about 13%. After purification, the impurities in multiwall carbon nanotube were dramatically down to about 2%. The decomposition temperature of the multiwall carbon nanotube without purification was about 623°C. After purification, the decomposition temperature of the multiwall carbon nanotube sample was increased to about 670°C. It was due to the decrease of the content of the non-nanotube carbon in multiwall carbon nanotube after purification.

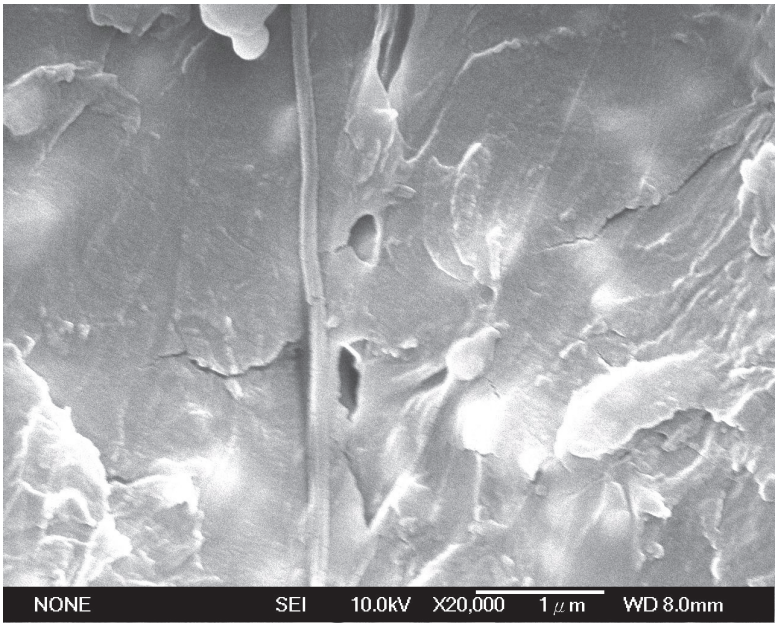

Fig. 6. The surface of the CNT modified bone cement observed using SEM

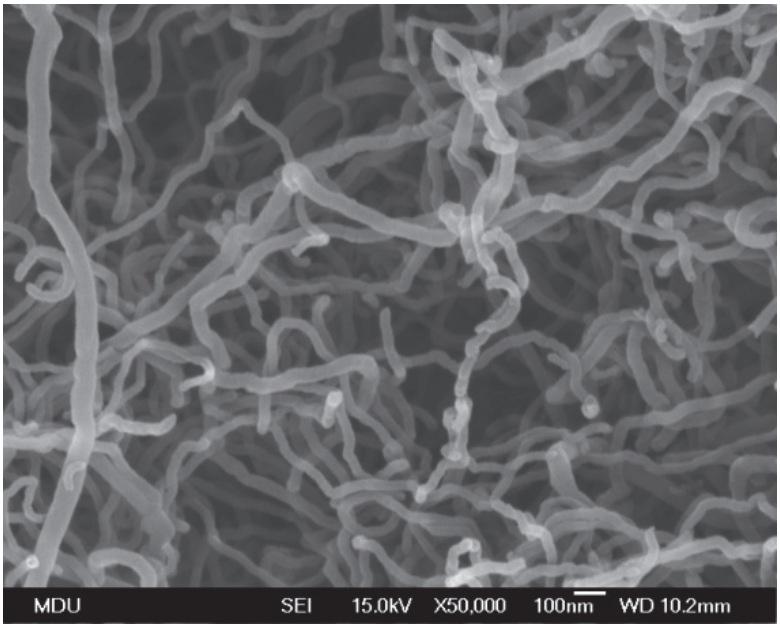

Fig. 7. The SEM image of the multiwall carbon nanotube without purification

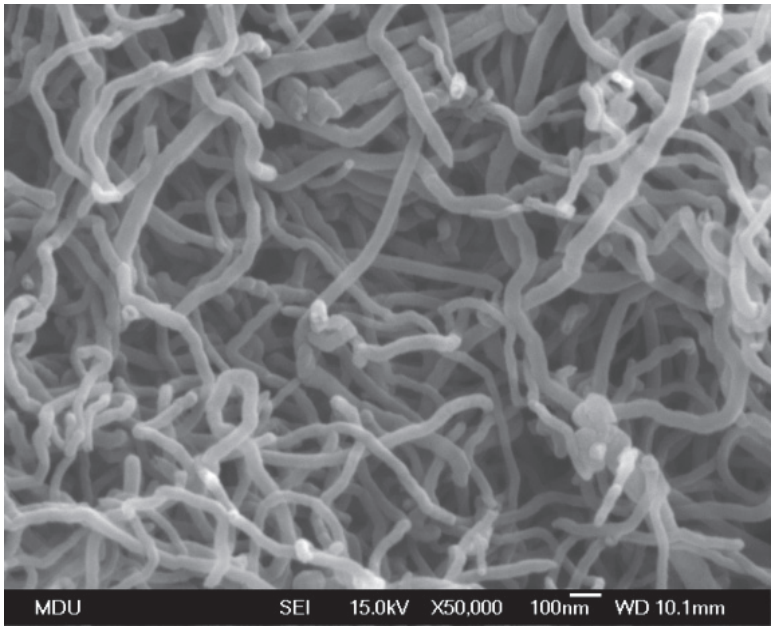

Fig. 8. The SEM image of the multiwall carbon nanotube after purification

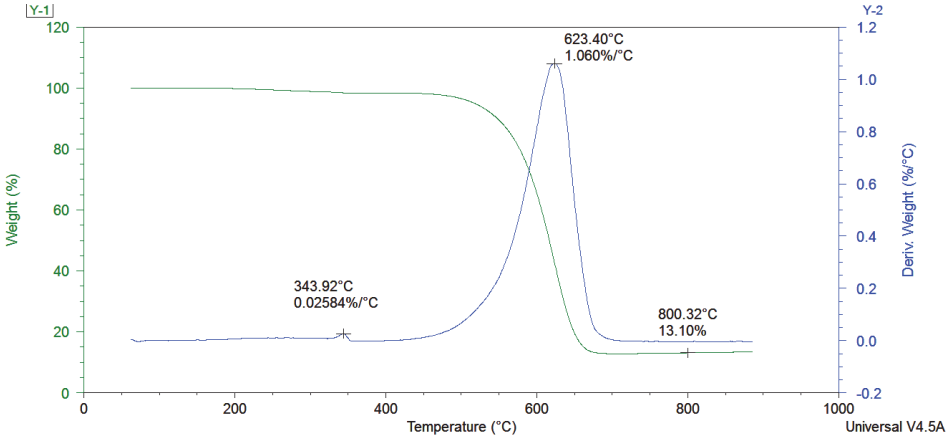

Fig. 9. The TGA curve of the multiwall carbon nanotube sample without purification

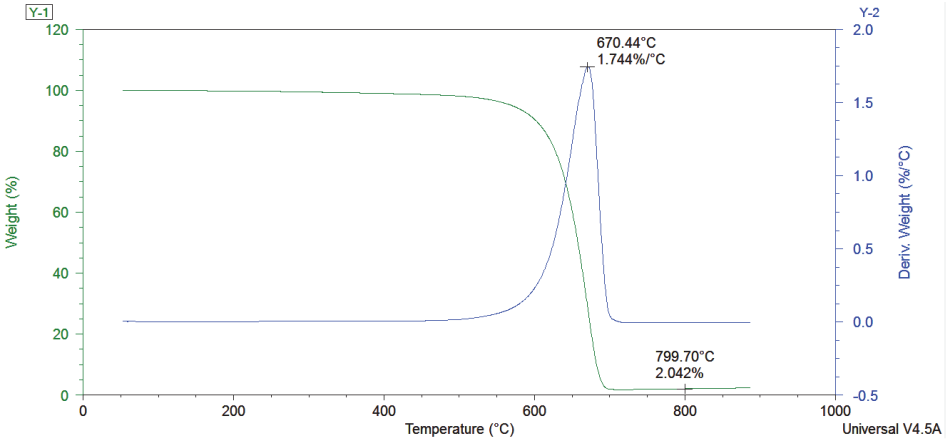

Fig. 10. The TGA curve of the multiwall carbon nanotube sample after purification

Figure 11 is the temperature profile of the curing acrylic bone cement modified by multiwall carbon nanotube. The maximum curing temperature of the acrylic bone cement modified by multiwall carbon nanotube was about 60°C. Figure 12 is the temperature profile of the curing acrylic bone cement without modification of multiwall carbon nanotube. Since the multiwall carbon nanotube was first to be prepared as PMMA/carbon nanotube powder, the PMMA/carbon nanotube powder as a pre-polymerized composite was not reacted further during the curing of the bone cement. Therefore, the curing temperature of the acrylic bone cement modified by multiwall carbon nanotube should be similar to that of the acrylic bone cement without modification of multiwall carbon nanotube.

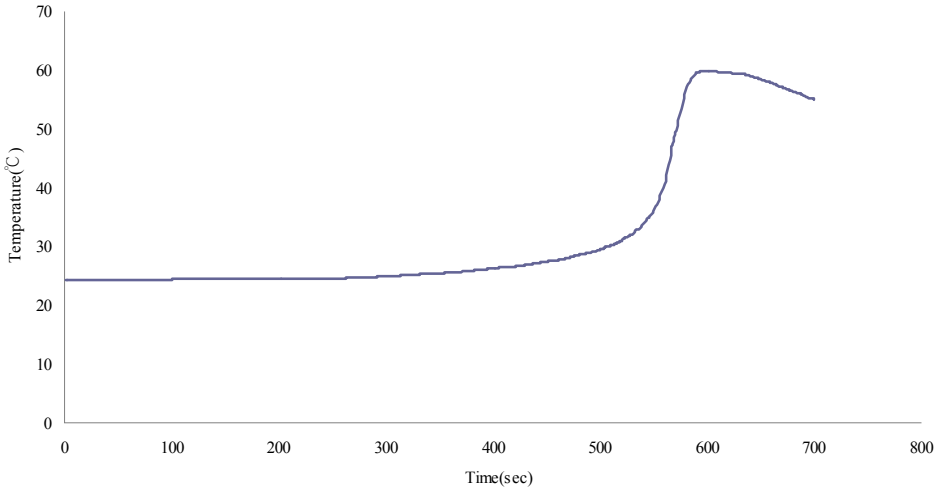

Fig. 11. The temperature profile of the curing acrylic bone cement modified by multiwall carbon nanotube

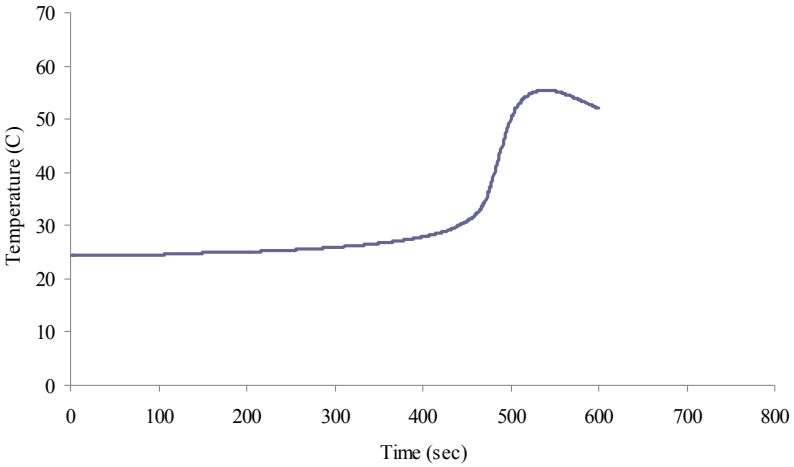

Fig. 12. The temperature profile of the curing acrylic bone cement without modification of multiwall carbon nanotube

3. Conclusion

In this study, we have prepared a new type of bone cement reinforced with carbon nanotube. In order to achieve better dispersion of carbon nanotube in bone cement, we first fabricated PMMA/CNT composites and then ground them as powder form to be introduced into bone cement. This kind of modified bone cement exhibits excellent material properties such as tensile and compressive strength. The results show potential usage in clinical applications.

4. Acknowledgment

The author would like to thank National Science Council, Taiwan for financial support under grant contract NSC 97-2221-E-224-068-. My students, Chiao-li Huang and Randy Hsu, did a lot of work in this study.

5. References

Basgorenay, B; Ulubayram, K.; Serbetci, K.; Onurhan, E. & Hasirci1, N. (2006). Preparation, Modification, and Characterization of Acrylic Cements. J Appl Polym Sci Vol.99, pp. 3631–3637

Cooper, C. A.; Ravich, D.; Lips, D.; Mayer J. & Wagner, H. D. (2002). Distribution and alignment of carbon nanotubes and nano fibrils in a polymer matrix. Composites Science and Technology. Vol.62, pp. 1105 –1112

Harper, E. J. & Bonfield, W. (2000). Tensile Characteristics of Ten Commercial Acrylic Bone Cements. J Biomed Mater Res (Appl Biomater). Vol.53, pp. 605–616

Iijima, S. (1991). Helical microtubules of graphitic carbon. Nature Vol.354, pp. 56 – 58

Jia, Z.; Wang, Z.; Xu, C.; Liang, J.; Wei B.; Wu D. & Zhu, S. (1999). Study on poly(methyl methacrylate):carbon nanotube composites. Materials Science and Engineering A. Vol.271, pp. 395–400

Jin, Z.; Pramoda, K. P.; Xu, G. & Goh, S. H. (2001). Dynamic mechanical behavior of melt-processed muti-walled carbon nanotube/poly(methyl methacrylate) composites. Chemical Physics Letters Vol.337, pp. 43-47

Kearns, J. C. & Shambaugh R. L. (2002). Polypropylene fibers reinforced with carbon nanotubes. Journal of Applied Polymer Science. Vol.86, pp. 2079-2084

Kwon, S. Y.; Cho, E. H. & Kim, S. S. (2007). Preparation and Characterization of Bone Cements Incorporated With Montmorillonite. J Biomed Mater Res Part B:Appl Biomater Vol.83B, pp. 276–284

Park, J. B. & Lakes, R. S. (1992). Biomaterials: An introduction, 2nd Edition, Plenum Publishing Corporation, ISBN 0306439921, New York, USA

Saha, S. & Pal, S. (1986). Mechanical characterization of commercially made carbon-fiber-reinforced polymethylmethacrylate. Journal of Biomedical Materials Research, Vol.20, pp. 817-826

Saha, S. & Pal, S. (1984). Mechanical properties of bone cement: A review. Journal of Biomedical Materials Research, Vol.18, pp. 435-462

Stephan, C. ; Nguyen, T. P.; de la Chapelle, M. L. ; Lefrant, S. ; Journet, C. & Bernier, P. (2000). Characterization of singlewalled carbon nanotubes-PMMA composites. Synthetic Metals. Vol.108, pp. 139-149

Usui, Y.; Aoki, K.; Narita, N.; Murakami, N., Nakamura, I.; Nakamura, K.; Ishigaki, N.; Yamazaki, H.; Horiuchi, H.; Kato, H.; Taruta, S.; Kim Y. A.; Endo, M. & Saito, N. (2008). Carbon Nanotubes with High Bone-Tissue Compatibility and Bone-Formation Acceleration Effects. Small. Vol.4, No.2, pp. 240 – 246

Vallo, C. I.; Abraham, G. A.; Cuadrado, T. R. & Roman, J. S. (2004). Influence of Cross-Linked PMMA Beads on the Mechanical Behavior of Self-Curing Acrylic Cements. J Biomed Mater Res Part B: Appl Biomater Vol.70B, pp. 407–416

19

Single-Walled Carbon Nanotubes as a Molecular Heater for Thermoresponsive Polymer Gel Composite

Tsuyohiko Fujigaya and Naotoshi Nakashima
Department of Applied Chemistry, Graduate School of Engineering, Kyushu University, Japan

1. Introduction

The structural stiffness, effective optical absorption ranging from UV to IR region and efficient photothermal conversion of the carbon nanotubes (CNTs) are attractive feature as a molecular heater, which can be useful for therapy, actuator and so on. Dai et al. reported that the near-IR (NIR) irradiation to a living HeLa cell after uptaking a CNTs/DNA composite caused death of the cells (Kam, et al., 2005) due to the intense local heating triggered by the NIR irradiation. We have described that pulsed-NIR irradiation of CNTs wrapped by an anthracene-pendanted polymer allowed the dissociation of the polymer from the CNTs surface followed by aggregation of the CNTs, in which the CNTs act as a "molecular heater" that triggers removal of the polymer from the SWNT surface.(Narimatsu, et al., 2006)

On the other hand, thermoresponsive polymer gels, which show phase transitions, are of interests in wide areas of science and technology from the aspects of both fundamental (experimental and theory) and applications (Bohidar, et al., 2003). Poly(*N*-isopropylacrylamide) (PNIPAM) (Hirotsu, et al., 1987; Schild, 1992) and its derivatives are well-known thermoresponsive materials, which show a phase transition triggered by external stimuli such as the solvent composition, (Katayama, et al., 1984) pH, (Tanaka, et al., 1980) ionic strength, (Tanaka, et al., 1980) electric field (Tanaka, et al., 1982) and light. (Ishikawa, et al., 1993; Juodkazis, et al., 2000; Mamada, et al., 1990; Nayak & Lyon, 2004; Suzuki & Tanaka, 1990) Among the various light sources, NIR laser light is a fascinating stimulus especially from a biomedical point of view, because biomedical tissues have a slight absorption in the NIR region, (Weissleder, 2001) which enable remote stimulation of the NIR absorbent in the body from the outside.

The combination of CNTs with PNIPAM would expect to trigger the phase transition of PNIPAM with NIR irradiation through photothermal conversion of CNTs. In this article, we propose the utilization of single-walled carbon nanotubes (SWNTs) as a photon antenna that serves as an effective "molecular heater" around the NIR region.

2. Photoinduced phase transition of thermoresponsive gel

2.1 Preparation of the SWNTs/PNIPAM gel composite

SWNTs are hydrophobic materials with a high aspect ratio and are strongly bundled to each other, thus the dispersion of the SWNTs in organic and inorganic solvents is quite difficult

to give an aggregation in the solvent as shown in Fig. 1a.(Nakashima & Fujigaya, 2007) Yodh et al.(Islam, et al., 2004) used a surfactant as a dispersant of the SWNTs in the preparation of a SWNT/PNIPAM gel in an aqueous solution, and examined liquid crystalline nature of the composite gel. However, the addition of anionic surfactants dramatically increases the transition temperatures (T_c) of the PNIPAM in an aqueous system.(Kokufuta, et al., 1993) To avoid such a problem, we introduced carboxylate groups onto the SWNTs surface by treating with strong acid to improve the dispersibility of the SWNTs in an aqueous system. The obtained acid-treated SWNTs were dispersed in deionized water with only mild shaking (Fig. 1b). The SWNT/PNIPAM composite gel preparations were carried out according to the typical procedure of PNIPAM gelation (Tanaka, 1978) in the absence of the SWNTs.

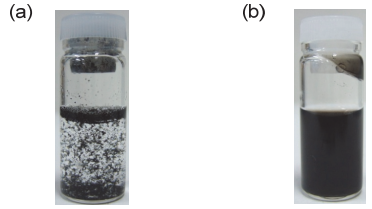

Fig. 1. SWNT dispersion solutions, (a) As-prepared SWNT dispersion in water. (b) Acid-treated SWNT dispersion in water.

The visible-NIR spectrum of the synthesized composite gel (Fig. 2a; inset) showed absorption over a wide range of the spectrum (solid line in Fig. 2a), while the gel without the SWNTs has no absorption in the visible-NIR region (dotted line in Fig. 2a). The composite gel was a transparent grey-color at temperatures below 23 °C, while upon heating in a temperature-controlled water bath, the gel changed to opaque at around 34.6 °C, suggesting that the transition temperature (T_c) of the SWNT/PNIPAM composite gel was virtually identical with that (T_c = 34.0 ˚C) of the SWNTs/PNIPAM gel (control sample). The phase transition of the PNIPAM gel was also investigated using UV-visible spectroscopy and differential scanning calorimetry (DSC). By plotting the absorbance at 600 nm, the transition temperature is determined to be ca. 33 °C (Fig. 2b). The T_c of the SWNTs/PNIPAM gel both upon heating and cooling were virtually identical to that of the gel without the SWNTs prepared as a control (Fig. 2c). In DSC, the endothermic peaks were appeared at around 35 °C for both the SWNT/PNIPAM and the PNIPAM gel (Fig. 2d), which agreed well with the results described above. It is clear that the SWNTs in the composite gel have virtually no effect on the phase transition temperature of the PNIPAM gel.

2.2 NIR irradiation to SWNTs/PNIPAM gel

We used the SWNTs as a "molecular heater" for the thermal phase transition of the composite gels. NIR laser irradiation experiments for the SWNT/PNIPAM gel and the PNIPAM gel were carried out for the gel tubes prepared and drawn from the capillary tube with inner diameter around 200 μm. As shown in Fig. 3a, upon irradiation with the NIR light centered at 1064 nm, the composite gel tube (initial diameter $d_0 \approx 240$ μm) containing the SWNTs become a smaller diameter ($d \approx 80$ μm) after 15 sec. As plotted in Fig. 3b that after turning off the irradiation, the shrunken gel gradually swells and becomes around 200

μm in diameter after about 67 sec. The further shrink-swell experiment upon ON/OFF irradiations was described in following session.

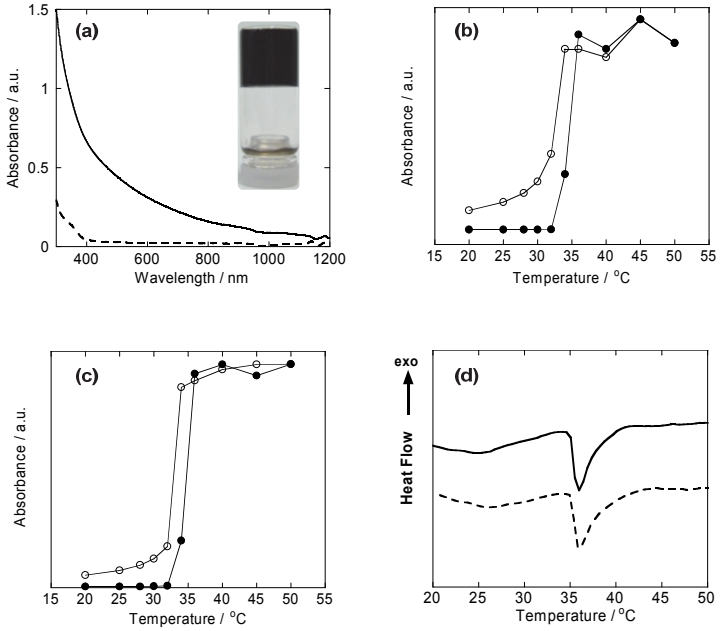

Fig. 2. Characterizations of a SWNT/PNIPAM gel, (a) Visible-NIR spectra of a SWNT/PNIPAM gel (solid line) and a PNIPAM gel (dotted line) at 20 °C. inset; photo of SWNT/PNIPAM gel (b) Temperature dependence of the optical absorption at 600 nm of a SWNT/PNIPAM gel was recorded for a heating process (solid circle) and a cooling process (open circle). (c) Temperature dependence of the optical absorption at 600 nm of a PNIPAM gel (controlled sample) upon heating process (solid circle) and a cooling process (open circle). (d) DSC curves of the gels of SWNT/PNIPAM gel (solid line) and PNIPAM gel (dotted line).

A stronger NIR laser power (> 1.2 W) has been reported to increase the temperature through the photothermal conversion of water.(Ishikawa, et al., 1996) However, this effect is excluded under our experimental conditions since the 210-mW NIR irradiation to the gel (controlled sample) prepared from the single component of PNIPAM showed no such volume phase transition even after the NIR-laser irradiation. It is conclusive that the NIR light irradiation to the SWNT/PNIPAM gel caused the phase transition of the PNIPAM gel via the photothermal conversion of the SWNTs. This contrasting result between the SWNT/PNIPAM gel and PNIPAM gel is the consequence of NIR absorption of the SWNT/PNIPAM gel at around 1064 nm (solid line in Fig. 2a), whereas the gel without the SWNTs has no absorption in the NIR region (dotted line in Fig. 2a). The proposed mechanism is that the local heating of the SWNTs due to the irradiation raises the temperature of the water around the irradiation spot in the gel over 35 °C, which induces the phase transition of the PNIPAM gel as discussed for the visible-light induced phase transition of the PNIPAM.(Suzuki & Tanaka, 1990) Here, the SWNTs act as a "molecular heater" to induce the phase transition of the PNIPAM in the composite gel.

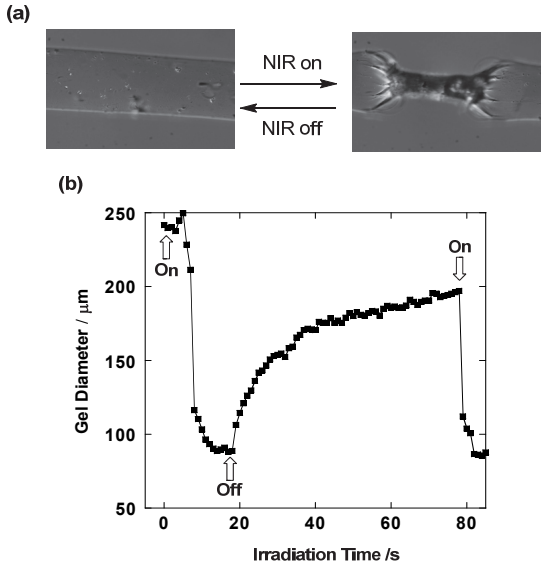

Fig. 3. NIR-induced phase transition, (a) NIR laser-driven volume change of a SWNT/PNIPAM gel shown by optical microscopic images. (b) Plot of the diameter of the SWNT/PNIPAM gel plotted as a function of time.

The response time of the volume change can be controlled by changing the concentration of the SWNTs as well as the power of the NIR laser light. The d/d_0 values obtained by the 210-mW or 390-mW irradiations of the composite gels synthesized using the different concentrations of the acid-treated SWNTs in water (2.0, 1.0, 0.5, 0.25, and 0.13 mg/mL) are plotted as a function of the irradiation time in Fig. 4a (210-mW irradiation) and Fig. 4b (390-mW irradiation). In the case of the 210-mW irradiation, the NIR-driven volume change in the gel samples synthesized at the concentrations of acid-treated aqueous SWNTs=2.0, 1.0, and 0.5 mg/mL almost finished in 4, 5, and 6 sec, respectively, whereas the gels synthesized from the lower concentration of the SWNTs = 0.25 and 0.13 mg/mL showed no phase transition.
On the other hand, at a 390-mW irradiation, the gels synthesized at the concentration of the SWNTs= 2.0, 1.0, 0.5, and 0.25 mg/mL shrunk within 2, 2, 5, and 12 sec, respectively, while the gel prepared at SWNTs=0.13 mg/mL showed no change. The absence of the phase transition observed for the gels from the SWNTs=0.25 and 0.13 mg/mL upon 210-mW irradiation and SWNTs=0.13 mg/mL upon 390-mW irradiation suggests the importance of the initial process, that is, the dark spot generated on the focal point enhances the absorption of the NIR light in that region, which accelerates the heating of the gels. The rate of this initial process varies with the concentration of the SWNTs as well as the NIR laser irradiation power. It is clear that the higher-powered light irradiation and the higher concentrations of the SWNTs in the gels render the composite gels a faster response. Of interest, for the gels especially with 2.0 and 1.0 mg/mL concentrations, we observed a bubble generation from the center of the irradiation spot upon the 390-mW irradiation. This phenomenon indicates that the temperature at the spots in the gels reached over 100 ˚C due to the photothermal conversion of the SWNTs. All the obtained results guarantee that the phase transition of the composite gels is triggered by photon absorption of the SWNTs in the NIR region.

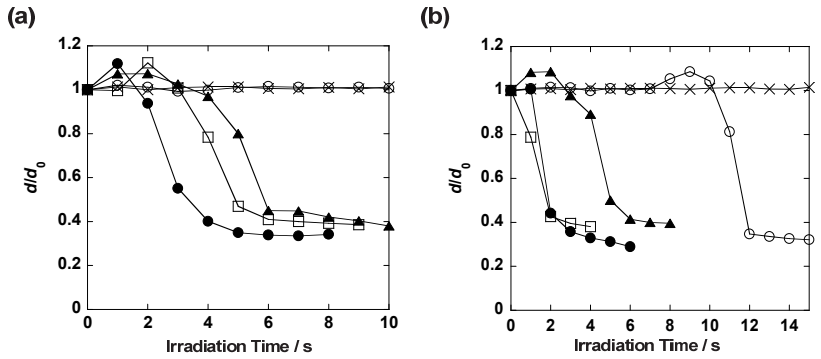

Fig. 4. Effect of SWNT concentration, The d/d_0 values of the composite gels synthesized using the different concentrations of acid-treated aqueous SWNTs = 2.0 (•), 1.0 (□), 0.5 (▲), 0.25 (○), and 0.13 (x) mg/mL on a (a) 210-mW and (b) 390-mW NIR laser irradiation plotted as a function of irradiation time.

2.3 Durability of SWNTs upon NIR irradiation

The SWNTs possess a robust structures arising from their rigid fused aromatic structures, and thus the SWNT-composite gels are expected to show high durability for the repeated ON/OFF-laser irradiation. We carried out an endurance test using the hybrid gel under optical micrograph monitoring, in which the tests were conducted by a programmed NIR laser operation repeated with ON irradiation for ca. 4 sec, followed by OFF irradiation for 55 sec to ensure the shrink-swell cycles (Fig. 5). Amazingly, no notable deterioration of the gel actuation was observed even after the 1200-cycle operation. As shown in Fig. 6, the Raman spectra of the gels before (dotted line) and after (solid line) the endurance test supports this durability, namely, both spectra exhibit virtually identical G/D (Graphite/Defect) ratios, which guarantee that the SWNTs remain structurally intact.

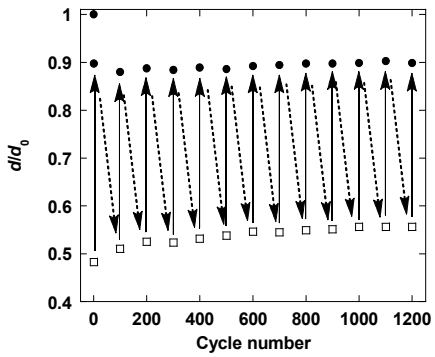

Fig. 5. Durability of the composite gel, The d/d_0 values of a SWNT/PNIPAM gel for ON (open square)/OFF (solid circle) switching of the NIR laser light irradiation plotted as a function of the cycle number. Data are collected every 100 cycles to avoid complication.

It is readily expected that the composite gel system can tolerate additional operations of more than 1200 cycles. We tested the gold nanorod (Au-NR)-mediated systems(Gorelikov, et al., 2004; Sershen, et al., 2005; Sershen, et al., 2000; Sershen, et al., 2001; Shiotani, et al., 2007) as another candidate for the NIR actuation of PNIPAM gels since Au-NR has an absorbance in the NIR region. The extinction coefficient of the Au-NR/PNIPAM mixture at 1064 nm is matched to that of the SWNT/PNIPAM mixture used in the endurance test for the fair comparison. Au-NR in the Au-NR/PNIPAM gel caused an aggregation of the particles after the 1200-cycle durability test, namely, we observed a blue shift in the peak that stemmed from the plasmon band of Au-NR at around 800 nm. It is evident that the SWNT/NIPAM gels have a stronger durability for the NIR irradiation.

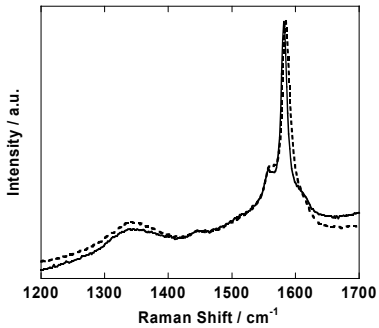

Fig. 6. Estimation of damage for SWNTs, Raman spectra of the gel before (dotted line) and after (solid line) the 1200-cycle irradiations.

3. Preparation and applications of SWNTs/PNIPAM gel using pristine SWNT (Fujigaya, et al., 2011)

3.1 Preparation of the SWNTs/PNIPAM gel composite

One of the goals of the study is to design and fabricate a NIR laser-driven drug-releasing system using isolated SWNTs as the material, in which the SWNTs having large surface areas embedded in a polymer gel serve as an efficient drug reservoir through physisorption of the molecules onto SWNTs. π-conjugating graphitic surface induces a molecular adsorption thorough many different interaction mode such as π–π, hydrophobic and van der Waals interactions. To realize an effective adsorption of the drug typically have a hydrophobic nature, employment of pristine SWNTs is essential since the surface of acid-treated SWNT possess many carboxylic group and turned to hydrophilic nature.

The preparation strategy of the composite gel are illustrated in Fig. 7. The composite gel composed of pristine SWNTs was prepared by the gelation of NIPAM in the presence of pristine SWNTs individually dissolved in an aqueous solution of the sodium dodecyl benzenesulfonic acid sodium salt (SDBS). SDBS was chosen as an SWNT dispersant since it is known to individually dissolve the SWNTs quite efficiently by encapsulating the SWNTs into the interior of the SDBS micelle in aqueous media.(McDonald, et al., 2006) The composite SWNT/PNIPAM gel was almost transparent similar with a PNIPAM gel without SWNT and slightly grey-colored due to the presence of a SWNTs. The mesh size of the SWNT/PNIPAM gel in aqueous media was determined by dynamic light scattering (DLS) to be around 10~20 nm (data not shown) which well agreed with previous reports.(Canal &

A. Peppas, 1989; Ishidao, et al., 1997) The observation of the intense photoluminescence (PL) signals from the composite gel guaranteed the isolation of the SWNTs even after the gelation since the PL signals are proved to be detected only from the individually isolated SWNTs (Fig. 8a).(O'Connell, et al., 2002)

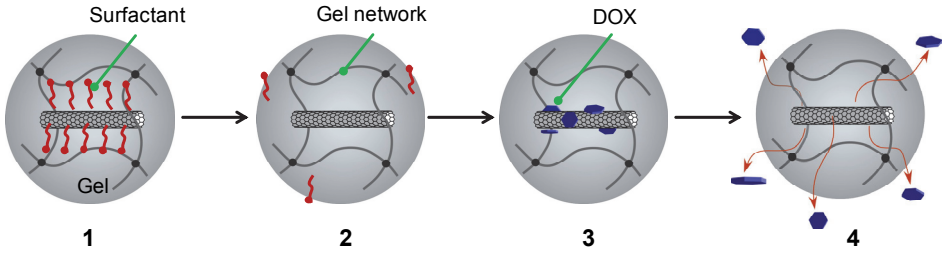

Fig. 7. Schematic illustration showing the strategy of this study. Stage **1**, Gelation carried out in an SDBS (dark blue) solution produces an SDBS-adsorbed SWNT in the gel. Stage **2**, SDBS on the SWNT surface are removed by dipping the gel in Milli-Q water. Stage **3**, The adsorption of drug molecules (red), occurs on the "vacant" SWNT surfaces through π-π and hydrophobic interactions. Stage **4**, The drug molecules on SWNT surfaces detach from the surfaces by a pH change or NIR laser irradiation by a photothermal conversion effect of the SWNTs.

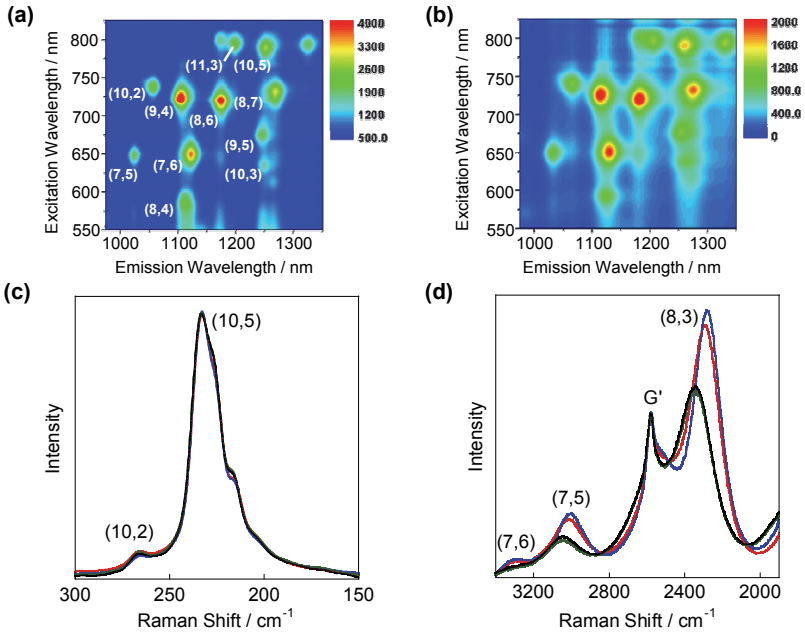

Fig. 8. Isolation of SWNTs in PNIPAM gel, (a,b) 2D PL mapping of the SWNT/PNIPAM gel before (a) and after (b) dipping in Milli-Q water for 72 h. (c,d) Raman spectra of the gel normalized at the (10,5) peak and G' peak for c and d, respectively; the red, blue, green and black lines show the spectra after the immersion in water for 24, 48, and 72 h, respectively.

In order to remove the SDBS molecules from the surfaces of the SWNTs, the composite gel was immersed in a large amount of Milli-Q water for 72 h. The Raman spectra of the SWNTs in the composite gel were monitored during the immersion in water by measuring the radial breathing mode (RBM) (Fig. 8c) together with the PL signals(Jeng, et al., 2006; Moore, et al., 2003) (Fig. 8b). We recognized that the PL peak from the (8,3) SWNT bathochromically shifts from 2290 to 2350 cm^{-1} due to the increase in the micropolarity around the SWNTs as reported in the literature (Fig. 8d).(Jeng, et al., 2006; Moore, et al., 2003; Strano, et al., 2003) Such a clear shift as well as the decrease in the peak intensity after the immersion in water indicated that the SDBS molecules were removed from the SWNT surfaces and replaced by water molecules.(Strano, et al., 2003) In order to confirm the removal of the SDBS from the SWNT surfaces in the composite gel, we measured the X-ray photoelectron spectrum (XPS) of the SWNT/PNIPAM gel after drying, and found that the sulfur signal almost disappeared in the sample after the immersion in water (Fig. 9).

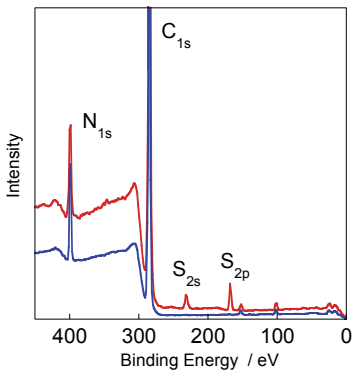

Fig. 9. X-ray photoelectron spectra, The spectra of SDBS/SWNT/PNIPAM gel before (red line) and after (blue line) immersion in deionized water.

Moreover, it is also important to emphasize that we observed a clear PL from the SWNTs in the gel after the immersion, whose PL-mapping (Fig. 8b) is virtually identical with that before the immersion (Fig. 8a). This suggests that the SWNTs remained in an isolated state even after the removal of the SDBS molecules. The Raman data also support this, namely, the intensities of the (10,2) RBM peak of the gel before and after immersion at around 267 cm^{-1}, which is known as an indicator for the evaluation of the degree of the SWNT aggregation,(Ericson & Pehrsson, 2005; Fujigaya, et al., 2009; Heller, et al., 2004; Kumatani & Warburton, 2008; Luo, et al., 2006; O'Connell, et al., 2004; Strano, et al., 2003) are virtually identical (Fig. 8c). The obtained results are in sharp contrast to those previously reported, in which the SWNTs aggregate after removal of the dispersants.(Chen, et al., 2008; Ikeda, et al., 2009; Ishibashi & Nakashima, 2006; Nobusawa, et al., 2008) We suggest that the SWNTs (~ 1 μm) penetrated the three-dimensional gel network structure having a 10~20-nm mesh to form the semi-interpenetrating network (semi-IPN) structure,(Gong, et al., 2003) and the formed structure serves to prevent further assembling (aggregation) of the SWNTs even in the absence of the dispersants. To our surprise, PL signals were also observed from the re-swelled gel after drying in a vacuum, indicating that the isolated state of the SWNTs in the gel is highly stable in the three-dimensional gel framework.

3.2 Preparation of SWNT-encapsulated PAAM and PDMAAM composite gels

We also prepared the polyacrylamide (PAAM)- and poly(*N*,*N*-dimethylacrylamide) (PDMAAM)-based composite gels in a way similar to the SWNT/PNIPAM gel to explore the effect of the side chain structures of the polymers. Fig. 10 displayed the PL mapping of the SWNT/PAAM (Fig. 10a and 10b) and SWNT/PDMAAM) (Fig. 10c and 10d) before and after the SDBS removal from the gels. Although no visible aggregation was observed for both gels, we observed a drastic PL quenching in the SWNT/PAAM composite gel (Fig. 10b). We also observed a similar deterioration in the PL signals for the SWNT/PDMAAM

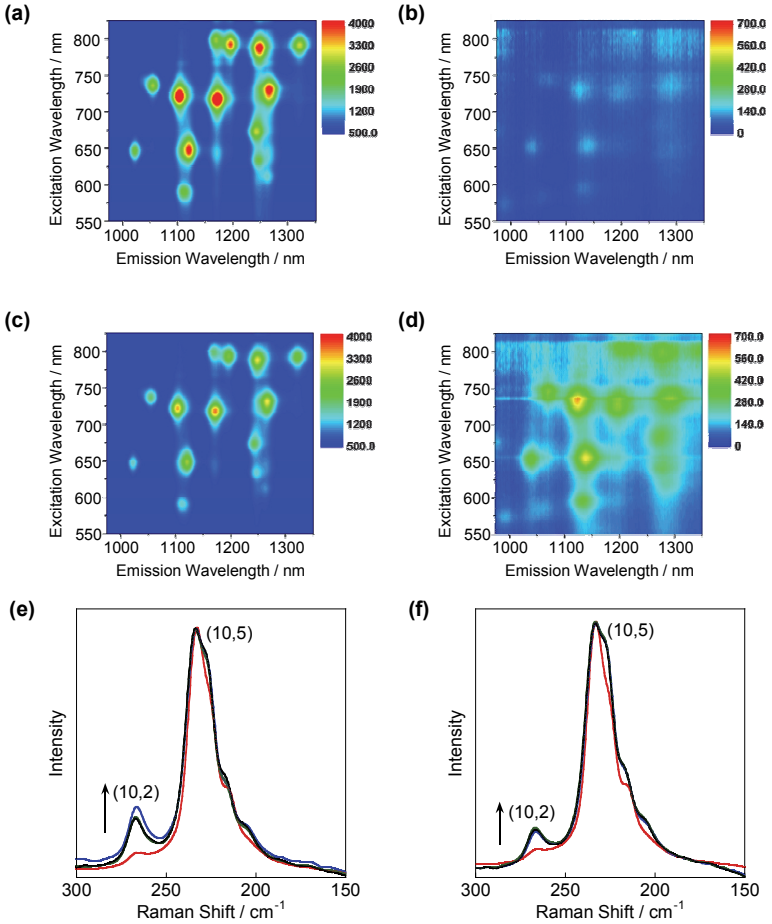

Fig. 10. Isolation of SWNTs in other gels, (a,b) 2D PL mapping of the SWNT/PAAM gel before (a) and after (b) dipping in Milli-Q water for 72 h. (c,d) 2D PL mapping of the SWNT/PDMAAM gel before (c) and after (d) dipping in Milli-Q water for 72 h. (e,f) Raman spectra of the SWNT/PAAM gel (e) and SWNT/PDMAAM gel (f) in the RBM region normalized at the (10,5) peak. The red lines show the initial spectra of the gels, and the blue, green and black lines are the spectra after the immersion for 24, 48, and 72 h, respectively.

gel (Fig. 10d), but the quenching degree is lower than that of the SWNT/PAAM composite gel. The Raman data agreed with the results, namely, we recognize larger (10,2) peaks in the RBM of the SWNT/PAAM after the removal (Fig. 10e) compared to that of the SWNT/PDMAAM (Fig. 10f). Considering the stable isolation of the SWNT in the PNIPAM gel, the CH-π interactions between the SWNTs and the polymer side chains are also considered to contribute to the SWNT isolation in the composite gels. The weaker CH-π interaction of the gel networks of PAAM and PDMAAM with the SWNTs allows to form small-sized bundled SWNTs, but the semi-IPN structure prevents to grow to visible-sized bundled SWNTs. Based on the chemical structures, it is readily expected that the intensities of such CH-π interactions are SWNT/PAAM < SWNT/PDMAAM < SWNT/PNIPAM, which is closely related the stable formation of the isolated SWNTs leading to a stronger PL intensity.

3.3 Drug holding and releasing from SWNT surface

Up to date, only several attempts for the stimuli responsive releasing of the physisorped molecules on SWNTs have been reported.(Ikeda, et al., 2009; Liu, et al., 2007; Nobusawa, et al., 2008) We showed a heat-driven desorption of pyrene-bearing vinyl monomer from SWNT surface.(Nakashima, et al., 2004) Dai et al. reported the detachment of doxorubicin hydrochloride (DOX) molecules from the SWNT surfaces upon lowering the pH of an aqueous media, which induces the increasing of hydrophilicity of the DOX due to the protonation.(Liu, et al., 2007) Redox active molecular detachment from SWNTs was performed with the Cu complex of the 2,2′-bipyridine derivative based on the geometry switching from the planner Cu^{II} complex to the tetrahedral Cu^{I} complex.(Nobusawa, et al., 2008) Light irradiation was also used as an external stimulus, in which the adsorbed malachite green unit (MG) was detached from the SWNT surfaces upon UV-driven ionization of MG.(Chen, et al., 2008)

All these previous studies, however, were carried out using SWNT dispersions and the detachment of the adsorbed molecules from the SWNT surfaces upon external stimuli resulted in the formation of insoluble SWNT aggregates.(Liu, et al., 2007) Additional sonication is required to dissolve the SWNT aggregates in solution. Thus, such irreversibility is inadequate especially *in vivo* application since the SWNT bundle possess a cytotoxic risk.(Wick, et al., 2007)

Dai et al. demonstrated the adsorption and pH responsive desorption of the DOX molecules, known as a cancer drug, on the SWNT surfaces dispersed in water with the aid of the lipid.(Liu, et al., 2007) In this study, we use the isolated SWNTs in the gels as the molecular reservoir to reach an efficient adsorption of the drug followed by a controlled release from the gels. Fig. 11a shows the absorption spectrum of the SWNT/PNIPAM gel before (red line) and after (blue line) dipping in a 1 mM DOX aqueous solution for 48 h. The DOX uptake after the dipping is evident since we see a clear peak around 490 nm due to the absorption of the DOX molecules. After the DOX uptake treatment, quenching of the PL intensity was observed for both the Raman (blue line in Fig. 11b) and PL spectrum (Fig. 11c), which might be induced by the adsorption of DOX molecules on the SWNT surfaces. In addition, the intensity of (10,2)SWNTs RBM peak around 270 cm^{-1} in the Raman spectrum increased slightly (Fig. 12), indicating the formation of the SWNT small bundles after the DOX uptake. This is in sharp contrast with the case without the gel, in which the DOX uptake caused visible aggregations of the SWNTs.(Liu, et al., 2007)

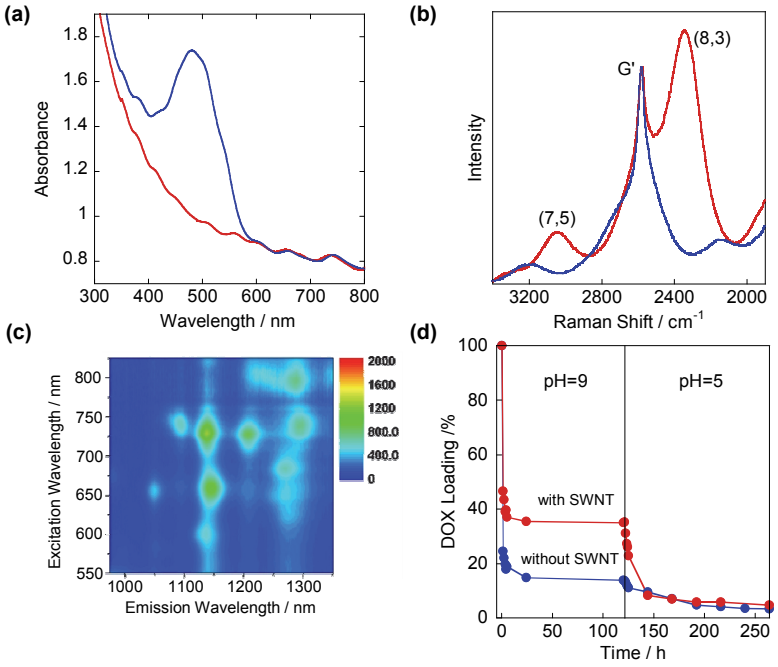

Fig. 11. DOX holding in the composite gel, (a) Absorption spectra of an SWNT/PNIPAM gel (red line) and an SWNT/PNIPAM gel dipped in a 1 mM DOX aqueous solution (blue line). (b) Raman spectra of the SWNT/PNIPAM gel before (red line) and after (blue line) dipping in a DOX solution. (c) 2D-PL mapping of the SWNT/PNIPAM gel after dipping in a DOX solution. (d) Plots of DOX loading of the SWNT/PNIPAM gel (red line) and the PNIPAM gel (blue line) as a function of dipping time. The gels after dipping in a DOX solution were washed with water for 1 min, followed by immersion in a NaOH aqueous solution (pH~9) for 122 h. The gels were then successively transferred into an HCl solution (pH~5).

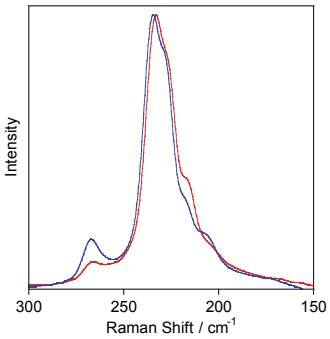

Fig. 12. Raman change after DOX holding, Raman spectra of SWNTs/PNIPAM gel. Raman spectra of SWNTs/PNIPAM gel before (red line) and after (blue line) incubation with 1 mM DOX solution for 2 days were illustrated.

The SWNT/PNIPAM gel was supposed to contain both bound DOX molecules on the SWNTs and unbound DOX. To remove the unbound DOX, the gel was immersed in an alkaline aqueous solution (pH~9). The absorption difference between the DOX-containing gel and the gel without DOX (red line in Fig. 11a) at 490 nm was monitored upon immersion and plotted after converting into the percentage of a DOX quantity based on the initial absorption difference (red line in Fig. 11d). DOX-containing PNIPAM gel without SWNTs was also prepared and monitored as a control sample (blue line in Fig. 11d). Large drops of the DOX quantities were observed after dipping, which corresponds to the removal of unbound DOX. After 24-h dipping, only 13.9% of the DOX remained in the PNIPAM gel, while 35.2% of the DOX remained for the SWNT/PNIPAM gel. The presence of bound DOX in PNIPAM suggested the fact that DOX was also bound on PNIPAM gel network. The large difference between two gels by 21.3% clearly indicated that the SWNTs act as a drug reservoir in the SWNT/PNIPAM gel to hold DOX through the interaction between the DOX and SWNT surfaces.

It has been reported that the interaction of the DOX and SWNT surface were weakened in the acidic aqueous solution (pH~5) due to the protonation of the amine group on the DOX.(Liu, et al., 2007) Indeed, successive immersion of the DOX-containing gels in an acidic (pH~5) aqueous solution leads to a DOX releasing from the SWNT/PNIPAM gel, and the quantity were reached almost identical to that in the PNIPAM gel under at the same condition (Fig. 11d). Therefore, the difference of DOX quantity between in the SWNT/PNIPAM and PNIPAM gels at pH~9 was confirmed as an amount of the DOX molecules on the SWNT surface and the quantity is calculated to be 2.7×10^{16} molecules. Such a high DOX loading would be due to the strong DOX affinity on large exposed SWNT surface.

3.4 Light-driven releasing of DOX from SWNT gels

Light is an attractive stimulus source from the viewpoints of its remote-controllability, quick responsibility, system simplicity, etc. We have reported that the NIR irradiation of the SWNT/PNIAPM gel induces a rapid volume phase transition of the gel due to an effective photo-thermal conversion of the SWNTs.(Fujigaya, et al., 2008) In this experiment, NIR irradiation of the DOX-containing SWNT/PNIPAM gel at pH~9 was carried out. The heat generation through the photothermal conversion of SWNTs caused by the NIR laser irradiation (1064 nm, spot size ~100 μm) rose the gel temperature to 35 °C (red line in Fig. 13b) and induced a volume phase transition of the gel observed under optical microscope (data not shown) similar to the previously reported result.(Fujigaya, et al., 2008) UV-vis absorption spectrum at the part of irradiated area (~10 μm) was measured by means of multi channel detector and characteristic S_{22} band from 600 to 800 nm together with DOX peak at around 490 nm were clearly observed (red line in Fig. 13a). However, almost no spectral change was observed after the NIR irradiation (blue line in Fig. 13a). This implies that the heat generation from the SWNTs did not result in releasing of the DOX from the gel. It is assumed that the quick shrinking of the gel (~2s) prevents the DOX release from the gel. Ineffective photothermal heating of the SWNTs (red line in Fig. 13b) owing to the light scattering of the shrunken gel might also disturb DOX release from the SWNTs.

In order to avoid shrinking of the gel, PDMAAM that exhibits no phase transition up to 90 °C was then incorporated as a component of a copolymer gel at the ratio of NIPAM:DMAAM=1:4. A copolymer gel containing the SWNTs showed no volume phase transition up to 90 °C (data not shown). Similar DOX loading (~ 40%) was successfully

obtained for the copolymer gel after incubation in a DOX solution followed by incubation in alkaline water. We carried out NIR irradiation of the SWNT/PNIPAM/PDMAAM gel. The DOX desorption from the SWNT surfaces was monitored (Fig. 13c) and plotted in Fig. 13d as a function of the irradiation time. An abrupt decrease in the absorbance of the DOX indicates the DOX releasing upon the NIR irradiation. The absence of gel shrinking

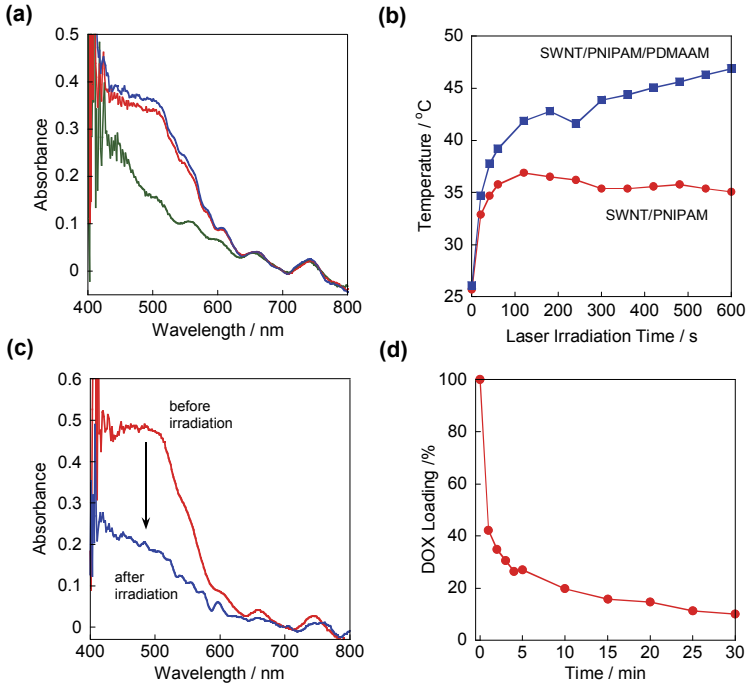

Fig. 13. DOX releasing upon NIR irradiation, (a) The absorption spectra of the SWNT/PNIPAM gel containing DOX molecules before (red line) and after (blue line) irradiation by an NIR laser light for 30 min (CW, 1064 nm, 160 mW). The gel was immersed in a NaOH solution during the laser irradiation. The absorption spectrum of the SWNT/PNIPAM gel not containing DOX is also shown by the green line. All spectra are normalized at 700 nm. Low S/N ratios of the spectra are due to the limitation of the observed area (~10 μm). (b) Temperatures of the gel surfaces of the SWNT/PNIPAM (red line) and SWNT/PNIPAM(1)/PDMAAM(4) (blue line) gels upon irradiation by an NIR laser light. The surface temperatures of the gels were monitored by an infrared thermography, and the temperatures of the gel surfaces are plotted as a function of the laser irradiation time. (c) Absorption spectra of a DOX-embedded SWNT/PNIPAM gel before (red line) and after (blue line) NIR (CW, 1064 nm, 120 mW) irradiation for 30 min in a NaOH solution. (d) Percentage of DOX loading in the SWNT/PNIPAM gel plotted as a function of the NIR irradiation time. Absorbance at 490 nm subtracted by the absorbance of an SWNT/PNIPAM (not containing DOX) was converted into a percentage based on the initial value. The spectra were measured using a multi-channel analyzer (exposure time: 20 ms, accumulation: 20 times).

(confirmed under optical microscope observation) and the smooth photothermal heating (blue line in Fig. 13b) leads to a successful DOX release from the gel as shown in Fig. 13c. It was revealed that 89.9% of the DOX molecules on the SWNT surfaces were released under a 30-min irradiation (Fig. 13d), which show a remarkable contrast with the DOX releasing in hot water (80 ^{o}C), in which ~70% of the DOX released after a 24-h heating.(Liu, et al., 2007) It is now evident that the NIR irradiation accelerates the releasing of the adsorbed DOX molecule compared to the conventional heating using a mechanical heater. Such an efficient drug holding and controlled releasing of the drug would be useful for an advanced drug delivery system (DDS).

4. Conclusion

In conclusion, we demonstrated the first NIR laser light-driven phase transition (volume change) of the SWNTs/PNIPAM composite gel, in which the SWNTs acted as a "molecular heater" to raise the local temperature of the gel via the photothermal conversion of the SWNTs. One notable advantage that we would like to emphasize in this system is the remarkable durability for ON/OFF switching actuated by the NIR laser irradiation for more than 1200 cycles.

In addition, SWNTs have been successfully isolated in hydrogel frameworks formed from PNIPAM and PNIPAM-PDMAAM due to the formation of semi-IPN structures, in which the CH-π of the gel side chains plays an important role in stabilizing the semi-IPN structures. The obtained gels were used as a molecular reservoir for molecules of biological importance, such as DOX, a cancer drug. Furthermore, we demonstrated pH- as well as photo-responsive releasing of the adsorbed molecule from the gels. Since the NIR light laser used in the photo-responsive releasing can penetrate the human body, the potential application for the use of a gel containing isolated SWNTs as an NIR-driven controllable releasing drug reservoir is expected.

5. Acknowledgment

This work was supported by a Grant-in-Aid for Scientific Research (B) (No.21350110) (for NN) and the Global COE Program "Science for Future Molecular Systems" from the Ministry of Education, Culture, Sports, Science and Technology, Japan.

6. References

Bohidar, H.B., Dubin, P. & Osada, Y. (2003) *Polymer Gels: Fundamentals and Applications.*, ACS, Washington, D.C. .

Canal, T. & A. Peppas, N. (1989). Correlation between mesh size and equilibrium degree of swelling of polymeric networks. *Journal of Biomedical Materials Research,* 23, pp. 1183, 1097-4636.

Chen, S., *et al.* (2008). Light-Controlled Single-Walled Carbon Nanotube Dispersions in Aqueous Solution. *Langmuir,* 24, pp. 9233, 0743-7463.

Ericson, L.M. & Pehrsson, P.E. (2005). Aggregation Effects on the Raman Spectroscopy of Dielectrophoretically Deposited Single-Walled Carbon Nanotubes. *Journal of Physical Chemistry B,* 109, pp. 20276, 1520-6106.

Fujigaya, T., Fukumaru, T. & Nakashima, N. (2009). Evaluation of dispersion state and thermal conductivity measurement of carbon nanotubes/UV-curable resin nanocomposites. *Synthetic Metals,* 159, pp. 827, 0379-6779.

Fujigaya, T., Morimoto, T. & Nakashima, N. (2011). Isolated single-walled carbon nanotubes in a gel as a molecular reservoir and its application to controlled drug release triggered by near-IR laser irradiation. *Soft Matter,* 7, pp. 2647, 1744-683X.

Fujigaya, T., Morimoto, T., Niidome, Y. & Nakashima, N. (2008). NIR Laser-Driven Reversible Volume Phase Transition of Single-Walled Carbon Nanotube/Poly(N-isopropylacrylamide) Composite Gels. *Advanced Materials (Weinheim, Germany),* 20, pp. 3610, 1521-4095.

Gong, J.P., Katsuyama, Y., Kurokawa, T. & Osada, Y. (2003). Double-network hydrogels with extremely high mechanical strength. *Advanced Materials (Weinheim, Germany),* 15, pp. 1155, 0935-9648.

Gorelikov, I., Field, L.M. & Kumacheva, E. (2004). Hybrid Microgels Photoresponsive in the Near-Infrared Spectral Range. *Journal of the American Chemical Society,* 126, pp. 15938, 0002-7863.

Heller, D.A., Barone, P.W., Swanson, J.P., Mayrhofer, R.M. & Strano, M.S. (2004). Using Raman Spectroscopy to Elucidate the Aggregation State of Single-Walled Carbon Nanotubes. *Journal of Physical Chemistry B,* 108, pp. 6905, 1520-6106.

Hirotsu, S., Hirokawa, Y. & Tanaka, T. (1987). Volume-phase transitions of ionized N-isopropylacrylamide gels. *Journal of Chemical Physics,* 87, pp. 1392, 0021-9606.

Ikeda, A., Totsuka, Y., Nobusawa, K. & Kikuchi, J.-i. (2009). Reversible solubilisation and precipitation of carbon nanotubes by temperature and pH control in water. *Journal of Materials Chemistry,* 19, pp. 5785, 0959-9428.

Ishibashi, A. & Nakashima, N. (2006). Individual dissolution of single-walled carbon nanotubes in aqueous solutions of steroid or sugar compounds and their Raman and near-IR spectral properties. *Chemistry--A European Journal,* 12, pp. 7595, 0947-6539.

Ishidao, T., *et al.* (1997). Mesh Sizes of Poly(N-Isopropylacrylamide) Gel in Aqueous Solution. *Journal of Chemical Engineering of Japan,* 30, pp. 162, 0021-9592.

Ishikawa, M., Misawa, H., Kitamura, N., Fujisawa, R. & Masuhara, H. (1996). Infrared laser-induced photo-thermal phase transition of an aqueous poly(N-isopropylacrylamide) solution in the micrometer dimension. *Bulletin of the Chemical Society of Japan,* 69, pp. 59, 0009-2673.

Ishikawa, M., Misawa, H., Kitamura, N. & Masuhara, H. (1993). Poly(N-isopropylacrylamide) microparticle formation in water by infrared laser-induced photo-thermal phase transition. *Chemistry Letters*, pp. 481, 0366-7022.

Islam, M.F., *et al.* (2004). Nematic Nanotube Gels. *Physical Review Letters,* 92, pp. 088303/1, 0031-9007.

Jeng, E.S., Moll, A.E., Roy, A.C., Gastala, J.B. & Strano, M.S. (2006). Detection of DNA Hybridization Using the Near-Infrared Band-Gap Fluorescence of Single-Walled Carbon Nanotubes. *Nano Letters,* 6, pp. 371, 1530-6992.

Juodkazis, S., *et al.* (2000). Reversible phase transitions in polymer gels induced by radiation forces. *Nature (London),* 408, pp. 178, 0028-0836.

Kam, N.W.S., O'Connell, M., Wisdom, J.A. & Dai, H. (2005). Carbon nanotubes as multifunctional biological transporters and near-infrared agents for selective cancer cell destruction. *Proceedings of the National Academy of Sciences of the United States of America,* 102, pp. 11600, 0027-8424.

Katayama, S., Hirokawa, Y. & Tanaka, T. (1984). Reentrant phase transition in acrylamide-derivative copolymer gels. *Macromolecules,* 17, pp. 2641, 0024-9297.

Kokufuta, E., Zhang, Y.Q., Tanaka, T. & Mamada, A. (1993). Effects of surfactants on the phase transition of poly(N-isopropylacrylamide) gel. *Macromolecules,* 26, pp. 1053, 0024-9297.

Kumatani, A. & Warburton, P.A. (2008). Characterization of the disaggregation state of single-walled carbon nanotube bundles by dielectrophoresis and Raman spectroscopy. *Applied Physics Letters,* 92, pp. 243123/1, 0003-6951.

Liu, Z., Sun, X., Nakayama-Ratchford, N. & Dai, H. (2007). Supramolecular Chemistry on Water-Soluble Carbon Nanotubes for Drug Loading and Delivery. *ACS Nano,* 1, pp. 50, 1936-0851.

Luo, Z., Doorn, S.K., Li, R. & Papadimitrakopoulos, F. (2006). Effects of aggregation and electron-phonon interactions on RBM spectral reconstruction of single walled carbon nanotubes. *Physica Status Solidi B: Basic Solid State Physics,* 243, pp. 3155, 0370-1972.

Mamada, A., Tanaka, T., Kungwatchakun, D. & Irie, M. (1990). Photoinduced phase transition of gels. *Macromolecules,* 23, pp. 1517, 0024-9297.

McDonald, T.J., Engtrakul, C., Jones, M., Rumbles, G. & Heben, M.J. (2006). Kinetics of PL Quenching during Single-Walled Carbon Nanotube Rebundling and Diameter-Dependent Surfactant Interactions. *Journal of Physical Chemistry B,* 110, pp. 25339, 1520-6106.

Moore, V.C., *et al.* (2003). Individually Suspended Single-Walled Carbon Nanotubes in Various Surfactants. *Nano Letters,* 3, pp. 1379, 1530-6992.

Nakashima, N. & Fujigaya, T. (2007). Fundamentals and applications of soluble carbon nanotubes. *Chemistry Letters,* 36, pp. 692, 0366-7022.

Nakashima, N., Okuzono, S., Tomonari, Y. & Murakami, H. (2004). Solubilization of carbon nanotubes with a pyrene-carrying polymer in water. *Transactions of the Materials Research Society of Japan,* 29, pp. 525, 1851665749.

Narimatsu, K., Niidome, Y. & Nakashima, N. (2006). Pulsed-laser induced flocculation of carbon nanotubes solubilized by an anthracene-carrying polymer. *Chemical Physics Letters,* 429, pp. 488, 0009-2614.

Nayak, S. & Lyon, L.A. (2004). Photoinduced Phase Transitions in Poly(N-isopropylacrylamide) Microgels. *Chemistry of Materials,* 16, pp. 2623, 0897-4756.

Nobusawa, K., *et al.* (2008). Reversible Solubilization and Precipitation of Carbon Nanotubes through Oxidation-Reduction Reactions of a Solubilizing Agent13. *Angewandte Chemie International Edition,* 47, pp. 4577, 1521-3773.

O'Connell, M.J., *et al.* (2002). Band gap fluorescence from individual single-walled carbon nanotubes. *Science,* 297, pp. 593, 0036-8075.

O'Connell, M.J., Sivaram, S. & Doorn, S.K. (2004). Near-infrared resonance Raman excitation profile studies of single-walled carbon nanotube intertube interactions: A direct comparison of bundled and individually dispersed HiPco nanotubes. *Physical Review B: Condensed Matter and Materials Physics,* 69, pp. 235415/1, 0163-1829.

Schild, H.G. (1992). Poly(N-isopropylacrylamide): experiment, theory and application. *Progress in Polymer Science,* 17, pp. 163, 0079-6700.

Schild, H.G., Muthukumar, M. & Tirrell, D.A. (1991). Cononsolvency in mixed aqueous solutions of poly(N-isopropylacrylamide). *Macromolecules,* 24, pp. 948, 0024-9297.

Sershen, S.R., *et al.* (2005). Independent optical control of microfluidic valves formed from optomechanically responsive nanocomposite hydrogels. *Advanced Materials (Weinheim, Germany),* 17, pp. 1366, 0935-9648.

Sershen, S.R., Westcott, S.L., Halas, N.J. & West, J.L. (2000). Temperature-sensitive polymer-nanoshell composites for photothermally modulated drug delivery. *Journal of Biomedical Materials Research,* 51, pp. 293, 0021-9304.

Sershen, S.R., Westcott, S.L., West, J.L. & Halas, N.J. (2001). An opto-mechanical nanoshell-polymer composite. *Applied Physics B: Lasers and Optics,* 73, pp. 379, 0946-2171.

Shiotani, A., Mori, T., Niidome, T., Niidome, Y. & Katayama, Y. (2007). Stable Incorporation of Gold Nanorods into N-Isopropylacrylamide Hydrogels and Their Rapid Shrinkage Induced by Near-Infrared Laser Irradiation. *Langmuir,* 23, pp. 4012, 0743-7463.

Strano, M.S., *et al.* (2003). The role of surfactant adsorption during ultrasonication in the dispersion of single-walled carbon nanotubes. *Journal of Nanoscience and Nanotechnology,* 3, pp. 81, 1550-7041

Suzuki, A. & Tanaka, T. (1990). Phase transition in polymer gels induced by visible light. *Nature,* 346, pp. 345, 0028-0836.

Suzuki, A. & Tanaka, T. (1990). Phase transition in polymer gels induced by visible light. *Nature (London, United Kingdom),* 346, pp. 345, 0028-0836.

Tanaka, T. (1978). Collapse of gels and the critical endpoint. *Physical Review Letters,* 40, pp. 820, 0031-9007.

Tanaka, T., *et al.* (1980). Phase transitions in ionic gels. *Physical Review Letters,* 45, pp. 1636, 0031-9007.

Tanaka, T., Nishio, I., Sun, S.T. & Ueno-Nishio, S. (1982). Collapse of gels in an electric field. *Science (Washington, DC, United States),* 218, pp. 467, 0036-8075.

Weissleder, R. (2001). A clearer vision for in vivo imaging. *Nature biotechnology,* 19, pp. 316, 1087-0156 FIELD Electronic Internat.Standard Doc. Number:.

Wick, P., *et al.* (2007). The degree and kind of agglomeration affect carbon nanotube cytotoxicity. *Toxicology Letters,* 168, pp. 121, 0378-4274.